frontiers | Research Topics

Environmental chemistry of mercury: Sources, pathways, transformations and impact

Edited by
Robert Peter Mason, David Amouroux, JiuBin Chen and Ashu Dastoor

Published in
Frontiers in Environmental Chemistry

ISSN 1664-8714
ISBN 978-2-8325-4368-9
DOI 10.3389/978-2-8325-4368-9

About Frontiers

Frontiers is more than just an open access publisher of scholarly articles: it is a pioneering approach to the world of academia, radically improving the way scholarly research is managed. The grand vision of Frontiers is a world where all people have an equal opportunity to seek, share and generate knowledge. Frontiers provides immediate and permanent online open access to all its publications, but this alone is not enough to realize our grand goals.

Frontiers journal series

The Frontiers journal series is a multi-tier and interdisciplinary set of open-access, online journals, promising a paradigm shift from the current review, selection and dissemination processes in academic publishing. All Frontiers journals are driven by researchers for researchers; therefore, they constitute a service to the scholarly community. At the same time, the *Frontiers journal series* operates on a revolutionary invention, the tiered publishing system, initially addressing specific communities of scholars, and gradually climbing up to broader public understanding, thus serving the interests of the lay society, too.

Dedication to quality

Each Frontiers article is a landmark of the highest quality, thanks to genuinely collaborative interactions between authors and review editors, who include some of the world's best academicians. Research must be certified by peers before entering a stream of knowledge that may eventually reach the public - and shape society; therefore, Frontiers only applies the most rigorous and unbiased reviews. Frontiers revolutionizes research publishing by freely delivering the most outstanding research, evaluated with no bias from both the academic and social point of view. By applying the most advanced information technologies, Frontiers is catapulting scholarly publishing into a new generation.

What are Frontiers Research Topics?

Frontiers Research Topics are very popular trademarks of the *Frontiers journals series*: they are collections of at least ten articles, all centered on a particular subject. With their unique mix of varied contributions from Original Research to Review Articles, Frontiers Research Topics unify the most influential researchers, the latest key findings and historical advances in a hot research area.

Find out more on how to host your own Frontiers Research Topic or contribute to one as an author by contacting the Frontiers editorial office: frontiersin.org/about/contact

Environmental chemistry of mercury: Sources, pathways, transformations and impact

Topic editors

Robert Peter Mason — University of Connecticut, United States
David Amouroux — UMR5254 Institut des Sciences Analytiques et de Physico-Chimie pour l'Environnement et les Matériaux (IPREM), France
JiuBin Chen — Institute of Geochemistry, Chinese Academy of Sciences
Ashu Dastoor — Environment and Climate Change Canada (ECCC), Canada

Citation

Mason, R. P., Amouroux, D., Chen, J., Dastoor, A., eds. (2024). *Environmental chemistry of mercury: Sources, pathways, transformations and impact*. Lausanne: Frontiers Media SA. doi: 10.3389/978-2-8325-4368-9

Table of contents

frontiers | Frontiers in Environmental Chemistry

TYPE Editorial
PUBLISHED 15 January 2024
DOI 10.3389/fenvc.2023.1358345

OPEN ACCESS

EDITED BY
Mika Erik Tapio Sillanpää,
University of Johannesburg, South Africa

REVIEWED BY
Juan Carlos Nóvoa-Muñoz,
University of Vigo, Spain

*CORRESPONDENCE
Robert Peter Mason,
robert.mason@uconn.edu

RECEIVED 19 December 2023
ACCEPTED 31 December 2023
PUBLISHED 15 January 2024

CITATION
Mason RP, Amouroux D, Dastoor A and Chen J (2024), Editorial: Environmental chemistry of mercury: sources, pathways, transformations and impact.
Front. Environ. Chem. 4:1358345.
doi: 10.3389/fenvc.2023.1358345

Editorial: Environmental chemistry of mercury: sources, pathways, transformations and impact

Robert Peter Mason[1]*, David Amouroux[2], Ashu Dastoor[3] and Juibin Chen[4]

[1]Department of Marine Sciences, College of Liberal Arts and Sciences, University of Connecticut, Groton, CT, United States, [2]IPREM, CNRS - Université de Pau et des Pays de l'Adour, Pau, France, [3]Environment and Climate Change Canada (ECCC), Burlington, ON, Canada, [4]Institute of Surface-Earth System Science, Tianjin Normal University, Tianjin, China

KEYWORDS

mercury, methylmercury, stable isotopes, atmosphere, ocean, freshwater, speciation (chemical), methylation

Editorial on the Research Topic
Environmental chemistry of mercury: sources, pathways, transformations and impact

In terms of inorganic pollutants that are globally distributed, mercury (Hg) is a global pollutant of major concern because of its ability to be transported globally via the atmosphere, and through the ocean and via river watersheds. It has been released into the environment from anthropogenic sources, from its intentional use, such as in artisanal and small-scale goldmining (ASGM), and because it is a trace element in coal, ores and other primary resources extracted and used by humans. Anthropogenic emissions globally far exceed the natural inputs of Hg to the biogeosphere. While it is primarily released as inorganic Hg, elevated levels of Hg as methylmercury (MeHg) in seafood and other foods is a health concern for humans and wildlife. Mercury is taken up into vegetation and soils, and into ocean surface waters primarily from the atmosphere, and can be released back to the atmosphere due to natural processes, including those that are anthropogenically enhanced, such as biomass burning and deforestation.

The exchange of Hg between the reservoirs of the biogeosphere, and the aquatic and atmospheric chemistry of Hg are complex, as it can exist in many different inorganic and organic forms, including elemental Hg, ionic Hg, and mono- and dimethylmercury, in the dissolved phase, while also binding to organic ligands in water or attached to particles. In the atmosphere, Hg is found mainly in the gaseous phase. The conversion of inorganic Hg to the more toxic methylated Hg forms is primarily mediated by bacteria and the factors influencing the net conversion (methylation) to methylated Hg are not yet fully understood. While most studies examine the environment chemistry of Hg using measurements of concentrations and kinetic and other chemical characterizations of the fate, transport and transformation of Hg, there is a growing number of studies that use the environmental fractionation of Hg stable isotopes, and differences in isotopic composition in different source materials to examine the origin and fate of Hg from industrial pollution.

Given the complexities of the environmental chemistry of Hg, and the lack of knowledge, and the advancement of techniques for quantifying Hg species in the biogeosphere, this Research Topic was defined to invite scientific contributions that examined the complex environmental chemistry of Hg and was designed to enhance the publication of new and exciting results. The paper in the Research Topic included those published prior to, and after, the 15th International Conference on Mercury as a Global Pollutant (ICMGP) that was held in July 2022 remotely because of the pandemic.

The papers published in this Research Topic examined the following aspects of Hg environmental chemistry by:

1. Examining the chemical speciation of Hg in air, and advances in speciation analysis of mercury (Gustin et al.).
2. Focusing on the examination of the methylation/demethylation pathways, Hg redox reactions, and interactions with of Hg with particles Lamborg et al. (dark reduction of Hg); Coulibaly et al. (Hg reduction); Cui et al. (Hg partitioning in the ocean); Despins et al. (Arctic Hg methylation).
3. Using stable mercury isotope to examine biogeochemical processes, transformations and transport of mercury Eckley et al.; Schwab et al. (both examining historical mercury contamination).
4. Examining the factors influencing mercury deposition over paleo timescales Nalbant et al. (tropical lake).
5. Through regional studies of mercury biogeochemical cycling, fate and transport Graham et al. (river); Fostier et al. (Amazon rain forest).

The papers in this Research Topic cover all aspects of Hg fate and transport and transformation in the biogeosphere with studies focused on the atmosphere, oceans, terrestrial landscapes and freshwater ecosystems, as well as examining the impacts of historical Hg contamination and the controlling factors on its fate and effects. These studies provide an insight into the important factors influencing the fate, transport and bioavailability of Hg in the environment, and demonstrate that while major advances in understanding have occurred, there is still more studies needed to further understand the factors controlling the formation and bioaccumulation of methylmercury and its impact on humans.

Author contributions

RM: Writing–original draft, Writing–review and editing. DA: Writing–original draft, Writing–review and editing. AD: Writing–original draft, Writing–review and editing. JC: Writing–original draft, Writing–review and editing.

Conflict of interest

The authors declare that the research was conducted in the absence of any commercial or financial relationships that could be construed as a potential conflict of interest.

The author(s) declared that they were an editorial board member of Frontiers, at the time of submission. This had no impact on the peer review process and the final decision.

Publisher's note

frontiers in Environmental Chemistry

ORIGINAL RESEARCH
published: 27 April 2021
doi: 10.3389/fenvc.2021.659085

Dark Reduction Drives Evasion of Mercury From the Ocean

Carl H. Lamborg[1], Colleen M. Hansel[2], Katlin L. Bowman[1], Bettina M. Voelker[3], Ryan M. Marsico[3], Veronique E. Oldham[2,4], Gretchen J. Swarr[2], Tong Zhang[2,5] and Priya M. Ganguli[2,6]*

[1] Department of Ocean Sciences, University of California, Santa Cruz, Santa Cruz, CA, United States, [2] Department of Marine Chemistry and Geochemistry, Woods Hole Oceanographic Institution, Woods Hole, MA, United States, [3] Department of Chemistry, Colorado School of Mines, Golden, CO, United States, [4] Graduate School of Oceanography, University of Rhode Island, Narragansett, RI, United States, [5] College of Environmental Science and Engineering, Nankai University, Tianjin, China, [6] Department of Geological Sciences, California State University, Northridge, CA, United States

Much of the surface water of the ocean is supersaturated in elemental mercury (Hg^0) with respect to the atmosphere, leading to sea-to-air transfer or evasion. This flux is large, and nearly balances inputs from the atmosphere, rivers and hydrothermal vents. While the photochemical production of Hg^0 from ionic and methylated mercury is reasonably well-studied and can produce Hg^0 at fairly high rates, there is also abundant Hg^0 in aphotic waters, indicating that other important formation pathways exist. Here, we present results of gross reduction rate measurements, depth profiles and diel cycling studies to argue that dark reduction of Hg^{2+} is also capable of sustaining Hg^0 concentrations in the open ocean mixed layer. In locations where vertical mixing is deep enough relative to the vertical penetration of UV-B and photosynthetically active radiation (the principal forms of light involved in abiotic and biotic Hg photoreduction), dark reduction will contribute the majority of Hg^0 produced in the surface ocean mixed layer. Our measurements and modeling suggest that these conditions are met nearly everywhere except at high latitudes during local summer. Furthermore, the residence time of Hg^0 in the mixed layer with respect to evasion is longer than that of redox, a situation that allows dark reduction-oxidation to effectively set the steady-state ratio of Hg^0 to Hg^{2+} in surface waters. The nature of these dark redox reactions in the ocean was not resolved by this study, but our experiments suggest a likely mechanism or mechanisms involving enzymes and/or important redox agents such as reactive oxygen species and manganese (III).

Keywords: mercury, evasion, elemental, dark, ocean, reactive oxygen species, manganese, global model

OPEN ACCESS

Edited by:
Martin Jiskra,
University of Basel, Switzerland

Reviewed by:
Jeroen E. Sonke,
UMR5563 Géosciences Environnement Toulouse (GET), France
Joachim Kuss,
Leibniz Institute for Baltic Sea Research (LG), Germany

****Correspondence:***
Carl H. Lamborg
clamborg@ucsc.edu

Specialty section:
This article was submitted to Inorganic Pollutants, a section of the journal Frontiers in Environmental Chemistry

Received: *27 January 2021*
Accepted: *23 March 2021*
Published: *27 April 2021*

Citation:
Lamborg CH, Hansel CM, Bowman KL, Voelker BM, Marsico RM, Oldham VE, Swarr GJ, Zhang T and Ganguli PM (2021) Dark Reduction Drives Evasion of Mercury From the Ocean. Front. Environ. Chem. 2:659085. doi: 10.3389/fenvc.2021.659085

INTRODUCTION

Mercury (Hg) is a toxic trace metal that is uniquely volatile. Current estimates place the rate of gross evasion of mercury (Hg) from the ocean to the atmosphere at about 17 Mmole y^{-1}, which is close to the sum of inputs to the ocean of 21 Mmole y^{-1} (e.g., Outridge et al., 2018). While these fluxes are nearly balanced in mass, they are very different in chemistry, with most of the input to the ocean from the atmosphere as Hg(II) and the Hg leaving the ocean to the air is mostly as Hg^0. Thus, a substantial amount of Hg(II) reduction must take place in the ocean to support the observed fluxes. We can put the sea-air flux in context by noting that the Outridge et al. estimate for the amount of Hg in the surface water is about 13 Mmole. This value, when combined with the flux information,

suggests a residence time of Hg in the surface ocean with respect to evasion of about 0.76 years and an apparent specific net reduction rate of 0.36 % day^{-1}. This apparent specific reduction rate is slower than that measured for gross production of Hg^0 from Hg(II) (e.g., Rolfhus, 1998; Costa and Liss, 1999; Whalin et al., 2007; Fantozzi et al., 2009; Qureshi et al., 2010; Soerensen et al., 2014; Kuss et al., 2015; Lee and Fisher, 2019). If gross reduction proceeds faster than the loss of Hg^0 from the surface ocean, then there must be substantial re-oxidation of Hg^0 prior to evasion (e.g., Soerensen et al., 2010). This sets up the possibility that the concentration of Hg^0 in the surface, one of the primary driving parameters for Hg evasion, is at or close to a steady-state set mostly by the redox recycling of Hg, and not the rate of evasion or net production.

To gain a greater understanding of the evasion of Hg from the ocean, much research has been conducted to understand the ways by which Hg(II) is reduced to Hg^0 in seawater. Light-dependent mechanisms are fast (specific reduction with respect to gross photoreduction under ambient light conditions: 0.39 to 1.53 h^{-1}) and reduction mechanisms that appear not to be light-dependent have been found to be many times slower (specific reduction: <0.1 to 0.23 h^{-1}; Rolfhus, 1998; Costa and Liss, 1999; Whalin et al., 2007; Fantozzi et al., 2009; Qureshi et al., 2010). However, when integrated over a water column, as done by Rolfhus and Fitzgerald (2004) and alluded to by Fantozzi et al. (2009) and Kuss et al. (2015), the importance of dark reduction mechanisms increases, perhaps even to dominance because the light-dependent reactions slow down as light diminishes.

One recent study in seawater deserves special attention, that of Kuss et al. (2015) in the Baltic Sea. Using shipboard incubations and a variety of amendments (e.g., filter-sterilizing, light-shading), they sought to apportion the Hg^0 produced within Baltic surface water between light and dark mechanisms. Their results suggested that about 59% was produced from light reactions (a combination of direct abiotic and indirect biotic) and about 41% from dark reactions (with some evidence that this process was at least partially biological). Kuss et al. noted, as did Rolfhus and Fitzgerald, that integrating to depths below the surface would likely boost the importance of dark reactions but did not calculate this.

The mechanism or mechanisms of Hg^{2+} reduction to Hg^0 in the dark are unclear. In the light, charge-transfer reactions seem to be most important as photoreduction of Hg^{2+} is most effective when Hg is complexed with photoactive dissolved organic matter (O'Driscoll et al., 2006). However, photoreduction can be enhanced through the production of reactive transients such as Fe(II) which in turn reduce Hg^{2+} (Zhang and Lindberg, 2001). Thus, it is reasonable that any redox intermediates of sufficient strength produced by non-photochemical means should also be able to reduce Hg^{2+}. Candidate species in the dark ocean most prominently include the reactive oxygen species (ROS) superoxide and hydrogen peroxide which have been shown to be actively produced by common marine heterotrophs (Diaz et al., 2013; Sutherland et al., 2019).

How relevant are the implications of these studies to the global ocean? The Baltic Sea is a low salinity and relatively eutrophicated marine environment, and the Long Island Sound where Rolfhus and Fitzgerald (2004) conducted their studies is an impacted marginal embayment and most of Whalin et al. (2007) work was conducted in estuarine environments. Thus, it remains uncertain as to how important dark reduction is in the open ocean. Here we describe experiments designed to provide additional constraint on the rates and possible mechanism(s) of dark reduction under such conditions and then place those rates in a global context through relatively simple modeling.

METHODS

Sample Collection

Samples for profiles, diel studies and production incubations were collected during the TORCH 2 cruise from September 20th to 29th, 2017 on board the *R/V Endeavor* (EN604; C. Hansel, Chief Scientist). Trace metal-clean water collection was accomplished using cleaned 8-L X-Niskin bottles deployed from a 12-place Seabird Electronics rosette (SBE 19plus/SBE 32, the trace-metal rosette or TMR). The rosette also carried a CTD-driven Auto-firing Module (AFM). The AFM was programmed to close Niskin bottles during up-casts at depths selected by examining water column profiles of temperature, salinity, photosynthetically active radiation (PAR) and chlorophyll fluorescence that were collected with the ship's non-clean CTD system immediately before the TMR was deployed. Samples for vertical profiles were retrieved at 4–6 depths (with Niskins doubled- or tripled-up to provide the necessary volume for various needs) that also included depths that would represent those for further incubation studies.

The stations occupied during TORCH 2 cruise are summarized in **Table 1** and shown in **Figure 1**. All except Station 4 can be characterized as continental shelf environments, while Station 4 is an off-shelf, more open ocean environment. The stations were selected to target a range of heterotrophic microbe activity, as reflected by a range of water temperature and primary production (**Figures S1**, **S2**).

Mercury Speciation

We measured the amount of dissolved total Hg and Hg^0 according to protocols described elsewhere (Lamborg et al., 2012 and references therein). In brief, duplicate ∼200 mL samples for dissolved total Hg were withdrawn from X-Niskins by peristaltic pump in a "clean bubble" by passing the fluid through Sterivex

TABLE 1 | Stations occupied during the TORCH 2 Cruise.

Station	Latitude/Longitude	Photic Depth[a] (m)	Approx. Water Depth (m)
1	40.8722/−71.69217	30.6	57
2	39.18884/−73.56232	30.0	44
3	37.77692/−74.56461	28.0	57
4	39.48669/−70.52424	84.8	2,482
5	41.18026/−67.92692	22.8	50
6	40.75594/−72.19386	32.4	43

[a] *defined as depth of 1% of surface irradiance.*

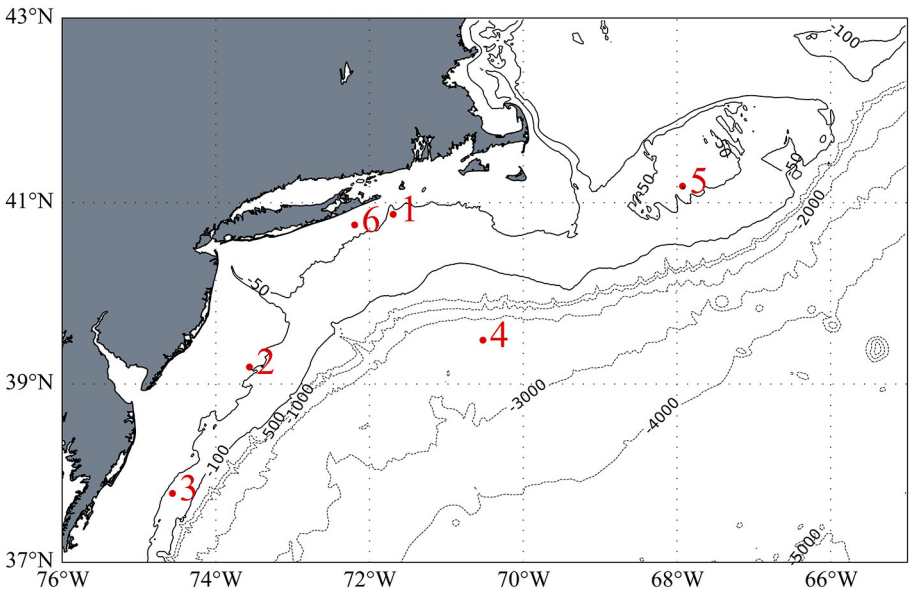

FIGURE 1 | Station locations for the TORCH 2 cruise. Isobaths on the continental shelf are shown in solid lines and are in 50-meter intervals. Those off the shelf are shown in dotted lines and denote 1,000-meter intervals. Bathymetric data from ETOPO1.

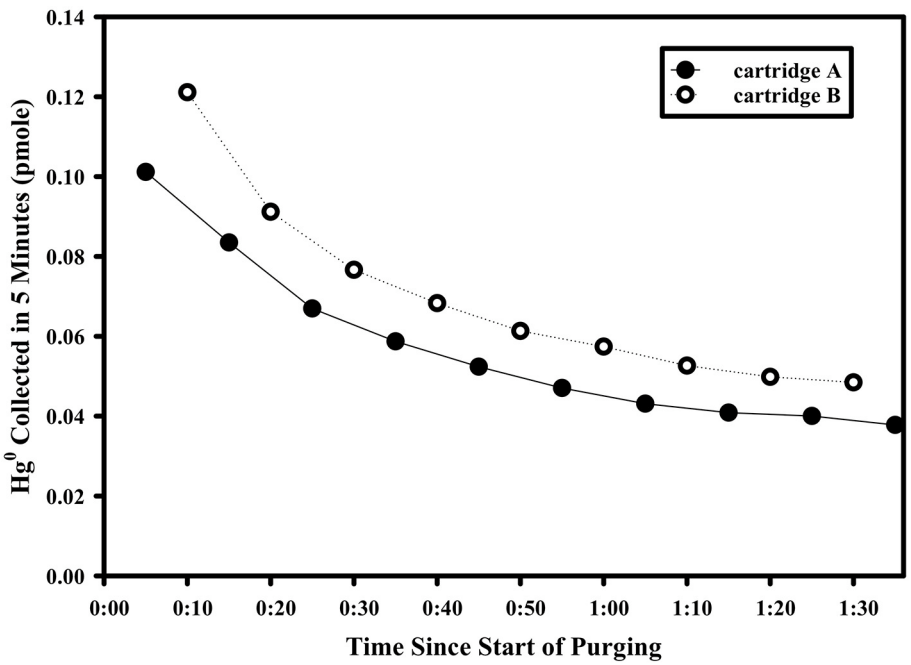

FIGURE 2 | Example time course of the Hg^0 mass purged from an experimental setup used to determine dark gross reduction rates. These data are from Station 6, with water filtered and taken from 30 m depth.

filter capsules with a nominal pore size of 0.2 μm and into 250-mL, acid-washed glass bottles (I-Chem). Similarly, but without filtration, duplicate ~1,800 mL samples for Hg^0 were withdrawn from the X-Niskins by gravity through a length of acid-washed C-Flex tubing positioned to avoid injecting bubbles. Samples for total Hg were then preserved with BrCl, while the samples for Hg^0 were immediately purged with high-purity N_2, with the gas effluent passing through a gold-coated sand trap to amalgamate Hg^0. Following purging, the volume of the sample purged was measured by graduated cylinder to the nearest 5 mL. The amount of Hg^0 so collected was determined by heating the trapping column onto the analytical trap of a Tekran 2600 Cold-vapor

Atomic Fluorescence Spectrometer (CVAFS), calibrated using a saturated vapor standard held at 15 °C (Tekran). Total Hg samples were also measured by purge-and-trap CVAFS after the excess BrCl was reduced by NH_2OH and the Hg(II) present reduced to Hg^0 by $SnCl_2$. Calibration was also accomplished using the vapor standard and checked with aqueous standards traceable to NIST.

Gross Hg^0 Production Incubations

The aphotic gross rate of Hg^0 production was measured in nominally 5-L sized samples supplemented with an extra ∼50 pmoles of Hg(II). Incubation samples were either filtered to 0.2 μm using Sterivex filters and peristaltic pumps directly out of the X-Niskins bottles or decanted unfiltered and held in acid-washed 10-L carboys. Shortly after filtering/decanting, the samples were spiked with Hg(II) and held in the dark and at room temperature for >18 h to allow the spike to fully complex with ambient ligands (Lamborg et al., 2003). For experiments where chemical amendments were made (see details below), the amendment was added just prior to the start of measurement and mixed with agitation. Before rate measurement, each sample-containing carboy was outfitted with a two-port cap. One port led to a sparging frit inside the carboy which was fed with room air that first passed through an Hg^0-trapping activated charcoal cartridge. The second port, which allowed sampling of the carboy headspace, led to the pumping inlet of a Tekran 2537 automated vapor Hg sampling/analysis unit. Altogether, the system allowed the Tekran 2537 to draw Hg^0-clean room air into the carboy, sparge the contents and take near-continuous (5 min sampling integration) measurements of the evolving gas. The carboy was kept at room temperature throughout the experiment and dark by covering with a black plastic sheet. A typical time course following attachment of the carboy to the analyzer is shown in **Figure 2**. Initially, the concentration of Hg^0 collected was high as a result of a combination of room air Hg^0 in the headspace of the carboy as well as some amount of Hg^0 generated from the Hg(II) spike added at least 18 h prior. The collected Hg^0 dropped rapidly, however, as this standing stock of Hg^0 was removed from headspace and solution, revealing a supported baseline amount of Hg^0 generated in solution. As the standing stock of Hg^0 in the carboy was decreased due to the continuous sparging, there was little opportunity for re-oxidation of produced Hg^0, so that the rate of Hg^0 removal would reach steady state with the rate of gross reduction (they differ by about 2% given an approximate 16 min residence time of supported Hg^0 in the carboy with respect to purging and an approximate 860 min with respect to dark oxidation). Sparging/measurement therefore continued until a stable baseline of 5 measurements, all within 10% of each other, was observed. Following the experiment, the final volume of seawater in the carboy was measured and a subsample taken for total Hg analysis as above. The final specific gross rate of production was calculated by dividing the average mass of Hg^0 collected during a sampling interval (5 min) by the mass of total Hg in the carboy (total Hg concentration multiplied by the final volume), to yield values with per time units. A system blank was also recorded by running an empty carboy for several cycles, and which always yielded Hg^0 concentrations in the effluent gas that were below detection (<0.01 ng Hg^0/m^3 of air).

Incubation Amendments

Away from the surface and a ready source of photons, reactive oxygen species (ROS) and other transient redox species (such as forms of manganese (Mn), iron (Fe), and copper (Cu) as well as biogenic reducing agents) seem the only source of electrons to drive Hg^0/Hg(II) speciation so far from equilibrium. Furthermore, ROS are generated extracellularly by common marine heterotrophs (Diaz et al., 2013) and within dark marine waters (e.g., Rose et al., 2008b; Zhang et al., 2016), making this suite of compounds worthy of study regarding Hg cycling in dark water. To explore the possible role of ROS in Hg(II) reduction, some gross reduction rate incubations were amended with either hydrogen peroxide (H_2O_2) or nicotinamide adenine dinucleotide (NADH). The first, H_2O_2 is a ROS formed either directly or via dismutation of another ROS species, superoxide (e.g., Blough and Zepp, 1995). The second, NADH, is a reducing equivalent carrier in wide use by bacteria and has been shown to stimulate ROS production both in bacterial culture and natural waters (Andeer et al., 2015; Zhang et al., 2016). Since NADH is only an indirect source of ROS and in case a change in Hg(II) reduction were observed following its addition to our incubations, superoxide dismutase (SOD) was also added to some amendments to act as a control. Superoxide dismutase acts to catalyze the destruction of superoxide to H_2O_2 at seawater pH's (e.g., Kieber et al., 2003). For incubations with H_2O_2 amended, 30% H_2O_2 (ACS grade) was diluted to a secondary stock (50 μM) and then added to the seawater samples to boost the concentration to ∼50 or 100 nM. For the superoxide amendments, enough NADH was added to initially raise its concentration to 200 μM through addition of a 5 mM stock solution (MP Biomedicals). For controls with SOD and NADH additions, enough SOD was added to raise the concentration to ∼50 kU/L through the use of a 4 kU/mL stock solution (Sigma).

In addition to ROS amendments, some gross reduction incubations were amended with Mn(III) in the form of Mn(III)-DFOB (desferrioxamine-B, as prepared in Madison et al., 2011). Manganese is a well-known redox facilitator in natural waters, but until recently it was thought that only the Mn(II) and Mn(IV) forms were present in environmentally relevant concentrations. There is a growing appreciation, however, that Mn(III), stabilized by organic complexing ligands, can comprise substantial and sometimes majority fractions of dissolved Mn especially in nearshore environments (e.g., Oldham et al., 2017). Thus, we explored whether this redox shuttle might also affect Hg(II) reduction. We added enough Mn(III), bound to desferrioximine-B (DFOB) as a stabilizer, to the incubations to raise the concentration to 500 nM. In addition, and as a control, we added a similar amount of just DFOB to see if affected Hg cycling on it own (presumably through complexation).

Superoxide Concentration Measurements

The *in-situ* concentration of the superoxide radical ($O_2^{\cdot-}$) was measured using the chemiluminescence method described by Rose et al. (2008a), with minor modifications (Sutherland et al.,

2020). Superoxide signals were measured by pumping unfiltered seawater (UFSW) or aged filtered seawater (AFSW) from dark bottles using a high accuracy peristaltic pump directly into a flow-through FeLume Mini system (Waterville Analytical, Waterville ME). For AFSW, seawater was filtered (0.2 μm), amended with 50 μM diethylene-triaminepentaacetic acid (DTPA, Sigma), and aged in the dark for at least 8 h in order to eliminate all particle- and metal-associated superoxide (remaining sources would be reactive DOC and/or soluble extracellular enzymes). Superoxide detection was based on the reaction between superoxide and a chemiluminescent probe, a methyl cypridina luciferin analog (MCLA, Santa Cruz Biotechnology; Rose et al., 2008a) as described by Roe et al. (2016). To minimize incidental room light exposure, seawater was pumped into the FeLume using opaque tubing (∼20 s transit time between sample bottle and FeLume). For each depth, the superoxide signals were measured within UFSW and AFSW for several minutes (∼2–4 min) to achieve a steady-state signal. At the end of each measurement, 800 U L^{-1} superoxide dismutase (SOD, Sigma) was added to seawater samples. A small fraction of the superoxide signal is a result of reagent auto-oxidation, thus this artifact is removed by taking the difference between two signals as follows. First, the chemiluminescent response, R, in the UFSW and AFSW was quantified relative to the SOD baseline, and converted to concentration using the calibration sensitivity, $S_{calibration}$ (Equation 1). Next, the total light-independent superoxide concentration was determined using the difference between the UFSW signal and AFSW signal (Equation 2, Roe et al., 2016). The primary assumption here is that the sources of superoxide in the AFSW are negligible; otherwise, the concentrations are underestimates of the true steady-state dark values.

$$\left[O_2^{\cdot-}\right]_{(UFSW\ or\ AFSW)} = \frac{R_{sample} - R_{sample+SOD}}{S_{calibration}} \quad (1)$$

$$\left[O_2^{\cdot-}\right]_{total} = \left[O_2^{\cdot-}\right]_{UFSW} - \left[O_2^{\cdot-}\right]_{AFSW} \quad (2)$$

Calibrations were conducted using potassium dioxide (Sigma) as detailed previously (Zhang et al., 2016). Briefly, a primary stock solution containing potassium dioxide was prepared and quantified spectrophotometrically (Abs_{240}). To prepare the calibration standards, the primary stock solution was further diluted with the calibration matrix to a final superoxide concentration of 5–41 nM. Both primary stock solution and calibration standards were prepared immediately before the analysis. The corresponding chemiluminescent signals were recorded and extrapolated back to the time when the primary standard was quantified, using first order decay kinetics. The half-life of superoxide in AFSW ranged from 0.26 to 0.49 min and the extrapolation time was 0.5–1 min. Calibration curves were constructed based on the linear regression of the natural logarithm extrapolated chemiluminescent signals vs. superoxide concentrations in the calibration standards. Calibrations yielded highly linear curves (e.g., $R^2 > 0.9$), with a sensitivity, $S_{calibration}$, of 0.16 ± 0.04 (average and standard deviation of different water depths) counts per pM.

Superoxide Production Rate Measurements

At a subset of stations and depths, superoxide decay rates within unfiltered waters were quantified. Decay rate constants of superoxide were determined by spiking in known concentrations of a calibrated potassium dioxide stock at levels ∼2–3 times measured *in situ* concentrations and measuring superoxide decay over time as discussed above. The decay constants were obtained by modeling data using a pseudo-first order decay equation (Shaked and Armoza-Zvuloni, 2013; Armoza-Zvuloni and Shaked, 2014). Waters were spiked with superoxide. Production rates were calculated using the measured steady-state superoxide concentrations and modeled decay rate constants for each water sample (Roe et al., 2016).

Ancillary Measurements

Several ancillary measurements were made using the ship's CTD rosette, including temperature, salinity, dissolved oxygen, chlorophyll fluorescence, beam transmission and photosynthetically active radiation (PAR). The depth of the photic zone was estimated by fitting an exponential curve through the PAR data, and then interpolating to find the depth at 1% of surface irradiance.

Modeling—Formulation

To examine the relative importance of dark and light reduction in Hg^0 production, we have constructed a relatively simple model of the production of Hg^0 in the oceanic water column by both light and dark mechanisms. The model seeks to estimate the specific gross rate of Hg^0 addition in the oceanic mixed layer (the layer in regular contact with the atmosphere and capable of supplying Hg^0 for evasion).

Assuming first-order kinetics, we modeled the Hg-specific, depth-integrated, gross production of Hg^0 from Hg(II) using the following equation:

$$SIP = \frac{k_{uvb}UVB(1 - e^{-\varepsilon_{uvb}z})}{\varepsilon_{uvb}} + \frac{k_{par}PAR(1 - e^{-\varepsilon_{par}z})}{\varepsilon_{par}} + k_{dark}\left(Q_{10}{}^{\frac{T-25}{10}}\right)z \quad (3)$$

where SIP is the specific (Hg(II)-normalized) integrated Hg^0 production, k_{uvb} and k_{par} are the photochemical Hg(II) reduction

TABLE 2 | Summary of Parameters Used in the Hg^0 Gross Production Model.

Parameter	Value	Units	References
k_{UVB}	0.044 ± 0.004	$m^2\ kJ^{-1}$	Kuss et al., 2015
k_{PAR}	4.2 ± 1.8	$\times 10^{-4}\ m^2\ W^{-1}\ day^{-1}$	Qureshi et al., 2010
ε_{uvb}	0.5 ± 0.1	m^{-1}	Johannessen et al., 2003
ε_{par}	0.030 ± 0.006	m^{-1}	Morel, 1988
k_{dark}	0.168 ± 0.048	day^{-1}	This study
Q_{10}	2	unitless	Lee and Fisher, 2019

rate constants for UV-B and PAR at the surface (respectively), ε_{uvb} and ε_{par} are the exctintion coefficients for UV-B and PAR, k_{dark} is the reduction rate constant for non-photochemical pathways at 25°C, Q_{10} is the temperature dependence coefficient of k_{dark}, z is the depth of the mixed layer and T is the temperature of the mixed layer in °C. The units and values of these terms are summarized in **Table 2**. Overall, the gross Hg-specific, depth-integrated Hg^0 production rate has units of meters per day. The first two terms represent the depth-integrated production of Hg^0 by light-dependent reactions, including abiological photoreduction of Hg(II) complexes by UV-B and the indirect reduction of Hg(II) by phytoplankton during photosynthesis (PAR-dependent term). The rate constants used are those taken from experimental data (Qureshi et al., 2010; Kuss et al., 2015), and assumed to follow an exponential decay in value with depth according to extinction coefficients appropriate for the wavelengths of light involved in those reactions (UV-B for abiological reactions and PAR for biological reactions). The third term is the depth-integrated production of Hg^0 by dark reactions, assumed to be directly or indirectly related to the activity of heterotrophic microbes. The rate constant here comes from our experiments described above but adjusted for

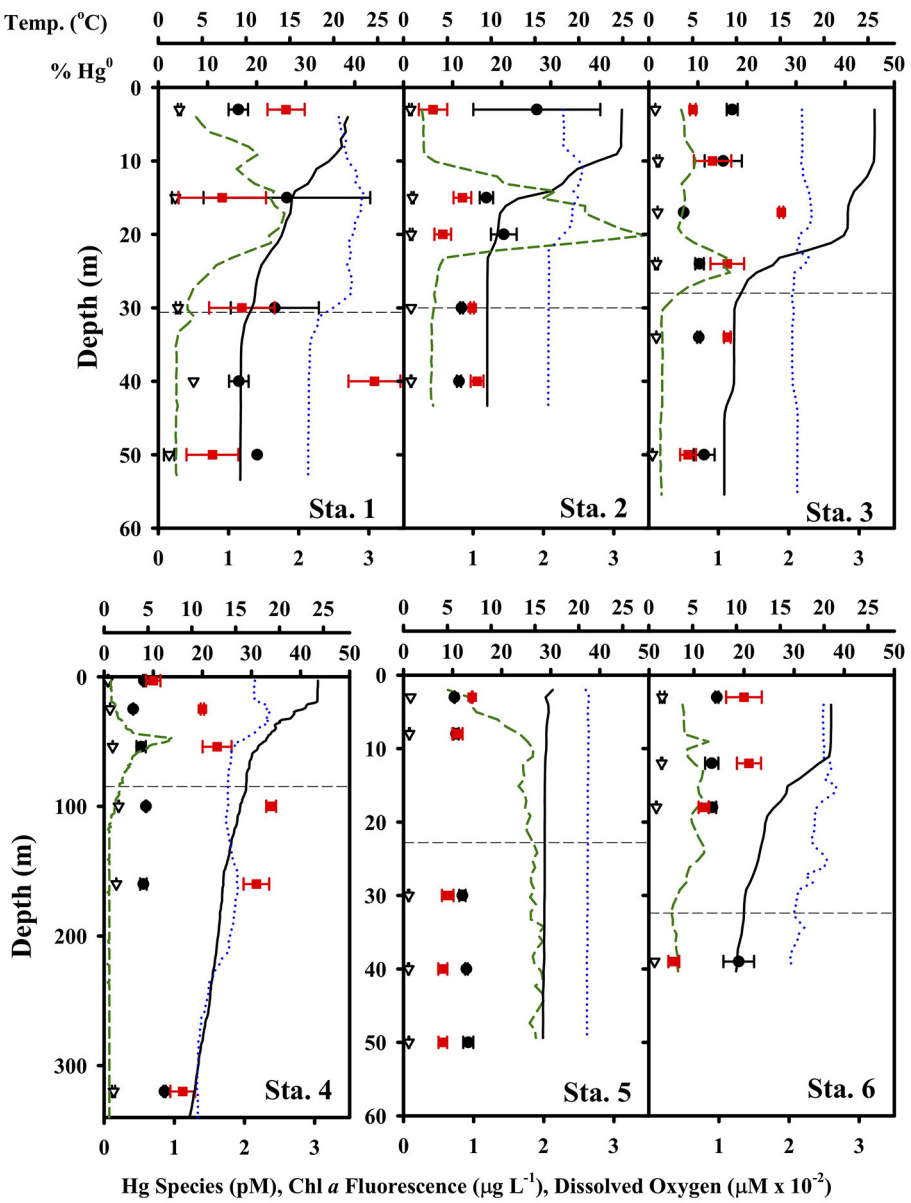

FIGURE 3 | Hg species concentrations and ancillary parameters at each TORCH 2 station. Notice the different depth axis scale for Station 4. In each panel, the black circles are total dissolved Hg, the red circles are percent of total Hg as Hg^0, the green dashed line is chlorophyll-a fluorescence (in µg/L concentration equivalents), the black line is temperature, and the blue dotted line is dissolved oxygen.

temperature using a Q_{10} value of 2 (Lee and Fisher, 2019), and which is typical for biological processes. This term might also be expected to have other dependencies related to the activity of bacteria in a given location, including for example primary production. We do not as yet know whether such dependency exists or how to parameterize it and so have left it out. This issue is taken up later as one of the caveats of the model. Temperature within the mixed layer is assumed constant with depth. We could have also included a term for the delivery of Hg^0 from below the mixed layer as a consequence of vertical eddy diffusion, but initial calculations suggested this term was small enough to ignore. This simplification ignores Hg^0 produced below the mixed layer that might find its way to the surface following seasonal entrainment (deepening of the mixed layer; e.g., Strode et al., 2007; Soerensen et al., 2010) and is therefore a likely low-end estimate for the rate of Hg^0 in-growth in the mixed layer. The values used in the equation are summarized in **Table 2**.

Climatologies for Light, Temperature, and Mixed Layer Depth

To apply these calculations to environmental conditions in different locations, we focused our analyses on 4 months that represent the progression of sunlight and other seasonal conditions (December, March, June, September). We also drew on several publicly available climatologies and recast them in terms of zonal averages over open ocean areas.

The first climatology we used was a two decade long record (1979–2000) of modeled and ground-truthed UV-B irradiances from NCAR (https://www2.acom.ucar.edu/modeling/tuv-download; accessed August 2018, data updated February 2017, **Figure S1**; Lee-Taylor and Madronich, 2007). This climatology includes the effects of sun angle and attenuation by atmospheric ozone and clouds. As this climatology includes data for UV-B flux to both land and ocean, a land mask was applied to the values prior to calculation of zonal averages and the original latitudinal resolution of 1 degree was converted to 2 degrees. The values provided by the NCAR dataset are presented in units of kJ m^{-2} $month^{-1}$ which we adjusted to kJ m^{-2} d^{-1} for the purposes of comparison to our dark reduction. The UV-normalized, specific Hg(II) reduction rate suggested by Qureshi et al. (2010) was 0.044 ± 0.004 m^2 kJ^{-1}. We used this value multiplied by the zonally averaged UV-B climatology to get the specific Hg(II) reduction rate (k_{uvb}, in units of d^{-1}) in surface waters as a function of latitude and time of the year.

The second climatology we incorporated was for PAR so that the contribution of phytoplankton on Hg(II) reduction could be examined. For this purpose, we used downwelling irradiance estimated from the Aqua-MODIS satellite-based radiometer. The data include monthly averages of a time span ∼from 2002 to 2017 made available by NASA (https://oceandata.sci.gsfc.nasa.gov/MODIS-Aqua/Mapped/Monthly_Climatology/9km/par), with data updated within the last two years. The original values are served at 9 km resolution which we converted to 2-degree zonal averages, with land values removed. Original units are in einsteins m^{-2} s^{-1}, which we transformed to W m^{-2} through comparison to NLDAS data to facilitate use with the rate measurements of Kuss et al. (2015). The zonal averages are shown in **Figure S4**.

The third climatology employed in our model was for global sea surface temperature. These data were retrieved from NCEP (https://ftp.emc.ncep.noaa.gov/cmb/sst/oimonth_v2/) and consisted of combined satellite and *in-situ* measurements (Reynolds et al., 2002; **Figure S5**). For use in the model, we assumed that these values were representative of the temperature in the local mixed layer. The original data set was provided in 1-degree resolution, from which we generated 2-degree averages for our analysis.

A fourth climatology applied to our model was that for ocean mixed layer depth developed by de Boyer Montégut et al. (2004), accessed at http://www.ifremer.fr/cerweb/deboyer/mld/home.php and shown in **Figure S6**. This dataset was provided in 2-degree resolution and was used without further modification.

To compare Hg^0 production speeds to evasion piston velocities, we also made use of a surface wind speed climatology. We used the Blended Sea Wind product from NOAA, which is the result of NCEP Reanalysis 2 (www.ncdc.noaa.gov/data-access/marineocean-data/blended-global/blended-sea-winds; Zhang et al., 2006). This data set is a monthly climatology making use of data collected from 1995 to 2005 and at 0.25-degree resolution (**Figure S7**). To appropriately combine with our other datasets, we averaged the data down to 2-degree resolution first, and then generated zonal averages. The zonal average data was then converted to a gas exchange piston velocity using the formula of Wanninkhof (1992), including incorporating modifications for sea surface temperature on the Schmidt Number for Hg^0 from our zonally average temperature data mentioned above.

RESULTS AND DISCUSSION

Species Distributions

The concentration of the Hg species ranged from 0.41 to 2.47 pM for total dissolved Hg and 0.05 to 0.3 pM for Hg^0, with relatively little variation vertically at the shelf stations (**Figure 3**). At Station 4 in deeper water, the profile revealed a peak in percent of total Hg as Hg^0 within the thermocline and below the photic zone. This sort of profile observed at Station 4 is comparable to that observed in other open ocean conditions, where Hg^0 and percent of total Hg as Hg^0 often look "nutrient-like" in character, and total Hg to a lesser extent as well (e.g., Bowman, 2014; Bowman et al., 2020). There were no obvious correlations between total Hg, Hg^0 and percent of total as Hg^0 and any of the ancillary parameters shown in **Figure 3** (temperature, chlorophyll *a* fluorescence and dissolved oxygen). Dissolved oxygen was never particularly low (range was 192 to 293 μM), though it did tend to decrease below the mixed layer and photic zone. Thus, the concentration of Hg^0 was always many orders of magnitude above that predicted by equilibrium given the redox properties of the Hg^0/Hg(II) couple (e.g., Whalin et al., 2007).

Concentrations of Hg^0 were supersaturated at all depths and at all stations if the atmospheric concentrations were assumed to be 1.5 ng Hg^0 m^{-3} (Soerensen et al., 2013) and ranged from 160 to 1,140%. Degrees of supersaturation tended to vary only slightly with depth between about 300 and 400% supersaturation. At shelf

stations, the degree of supersaturation was highest in the surface and fell off below the photic zone, while at Station #4 there was a peak in supersaturation just below the photic zone.

Diel Cycling

At two stations, #2 and 6, we conducted diel samplings, where the species were measured at three different depths over the course of 17 and 29 h, respectively (**Figure 4**). No significant trend in any of the Hg species was observed at these locations over time, suggesting little overall net effect of light on Hg^0 production. The depths studied included those at the surface (3 m for St. 2 and 6), chlorophyll max (12 and 18 m for St. 6) as well as below the local photic zone (30 and 40 m for St. 2; 39 m for St. 6), and while the concentrations of Hg species were different at the different depths, the temporal trends were the same. These two observations together discourage the view that vertical mixing could have mixed away a photochemical signal making the system appear to have little diel trending. A lack of

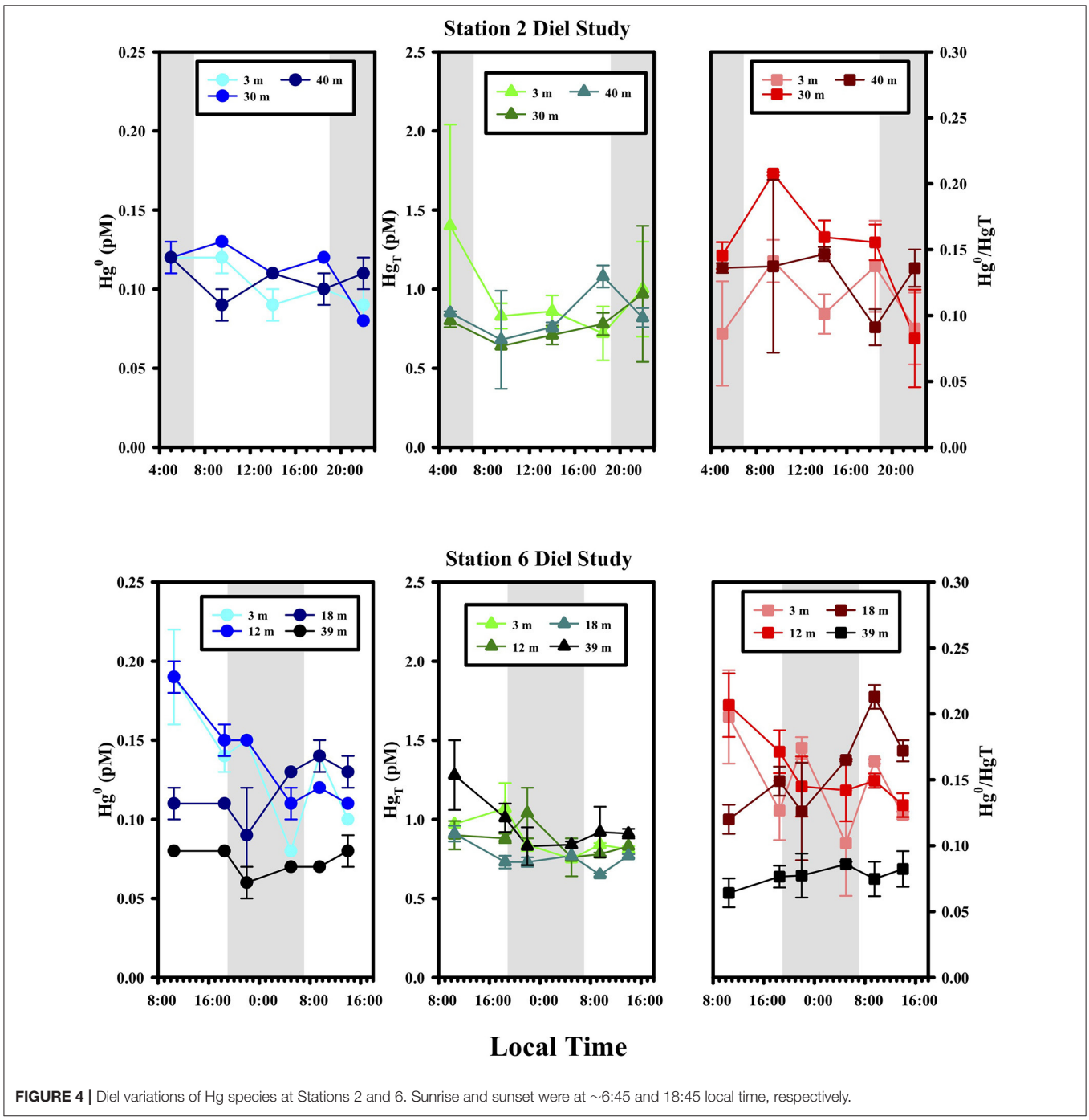

FIGURE 4 | Diel variations of Hg species at Stations 2 and 6. Sunrise and sunset were at ~6:45 and 18:45 local time, respectively.

diel cycling has been noted in other open ocean locations for example by groups using high-resolution underway sampling of Hg^0 in surface waters (e.g., Andersson et al., 2008; Mason et al., 2017). However, there are studies that have reported diel changes in Hg^0 concentrations (e.g., Fantozzi et al., 2007; Tseng et al., 2012) and we return to the issue of whether diel cycling should be expected or not below.

Gross Reduction Rate Incubations

To begin to probe the underlying mechanisms of Hg reduction, we conducted gross dark reduction incubations in water collected below the photic zone at stations #2, 3, 4 and 6, and depths were 40, 34, 160, and 39 m, respectively. The role of particles was assessed by comparing Hg(II) reduction in unfiltered and filtered waters (**Figure 5**). The specific gross rate of Hg(II) reduction in unfiltered samples averaged 0.007 ± 0.002 h^{-1}, with no discernible trend among stations. The filtered results were more variable, with the specific rates at Stations #2 and 4 essentially the same as the unfiltered, but at Stations #3 and 6 less than and greater than the unfiltered, respectively. While these results are difficult to interpret, they indicate that filtering does not universally result in a substantial loss of reduction power. Thus, the presence of cells and particulates does not appear necessary for robust dark reduction to take place. Nevertheless, this does not imply that microbes are not involved in dark Hg(II) reduction, but just that reduction can occur without active cells. In fact, we previously observed that Hg(II) reduction in brackish water is facilitated by dissolved compounds that reside in the 3–10 kDa size range (data not shown), which implies the involvement of extracellular enzymes. Thus, it is possible that microbes are required for Hg reduction via the production of dissolved metabolites or extracellular enzymes that promote the reduction reaction.

In addition to the filtered/unfiltered treatments, we also amended a subset of dark gross reduction measurement incubations with chemicals we hypothesized might be involved in promoting or inhibiting Hg reduction. Our initial hypotheses included ones that centered around the potential involvement, either directly or indirectly, of reactive oxygen species including superoxide and hydrogen peroxide. These transient species have redox potentials that lie in the middle of environmentally important redox couples (e.g., Fe, Mn, and Hg) and can therefore variously act as both oxidants and reductants, depending on the compounds with which they are presented. Production of the ROS superoxide ($O_2^{\cdot-}$) and hydrogen peroxide (H_2O_2) in natural waters has more recently been attributed in large part to light-independent reactions mediated by particles, presumably composed primarily of microbes (Rose et al., 2008b; Hansard et al., 2010; Roe et al., 2016; Zhang et al., 2016; Sutherland et al., 2020). As these ROS may influence the cycling of Hg, some of our amendment experiments either added exogenous ROS or stimulated ROS production by the resident microbial community.

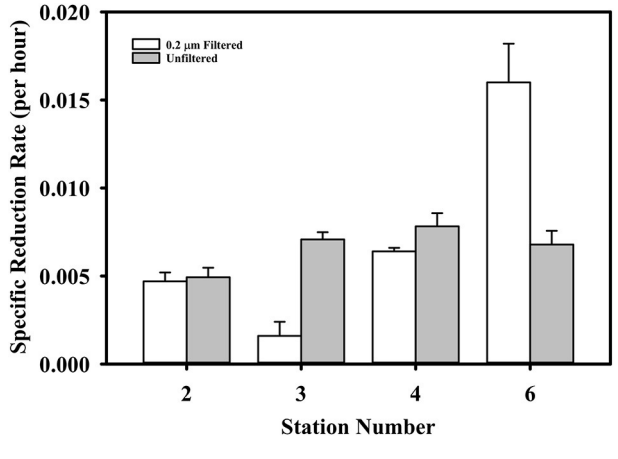

FIGURE 5 | The gross dark specific rate of Hg(II) reduction in filtered and unfiltered water from four TORCH 2 stations. See text for station details.

Figure 6 illustrates the results of amendments made to the seawater in our gross rate incubation experiments designed to explore the influence of ROS. In one set of incubations containing water collected from Station 2 at 40 m, H_2O_2 was added to bring the concentration in the incubation to either 50 or 100 nM. Typical continental shelf waters can be expected to have 10s to 100s of nM H_2O_2 (e.g., Miller and Kester, 1988; Miller et al., 2005). Thus, the amendments were substantial, but within an order of magnitude of the ambient concentrations. The addition of H_2O_2 either had no effect on the gross Hg(II) reduction rate (relative to the unamended control) in the case of unfiltered seawater, or about a 30% decrease in reduction rate in the case of filtered seawater. The absence of any effect in the unfiltered water suggests that the added H_2O_2 was degraded by particles that are presumably microbes. Indeed, the primary pathway of H_2O_2 degradation in the ocean is via microbial enzymatic activity (Moffett and Zafiriou, 1990).

Superoxide amendment in the incubations was achieved by stimulating superoxide production via NADH-based enzymes as conducted previously (Zhang et al., 2016). The addition of NADH to both filtered and unfiltered seawater saw a significant change in Hg(II) reduction only in the unfiltered treatment. In that treatment, specific gross reduction increased by about 30% (**Figure 6**). In a parallel study, laboratory experiments confirmed that NADH does not directly reduce Hg(II) (Marsico, 2015). The results of the two NADH treatments suggest that microbes can be involved in Hg(II) reduction and that this reduction can be stimulated through NADH addition. Including SOD with the NADH treatments (not shown) resulted in no statistically significant loss of the stimulated reduction, implying that the contribution to stimulated reduction activity from superoxide could not be resolved. Consistent with this, if we examine the concentrations of Hg^0, the ratio of Hg^0 to total Hg and light-independent steady-state superoxide concentrations from the cruise profiles together (**Figure 7**), we see no correlation and therefore no circumstantial support for the idea that superoxide contributes to Hg(II) reduction. Furthermore, if we compare the Hg species concentrations and ratios to light-independent superoxide production rates (**Figure 7**) there appears to be an inverse relationship (at least with the fraction of total as Hg^0). Therefore, it would seem that superoxide does not contribute

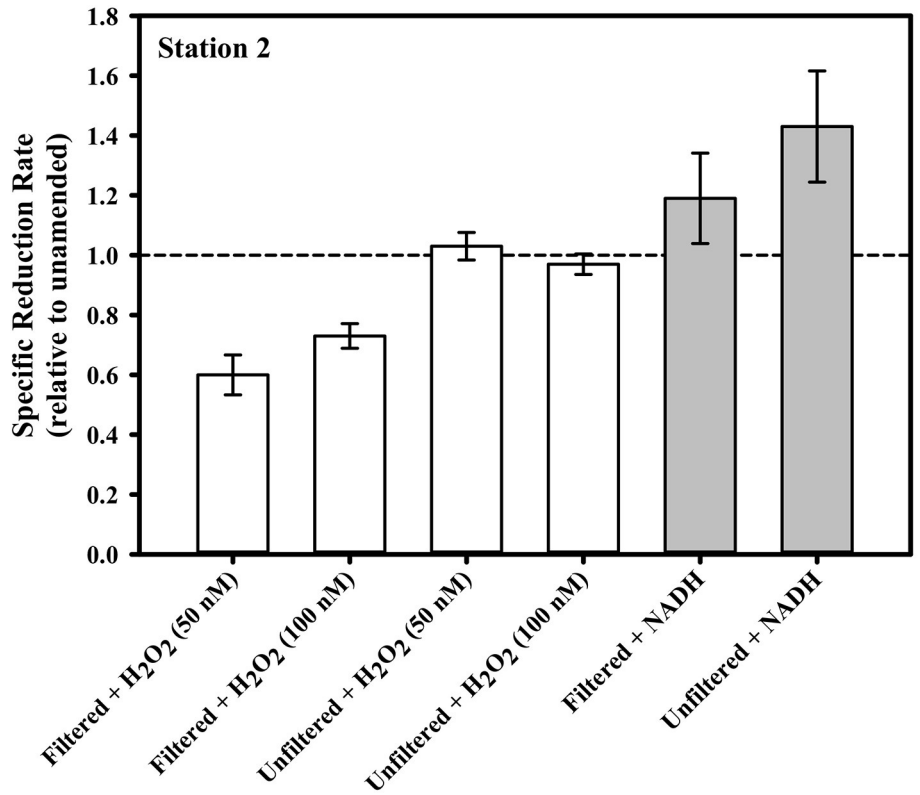

FIGURE 6 | The gross dark specific rate of Hg(II) reduction at Station 2 from water collected at 39 m, with various ROS-related amendments, shown relative to the local unamended control.

to Hg(II) reduction in seawater, or perhaps that under ambient conditions it instead is reacting with some other species which is more influential in Hg(II) reduction.

Another possible reactant of Hg is oxidized Mn species, including Mn(III)-L complexes. This is particularly interesting in this context because in a parallel study, Mn(III)-L was shown to be abundant within the water column of these sites (Oldham et al., 2020). In the filtered Mn(III)-DFOB amendment incubations, the gross specific rate of reduction jumped by about a factor of 20 relative to filtered but unamended (**Figure 8**). The filtered+DFOB-only treatment was indistinguishable from the unamended, suggesting the dramatic increase in Hg reduction was the result of the presence of the Mn(III), not DFOB, in solution. Interestingly, when the same pair of Mn(III)-DFOB and DFOB-only treatments were applied to unfiltered seawater, there was only a modest increase in the gross reduction rate when Mn(III) was present, and a decrease in the gross rate when DFOB alone was present. This suggests that when cells were present, the DFOB may have facilitated cell uptake of Hg(II) or otherwise rendered the Hg(II) in a form that was not available for reduction. When both Mn(III) and DFOB were present along with cells, the two apparent competing forces of increased reduction from the Mn vs. the sequestration from the DFOB+cell combination resulted in an increase in reduction that was modest.

As noted above, there was no discernible trend in the gross specific rate of Hg(II) reduction in unfiltered samples across our stations. This is interesting because the stations where our experiments were conducted include waters with a range in cell abundance from $0.4{\cdot}10^6$ to $2{\cdot}10^6$ bacterial cells mL^{-1} in aphotic waters (Sutherland et al., 2020) and perhaps a range in community activity as well. This suggests three possibilities: (1) Hg(II) reduction in the dark is not dependent on heterotrophic bacterial activity at all and whatever the agent responsible for Hg reduction was, had a uniform distribution or was at sufficient excess at all our stations, (2) cells at the lower abundance site had a higher per cell dark reduction rate than cells at the higher abundance sites, or (3) the rate of dark reduction, whatever the mechanism, is set by a slow step other than the reaction itself, for example the rate of release of Hg from a "hard-to-reduce" pool.

The gross specific rate measured here is also interesting in that it is slower than photochemical reduction, but still relatively fast. The dark rates we observed were similar to those reported earlier (e.g., Whalin et al., 2007), though perhaps better resolved. Thus, even in open ocean conditions and as suggested by others for coastal environments, depth-integrated dark reduction has the potential to provide more Hg^0 in the mixed layer than light reactions under conditions where the mixed layer depth is relatively deep.

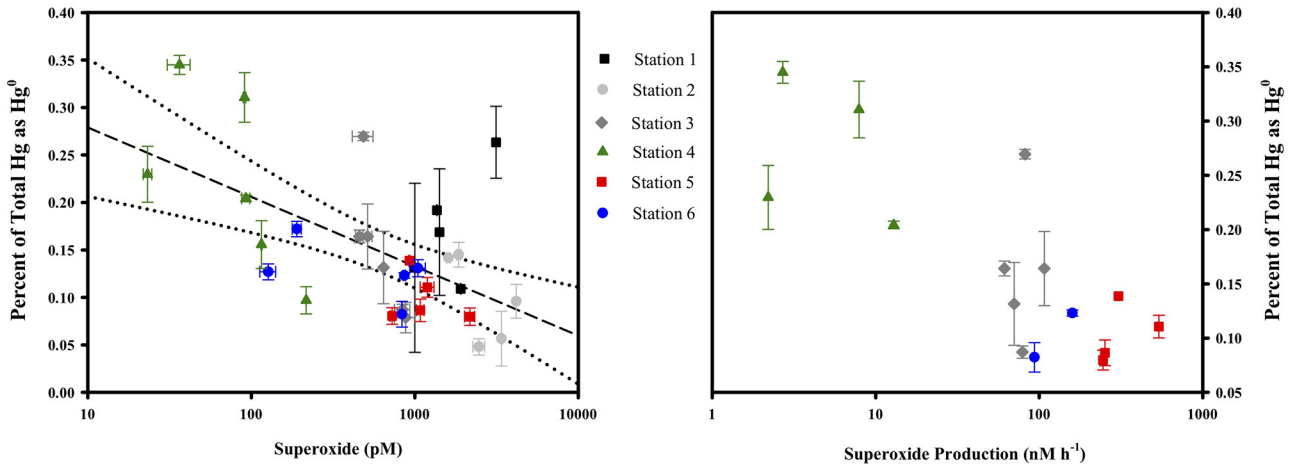

FIGURE 7 | The fraction of total Hg as Hg^0 compared to the light-independent, steady-state concentration of superoxide **(left)** and the rate of light-independent superoxide production in unfiltered water **(right)** at all stations and depths. For more details on the superoxide dynamics (see Sutherland et al., 2020).

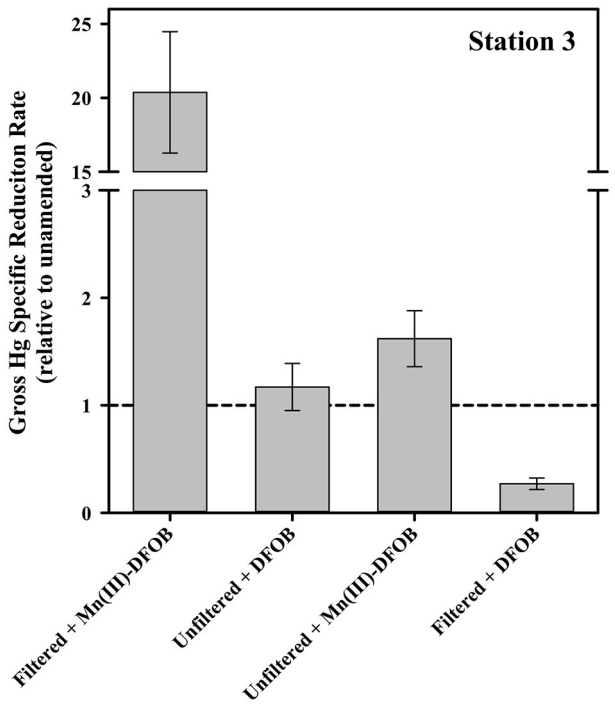

FIGURE 8 | The gross dark specific rate of Hg(II) reduction at Station 3 with Mn(III)-related amendments, shown relative to the local unamended control.

Zonally Averaged Modeling

To explore the hypothesis that depth-integrated dark reduction can be more important that light reduction, we used the model described above, driven with climatological data to get an estimate for the total, depth-integrated production rate of Hg^0 within the mixed layer and the apportionment of that production between light-dependent and -independent (dark) mechanisms. The results from these calculations are shown in **Figure 9** and summarized in **Table 3**. Several features of the model output are worth discussing. First, the overall rate of reduction varies dramatically with latitude, with tropical regions producing Hg^0 at a much faster specific rate than high latitude regions. Furthermore, as tropical latitudes make up a larger fraction of the ocean's area than do high latitudes, the model predicts that the tropical ocean is where the majority of Hg reduction takes place. This does not necessarily translate into higher evasional fluxes, however, as re-oxidation rates and wind speed will influence the specific rate of evasion. For example, as Kuss et al. (2011) noted, relatively high concentrations of Hg^0 can be found in tropical surface waters, but winds at these latitudes tend to be lower than at higher latitudes. Thus, they found maximal evasion fluxes (per unit area) in temperate waters.

The second major feature of the output to notice is that integrated dark specific reduction is faster than either of the light-dependent pathways, as well as the sum of the two, except in high and temperate latitudes during local summer. The abiological (photochemical) light reduction pathway is everywhere greater than the phytoplankton pathway as well. Therefore, the model predicts that temperature, which is the primary control on dark reduction, is the critical modulator of Hg^0 specific production and explains why warm tropical waters dominate global specific reduction. In addition to high specific reduction, the tropics also experience high loadings of Hg(II) to the ocean from their relatively high precipitation depths, which when combined to vigorous reduction, leads to high Hg^0 concentrations and high evasion rates in and around the intertropical convergence zone (Kuss et al., 2011; Soerensen et al., 2013, 2014; He and Mason, 2020).

Comparing the residence times of Hg^0 in the mixed layer with respect to reduction/oxidation and evasion reveals that in most locations oxidation is a bigger gross sink for Hg^0 from the mixed layer than is evasion. **Figure 10** portrays this by calculating the ratio of the residence time of Hg^0 with respect to

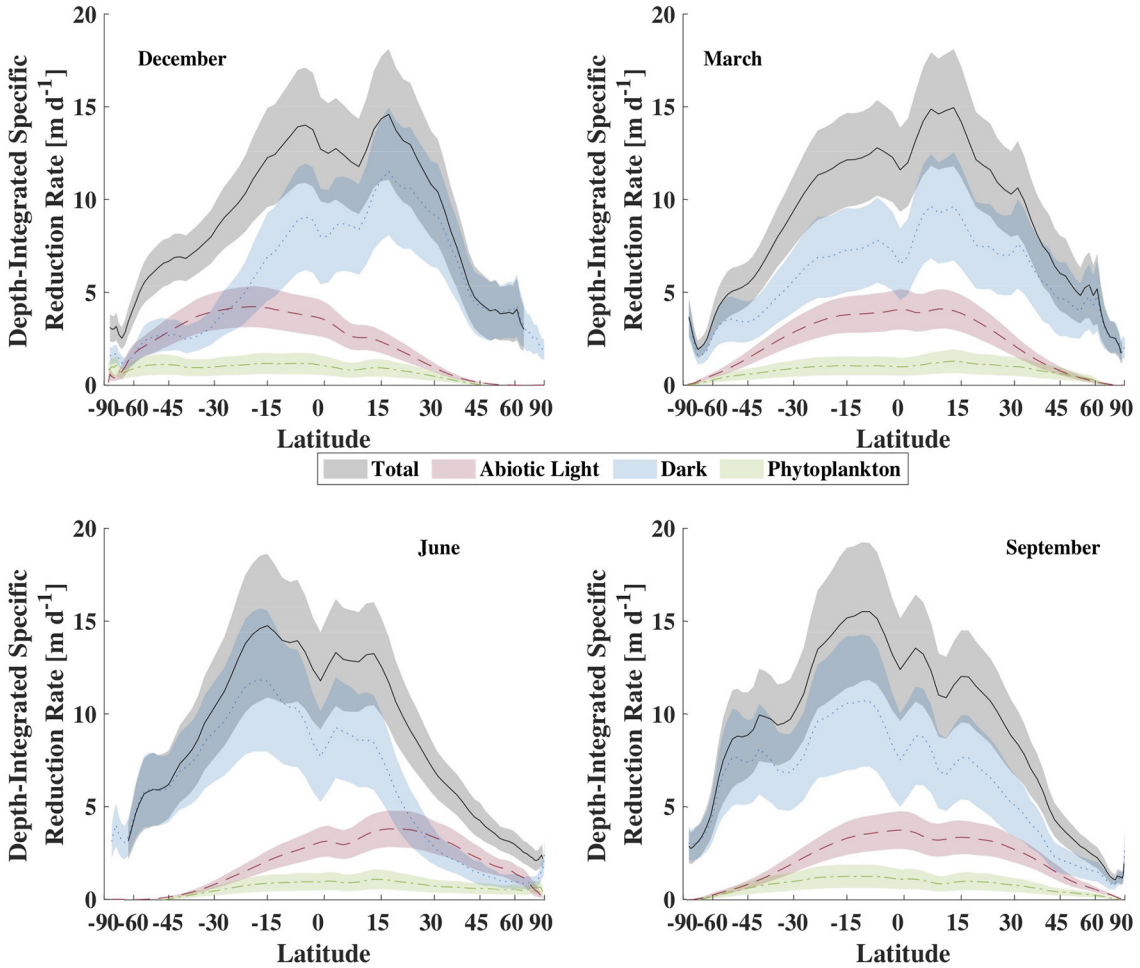

FIGURE 9 | Comparison of the zonal-averaged depth-integrated Hg specific reduction rate for representative months, in units of meters per day. The lines are the mean value while the shaded areas are the ± 1 standard deviation envelope.

evasion, divided by the residence time with respect to production from Hg(II):

$$R = \frac{k_{red}\,[Hg(II)]ML}{k_{piston}\,[Hg^0]} \tag{4}$$

where k_{red} is the overall reduction rate constant, ML is the depth of the mixed layer, and k_{piston} is the gas exchange piston velocity. In **Figure 10**, the ratio of Hg^0 to Hg(II) in the mixed layer is assumed to be 0.5 everywhere, which is undoubtedly an overestimate for most locations, but which means that the ratio is likely larger in most places. As the value is much larger than one under most conditions, this implies that oxidation of Hg^0 is a larger sink than evasion and therefore the steady-state concentration of Hg^0 is set by redox cycling more or less independently of the strength of evasion. As evasion is driven in part by the dissolved Hg^0 concentration, this in turn implies that evasion rates are driven by the balance between oxidation and dark reduction, and not gross reduction rates. **Figure 10** suggests that the speeds of redox and evasion approach each other at high latitudes allowing evasion to remove more of the Hg^0 after it is produced and before it can be oxidized. Under these conditions, it is possible for the speed of gross reduction to be more influential on evasion rates. As reduction rates are their highest in warm water with a shallow mixed layer, we should expect high latitudes in the summer hemispheres to exhibit relatively large net fluxes of Hg^0 and possibly see diel cycling if mixed layer depths are shallow.

Modeling Caveats

One potential weakness of this modeling approach is the oversimplified view of the ocean mixed layer. A truly well-mixed surface layer is one with uniformly short residence times at all depths and is required in our model to justify our mathematical arguments described above. However, Franks (2014) pointed out that while a layer of uniform properties like temperature and salinity might be identified from data, this is an imperfect proxy for a surface turbulent layer in which the residence time at any one depth is truly short. Franks summarized several forces that can contribute to turbulence and true mixing, and found that only two, convection and Langmuir circulation, are capable

TABLE 3 | Model result summary.

Region[a]	% of Ocean Area	Temp. Range (°C)	Total DISR[b] (m d^{-1})	Dark DISR (m d^{-1})	Light DISR (m d^{-1})	Piston Velocity (m d^{-1})
High latitudes (Summer)	13	−1.9 to 5.4	2.7 ± 0.5	1.4 ± 0.5	0.7 ± 0.5	5.1 ± 1.4
High latitudes (Winter)	13	−1.8 to 3.2	3.6 ± 0.4	3.0 ± 0.8	0 ± 0	11 ± 3
Temperate latitudes (Summer)	37	1.8 to 22.5	5.6 ± 1.4	2.1 ± 0.7	2.7 ± 0.7	4.3 ± 2.2
Temperate latitudes (Winter)	37	1.2 to 20.5	6.5 ± 2.1	6.1 ± 1.7	0.3 ± 0.3	8.3 ± 2.4
Tropics	50	19.2 to 28.5	12 ± 2	8.4 ± 2.3	3.0 ± 1.0	2.5 ± 0.5
Global average (Annual)	100	13.0 ± 11.2	8 ± 4	5 ± 3	1.7 ± 1.4	5.5 ± 3.9

[a]*Here, we take "high latitudes" to be those above 60°, "temperate latitudes" to be those between 30 and 60°, and the "tropics" to be between 30° north and south.*
[b]*DISR, depth-integrated specific reduction rate.*

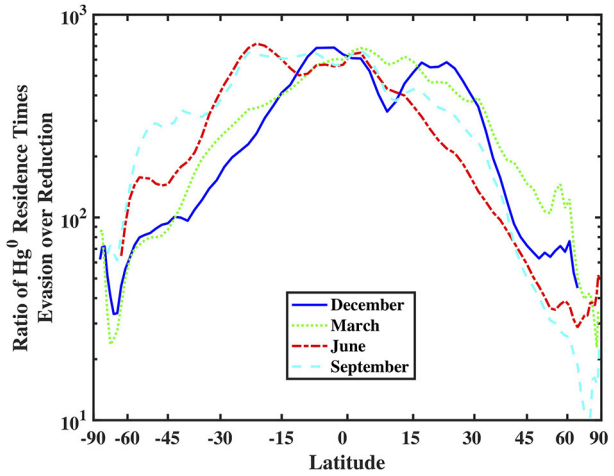

FIGURE 10 | Comparison of the zonal-averaged depth-integrated Hg specific reduction rate (in units of meters per second) and piston velocity (*k* value in the gas-exchange model, also in units of meters per second).

of providing turbulence and mixing deeper than a few meters. While these two forces can act at any time and result in relatively rapid mixing, they tend to occur discontinuously and are more important in the evening, in cooler seasons, and under strong and steady winds. Thus, our use of the mixed layer climatology of de Boyer Montegut et al. could overestimate the depth of turbulent mixing on any given day, and may even have some diel and seasonal bias as well. This could be tested by looking for any temporal trends in the various high resolution surface Hg^0 data sets that are becoming more common (Andersson et al., 2011; Soerensen et al., 2014; Mason et al., 2017; DiMento et al., 2019). Some observers using more conventional datasets have already reported seeing diel trends. For example, Tseng and colleagues reported trends in the South China Sea, as did Fantozzi et al. in the Mediterranean and DiMento et al. in the Arctic (Fantozzi et al., 2009; Tseng et al., 2013; DiMento et al., 2019). But as we noted in our own data (see **Figure 4**), this is far from universal. Therefore, we suggest that when the depth of real mixing, as opposed to the conventional definition we've used here, is deeper than the "critical depth" for Hg reduction (the depth at which integrated dark reduction equals integrated light reduction and analogous to the concept in primary production; Franks, 2014), dark reduction will dominate Hg^0 production and observers will see little evidence of diel cycling. This would imply that those cases where diel cycles have been observed were therefore situations where the depth of real mixing was shallower than the critical depth.

A second important caveat to this model is that we have assumed a temperature dependence to dark Hg reduction on the basis that the production of reducing equivalents in the dark almost certainly has to be biological in nature. Assuming this is true, then all the various factors that affect dark biological Hg reduction should also be included. One of the most important is likely to be primary production within the photic zone, as this is the source of fixed carbon to bacteria that may be reducing Hg. However, we have not attempted to include primary production as a variable in our model because we simply lack information on how this might affect Hg reduction. Our prediction is that greater bacterial production should increase Hg reduction, though our range of studies did not seem to bear this out. Assuming it is true, however, then dark Hg reduction might be expected to have a spatial trend similar to that of phytoplankton-driven Hg reduction. If this were true, then it would suggest that our model currently overestimates Hg reduction in the winter hemisphere at mid-latitudes, where production is relatively low but temperatures are warm. We do not believe this will change the overall conclusion that dark reduction dominates in most places, but this is clearly an important topic for further research.

Implications

The combination of measurement and modeling presented here argues that dark reduction, rather than light-driven reduction, is responsible for most of the Hg^0 produced in and evaded from the global surface ocean. As this reduction produces concentrations of Hg^0 that are dramatically out of equilibrium, they must be actively supported by a ready supply of reducing agents that are likely of biological origin. This implies that factors affecting the activity of marine heterotrophs within the mixed layer can subsequently affect the production and evasion of Hg^0 from the ocean. Such factors include temperature and primary productivity, both of which are likely to change in the future and in ways that are hard to predict. For example, warming should stimulate heterotrophic activity and could enhance primary

productivity (e.g., Behrenfeld, 2011), both of which should enhance Hg evasion according to our results. But warming would also result in a shoaling of the mixed layer and restriction of new production, both of which should decrease the importance of dark biological reduction. More study of the temperature and biological sensitivities of Hg redox are needed to make predictions regarding the future of the marine Hg cycle.

DATA AVAILABILITY STATEMENT

The datasets presented in this study can be found in online repositories. The names of the repository/repositories and accession number(s) can be found at: https://www.bco-dmo.org/dataset/765327/data.

AUTHOR CONTRIBUTIONS

CL, CH, and BV designed the experiments. All authors contributed to data collection and writing.

FUNDING

This work was supported by NSF Grant OCE-1355720 (to CH, CL, and BV).

ACKNOWLEDGMENTS

Thanks to the captain and crew of the *R/V Endeavor*, as well as the science crew of the TORCH2 cruise, with special thanks to Alison Agather, Lindsey Starr, and Bill Fanning. Thanks to Mak Saito, Brian Guest, and the Winch Pool staff at WHOI for sampling equipment assistance. Thanks to Asif Qureshi, Joachim Kuss, Mathis Hain, and Jessica McCarty for data sharing, help with remote sensing data and data presentation advice. Thanks to Jerome Fietcher for discussion of mixed layers. Thanks also the insightful comments of two reviewers.

SUPPLEMENTARY MATERIAL

The Supplementary Material for this article can be found online at: https://www.frontiersin.org/articles/10.3389/fenvc.2021.659085/full#supplementary-material

Figure S1 | Sea surface temperature (°C) in the NW Atlantic at the time of TORCH 2 cruise as collected by the MODIS instrument on the Aqua satellite. The figure depicts average values from 9/17/2017 to 9/23/2017.

Figure S2 | Concentration of chlorophyll-a (mg L^{-1}) in the NW Atlantic at the time of TORCH 2 cruise as collected by the MODIS instrument on the Aqua satellite. The figure depicts average values from 9/17/2017 to 9/23/2017.

Figure S3 | Zonal-averaged surface UV-B flux in units of kJ m^{-2} d^{-1} for representative months.

Figure S4 | Zonal-averaged surface photosynthetically active radiation (PAR; units of kJ m^{-2} d^{-1}) flux for representative months.

Figure S5 | Zonal-averaged sea surface temperature in degrees Celsius for representative months.

Figure S6 | Zonal-averaged mixed layer depth in meters for representative months.

Figure S7 | Zonal-averaged surface winds in meters per second for representative months.

REFERENCES

Andeer, P. F., Learman, D. R., McIlvin, M., Dunn, J. A., and Hansel, C. M. (2015). Extracellular haem peroxidases mediate Mn (II) oxidation in a marine *Roseobacter* bacterium via superoxide production. *Environ. Microbiol.* 17, 3925–3936. doi: 10.1111/1462-2920.12893

Andersson, M. E., Gardfeldt, K., and Wangberg, I. (2008). A description of an automatic continuous equilibrium system for the measurement of dissolved gaseous mercury. *Anal. Bioanal. Chem.* 391, 2277–2282. doi: 10.1007/s00216-008-2127-4

Andersson, M. E., Sommar, J., Gardfeldt, K., and Jutterstrom, S. (2011). Air-sea exchange of volatile mercury in the North Atlantic Ocean. *Mar. Chem.* 125, 1–7. doi: 10.1016/j.marchem.2011.01.005

Armoza-Zvuloni, R., and Shaked, Y. (2014). Release of hydrogen peroxide and antioxidants by the coral *Stylophora pistillata* to its external milieu. *Biogeosciences* 11, 4587–4598. doi: 10.5194/bg-11-4587-2014

Behrenfeld, M. (2011). Uncertain future for ocean algae. *Nat. Clim. Chang.* 1, 33–34. doi: 10.1038/nclimate1069

Blough, N. V., and Zepp, R. G. (1995). "Reactive oxygen species in natural waters," in *Active Oxygen in Chemistry,* eds C. S. Foote, J. S. Valentine, A. Greenberg, and J. F. Liebman (Dordrecht: Springer Netherlands), 280–333.

Bowman, K. L. (2014). *Mercury Distributions and Cycling in the North Atlantic and Eastern Tropical Pacific Oceans*. Dayton, OH: Wright State University.

Bowman, K. L., Lamborg, C. H., and Agather, A. M. (2020). A global perspective on mercury cycling in the ocean. *Sci. Tot. Environ.* 710:136166. doi: 10.1016/j.scitotenv.2019.136166

Costa, M., and Liss, P. S. (1999). Photoreduction of mercury in sea water and its possible implications for Hg-0 air-sea fluxes. *Mar. Chem.* 68, 87–95. doi: 10.1016/S0304-4203(99)00067-5

de Boyer Montégut, C., Madec, G., Fischer, A. S., Lazar, A., and Iudicone, D. (2004). Mixed layer depth over the global ocean: an examination of profile data and a profile-based climatology. *J. Geophys. Res. Oceans* 109:C12003. doi: 10.1029/2004JC002378

Diaz, J. M., Hansel, C. M., Voelker, B. M., Mendes, C. M., Andeer, P. F., and Zhang, T. (2013). Widespread production of extracellular superoxide by heterotrophic bacteria. *Science* 340, 1223–1226. doi: 10.1126/science.1237331

DiMento, B. P., Mason, R. P., Brooks, S., and Moore, C. (2019). The impact of sea ice on the air-sea exchange of mercury in the Arctic Ocean. *Deep Sea Res. Pt. I Oceanogr. Res. Pap.* 144, 28–38. doi: 10.1016/j.dsr.2018.12.001

Fantozzi, L., Ferrara, R., Frontini, F. P., and Dini, F. (2007). Factors influencing the daily behaviour of dissolved gaseous mercury concentration in the Mediterranean Sea. *Mar. Chem.* 107, 4–12. doi: 10.1016/j.marchem.2007.02.008

Fantozzi, L., Ferrara, R., Frontini, F. P., and Dini, F. (2009). Dissolved gaseous mercury production in the dark: evidence for the fundamental role of bacteria in different types of Mediterranean water bodies. *Sci. Tot. Environ.* 407, 917–924. doi: 10.1016/j.scitotenv.2008.09.014

Franks, P. J. S. (2014). Has Sverdrup's critical depth hypothesis been tested? Mixed layers vs. turbulent layers. *ICES J. Mar. Sci.* 72, 1897–1907. doi: 10.1093/icesjms/fsu175

Hansard, S. P., Vermilyea, A. W., and Voelker, B. M. (2010). Measurements of superoxide radical concentration and decay kinetics in the Gulf of Alaska. *Deep Sea Res. Pt. I Oceanogr. Res. Pap.* 57, 1111–1119. doi: 10.1016/j.dsr.2010.05.007

He, Y. P., and Mason, R. P. (2020). "Comparison of air-sea exchange of mercury from the GEOTRACES GP15 cruise with data from other cruises in the Pacific Ocean: from similarity to discrepancy," in *Ocean Sciences* (San Diego, CA: American Geophysical Union).

Johannessen, S. C., Miller, W. L., and Cullen, J. J. (2003). Calculation of UV attenuation and colored dissolved organic matter absorption spectra from measurements of ocean color. *J. Geophys. Res. Oceans* 108:13. doi: 10.1029/2000JC000514

Kieber, D. J., Peake, B. M., and Scully, N. M. (2003). Reactive oxygen species in aquatic. *UV Effects Aquat. Organ. Ecosyst.* 1:251. doi: 10.1039/9781847552266-00251

Kuss, J., Wasmund, N., Nausch, G., and Labrenz, M. (2015). Mercury emission by the baltic sea: a consequence of cyanobacterial activity, photochemistry, and low-light mercury transformation. *Environ. Sci. Technol.* 49, 11449–11457. doi: 10.1021/acs.est.5b02204

Kuss, J., Zülicke, C., Pohl, C., and Schneider, B. (2011). Atlantic mercury emission determined from continuous analysis of the elemental mercury sea-air concentration difference within transects between 50°N and 50°S. *Global Biogeochem. Cycles* 25:GB3021. doi: 10.1029/2010GB003998

Lamborg, C. H., Hammerschmidt, C. R., Gill, G. A., Mason, R. P., and Gichuki, S. (2012). An intercomparison of procedures for the determination of total mercury in seawater and recommendations regarding mercury speciation during GEOTRACES cruises. *Limnol. Oceanogr. Methods* 10, 90–100. doi: 10.4319/lom.2012.10.90

Lamborg, C. H., Tseng, C. M., Fitzgerald, W. F., Balcom, P. H., and Hammerschmidt, C. R. (2003). Determination of the mercury complexation characteristics of dissolved organic matter in natural waters with "reducible Hg" titrations. *Environ. Sci. Technol.* 37, 3316–3322. doi: 10.1021/es0264394

Lee, C. S., and Fisher, N. S. (2019). Microbial generation of elemental mercury from dissolved methylmercury in seawater. *Limnol. Oceanogr.* 64, 679–693. doi: 10.1002/lno.11068

Lee-Taylor, J., and Madronich, S. (2007). *Climatology of UV-A, UV-B, and erythemal radiation at the Earth's surface, 1979-2000.* Boulder, CO: NCAR Technical Note NCAR/TN-474+STR, NCAR.

Madison, A. S., Tebo, B. M., and Luther, I. I. I., G. W. (2011). Simultaneous determination of soluble manganese (III), manganese (II) and total manganese in natural (pore) waters. *Talanta* 84, 374–381. doi: 10.1016/j.talanta.2011.01.025

Marsico, R. M. (2015). *Implications of Widespread Dark Production and Decay of Reactive Oxygen Species in Natural Waters*. Golden, CO: Colorado School of Mines.

Mason, R. P., Hammerschmidt, C. R., Lamborg, C. H., Bowman, K. L., Swarr, G. J., and Shelley, R. U. (2017). The air-sea exchange of mercury in the low latitude Pacific and Atlantic Oceans. *Deep Sea Res. Pt. I Oceanogr. Res. Pap.* 122, 17–28. doi: 10.1016/j.dsr.2017.01.015

Miller, G. W., Morgan, C. A., Kieber, D. J., King, D. W., Snow, J. A., Heikes, B. G., et al. (2005). Hydrogen peroxide method intercomparision study in seawater. *Mar. Chem.* 97, 4–13. doi: 10.1016/j.marchem.2005.07.001

Miller, W. L., and Kester, D. R. (1988). Hydrogen peroxide measurement in seawater by (p-hydroxyphenyl)acetic acid dimerization. *Anal. Chem.* 60, 2711–2715. doi: 10.1021/ac00175a014

Moffett, J., and Zafiriou, O. (1990). An investigation of hydrogen peroxide chemistry in seawater by isotope ratio mass spectrometry using 18O2 and H218O2. *Limnol. Oceanogr.* 35, 1221–1229.

Morel, A. (1988). Optical modeling of the upper ocean in relation to its biogenous matter content (case I waters). *J. Geophys. Res. Oceans* 93, 10749–10768. doi: 10.1029/JC093iC09p10749

O'Driscoll, N. J., Siciliano, S. D., Lean, D. R. S., and Amyot, M. (2006). Gross photoreduction kinetics of mercury in temperate freshwater lakes and rivers: application to a general model of DGM dynamics. *Environ. Sci. Technol.* 40, 837–843. doi: 10.1021/es051062y

Oldham, V. E., Lamborg, C. H., and Hansel, C. M. (2020). The spatial and temporal variability of Mn speciation in the coastal Northwest Atlantic Ocean. *J. Geophys. Res. Oceans* 125:e2019JC015167. doi: 10.1029/2019JC015167

Oldham, V. E., Mucci, A., Tebo, B. M., and Luther, G. W. III (2017). Soluble Mn(III)-L complexes are abundant in oxygenated waters and stabilized by humic ligands. *Geochim. Cosmochim. Acta* 199, 238–246. doi: 10.1016/j.gca.2016.11.043

Outridge, P. M., Mason, R. P., Wang, F., Guerrero, S., and Heimbürger-Boavida, L. E. (2018). Updated global and oceanic mercury budgets for the United Nations Global Mercury Assessment 2018. *Environ. Sci. Technol.* 52, 11466–11477. doi: 10.1021/acs.est.8b01246

Qureshi, A., O'Driscoll, N. J., MacLeod, M., Neuhold, Y. M., and Hungerbuhler, K. (2010). Photoreactions of mercury in surface ocean water: gross reaction kinetics and possible pathways. *Environ. Sci. Technol.* 44, 644–649. doi: 10.1021/es9012728

Reynolds, R. W., Rayner, N. A., Smith, T. M., Stokes, D. C., and Wang, W. (2002). An improved *in situ* and satellite SST analysis for climate. *J. Clim.* 15, 1609–1625. doi: 10.1175/1520-0442(2002)015andlt;1609:AIISASandgt;2.0.CO;2

Roe, K. L., Schneider, R. J., Hansel, C. M., and Voelker, B. M. (2016). Measurement of dark, particle-generated superoxide and hydrogen peroxide production and decay in the subtropical and temperate North Pacific Ocean. *Deep Sea Res. Pt. I Oceanogr. Res. Pap.* 107, 59–69. doi: 10.1016/j.dsr.2015.10.012

Rolfhus, K. R. (1998). *The production and distribution of elemental hg in a coastal marine environment* [Ph.D.dissertation]. University of Connecticut, Stamford, CT, United States.

Rolfhus, K. R., and Fitzgerald, W. F. (2004). Mechanisms and temporal variability of dissolved gaseous mercury production in coastal seawater. *Mar. Chem.* 90, 125–136. doi: 10.1016/j.marchem.2004.03.012

Rose, A. L., Moffett, J. W., and Waite, T. D. (2008a). Determination of superoxide in seawater using 2-Methyl-6-(4-methoxyphenyl)-3,7-dihydroimidazo[1,2-a]pyrazin-3(7H)-one *c* chemiluminescence. *Anal. Chem.* 80, 1215–1227.doi: 10.1021/ac7018975

Rose, A. L., Webb, E. A., Waite, T. D., and Moffett, J. W. (2008b). Measurement and implications of nonphotochemically generated superoxide in the equatorial Pacific Ocean. *Environ. Sci. Technol.* 42, 2387–2393. doi: 10.1021/es7024609

Shaked, Y., and Armoza-Zvuloni, R. (2013). Dynamics of hydrogen peroxide in a coral reef: sources and sinks. *J. Geophys. Res. Biogeosci.* 118, 1793–1801. doi: 10.1002/2013JG002483

Soerensen, A. L., Mason, R. P., Balcom, P. H., Jacob, D. J., Zhang, Y., Kuss, J., et al. (2014). Elemental mercury concentrations and fluxes in the tropical atmosphere and ocean. *Environ. Sci. Technol.* 48, 11312–11319. doi: 10.1021/es503109p

Soerensen, A. L., Mason, R. P., Balcom, P. H., and Sunderland, E. M. (2013). Drivers of surface ocean mercury concentrations and air–sea exchange in the west atlantic ocean. *Environ. Sci. Technol.* 47, 7757–7765. doi: 10.1021/es401354q

Soerensen, A. L., Sunderland, E. M., Holmes, C. D., Jacob, D. J., Yantosca, R. M., Skov, H., et al. (2010). An improved global model for air-sea exchange of mercury: high concentrations over the North Atlantic. *Environ. Sci. Technol.* 44, 8574–8580. doi: 10.1021/es102032g

Strode, S. A., Jaegle, L., Selin, N. E., Jacob, D. J., Park, R. J., Yantosca, R. M., et al. (2007). Air-sea exchange in the global mercury cycle. *Glob. Biogeochem. Cycles* 21:GB1017. doi: 10.1029/2006GB002766

Sutherland, K. M., Coe, A., Gast, R. J., Plummer, S., Suffridge, C. P., Diaz, J. M., et al. (2019). Extracellular superoxide production by key microbes in the global ocean. *Limnol. Oceanogr.* 64, 2679–2693. doi: 10.1002/lno.11247

Sutherland, K. M., Grabb, K. C., Karolewski, J. S., Plummer, S., Farfan, G. A., Wankel, S. D., et al. (2020). Spatial heterogeneity in particle associated dark superoxide production within productive coastal waters. *J. Geophys. Res. Oceans* 125:e2020JC016747. doi: 10.1029/2020JC016747

Tseng, C. M., Lamborg, C. H., and Hsu, S. C. (2013). A unique seasonal pattern in dissolved elemental mercury in the South China Sea, a tropical and monsoon-dominated marginal sea. *Geophys. Res. Lett.* 40, 167–172. doi: 10.1029/2012GL054457

Tseng, C. M., Liu, C. S., and Lamborg, C. (2012). Seasonal changes in gaseous elemental mercury in relation to monsoon cycling over the northern South China Sea. *Atmos. Chem. Phys.* 12, 7341–7350. doi: 10.5194/acp-12-7341-2012

Wanninkhof, R. (1992). Relationship between wind-speed and gas-exchange over the ocean. *J. Geophys. Res. Oceans* 97, 7373–7382. doi: 10.1029/92JC00188

Whalin, L., Kim, E. H., and Mason, R. (2007). Factors influencing the oxidation, reduction, methylation and demethylation of mercury species in coastal waters. *Mar. Chem.* 107, 278–294. doi: 10.1016/j.marchem.2007.04.002

Zhang, H., and Lindberg, S. E. (2001). Sunlight and iron(III)-induced photochemical production of dissolved gaseous mercury in freshwater. *Environ. Sci. Technol.* 35, 928–935. doi: 10.1021/es001521p

Zhang, H.-M., Bates, J. J., and Reynolds, R. W. (2006). Assessment of composite global sampling: sea surface wind speed. *Geophys. Res. Lett.* 33:L17714. doi: 10.1029/2006GL027086

Zhang, T., Hansel, C. M., Voelker, B. M., and Lamborg, C. H. (2016). Extensive dark biological production of reactive oxygen species in brackish and freshwater ponds. *Environ. Sci. Technol.* 50, 2983–2993. doi: 10.1021/acs.est.5b03906

Conflict of Interest: The authors declare that the research was conducted in the absence of any commercial or financial relationships that could be construed as a potential conflict of interest.

frontiers in Environmental Chemistry

ORIGINAL RESEARCH
published: 14 May 2021
doi: 10.3389/fenvc.2021.660267

The Effect of Particle Composition and Concentration on the Partitioning Coefficient for Mercury in Three Ocean Basins

Xinyun Cui[1]*, *Carl H. Lamborg*[1], *Chad R. Hammerschmidt*[2], *Yang Xiang*[1] and *Phoebe J. Lam*[1]

[1] Department of Ocean Sciences, University of California, Santa Cruz, Santa Cruz, CA, United States, [2] Department of Earth and Environmental Sciences, Wright State University, Dayton, OH, United States

OPEN ACCESS

Edited by:
Anne L. Soerensen, Swedish Museum of Natural History, Sweden

Reviewed by:
Emily Seelen, University of Southern California, United States
Yanxu Zhang, Nanjing University, China
Seunghee Han, Gwangju Institute of Science and Technology, South Korea

***Correspondence:**
Xinyun Cui
xcui12@ucsc.edu

Specialty section:
This article was submitted to Inorganic Pollutants, a section of the journal Frontiers in Environmental Chemistry

Received: 29 January 2021
Accepted: 12 April 2021
Published: 14 May 2021

Citation:
Cui X, Lamborg CH, Hammerschmidt CR, Xiang Y and Lam PJ (2021) The Effect of Particle Composition and Concentration on the Partitioning Coefficient for Mercury in Three Ocean Basins. Front. Environ. Chem. 2:660267. doi: 10.3389/fenvc.2021.660267

The downward flux of sinking particles is a prominent Hg removal and redistribution process in the ocean; however, it is not well-constrained. Using data from three U.S. GEOTRACES cruises including the Pacific, Atlantic, and Arctic Oceans, we examined the mercury partitioning coefficient, K_d, in the water column. The data suggest that the K_d varies widely over three ocean basins. We also investigated the effect of particle concentration and composition on K_d by comparing the concentration of small-sized (1–51 μm) suspended particulate mass (SPM) as well as its compositional fractions in six different phases to the partitioning coefficient. We observed an inverse relationship between K_d and suspended particulate mass, as has been observed for other metals and known as the "particle concentration effect," that explains much of the variation in K_d. Particulate organic matter (POM) and calcium carbonate ($CaCO_3$) dominated the Hg partitioning in all three ocean basins while Fe and Mn could make a difference in some places where their concentrations are elevated, such as in hydrothermal plumes. Finally, our estimated Hg residence time has a strong negative correlation with average log bulk K_d, indicating that K_d has significant effect on Hg residence time.

Keywords: partitioning, GEOTRACES, particle concentration, particle composition, marine particles, mercury

INTRODUCTION

Removal of trace elements by particle scavenging has a first-order control on their concentrations in the ocean (Anderson, 2014). This is true for mercury (Hg) as well: particle scavenging represents the ultimate sink for Hg from the ocean over centuries, and it is eventually back to the deep mineral reservoir on the timescales of glacial cycle (e.g., Amos et al., 2013). At present, the global burial flux for Hg in ocean sediments is not very well-constrained but likely lies between the value of 1.2 $\mu g\ m^{-2}\ y^{-1}$ in open ocean conditions and 1,200 $\mu g\ m^{-2}\ y^{-1}$ in hyper-accumulating regions like the Antarctic margin (Soerensen et al., 2016; Zaferani et al., 2018). Models have suggested that the global burial flux falls between 1.7 and 7 $\mu g\ m^{-2}\ y^{-1}$ (e.g., Outridge et al., 2018; Tesán Onrubia et al., 2020). Given the current oceanic inventory of Hg, these burial fluxes suggest a residence time of Hg of about 520 years (Outridge et al., 2018).

Mercury likely finds its way from solution onto suspended and sinking particles via processes that John and colleagues have called "regenerative scavenging" (John and Conway, 2014; Lamborg et al., 2016). This mechanism is unlike that exhibited by trace elements such as thorium, for which reversible partitioning appears to occur and results in steady-state particle-/aqueous-phase ratios that are dependent on the composition of the particulate phase (Bacon and Anderson, 1982; Chase et al., 2002; Hayes et al., 2015). In regenerative scavenging, some irreversible process such as biological uptake in surface waters is responsible for the movement of an element from the solution- to the particle-phase initially, and the return reaction is only accomplished when the particles themselves are altered or destroyed, forcing the trace elements (and macro-material) back into solution followed by re-association with the altered particles. A combination of non-reversible and reversible processes broadly describes the nature of all "hybrid-type" elements and thus we should expect that their distribution in and removal from the ocean to be controlled by regenerative scavenging. To best understand and describe such cycling, we would benefit from a study of the kinetics of sorption, desorption, uptake, and remineralization as has been done for thorium (e.g., Lerner et al., 2018). However, unlike for thorium, sources of Hg are not well-known making a mass balance inverse approach more difficult, and we are therefore forced to rely on some proxy information to guide our understanding. The empirical distribution coefficient (K_d) is one such proxy and has been used extensively in modeling studies for a variety of elements (e.g., Honeyman and Santschi, 1989). However, in the case of Hg it has been noted that the value of K_d remains poorly constrained (Zhang et al., 2014). We recently examined the magnitude and variability of K_d of Hg in the Atlantic Ocean using data generated from the U.S. GEOTRACES and found that K_d values were substantially higher than had been assumed in the past and that the particle phase with the strongest apparent affinity for Hg was manganese oxide (MnO_2), followed by iron oxyhydroxide [$Fe(OH)_3$], particulate organic matter (POM), calcium carbonate ($CaCO_3$), and lithogenic particles in decreasing order (Lamborg et al., 2016). However, as the oxide phases represented only a small fraction of total particulate mass (0.8% for iron and 0.1% for manganese), their apparent contribution to overall Hg sorption (if indeed Hg is to be found in marine particles as a result of sorption) was modest. Instead, POM was the most important phase with its sorption fraction at 36%, $CaCO_3$ next at 30%, and lithogenic phase at 29%. These findings supported the generally held hypothesis that POM is highly influential in determining the phase distribution of Hg in the environment (Fitzgerald and Lamborg, 2014). However, it also suggested that the influence of POM is not exclusive and perhaps not even responsible for the majority of Hg partitioned to the particle phase. In this manuscript, we extended the Lamborg et al. (2016) Atlantic examination to two additional basins including the eastern tropical South Pacific Ocean and the Western Arctic Ocean. We also subject the datasets to additional statistical analyses in search of a predictive model of Hg phase partitioning. The analysis here makes use of total dissolved and particulate Hg but could be performed on monomethylmercury as well. The contributions of monomethylmercury to total dissolved and particulate Hg are relatively small and so were not removed prior to our calculations. Therefore, the K_d values derived using total Hg values are close approximations for the Hg(II) form.

METHODS

Data Used

All datasets used here are from U.S. GEOTRACES cruises, including the East Pacific zonal transect (nickname EPZT; GEOTRACES transect number GP16, cruise identifier TN303), the North Atlantic zonal transect (NAZT, GA03; KN199-04 and KN204-1), and the Western Arctic (GN01; HLY1502). We used data from 58 stations in total with 22 in the Pacific, 17 in the Atlantic and 19 stations in the Arctic Ocean (**Figure 1**). All data used were from the BCO-DMO data repository.

The Hg data have all been published previously, with the dissolved and particulate total mercury data from Agather et al. (2019) (GN01) and Bowman et al. (2015, 2016) (GA03 & GP16). The published particle mass and composition data are from Lam et al. (2015, 2018), Xiang and Lam (2020). Due to lack of access to large-size-fraction (>51 μm; LSF) samples for Hg analysis, we only used small-size-fraction (1–51 μm; SSF) particle composition and particulate Hg data in our mercury partition coefficient analysis. Note that the original collected data are linked with "flags" indicating the data quality, in order to have convincing results, we made sure that all parameters we used were identified as either "good" (Quality Flag = 2) or "possibly good" (QF = 3) quality at the same depth.

Partition Coefficient (K_d) Analysis

Here, the partition coefficient (K_d) is defined as the apparent affinity of mercury for marine particles. This concept was inspired from studies of Bacon et al. (1976) and Baskaran and Santschi (1993). K_d is calculated as:

$$K_d = \frac{C_p}{C_d} \times \frac{1}{SPM} \quad (1)$$

where C_p and C_d represent the concentration of Hg in particulate and dissolved phases, respectively, and SPM is the suspended particulate mass (kg L^{-1}). This results in K_d having units of volume per mass, conventionally as L kg^{-1}. Here C_d represents the concentration passing a 0.2-μm filter and therefore includes both dissolved and colloidal Hg. Particle sampling depths at each station were not exactly the same as the dissolved phase, thus, to calculate partition coefficients, we estimated concentrations of the dissolved phase by linear interpolation (using the MATLAB routine "interp1") to the depths of particle phase samples.

In order to better understand how bulk partition coefficients relate to particle composition, a six-end member mixing model was applied, which is similar to the one developed by Hayes et al. (2015) for thorium isotopes. The contribution of each major

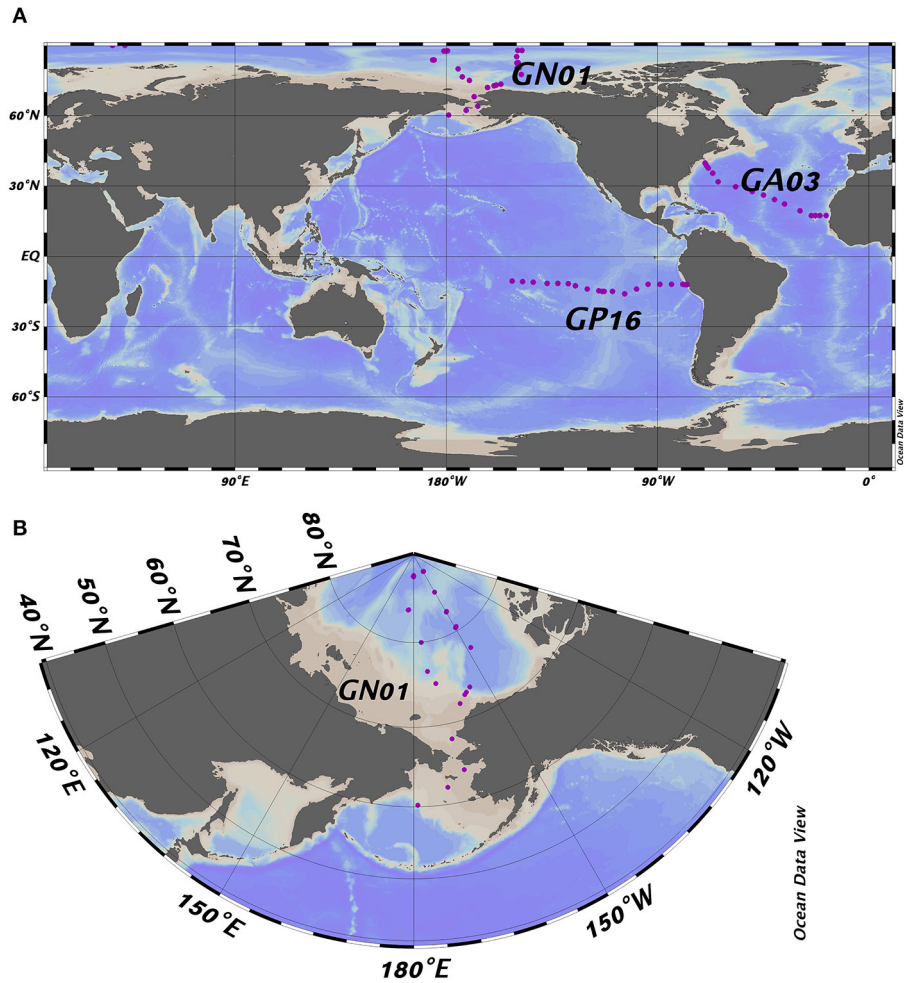

FIGURE 1 | (A) Full map of the three GEOTRACES cruises including GP16, GA03, and GN01; **(B)** Zoomed in map of GN01. Purple dots represent the location of the sampling stations referred to in the text.

particle phase to the measured bulk K_d is represented by the following formula:

$$K_d = \sum_{1}^{6} (K_d)_i \cdot f_i = (K_d)_1 \cdot f_1 + (K_d)_2 \cdot f_2 + (K_d)_3 \cdot f_3 + (K_d)_4 \cdot f_4 + (K_d)_5 \cdot f_5 + (K_d)_6 \cdot f_6 \quad (2)$$

where K_d is the observed bulk partition coefficient, $(K_d)_i$ is the apparent partition coefficient for pure phase i, f_i is the fraction of certain particle phase i over particulate mass, and I = 1(POM), 2($CaCO_3$), 3(Opal), 4(lithogenic), 5(MnO_2), 6($Fe(OH)_3$). The $(K_d)_i$, which we and Hayes call the intrinsic K_d, was calculated using non-negative least-squares regression ("lsqnonneg") in MATLAB for individual basin datasets, as well as some sub-basin datasets:

$$\begin{bmatrix} f_1^1 & f_2^1 & f_3^1 & f_4^1 & f_5^1 & f_6^1 \\ f_1^2 & f_2^2 & f_3^2 & f_4^2 & f_5^2 & f_6^2 \\ f_1^3 & f_2^3 & f_3^3 & f_4^3 & f_5^3 & f_6^3 \\ \vdots & \vdots & \vdots & \vdots & \vdots & \vdots \\ f_1^N & f_2^N & f_3^N & f_4^N & f_5^N & f_6^N \end{bmatrix} \times \begin{bmatrix} (K_d)_1 \\ (K_d)_2 \\ (K_d)_3 \\ \vdots \\ (K_d)_6 \end{bmatrix} = \begin{bmatrix} K_d^1 \\ K_d^2 \\ K_d^3 \\ \vdots \\ K_d^N \end{bmatrix} \quad (3)$$

To estimate the standard error of the derived intrinsic K_d values, we used the jackknife re-sampling technique suggested by Hayes et al. (2015) and Efron and Stein (1981).

Principal Component Analysis of Bulk K_d and Particle Composition

We performed PCA on the partition coefficient and particle composition data to see if a few principal components (PCs), or linear combinations of the original variables, could explain a large proportion of the total variance in dataset being considered. Therefore, PCA was conducted on the following seven variables: bulk log K_d, f_{POM}, f_{CaCO3}, f_{opal}, $f_{lithogenic}$, f_{MnO2}, $f_{Fe(OH)3}$, in order to analyze the relationship between bulk K_d and particle

composition fraction among three different ocean basins. Since the units and magnitude of the 7 variables are different, prior to PCA the sample data were mean-centered and normalized by standard deviation ("zscore" function in MATLAB). The PCA itself was performed using the MATLAB function "pca". In addition, we constructed biplots of loadings and scores associated with PC's 1 and 2 to visualize the results, which interprets the correlation for each of the original variables as well as the direction of increasing values.

Principal Component Analysis of Residual K_d and Particle Composition

We did linear regression to model the relationship between SPM and bulk K_d. The residuals K_d data were calculated as the vertical distance in the Y-axis between each data point and the fitted line and represent the portion of K_d not explained by SPM. Following the same data processing strategy as in section Principal Component Analysis of bulk K_d and particle composition, we performed PCA on the residuals and particle composition data to examine whether this would better reveal a particle composition effect.

RESULTS AND DISCUSSION

In this section, we present our data results and employ a model to demonstrate the particle concentration and composition effect on Hg partitioning. In addition to discussion on some special features of K_d, we extended the study of K_d on Hg residence time at the end.

Dissolved and Particulate Hg Profiles

The mean and median concentrations of dissolved and particulate total mercury for the three ocean basins were calculated in the surface (above 100 m), as well as every 500 m depth in the deep water (below 100 m; **Figure 2**). Overall, the concentration of dissolved Hg in the Arctic was the highest (around 1.1 pM) at the surface, as a result of riverine input, atmospheric deposition and ice melt (e.g., Fitzgerald et al., 2005; Agather et al., 2019), and decreased to ∼0.5 pM at depth. In contrast, the dissolved Hg in the Pacific and Atlantic Ocean was distributed in a more nutrient-like way, characterized by a slight increasing trend with depth. Note that there was a maximum at 3,500 m in the Atlantic is due to the influence of the TAG hydrothermal vent where total dissolved Hg increased to 13 pM.

The particulate Hg started with the highest concentration at the surface in all basins, attenuating quickly below the photic zone and reaching the minimum at about 1,000 m. In the Pacific Ocean, a strong hydrothermal plume led to abnormally high concentrations of particulate Hg in deep water (between 2,500 and 3,500 m), accompanied by high variability as well. Similarly, the SPM concentration in the three ocean basins attenuated with depth. At the surface, the mean SPM concentration in the Arctic was around 6 times greater than that in the Pacific and Atlantic, resulting from the extremely high SPM over the continental shelf (Xiang and Lam, 2018). The median surface SPM concentration in the Arctic was the lowest of the three basins, however, reflecting the very oligotrophic Canadian Basin in the Western Arctic Ocean (Xiang and Lam, 2020). A maximum occurred in the deep ocean of the Atlantic due to the influence of strong bottom nepheloid layers in the Deep Western Boundary Current (Lam et al., 2015).

Bulk Partition Coefficient (K_d) for the Three Ocean Basins

Bulk partition coefficient values varied widely over the whole dataset, ranging in order from 10^4 to 10^8 L kg^{-1} (**Figure 3**). In the Pacific, the bulk partition coefficients were extremely high, with an average order of magnitude of 10^7 (range: 5.05×10^5-1.63×10^8 L kg^{-1}; log K_d = 5.70–8.21). The bulk K_d values from the Atlantic, in contrast, were lowest and ranged from 2.60×10^5 to 6.73×10^7 L kg^{-1} (log K_d = 5.41–7.83). Compared to these two ocean basins, the K_d value from the Arctic Ocean were modestly lower and ranged from 9.70×10^4 to 6.99×10^7 L kg^{-1} with an average on the order of 10^6. Summary K_d statistics are presented in **Supplementary Table 1**. As previously noted by Lamborg et al. (2016), these K_d values are substantially higher than those previously reported for freshwaters, sediment porewaters over continental shelves (∼10^4 L kg^{-1}) (e.g., Hammerschmidt and Fitzgerald, 2004) and coastal waters (10^5-10^6 L kg^{-1}) (e.g., Balcom et al., 2008).

Intrinsic K_d

End-member coefficients, or intrinsic K_d, were calculated for each of the six particle phases in the SSF in all three cruises, including POM, $CaCO_3$, opal, lithogenic, Mn oxides, and Fe oxyhydroxides. The value of intrinsic K_d and composition fractions are summarized in **Table 1**. Overall, the intrinsic K_d values varied between ocean basins. One commonality, however, was that the intrinsic K_d for opal could not be defined using this method in any of the three ocean basins. The intrinsic K_d for POM, $CaCO_3$, and lithogenic phases could always be estimated, but had different values. As for Fe and Mn, the contribution to sorption of Hg could be evident when their concentrations were high, typically observed in hydrothermal vents. Otherwise, their influence on Hg partitioning was negligible.

If there is really is such a thing as an "intrinsic K_d" that expresses the stickiness of Hg to a measured particle phase, the calculated values should be homogeneous everywhere in the ocean. However, an examination of our results suggests that this might not be true. We applied the Z-test based on intrinsic K_d values and their standard deviations (**Table 1**), setting the confidence interval to 95%, to test whether the intrinsic K_d values for each particle phase were significantly different between basins. Generally speaking, intrinsic K_d between ocean basins were similar for some phases but significantly different for others. For instance, intrinsic K_d values of POM in three ocean basins were significantly different ($P < 0.05$). In contrast, the values for $CaCO_3$ of three ocean basins were statistically indistinguishable ($P > 0.05$). This suggests that the precise composition of POM with respect to its ability to scavenge Hg varies between ocean basins but that $CaCO_3$ does not (or varies less). Since the three cruises were sampled in different seasons and different environments, the dominant plankton were likely not the same in the three ocean basins, and the components of collected POM

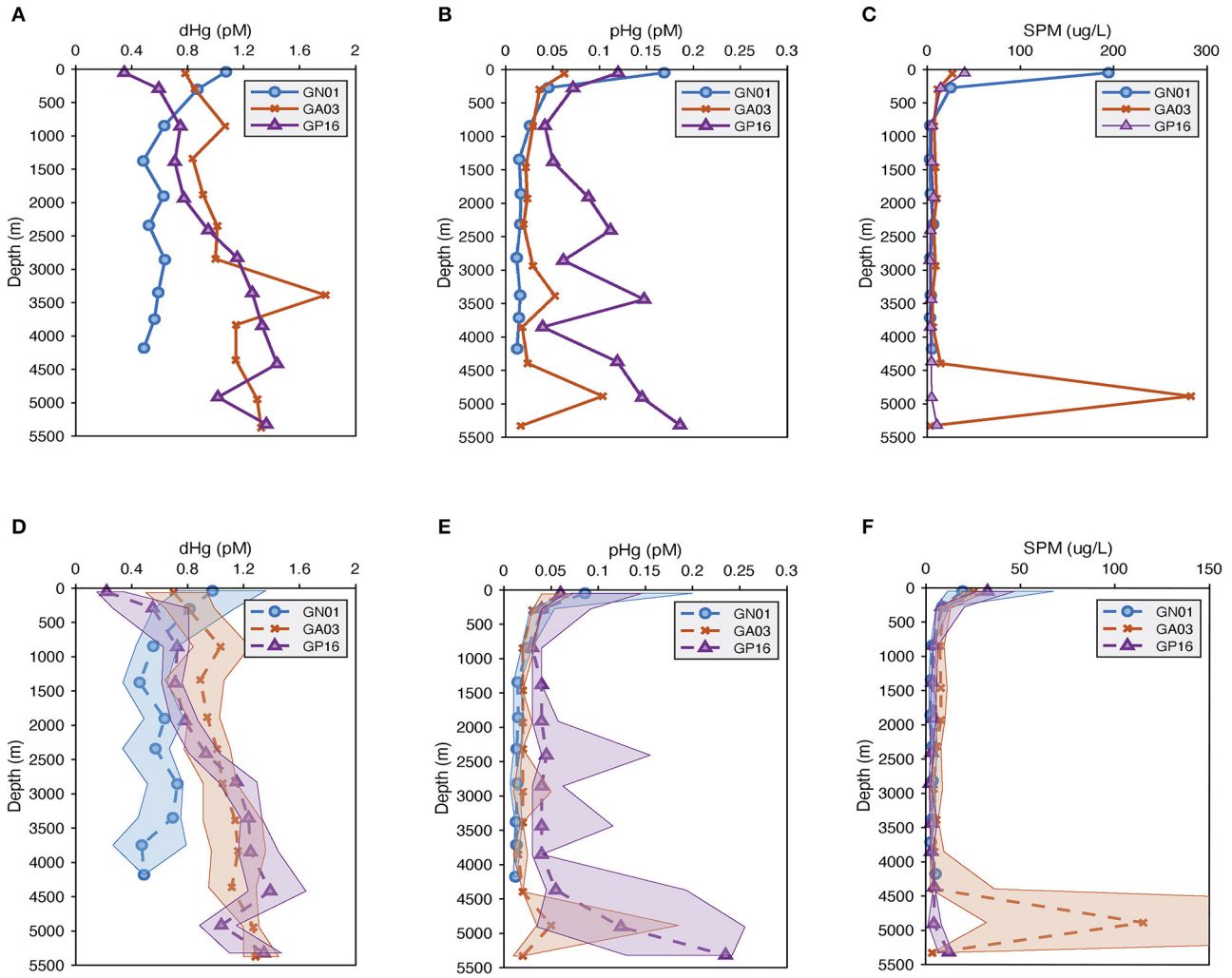

FIGURE 2 | (A–C) are average vertical profiles of dissolved and particulate Hg (pM) as well as suspended particulate matter (SPM) (μg/L) from three US GEOTRACES cruises; while **(D–F)** are median vertical profiles of dissolved and particulate Hg (pM) as well as suspended particulate matter (SPM) (μg/L), and the shade is 25 to 75 percentiles for the median plots.

presumably varied with different plankton. The intrinsic K_d of the lithogenic phase in the Arctic Ocean was different from those in the Pacific and Atlantic Oceans. This is perhaps not surprising, since "lithogenic particles" is a category that represents a diverse range of aluminosilicate minerals, which might be expected to have different sorption characteristics for Hg (e.g., Biscaye, 1965; Darby, 1975). Interestingly, intrinsic K_d values of Mn had no significant difference ($P > 0.05$) in the Pacific and Arctic Ocean, while intrinsic K_d values of Fe were significantly different ($P < 0.05$) between the Pacific and the Atlantic Ocean. The Fe intrinsic K_d differences between basins implies a qualitative difference in the Fe itself, but this remains to be explored.

PCA of Hg Partitioning and Particle Composition

The PCA results are summarized in **Table 2**, which includes 7 variables (the bulk K_d value and the fraction of the six particle fractions), loadings of the first three principal components (PC) and their contribution in explaining the total variance. In the East Pacific, the first three principal components explained 77.64% of variation of the seven variables with 35.33% explained by PC1, 22.78% explained by PC2, and 19.53% explained by PC3. The highest loadings for PC1 were the fractions of Fe and Mn, both of which were positively correlated with bulk K_d, which could result from the hydrothermal plume (Lam et al., 2018). For PC2, the relative fractions of POM had strong positive loadings, while f_{CaCO3}, f_{litho}, and f_{opal} were negatively loaded, which means the organic matter was anticorrelated with minerals. This negative correlation reflects the variation in depth: decreasing POM and increasing lithogenic particles with depth (Lam et al., 2018). The fractions of $CaCO_3$ and opal were strongly anticorrelated in PC3 (**Table 2, Figure 4**), which might reflect the variation of region: higher opal in the coastal region, abundant $CaCO_3$ in the open ocean (Lam et al., 2018). In the Atlantic, 63.85% of

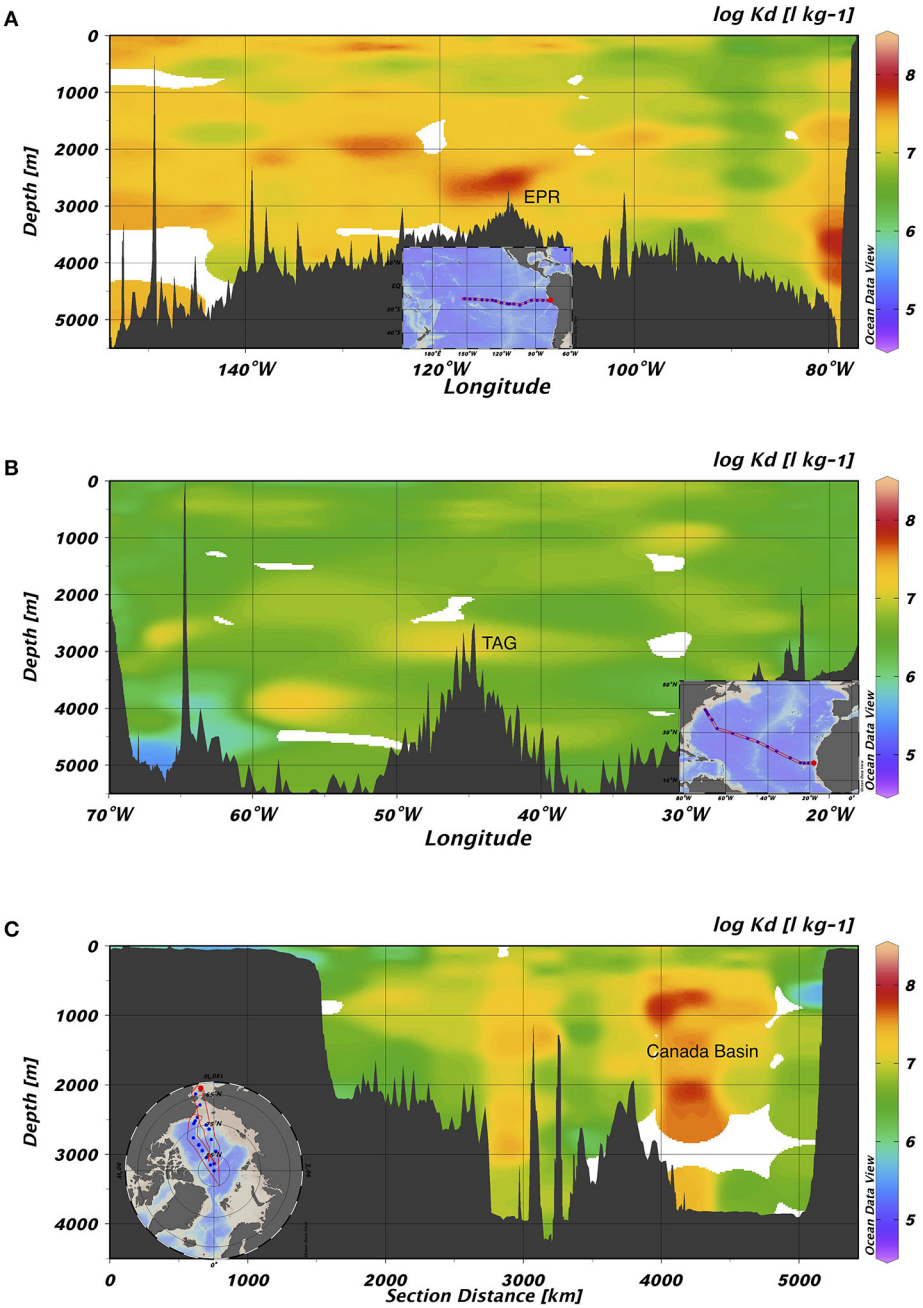

FIGURE 3 | Section views of log Kd (L kg^{-1}) values in **(A)** GP16, **(B)** GA03, and **(C)** GN01. The highest value on average was found in the Pacific, while the lowest on average was found in the Atlantic. EPR represents East Pacific Rise; TAG represents Trans-Atlantic Geotraverse hydrothermal field located on Mid-Atlantic Ridge.

total variance was explained by the first three components with 30.56% explained by PC1, 17.64% explained by PC2, and 15.65% explained by PC3. Based on our observations, in PC1, bulk K_d and the fractions of POM were anticorrelated with fractions of lithogenic particles and Mn, reflecting the depth variation of POM and lithogenic particles (Lam et al., 2015). For PC2, the fraction of $CaCO_3$ was strongly correlated with bulk K_d, and for PC3 the fractions of opal were anticorrelated with Fe and Mn. Additionally, the first three principal components of the Arctic dataset explained 77.92% of the total variance, where PC1 explained 39.15%, PC2 explained 35.61%, and PC3 explained 13.16%. The highest loadings of PC1 were observed from the fractions of lithogenic particles and POM, which could be the consequence of variations in depth and/or region (Xiang and Lam, 2020), whereas PC2's highest loadings were mainly from bulk K_d, and the fractions of Mn, $CaCO_3$ and opal. The f_{CaCO3}

TABLE 1 | The log intrinsic K_d^i (l kg^{-1}) of Hg for six particle composition in the small size fraction (SSF) in the Pacific, Atlantic, and Arctic ocean, respectively, and their relative standard deviation (r.s.d.) as well as particle composition mass contribution (f; %).

	Pacific			Atlantic			Arctic		
	log K_d^i	r.s.d. (%)	f_i (%)	log K_d^i	r.s.d. (%)	f_i (%)	log K_d^i	r.s.d. (%)	f_i (%)
POM	7.24	0.40	48 ± 23	6.67	0.64	42 ± 21	6.94	1.24	45 ± 23
$CaCO_3$	7.02	0.56	33 ± 19	6.86	1.13	28 ± 11	8.23	15.56	2 ± 2
Opal	n.a.	n.a.	9 ± 8	n.a.	n.a.	4 ± 3	n.a.	n.a.	17 ± 13
Lithogenic	7.37	1.57	6 ± 12	6.29	5.04	25 ± 20	6.50	0.78	34 ± 27
Mn	7.25	27.45	0.4 ± 0.9	n.a.	n.a.	0.1 ± 0.2	7.90	19.46	2 ± 2
Fe	8.20	2.08	3 ± 10	6.75	2.05	0.7 ± 5.0	n.a.	n.a.	1 ± 1

n.a., not available yet.

TABLE 2 | The first three principal component loadings, percentage of variance explained by each principal component, and their cumulative percentage of total variance including bulk K_d and six particle compositions in the small size fraction of particles.

	Variables	PC1	PC2	PC3
Pacific	Bulk K_d	0.4079	0.2223	0.119
	f_{POM}	−0.4285	0.5769	−0.0387
	f_{CaCO3}	0.1283	−0.4739	0.6401
	f_{Opal}	−0.0138	−0.276	−0.6346
	f_{Litho}	0.1558	−0.4298	−0.3948
	f_{Mn}	0.5604	0.2188	−0.0613
	f_{Fe}	0.5432	0.2906	−0.1107
	% of variance	35.33	22.78	19.53
	Cumulative %	35.33	58.11	77.64
Atlantic	Bulk K_d	0.331	0.4279	0.2871
	f_{POM}	0.6219	−0.3042	−0.1263
	f_{CaCO3}	−0.0499	0.8387	−0.1478
	f_{Opal}	−0.225	0.0063	−0.4912
	f_{Litho}	−0.6164	−0.1421	0.1033
	f_{Mn}	−0.2649	−0.0137	0.3205
	f_{Fe}	0.0196	−0.0208	0.7247
	% of variance	30.56	17.64	15.65
	Cumulative %	30.56	48.2	63.85
Arctic	Bulk K_d	−0.0604	0.6125	−0.2405
	f_{POM}	−0.5367	0.09	−0.2946
	f_{CaCO3}	0.1441	0.4497	0.4808
	f_{Opal}	−0.2857	−0.4226	0.5921
	f_{Litho}	0.5816	0.0533	−0.1112
	f_{Mn}	−0.167	0.4706	0.4886
	f_{Fe}	0.4897	−0.1077	0.1501
	% of variance	39.15	25.61	13.16
	Cumulative %	39.15	64.76	77.92

and f_{Mn} were positively correlated with bulk K_d while f_{opal} was negatively correlated with bulk K_d. PC3's highest loadings were the fractions of Mn, $CaCO_3$ and opal which were positively correlated with each other.

From the biplots of scores and loadings (**Figure 4**), the K_d loadings were strongest with PC1 in the Pacific, and PC2 in the Atlantic and Arctic. As already noted above, PC1 in the Pacific was most strongly associated with Fe and Mn oxides, implying a significant influence of those phases on the overall value of K_d. This is likely due to the influence of hydrothermal Fe- and Mn-rich particles sorbing Hg from seawater. In the Atlantic and Arctic, PC2 was also strongly loaded with $CaCO_3$, and relatively poorly loaded for POM, implying a major role of $CaCO_3$ in Hg sorption in those basins, but less of a role for POM.

Furthermore, the biplots loadings (**Figure 4**) for each ocean basins suggested that the PC1 and PC2 could be driven by different variables. The significant strong positive loadings in PC1 for both Mn, Fe and bulk K_d in the Pacific imply that this PC was related to some natural processes that affected bulk K_d in a similar manner with Mn and Fe in the Pacific. Similarly, PC2 has strong positive loadings for Mn and bulk K_d in the Arctic also suggested these two variables behaves similarly and closely correlated with each other, since the high absolute and relative concentrations of manganese oxides were observed in the Arctic halocline and deep water, leading to strong scavenging of various elements (Xiang and Lam, 2020). However, there is no significant correlation between f_{MnO2} and log K_d in the Atlantic, suggesting that f_{MnO2} can't be the only control on log K_d globally. Meanwhile, f_{MnO2} is very low in the Atlantic, possibly accounting for its little influence in scavenging Hg.

Particle Concentration and Composition Effects on Partition Coefficient

Particle Concentration Effect

We began our investigation of the potential drivers of K_d by examining the effect of particle concentration on the partitioning of Hg. The linear regression model in **Figure 5** shows the relationship between log SPM (μg L^{-1}) and log bulk K_d (L kg^{-1}) for the three ocean basins. A significant inverse correlation was observed in all basins, which is consistent with the findings reported by Moran et al. (1996). Similar inverse relationships were observed between log K_d of ^{210}Pb and ^{210}Po and SPM in these transects (Tang et al., 2017; Bam et al., 2020). The inverse relationship between K_d and SPM, also known as "the particle concentration effect" (Honeyman et al., 1988), can be explained by at least three mechanisms. The first one centers

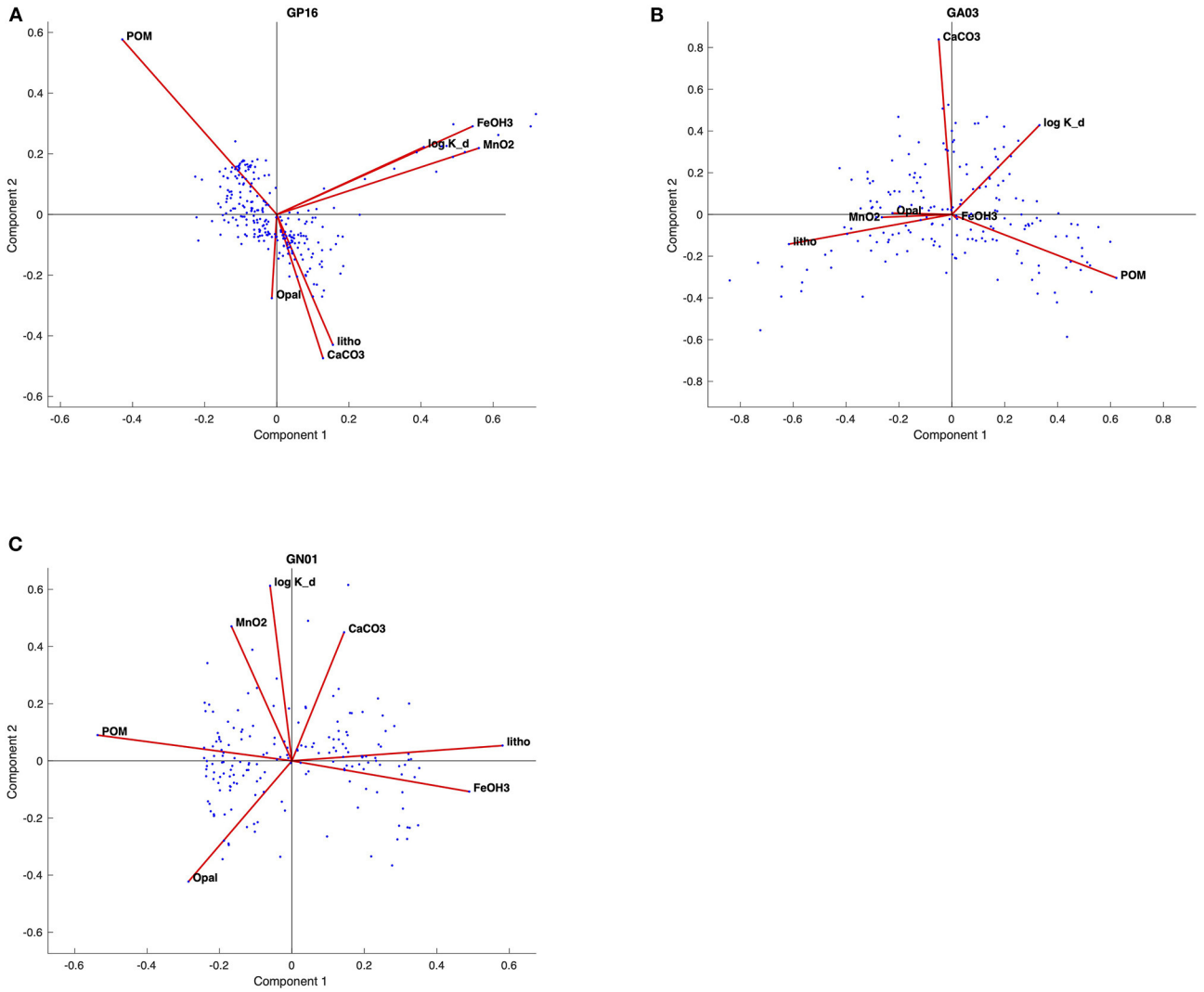

FIGURE 4 | Biplots of principal component (PC1 and PC2) for the **(A)** GP16, **(B)** GA03, and **(C)** GN01, respectively. The red lines represent loadings for each variable; blue dots represent the scores for each observation.

around the effects of colloidal chemistry on metal distributions within the particulate phase (e.g., Honeyman and Santschi, 1989; Benoit and Rozan, 1999; Bam et al., 2020). Assuming Hg species sorb to colloids and as colloids are too small to be collected by conventional filtration, GEOTRACES sampling methods tend to count colloids as "dissolved" and thereby result in a smaller K_d value for Hg than the ideal circumstance when colloids are properly accounted for in the particle pool. Furthermore, the proportion of colloids over the particulate mass is generally thought to increase with SPM concentrations, leading to a negative K_d vs. SPM slope (Moran et al., 1996). Indeed, based on two observed relationships between colloidal and SPM concentrations, Moran et al. (1996) modeled the percent of colloidal Hg on the particle mass and found that it tends to increase with SPM concentrations if SPM are $<10^4$ μg L^{-1}. A second possibility is that particle mass is not a good proxy for available particle surface sorption sites for Hg. The material reported here as SPM at a specific location is made up of many individual particles that vary in size, with the number of small particles generally being much greater than the number of large particles (e.g., Stemmann and Boss, 2012). Particle size distributions vary between different samples, and therefore each SPM sample has varying proportions of large and small constituents. Samples in high productivity regions with high SPM can also be expected to have a relatively high proportion of large particles (e.g., diatom cells), while low SPM samples are more prevalent in oligotrophic regions where cells are mostly small (e.g., picoplankton). Thus, we might expect that the smaller the SPM is, the more Hg scavenged by a given particle mass as a consequence of larger surface area-to-volume ratios for smaller particles. As area-to-volume ratios scale with the inverse of particle size, one might predict that a bulk K_d

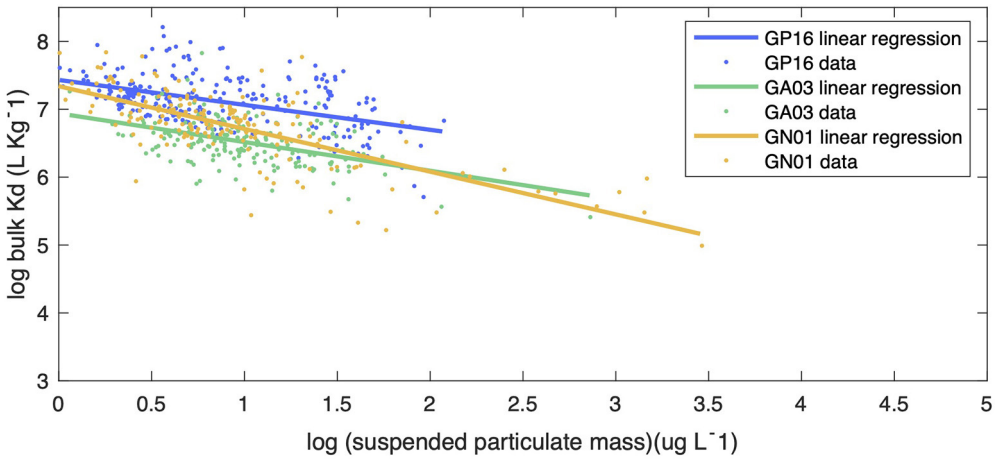

FIGURE 5 | The linear regression between log bulk Kd (l kg^{-1}) and particle concentration (log SPM in ug l^{-1}) in the small size fraction for Pacific (blue line), Atlantic (green line), and Arctic (yellow line) oceans. The slopes of linear regression for each ocean basins were −0.367, −0.423, −0.629, with statistics R-squared equals 0.2155, 0.2218, 0.5338, respectively. The slope of the Arctic was significantly different from the slopes of the Pacific and the Atlantic by applying *Z*-test, with statistics $P < 5\%$.

vs. SPM plot should resemble an inverse curve. However, no discernible trend between the total SPM concentration (Total SPM = SSF SPM + LSF SPM) and fSSF, the mass fraction of small particles over total particles (fSSF = SSF SPM/Total SPM) during the same cruises, was evident (**Figure 6**). The fSSF is an analog to the slope of the particle mass-size spectrum (Xiang et al., 2020) or the number-size spectrum (e.g., Cael and White, 2020), a higher fSSF implies more abundance of small particles. Hence, it is likely that the particle size did not change with SPM concentrations in particles. Therefore, the "particle-size hypothesis" appears unsupported by these datasets. A third possibility for the apparent particle concentration effect is a kinetic explanation. The ratio of the adsorption to desorption rate constant, normalized by SPM, can be thought of, in some circumstances, as a kinetic representation of K_d (Honeyman et al., 1988). In a kinetic study of the adsorption and desorption of thorium, both the adsorption and desorption rate constants were found to increase with SPM, but at different rates, such that their ratio normalized by SPM also decreased with SPM, much like the classic particle concentration effect (Lerner et al., 2017). Although this kinetic explanation for the apparent particle concentration effect has so far only been observed for thorium, it is a potential alternative to explain the particle concentration effect that does not rely on colloids. This then leaves the influence of colloids, and perhaps the kinetics of particle attachment and detachment, as the possible explanations for the K_d vs. SPM trends observed in our data.

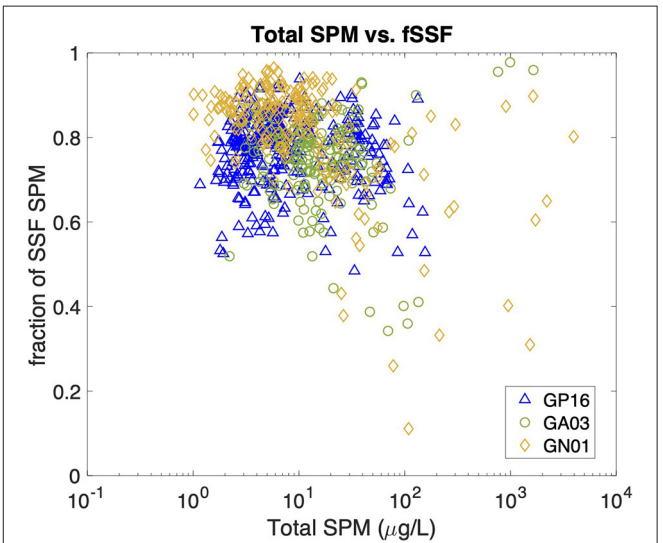

FIGURE 6 | Scatter plot between Total SPM concentrations (unit: μg/L) and the fraction of SSF particles (fSSF) in all three cruises. The Total SPM is calculated as SSF SPM+ LSF SPM, and the fSSF as SSF SPM/Total SPM.

Particle Composition Effect

Additionally, we argue that variations in bulk K_d also partly result from the particle composition effect. The decreasing trend in bulk K_d with SPM (**Figure 5**) clearly shows the influence of SPM, but the variations around this trend are still worth being investigated. We assumed this variation is from particle composition. Different statistical methods were employed to obtain the information about the impact of particle composition on partition coefficient.

In some specific regions, the value of bulk K_d was clearly driven by the SPM concentration. For example, high concentrations of SPM in the deep water of the western Atlantic (Lam et al., 2015) corresponded to low bulk K_d. Similarly, the Arctic continental shelf also had abundant SPM (Xiang and Lam, 2020), coinciding with low bulk K_d values. At the other end of the SPM spectrum, high K_d values were found in Arctic mid-waters where SPM was low. This was not universally true, however, as demonstrated by much higher bulk K_d in relatively low SPM

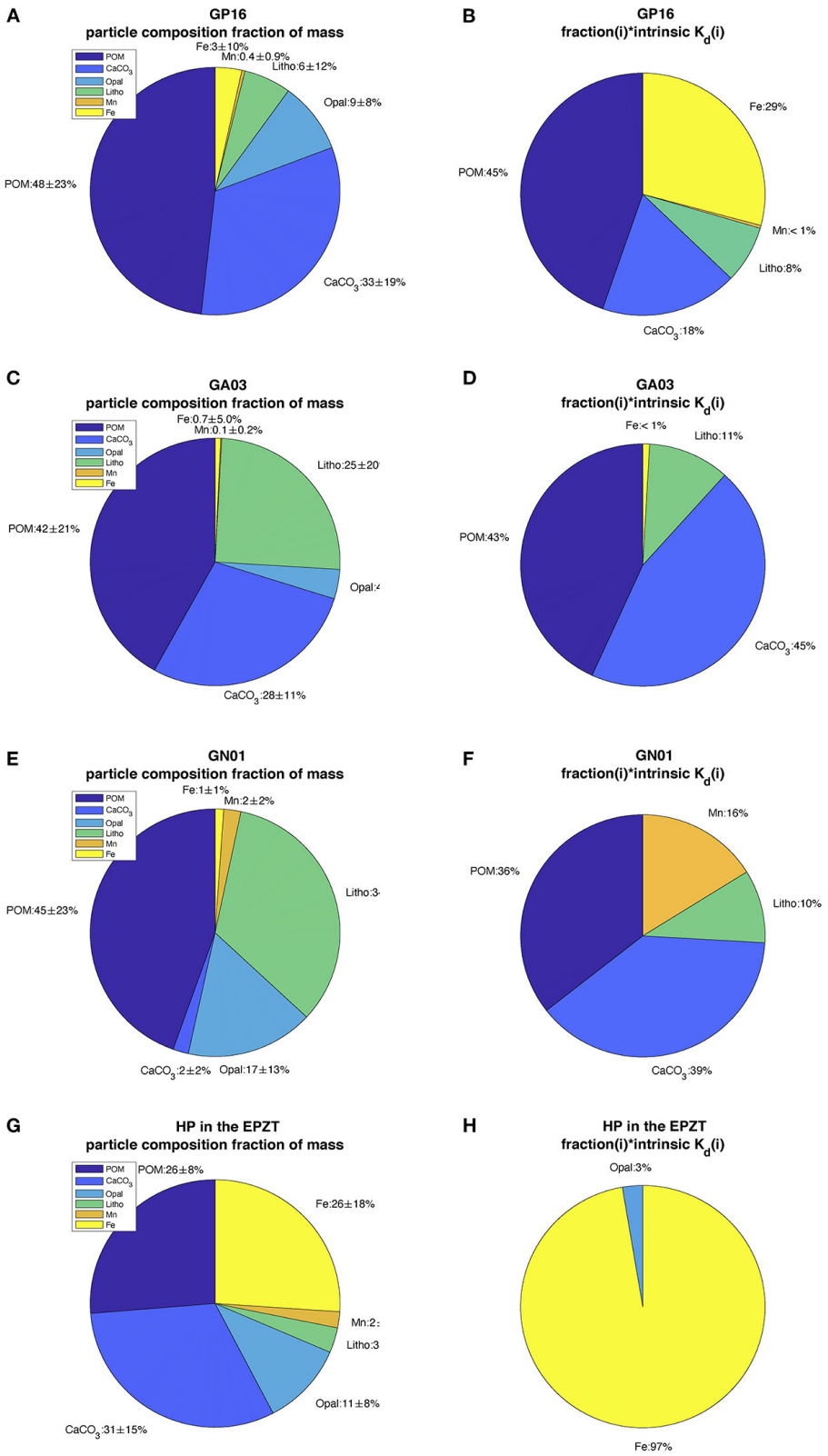

FIGURE 7 | The pie charts **(A,C,E,G)** described the mean and standard deviation of particle composition fraction of mass in the Pacific (GP16), Atlantic (GA03), Arctic (GN01), and hydrothermal plume in EPZT; chart **(B,D,F,H)** described the mean proportion of each composition fraction multiplying their intrinsic Kd in four regions above, respectively.

water in the Canada Basin in the Western Arctic Ocean. We take this to be evidence of another factor that influences the bulk K_d, namely the particle composition effect. This effect is described by the intrinsic K_d values in each basin and which can be better understood by multiplying the mean compositional fraction for each particle phase by the intrinsic K_d we calculated (**Figure 7**). The corresponding value, when compared to those of other phases, expresses the relative importance for each phase in sorbing Hg from solution (if that kind of chemistry does in fact occur). The resulting pie charts indicate that for these three oceans, POM and $CaCO_3$ dominate Hg partitioning. This trend holds across all the basins despite there being large variations in the abundance of $CaCO_3$ as a result of compensatory changes in the intrinsic K_d for that phase (**Table 1**). Moreover, the contributions of lithogenic material to bulk K_d were also quite similar in the three oceans, with percentages from 9 to 11%, while the fraction of it was distinct everywhere.

It is worth noting that Fe contributions to bulk K_d were quite variable and were high only in the Pacific, caused by relatively high Fe fraction in particles released in a hydrothermal plume. Similarly, the abundant Mn observed in the Arctic also accounted for a large part of the bulk K_d. Therefore, we can see that Mn and Fe had strong adsorption affinities to Hg in some regions despite their relatively low concentration level in particles. The strong sorption affinity of Mn is apparently not only for Hg but also to ^{234}Th, ^{231}Pa, ^{210}Po, and ^{210}Pb (Hayes et al., 2015; Lerner et al., 2018; Bam et al., 2020). As noted above and discussed below, there was no resolvable intrinsic K_d value for opal and so it does not appear in the pie charts of **Figure 7**. This implies that opal plays a minor role in the partitioning of Hg into the particle phase, at least in these three basins.

In **Figure 5**, bulk K_d data from the three oceans were scattered around the regression lines with SPM. We examine the hypothesis that the residuals to the SPM relationship, which are the vertical distance between each data point and the regression lines, might be explained by particle composition. Hence, we applied PCA to see the relationship between residuals of log K_d and particle phases. The PCA results are presented in **Supplementary Table 2**. In the Pacific, the highest loadings for PC1 were the fractions of Fe and Mn, which were positively associated; for PC2, POM, $CaCO_3$ and the residuals had the highest loadings, where POM correlated positively with residuals whereas $CaCO_3$ correlated negatively with residuals. Information from PC1 suggests that POM was also a crucial factor that led to the variance of K_d in the Atlantic; $CaCO_3$ had a positive association with residuals in the Arctic from PC2.

Besides PCA, we applied the least squares regression of particle composition fraction to the K_d residuals of the SPM regression, which we called the "intrinsic residual K_d" (K_d^*) (**Table 3**).

$$residuals = \sum_{1}^{6} \left(K_d^*\right)_i \cdot f_i = \left(K_d^*\right)_1 \cdot f_1 + \left(K_d^*\right)_2 \cdot f_2 + \left(K_d^*\right)_3 \cdot f_3 + \left(K_d^*\right)_4 \cdot f_4 + \left(K_d^*\right)_5 \cdot f_5 + \left(K_d^*\right)_6 \cdot f_6 \quad (4)$$

TABLE 3 | The coefficients to the least squares regression of the residual K_d^* (L kg^{-1}) of Hg for six particle composition fractions (Equation 4) in the small size fraction (SSF) in the Pacific, Atlantic, and Arctic ocean, respectively.

	Pacific K_d^*	Atlantic K_d^*	Arctic K_d^*
POM	2.21	2.12	3.11
$CaCO_3$	−0.14	1.41	0.45
Opal	−0.69	−3.58	−1.64
Lithogenic	2.00	0.52	0.40
Mn	−10.97	4.39	−0.93
Fe	10.18	1.29	14.20

The statistical R squared for each ocean were 0.3972, 0.0625, 0.1288.

In general, the particle composition explained the 39.72% of variance of residuals in the Pacific Ocean, 6.25% of variance of residuals in the Atlantic Ocean and 12.88% of variance of residuals in the Arctic Ocean. In the Pacific, Mn and Fe had a strong correlation with residuals compared with other particle phases. Mn could result in lower K_d while Fe contributed to a higher K_d. $CaCO_3$ and lithogenic particles have little effect in driving bulk K_d to be lower than the regression line (**Figure 5**), while POM has a positive feedback on bulk K_d. In the Atlantic, POM, $CaCO_3$, lithogenic phase and Fe lead to positive residuals that makes bulk K_d higher above the fitting line (**Figure 5**). Additionally, POM, lithogenic phase have strong positive correlation with residuals in the Arctic, while Mn led to smaller K_d values in the Arctic.

By adding R-squared values that are generated from the linear regression model of SPM and K_d (**Figure 5**) to R-squared values from least squares regression above, we could have a general view of how much variation of partition coefficient that can be demonstrated by both particle concentration and composition effect. Overall, the SPM combined particle composition explained the 61.27% of variance of K_d in the Pacific, 28.43% of variance of K_d in the Atlantic, and 66.26% of variance of K_d in the Arctic. However, these values were possibly overestimated, since SPM and composition effect are not completely independent in our model. Despite that residuals to the SPM regression remove the effect of particle concentration which represents a pure composition effect on K_d, the regression of log K_d against SPM carries some particle composition effect information which we don't know how to eliminate so far.

Special Features: Hydrothermal Plume and Coast

Part of the reason for the exceptionally high K_d values observed from the EPZT cruise dataset was the presence of high Fe at stations/depths associated with the continental shelf and East Pacific Rise hydrothermal plume. Thus, we separated the EPZT data into three subsets based on the dissolved Fe concentrations reported by Resing et al. (2015), including a coastal margin (stations 1–5), hydrothermal vents (stations 18, 20, 21, 25, 26, where depth was between 2,200 and 3,000 m) and open ocean (the rest of stations and depths). The bulk K_d values for the

coastal margin subset were lower than the average (between 5.05 $\times$ 10^5 to 7.84 $\times$ 10^7 L kg^{-1}; log K_d = 5.70–7.89), whereas higher than average bulk K_d value were observed in hydrothermal vent subset (from 1.26 $\times$ 10^7 to 1.63 $\times$ 10^8 L kg^{-1}; log K_d = 7.10–8.21). The bulk K_d value of the open ocean subset was between 1.92 $\times$ 10^6 and 8.85 $\times$ 10^7 L kg^{-1} (log K_d = 6.28–7.95). The intrinsic K_d values in each subset are summarized in **Table 4**. Interestingly, the pattern of intrinsic K_d values was very different between these three regions, similarly resulted from what we discussed in section Intrinsic K_d. In the coastal data subset, only carbonate and lithogenic particle fractions were able to explain bulk K_d variability and in the hydrothermally influenced samples, only the opal and Fe phases gave resolved intrinsic K_d values. The remaining, open-ocean samples/sites appeared influenced by a broader range of phases, including opal, but not for either lithogenic or Fe phases.

The Lack of a Resolved Intrinsic K_d for Opal

Zaferani et al. have recently documented uncommonly high sediment accumulation fluxes of Hg that are also associated with high opal fluxes along parts of the Antarctic margin (e.g., Zaferani et al., 2018; Zaferani and Biester, 2020). This is seemingly inconsistent with our finding that there is little correlation between the values of bulk K_d and f_{opal} in overall datasets, resulting in undefined values for the intrinsic K_d for Hg-opal, and implying either that biogenic silica is a poor sorbent material for Hg or that diatoms are not particularly effective at taking up Hg. The first of these two possibilities are more likely as the high Hg fluxes on the Antarctic margin could be due more to high productivity, and therefore high abundance of particulate organic matter, rather than the opal associated with that productivity. Furthermore, diatoms appear to effectively bioaccumulate Hg (Mason et al., 1996; Bełdowska et al., 2018). The lack of a resolved K_d contribution from opal in the multivariate linear regression is an expression of an apparent lack of co-variation between K_d and f_{opal} and is consistent with both the simple correlation matrix view of the data as well as the PCA, both of which show little co-variation of Hg K_d and f_{opal} in the full datasets. One important caveat to this discussion is that two of the Pacific sub-datasets (open ocean and hydrothermal plume; **Table 4**), did have resolved intrinsic K_d's for opal, and the values were quite high. This was especially surprising as these were locations in the Pacific with the lowest fraction of particle mass as opal. With our current datasets, this behavior is difficult to explain and is worthy of further study.

Possible Biological Control on K_d in Surface Waters

In surface water, we found higher bulk K_d values in the open ocean compared to the continental margin (water depth < 200 m; **Figure 3**). This could be the result of the concentration effect as margin water tends to be higher in SPM than open ocean water. It could also be due to a difference in the mechanism by which Hg becomes associated with particles. In deeper waters, this should only be a consequence of sorption, while in surface waters could also be from biological uptake. If this is true, then variations in the value of bulk K_d might be determined by an "uptake efficiency." In coastal regions, even though the biological activity is high, the uptake efficiency of Hg might be limited by the size of microbes based on Michaelis-Menten kinetics: more effective uptake occurs in the open ocean, where small size microbes with high uptake rate survive. In order to test this hypothesis, we examined the regression of log bulk K_d against log SPM in both shallow water (above 100 m) and deep water (below 100 m), separately, for three ocean basins. Then, we compared regression slopes between shallow and deep water by applying *Z*-test. Assuming that the particle concentration effect controls the K_d in deep water, if microbes were to passively adsorb Hg (like particle scavenging) in the surface, we would expect to see no difference between slopes in the shallow and deep water. In contrast, if microbes actively taking up Hg in the surface is responsible for the higher open ocean surface K_d, we might expect to observe a significantly different slope in shallow water compared to deep water, because K_d was not controlled by particle concentration effect.

The statistical results were summarized in **Supplementary Table 3**. Through the comparison of slopes of regression in shallow and deep seawater, we noticed that the slopes between shallow and deep water were not significantly different in the Atlantic and Arctic Ocean, suggesting the passive adsorption might take over in the surface seawater, therefore, we can deem that particle scavenging dominate the whole Atlantic and Arctic Ocean. However, the slope analysis failed the

TABLE 4 | The log intrinsic K^i_d (l kg^{-1}) of Hg for six particle composition in the small size fraction (SSF) in coastal margin, hydrothermal plume, and open ocean of the Pacific, respectively, and their relative standard deviation (r.s.d.) as well as particle composition mass contribution (f; %).

	Coastal margin			Hydrothermal plume			Open ocean		
	Intrinsic log K_d (l kg^{-1})	r.s.d. (%)	Typical contribution to particle mass (%)	Intrinsic log K_d (l kg-1)	r.s.d. (%)	Typical contribution to particle mass (%)	Intrinsic log K_d (l kg−1)	r.s.d. (%)	Typical contribution to particle mass (%)
POM	n.a.	n.a.	62 ± 19	n.a.	n.a.	26 ± 8	7.27	0.46	50 ± 23
$CaCO_3$	7.83	9.20	14 ± 8	n.a.	n.a.	31 ± 15	6.56	0.68	37 ± 18
Opal	n.a.	n.a.	22 ± 10	7.07	7.65	11 ± 8	7.81	5.52	6 ± 4
lithogenic	7.62	7.17	12 ± 17	n.a.	n.a.	3 ± 4	n.a.	n.a.	5 ± 10
Mn	n.a.	n.a.	0.03 ± 0.07	n.a.	n.a.	2 ± 2	8.86	1.24	0.2 ± 0.3
Fe	n.a.	n.a.	0.6 ± 0.4	8.25	7.75	26 ± 18	n.a.	n.a.	1 ± 2

Z-test in the Pacific, the result of statistical difference between shallow and deep water is consistent with our hypothesis of active biological uptake control in the surface. Despite this observed difference, more evidence needs to be collected in order to support the phenomenon in the Pacific, we cannot assert the conclusion of surface domination of biological uptake on K_d, since the special feature in Hydrothermal Plume could also give rise to this difference between shallow and deep water.

Model Evaluation: Observed vs. Predicted

To test the robustness of the six end-member model, we substituted calculated values from **Table 1** (intrinsic K_d) into Equation 2 to obtain the predicted K_d values for each sample (Tang et al., 2017). We then looked at the correlation between observed and predicted K_d through linear regressions and treating the ocean basins separately. The analysis of the coefficient of determination (R^2) revealed that 12% of total variance was explained by the predicted *vs.* observed K_d regression model in Pacific (without hydrothermal plume data), while 14% of Atlantic K_d and 27% of Arctic K_d were explained by the linear regression of predicted against observed K_d (PO regression), respectively ($P < 0.0001$).

Furthermore, all the slopes were far from 1, the shape of linear regression in **Figure 8** suggested that this model overestimates observed K_d at low value while underestimates at high value. The y-intercepts from PO regression were different from 0. Therefore, based on the analysis of R^2, slope and y-intercept, this model failed to describe the characteristic of variability of observed K_d well. However, when we re-did the linear regression on extracted data from hydrothermal vents in the Pacific only (**Figure 8D**), the slope was 0.89 with R^2 0.84. This good agreement occurred because iron oxyhydroxides were a significant fraction of particle mass (26%) and thus dominated the adsorption (97%) in the whole hydrothermal plume area (**Figures 7G,H**). This evaluation is informative, suggesting we need to look for a new way to express the partition coefficient in the future.

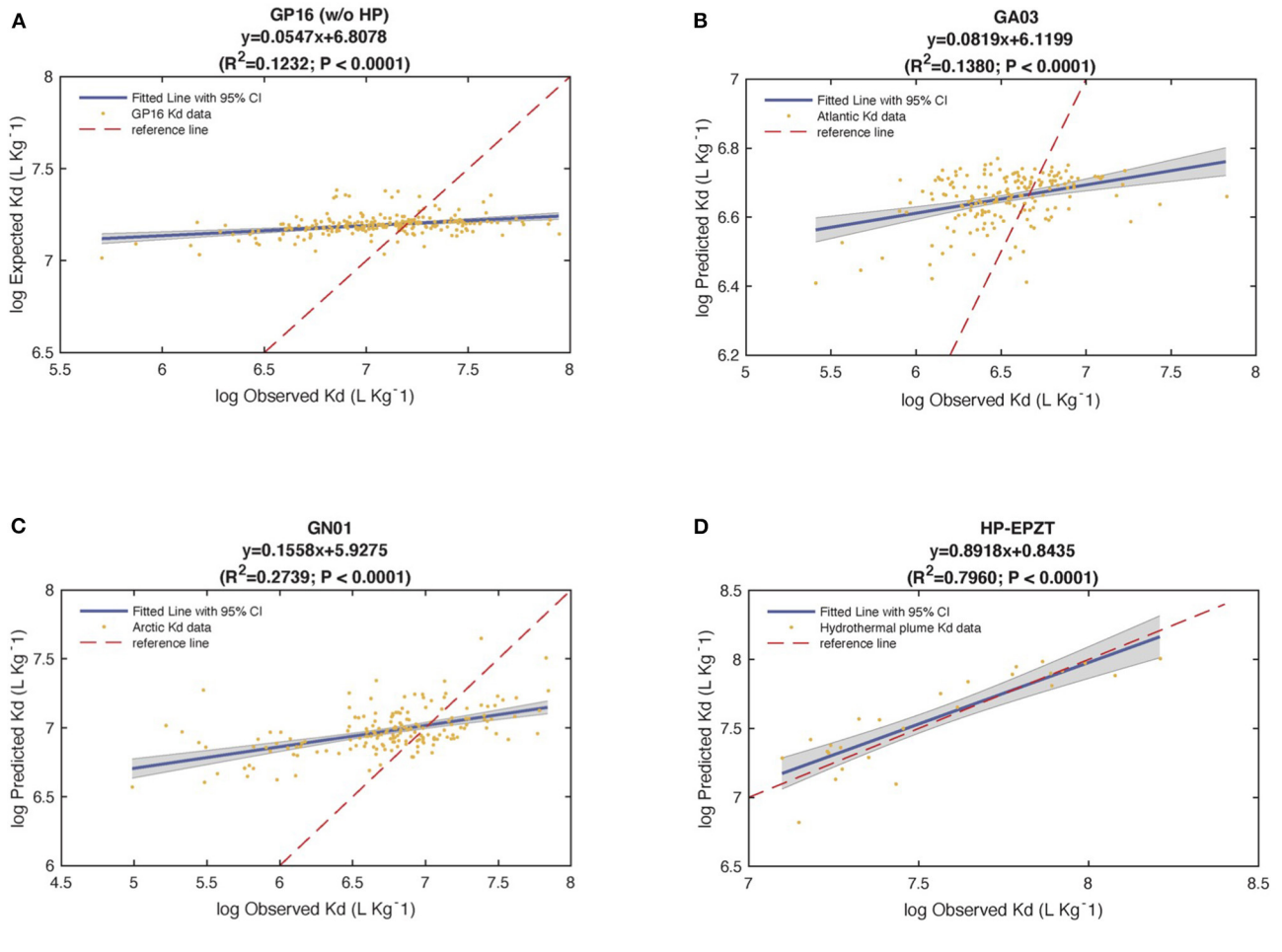

FIGURE 8 | The statistical results of the regression of observed (Obs) vs. predicted (Pre) K_d values in **(A)** the Pacific Ocean (GP16) without Hydrothermal Plume (HP), **(B)** the Atlantic Ocean (GA03), **(C)** the Arctic Ocean (GN01), and **(D)** Hydrothermal plume in the EPZT. Bule solid line is linear regression fitted line, red dash line is a reference line y = x.

TABLE 5 | Summary of estimated Hg inventory (10^3 pM·m), Hg burial flux (pmole m^{-2} d^{-1}) with asymmetric standard deviation, Hg residence time (year), as well as averaged log K_d (log L Kg^{-1}) in the Pacific, Atlantic, and Arctic Ocean, respectively.

	Pacific	Atlantic	Arctic
Hg inventory (10^3 pM·m)	5.29	5.90	2.56
log Hg burial flux (log pmole m^{-2} d^{-1})	2.15 ± 0.43	1.56 ± 0.38	1.31 ± 0.18
Hg burial flux (pmole m^{-2} d^{-1})	142.73, +240.0116, −89.50	36.31, +14.48, −21.17	20.23, +10.26, −6.81
Residence time (year)	102	445	347
log K_d (log L Kg^{-1})	7.11 ± 0.38	6.52 ± 0.32	6.74 ± 0.53

The correlation between residence time and log K_d was strongly negative correlation coefficient $t = -0.995$, $R^2 = 0.991$.

Implication of Hg Residence Time

To some extent, the K_d determines the downward Hg flux from the surface ocean, and further influences the Hg burial flux to marine sediments, which give us insights into the residence time of Hg in the ocean.

Here, we calculated the Hg inventory in each ocean basin by integrating the dissolved Hg with depth (**Table 5**). Due to a lack of Hg burial flux on a global scale, we used information about the particulate Hg flux into the deep ocean to estimate the burial flux. The particulate Hg flux was derived based on the bulk particle flux from the same cruises (Xiang et al., 2020). To convert to Hg flux, we multiplied the particle flux by the concentration ratios between particulate Hg and SPM for each sample. The underlying assumptions are: (1) particulate Hg follows the particle size distribution of bulk particles; (2) particulate Hg has the same sinking velocity as bulk particles. We then estimated the mean of the logarithmic transformed Hg sinking fluxes below 3,500 m in each ocean basin, and assumed the average sinking flux in the deep ocean equal to burial flux. Overall, our estimates of the Hg burial flux were an order of magnitude higher in the Pacific than the Arctic and Atlantic Ocean (**Table 5**). In the Arctic Ocean, the Hg burial flux (20.23, +10.26, −6.81 pmole m^{-2} d^{-1}) was in a similar range compared to Tesán Onrubia et al. (2020) (outer shelf: 51 ± 35 pmole m^{-2} d^{-1}; central Arctic Ocean: 11 ± 8 pmole m^{-2} d^{-1}). Note that the uncertainty of burial flux were not the same because they were transformed back from logarithmic to their original scale. Additionally, the Hg burial fluxes in the Atlantic and Arctic were in line with the globally averaged Hg fluxed from deep ocean to sediments reported by Outridge et al. (2018), which was 0.60 kt/y.

On the basis of estimated Hg inventory and burial fluxes, Hg residence times in three ocean basins were calculated (**Table 5**). A strong negative correlation between log bulk K_d and residence time was observed in our analysis, suggesting that K_d could have a significant impact on Hg residence time. Given the higher bulk K_d observed in the Pacific, our estimates of the Hg residence time in the Pacific are the shortest among all oceans, ∼102 years, lower than previous studies (∼350 yrs, e.g., Gill and Fitzgerald, 1988). The residence time of Hg is the longest in the Atlantic. It should be noted that, however, our Stokes' law-based method might overestimate the Hg burial fluxes compared to conventional but limited sediment trap-based observations (e.g., Munson et al., 2015), which could lead to shorter residence time. Future modeling and field observation efforts are needed to better constrain the Hg burial flux and thereby Hg residence time on a global scale.

CONCLUSION

In general, we investigated into the Hg partition coefficient (K_d) in the water column across the Pacific, Atlantic and Arctic Ocean, and analyzed the impact of particle concentration and composition on variation of K_d. The higher K_d were observed in the Pacific, while modestly lower and lowest K_d were observed in the Arctic and Atlantic Ocean, respectively. The log bulk K_d of Hg was inversely correlated with log SPM concentration, known as "particle concentration effect." The analysis of intrinsic K_d across three ocean basins indicated that affinity of Hg to particle composition is not constant everywhere, and its variation depends on regions and phase concentration. Fe and Mn oxides have highly strong affinity to Hg in the water column despite their low relative abundance in particles, which could be dominant phases in some special regions like the hydrothermal plume, POM and $CaCO_3$ were important drivers of K_d as well. Further, the end member mixing model has limited ability to describe the observed K_d for the entire ocean possibly as a result of changing water chemistry and mineralogy of particles. Overall, the SPM combined particle composition explained the 28–66% of variance of K_d over three ocean basins. The strong negative correlation between Hg residence time and average log bulk K_d implied that varying K_d might determine the timescale of marine Hg cycling indirectly.

DATA AVAILABILITY STATEMENT

Publicly available datasets were analyzed in this study. This data can be found at: https://www.bco-dmo.org.

AUTHOR CONTRIBUTIONS

XC and CL conceived of the presented idea and took the lead in writing the manuscript. XC performed the computations and analytical calculation. PL and YX collected the SPM datasets. CH and CL collected Hg datasets. All authors provided critical feedback and contributed to the final manuscript.

FUNDING

XC was supported during the analysis and writing of this current work by the Chinese Scholarship Council. Original support for collection and analysis of these samples came from the U.S. National Science Foundation in grants to CL and CH

(OCE 1534315; OCE 1434653; OCE 1132515; OCE 1232760; OCE 0928191).

ACKNOWLEDGMENTS

We thank the captains and crews of GEOTRACES cruises GN01, GA03, and GP16, as well as the scientific crews who collected the samples. The underlying data are archived at BCO-DMO (https://www.bco-dmo.org.) and we thank their on-going efforts regarding data quality and access. We also thank the US and International GEOTRACES offices for pre-COVID travel support and publicity. We thank Claudie Beaulieu for advice with PCA.

SUPPLEMENTARY MATERIAL

The Supplementary Material for this article can be found online at: https://www.frontiersin.org/articles/10.3389/fenvc.2021.660267/full#supplementary-material

REFERENCES

Agather, A. M., Bowman, K. L., Lamborg, C. H., and Hammerschmidt, C. R. (2019). Distribution of mercury species in the Western Arctic ocean (US GEOTRACES GN01). *Mar. Chem.* 216:103686. doi: 10.1016/j.marchem.2019.103686

Amos, H. M., Jacob, D. J., Streets, D. G., and Sunderland, E. M. (2013). Legacy impacts of all-time anthropogenic emissions on the global mercury cycle. *Glob. Biogeochem. Cycles* 410–421. doi: 10.1002/gbc.20040

Anderson, R. F. (2014). "8.9 - Chemical tracers of particle transport," in *Treatise on Geochemistry (Second Edition),* eds. H. D. Holland and K. K. Turekian (Oxford: Elsevier), 259–280. doi: 10.1016/B978-0-08-095975-7.00609-4

Bacon, M., Spencer, D., and Brewer, P. (1976). 210Pb/226Ra and 210Po/210Pb disequilibria in seawater and suspended particulate matter. *Earth Planet. Sci. Lett.* 32, 277–296. doi: 10.1016/0012-821X(76)90068-6

Bacon, M. P., and Anderson, R. F. (1982). Distribution of thorium isotopes between dissolved and particulate forms in the deep sea. *J. Geophys. Res.* 87, 2045–2056. doi: 10.1029/JC087iC03p02045

Balcom, P. H., Hammerschmidt, C. R., Fitzgerald, W. F., Lamborg, C. H., and O'connor, J. S. (2008). Seasonal distributions and cycling of mercury and methylmercury in the waters of New York/New Jersey harbor estuary. *Mar. Chem.* 109, 1–17. doi: 10.1016/j.marchem.2007.09.005

Bam, W., Maiti, K., Baskaran, M., Krupp, K., Lam, P. J., and Xiang, Y. (2020). Variability in 210Pb and 210Po partition coefficients (Kd) along the US GEOTRACES Arctic transect. *Mar. Chem.* 219:103749. doi: 10.1016/j.marchem.2020.103749

Baskaran, M., and Santschi, P. H. (1993). The role of particles and colloids in the transport of radionuclides in coastal environments of Texas. *Mar. Chem.* 43, 95–114. doi: 10.1016/0304-4203(93)90218-D

Bełdowska, M., Zgrundo, A., and Kobos, J. (2018). Mercury in the diatoms of various ecological formations. *Water Air Soil Pollut.* 229:168. doi: 10.1007/s11270-018-3814-1

Benoit, G., and Rozan, T. F. (1999). The influence of size distribution on the particle concentration effect and trace metal partitioning in rivers. *Geochim. Cosmochim. Acta* 63, 113–127. doi: 10.1016/S0016-7037(98)00276-2

Biscaye, P. E. (1965). Mineralogy and sedimentation of recent deep-sea clay in the atlantic ocean and adjacent seas and oceans. *GSA Bull.* 76, 803–832. doi: 10.1130/0016-7606(1965)76[803:MASORD]2.0.CO;2

Bowman, K. L., Hammerschmidt, C. R., Lamborg, C. H., and Swarr, G. (2015). Mercury in the North Atlantic ocean: the U.S. GEOTRACES zonal and meridional sections. *Deep Sea Res. Part II Top. Stud. Oceanogr.* 116, 251–261. doi: 10.1016/j.dsr2.2014.07.004

Bowman, K. L., Hammerschmidt, C. R., Lamborg, C. H., Swarr, G. J., and Agather, A. M. (2016). Distribution of mercury species across a zonal section of the eastern tropical South Pacific ocean (U.S. GEOTRACES GP16). *Mar. Chem.* 186, 156-166. doi: 10.1016/j.marchem.2016.09.005

Cael, B., and White, A. E. (2020). Sinking versus suspended particle size distributions in the North Pacific subtropical gyre. *Geophys. Res. Lett.* 47:e2020GL087825. doi: 10.1029/2020GL087825

Chase, Z., Anderson, R. F., Fleisher, M. Q., and Kubik, P. W. (2002). The influence of particle composition and particle flux on scavenging of Th, Pa and Be in the ocean. *Earth Planet. Sci. Lett.* 204, 215–229. doi: 10.1016/S0012-821X(02)00984-6

Darby, D. A. (1975). Kaolinite and other clay minerals in Arctic ocean sediments. *J. Sediment. Res.* 45, 272–279. doi: 10.1306/212F6D34-2B24-11D7-8648000102C1865D

Efron, B., and Stein, C. (1981). The jackknife estimate of variance. *Ann. Stat.* 9, 586–596. doi: 10.1214/aos/1176345462

Fitzgerald, W. F., Engstrom, D. R., Lamborg, C. H., Tseng, C.-M., Balcom, P. H., and Hammerschmidt, C. R. (2005). Modern and historic atmospheric mercury fluxes in northern Alaska: global sources and arctic depletion. *Environ. Sci. Technol.* 39, 557–568. doi: 10.1021/es049128x

Fitzgerald, W. F., and Lamborg, C. H. (2014). "Geochemistry of mercury in the environment," in *Treatise on Geochemistry,* ed. B. S. Lollar (Oxford: Elsevier), 91–129. doi: 10.1016/B978-0-08-095975-7.00904-9

Gill, G. A., and Fitzgerald, W. F. (1988). Vertical mercury distributions in the oceans. *Geochim. Cosmochim. Acta* 52, 1719–1728. doi: 10.1016/0016-7037(88)90240-2

Hammerschmidt, C. R., and Fitzgerald, W. F. (2004). Geochemical controls on the production and distribution of methylmercury in near-shore marine sediments. *Environ. Sci. Technol.* 38, 1487–1495. doi: 10.1021/es034528q

Hayes, C. T., Anderson, R. F., Fleisher, M. Q., Vivancos, S. M., Lam, P. J., Ohnemus, D. C., et al. (2015). Intensity of Th and Pa scavenging partitioned by particle chemistry in the North Atlantic ocean. *Marine Chem.* 170, 49–60. doi: 10.1016/j.marchem.2015.01.006

Honeyman, B. D., Balistrieri, L. S., and Murray, J. W. (1988). Oceanic trace metal scavenging: the importance of particle concentration. *Deep Sea Res. Part A Oceanogr. Res. Pap.* 35, 227–246. doi: 10.1016/0198-0149(88)90038-6

Honeyman, B. D., and Santschi, P. H. (1989). A brownian-pumping model for oceanic trace-metal scavenging - evidence from Th-isotopes. *J. Marine Res.* 47, 951–992. doi: 10.1357/002224089785076091

John, S. G., and Conway, T. M. (2014). A role for scavenging in the marine biogeochemical cycling of zinc and zinc isotopes. *Earth Planet. Sci Lett.* 394, 159–167. doi: 10.1016/j.epsl.2014.02.053

Lam, P. J., Lee, J.-M., Heller, M. I., Mehic, S., Xiang, Y., and Bates, N. R. (2018). Size-fractionated distributions of suspended particle concentration and major phase composition from the U.S. GEOTRACES eastern Pacific zonal transect (GP16). *Marine Chem.* 201, 90–107. doi: 10.1016/j.marchem.2017.08.013

Lam, P. J., Ohnemus, D. C., and Auro, M. E. (2015). Size-fractionated major particle composition and concentrations from the US GEOTRACES North Atlantic zonal transect. *Deep Sea Res. Part II Top. Stud. Oceanogr.* 116, 303–320. doi: 10.1016/j.dsr2.2014.11.020

Lamborg, C. H., Hammerschmidt, C. R., and Bowman, K. L. (2016). An examination of the role of particles in oceanic mercury cycling. *Philos. Trans. A Math. Phys. Eng. Sci.* 374:20150297. doi: 10.1098/rsta.2015.0297

Lerner, P., Marchal, O., Lam, P. J., Buesseler, K., and Charette, M. (2017). Kinetics of thorium and particle cycling along the US GEOTRACES north Atlantic transect. *Deep Sea Res. Part I Oceanogr. Res. Pap.* 125, 106–128. doi: 10.1016/j.dsr.2017.05.003

Lerner, P., Marchal, O., Lam, P. J., and Solow, A. (2018). Effects of particle composition on thorium scavenging in the north Atlantic. *Geochim. Cosmochim. Acta* 233, 115–134. doi: 10.1016/j.gca.2018.04.035

Mason, R. P., Reinfelder, J. R., and Morel, F. M. (1996). Uptake, toxicity, and trophic transfer of mercury in a coastal diatom. *Environ. Sci. Technol.* 30, 1835–1845. doi: 10.1021/es950373d

Moran, S., Yeats, P., and Balls, P. (1996). On the role of colloids in trace metal solid-solution partitioning in continental shelf waters: a comparison of model results and field data. *Cont. Shelf Res.* 16, 397–408. doi: 10.1016/0278-4343(95)98840-7

Munson, K. M., Lamborg, C. H., Swarr, G. J., and Saito, M. A. (2015). Mercury species concentrations and fluxes in the central tropical Pacific ocean. *Glob. Biogeochem. Cycles* 29, 656–676. doi: 10.1002/2015GB005120

Outridge, P. M., Mason, R. P., Wang, F., Guerrero, S., and Heimbürger-Boavida, L. E. (2018). Updated global and oceanic mercury budgets for the united nations global mercury assessment 2018. *Environ. Sci. Technol.* 52, 11466–11477. doi: 10.1021/acs.est.8b01246

Resing, J. A., Sedwick, P. N., German, C. R., Jenkins, W. J., Moffett, J. W., Sohst, B. M., et al. (2015). Basin-scale transport of hydrothermal dissolved metals across the South Pacific Ocean. *Nature* 523, 200–203. doi: 10.1038/nature14577

Soerensen, A. L., Jacob, D. J., Schartup, A. T., Fisher, J. A., Lehnherr, I., St. Louis, V. L., et al. (2016). A mass budget for mercury and methylmercury in the Arctic ocean. *Global Biogeochem. Cycles* 30, 560–575. doi: 10.1002/2015GB005280

Stemmann, L., and Boss, E. (2012). Plankton and particle size and packaging: from determining optical properties to driving the biological pump. *Ann. Rev. Mar. Sci.* 4, 263–290. doi: 10.1146/annurev-marine-120710-100853

Tang, Y., Stewart, G., Lam, P. J., Rigaud, S., and Church, T. (2017). The influence of particle concentration and composition on the fractionation of Po-210 and Pb-210 along the north Atlantic GEOTRACES transect GA03. *Deep Sea Res. Part I Oceanogr. Res. Pap.* 128, 42–54. doi: 10.1016/j.dsr.2017.09.001

Tesán Onrubia, J. A., Petrova, M. V., Puigcorbé, V., Black, E. E., Valk, O., Dufour, A., et al. (2020). Mercury export flux in the Arctic ocean estimated from 234Th/238U disequilibria. *ACS Earth Space Chem.* 4, 795–801. doi: 10.1021/acsearthspacechem.0c00055

Xiang, Y., and Lam, P. J. (2018). "Comparisons of size-fractioned suspended particles in three different basins from the US GEOTRACES NAZT (GA03), EPZT (GP16) and Arctic (GN01) Cruises," in *2018 Ocean Sciences Meeting* (Portland, OR: AGU).

Xiang, Y., and Lam, P. J. (2020). Size-Fractionated compositions of marine suspended particles in the western Arctic ocean: lateral and vertical sources. *J. Geophys. Res. Oceans* 125:e2020JC016144. doi: 10.1029/2020JC016144

Xiang, Y., Lam, P. J., and Burd, A. B. (2020). *Controls on Sinking Velocities and Mass Fluxes of Size-Fractionated Marine Particles in Recent U.S. GEOTRACES Cruises.* Available online at: https://essoar.org.

Zaferani, S., and Biester, H. (2020). Biogeochemical processes accounting for the natural mercury variations in the southern ocean diatom ooze sediments. *Ocean Sci. Discuss.* 2020, 1–22. doi: 10.5194/os-16-729-2020

Zaferani, S., Pérez-Rodríguez, M., and Biester, H. (2018). Diatom ooze—a large marine mercury sink. *Science* 361, 797–800. doi: 10.1126/science.aat2735

Zhang, Y., Jaeglé, L., and Thompson, L. (2014). Natural biogeochemical cycle of mercury in a global three-dimensional ocean tracer model. *Global Biogeochem. Cycles* 28, 2014GB004814. doi: 10.1002/2014GB004814

Conflict of Interest: The authors declare that the research was conducted in the absence of any commercial or financial relationships that could be construed as a potential conflict of interest.

frontiers in Environmental Chemistry

ORIGINAL RESEARCH
published: 14 June 2021
doi: 10.3389/fenvc.2021.660058

Abiotic Reduction of Mercury(II) in the Presence of Sulfidic Mineral Suspensions

Mariame Coulibaly[1,2], *Nashaat M. Mazrui*[1,3], *Sofi Jonsson*[1,4] *and Robert P. Mason*[1]*

[1]Departments of Marine Sciences and Chemistry, University of Connecticut, Groton, CT, United States, [2]Ecole Normale Superieure d'Abidjan, Abidjan, Côte d'Ivoire, [3]Okavango Research Institute, University of Botswana, Maun, Botswana, [4]Department of Environmental Science, Stockholm University, Stockholm, Sweden

Monomethylmercury (CH_3Hg) is a neurotoxic pollutant that biomagnifies in aquatic food webs. In sediments, the production of CH_3Hg depends on the bacterial activity of mercury (Hg) methylating bacteria and the amount of bioavailable inorganic divalent mercury (Hg^{II}). Biotic and abiotic reduction of Hg^{II} to elemental mercury (Hg^0) may limit the pool of Hg^{II} available for methylation in sediments, and thus the amount of CH_3Hg produced. Knowledge about the transformation of Hg^{II} is therefore primordial to the understanding of the production of toxic and bioaccumulative CH_3Hg. Here, we examined the reduction of Hg^{II} by sulfidic minerals ($FeS_{(s)}$ and $CdS_{(s)}$) in the presence of dissolved iron and dissolved organic matter (DOM) using low, environmentally relevant concentrations of Hg and ratio of Hg^{II}:$FeS_{(s)}$. Our results show that the reduction of Hg^{II} by Mackinawite ($FeS_{(s)}$) was lower (<15% of the Hg^{II} was reduced after 24 h) than when Hg^{II} was reacted with DOM or dissolved iron. We did not observe any formation of Hg^0 when Hg^{II} was reacted with $CdS_{(s)}$ (experiments done under both acidic and basic conditions for up to four days). While reactions in solution were favorable under the experimental conditions, Hg was rapidly removed from solution by co-precipitation. Thermodynamic calculations suggest that in the presence of $FeS_{(s)}$, reduction of the precipitated Hg^{II} is surface catalyzed and likely involves S^{-II} as the electron donor. The lack of reaction with CdS may be due to its stronger M-S bond relative to FeS, and the lower concentrations of sulfide in solution. We conclude that the reaction of Hg with $FeS_{(s)}$ proceeds *via* a different mechanism from that of Hg with DOM or dissolved iron, and that it is not a major environmental pathway for the formation of Hg^0 in anoxic environments.

Keywords: mercury, reduction, iron sulfide, cadmium sulfide, dissolved organic matter

OPEN ACCESS

Edited by:
Martin Jiskra,
University of Basel, Switzerland

Reviewed by:
Amrika Deonarine,
Texas Tech University, United States
Daniel Steven Grégoire,
University of Waterloo, Canada

***Correspondence:**
Robert P. Mason
robert.mason@uconn.edu

Specialty section:
This article was submitted to Inorganic Pollutants, a section of the journal Frontiers in Environmental Chemistry

Received: *28 January 2021*
Accepted: *27 May 2021*
Published: *14 June 2021*

Citation:
Coulibaly M, Mazrui NM, Jonsson S and Mason RP (2021) Abiotic Reduction of Mercury(II) in the Presence of Sulfidic Mineral Suspensions. Front. Environ. Chem. 2:660058. doi: 10.3389/fenvc.2021.660058

INTRODUCTION

Mercury (Hg) is considered as a global and high-priority pollutant (Clarkson and Magos, 2006; Mergler et al., 2007). While it is released as elemental or divalent Hg (Hg^0 and Hg^{II}) from natural and anthropogenic sources (Driscoll et al., 2013), the main concern lies with the accumulation of Hg as monomethylmercury (CH_3Hg) in aquatic food webs (Eagles-Smith et al., 2018; Sunderland et al., 2018). Production of CH_3Hg in aquatic systems from Hg^{II} is facilitated by microorganisms carrying the Hg-methylation genes (*HgcA* and *HgcB*-genes) primarily in anoxic environments, such as in sediments, soils or on resuspended particles (Parks et al., 2013; Podar et al., 2015). The production of CH_3Hg is controlled by the composition of the bacterial community, bacterial activity and the

availability of Hg^{II} for bacterial uptake (Benoit et al., 2003; Fitzgerald et al., 2007; Compeau and Bartha, 1985; Gilmour et al., 1992). In environments where Hg methylation rates are typically high, the amount of Hg^{II} available to Hg methylating bacteria is controlled by competition between adsorption of Hg to the solid phase, the chemical speciation in the dissolved phase as well as removal processes, such as reduction of Hg^{II} to volatile elemental Hg (Hg^0).

Under anoxic conditions, Hg can be reduced to Hg^0 *via* biotic and abiotic processes (Spangler et al., 1973; Steffan et al., 1988). Abiotic processes include photoreduction (Garcia et al., 2005; O'Driscoll et al., 2006; Whalin et al., 2007), which is likely limited in anoxic environments, and chemical reduction of Hg^{II} in the presence of organic matter (Baohua et al., 2011; Zheng et al., 2012; Chakraborty et al., 2015; Jiang et al., 2015) or mineral-associated ferrous iron (Charlet et al., 2002; Jeong et al., 2010; Remy et al., 2015; Richard et al., 2016; O'Loughlin et al., 2003). For the latter pathway, several iron-containing minerals have been suggested to reduce Hg, including hydrous ferric oxide (Richard et al., 2016), siderite (Ha et al., 2017) and clay (Peretyazhko et al., 2006a). Recently, reduction of Hg on iron sulfide mineral surfaces was also suggested (Bone et al., 2014), although the mechanism was not completely determined. In anoxic environments, the competition between inorganic sulfide phases and organic matter likely control the bioavailability of Hg as both complex Hg strongly and likely influence important reactions such as Hg^{II} reduction (Skyllberg and Drott, 2010).

The affinity of Hg^{II} for mineral surfaces, especially sulfide containing minerals, has been well documented (Jeong et al., 2008; Jeong et al., 2010; Skyllberg and Drott, 2010). Studies examining the sorption to mackinawite showed that Hg can replace iron in the mineral, forming black meta-cinnabar (β-$HgS_{(s)}$) and red cinnabar (α-$HgS_{(s)}$)-like structures, and this was the primary reaction. Both the sorption and co-precipitation of Hg with $FeS_{(s)}$ has been shown to influence its methylation by bacteria (Rivera et al., 2019). Whether Hg^{II} can also be reduced on interaction with iron sulfide minerals remains less clear but has been speculated to occur in anoxic contaminated sediments (Han et al., 2020).

Most researchers who also investigated the reaction between Hg^{II} and $FeS_{(s)}$, did not detect Hg^0 (Liu et al., 2008; Jeong et al., 2010; Skyllberg and Drott, 2010). However, cinnabar and Hg^0 were formed when Hg^{II} interacted with pyrite and troilite (Bower et al., 2008). Only one work so far has reported the reduction of mercury by $FeS_{(s)}$ (Bone et al., 2014). This work suggested that Hg^0 was generated from the reduction of Hg^{II}-S^{-II} species in the presence of $FeS_{(s)}$, but that adsorption of Hg to the solid was not necessary for the reaction, suggesting a reaction involving Hg complexes in solution. Thermodynamically, whether the reaction occurs in solution or at the mineral surface is likely controlled by solution chemistry and the Hg concentration. The relative importance also likely depends on the fractionation of Hg between the dissolved and solid phases, which depends on its concentration, pH and sulfide concentration (Supporting Information (SI), **Supplementary Tables S1, S2**). Combining the precipitation reaction with that of a major dissolved Hg species in solution under sulfidic conditions results in the overall reaction shown below for Hg co-precipitation:

$$Hg(SH)_2 = HgS_{(s)} + H^+ + HS^- \qquad \text{Log K} = -0.9$$

where the solid is either from solution saturation or from co-precipitation:

$$FeS_{(s)} + Hg(SH)_2 = HgS_{(s)} + Fe^{2+} + 2HS^- \qquad \text{Log K} = -4.4$$

One important difference in the studies to date, as noted by Bone et al. (2014), is the difference in the Hg^{II}:$FeS_{(s)}$ ratio. In many studies this is higher than the molar ratio found in the environment, which ranges from 3×10^{-3} to $\sim 10^{-7}$ for regionally contaminated and uncontaminated locations. The studies of Bone et al. used a range from 0.4 to 20×10^{-3}, which is at the high end of the environmental range, but lower than the ratios of Jeong et al. (2010), for example, ($>10^{-2}$). We therefore proposed to do our follow-up studies at more environmentally-relevant concentrations to further investigate how this ratio may influence the experimental results.

In contrast to the differences in reaction mechanisms in the presence of $FeS_{(s)}$, reactions of Hg^{II} with reduced sulfur have been documented in several studies showing the reduction of Hg by sulfite (Van Loon et al., 2001; Feinberg et al., 2015). According to other previous work, Fe^{II} also plays an important role in the reduction of Hg^{II} to Hg^0 by reduced iron species including magnetite, green rust, haematite and siderite (Ona-Nguema et al., 2002; Peretyazhko et al., 2006b; Wiatrowski et al., 2009; Ha et al., 2017). Given the reactions noted above, and the literature, whether Hg reduction would occur in solution or on the solid surface will depend on the environmental conditions. As noted, most prior studies have been done at high concentrations given the analytical tools used to evaluate the interactions, and this study was therefore designed to examine Hg interactions at low Hg concentrations, and to examine if there was the potential for Hg reduction in such environments. Further, the study was aimed at probing the potential reaction pathways for formation of Hg^0 in such systems. The potential reactions include reactions of dissolved or solid-phase Hg with reduced species (Fe(II), S(-II) or other reduced S species). As always, in such systems the interactions are complex as there is the potential for abiotic transformations of Fe and S (e.g., Fe^{3+} being reduced by HS^-).

Besides interactions with inorganic solids, Hg speciation in natural systems is strongly influenced by dissolved organic matter (DOM) (Ravichandran, 2004; Slowey, 2010; Gerbig et al., 2011b; Muresan et al., 2011; Jeremiason et al., 2015). Studies have shown the importance of DOM, not just as a group of Hg-binding ligands, but also due to its impact on Hg^{II}–$S^{-II}_{(aq)}$ reactions and on the stability of $HgS_{(s)}$ (Ravichandran et al., 1998; Waples et al., 2005; Deonarine and Hsu-Kim, 2009; Skyllberg and Drott, 2010; Gerbig et al., 2011a). Indeed, it has been reported that $HgS_{(s)}$ nanoparticle dissolution is mediated by DOM (Slowey, 2010). In addition, research indicating the potential for DOM to reduce Hg^{II} was shown by a positive correlation between dissolved organic carbon (DOC) concentration and Hg^0 production (Rocha et al., 2003; Park et al., 2008). These results are

however contradicted by other studies which found a negative correlation between DOC concentration and Hg^0 production (Amyot et al., 1997; Garcia et al., 2005; O'Driscoll et al., 2006; Mauclair et al., 2008), which was explained by the influence of complexation on Hg reduction. Some studies have demonstrated that under anoxic dark conditions, DOM can rapidly convert Hg^{II} to Hg^0 at very low DOM concentrations (up to ~70% at 0.2 mg/L) (Baohua et al., 2011; Zheng et al., 2012). However, according to others, there is no Hg reduction by DOM in dark environments (Matthiessen, 1998). Photo-reduction is considered the main abiotic process responsible for the conversion of Hg^{II} to Hg^0 in natural systems, and studies show that this reduction process is enhanced by the presence of DOM (Allard and Arsenie, 1991; Costa and Liss, 2000). However, DOM could also reduce Hg reduction by altering light penetration. It is unlikely that photochemical processes are important in most anoxic environments.

To further understand the potential for Hg reduction in the presence of mineral surfaces, and to examine the potential reduction pathways, we investigated the production of Hg^0 from Hg^{II} in the presence of two sulfidic minerals, $FeS_{(s)}$ and $CdS_{(s)}$, under anoxic and dark conditions. We hypothesized that under the experimental conditions, Hg would be co-precipitated onto the solid surface and that the Hg reduction reaction will involve a surface interaction. To explore the role of surfaces and S^{-II} or Fe^{II} as electron donors for the Hg^{II} reduction, Hg^0 production rates at different pH values and Hg^{II}: $FeS_{(s)}$ ratios were examined, and contrasted to reactions of Hg^{II} with dissolved Fe^{II}. Additionally, reactions with $CdS_{(s)}$ were examined as this could help interpret the reaction mechanisms. While $FeS_{(s)}$ and pyrite (FeS_2) are ubiquitous minerals in environmental settings, the presence of $CdS_{(s)}$ is also likely given its low solubility (Stumm and Morgan, 1996). These results were compared and discussed along with the thermodynamic aspects of the potential reduction pathways. In addition, the effect of DOM on the efficiency of any metal sulfide reactive barriers was examined by looking at the reduction of Hg^{II} by sulfidic minerals ($FeS_{(s)}$ and $CdS_{(s)}$) in presence of dissolved organic matter (DOM).

MATERIALS AND METHODS

Preparation of Materials

All solutions used in the experiments were prepared under an inert atmosphere using a glovebox (N_2 atmosphere) and using MQ-water ($\Omega < 18.2$) degassed by purging boiling water with N_2 for 20 min and as it cooled to room temperature. Sulfide minerals ($FeS_{(s)}$ and $CdS_{(s)}$) were synthesized and characterized as described elsewhere (Jonsson et al., 2016). Briefly, disordered $FeS_{(s)}$ was synthesized by adding 100 ml of 0.6 M Na_2S to 100 ml of 0.6 M Mohr's salt ($(NH_4)_2Fe(II)(SO_4)_2{\cdot}6H_2O$); and $CdS_{(s)}$ by adding 25 ml of 0.6 M Na_2S to 25 ml of 0.6 M $Cd(NO_3)_2{\cdot}4H_2O$.

The minerals were characterized using X-ray Diffraction Crystallography (XRD) and Brunauer–Emmett–Teller (BET) measurements (Jonsson et al., 2016). XRD studies were conducted by Rigaku UltimaIV diffractometer with Cu Kα radiation ($\lambda = 1.5418$ Å) operating at a beam voltage of 40 kV and beam current of 45 mA. The patterns were acquired at a scan rate of $2^{\circ}min^{-1}$, from 0 to 80 degrees in the 2θ range. BET surface-area measurements were performed using nitrogen sorption experiments conducted on a Quantochrome Nova 2000e instrument. All the samples were degassed for 5 h before analysis. Specific surface area was calculated using the adsorption isotherm within $0.05 < P/P0 < 0.3$ range, where P/P0 is the relative pressure.

The $Hg_{(aq)}$ working standard was prepared from a 1,000 ppm $Hg_{(aq)}$ stock solution (Merck, Allemagne, 1,000 mgL^{-1} Hg in 1.00 M HNO_3) and then adjusted using 2–8 M $KOH_{(aq)}$ to obtain the desired pH. Mercury working solutions were prepared daily for each experiment. The ferrous iron solution was prepared by dissolving Mohr's salt in MQ-water. The DOM isolates used were extracted from surface waters collected at the shelf break of the North Atlantic Ocean and on the western side of Long Island Sound (United States) (Mazrui et al., 2018). The extraction procedure involved passing 0.2 µm filtered seawater through a modified benzene styrene polymer cartridge (Bond Elut) at a rate of <4 ml/min (Dittmar et al., 2008). The cartridge was then rinsed with dilute HCl, dried and the adsorbed DOM eluted with methanol and acetone. DOM dissolved in organic solvent was dried at 40°C using a Nitrogen evaporator (N-EVAP 111). Stock solutions of DOM were prepared by dissolving approximately 0.1 g of the DOM in 100 ml of degassed purified water. The solutions were then filtered through a 0.02 µm PTFE syringe filter, adjusted to pH 7–8, using dilute HCl/KOH and stored in the dark in airtight containers at 4°C until use.

Mercury Reduction Experiments and Analysis of Hg^0

The reduction of Hg^{II} in the presence of $FeS_{(s)}$, $CdS_{(s)}$, $Fe^{II}_{(aq)}$ or DOM was tested by adding $Hg^{II}_{(aq)}$ to slurries of $FeS_{(s)}$ or $CdS_{(s)}$ or solutions of $Fe^{II}_{(aq)}$ or DOM in acid cleaned glass vials (total volume of 10 ml). The samples were then incubated in the glove box under anoxic and dark conditions (foil-wrapped sealed serum bottles) to prevent photochemical reactions. Each experimental set was done in triplicate ($n = 3$) at room temperature. At the end of each experiment, vials were removed from the glove box and produced $Hg^0_{(g)}$ collected onto Goldtrap™(Supelco) traps. For the collection, two tubes were inserted through the septum of the vial. One tube was used to purge the headspace of the vial with Argon (Ar) at a rate of 200 ml/min for 20 min, while the other collected the purged gasses onto a gold trap. Collected $Hg^0_{(g)}$ was then analyzed using a Cold Vapor Atomic Fluorescence Spectrophotometer (CVAFS) (Tekran, model 2,500) after thermal desorption of the Hg^0 from the gold-traps. A calibration curve was prepared by analyzing 10–200 µL of air saturated with $Hg^0_{(g)}$ from a vial containing $Hg^0_{(g)}$ at a known temperature.

Based on the BET determined surface area (Jonsson et al., 2016), concentrations of $FeS_{(s)}$ and $CdS_{(s)}$ in the experiments were adjusted to have a concentration, reported as surface area to volume of solution ratio, of 1, 5, and 30 m^2L^{-1}. This is equivalent to 0.02, 0.09, and 0.54 g L^{-1} for $FeS_{(s)}$ and 0.01, 0.07, and 0.41 g L^{-1}

for $CdS_{(s)}$, respectively. Samples containing $FeS_{(s)}$ or $CdS_{(s)}$ and 50 pM Hg^{II} were equilibrated for 24 h under dark conditions at pH 5–8 for the initial experiments. The production of purgeable Hg^0 was measured after 24 h in the mixtures and control solutions consisting of degassed MQ water and 50 pM Hg^{II}. In a similar manner, reduction of Hg^{II} by DOM or Fe^{II} was tested by incubating 10 ml of experimental solutions containing 5.0 mg C/L of DOM (24 h and pH 7–8) or 1 mM Fe^{II} (0–4.5 h and pH 5 and 7.5) and 50 pM of Hg^{II}. Experiments were also performed over time at a pH of 7–8 in the presence of $FeS_{(s)}$ at different Hg^{II}:$FeS_{(s)}$ ratios to examine the impact on the reaction rate.

Analysis of Dissolved Fe(II)

After the incubation period, experimental solutions containing $FeS_{(s)}$ slurries were filtered through a 0.02 μm PTFE syringe filter and prepared for Fe^{II} analysis inside the glove box. Samples for Fe^{II} analysis were removed from the glove box and immediately analyzed for the concentration of aqueous Fe^{II} using the ferrozine method (Vollier et al., 2000). Briefly, ferrozine (monosodium salt hydrate of 3-(2-pyridyl)-5, 6-diphenyl-1, 2, 4-triazine-p,p′-disulfonic acid) was reacted with dissolved iron to form a stable magenta complex which absorbs in the visible region at 562 nm. A PharmaSpec UV-1700 UV−Vis spectrometer (Shimadzu) was then used to detect the complex before and after a reduction step with hydroxylamine.

Thermodynamic Calculations and Rate Calculations

The potential reactions that could occur were examined using calculations of the respective equilibrium constants and the free energy (ΔG) of the reaction under the experimental conditions. The concentration of dissolved Fe ($Fe(II)_T$) and sulfide ($S(-II)_T$), and the individual species (principally Fe^{2+} and FeS^0, with the potential for $FeOH^+$, $FeCl^+$, and $FeSO_4{}^0$ being present at higher pH and anion concentrations) was calculated using the solubility model for $FeS_{(s)}$ of Rickard (2006) which considers that the Fe(II) concentration is determined by a solubility reaction and an equilibrium reaction:

$$FeS_{(s)} + 2H^+ = Fe^{2+} + H_2S \qquad \log K = 3.5$$

$$FeS_{(s)} = FeS^0 \qquad \text{Log } K = -5.7$$

where FeS^0 represents a series of $(FeS)_x$ cluster compounds that form in the presence of $FeS_{(s)}$. The Hg speciation and interaction with $FeS_{(s)}$ was modeled using constants from Skyllberg and Drott (2010), Stumm and Morgan (1996). Equilibrium constants for the redox reactions were from Stumm and Morgan (1996). The results of the thermodynamic calculations are detailed in **Supplementary Tables S1, S2**; **Tables 1–3**. **Supplementary Table S1** details the solubility of $FeS_{(s)}$ across the pH range used in the experiments, **Supplementary Table S2** contains a listing of the examined reactions while **Table 1** details the concentrations used in the calculations at pH 7. The calculated free energies of the various reactions are contained in **Tables 2**, **3**. The concentrations of Hg^0 were those measured in the experiments and it was assumed that the total concentration of oxidized forms (sulfate and Fe(III)) were low, (respectively, 0.1 μM and 1 nM) given that these were primarily produced by reduction of Hg^{II}, or were present as trace constituents in the experimental solution. Their dissolved speciation was taken into account in the calculations.

The rates of reaction were calculated using the Hg^0 data and with an assumption of a pseudo first order reaction as the concentration of Hg^0 (<50 pM) is at least five orders of magnitude higher than the concentrations of Fe^{II}, S^{-II} in solution or in the solid phase. Additionally, under the experimental conditions, <1% of the solid is dissolved at equilibrium. Therefore, the assumption of a pseudo first order is valid.

RESULTS

To test the reduction of Hg^{II} in the presence of $FeS_{(s)}$, we initially quantified the amount of purgeable Hg^0 from pH controlled slurries containing 0.09 g/L $FeS_{(s)}$ (corresponding to a surface area concentration of 5 m^2L^{-1}) and 50 pM Hg^{II} that were incubated under anaerobic and dark conditions. In control samples where no $FeS_{(s)}$ was added (pH ranging from 5 to 8) less than 2% of the initially added Hg^{II} was lost as Hg^0 after 24 h of incubation (**Figure 1**). In $FeS_{(s)}$ mineral suspension, however, ~12–~15% of the total Hg^{II} was reduced, and the amount of Hg^0 produced increased with pH. Overall, the amount of Hg^0 produced doubled at pH 8 compared to that at pH 5, and this difference was statistically significant, although the differences in the production rate at the higher pH values were not. Overall, the effect of pH was greater at lower pH. However, the production of Hg^0 (<15% of the initial Hg^{II}) remained very low compared to the levels observed during the interaction of Hg^{II}-ferric oxide or Hg^{II} DOM experiments (Zheng et al., 2012; Ha et al., 2017), or in the presence of Fe(II) alone in our studies, as discussed further below.

To further explore reaction kinetics, net reduction of Hg^{II} was tested as a function of reaction time (1 h–3 days) and mineral surface area concentration (1–30 m^2L^{-1}) at a pH of 7–8. At all tested mineral surface area concentrations, the reduction rate of Hg^{II} was rapid within the first hour (>1 $pmolL^{-1}h^{-1}$), and most Hg^0 was produced within the first hour of the experiment (**Figure 2**). The initial average rates of production are compiled in **Table 4** assuming the reaction was first order, and while the initial rates appeared to increase with surface area, these differences were not statistically significant as rates were respectively, 0.78 ± 0.50, 0.92 ± 0.07 and 1.09 ± 0.16 h^{-1}. The concentration of Hg^0 formed then gradually increased at a slower rate (<0.2 $pmolL^{-1}h^{-1}$) to reach a maximum after 48 h. At this equilibration point, the production of Hg^0 was slow relative to that in the first hour, and accumulated Hg^0 concentrations reached a plateau concentration. After the first hour, the rates of reduction were an order of magnitude lower (**Table 4**) and the rates appeared more related to the relative $FeS_{(s)}$ surface area, increasing with the amount of $FeS_{(s)}$ present. At $FeS_{(s)}$ surface concentration of 1, 5 and 30 m^2L^{-1} of $FeS_{(s)}$ suspensions,

TABLE 1 | Concentrations used to determine the free energy of reactions (**Tables 2**, **3**) at pH 7. Values for individual forms of Hg, Fe and S are calculated using the equations in **Supplementary Table S2**. The Hg_T and Hg^0 concentrations are based on the added and measured Hg concentrations. The total sulfide and Fe(II) concentrations are based on the solubility data of (Rickard, 2006) for $FeS_{(s)}$ (**Supplementary Table S1**). A total Fe(III) concentration of 1 nM and a sulfate concentration of 0.1 μM is assumed. For Cd, the concentration is derived from the solubility product reaction.

Chemical species	Calculated/measured conc. (M)	Chemical species	Calculated/measured conc. (M)
pH	7	$Fe(OH)_2^+$	7.5×10^{-10}
Total sulfide	9.5×10^{-6}	Initial Hg_T	5×10^{-11}
HS-	9.5×10^{-6}	Hg^0	5×10^{-12}
$Fe(II)_T$	1.1×10^{-5}	Hg^{2+}	1×10^{-39}
Fe^{2+}	7.5×10^{-6}	$Hg(SH)_2$	1.4×10^{-11}
$Fe(III)_T$	10^{-9}	Cd^{2+}	2.1×10^{-11}
Fe^{3+}	1.5×10^{-17}	Total sulfate	10^{-7}

TABLE 2 | Calculated free energies of the various potential reactions discussed in the text based on the concentrations in **Table 1**, and writing the reactions in terms of the major dissolved forms of the metals and sulfide at pH 7. All solids are assumed to have an activity of 1. The redox calculations are done assuming the presence of 5 pM Hg^0.

Reaction	Log K	Log Q	ΔG (kJ/mol)	React. #
$FeS(s) + Hg(SH)_2 = HgS(s) + Fe^{2+} + 2SH^-$	−4.4	−6.59	−4.72	1
$CdS(s) + Hg(SH)_2 + H_2O = HgS(s) + CdOHS^- + H^+ + SH^-$	−19.2	−18.5	3.74	2
$Hg(SH)_2 + 2Fe^{2+} + 2H_2O = Hg^0 + 2Fe(OH)_2^+ + 4H^+ + 2SH^-$	−55.4	−67.9	−71.3	3
$HgS(s) + 2Fe^{2+} + 4H_2O = Hg^0 + 2Fe(OH)_2^+ + 3H^+ + HS^-$	−54.5	−45.8	49.8	4
$HgS(s) + H_2O = Hg^0 + ¼SO_4^{2-} + ¼H^+ + ¾HS^-$	−24.4	−25.9	−3.4	5
$Hg(SH)_2 + H_2O = Hg^0 + ¼SO_4^{2-} + 2¼H^+ + 1¾HS^-$	−25.3	−27.5	−17.9	6
$HgS(s) = Hg^0 + S^0(s)$	−12.5	−11.3	6.84	7
$Fe(OH)_2^+ + 1/8HS^- + 7/8H^+ = 1/8SO_4^{2-} + Fe^{2+} + 1½H_2O$	15.1	10.0	−28.8	8

TABLE 3 | Calculated free energies for the reactions involving Hg co-precipitation and Hg(II) reduction at the different pH values of the experiments.

Reaction	pH = 5	6	7	8
$FeS(s) + Hg(SH)_2 = HgS(s) + Fe^{2+} + 2SH^-$	7.8	−0.4	−4.8	−7.4
$Hg(SH)_2 + 2Fe^{2+} + 2H_2O = Hg^0 + 2Fe(OH)_2^+ + 4H^+ + 2SH^-$	−4.54	−39.67	−71.3	−106.7
$HgS(s) + 2Fe^{2+} + 4H_2O = Hg^0 + 2Fe(OH)_2^+ + 3H^+ + HS^-$	73.17	58.01	49.8	31.62
$HgS(s) + H_2O = Hg^0 + ¼SO_4^{2-} + ¼H^+ + ¾HS^-$	13.46	3.67	−3.46	−12.16
$Hg(SH)_2 + H_2O = Hg^0 + ¼SO_4^{2-} + 2¼H^+ + 1¾HS^-$	10.93	−7.61	−17.88	−29.30
$Fe(OH)_2^+ + 1/8HS^- + 7/8H^+ = 1/8SO_4^{2-} + Fe^{2+} + 1½H_2O$	−32.48	−29.80	-29.25	−24.52

respectively, ~12, ~15 and ~17% of the Hg^{II} was reduced over the course of 24 h.

While the formation of Hg^0 increased with surface area, the relationship was not linear. Several studies on the reduction of Hg^{II} in the presence of iron oxide minerals have shown that the minimum equilibration time necessary for the production of Hg^0 was 24 h (Wiatrowski et al., 2009; Ha et al., 2017), and our results also suggest that the system is approaching steady state over a similar time period, even though our studies were done at much lower ratios of Hg^{II}:$FeS_{(s)}$. The initial high rate of reduction followed by slower formation of Hg^0 suggests that competing reactions are occurring. Initially there would be high concentrations of dissolved Hg in solution but given the experimental conditions, the dissolved Hg would rapidly decrease due to co-precipitation of $HgS_{(s)}$ on the $FeS_{(s)}$ surface, or through surface complexation, as discussed below.

The reduction of Hg^{II} by cadmium sulfide ($CdS_{(s)}$) was investigated at a $CdS_{(s)}$ concentration corresponding to a surface area concentration of 5 m^2L^{-1} and Hg^{II} concentration of 50 pM. During the entire duration of the experiment (up to 4 days), measurements indicated that less than 2% of the total Hg was reduced with $CdS_{(s)}$ (**Figure 3**). The fraction of Hg^{II} reduced to Hg^0 was thus similar to the reduction observed in controls, suggesting that the presence of $CdS_{(s)}$ did not significantly enhance Hg reduction.

To examine the impact of DOM on the reduction of Hg, aqueous solutions of Hg^{II} were reacted with two different DOM extracts, obtained from waters collected at the shelf break of the North Atlantic Ocean (DOM1) and from western Long Island Sound (DOM2) (Mazrui et al., 2018). The two DOM were characterized by determining their optical properties (**Supplementary Table S3**). The Specific Ultraviolet Absorption ($SUVA_{254}$), calculated as absorption at 254 nm divided by the DOC concentration, is a measure of the aromaticity of the DOM. The absorption ratio (ratio of absorbance at 250–365 nm), on the other hand, is a measure

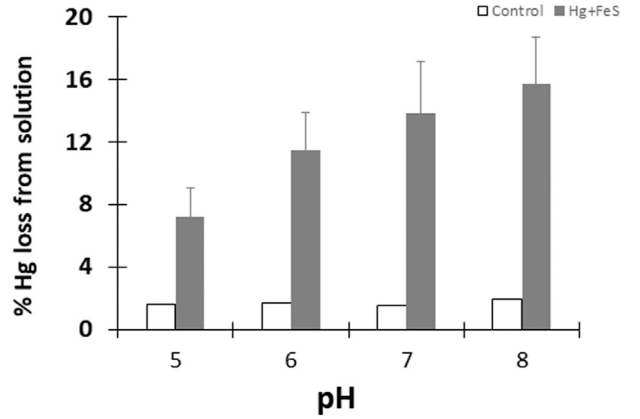

FIGURE 1 | Percentage of Hg^0 produced after 24 h in the presence (grey bars) and absence (white bars) of FeS_m at different pH. Reactions done under dark and anoxic conditions with 50 pM Hg^{II} and $FeS_{(s)}$ at a surface area to volume of solution ratio of 5 m^2/L. Error bars show mean ± standard deviation (n = 3).

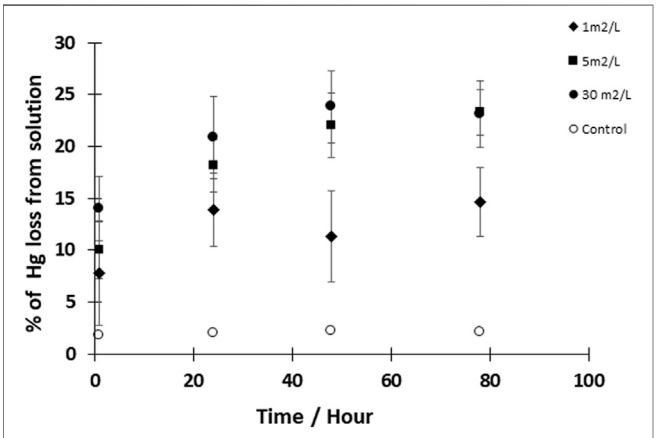

FIGURE 2 | Kinetics of Hg^{II} reduction by $FeS_{(s)}$. Experimental solutions contained 50 pM Hg^{II} and $FeS_{(s)}$ at a concentration of 1, 5, and 30 m^2/L (surface area to volume of solution ratio). Reactions were performed at pH 7–8 under dark and anoxic conditions. Error bars represent mean ± standard deviation (n = 3).

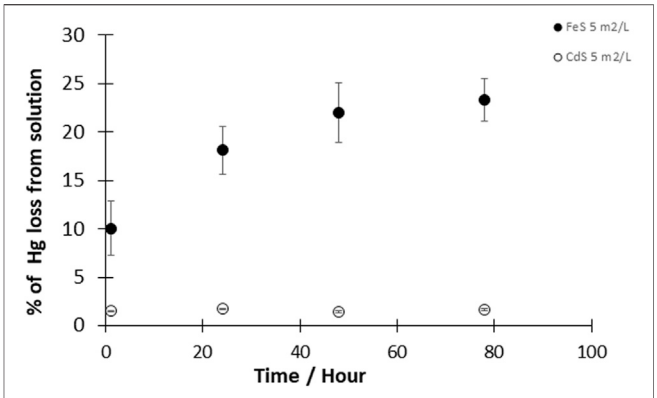

FIGURE 3 | Kinetics of the reaction of Hg^{II} with $CdS_{(s)}$ and FeS(s). Experimental solutions contained 50pM Hg^{II} and 5 m^2/L $CdS_{(s)}$ or 5 m^2/L $FeS_{(s)}$ (given as surface area to volume of solution ratio). Reactions were performed at pH 7–8 under dark and anoxic conditions. Error bars represent the mean ± standard deviation (n = 3).

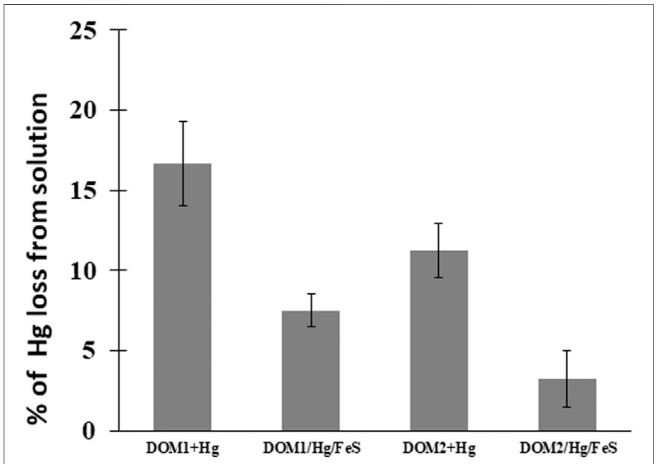

FIGURE 4 | Percent Hg^{II} converted to Hg^0 after 24 h of reacting 50 pM Hg^{II}, 5 mg C/L DOM and 5 $m^2L^{-1}FeS_{(s)}$ at pH 7–8 under dark and anoxic conditions. Error bars represent mean ± standard deviation (n = 3).

TABLE 4 | Calculated rates of reaction in the presence of different amounts of $FeS_{(s)}$ and over time at a pH of 7–8.

Surf. Area (m^2/L)	Rate (hr^{-1})	Rate (x 10^{-2} hr^{-1})	Rate (x 10^{-2} hr^{-1})	Rate (x 10^{-2} hr^{-1})
	0–1 h	1–24 h	24–48 h	1–48 h
1	0.78	1.3	−0.4	0.43
5	0.92	1.3	0.37	0.81
30	1.09	0.8	0.26	0.53

of the molecular weight of the DOM. Since high molecular weight DOM absorbs more strongly at longer wavelengths than low molecular weight DOM, a lower absorption ratio indicates that the DOM has a higher relative molecular weight. Here, we found that DOM2 had a lower absorption ratio and a higher $SUVA_{254}$ than DOM1. We also found that DOM1 had a proteinaceous fluorescence signal (intense emission at a lower wavelength) similar to tyrosine and tryptophan emissions while DOM2 had

a humic-like fluorescence signal (**Supplementary Figure S1**), which likely reflects differences in the amount of allochthonous vs. autochthonous DOM sources. Thus, DOM2 had more humic characteristics, i.e., of more allochthonous origin, hydrophobic and aromatic, with a lower nitrogen content and a higher phenolic and sulfur content than DOM1.

At pH 7–8, 17% of the added Hg^{II} in the DOM1 sample was reduced to Hg^0 after 24 h, whereas ~12% was reduced by DOM2 (**Figure 4**), indicating a slower reaction rate of the latter. The maximum reduction was obtained after 48 h, with ~25% of the Hg^{II} reduced by DOM1. This result is consistent with some previous studies of Hg^{II} reduction by DOM in the absence of light (Zheng et al., 2012; Chakraborty et al., 2015).

The reducing capacity of $FeS_{(s)}$ in the presence of the two different DOM was further investigated to examine the impact of both as thiols ligands can affect both the dissolved concentration and the speciation of Hg^{II} (**Figure 4**). The total concentrations of Hg^0 produced decreased in the presence of $FeS_{(s)}$ for both DOM1 (55% decrease) and DOM2 (71% decrease). In contrast to reduction of Hg^{II} at pH 7–8 within 24 h with DOM only, added $FeS_{(s)}$ decreased Hg^0 production. The produced Hg^0 was lower however than in the presence of $FeS_{(s)}$ alone (**Figure 1**), indicating that the presence of DOM hindered the reduction when a solid surface was present, but enhancing the reduction in its absence. This may suggest that at pH 7–8 the reaction likely involves Hg associated with the $FeS_{(s)}$ and not dissolved Hg, but the influence of DOM may also be due to its binding to the $FeS_{(s)}$ surface, thereby reducing the extent of the reaction.

Finally, to examine the role of dissolved vs. solid phase reactions, Hg^0 production was evaluated in the presence of dissolved Fe(II) at two different pH values. The rate of production was higher in these homogeneous solutions (e.g., $1.32\ h^{-1}$ for the first hr at pH 7) than in the presence of $FeS_{(s)}$ ($0.78–1.09\ h^{-1}$; **Table 1**) although the dissolved Fe(II) used in these experiments was higher than that found in equilibrium with the solid.

DISCUSSION

Hg Reduction by $FeS_{(s)}$

In most studies looking at the interactions of Hg^{II} and $FeS_{(s)}$, the products obtained were the stable species β-$HgS_{(s)}$, and Hg^0 was not detected suggesting that the primary interaction was an exchange reaction with the release of Fe^{2+} from $FeS_{(s)}$ with concomitant β-HgS formation. This is essentially a cation exchange reaction driven by the thermodynamic favorability of precipitating $HgS_{(s)}$ (Jeong et al., 2008; Jeong et al., 2010; Skyllberg and Drott, 2010):

$$FeS_{(s)} + Hg(SH)_2 = HgS_{(s)} + 2HS^- + Fe^{2+} \qquad \log K = -4.4$$

The reaction is favorable under the experimental conditions except at the lower pH ($\Delta G = -4.72$ kJ/mol at pH 7 and 7.8 kJ/mol at pH 5; **Table 3**). Therefore, reduction of dissolved Hg could only occur initially, before Hg^{II} is co-precipitated. Bone et al. (2014), however, suggested that Hg^0 was generated from the reduction of Hg^{II} by $FeS_{(s)}$. They formulated a reduction hypothesis starting from Hg^{II} adsorption to the mineral. Nevertheless, they could not conclusively verify the role of the reductant—S^{-II} or Fe^{II} in Hg^{II} reduction, and overall, the role of S^{-II} or Fe^{II} as electron donors in Hg^{II} reduction appears to vary according to the ratio of Hg^{II}:$FeS_{(s)}$. Similar to the Bone et al. hypothesis, others (Hua and Deng, 2008; Hyun et al., 2012) suggested that U(VI) reduction by mackinawite or amorphous $FeS_{(s)}$ occurred following U(VI) adsorption onto the mineral surface and simultaneous release of Fe^{II}. They proposed that once sorbed to the mackinawite surface, either the surface U(VI) is reduced by S^{-II} at the Fe^{II} depleted mackinawite surface or the dissolved U(VI) is reduced by dissolved HS^- released by congruent dissolution of mackinawite. Kirsch et al. (2008) come to a similar conclusion for their studies of antimony. However, in contrast to U(VI), Hg is known to have a high affinity for reduced S even in substantially oxic environments (Wolfenden et al., 2005). In our experiments, co-precipitation reduces the dissolved Hg in solution and so while the reactions in the dissolved phase with Fe^{II} or S^{-II} may be favorable (Reactions 3 and 6 in **Table 2**), they are unlikely to be the only reactions occurring over time. Indeed, the reactions were slower in the presence of the $FeS_{(s)}$ suggesting that interaction of Hg with the solid is occurring, as predicted by the thermodynamic calculations at pH 7 and 8 (**Tables 2**, **3**).

The reaction of Hg^{II} with the surface is pH dependent, as pH affects both the dissolved speciation of Hg^{II} and sulfide, and the surface charge on the mineral. The point of zero charge (PZC) for mackinawite is around 7.5 (Wolthers et al., 2005) and so under the experimental conditions the surface is either positively charged or near neutral, and thus would not hinder the interaction of the dissolved Hg complexes with the surface. At the lower pH values, the uncharged Hg-sulfide complex dominates in solution but becomes less important as the pH increases. Overall, the noted pH effect on the reduction reaction is likely not related to the impact of pH on the interaction of Hg with the mineral surface. However, the precipitation of $HgS_{(s)}$ becomes less favorable at low pH. The reactions on the surface and in solution involving Hg^{II} reduction become more favorable at higher pH, primarily due to the decreasing concentrations of Fe(II) and HS^- with increasing pH (**Table 3**). Furthermore, the experimental pH effect is relatively small with the increase in Hg^0 production increasing by less than a factor of 2 for a change in $[H^+]$ of 10^3.

Most studies on the interactions between Hg^{II} and minerals show that the production of Hg^0 increases with the pH of the solution (Wiatrowski et al., 2009; Bone et al., 2014; Ha et al., 2017). The results reported by Andersson (1979) on the interaction between Hg^{II} and $Fe_2O_3.nH_2O$ found that the amount of reduced Hg^{II} increased with pH, from pH values of 6.2–8.5. The same result has been observed by Patterson et al. (1997) with the interaction between chromium and $FeS_{(s)}$. Thus, our results agree with these studies with the best rate of reduction at pH 7–8. The influence of pH on the production of Hg^0 in the range 7–8 could be explained by the formation of the dissolved species $FeOH^+$ in these studies, which increases in relative

TABLE 5 | Measured concentrations of Fe^{II} in iron sulfide suspensions.

Surface area	Concentrations of Fe(II) in FeS suspensions (μM) in absence of mercury	
(m^2/L)	pH = 7–8	pH = 5–6
1	25 ± 2	–
5	136.6 ± 5.5	165.8 ± 7
10	203 ± 15	198 ± 23
30	466 ± 14.3	540 ± 17

concentration with pH, as shown by Amirbahman et al. (2013), although this reaction is unlikely to be occurring in our experiments (**Table 3**). Our results showed an increase in reduction with increased mineral surface area, suggesting that co-precipitated $HgS_{(s)}$ is likely involved in the reaction. Other studies on heterogeneous reduction have demonstrated that the formation of surface complexes is responsible for the enhanced reaction rate (Liu et al., 2008; Pecher et al., 2002; Schwarzenbach and Stone, 2003) and this adsorption depends on the pH (Kim et al., 2004; Miretzky et al., 2005). We conclude that this explains why the increase in pH promotes the reduction of Hg^{II}.

At the low concentrations of Hg used in our experiments compared to the other studies mentioned above, the amount of Fe^{2+} released into solution from the co-precipitation of Hg onto the mineral surface is small compared to the Fe^{2+} in solution in equilibrium with the solid phase. The following reactions determine the dissolved Fe(II) and total S(-II) concentrations in equilibrium with the solid (Stumm and Morgan, 1996; Wolthers et al., 2005; Rickard, 2006; **Supplementary Tables S1, S2**):

$$FeS_{(s)} + H^+ = Fe^{2+} + HS^- \qquad log\,K = -2.23$$
$$FeS_{(s)} = FeS^0_{(aq)} \qquad log\,K = -5.7$$
$$H_2S = H^+ + HS^- \qquad log\,K = -7.1$$
$$Fe^{2+} + OH^- = FeOH^+ \qquad log\,K = 4.5$$

While $FeOH^+$ is the dominant complex formed in solution in the absence of sulfide, the principal form is the free ion. In the presence of sulfide, FeS^0 is also found where this represents a series of cluster compounds with 1:1 stoichiometry (Rickard, 2006), and is present at a fixed concentration in equilibrium with the solid. The total dissolved Fe^{II} concentration depends on both the pH and the sulfide concentration (**Supplementary Table S1**). At pH 5.5, $FeOH^+$ is insignificant but increases to about 10% of the total Fe^{II} at pH 8, according to the thermodynamic calculations. The calculations, based on Rickard (2006), predict a dissolved Fe^{II} concentration of 182 μM at pH 5 and 3.7 μM at pH 8. Our measurements (**Table 5**) found slightly higher concentrations at higher pH and less of a pH effect (e.g., 137 μM at pH 7–8 and 166 μM at pH 5–6 for 5 m^2/L $FeS_{(s)}$), and also that the dissolved Fe^{II} increased with the amount of $FeS_{(s)}$ added, suggesting that the assumption of a pure solid (activity = 1) is likely not completely valid for our studies, likely due to the amorphous nature of the solid used. While we did not measure sulfide concentrations, the predicted dissolved concentration (total $S^{-II}_{(aq)} \sim Fe^{II}_{(aq)}$) is not high enough to precipitate the majority of the dissolved Hg as $HgS_{(s)}$ (**Table 1**), and much of the Hg^{II} is in solution initially as $Hg(SH)_2$, and its deprotonated forms (HgS_2H^- and HgS_2^{2-}) (Skyllberg and Drott, 2010).

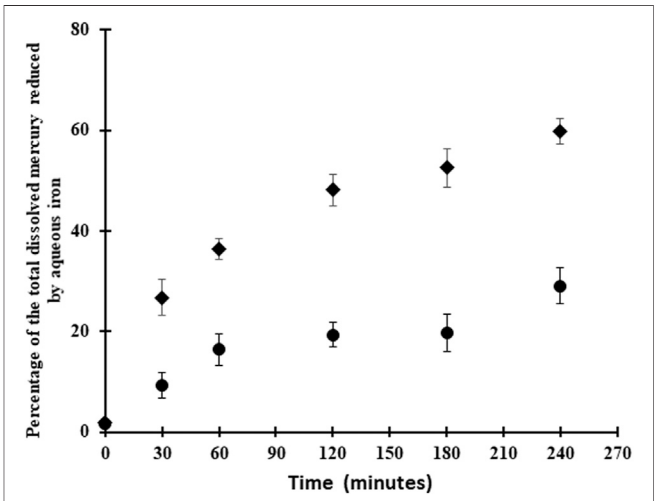

FIGURE 5 | Kinetics of Hg^{II} (50 pM) reduction by Fe^{II} (1 mM) at pH 5 (circle) and 7.5 (square).

Reduction Mechanisms

The source of the electrons for the reduction of Hg^{II} is either from a redox reaction on the surface involving the mineral constituents, or a reaction with dissolved reduced ions, either Fe^{II} or S^{-II}. If sulfide was being oxidized during the reduction of Hg, then one would predict this should have occurred in the presence of the $CdS_{(s)}$, but no reduction was observed. The equilibrium dissolved S^{-II} and Cd^{II} concentrations in the presence of the solid (K = −14.36 for $CdS_{(s)} + H^+ = Cd^{2+} + HS^-$) are lower, however, than in the presence of $FeS_{(s)}$, and thus the reduction in the presence of $CdS_{(s)}$ would be less favorable even if S^{-II} was the reductant. Thermodynamic calculations suggest the concentration of sulfide is at low nM levels in the presence of $CdS_{(s)}$ and that the co-precipitation reaction of Hg with the $CdS_{(s)}$ is not thermodynamically favorable (**Table 2**). Thus, the lack of reaction in this case does not necessarily negate the role of sulfide oxidation in Hg reduction.

The other potential reductant is Fe^{II} for the reactions in the presence of the $FeS_{(s)}$, as it is with the reactions in the presence of dissolved Fe^{II}, and no surfaces (**Figure 5**). Thermodynamically the reaction is favorable in solution ($\Delta G = -71.3$ kJ/mol at pH 7) under the experimental conditions (**Tables 2**, **3**), even given the low concentration of Hg^{II} relative to Fe^{II} and HS^-, and with the assumption that Fe^{III} is low (**Table 1**):

$$Hg(SH)_2 + 2Fe^{2+} + 2H_2O = Hg^0 + 2Fe(OH)_{2^+} + 4H^+ + 2HS^-$$
$$Log\,K = 55.4$$

Thus, while Hg remains in solution, the reaction will proceed and this likely accounts for the initial formation of Hg^0 in the initial time period, and could account for some of the trend seen with pH. However, as the concentration of dissolved Hg^{II} decreases as Hg is precipitated onto the $FeS_{(s)}$, this reaction will no longer occur. The time series measurements were made at pH 7–8 where co-precipitation is a favorable reaction, thereby decreasing the dissolved concentration of Hg over time. The differences in the rate of reaction in homogeneous solution (**Figure 5**) and in the presence of $FeS_{(s)}$ (**Figure 2**) indicates that the majority of the Hg^{II} is being co-precipitated or surface absorbed to the solid.

Another mechanism is therefore needed to account for the Hg^0 formation at later times. The reaction of co-precipitated $HgS_{(s)}$ with Fe(II) is not favorable (**Table 3**) and therefore the reaction that occurs with the precipitated Hg does not involve Fe(II):

$$HgS_{(s)} + 2Fe^{2+} + 4H_2O = Hg^0_{(aq)} + 2Fe(OH)^+_2 + 3H^+ + 2HS^-$$
$$\log K = -54.5$$

Overall, we conclude that Fe^{II} or $FeOH^+$ is not the reductant in our experiments after the Hg has co-precipitated onto the solid. Thus, there is a difference in the mechanisms for the reduction of Hg^{II} in the presence of $FeS_{(s)}$ and with dissolved Fe^{II} (Jeong et al., 2010; Richard et al., 2016). Note, however, that at pH 5 the precipitation reaction is not thermodynamically favorable and therefore the reactions in solution dominate, with Fe^{II} being the primary reductant (**Table 3**).

Alternatively, the reductant could be S^{-II}, and the reason for the low reaction in the presence of $CdS_{(s)}$ is probably because of the low sulfide concentration in equilibrium with the solid. The potential reaction is thermodynamically favorable, even under the low concentrations of the experimental conditions, for both the reactions in the water and that with the solid, except at the lower pH levels (**Table 3**):

$$Hg(SH)_2 + H_2O = Hg^0_{(aq)} + \tfrac{1}{4}SO_4^{2-} + 1\tfrac{3}{4}HS^- + 2\tfrac{1}{4}H^+ \quad \log K = -25.3$$

and

$$HgS_{(s)} + H_2O = Hg^0_{(aq)} + \tfrac{1}{4}SO_4^{2-} + \tfrac{3}{4}HS^- + \tfrac{1}{4}H^+ \quad \log K = -24.4$$

The equations represent either oxidation of dissolved sulfide or of the S^{-II} associated with the $HgS_{(s)}$. Overall, again, these calculations suggest that the reaction later in the experimental time period does not involve dissolved reduced species and that the reduction involves reactions within the solid, with the electrons being provided from the oxidation of S^{-II} by an electron transfer reaction at the surface, followed by the release of Hg^0 into solution. Overall, these results suggest that initially in the experiments, the dissolved Hg is being reduced by either Fe(II) or HS^-, but that later in the experiment the reaction only involves reduced S. If Fe^{II} is being oxidized, the Fe^{III} produced would likely remain adsorbed on the solid, but it is also likely that the Fe(III) would be reduced back to Fe(II) by the sulfide in solution as this reaction is favorable under the experimental conditions ($\Delta G = -28.8$ kJ/mol at pH 7; **Tables 2**, **3**). Thus, once the Hg is co-precipitated onto the $FeS_{(s)}$ surface, whether the reaction involves initially S(−II) or Fe(II) is somewhat academic as the final products will be the same because of the reduction of any Fe(III) produced.

If the reaction involves sulfide oxidation, the fate would depend on the degree of oxidation of S^{-II}. It is likely that some intermediate product, such as elemental sulfur (S^0), could result, rather than complete oxidation to sulfate. Indeed, an electron exchange reaction between Hg^{II} and S^{-II} could potentially occur with the formation of Hg^0 and elemental S. Given the uncertainty in the equilibrium constants (Stumm and Morgan, 1996; Skyllberg and Drott, 2010), and assuming pure solids are formed, the reaction is near equilibrium at pM Hg^0 concentrations (i.e., $[Hg^0] \sim K$; **Table 2**, Reaction #7):

$$HgS_{(s)} = Hg^0_{(aq)} + S^0_{(s)}$$
$$\log K = -12.5 \text{ and } \Delta G = 6.84\,\text{kJ/mol at 5 pM } Hg^0$$

As mentioned earlier, the lack of a reaction with $CdS_{(s)}$ is likely because of the lack of precipitation of $HgS_{(s)}$ on the surface at the low sulfide concentrations found in equilibrium with the solid phase, and the low sulfide concentration in solution. This is because of the stronger M-S bond in $CdS_{(S)}$ compared to $FeS_{(S)}$.

Furthermore, as noted above, the increase in the amount of mineral surface of mackinawite (**Figure 2**) slightly influences the quantities of Hg^0 produced. With 30 m^2L^{-1} of $FeS_{(s)}$, the reduction reached a maximum of 11 pM of Hg^0 after 24 h of reaction, while this maximum was 6.9 pM for 1 m^2L^{-1} of $FeS_{(s)}$. These results indicate that a surface catalytic role of precipitated $HgS_{(s)}$ on mackinawite is involved in the production of Hg^0. Wiatrowski et al. (2009) demonstrated that the kinetics of Hg^{II} reduction by magnetite systematically varies as a function of magnetite concentration. Amirbahman et al. (2013)'s study on the kinetics of Hg^{II} reduction by Fe^{II} suggested that the mineral phases are important factors affecting the rate of the mercury reductive pathways, and O'Loughlin et al. (2020) showed that there were differences in the reaction rates in the presence of Fe^{II}-containing clays. However, Jeong et al. (2010) have shown that the adsorption of Hg^{II} onto the surfaces of mackinawite only occurs below a certain molar ratio of Hg^{II} and $FeS_{(s)}$, which implies that the ratio of Hg^{II}:$FeS_{(s)}$ could also influence the production of Hg^0. This ratio in our study was 5–7 orders of magnitude lower than that of Jeong et al. (2010).

In summary, our study indicated that mercury reduction by $FeS_{(s)}$ is kinetically slow and the production of Hg^0 is small compared to other potential reduction pathways in environmental ecosystems, such as Hg^{II} reduction in the presence of dissolved Fe^{II} or DOM, and also appears to occur *via* a different mechanism. The experiments were carried out with excess $FeS_{(s)}$ concentrations so the reaction can therefore be described according to pseudo first order kinetics. The overall reaction rate constants obtained are k = $67 \times 10^{-3}\ h^{-1}$; $85 \times 10^{-3}\ h^{-1}$; and $92 \times 10^{-3}\ h^{-1}$, respectively, for 1, 5, and 30 m^2/L of $FeS_{(s)}$. These values are similar in terms of the link between reaction rate constant and mineral concentration noted in some studies (Wiatrowski et al., 2009; Amirbahman et al., 2013; Ha et al., 2017). However, our experimental data show that the average net rate of Hg^{II} reduction by $FeS_{(s)}$, assuming first order kinetics over the experimental time period, is lower than Hg^{II} reduction by humic substances ($1.6–2.1 \times 10^{-2}\ h^{-1}$; Chakraborty et al., 2015), minerals such as clay ($1.74 \times 10^{-1}\ h^{-1}$) (Peretyazhko et al., 2006a), hematite from phlogopite ($6.60 \times 10^{-1}\ h^{-1}$) or magnetite (Wiatrowski et al., 2009). These results confirm that the production rate of Hg^0 is a function of the nature of the mineral (i.e., oxide or sulfide), and likely the form of Hg adsorbed or precipitated on the surface of the mineral.

Reaction With Dissolved Iron

Overall, under our experimental conditions, the homogeneous Hg reduction in presence of aqueous Fe^{II} without mineral surfaces was more favorable than the experiments in presence of $FeS_{(s)}$ mineral (**Figure 5**), which is consistent with the thermodynamic calculations (**Table 3**). The initial reaction rate was 20–70% higher for the aqueous Fe^{II} experiments. However, the concentration of Fe^{II} in the homogeneous experiments was much higher than in the mineral studies and this could potentially account for the higher conversion rate to Hg^0, although the rate should be similar given that the initial Hg^{II} concentration was the same, and the Fe^{II} concentrations in both cases is substantially higher and not rate limiting Rather, the mechanisms are likely different for the two situations. Although several authors have shown the role of surface-catalysis by iron minerals on the rate of mercury reduction, our data (**Figure 5**) shows fast reduction of mercury in presence of aqueous Fe^{II}. In contrast, Ha et al. (2017) indicated that mercury reduction by aqueous ferrous iron in the absence of a solid phase was kinetically slow. Pasakarnis et al. (2013), Amirbahman et al. (2013) suggested that Hg^I sorbed onto the mineral surface during the transformation of Hg^{II} to Hg^0 and acts as a surface-catalyst in this reaction. Peretyazhko et al. (2006b) demonstrated that adsorption of Fe^{II} to the haematite surface created very reactive sites for the reduction of Hg^{II}, while in the absence of haematite particles, no production of Hg^0 occurred. The difference between this study and previous studies mentioned above might be due to the low concentration of Fe^{II} in the $FeS_{(s)}$ suspensions or more likely because the reaction proceeds *via* a different mechanism once the Hg is co-precipitated.

Effect of Dissolved Organic Matter

It is well known that dissolved organic matter (DOM) has a strong interaction with mercury and other trace metals affecting their speciation, mobility and toxicity (Buffle, 1988). Under abiotic dark conditions in aquatic systems, DOM participates in the conversion of Hg^{II} to Hg^0 but also contributes to the strong complexation of Hg^{II} (Ravichandran et al., 1998; Deonarine and Hsu-Kim, 2009; Zheng and Hintelmann 2010; Zheng et al., 2012; Han et al., 2007). This complexation is attributed to reduced sulfur ligands (Waples et al., 2005; Merritt and Amirbahman, 2007). Indeed, DOM is a mixture of molecular organic compounds with a large number of hydrophilic functional groups: carboxylic (COOH), phenolic and/or alcoholic (OH), carbonyl (C=O) and amine groups (NH_2). Reduced sulfur groups also exist in different oxidation states (R-SH, R-S=S-R and R-SO_3H). Chakraborty et al. (2015) showed that the ratio of the–COOH/−OH groups and the sulfur content in the humic substances reveal a strong competition between complexation and reduction of Hg^{II}. They suggested that several parameters such as pH, total sulfur content, the −COOH/−OH ratio and salinity influenced the reduction of Hg^{II} in presence of DOM. In our studies, the less humic DOM1 reduced Hg at a higher rate than that with DOM2, and this is consistent with the data of Chakraborty et al. (2015) who showed that the rate of reduction was higher for humic material with less total S, or a higher ratio of carboxylic to thiol groups. As discussed above and shown in **Supplementary Figure S1**, DOM2 has more humic character while DOM1 is more protein-like in terms of its fluorescence.

We observed that the Hg^{II} reduction by DOM was diminished in presence of $FeS_{(s)}$, whatever the characteristics of the experiment (**Figure 4**). Calculations of the speciation of dissolved Hg in the presence of $FeS_{(s)}$ and DOM at the concentrations used in the experiment, using the RSH:DOM ratios determined by Seelen (2018) for comparable coastal waters and the $Hg(SR)_2$ binding constant from Skyllberg and Drott (2010), suggest that a small fraction of the Hg—5–10% depending on the DOM was organically complexed during the experiments. This is consistent with the results that showed the extent of reduction in the presence of $FeS_{(s)}$ and DOM was lower than that of $FeS_{(s)}$ alone. Overall, we conclude that the presence of DOM increases the barrier to Hg reduction by sulfide surfaces, and likely also has a similar effect for other reductive surfaces.

Mishra et al. (2011) observed that the Hg^{II} reduction by magnetite and green rust was severely diminished in the presence of bacterial biomass, suggesting inhibition by surface sulfhydryl groups. These experiments suggest that the conditions of the experiment likely determine whether Hg is primarily bound to the reduced S in DOM or the inorganic reduced sulfide in $FeS_{(s)}$, or is removed by co-precipitation. Furthermore, in most of the studies on the interaction between Hg^{II} and $FeS_{(s)}$, the products obtained were the stable solids metacinnabar, cinnabar, and Hg associated with iron sulfides (Jeong et al., 2008; Liu et al., 2008; Skyllberg and Drott, 2010) suggesting Fe^{II} present in $FeS_{(s)}$ suspension acts as an electron donor in the production of Hg^0. However, in the presence of DOM and $FeS_{(s)}$, this mechanism could be changed as DOM likely keeps the Hg in solution and prevents its interaction with the solid phase, although our calculations show that the extent of complexation was small. However, depending on the pH, the DOM can also interact with the

mineral surface and therefore hinder the co-precipitation of Hg^{II} and any surface reactions. Dissolved organic matter is known to play a dual role in $HgS_{(s)}$ formation and stabilization (Slowey, 2010; Gerbig et al., 2011a), creating a competition between its complexation of Hg and Hg adsorption to the iron sulfide (Skyllberg and Drott, 2010) and, influencing, through its complexation of dissolved Hg, the dissolution of cinnabar (Ravichandran et al., 1998; Waples et al., 2005). We conclude that our data showing that Hg^{II} reduction in presence of both DOM and $FeS_{(s)}$ was less than found in the presence of either DOM or $FeS_{(s)}$ only, is because of the competition between $FeS_{(s)}$ and DOM for complexation and the extent of HgS formation (Skyllberg and Drott, 2010). The Hg^{II} would be less available for reduction by DOM, Fe^{II} or $FeS_{(s)}$ under these conditions. Zhu et al. (2013) have shown that the strength of Fe^{II} as a reducing agent is affected by DOM during the reduction of 2-nitrophenol (2-NP) in TiO_2 suspensions. Overall, the Hg^{II} reduction in presence of DOM or mineral phases involves complicated reaction pathways but the presence of DOM increases the barrier to reduction.

Environmental Implications

Our study demonstrates that Hg^{II} can be reduced to Hg^0 in the presence of $FeS_{(s)}$ but the extent of reduction is slow compared to that found with hydrous ferric oxide, with dissolved Fe(II) and in the presence of DOM. The data presented herein show clearly that in the presence of sulfide surfaces, Hg^{II} is less available for reduction. However, our results also showed that there was no Hg^0 production in presence of $CdS_{(s)}$ in contrast to $FeS_{(s)}$, suggesting that the presence of a sulfide surface is not sufficient for this reaction to occur (**Figure 4**). The concentration of sulfide in solution also plays a role in controlling the extent of the reaction. Neither $FeS_{(s)}$ nor $CdS_{(s)}$ enhanced Hg^{II} reduction compared to DOM or Fe^{II}. Based on thermodynamic calculations (**Tables 2**, **3**; **Supplementary Table S2**), we suggest that S^{-II} was the likely electron donor for reduction of precipitated Hg^{II} in the presence of $FeS_{(s)}$, and its higher concentration in the $FeS_{(s)}$ solutions compared to the $CdS_{(s)}$ solutions accounts for the differences in the Hg^0 formation. At low pH in the presence of $FeS_{(S)}$, precipitation of Hg^{II} is unlikely to occur and in this instance, reactions in solution are likely controlling the rate of reduction. We therefore suggest that while the Hg does not need to be adsorbed to the surface for the reaction to proceed, this is the likely fate of Hg in the presence of FeS solids under environmental conditions.

Extrapolating these findings to environmental conditions, we suggest that chemical reduction of Hg^{II} is complex in anoxic environments, such as sediment, with many potential reaction pathways. This reaction is influenced by ferrous iron, minerals, sulfide, DOM and interactions between the different compounds and solid phases. However, we conclude that the presence of $FeS_{(s)}$ in environmental sediments is not the major driver of the formation of Hg^0 in such systems as the reactions are slow once the Hg interacts with the mineral surface. Other reduction pathways are much more favorable with dissolved reductants (reduced Fe and S species). Furthermore, this study shows the influence of DOM on the reaction between Hg and $FeS_{(s)}$ and that its presence needs to be considered because DOM affects mercury transformation and mercury reactivity toward minerals, as shown by Skyllberg and Drott (2010). The type of DOM also influences the rate of reaction, as it does complexation.

Overall, processes that convert Hg^{II} to Hg^0 under anoxic conditions are important mitigators of the production and bioaccumulation of CH_3Hg as reduction potentially removes ionic Hg from the system where it could otherwise be methylated. More research at lower Hg concentrations is needed to further understand the primary reactions that are occurring and the potential role of DOM and pH in controlling the rates of Hg reduction.

DATA AVAILABILITY STATEMENT

All the data related to this study are included in the article/ **Supplementary Material**. The validated concentration datasets for this study will be provided on valid request. The data will be submitted to the University of Connecticut's data archiving facility to make it available upon request. The data will also be made available through Mason's research website: mason.mercury.uconn.edu.

AUTHOR CONTRIBUTIONS

All authors contributed to the design of the study. MC lead and conducted most of the laboratory work. NMM and SJ contributed with material (extracted DOM, lab-synthesized $FeS_{(s)}$ and $CdS_{(s)}$) and with labwork. MC and RPM wrote the paper with inputs from SJ and NMM.

FUNDING

The research was funded through the Fulbright Visiting Scholar Program to MC which supported her stay in United States (Grantee ID 68150507). SJ acknowledges funding from the Swedish Research Council (International Postdoc grant 637–2014–54). NM and RM acknowledge partial funding from the National Science Foundation Environmental Chemical Science program (Award # 1607913 to RM and J. Zhao).

ACKNOWLEDGMENTS

Staff and students from the labs of RM (University of Connecticut) are acknowledged for valuable discussions during the study. MC thanks the Fulbright Program for providing the scholarship; the Department of Marine Sciences and Chemistry, University of Connecticut for the reception within the department and for the help received; all staff and students of the RM lab for their help.

SUPPLEMENTARY MATERIAL

The Supplementary Material for this article can be found online at: https://www.frontiersin.org/articles/10.3389/fenvc.2021.660058/full#supplementary-material

REFERENCES

Allard, B., and Arsenie, I. (1991). Abiotic Reduction of Mercury by Humic Substances in Aquatic System - an Important Process for the Mercury Cycle. *Water Air Soil Pollut.* 56 (1), 457–464. doi:10.1007/bf00342291

Amirbahman, A., Kent, D. B., Curtis, G. P., and Marvin-Dipasquale, M. C. (2013). Kinetics of Homogeneous and Surface-Catalyzed Mercury(II) Reduction by Iron(II). *Environ. Sci. Technol.* 47 (13), 7204–7213. doi:10.1021/es401459p

Amyot, M., Gill, G. A., and Morel, F. M. M. (1997). Production and Loss of Dissolved Gaseous Mercury in Coastal Seawater. *Environ. Sci. Technol.* 31, 3606–3611. doi:10.1021/es9703685

Andersson, A. (1979). "Mercury in Soils," in *The Biogeochemistry of Mercury in the Environment*. Editor O. Nriagu (Amsterdam, The Netherlands: Elsevier, North-Holland Biomedical Press), 79–112.

Baohua, G., Yongrong, B., Carrie, L. M., Wenming, D., Xin, J., and Liang, L. (2011). Mercury Reduction and Complexation by Natural Organic Matter in Anoxic Environments. *PNAS* 108, 1479–1483. doi:10.1109/iccsn.2011.6014680

Benoit, J. M., Gilmour, C. C., Heyes, A., Mason, R. P., and Miller, C. L. (2003). "Geochemical and Biological Controls over Methylmercury Production and Degradation in Aquatic Ecosystems," in *Biogeochemistry of Environmentally Important Trace Elements. Acs Symposium Series*, 262–297.

Bone, S. E., Bargar, J. R., and Sposito, G. (2014). Mackinawite (FeS) Reduces Mercury(II) under Sulfidic Conditions. *Environ. Sci. Technol.* 48 (18), 10681–10689. doi:10.1021/es501514r

Bower, J., Savage, K. S., Weinman, B., Barnett, M. O., Hamilton, W. P., and Harper, W. F. (2008). Immobilization of Mercury by Pyrite (FeS2). *Environ. Pollut.* 156 (2), 504–514. doi:10.1016/j.envpol.2008.01.011

Buffle, J. (1988). *Complexation Reactions in Aquatic Systems: An Analytical Approach*. Chichester: Ellis Horwood Ltd.

Chakraborty, P., Vudamala, K., Coulibaly, M., Ramteke, D., Chennuri, K., and Lean, D. (2015). Reduction of Mercury (II) by Humic Substances-Influence of pH, Salinity of Aquatic System. *Environ. Sci. Pollut. Res.* 22 (14), 10529–10538. doi:10.1007/s11356-015-4258-4

Charlet, L., Bosbach, D., and Peretyashko, T. (2002). Natural Attenuation of TCE, as, Hg Linked to the Heterogeneous Oxidation of Fe(II): An AFM Study. *Chem. Geology* 190, 303–319. doi:10.1016/s0009-2541(02)00122-5

Clarkson, T. W., and Magos, L. (2006). The Toxicology of Mercury and its Chemical Compounds. *Crit. Rev. Toxicol.* 36 (8), 609–662. doi:10.1080/10408440600845619

Compeau, G. C., and Bartha, R. (1985). Sulfate-Reducing Bacteria: Principal Methylators of Mercury in Anoxic Estuarine Sediment. *Appl. Environ. Microbiol.* 50 (2), 498–502.

Costa, M., and Liss, P. (2000). Photoreduction and Evolution of Mercury from Seawater. *Sci. Total Environ.* 261 (1-3), 125–135. doi:10.1016/s0048-9697(00)00631-8

Deonarine, A., and Hsu-Kim, H. (2009). Precipitation of Mercuric Sulfide Nanoparticles in NOM-Containing Water: Implications for the Natural Environment. *Environ. Sci. Technol.* 43 (7), 2368–2373. doi:10.1021/es803130h

Dittmar, T., Koch, B., Hertkorn, N., and Kattner, G. (2008). A Simple and Efficient Method for the Solid-phase Extraction of Dissolved Organic Matter (SPE-DOM) from Seawater. *Limnol. Oceanogr. Methods* 6, 230–235. doi:10.4319/lom.2008.6.230

Driscoll, C. T., Mason, R. P., Chan, H. M., Jacob, D. J., and Pirrone, N. (2013). Mercury as a Global Pollutant: Sources, Pathways, and Effects. *Environ. Sci. Technol.* 47 (10), 4967–4983. doi:10.1021/es305071v

Eagles-Smith, C. A., Silbergeld, E. K., Basu, N., Bustamante, P., Diaz-Barriga, F., Hopkins, W. A., et al. (2018). Modulators of Mercury Risk to Wildlife and Humans in the Context of Rapid Global Change. *Ambio* 47 (2), 170–197. doi:10.1007/s13280-017-1011-x

Feinberg, A. I., Kurien, U., and Ariya, P. A. (2015). The Kinetics of Aqueous Mercury(II) Reduction by Sulfite over an Array of Environmental Conditions. *Water Air Soil Pollut.* 226 (4). doi:10.1007/s11270-015-2371-0

Fitzgerald, W. F., Lamborg, C. H., and Hammerschmidt, C. R. (2007). Marine Biogeochemical Cycling of Mercury. *Chem. Rev.* 107 (2), 641–662. doi:10.1021/cr050353m

Garcia, E., Amyot, M., and Ariya, P. A. (2005). Relationship between DOC Photochemistry and Mercury Redox Transformations in Temperate Lakes and Wetlands. *Geochi. Cosmochim. Acta* 69 (8), 1917–1924. doi:10.1016/j.gca.2004.10.026

Gerbig, C. A., Kim, C. S., Stegemeier, J. P., Ryan, J. N., and Aiken, G. R. (2011a). Formation of Nanocolloidal Metacinnabar in Mercury-DOM-Sulfide Systems. *Environ. Sci. Technol.* 45 (21), 9180–9187. doi:10.1021/es201837h

Gerbig, C. A., Ryan, J. N., and Aiken, G. R. (2011b). "The Effects of Dissolved Organic Matter on Mercury Biogeochemistry," in *Environmental Chemistry and Toxicology of Mercury* Editors Y. Cai, G. Liu, and N. O'Driscoll (New York, NY: Wiley), 259–292. doi:10.1002/9781118146644.ch8

Gilmour, C. C., Henry, A. E., and Mitchell, R. (1992). Sulfate stimulation of mercury methylation in freshwater sediments. *Environ. Sci. Technol.* 26 (11), 2281–2287. doi:10.1021/es00035a029

Ha, J., Zhao, X., Yu, R., Barkay, T., and Yee, N. (2017). Hg(II) Reduction by Siderite ($FeCO_3$). *Appl. Geochem.* 78, 211–218. doi:10.1016/j.apgeochem.2016.12.017

Han, S., Lehman, R. D., Choe, K. Y., and Gill, G. A. (2007). Chemical and physical speciation of mercury in Offatts Bayou: A seasonally anoxic bayou in Galveston Bay. *Limnol. Oceanogr.* 52 (4), 1380–1392. doi:10.4319/lo.2007.52.4.1380

Han, Y.-S., Kim, S.-H., Chon, C.-M., Kwon, S., Kim, J. G., Choi, H. W., et al. (2020). Effect of FeS on Mercury Behavior in Mercury-Contaminated Stream Sediment: A Case Study of Pohang Gumu Creek in South Korea. *J. Hazard. Mater.* 393, 122373. doi:10.1016/j.jhazmat.2020.122373

Hua, B., and Deng, B. (2008). Reductive Immobilization of Uranium(VI) by Amorphous Iron Sulfide. *Environ. Sci. Technol.* 42 (23), 8703–8708. doi:10.1021/es801225z

Hyun, S. P., Davis, J. A., Sun, K., and Hayes, K. F. (2012). Uranium(VI) Reduction by Iron(II) Monosulfide Mackinawite. *Environ. Sci. Technol.* 46 (6), 3369–3376. doi:10.1021/es203786p

Jeong, H. Y., Lee, J. H., and Hayes, K. F. (2008). Characterization of Synthetic Nanocrystalline Mackinawite: Crystal Structure, Particle Size, and Specific Surface Area. *Geochimica et Cosmochimica Acta* 72 (2), 493–505. doi:10.1016/j.gca.2007.11.008

Jeong, H. Y., Sun, K., and Hayes, K. F. (2010). Microscopic and Spectroscopic Characterization of Hg(II) Immobilization by Mackinawite (FeS). *Environ. Sci. Technol.* 44 (19), 7476–7483. doi:10.1021/es100808y

Jeremiason, J. D., Portner, J. C., Aiken, G. R., Hiranaka, A. J., Dvorak, M. T., Tran, K. T., et al. (2015). Photoreduction of Hg(II) and Photodemethylation of Methylmercury: The Key Role of Thiol Sites on Dissolved Organic Matter. *Environ. Sci. Process. Impacts* 17 (11), 1892–1903. doi:10.1039/c5em00305a

Jiang, T., Skyllberg, U., Wei, S., Wang, D., Lu, S., Jiang, Z., et al. (2015). Modeling of the Structure-specific Kinetics of Abiotic, Dark Reduction of Hg(II) Complexed by O/N and S Functional Groups in Humic Acids while Accounting for Time-dependent Structural Rearrangement. *Geochim. Cosmochim. Acta* 154, 151–167. doi:10.1016/j.gca.2015.01.011

Jonsson, S., Mazrui, N. M., and Mason, R. P. (2016). Dimethylmercury Formation Mediated by Inorganic and Organic Reduced Sulfur Surfaces. *Sci. Rep.* 6. doi:10.1038/srep27958

Kim, C. S., Rytuba, J. J., and Brown, G. E. (2004). EXAFS Study of Mercury(II) Sorption to Fe- and Al-(hydr)oxides. *J. Colloid Interf. Sci.* 271 (1), 1–15. doi:10.1016/s0021-9797(03)00330-8

Kirsch, R., Scheinost, A. C., Rossberg, A., Banerjee, D., and Charlet, L. (2008). Reduction of Antimony by Nano-Particulate Magnetite and Mackinawite. *Mineral. Mag.* 72, 185–189. doi:10.1180/minmag.2008.072.1.185

Liu, J., Valsaraj, K. T., Devai, I., and DeLaune, R. D. (2008). Immobilization of Aqueous Hg(II) by Mackinawite (FeS). *J. Hazard. Mater.* 157 (2-3), 432–440. doi:10.1016/j.jhazmat.2008.01.006

Matthiessen, A. (1998). Reduction of Divalent Mercury by Humic Substances - Kinetic and Quantitative Aspects. *Sci. Total Environ.* 213, 177–183. doi:10.1016/s0048-9697(98)00090-4

Mauclair, C., Layshock, J., and Carpi, A. (2008). Quantifying the Effect of Humic Matter on the Emission of Mercury from Artificial Soil Surfaces. *Appl. Geochem.* 23 (3), 594–601. doi:10.1016/j.apgeochem.2007.12.017

Mazrui, N. M., Seelen, E., King'ondu, C. K., Thota, S., Awino, J., Rouge, J., et al. (2018). The Precipitation, Growth and Stability of Mercury Sulfide

Nanoparticles Formed in the Presence of marine Dissolved Organic Matter. *Environ. Sci. Process. Impacts* 20 (4), 642–656. doi:10.1039/c7em00593h

Mergler, D., Anderson, H. A., Chan, L. H. M., Mahaffey, K. R., Murray, M., Sakamoto, M., et al. (2007). Methylmercury Exposure and Health Effects in Humans: A Worldwide Concern. *AMBIO: A J. Hum. Environ.* 36 (1), 3–11. doi:10.1579/0044-7447(2007)36[3:meahei]2.0.co;2

Merritt, K. A., and Amirbahman, A. (2007). Mercury Mobilization in Estuarine Sediment Porewaters: A Diffusive Gel Time-Series Study. *Environ. Sci. Technol.* 41 (3), 717–722. doi:10.1021/es061659t

Miretzky, P., Bisinoti, M. C., and Jardim, W. F. (2005). Sorption of Mercury (II) in Amazon Soils from Column Studies. *Chemosphere* 60 (11), 1583–1589. doi:10.1016/j.chemosphere.2005.02.050

Mishra, B., O'Loughlin, E. J., Boyanov, M. I., and Kemner, K. M. (2011). Binding of HgIIto High-Affinity Sites on Bacteria Inhibits Reduction to Hg0by Mixed FeII/IIIPhases. *Environ. Sci. Technol.* 45 (22), 9597–9603. doi:10.1021/es201820c

Muresan, B., Pernet-Coudrier, B., Cossa, D., and Varrault, G. (2011). Measurement and Modeling of Mercury Complexation by Dissolved Organic Matter Isolates from Freshwater and Effluents of a Major Wastewater Treatment Plant. *Appl. Geochem.* 26 (12), 2057–2063. doi:10.1016/j.apgeochem.2011.07.003

O'Driscoll, N. J., Siciliano, S. D., Lean, D. R. S., and Amyot, M. (2006). Gross Photoreduction Kinetics of Mercury in Temperate Freshwater Lakes and Rivers: Application to a General Model of DGM Dynamics. *Environ. Sci. Technol.* 40 (3), 837–843. doi:10.1021/es051062y

O'Loughlin, E. J., Kelly, S. D., Kemner, K. M., Csencsits, R., and Cook, E. R. (2003). Reduction of AgI, AuIII, CuII, and HgII by FeII/FeIII hydroxysulfate green rust. *Chemosphere* 53 (5), 437–446. doi:10.1016/S0045-6535(03)00545-9

O'Loughlin, E. J., Boyanov, M. I., Kemner, K. M., and Thalhammer, K. O. (2020). Reduction of Hg(II) by Fe(II)-bearing Smectite clay Minerals. *Minerals* 10 (12), 1079. doi:10.3390/min10121079

Ona-Nguema, G., Abdelmoula, M., Jorand, F., Benali, O., Block, J.-C., and Génin, J.-M. R. (2002). Iron(II,III) Hydroxycarbonate green Rust Formation and Stabilization from Lepidocrocite Bioreduction. *Environ. Sci. Technol.* 36 (1), 16–20. doi:10.1021/es0020456

Park, J.-S., Oh, S., Shin, M.-Y., Kim, M.-K., Yi, S.-M., and Zoh, K.-D. (2008). Seasonal Variation in Dissolved Gaseous Mercury and Total Mercury Concentrations in Juam Reservoir, Korea. *Environ. Pollut.* 154 (1), 12–20. doi:10.1016/j.envpol.2007.12.002

Parks, J. M., Johs, A., Podar, M., Bridou, R., Hurt, R. A., Smith, S. D., et al. (2013). The Genetic Basis for Bacterial Mercury Methylation. *Science* 339 (6125), 1332–1335. doi:10.1126/science.1230667

Pasakarnis, T. S., Boyanov, M. I., Kemner, K. M., Mishra, B., O'Loughlin, E. J., Parkin, G., et al. (2013). Influence of Chloride and Fe(II) Content on the Reduction of Hg(II) by Magnetite. *Environ. Sci. Technol.* 47 (13), 6987–6994. doi:10.1021/es304761u

Patterson, R. R., Fendorf, S., and Fendorf, M. (1997). Reduction of Hexavalent Chromium by Amorphous Iron Sulfide. *Environ. Sci. Technol.* 31 (7), 2039–2044. doi:10.1021/es960836v

Pecher, K., Haderlein, S. B., and Schwarzenbach, R. P. (2002). Reduction of Polyhalogenated Methanes by Surface-Bound Fe(II) in Aqueous Suspensions of Iron Oxides. *Environ. Sci. Technol.* 36, 1734–1741. doi:10.1021/es011191o

Peretyazhko, T., Charlet, L., and Grimaldi, M. (2006a). Production of Gaseous Mercury in Tropical Hydromorphic Soils in the Presence of Ferrous Iron: A Laboratory Study. *Eur. J. Soil Sci.* 57 (2), 190–199. doi:10.1111/j.1365-2389.2005.00729.x

Peretyazhko, T., Charlet, L., Muresan, B., Kazimirov, V., and Cossa, D. (2006b). Formation of Dissolved Gaseous Mercury in a Tropical lake (Petit-Saut Reservoir, French Guiana). *Sci. Total Environ.* 364 (1-3), 260–271. doi:10.1016/j.scitotenv.2005.06.016

Podar, M., Gilmour, C. C., Brandt, C. C., Soren, A., Brown, S. D., Crable, B. R., et al. (2015). Global Prevalence and Distribution of Genes and Microorganisms Involved in Mercury Methylation. *Sci. Adv.* 1, e1500675. doi:10.1126/sciadv.1500675

Ravichandran, M., Aiken, G. R., Reddy, M. M., and Ryan, J. N. (1998). Enhanced Dissolution of Cinnabar (Mercuric Sulfide) by Dissolved Organic Matter Isolated from the Florida Everglades. *Environ. Sci. Technol.* 32, 3305–3311. doi:10.1021/es9804058

Ravichandran, M. (2004). Interactions between Mercury and Dissolved Organic Matter-Aa Review. *Chemosphere* 55 (3), 319–331. doi:10.1016/j.chemosphere.2003.11.011

Remy, P.-P., Etique, M., Hazotte, A. A., Sergent, A.-S., Estrade, N., Cloquet, C., et al. (2015). Pseudo-first-order Reaction of Chemically and Biologically Formed green Rusts with HgII and C15H15N3O2: Effects of pH and Stabilizing Agents (Phosphate, Silicate, Polyacrylic Acid, and Bacterial Cells). *Water Res.* 70, 266–278. doi:10.1016/j.watres.2014.12.007

Richard, J.-H., Bischoff, C., Ahrens, C. G. M., and Biester, H. (2016). Mercury (II) Reduction and Co-precipitation of Metallic Mercury on Hydrous Ferric Oxide in Contaminated Groundwater. *Sci. Total Environ.* 539, 36–44. doi:10.1016/j.scitotenv.2015.08.116

Rickard, D. (2006). The Solubility of FeS. *Geochim. Cosmochim. Acta* 70, 5779–5789. doi:10.1016/j.gca.2006.02.029

Rivera, N. A., Bippus, P. M., and Hsu-Kim, H. (2019). Relative Reactivity and Bioavailability of Mercury Sorbed to or Coprecipitated with Aged Iron Sulfides. *Environ. Sci. Technol.* 53 (13), 7391–7399. doi:10.1021/acs.est.9b00768

Rocha, J., Sargentini, E., Jr, Zara, L. F., Rosa, A. H., Santos, A. D., and Burba, P. (2003). Reduction of Mercury(II) by Tropical River Humic Substances (Rio Negro)-Part II. Influence of Structural Features (Molecular Size, Aromaticity, Phenolic Groups, Organically Bound Sulfur). *Talanta* 61 (5), 699–707. doi:10.1016/s0039-9140(03)00351-5

Schwarzenbach, R. P., and Stone, A. T. (2003). Mineral Surface Catalysis of Reactions between Fe^{II} and Oxime Carbamate Pesticides. *Geochimica et Cosmochimica Acta* 67, 2775–2791. doi:10.1016/s0016-7037(03)00281-3

Seelen, E. A. (2018). A Multi-Estuary Appraoch to Better Understand the Sources and Fate of Methylmercury within Estuarine Water Columns. PhD thesis (Storrs, CT: University of Connecticut), 168.

Skyllberg, U., and Drott, A. (2010). Competition between Disordered Iron Sulfide and Natural Organic Matter Associated Thiols for Mercury(II)-An EXAFS Study. *Environ. Sci. Technol.* 44 (4), 1254–1259. doi:10.1021/es902091w

Slowey, A. J. (2010). Rate of Formation and Dissolution of Mercury Sulfide Nanoparticles: The Dual Role of Natural Organic Matter. *Geochimica et Cosmochimica Acta* 74 (16), 4693–4708. doi:10.1016/j.gca.2010.05.012

Spangler, W. J., Spigarelli, J. L., Rose, J. M., Flippin, R. S., and Miller, H. H. (1973). Degradation of Methylmercury by Bacteria Isolated from Environmental Samples. *Appl. Microbiol.* 25 (4), 488–493. doi:10.1128/aem.25.4.488-493.1973

Steffan, R. J., Korthals, E. T., and Winfrey, M. R. (1988). Effects of Acidification on Mercury Methylation, Demethylation, and Volatilization in Sediments from an Acid-Susceptible lake. *Appl. Environ. Microbiol.* 54 (8), 2003–2009. doi:10.1128/aem.54.8.2003-2009.1988

Stumm, W., and Morgan, J. J. (1996). *Aquatic Chemistry*. New York: John Wiley & Sons.

Sunderland, E. M., Li, M., and Bullard, K. (2018). Decadal Changes in the Edible Supply of Seafood and Methylmercury Exposure in the United States. *Environ. Health Perspect.* 126 (1), 017006. doi:10.1289/ehp2644

Van Loon, L. L., Mader, E. A., and Scott, S. L. (2001). Sulfite Stabilization and Reduction of the Aqueous Mercuric Ion: Kinetic Determination of Sequential Formation Constants. *J. Phys. Chem. A.* 105 (13), 3190–3195. doi:10.1021/jp003803h

Vollier, E., Inglett, P. W., Hunter, K., Roychoudhury, A. N., and Cappellen, P. V. (2000). Book Reviews. *Housing Stud.* 15, 785–790. doi:10.1080/02673030050134619

Waples, J. S., Nagy, K. L., Aiken, G. R., and Ryan, J. N. (2005). Dissolution of Cinnabar (HgS) in the Presence of Natural Organic Matter. *Geochim. Cosmochim. Acta* 69 (6), 1575–1588. doi:10.1016/j.gca.2004.09.029

Whalin, L., Kim, E.-H., and Mason, R. (2007). Factors Influencing the Oxidation, Reduction, Methylation and Demethylation of Mercury Species in Coastal Waters. *Mar. Chem.* 107 (3), 278–294. doi:10.1016/j.marchem.2007.04.002

Wiatrowski, H. A., Das, S., Kukkadapu, R., Ilton, E. S., Barkay, T., and Yee, N. (2009). Reduction of Hg(II) to Hg(0) by Magnetite. *Environ. Sci. Technol.* 43 (14), 5307–5313. doi:10.1021/es9003608

Wolfenden, S., Charnock, J. M., Hilton, J., Livens, F. R., and Vaughan, D. J. (2005). Sulfide Species as a Sink for Mercury in lake Sediments. *Environ. Sci. Technol.* 39 (17), 6644–6648. doi:10.1021/es048874z

Wolthers, M., Charlet, L., van Der Linde, P. R., Rickard, D., and van Der Weijden, C. H. (2005). Surface Chemistry of Disordered Mackinawite (FeS). *Geochimica et Cosmochimica Acta* 69 (14), 3469–3481. doi:10.1016/j.gca.2005.01.027

Zheng, W., and Hintelmann, H. (2010). Isotope Fractionation of Mercury during its Photochemical Reduction by Low-Molecular-Weight Organic Compounds. *J. Phys. Chem. A.* 114 (12), 4246–4253. doi:10.1021/jp9111348

Zheng, W., Liang, L., and Gu, B. (2012). Mercury Reduction and Oxidation by Reduced Natural Organic Matter in Anoxic Environments. *Environ. Sci. Technol.* 46 (1), 292–299. doi:10.1021/es203402p

Zhu, Z., Tao, L., and Li, F. (2013). Effects of Dissolved Organic Matter on Adsorbed Fe(II) Reactivity for the Reduction of 2-nitrophenol in TiO2 Suspensions. *Chemosphere* 93 (1), 29–34. doi:10.1016/j.chemosphere.2013.04.053

Conflict of Interest: The authors declare that the research was conducted in the absence of any commercial or financial relationships that could be construed as a potential conflict of interest.

frontiers | Frontiers in Environmental Chemistry

TYPE Original Research
PUBLISHED 20 December 2022
DOI 10.3389/fenvc.2022.1058890

OPEN ACCESS

EDITED BY
Robert Peter Mason,
University of Connecticut, United States

REVIEWED BY
Amrika Deonarine,
Texas Tech University, United States
Brett Poulin,
University of California, Davis,
United States
Daniel Steven Grégoire,
Carleton University, Canada

*CORRESPONDENCE
Lorenz Schwab,
lorenz.schwab@univie.ac.at

SPECIALTY SECTION
This article was submitted to Inorganic Pollutants,
a section of the journal
Frontiers in Environmental Chemistry

RECEIVED 30 September 2022
ACCEPTED 06 December 2022
PUBLISHED 20 December 2022

CITATION
Schwab L, Rothe FM, McLagan DS, Alten A, Kraemer SM, Biester H and Wiederhold JG (2022), Large extent of mercury stable isotope fractionation in contaminated stream sediments induced by changes of mercury binding forms.
Front. Environ. Chem. 3:1058890.
doi: 10.3389/fenvc.2022.1058890

Large extent of mercury stable isotope fractionation in contaminated stream sediments induced by changes of mercury binding forms

Lorenz Schwab[1,2]*, Florian M. Rothe[1], David S. McLagan[3,4,5], Alexandra Alten[3], Stephan M. Kraemer[1], Harald Biester[3] and Jan G. Wiederhold[1,6]

[1]Department for Environmental Geosciences, Centre for Microbiology and Environmental System Science, University of Vienna, Vienna, Austria, [2]Doctoral School in Microbiology and Environmental Science, University of Vienna, Vienna, Austria, [3]Institute of Geoecology, Technical University of Braunschweig, Braunschweig, Germany, [4]Department of Geological Sciences and and Geological Engineering, Queen's University, Kingston, ON, Canada, [5]School of Environmental Studies, Queen's University, Kingston, ON, Canada, [6]German Federal Institute of Hydrology (BfG), Qualitative Hydrology, Koblenz, Germany

Mercury (Hg) release from contaminated legacy sites is a large contributor to riverine ecosystems and can represent a significant local and regional environmental issue even long after the initial site contamination. Understanding processes of in-stream species transformation is therefore important to assess the fate and bioavailability of the released Hg. In this study, we investigated in-stream Hg transformation processes with analyses of Hg binding forms and Hg stable isotopes. Stream sediments were collected downstream of a former kyanization facility (Black Forest, SW Germany), where highly soluble Hg(II)-chloride ($HgCl_2$) was used as an anti-fouling agent to treat timber. Exfiltration of partly anoxic, contaminated groundwater with Hg concentrations of up to 700 µg L^{-1} into the adjacent Gutach stream is the main source of Hg to sediments. Total Hg concentrations in the stream bottom sediments (<2 mm) ranged from background values of 6.3 µg kg^{-1} upstream of the contaminated site to 77 mg kg^{-1} near the location of exfiltration of contaminated groundwater. A five-step sequential extraction procedure and Hg pyrolytic thermal desorption (PTD) analyses indicated changes in Hg binding forms in the sediments along the flow path towards a higher proportion of organically bound Hg. A large shift towards negative δ^{202}Hg values was observed downstream of the contaminated site (change of ≈2‰) along with a minor offset in mass-independent fractionation. Binary mixing models based on Hg isotope ratios using one industrial and different natural background endmembers were tested to estimate their respective contribution of Hg to the sediments but failed to produce plausible allocations. Based on the observed changes in isotopic composition, total Hg concentrations and Hg binding forms, we propose that the large extent of fractionation observed in downstream sediments is the result of a combination of kinetic isotope effects during sorption, redistribution of Hg within the sediment and the preferential

transport of Hg associated with the sediment fine fraction. These results highlight the importance of transformation processes when assessing the sources and fate of Hg in environmental systems and show limitations of using simple mixing models based on Hg stable isotopes.

KEYWORDS

mercury stable isotopes, stream sediment, source tracing, species transformation processes, contaminated legacy sites

1 Introduction

Mercury (Hg) is a global pollutant emitted by natural processes and human activities (Selin, 2009; Streets et al., 2019; UN Environment, 2019). The use of Hg in industrial processes has created local Hg contamination hotspots in different ecosystems around the world (Eckley et al., 2020), which continue to represent a significant source of Hg to the atmosphere and aquatic systems (Kocman et al., 2013). This anthropogenic legacy Hg, released and deposited previously, is recycled through re-emission and links past human activities to current environmental Hg cycling (Cooke et al., 2020). Once released, the main concern with respect to human exposure is Hg transformation into methylmercury, which bioaccumulates in aquatic organisms (Ullrich et al., 2001; Branfireun et al., 2020; Bravo and Cosio, 2020) and presents the main Hg uptake pathway for humans through fish consumption (Lavoie et al., 2018). Rivers represent an important long-range transport pathway, connecting contaminated legacy sites to estuaries and coastal zones (Horvat et al., 1999; Araujo et al., 2017) and are the largest source of Hg to coastal oceans (Liu et al., 2021). Understanding Hg transport from the release of Hg in the stream along the flow path to the river mouth is of critical interest.

The fate of Hg in environmental compartments such as river systems largely depends on its chemical speciation (Liu et al., 2011a). The majority of Hg released to the environment is in the form of inorganic Hg(0) or Hg(II) compounds (Eckley et al., 2020). Transformation processes in aquatic systems include the association/dissociation with numerous organic and inorganic ligands, sorption/desorption, precipitation/dissolution, oxidation/reduction, methylation/demethylation and volatilization/deposition to/from the atmosphere (Liu et al., 2011b). In addition to these biogeochemical transformations, physical transport mechanisms are of special interest in the case of fluvial Hg transport, which in most systems occurs predominantly in particulate form (Amos et al., 2014), because discharge velocity and energy control particle entrainment, suspension and ultimately transport (Boszke et al., 2004; Kocman et al., 2011; Kelly and Rudd, 2018). The partitioning of Hg at the particle-solution interface also affects its availability for methylating microorganisms and biological uptake (Hsu-Kim et al., 2013; Zhang et al., 2019).

Despite all the recent advances in understanding Hg biogeochemical cycling in the environment, many questions regarding Hg transformation processes and mechanisms remain unanswered (Gustin et al., 2020). The determination of the exact speciation of Hg in environmental samples remains challenging, leaving the determination of operationally defined pools as the most common method to assess the mobility, bioavailability and changes in Hg binding forms. There are numerous sequential extraction protocols (SEP) aiming to separate Hg into specified pools (Issaro et al., 2009; Fernández-Martínez and Rucandio, 2013; Reis et al., 2016). Other than chemical extractions, pyrolytic thermal desorption (PTD) analyses use the release of different Hg compounds at specific temperatures and are an effective method for the identification of the presence of Hg(0) (released at low temperatures) and Hg^{2+} sulfides and sulfates released at high temperatures) (Biester and Scholz, 1997; Reis et al., 2015; Rumayor et al., 2016).

Mercury stable isotope ratios are a potential tracer for sources and pathways of Hg in the environment and have been applied as a tool in an increasing number of field studies for source attribution and transport processes in stream systems contaminated by different sources such as former Hg mines (e.g., Foucher et al., 2013; Smith et al., 2015a; Baptista-Salazar et al., 2018; Pribil et al., 2020), gold mining or processing activities (e.g., Donovan et al., 2016; Marshall et al., 2018; Goix et al., 2019), chlor-alkali or other industrial activities (e.g., Donovan et al., 2014; Washburn et al., 2017; Demers et al., 2018; Grigg et al., 2018; Reinfelder and Janssen, 2019; Crowther et al., 2021; Janssen et al., 2021). In addition to mass-dependent fractionation (MDF), Hg isotopes also exhibit mass-independent fractionation (MIF) related to the magnetic isotope effect (MIE) and the nuclear volume effect (NVE, also known as nuclear field shift effect) (Blum and Bergquist, 2007; Bergquist and Blum, 2009). Fewer processes have been demonstrated to induce MIF (e.g., photochemical redox transformations) and it is therefore considered to be a more conservative tracer than MDF and might be conserved during accumulation in soils or plants (Bergquist and Blum, 2009; Sonke, 2011).

Simple binary mixing models based on δ^{202}Hg isotope signatures and inverse total Hg concentrations (1/THg) have been applied to estimate source contributions of two different sources or an industrial source versus background contribution to sediments and soils in numerous studies (Foucher et al., 2009; Feng et al., 2010; Feng et al., 2019; Ma et al., 2013; Gray et al., 2015; Guédron et al., 2016; Yin et al., 2016; Washburn et al., 2017;

Washburn et al., 2018; Woerndle et al., 2018; Zhang et al., 2018; Zhang et al., 2020; Zhu et al., 2018; Goix et al., 2019; Reinfelder and Janssen, 2019; Pribil et al., 2020; Tsui et al., 2020). Mixing models were also extended to include the relationship between MDF vs. MIF instead of MDF vs. 1/THg (Liu et al., 2011c; Lepak et al., 2015; Chen et al., 2016; Meng et al., 2019; Janssen et al., 2021) and in some studies the two-endmember mixing models were extended to include three or more endmembers (e.g., Bartov et al., 2013; Yin et al., 2018; Jung et al., 2021; Jung et al., 2022; Chen et al., 2022) or additional parameters such as carbon stable isotopes (Campeau et al., 2022). Binary mixing models require the precise definition of two distinct endmembers (e.g., contaminant and natural background) with a sufficiently different isotopic composition (Foucher et al., 2009). These mixing models are based on a linear relationship between δ^{202}Hg and 1/THg and assume that the isotopic composition of samples between the endmembers is the result of conservative mixing of these two distinct endmembers.

Compared to source tracing, the application of Hg isotopes for process tracing in rivers is more limited (Washburn et al., 2017; Demers et al., 2018; Crowther et al., 2021; McLagan et al., 2022a). Mercury transformation processes in river systems have also been investigated using stable Hg isotope signatures, for example, partitioning among dissolved and particulate phases (Washburn et al., 2017; Demers et al., 2018), methylation of inorganic Hg (Donovan et al., 2016) or photodegradation of methylmercury (Tsui et al., 2013).

Here we assessed Hg stable isotopes as a tool to trace Hg sources, understand Hg transport processes and identify changes in Hg binding forms in contaminated freshwater environments. For this purpose, we investigated stream sediments contaminated by continuous release of Hg from a former industrial site where timber was treated with a 0.67% solution of highly soluble mercuric chloride ($HgCl_2$) for preservation in a process called kyanization (Troschel, 1916; Nowak, 1952; Kallipoliti, 2010). The combination of analyses of Hg binding forms employing a SEP and PTD with Hg stable isotope analysis is expected to provide additional information about the processes governing the biogeochemical changes and the transport mechanism in the stream sediments. With our study we address the question whether the highly mobile $HgCl_2$ originally released at the contamination source changes its binding forms during the transport along the stream and will be retained in sediments. Further, we investigate if this change in binding forms is reflected in the different isotopic compositions of Hg in sediment samples and if differences in Hg isotope ratios in bulk sediments compared to the fine fraction can provide additional information about the dominant transport mechanisms and the changes in binding forms. The objective is to assess in-stream processes that can explain the observed shifts in Hg binding forms and isotopic composition. This contamination case further provides an excellent opportunity to investigate the potential fractionation of Hg isotopes in a stream system and an assessment of the suitability of Hg isotopes and endmember mixing models as a source tracing tool.

2 Materials and methods

2.1 Site description

All stream sediment and stream water samples were collected in the vicinity of a former wood impregnation facility located in the Black Forest (South-West Germany, 830 m a.s.l.; site A in McLagan et al., 2022b, site C in Richard et al., 2016b). From the late 19th century until the early 1960s, $HgCl_2$ was used in the kyanization process as a wood preservation agent at this site. Extensive contamination of soil and groundwater resulted from spillages and drying of treated wood on unsealed ground (Heckmann, 2002; Eisele, 2004). The facility is divided into northern and southern parts by the Gutach stream (Figure 1), which was dammed by a small barrage in 1968/69, creating a small artificial pond (Okalsee) at the western end of the site (Eisele, 2004) (photos provided in Supplementary Section S1). This did not only affect the sediment transport from the upstream part of Gutach stream, which features a natural brownwater lake "Titisee" a few km upstream, but also the location of the streambed was slightly altered at that time. The northern part of the former industrial area has been developed into a commercial shopping area with stores and parking lots in 2002/03 (Eisele, 2004). The southern part is today occupied by several smaller company buildings, but also exhibits larger open areas with unsealed land surfaces. There are two vertically arranged aquifers with mostly south-eastern flow direction. The upper groundwater body is in exchange with the stream *via* exfiltration of Hg contaminated groundwater (Heckmann, 2002; Schuler, 2012).

The (hydro)geology of the area is dominated by Quaternary fluvial sediments overlaying Paleozoic granite basement (LGRB, 2021). Between lake Titisee and the former kyanization site, there is only a small altitude gradient and Gutach stream is flowing at a slow velocity. Shortly after the confluence with the Josbach stream (see Figure 1) the terrain gets steeper and the flow velocities increase resulting in a streambed consisting of coarser gravel and stones with only little fine-grained particles settling (Gonser and Schwoerbel, 1985; Schuler, 2012). After the confluence with the Haslach stream the name changes to Wutach. The river Wutach is a tributary of the river Rhine, which ultimately drains to the North Sea. The mean discharge of the Wutach is 6 $m^3 s^{-1}$, but due to the close relation to rainfall and snowmelt events, it can increase to >100 $m^3 s^{-1}$ during high discharge events (see precipitation and discharge data in Supplementary Section S2), where large amounts of sediments can be mobilized (Ortlepp, 1997).

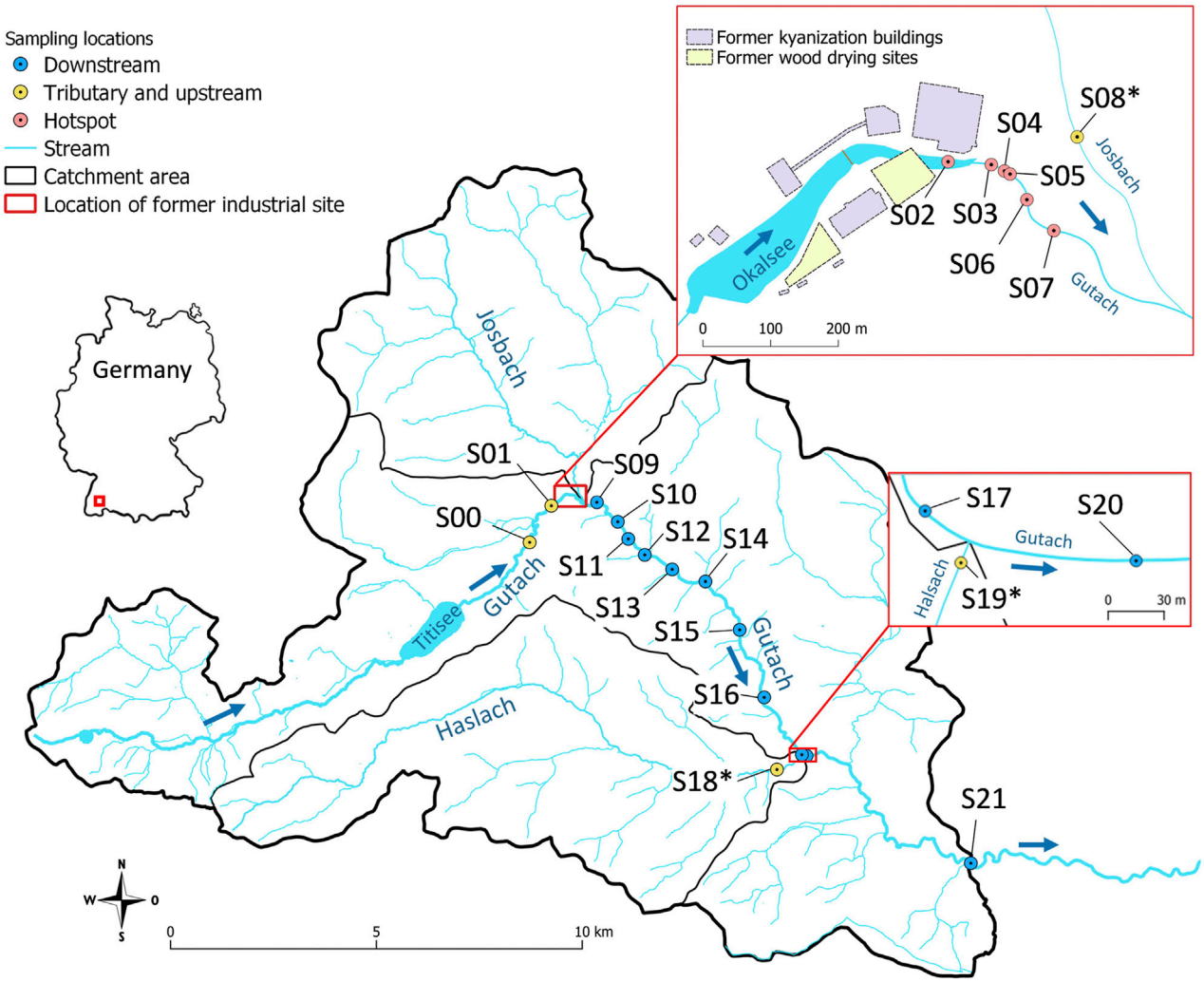

FIGURE 1
Location of the sampling sites. Samples from tributary creeks are denoted with an asterisk.

2.2 Sampling and sample preparation

Sediment samples from Gutach stream were collected at and downstream of the former industrial site (n = 17, see Figure 1) in 2018 and 2019. Two additional samples were collected upstream of the contaminated site (S00 and S01) to assess background Hg concentration and isotope signatures in the Gutach sediment. Additionally, sediment samples from the two main tributary streams Josbach (S08*) and Haslach (S18* and S19*) were collected to assess their potential influence. The location of all sampling points is displayed in Figure 1. Sampling campaigns were carried out in months with comparably low precipitation and discharge (Supplementary Figures S2.1, S2.2). All sampling equipment was washed thoroughly and rinsed with stream water at the respective sampling location. Sediment samples were taken from the uppermost <5 cm with a hand shovel. Multiple grabs randomly distributed across the streambed were combined at each location to optimize representative sampling of the heterogeneous streambed and until a sufficient amount of sediment was collected (100–200 g, <2 mm). Samples were homogenized using a stainless-steel spatula and directly sieved to <2 mm in the field and filled into 180 ml polypropylene (PP) containers for transport to the laboratory. Stream water samples were filtered through 0.45 µm cellulose acetate (CA) filters into 50 ml PP vials and stabilized with 1% (v/v) BrCl (0.2 M BrCl in concentrated HCl, prepared according to Bloom et al. (2003). Electrical conductivity, pH and temperature of the stream water were measured in the field with respective electrodes (Supplementary Table S6). Sediment samples were dried at 60°C for 48 h. Samples used for PTD were not dried to avoid

loss of Hg(0). An aliquot of the dried samples was dry-sieved to <125 µm to compare Hg concentrations and isotope ratios of the fine fraction with bulk sediments and assess its role for transport and transformation processes. Relative mass proportions were calculated using the mass of the <125 µm fraction in relation to the total mass of sieved aliquots. An aliquot of the <2 mm fraction was milled with a vibrating ball mill for 30 s at 30 vibrations per second (Retsch MM 400).

2.3 Analyses

Total carbon (C), hydrogen (H), nitrogen (N) and sulfur (S) concentrations were determined using an elemental analyzer (Elementar, VarioMacro). Organic and inorganic carbon contents of the sediment samples were determined using a multiphase carbon analyzer (LECO RC612, Leco Corporation). For this analysis, an aliquot of the milled <2 mm fraction was heated from 105°C to 1,000°C at a rate of 5°C min^{-1}. A peak separator was set at 550°C to distinguish between organic and inorganic carbon. Because the Leco analyzer contains parts made of gold, which could be damaged by the introduction of samples with elevated Hg contents, the total C of samples with Hg concentrations >1 mg kg^{-1} were analyzed by combustion and infra-red detection using a DIMA 1000NT (Dimatec). The organic carbon content of these samples was determined after removing the inorganic carbon fraction with concentrated HCl by the "carbonate-bomb" method (Müller and Gastner, 1971). Characterization of organic carbon was performed by Fourier-transform infrared spectroscopy (FTIR; Cary 630 FTIR Spectrometer, Agilent Technologies) on selected samples (details see Supplementary Section S8). Major elements were analyzed by ICP-OES (ICP-OES 5110, Agilent Technologies) on aqua regia digests (HNO_3:HCl (1:3)). Samples were digested on a hotplate at 85°C for 2 h after the addition of 12 ml aqua regia to 0.5 g of sediment in loosely capped 50 ml PP vials. Aqua regia was refilled to 12 ml and digested for another hour, then filled to 50 ml with ultrapure water and filtered through 0.45 µm CA filters. Elemental analysis was further conducted on selected samples by energy dispersive X-ray fluorescence (XRF) spectrometry on wax pellets of the milled <2 mm fraction. The mineralogical composition of the milled bulk stream sediments was examined using X-ray diffraction and the COD database (XRD, Rigaku MiniFlex 600).

For THg analysis aqua regia extracts with BrCl (8 ml of conc. HCl, 3 ml of conc. HNO_3 and 1 ml of conc. BrCl) of both <2 mm and <125 µm sediment fractions were analyzed for total Hg and, if concentrations allowed, also for Hg stable isotopes. Extractions were carried out in 50 ml PP centrifuge vials covered with perforated parafilm. Digests were run overnight (20–24 h) on a lateral shaker at 170 rpm. Samples were then diluted with 36 ml of ultrapure water (18.2 MΩ cm), resuspended and centrifuged at 3,000 rcf for 20 min (Herolab HiCen 21°C). After centrifugation, the supernatants were passed through 0.45 µm CA filters.

A five-step sequential extraction protocol (SEP) was carried out on selected sediment samples (<2 mm, not milled) based on the method described in Bloom et al. (2003) (for details see Supplementary Section S3). This method separates Hg into operationally defined fractions using the following extraction agents: deionized water (F1), 0.01 M HCl/0.1 M CH_3COOH (F2), 1 M KOH (F3), 12 M HNO_3 (F4), aqua regia (F5). Major elements in extracts were analyzed by ICP-OES (Supplementary Figure S3.1). The pH of sediment samples was measured for selected samples in the F1 extract (Supplementary Table S7). Pyrolytic thermal desorption (PTD) analysis was applied to characterize Hg binding forms similar to the procedure described in Biester and Scholz (1997). Aliquots of the untreated sediment samples were continuously heated to 650°C at a rate of 1°C per second in an N_2 gas flow and the Hg release was measured as a function of temperature using atomic absorption spectrometry. The obtained release curves were compared to the characteristic release curves of Hg reference compounds (for details see Supplementary Section S4). Although both methods provide valuable and often complementary information about the nature of the dominant Hg compounds and their binding to different matrix components in the investigated sediments, it is important to realize that no individual chemical Hg species can be separated and identified in most cases.

Total Hg concentrations were determined on a direct mercury analyzer (DMA-80, Milestone Inc.) using thermal decomposition, amalgamation and subsequent atomic absorption spectrometry on the milled sample aliquots following EPA method 7473 (EPA, 2000). High Hg concentration samples from the hotspot area (S05-S07) were not included in this analysis because impractically low sample masses would have been required to remain within the calibration range of the instrument. Mercury concentrations of aqua regia and SEP extracts were analyzed using cold vapor atomic absorption/fluorescence spectrometry (CV-AAS/AFS, DMA-80L, Milestone Inc.) after pre-reduction of the samples with hydroxylamine-hydrochloride solution (NH_2OH·HCl) and online reduction of Hg^{2+} to Hg(0) by $SnCl_2$ following EPA method 1631 (EPA, 2002). Certified reference material (ERM CC-018) was extracted in parallel with samples as quality control and yielded recoveries of 93.3% ± 8.6% (SD, n = 4) for aqua regia digests and 87.4% ± 8.4% (SD, n = 4) for the sum of the five extracts in the sequential extraction protocol. All reagent blanks were below the limit of quantification. Stream water samples were analyzed using cold vapor atomic fluorescence spectrometry (CV-AFS, Mercur Analytic Jena) except for additional samples collected at later sampling events which were analyzed using the DMA-80L. Water samples are labeled in the same order as sediments (W00-W21) and were collected at the same location.

For isotope analysis, sediment samples with low Hg concentrations were pre-concentrated using combustion and trap with the DMA-80 direct mercury analyzer previously tested and successfully applied in our laboratory (McLagan et al., 2022b; McLagan et al., 2022a). Samples were weighed into sample boats (0.2–17 g, max. 1 g per boat), combusted and

the released Hg purged into an oxidizing trap consisting of 5 ml 40% (v/v) inverse aqua regia (HNO_3:BrCl (3:1)) as described in Janssen et al. (2019). The efficacy of the method was tested by preparing different reference materials and calculating recoveries with 1SD variation (BCR-482: 103% ± 12%, n = 13; CC-141: 95% ± 4%, n = 16; NIST-3133: 102% ± 4%, n = 12). Mercury isotope ratios of aqua regia digests and selected sequential extracts were determined with a Nu Plasma II multi-collector inductively coupled plasma mass spectrometer (MC-ICP-MS, Nu Instruments) connected to an HGX-200 cold vapor system (Teledyne Cetac) for Hg introduction and an Aridus II desolvating nebulizer (Teledyne Cetac) for Tl introduction. Mass bias and instrument drift were corrected using NIST-3133 standard-sample bracketing and element doping with NIST-997 Tl standard. Measurement sessions were conducted at concentrations of either 2.5 μg L^{-1}, 5 μg L^{-1} or 10 μg L^{-1} Hg with concentration-matched bracketing standards. Standards and samples were diluted in a 1% (v/v) BrCl matrix to an acid strength of <10% (v/v). Isotope data are reported as δ-values in permille relative to NIST-3133 calculated according to Eq. 1:

$$\delta^{xxx}Hg\,(‰) = \left(\frac{\frac{^{xxx}Hg}{^{198}Hg}sample}{\frac{^{xxx}Hg}{^{198}Hg}NIST{-}3133} - 1\right)*1000 \qquad (1)$$

Mass-independent fractionation (MIF) is reported as deviation from the theoretically predicted mass-dependent fractionation (MDF) using the following Eq. 2:

$$\Delta^{xxx}Hg = \delta^{xxx}Hg - \left(\delta^{202}Hg*\beta^{xxx}\right) \qquad (2)$$

The β^{xxx} values of ^{199}Hg, ^{200}Hg, ^{201}Hg and ^{204}Hg isotopes are 0.2520, 0.5024, 0.7520, and 1.4930, respectively (Blum and Bergquist, 2007). Assessment of accuracy and precision of the isotope analysis was done by regular measurements of the secondary standard "ETH Fluka". Results were consistent with previous analyses of different laboratories (Smith et al., 2015a; Jiskra et al., 2017; Obrist et al., 2017; Grigg et al., 2018; Brocza et al., 2019; Goix et al., 2019; McLagan et al., 2022b). The overall reproducibility (2SD, n = 69) was ±0.15‰ for δ^{202}Hg and ±0.06‰ for Δ^{199}Hg and Δ^{201}Hg, but the standard deviations (2SD) reported for individual sample measurements correspond to the respective session reproducibility of "ETH Fluka" (overview in Supplementary Table S5.1).

3 Results

3.1 Stream water and sediment characterization

Background Hg concentrations, measured in Gutach stream before the contaminated area and the tributary streams, were below the detection limit except for W19* (0.6 ng L^{-1}) consistent with previously reported low background Hg concentrations between 1.1 and 4.1 ng L^{-1} (Bischoff et al., 2015). Close to the former kyanization facility, between the artificial pond and the confluence with the Josbach stream (hereafter called "hotspot samples," see Figure 1 inset), the water samples show elevated Hg concentrations reaching up to 835.4 ng L^{-1} at W05 (Supplementary Table S6), indicating exfiltration of contaminated groundwater (for details see Supplementary Section S6). This is supported by elevated THg concentrations in groundwater samples from a well close to the location where groundwater was exfiltrating ranging from 78 to 555 μg L^{-1} in five measurement campaigns (McLagan et al., 2022b; cf. sample WA10). "Hotspot" water samples were also characterized by elevated electrical conductivity (EC) and higher dissolved Fe and Mn concentrations than both upstream and downstream samples. After the confluence with Josbach stream (hereafter called "downstream samples") the dissolved Hg concentrations remain elevated (14.8–50.8 ng L^{-1}, Supplementary Table S6) up to and including the most distant sample (W21) approximately 16.5 km along the Gutach-Wutach channel. Stream water field parameters are summarized in Supplementary Table S6.

The pH of sediment samples ranged from 6.0 to 7.0 (Supplementary Table S7). The fine fraction (<125 μm) made up only a small mass proportion of 0.3% (S20) to 7.5% (S05) of the bulk sample mass (Supplementary Table S7). The peak identification of XRD patterns showed that the mineralogy is dominated by quartz and plagioclase feldspars such as albite and anorthite. There is some variation in the intensity of the major peaks and the occurrence of minor peaks between the sediment samples indicating a different relative composition and abundance of these minerals, but no clear distinction between the Gutach stream sediments and sediments from tributaries could be made based on mineralogical composition (XRD patterns are provided in Supplementary Section S9). Elemental composition results from ICP-OES and XRF measurements show that some of the samples from near the former industrial facility exhibit increased concentrations of contaminants related to former usage and release from the site (Pb, Cr, Zn) and higher concentrations of Fe, Mn and Ca (Supplementary Tables S10.1, S10.2). The XRF data also shows higher concentrations of Cl, S and P concentrations for the most contaminated samples. For Fe and Mn this is likely caused by the exfiltration of anoxic groundwater and subsequent oxidation and precipitation and settling of Fe and Mn. However, XRD patterns do not allow the identification of Fe or Mn minerals as a component of the sediment samples, either because of their poorly-crystalline structure or their low relative abundance. The FTIR spectra showed subtle differences in absorbance among the selected samples indicating a slightly higher proportion of organic matter in sediments S05 and S08* (Supplementary Figures S8.1, S8.2). The total carbon (TC) content of the bulk sediments in Gutach stream and the tributaries ranged from 0.16% to 1.02% (details see Supplementary Table S7 and Supplementary Figure

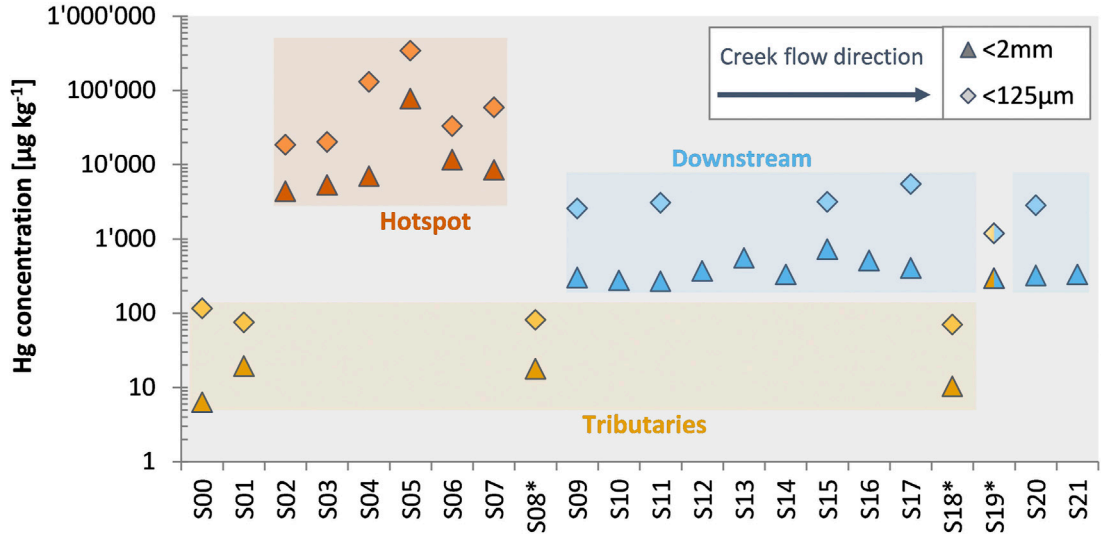

FIGURE 2
Total mercury (THg) concentrations in bulk (<2 mm) and fine (<125 µm) fractions of the sediment samples. Samples are displayed in the flow direction from S00 to S21. Tributary creeks are marked with an asterisk. Sample S19* was collected only about 10 m upstream of the confluence with the Gutach creek and might be affected by the Gutach during high discharge events. Error bars are smaller than data symbols. Accuracy and precision of THg measurements was assessed by replicate analysis of reference materials: NIST-3133 (recovery: 103% ± 3%, 1SD, n = 108) for DMA-80L; ERM CC-141 (recovery: 96% ± 6%, 1SD, n = 20) and NIST-2711 (recovery: 105% ± 7%, 1SD, n = 8) for DMA-80.

S7). Most of the carbon was present as organic carbon (86% ± 8%) (Supplementary Table S7). Overall, the differences in the elemental and mineralogical composition were not very pronounced and did not allow an estimate of the sediment contribution from each tributary stream. An overview of the sediment characterization is presented in Supplementary Section S7.

3.2 Hg concentrations and binding forms

Total mercury (THg) concentrations in bulk sediment and fine fraction (<125 µm) samples varied strongly along the investigated section of Gutach stream. Bulk sediments from upstream of the former wood treatment facility (S00 and S01), which can be considered as natural background, had low THg concentrations in the bulk (6.32 µg kg^{-1} and 19.3 µg kg^{-1}, respectively) and fine (115 µg kg^{-1} and 74.9 µg kg^{-1}, respectively) fractions (Figure 2). The hotspot samples (S02-S07) are impacted by the contamination case and showed highly elevated THg concentrations ranging from 4.37 mg kg^{-1} to 77.0 mg kg^{-1} in bulk sediments (S02–S07). For these samples, the fine fraction also had much higher THg concentrations of up to 340 mg kg^{-1} (S05). The downstream samples showed a higher Hg concentration (range from 267 to 726 µg kg^{-1}) than the background values of the Gutach or the tributaries indicating an influence of the Hg contamination case as far as 16.5 km downstream of the source. Both the Josbach and Haslach streams had similarly low Hg concentrations as the uncontaminated upstream Gutach stream in both fractions. One of the samples from the Haslach stream however had elevated THg concentrations [S19*: 296 µg kg^{-1} (<2 mm) and 1.19 mg kg^{-1} (<125 µm)]. Sample S19* was collected near the confluence with the Gutach stream and considering the differences in Hg concentrations between S18* and S19* an influence or mixture of contaminated sediments cannot be excluded, especially during high discharge events. The fine fraction had systematically higher Hg concentrations in all investigated samples by a factor of 4.4–21.7 in comparison to the respective coarse fraction (≥125 µm–<2 mm). Most of the total Hg was nonetheless associated with the coarse fraction (61%–97%) because the fine fraction made up only a small mass proportion of the bulk sample.

Both SEP and PTD of bulk sediments showed a distinct shift of the Hg binding form of hotspot sediments directly affected by exfiltrating groundwater compared to sediments from the tributaries and the downstream sediments. The PTD release curve of hotspot samples started at 180°C with a peak maximum of around 250°C while the release curve for downstream sediments shifted to higher temperatures with a start at 250°C and a peak maximum at 300°C (Figure 3B). None of the samples showed any Hg(0) as would be indicated by a low release temperature of around 100°C or lower. Although there are a large number of potential Hg^{2+} species with maximum release peaks between 200 and 300°C, including $HgCl_2$, metacinnabar (β-HgS), Hg adsorbed to $Fe(OH)_3$ as well as Hg bound to organic matter and humic acids (Biester and Scholz, 1997; Rumayor et al., 2016; McLagan et al., 2022b), the consistent shift in peak maxima gives further weight to the interpretation of a shift in binding

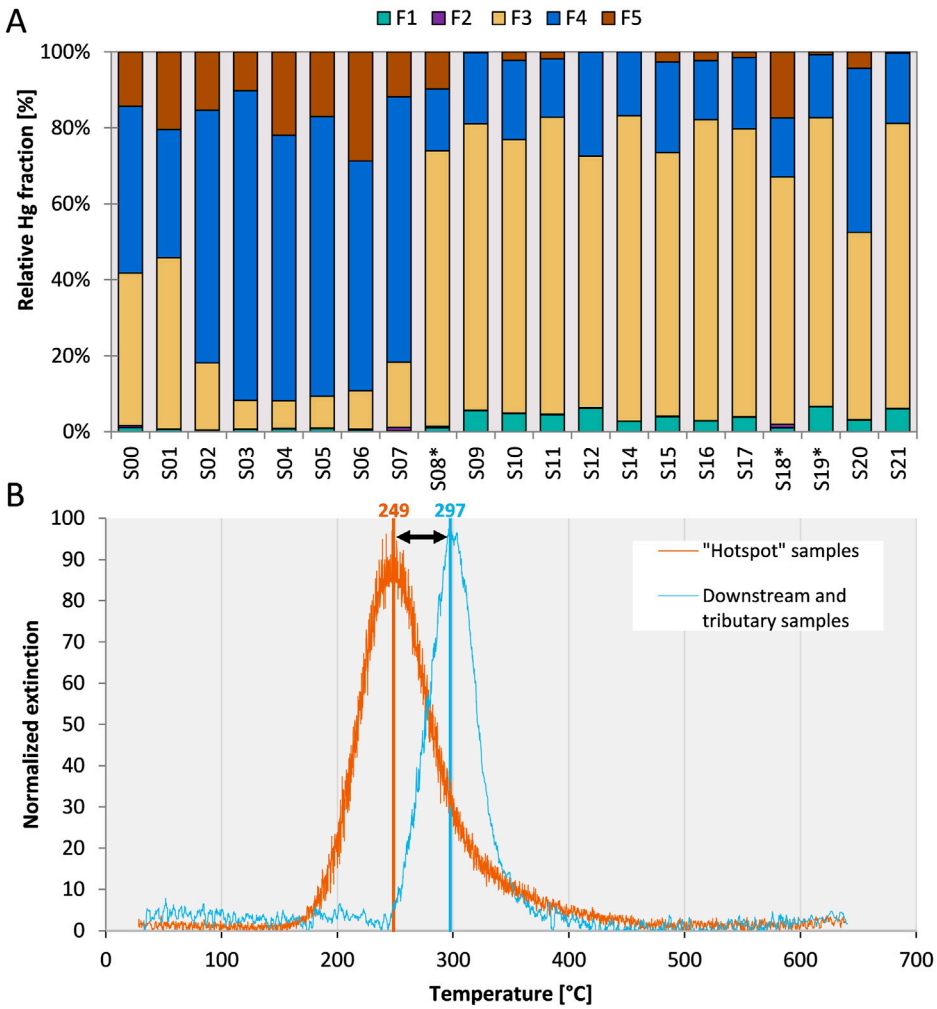

FIGURE 3
(A) Results of the SEP displayed as Hg pools normalized to the sum of extracts (sum of extracts = 100%). Samples from tributary creeks are marked with an asterisk. The performance of the SEP was assessed with repeated extractions of the reference material ERM CC-018 (F1: 0.13% ± 0.05%; F2: 0.02% ± 0.01%; F3: 3.9% ± 1.1%; F4: 77.9% ± 4.7%; F5: 3.6% ± 3.6%, Sum of extracts: 87.8% ± 8.4%. *n* = 5). **(B)** Moving average of PTD release peaks of sediments from "hotspot" section (S02-S07, peak centers ranging from 232 to 257°C) and downstream plus tributary creek sediments (peak centers ranging from 292 to 304°C). Signals were normalized to the maximum extinction of individual samples. See Supplementary Table S4 for peaks of individual samples.

forms in downstream sediments (Supplementary Figures S4.1–S4.3). The presence of metacinnabar should be indicated by a second peak shoulder or a peak at higher temperatures, which was not observed in the samples. There was a slight tailing in the release curve of S02 which could be attributed to sulfidic Hg, but slight differences in release curves can also be caused by differences in the sample matrix (e.g., grain size) and Hg concentrations (Biester and Scholz, 1997; Baptista-Salazar et al., 2017; Petranich et al., 2022). Generally, Hg associated with organic matter (humic acid in case of the standard) has a release temperature that is slightly higher than Hg associated with Fe or other "matrix-bound" Hg forms (around 300°C, see Supplementary Figure S4.3) and the observed shift can be interpreted as a change in Hg binding form towards a higher proportion of organic matter bound Hg in downstream sediments (Biester et al., 2000; Baptista-Salazar et al., 2018).

For hotspot samples (S02–S07), most of the Hg was extracted in the F4 step (60%–80%) targeting strongly complexed Hg (Figure 3A) The relative proportion of the F5 pool (residual Hg, HgS) decreased from 10%–22% in hotspot samples to <5% after the confluence with Josbach stream, suggesting a minor role of sulfide-bound Hg in these sediments. For the hotspot samples, approximately 10% of Hg was extracted in the F3 fraction, which is associated with Hg bound to organic matter. This pool had a much higher relative abundance in the samples after the confluence with Josbach stream (66%–80%) and to a slightly

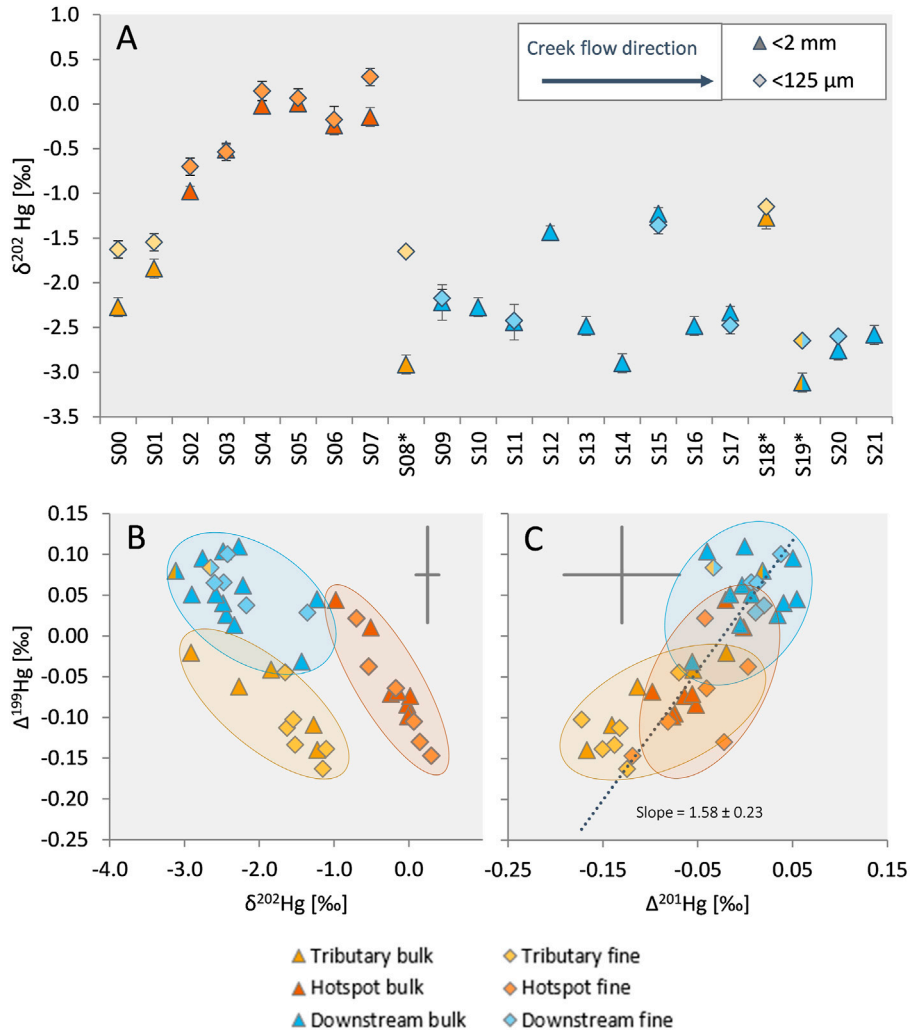

FIGURE 4
(A) δ^{202}Hg (MDF) of bulk and fine sediment samples. Samples are displayed in flow direction from S00 to S21. Tributary creeks are marked with an asterisk. Hotspot and downstream section are indicated by colored symbols as in Figure 2. Error bars indicate 2SD based on the standard reproducibility of the measurement session, but are smaller than symbol size in some cases. **(B)** Relationship of MDF (δ^{202}Hg) and MIF (Δ^{199}Hg). **(C)** Relationship of Δ^{201}Hg and Δ^{199}Hg. The dotted line represents a York regression for combined bulk and fine sediment samples calculated using the IsoplotR package in R (Vermeesch, 2018). The grey crosses indicate the average 2SD for the respective parameter.

lower degree in the uncontaminated Gutach. In absolute terms, the pool of Hg in the F3 pool was larger in the hotspot samples compared to the downstream samples, despite the lower relative abundance. Especially with samples that are not pure compounds but more complex mixtures, several issues can influence the results of SEP (Kim et al., 2003; Hall et al., 2005; Hall and Pelchat, 2005) and resorption of Hg can cause the release of more labile Hg in later extraction steps. In the case of the hotspot samples, the concentrations are high and incomplete removal of organically bound Hg or resorption of Hg during the F3 step causing a later extraction in step F4 cannot be completely ruled out. Even though the sediment composition has a large effect on Hg adsorption (Pelcová et al., 2010), the general sediment characterization (elemental and mineralogical composition) did not indicate clear shifts in the sediment composition between the sampling locations. Differences in organic matter content can also not explain the shift towards a higher proportion of organically bound Hg. There is only a weak relationship between TOC content and absolute Hg extracted in F3 (p = 0.06, R^2 = 0.235) and no relationship between TOC content and the relative Hg fraction extracted in F3 (p = 0.42, R^2 = 0.047) (Supplementary Figure S3.3). With general sediment characterization and TOC having no apparent relationship to Hg binding forms, we measured Hg isotope ratios to further investigate the reasons for the observed changes in Hg binding forms.

3.3 Hg isotope composition of bulk and fine sediment fractions

Along the investigated section of Gutach stream, large variations in the isotopic composition of Hg in sediments were observed in both bulk and fine fraction samples, with a notable shift of δ^{202}Hg values towards more negative values in downstream sediments (Figure 4A). Gutach stream samples from upstream with very low Hg concentrations can be used to approximate the background Hg isotope signature of uncontaminated Gutach stream sediment. Both samples from upstream of the site had highly negative δ^{202}Hg values of −2.27‰ ± 0.11‰ (S00) and −1.84‰ ± 0.11‰ (S01). The background sample from Josbach stream had a lighter isotopic composition (S08*; −2.91‰ ± 0.11‰) than Gutach upstream samples while Haslach stream had an isotopic composition that is distinct from the Gutach and Josbach streams. Like THg, the two samples of the Haslach stream were also isotopically different. The sample from further up the gorge (S18*) had a less negative δ^{202}Hg value (−1.27‰ ± 0.11‰) compared to the sample close to the confluence (S19*; −3.12‰ ± 0.11‰). As mentioned earlier, S19* was likely influenced by contaminated Gutach sediments and water and the background of Haslach stream is better represented by S18*. The bulk isotope signature of the sediment samples from the hotspot section (S02-S07) had a δ^{202}Hg value of −0.31‰ ± 0.37‰ (1SD, n = 6), which is close to values in the groundwater (McLagan et al., 2022b). Exfiltration of contaminated groundwater is expected to be the major source of Hg in Gutach stream and the analysis of groundwater from the most contaminated wells at the former kyanization site showed mean δ^{202}Hg values of −0.20‰ ± 0.07‰ and Δ^{199}Hg values of −0.07‰ ± 0.03‰ indicated little to no mass-independent fractionation in the aquifer [1SD, wells WA7 and WA10a in McLagan et al. (2022b)]. The isotopic compositions of contaminated groundwater and hotspot sediments were remarkably similar, indicating that exfiltration is likely the dominant source of Hg in these samples and an influence of contaminated surface runoff and erosion of contaminated soil from the site is of minor importance and likely restricted to heavy rainfall events. For the downstream sediments a shift towards remarkably light δ^{202}Hg values of −2.35‰ ± 0.37‰ (1SD, n = 12) was observed. The isotopic composition of the fine fraction showed an offset with more positive δ^{202}Hg values compared to the bulk fraction (in 13 out of 16 samples; Figure 4A). The offset was most pronounced in the hotspot and the tributary samples, whereas the downstream samples exhibited no clear δ^{202}Hg difference between the size fractions. Apart from this offset, the isotopic composition of the fine fraction followed the same general trends and changes observed for the bulk sediments. The extent of MIF observed in the sediment samples was very low. No even-mass MIF beyond the analytical uncertainty was observed (Supplementary Table S5.2) suggesting no significant contribution of Hg to the sediments from atmospheric precipitation or dry deposition (Gratz et al., 2010; Chen et al., 2012). However, there was a minor shift in odd-mass MIF (Δ^{199}Hg and Δ^{201}Hg, see Figures 4B, C) towards higher values (~0.1‰) in downstream samples compared to hotspot or tributary sediments.

4 Discussion

4.1 Mixing model based on MDF and Hg concentrations

To test the hypothesis of conservative mixing of natural Hg and industry-derived mercury, a binary mixing model was applied according to eqs 3, 4:

$$f_{ind} * \delta^{202}Hg_{ind} + f_{nat} * \delta^{202}Hg_{nat} = \delta^{202}Hg_{sediment} \quad (3)$$

$$f_{ind} + f_{nat} = 1 \quad (4)$$

In the model f_{nat} and f_{ind} represent the fractions of Hg originating from natural background and industrial contamination, respectively. The isotopic signature of the endmembers in the model are defined as $\delta^{202}Hg_{ind}$ representing the industrial contamination source (exfiltrating groundwater) and $\delta^{202}Hg_{nat}$ of different natural background samples (Figure 5A). The exact isotopic signature of the industrial endmember is difficult to determine since there is no record of $HgCl_2$ solutions that were used at the site and Hg exfiltrating from the groundwater has potentially already undergone transformation processes as it interacts with the aquifer material (McLagan et al., 2022b). Nonetheless, we consider δ^{202}Hg values of highly contaminated groundwater wells to be the closest estimate of the industrial Hg isotope source signature for this study. The second endmember, the natural background signature is equally difficult to define. Five approaches were tested with different assumptions made about the regional background signature (details see Supplementary Section S11).

The bulk isotope signatures of the sediment samples from the hotspot section had a δ^{202}Hg value of −0.31‰ ± 0.37‰ which is close to that of the groundwater (−0.20‰ ± 0.07‰). For the allocation of Hg in the hotspot samples, the mixing models predicted that most of the Hg (63%–100%) is derived from exfiltrating groundwater. The model using Haslach stream as natural endmember predicted a lower contribution (only 27% for S02) in the hotspot samples, which is very unlikely based on the remarkably high Hg concentrations in these samples and the low background concentration. For most of the downstream samples, only a small amount of Hg was allocated to the industrial source. The industrial contribution ranged between 0% and 3% (Gutach

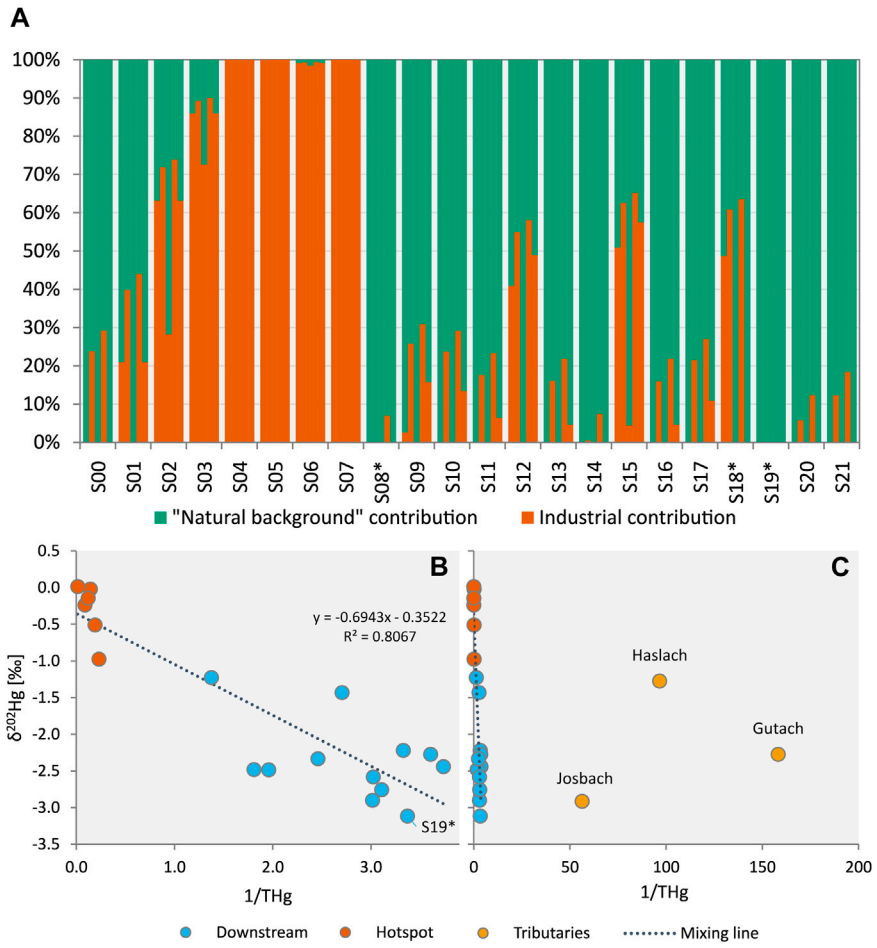

FIGURE 5
(A) Results of two endmember mixing models, each one using a different natural background endmember from left to right: Gutach upstream sample S00 (δ^{202}Hg = −2.27‰), Josbach S08* (δ^{202}Hg = −2.91‰), Haslach S18* (δ^{202}Hg = −1.27‰), S19* (δ^{202}Hg = −3.12‰) and an approach using average δ^{202}Hg values of tributaries after each confluence (see Supplementary Section S11). **(B)** Plot of δ^{202}Hg values of creek sediments versus 1/THg (mg kg^{-1} basis). Excluding the tributary and upstream sediments (Gutach S00, Josbach S08* and Haslach S18*) used as endmembers in the mixing models results in a good fit for the linear regression (mixing line) with a hypothetical endmember with a very low δ^{202}Hg value and sufficiently high Hg concentrations (e.g. δ^{202}Hg ≈ −3.0‰ and 0.25 mg kg^{-1} Hg). **(C)** This panel shows that δ^{202}Hg values of creek sediments do not lie between the industrial endmember (δ^{202}Hg ≈ −0.22‰) and the δ^{202}Hg values of sediments of the tributary creeks and the Gutach upstream sample.

endmember), 0%–26% (Josbach endmember), 0%–31% (S19* endmember) and 0%–16% (mixed endmember). Only for the S19* endmember the downstream sediments plot along the mixing line (Figure 5B). However, for S19* an influence of contaminated Gutach sediment or stream water is likely and it is questionable if S19* can be regarded as "natural background." The downstream sediments had Hg concentrations between 268 and 727 µg kg^{-1}, which is more than 15-fold higher than the background samples (6.3–17.8 µg kg^{-1} Hg). There is no known other major Hg source in the area and based on this difference in Hg concentrations the contribution of industrial Hg is expected to be >90%. Irrespective of the chosen natural background endmember the contribution of industrial Hg is therefore largely underestimated in the mixing models. Due to the low background Hg concentrations, a significant contribution of Hg from other sources within the tributary catchment area (industrial or natural/geogenic) to the total Hg budget in Gutach stream sediments through conservative mixing seems unlikely, even for endmembers with a light isotope signature such as Josbach stream (Figure 5C). Extending the mixing model with MIF values (Δ^{199}Hg) would be one option to add a more conservative dimension to the system. The extent of odd-mass MIF in our samples was however small. Plotting MDF and MIF values against each other reveals that the downstream sediments do not lie

between the hotspot samples, with a similar isotopic composition as the industrial endmember, and the tributary sediments which can be regarded as natural background endmember (Figure 4B).

Both MDF and MIF suggest that the downstream samples are at least partially affected by processes causing isotope fractionation and not conservative transport and mixing of the industrial source (exfiltrating contaminated groundwater) with Hg in sediments derived from natural sources. The change in the binding form, as indicated by SEP and PTD, further implies transformation processes within the sediment or between the sediment and the liquid phase which in turn could lead to isotope fractionation.

4.2 Isotope fractionation mechanisms

The shift towards higher release temperatures in PTD and the higher proportion of Hg extractable in F3 in the downstream samples compared to hotspot samples both indicated a higher proportion of organically bound Hg. This observed shift can be the result of in-stream transformation (e.g., from F4 extractable Hg to an F3 extractable form) as well as preferential transport of different Hg pools. Many biotic and abiotic Hg species transformation processes can cause fractionation of Hg isotopes and the identification of the exact processes involved in the isotopic fractionation is challenging. Comparing the expected fractionation effects of different processes with the Hg isotope ratios in the stream sediments, provides the means to narrow down the drivers of the observed isotopic offset between hotspot and downstream samples. In the following section the potential influence of different processes on the Hg isotopic composition in Gutach stream after the exfiltration of contaminated groundwater are discussed. This allows to exclude certain processes and identify more probable mechanisms that explain the observed variability in isotope ratios.

Mercury is microbially methylated under anoxic conditions in aquatic environments (Hsu-Kim et al., 2013; Tang et al., 2020). However, the conditions in Gutach stream are predominantly oxic and potential methylation is presumably restricted to localized areas (e.g., still water areas with low flow velocities and floodplains). Methylmercury (MeHg) would be extracted in the F3 step of SEP (Bloom et al., 2003) which is found in a higher proportion in downstream sediments. Methylation was also found to cause mass-dependent isotope fractionation leading to an enrichment of light isotopes in the produced methylmercury (Janssen et al., 2016; Zhang et al., 2022) and is further isotopically fractionated throughout environmental reactions in the water column and internal cycling within biological tissue (Rosera et al., 2022). If methylation takes place in Gutach sediments, this could only change the isotopic composition of the bulk sediment to the observed negative δ^{202}Hg values if MeHg is accumulating and the remaining Hg(II) is preferentially removed. Additionally, MeHg usually contributes only a minor part of total Hg in river sediments (Skyllberg, 2012) and Hg methylation is therefore not expected to result in a measurable shift of the overall isotopic signature of the sediments.

The minor offset in MIF observed in downstream sediments compared to hotspot sediments suggests an influence of in-stream fractionation affecting both the MDF and MIF signals of sediment samples, such as, for example, redox processes. Based on experimental studies the ratio of Δ^{199}Hg and Δ^{201}Hg has been proposed to be indicative of specific fractionation processes. These experiments include photoreduction of Hg(II) (slope = 1.00 ± 0.02) (Bergquist and Blum, 2007), photoreduction of Hg(II) at different Hg/DOC ratios (slopes ranging from 1.19 ± 0.02 to 1.31 ± 0.14) (Zheng and Hintelmann, 2009) and photoreduction of MeHg (slope = 1.36 ± 0.02) (Bergquist and Blum, 2007). Experiments investigating reactions influenced by the nuclear volume effect (NVE) showed different characteristic slopes of 1.61 ± 0.06 for abiotic reduction of Hg(II) by DOM (Zheng and Hintelmann, 2010b) and 1.54 ± 0.22 for equilibrium fractionation between dissolved Hg(II) species and thiol-bound Hg (Wiederhold et al., 2010) which is close to the theoretically predicted value of 1.65 for NVE (Wiederhold et al., 2010). Applying this slope as diagnostic tool in stream sediments, Washburn et al. (2019) suggested that Hg in the investigated rivers was influenced by Hg photoreduction (observed Δ^{199}Hg/Δ^{201}Hg slopes of 1.57 ± 0.49 and 1.40 ± 0.27). In our study the slope of the orthogonal regression (York et al., 2004) of the relationship between Δ^{199}Hg and Δ^{201}Hg of all sediment samples (fine and bulk) is 1.58 ± 0.23 (Figure 4C). The slope of separate regressions for the bulk sediments only (1.57 ± 0.31) and the fine fraction only (1.62 ± 0.34) showed similar trends. For hotspot and downstream samples this slope indicates an influence of processes involving isotope fractionation influenced by NVE rather than photoreduction. The slope of the regression for the tributary samples only however is 0.95 ± 0.70, closer to values reported for Hg affected by photochemical reduction (Bergquist and Blum, 2007; Zheng and Hintelmann, 2009). Microbial reduction of Hg(II) to Hg(0) (Kritee et al., 2008, 2013), photochemical reduction by organic compounds (Zheng and Hintelmann, 2010a; Motta et al., 2020) and dark abiotic reduction (Zheng and Hintelmann, 2010b) are known to impart MDF as well as MIF. However, the PTD results do not indicate the presence of Hg(0) in the sediment samples. The fact that Hg(0) is not present in the sediments does not entirely exclude an influence of reduction processes because Hg(0) could easily volatilize to the atmosphere. The effects of reduction processes would nonetheless be detectable in the remaining Hg pool in sediments by causing a shift towards heavier δ^{202}Hg values along the flow path as reduction of Hg(II) leads to an enrichment of light isotopes in the produced Hg(0) fraction. This is opposite to the observed shift towards lighter isotopic composition in downstream samples.

Formation of Hg(0) in the aquifer of this site has been demonstrated (McLagan et al., 2022b) and in certain groundwater wells at the contamination site Hg(0) has been detected (Richard et al., 2016b) which could potentially exfiltrate to the stream despite the dominant species being inorganic Hg(II). Data on isotope fractionation during Hg(0) oxidation in aqueous systems is still limited, but dark abiotic oxidation of dissolved Hg(0) has been shown to enrich heavier isotopes in the oxidized Hg(II) and shift Δ^{199}Hg to more negative values (Zheng et al., 2019). Exfiltration of Hg(0) and subsequent oxidation is therefore an unlikely cause of the observed negative δ^{202}Hg values in downstream sediment samples and the minor offset in Δ^{199}Hg towards more positive values.

The groundwater at the investigated site showed changing redox states, and the importance of hydrous ferric oxides for the retention of Hg in parts of the adjacent groundwater aquifer has been demonstrated by Richard et al. (2016a). If dissolved Fe(II) exfiltrates with anoxic groundwater it will rapidly precipitate as ferrihydrite and other poorly-crystalline hydrous ferric oxides with a large reactive surface when it enters the well-mixed oxic stream water. These Fe-phases can function as a temporary sink for Hg through sorption and co-precipitation. Hg(II) sorption to goethite as a model compound for Fe-oxides under equilibrium conditions was reported to cause an overall δ^{202}Hg fractionation of ~−0.4‰ (Jiskra et al., 2012). In experiments, the precipitation of metacinnabar (β-HgS) and montroydite (HgO) caused an enrichment of light isotopes in the precipitates relative to the dissolved fraction by a factor of up to −0.63‰ (Smith et al., 2015b). Immediate precipitation of a small fraction of Hg exfiltrating from groundwater as HgO or β-HgS could also cause hotspot sediments to have a slightly lighter isotopic composition than the exfiltrating groundwater, shifting the isotope ratios in the observed direction. However, the release curves of the PTD do not indicate the presence of HgO or β-HgS in the sediment samples (except for S02 to a minimal extent). If Hg precipitated, then more likely as co-precipitates with hydrous ferric oxides. A large fraction of Hg in the hotspot sediments is extracted in steps F4 and F5, the steps in which the majority of Fe is extracted, and thus in which Hg associated with Fe-oxides is expected to be released (Supplementary Figure S3.1). The determined equilibrium fractionation factors are however not large enough to explain the large extent of fractionation observed in the downstream sediments solely based on equilibrium sorption to Fe oxides or precipitation of Hg as HgO or β-HgS. Precipitation of Hg with mineral phases and subsequent sorption on these mineral phases is rather expected directly after the exfiltration of contaminated groundwater in the hotspot area immobilizing Hg in sediments in the hotspot section without causing a large shift in isotopic composition.

Organic matter is one of the primary parameters controlling Hg sorption and mobility in natural aquatic systems due to the formation of extremely strong ionic bonding between Hg and reduced sulfur (S) or thiol groups (-SH) commonly present in aquatic organic matter (Ravichandran, 2004; Skyllberg et al., 2006; Wang et al., 2022). Mercury exfiltrating as inorganic Hg(II) with contaminated groundwater is expected to rapidly bind to organic sorption sites in the bottom sediments as well as algae and biofilms. However, it has been suggested that Hg in highly contaminated areas is also adsorbed onto mineral fractions of sediments because high-affinity organic matter sorption sites are rapidly saturated by high Hg concentrations (Hissler and Probst, 2006). Similarly, high-affinity sites associated with colloidal DOM may quickly become saturated after initial exposure and the remaining Hg may become associated with lower affinity sites and larger particulates (Washburn et al., 2017). The high THg concentrations in hotspot sediments suggest rapid removal of Hg from the water phase by sorption of Hg to the bottom sediments. Relative proportions in SEP indicate the formation of poorly soluble high-concentration Hg pools (released in SEP steps F4 and F5) in that section of the stream, but the absolute pool size of F3 is also larger in the hotspot sediments compared to downstream sediments highlighting the importance of organic matter in the retention of Hg in the hotspot section. Sorption of Hg to organic matter is expected to cause isotope fractionation as shown by equilibrium sorption experiments of dissolved Hg(II) on thiols which is associated with an enrichment of light isotopes (δ^{202}Hg) in the sorbed fraction in the range of −0.53‰ (for $HgCl_2$) and −0.62‰ (for $Hg(OH)_2$) (Wiederhold et al., 2010). Like sorption to goethite, the enrichment factors for equilibrium sorption to functional groups (thiol, carboxyl) of organic matter alone are not large enough to explain the negative δ^{202}Hg values observed in downstream sediments. Exchange experiments between dissolved Hg(II) species and solid bound Hg(II) on carboxyl- and thiol-resins or goethite indicated that kinetic effects may play an important role in metal isotope fractionation during sorption (Jiskra et al., 2014). The timeframe to reach equilibrium in these experiments was days to several months depending on the properties of the dissolved ligand phase. In a dynamic, open system such as Gutach stream, the contact time of dissolved Hg(II) and sorption sites in the bottom sediment is likely not sufficiently long to reach complete equilibrium conditions. Thus, an influence of initial kinetic effects on isotope fractionation during sorption and transport of Hg in the water phase and suspended particles needs to be considered.

Dissolved Hg concentrations in Gutach stream remain elevated at downstream sampling locations (14.8–50.8 ng L^{-1}; Supplementary Table S6). There are two possible explanations for these elevated dissolved Hg concentrations: 1.) The majority of Hg remains in the liquid phase after the exfiltration of contaminated groundwater in soluble forms or associated with high affinity sorption sites of DOM and is transported in the stream water over long distances. 2.) The contaminated bottom sediments constantly release Hg and sustain elevated Hg concentrations in stream water. In the first case most of the released Hg remains in the liquid phase and only a small fraction of Hg is sorbed to the bottom sediments. The observed shift

towards negative δ^{202}Hg values would result from preferential sorption of light isotopes. The large extent of fractionation could be explained by the short contact time which doesn't allow the establishment of equilibrium conditions (Jiskra et al., 2014). An initial kinetic effect with minor re-equilibration can lead to a larger extent of fractionation compared to equilibrium sorption experiments. The removal of only a small pool of Hg enriched in light isotopes would cause a minimal (negligible) change in the isotope signature of the large remaining dissolved Hg pool that cannot be analytically resolved in downstream samples.

In the second case, the Hg pool size in bottom sediments needs to be large enough to constantly release Hg and sustain elevated Hg concentrations in stream water. Our results showed that the largest amount of Hg in Gutach stream sediments was associated with the coarse fraction (61%–97%), similar to results reported by Xu et al. (2021), Hissler and Probst (2006) and Smith et al. (2015a). The proportion of Hg released from bulk sediments in the water-soluble pool in downstream samples was higher compared to hotspot samples, but still relatively small (4.3% ± 1.3%). The overall pool size of this labile Hg fraction in sediments can nonetheless be large considering the overall mass of the sediments. Crowther et al. (2021) hypothesized that abundant Hg in strongly-bound fractions (F4 and F5 steps in SEP) may continuously be remobilized, contributing small amounts of Hg to both the weakly-bound Hg pools in sediments (F1 step in SEP) and replenishing dissolved Hg in the stream water. A similar redistribution of Hg in Gutach stream is plausible, however the transformations of Hg binding forms observed in PTD and SEP suggest that Hg is re-adsorbed to organic matter (F3 in SEP) rather than the water-soluble pool. The Hg pool mobilized from contaminated bulk sediments is expected to be isotopically heavier to an extent similar to that expected from equilibrium sorption experiments (δ^{202}Hg difference 0.3‰ to 0.6‰) (Wiederhold et al., 2010; Jiskra et al., 2012). Leaching experiments also showed that the labile Hg pools mobilized from soils or mine waste (Stetson et al., 2009; Wiederhold et al., 2013; Yin et al., 2013) and aquifer material from drill cores contaminated with $HgCl_2$ (Brocza et al., 2019; McLagan et al., 2022b) were consistently enriched in heavier isotopes compared to bulk samples. Water extracts of contaminated sediments in Grigg et al. (2018) and Crowther et al. (2021) however were not significantly different from bulk sediments showing that the extent of Hg fractionation during leaching is site-specific, depending on Hg speciation, geochemical conditions and spatial heterogeneity. The limited data of isotope ratios in SEP extracts in this study showed that both the F1 and F3 extracts of the most contaminated sediment samples (S05 and S02) had a heavier δ^{202}Hg value compared to the bulk sample (Supplementary Figure S3.3) suggesting that Hg mobilized and re-adsorbed is indeed isotopically heavier and the Hg associated with the bulk sediments isotopically lighter. Complementary to MDF, sorption of Hg in equilibrium experiments was also associated with a small extent of odd-mass MIF related to NVE, resulting in a Δ^{199}Hg/Δ^{201}Hg slope of 1.54 (Wiederhold et al., 2010). This is consistent with the results of sediment samples in this study. The extent of mass dependent enrichment of heavy isotopes is however again smaller (<1‰ difference) than the differences observed in the stream sediments and can only explain the observed variation when particle size and transport effects are included.

The redistribution of Hg to organic matter is likely also a redistribution to the finer sediment fractions due to the increase in specific reactive surface area with decreasing grain size (Kelly and Rudd, 2018; Dickson et al., 2019; Xu et al., 2021). The sediment fine fraction has often been observed to contain higher THg concentrations than bulk sediments (Kelly and Rudd, 2018). Previous studies also found slight differences in Hg isotopic composition between sediment size fractions, with the fine fraction exhibiting less negative δ^{202}Hg values than the coarse fraction (Donovan et al., 2014; Smith et al., 2015a). This difference was attributed to the input of Hg from isotopically distinct sources (contaminated streambanks and soils) that contribute to sediment size fractions to a different extent. While this may also be the case for sediments at our study site, including sediments from tributary streams not affected by direct industrial contamination that also exhibit a large offset between δ^{202}Hg values of the size fractions, we propose that the *in-situ* redistribution of Hg from the bulk sediments to organic matter in the fine fractions also leads to the isotopic difference between the size fractions which was observed in some samples (Figure 4). The differences between the size fractions are however not as pronounced and consistent as could be expected from this process because of preferential mobilization and removal of the fine fraction. It has been demonstrated that hydrological conditions can have an effect on Hg speciation in suspended matter of rivers (Lin et al., 2011; Baptista-Salazar et al., 2017; Yu et al., 2022). Particles of different size and composition exhibit different settling and resuspension behaviors, with the finer particles remaining suspended in water for much longer and being transported further (Kelly and Rudd, 2018). This can cause a separation of different Hg binding forms associated with these particles (Riscassi et al., 2016; Baptista-Salazar and Biester, 2019; Nair et al., 2022). Similar to the findings of Demers et al. (2018) that the suspended sediment load is "spiraling" downstream as it is deposited and resuspended from streambed biofilm, the sediment fine fraction is expected to act as a transport vector for Hg in Gutach stream. The observed difference between the hotspot section and the downstream sediments can also be attributed to the particle transport regime, which changes shortly after the Gutach stream and the Josbach stream converge. The hotspot section is relatively flat and right after the weir of the artificial Okalsee pond which will reduce the mobilization of coarse sediment in this section compared to the downstream section. The coarse fraction, and with it the largest Hg pool in Gutach stream, is expected to only be transported in

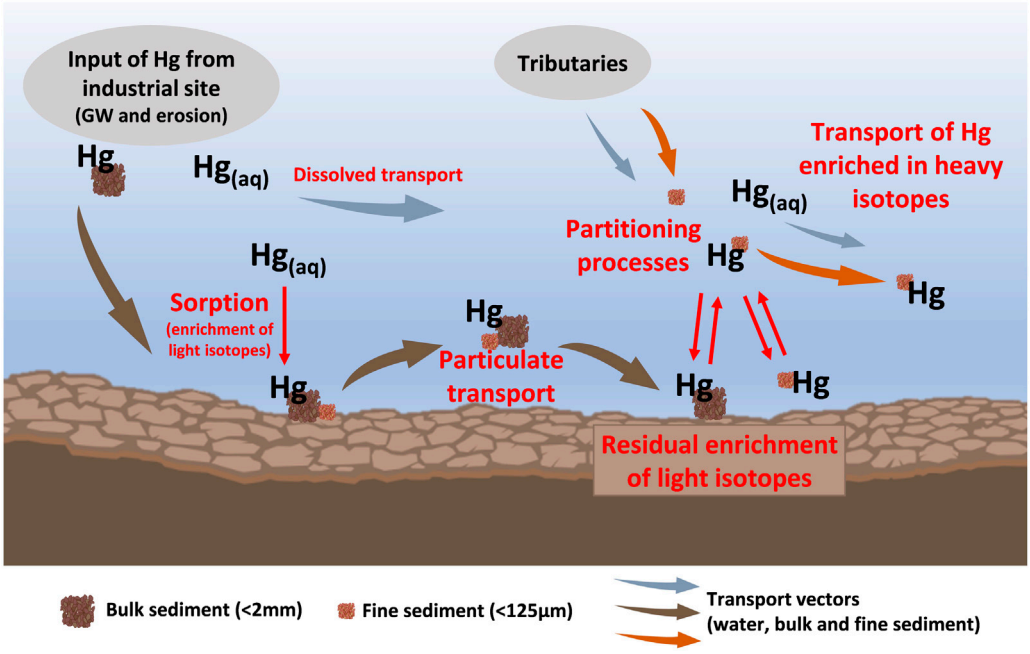

FIGURE 6
Conceptual model of the proposed mechanisms leading to the observed light δ^{202}Hg values in downstream sediments after the exfiltration of contaminated groundwater (GW) into the stream. Briefly, the processes involved include rapid sorption to the solid phase (including lower affinity sorption sites) after exfiltration of contaminated groundwater to the stream. Mercury is then mainly transported with particulate matter during high discharge events. Partitioning processes lead to a redistribution of Hg during the further transport, mobilizing Hg from the particulate phase and re-adsorbing to high affinity sites such as organic matter or fine fraction. The partitioning of Hg between the solid and liquid phase leads to isotopic fractionation and an enrichment of light isotopes in the residual phase. Hg re-adsorbed from the heavier pool is preferentially transported within the stream, leading to a large extent of Hg isotope fractionation in the residual Hg pool. Please note that this is a simplified visualization and not all potentially relevant components and processes are depicted.

the hotspot section during high discharge periods [~10 times per year (Ortlepp, 1997)]. Mercury associated with finer particles however can be more easily resuspended and transported during the prevalent low to moderate flow conditions. This difference in transport velocities between the sediment size fractions leads to a separation of these pools with an isotopic fractionation behavior that is different from what would be expected in a closed system batch experiment without transport. The continuous replenishment of fine sediment and suspended particulate matter during regular flow conditions in the downstream section and redistribution of Hg to organic matter in this sediment fraction removes the product of the partitioning process. In comparison to equilibrium fractionation, the extent of fractionation in systems with continuous removal of the product can be much larger. For such systems with removal of the reaction product a Rayleigh fractionation model describes the extent of fractionation more accurately and using the fractionation factors determined for equilibrium sorption processes in a Rayleigh model shows that the observed offset of about −2‰ in the remaining pool is possible if a very large relative fraction of Hg (~95%) has been redistributed and removed. Considering the much lower THg concentrations in downstream samples compared to hotspot samples, the removal of a large proportion of Hg from the sediments by partitioning processes, redistribution and preferential transport of remobilized Hg from sediment components which were previously affected by isotope fractionation between different components of the sediment is another possible explanation for the observed changes in Hg binding forms and isotope values (a conceptualization of this redistribution and fractionation mechanism is presented in Figure 6).

The observed change in Hg binding forms during the transport of Hg in Gutach stream may have implications for the methylation potential of Hg transported further downstream of the former $HgCl_2$ source. Methylation rates and bioavailability potentials are known to span over a large range depending on the binding form of Hg in sediments and local geochemical conditions (Jonsson et al., 2012; Zhang et al., 2019; Xu et al., 2021) and the amount of Hg removed in the F3 fraction has been reported to be correlated with Hg methylation potential for

aquatic sediments (Bloom et al., 2003; Brooks et al., 2017). The redistribution of Hg to organically bound Hg in downstream samples may therefore indicate a greater potential for Hg methylation and subsequent accumulation in the aquatic food web.

5 Conclusion

This study demonstrates that Hg released as highly soluble $HgCl_2$ from a contaminated site is rapidly sorbed to stream sediments and can be retained long-term followed by particulate transport and redistribution within the sediment. The observed large shift to negative $\delta^{202}Hg$ values in Gutach sediments downstream of the contaminated site stream could not be explained by conservative binary mixing models using industrially derived Hg from the former kyanization facility and natural background endmembers. All tested scenarios resulted in a large underestimation of the industrial contribution. More likely, transformation of Hg binding forms as indicated by the analysis of Hg binding forms together with transport processes have caused the large extent of isotopic fractionation. Based on the observed MDF and MIF signatures, we were able to conclude that several potentially relevant in-stream processes, which would lead to a fractionation causing an enrichment of heavy isotopes in the sediments such as methylation, precipitation or (photo-) reduction and evaporative losses to the atmosphere, were not able to influence the Hg budget in the studied stream system to a significant extent. The rapid sorption of Hg to the sediments is expected to retain a large fraction of the released Hg in the bulk sediments which is only transported during high discharge events, while Hg mobilized and re-adsorbed to organic matter in fine sediment fractions is expected to be removed also under the prevalent low to moderate flow conditions. This redistribution of Hg in the sediments results in an offset of $\delta^{202}Hg$ between bulk and fine sediments. The large extent of isotopic fractionation between hotspot and contaminated downstream sediments is proposed to be a combination of kinetic effects during the redistribution with the preferential transport of the fine fraction and the removal of the redistributed fraction preventing re-equilibration. These findings highlight the importance of processes governing the isotopic composition of environmental samples such as stream sediments impacted by a single point source of contamination and the apparent limitations of the application of conservative mixing models using Hg isotopes. Furthermore, the observed change in Hg binding form has implications for the potential of Hg to become available for methylation and subsequent accumulation in the aquatic food web. The combination of methods used in this study allowed to narrow down the processes leading to the observed large extent of Hg isotope fractionation. Given the complexity of the system and the influence of many different (biogeo)chemical and physical processes occurring simultaneously in a natural stream environment the exact allocation of governing processes is challenging and the proposed mechanisms still need to be verified and confirmed in future studies. Ideally, the sampling and isotopic analysis should target multiple sample matrices such as stream water, suspended particulate matter, and potentially biota, in addition to sediments. Although stream sediments may potentially provide an integrated record of past Hg releases from industrial sites, the interpretation of sediment Hg isotope data is complicated because the age (time of deposition) of a collected sediment sample is usually unknown as well as due to the difficulty of establishing mass balance estimates of Hg pool sizes and fluxes in such heterogeneous natural systems where transport is often dominated by hydrological extreme events. Concerning the interpretation of Hg isotope data, a more comprehensive understanding of the Hg isotope effects of certain processes is still lacking [e.g., (de)sorption and complexation under kinetically controlled conditions] and experiments under environmentally relevant conditions are needed to link field observations to laboratory studies. While SEP and PTD provide a useful general picture of dominant Hg binding forms, advances in spectroscopic techniques may allow obtaining more detailed information of the Hg speciation in environmental samples (e.g., Poulin et al., 2016; Xu et al., 2021; Nehzati et al., 2022) which in turn could potentially provide further insights into the mechanisms and processes involved. Moreover, recent advancements in analytical methods and sample preparation enable the analysis of Hg isotope ratios in many different matrices (e.g., water, suspended particulate matter, biota), also at very low Hg concentrations (e.g., Janssen et al., 2019; Yang et al., 2022) as well as species specific Hg isotope analysis (e.g., Rosera et al., 2022; Bouchet et al., 2022). We therefore recommend that the design of future process-oriented studies on the behavior and fate of Hg at contaminated sites and surrounding environmental systems should take advantage of these recent analytical advances and include the investigation of multiple sample matrices and the combination of different methods approaches to elucidate and disentangle the intricate mechanisms and processes controlling environmental Hg cycling.

Data availability statement

The original contributions presented in the study are included in the article/Supplementary Material, further inquiries can be directed to the corresponding author.

Author contributions

LS: Writing of original draft, fieldwork, sample analysis, data evaluation and visualization. FR: Fieldwork, sample

analysis, data evaluation. AA: FTIR analysis. DM: Fieldwork, sample analysis, manuscript reviews. SK: Manuscript reviews. HB: Study design and concept, manuscript reviews. JW: Study design and concept, fieldwork, sample analysis, data evaluation, manuscript reviews.

Funding

This research was funded by the Austrian Science Fund (FWF) grant I-3489-N28 and the German Research Foundation (DFG) grant BI 734/17-1.

Acknowledgments

The authors acknowledge Herwig Lenitz, Kurt Barmettler, Petra Schmidt, and Adelina Calean for analytical assistance and thank the Environmental Geochemistry Group at the University of Vienna for inspiring discussion. We thank the three reviewers for helpful comments.

Conflict of interest

The authors declare that the research was conducted in the absence of any commercial or financial relationships that could be construed as a potential conflict of interest.

Publisher's note

Supplementary material

The Supplementary Material for this article can be found online at: https://www.frontiersin.org/articles/10.3389/fenvc.2022.1058890/full#supplementary-material

References

Amos, H. M., Jacob, D. J., Kocman, D., Horowitz, H. M., Zhang, Y., Dutkiewicz, S., et al. (2014). Global biogeochemical implications of mercury discharges from rivers and sediment burial. *Environ. Sci. Technol.* 48, 9514–9522. doi:10.1021/es502134t

Araujo, B. F., Hintelmann, H., Dimock, B., Almeida, M. G., and Rezende, C. E. (2017). Concentrations and isotope ratios of mercury in sediments from shelf and continental slope at Campos Basin near Rio de Janeiro, Brazil. *Chemosphere* 178, 42–50. doi:10.1016/j.chemosphere.2017.03.056

Baptista-Salazar, C., and Biester, H. (2019). The role of hydrological conditions for riverine Hg species transport in the Idrija mining area. *Environ. Pollut.* 247, 716–724. doi:10.1016/j.envpol.2019.01.109

Baptista-Salazar, C., Hintelmann, H., and Biester, H. (2018). Distribution of mercury species and mercury isotope ratios in soils and river suspended matter of a mercury mining area. *Environ. Sci. Process. Impacts* 20, 621–631. doi:10.1039/c7em00443e

Baptista-Salazar, C., Richard, J. H., Horf, M., Rejc, M., Gosar, M., and Biester, H. (2017). Grain-size dependence of mercury speciation in river suspended matter, sediments and soils in a mercury mining area at varying hydrological conditions. *Appl. Geochem.* 81, 132–142. doi:10.1016/j.apgeochem.2017.04.006

Bartov, G., Deonarine, A., Johnson, T. M., Ruhl, L., Vengosh, A., and Hsu-Kim, H. (2013). Environmental impacts of the Tennessee Valley Authority Kingston coal ash Spill. 1. Source apportionment using mercury stable isotopes. *Environ. Sci. Technol.* 47, 2092–2099. doi:10.1021/es303111p

Bergquist, B. A., and Blum, J. D. (2007). Mass-dependent and -independent fractionation of Hg isotopes by photoreduction in aquatic systems. *Science* 318, 417–420. doi:10.1126/science.1148050

Bergquist, B. A., and Blum, J. D. (2009). The odds and evens of mercury isotopes: Applications of mass-dependent and mass-independent isotope fractionation. *Elements* 5, 353–357. doi:10.2113/gselements.5.6.353

Biester, H., Gosar, M., and Covelli, S. (2000). Mercury speciation in sediments affected by dumped mining residues in the drainage area of the Idrija mercury mine, Slovenia. *Environ. Sci. Technol.* 34, 3330–3336. doi:10.1021/es991334v

Biester, H., and Scholz, C. (1997). Determination of mercury binding forms in contaminated soils: Mercury pyrolysis versus sequential extractions. *Environ. Sci. Technol.* 31, 233–239. doi:10.1021/es960369h

Bischoff, C., Richard, J., and Biester, H. (2015). *Abschlussbericht Änderungen der Quecksilber, Arsen und Chromkonzentrationen durch Grundwasserexfiltration in die Gutach im Bereich der ehemaligen Kyanisieranlage Okal-Werk*. Braunschweig, Germany: Technical University of Braunschweig (unpublished).

Bloom, N. S., Preus, E., Katon, J., and Hiltner, M. (2003). Selective extractions to assess the biogeochemically relevant fractionation of inorganic mercury in sediments and soils. *Anal. Chim. Acta X.* 479, 233–248. doi:10.1016/S0003-2670(02)01550-7

Blum, J. D., and Bergquist, B. A. (2007). Reporting of variations in the natural isotopic composition of mercury. *Anal. Bioanal. Chem.* 388, 353–359. doi:10.1007/s00216-007-1236-9

Boszke, L., Kowalski, A., and Siepak, J. (2004). Grain size partitioning of mercury in sediments of the middle Odra River (Germany/Poland). *Water Air Soil Pollut.* 159, 125–138. doi:10.1023/B:WATE.0000049171.22781.bd

Bouchet, S., Tessier, E., Masbou, J., Point, D., Lazzaro, X., Monperrus, M., et al. (2022). *In situ* photochemical transformation of Hg species and associated isotopic fractionation in the water column of high-altitude lakes from the Bolivian altiplano. *Environ. Sci. Technol.* 56, 2258–2268. doi:10.1021/acs.est.1c04704

Branfireun, B. A., Cosio, C., Poulain, A. J., Riise, G., and Bravo, A. G. (2020). Mercury cycling in freshwater systems - an updated conceptual model. *Sci. Total Environ.* 745, 140906. doi:10.1016/j.scitotenv.2020.140906

Bravo, A. G., and Cosio, C. (2020). Biotic formation of methylmercury: A bio–physico–chemical conundrum. *Limnol. Oceanogr.* 65, 1010–1027. doi:10.1002/lno.11366

Brocza, F. M., Biester, H., Richard, J.-H., Kraemer, S. M., and Wiederhold, J. G. (2019). Mercury isotope fractionation in the subsurface of a Hg(II) chloride-contaminated industrial legacy site. *Environ. Sci. Technol.* 53, 7296–7305. doi:10.1021/acs.est.9b00619

Brooks, S., Eller, V., Dickson, J., Earles, J., Lowe, K., Mehlhorn, T., et al. (2017). Mercury content of sediments in east fork poplar creek: Current assessment and past trends. Available at: http://www.osti.gov/scitech/(Accessed August 8, 2022).

Campeau, A., Eklöf, K., Soerensen, A. L., Åkerblom, S., Yuan, S., Hintelmann, H., et al. (2022). Sources of riverine mercury across the Mackenzie River Basin; inferences from a combined Hg–C isotopes and optical properties approach. *Sci. Total Environ.* 806, 150808. doi:10.1016/j.scitotenv.2021.150808

Chen, J. Bin, Hintelmann, H., Feng, X. Bin, and Dimock, B. (2012). Unusual fractionation of both odd and even mercury isotopes in precipitation from Peterborough, ON, Canada. *Geochim. Cosmochim. Acta* 90, 33–46. doi:10.1016/j.gca.2012.05.005

Chen, J., Hintelmann, H., Zheng, W., Feng, X., Cai, H., Wang, Z. Z. Z., et al. (2016). Isotopic evidence for distinct sources of mercury in lake waters and sediments. *Chem. Geol.* 426, 33–44. doi:10.1016/j.chemgeo.2016.01.030

Chen, X., Zheng, L., Sun, R., Liu, S., Li, C., Chen, Y., et al. (2022). Mercury in sediment reflecting the intensive coal mining activities: Evidence from stable

mercury isotopes and Bayesian mixing model analysis. *Ecotoxicol. Environ. Saf.* 234, 113392. doi:10.1016/j.ecoenv.2022.113392

Cooke, C. A., Martínez-Cortizas, A., Bindler, R., and Sexauer Gustin, M. (2020). Environmental archives of atmospheric Hg deposition – a review. *Sci. Total Environ.* 709, 134800. doi:10.1016/j.scitotenv.2019.134800

Crowther, E. R., Demers, J. D., Blum, J. D., Brooks, S. C., and Johnson, M. W. (2021). Use of sequential extraction and mercury stable isotope analysis to assess remobilization of sediment-bound legacy mercury. *Environ. Sci. Process. Impacts* 23, 756–775. doi:10.1039/d1em00019e

Demers, J. D., Blum, J. D., Brooks, S. C., Donovan, P. M., Riscassi, A. L., Miller, C. L., et al. (2018). Hg isotopes reveal in-stream processing and legacy inputs in east fork poplar creek, oak ridge, Tennessee, USA. *Environ. Sci. Process. Impacts* 20, 686–707. doi:10.1039/c7em00538e

Dickson, J. O., Mayes, M. A., Brooks, S. C., Mehlhorn, T. L., Lowe, K. A., Earles, J. K., et al. (2019). Source relationships between streambank soils and streambed sediments in a mercury-contaminated stream. *J. Soils Sediments* 19, 2007–2019. doi:10.1007/s11368-018-2183-0

Donovan, P. M., Blum, J. D., Demers, J. D., Gu, B., Brooks, S. C., and Peryam, J. (2014). Identification of multiple mercury sources to stream sediments near Oak Ridge, TN, USA. *Environ. Sci. Technol.* 48, 3666–3674. doi:10.1021/es4046549

Donovan, P. M., Blum, J. D., Singer, M. B., Marvin-Dipasquale, M., and Tsui, M. T. K. (2016). Isotopic composition of inorganic mercury and methylmercury downstream of a historical gold mining region. *Environ. Sci. Technol.* 50, 1691–1702. doi:10.1021/acs.est.5b04413

Eckley, C. S., Gilmour, C. C., Janssen, S., Luxton, T. P., Randall, P. M., Whalin, L., et al. (2020). The assessment and remediation of mercury contaminated sites: A review of current approaches. *Sci. Total Environ.* 707, 136031. doi:10.1016/j.scitotenv.2019.136031

Eisele, G. (2004). Absicherbarkeit von Risiken beim Flächenrecycling, Forschungsbericht FZKA-BWPLUS. Available at: https://pudi.lubw.de/detailseite/-/publication/99447-Arbeitshilfe_Absicherbarkeit_von_Risiken_beim_Flächenrecycling.pdf.

EPA (2002). Method 1631, revision E: Mercury in water by oxidation, purge and trap, and cold vapor atomic fluorescence spectrometry. Available at: https://www.nemi.gov/methods/method_summary/9628/ (Accessed September 2, 2021).

EPA (2000). Method 7473, Mercury in solids and solutions by thermal decomposition, amalgamation, and atomic absorption spectrophotometry. Available at: https://www.epa.gov/esam/epa-method-7473-sw-846-mercury-solids-and-solutions-thermal-decomposition-amalgamation (Accessed December 9, 2022).

Feng, C., Pedrero, Z., Lima, L., Olivares, S., de la Rosa, D., Berail, S., et al. (2019). Assessment of Hg contamination by a Chlor-Alkali Plant in riverine and coastal sites combining Hg speciation and isotopic signature (Sagua la Grande River, Cuba). *J. Hazard. Mat.* 371, 558–565. doi:10.1016/j.jhazmat.2019.02.092

Feng, X., Foucher, D., Hintelmann, H., Yan, H., He, T., and Qiu, G. (2010). Tracing mercury contamination sources in sediments using mercury isotope compositions. *Environ. Sci. Technol.* 44, 3363–3368. doi:10.1021/es9039488

Fernández-Martínez, R., and Rucandio, I. (2013). Assessment of a sequential extraction method to evaluate mercury mobility and geochemistry in solid environmental samples. *Ecotoxicol. Environ. Saf.* 97, 196–203. doi:10.1016/j.ecoenv.2013.07.013

Foucher, D., Hintelmann, H., Al, T. A., and MacQuarrie, K. T. (2013). Mercury isotope fractionation in waters and sediments of the Murray Brook mine watershed (New Brunswick, Canada): Tracing mercury contamination and transformation. *Chem. Geol.* 336, 87–95. doi:10.1016/j.chemgeo.2012.04.014

Foucher, D., Ogrinc, N., and Hintelmann, H. (2009). Tracing mercury contamination from the idrija mining region (Slovenia) to the gulf of trieste using Hg isotope ratio measurements. *Environ. Sci. Technol.* 43, 33–39. doi:10.1021/es801772b

Goix, S., Maurice, L., Laffont, L., Rinaldo, R., Lagane, C., Chmeleff, J., et al. (2019). Quantifying the impacts of artisanal gold mining on a tropical river system using mercury isotopes. *Chemosphere* 219, 684–694. doi:10.1016/j.chemosphere.2018.12.036

Gonser, T., and Schwoerbel, J. (1985). Chemische und biologische Untersuchung des Gutach-Wutach-Flusssystems zwischen Neustadt und Weizener Steg. *Beih. Veröffentlichungen für Naturschutz Landschaftspfl. Baden-württemb* 44, 9–112. Available at: http://www.ephemeroptera-galactica.com/pubs/pub_g/pubgonsert1985p9.pdf (Accessed December 9, 2022).

Gratz, L. E., Keeler, G. J., Blum, J. D., and Sherman, L. S. (2010). Isotopic composition and fractionation of mercury in Great Lakes precipitation and ambient air. *Environ. Sci. Technol.* 44, 7764–7770. doi:10.1021/es100383w

Gray, J. E., Van Metre, P. C., Pribil, M. J., and Horowitz, A. J. (2015). Tracing historical trends of Hg in the Mississippi River using Hg concentrations and Hg isotopic compositions in a lake sediment core, Lake Whittington, Mississippi, USA. *Chem. Geol.* 395, 80–87. doi:10.1016/j.chemgeo.2014.12.005

Grigg, A. R. C., Kretzschmar, R., Gilli, R. S., and Wiederhold, J. G. (2018). Mercury isotope signatures of digests and sequential extracts from industrially contaminated soils and sediments. *Sci. Total Environ.* 636, 1344–1354. doi:10.1016/j.scitotenv.2018.04.261

Guédron, S., Amouroux, D., Sabatier, P., Desplanque, C., Develle, A. L., Barre, J., et al. (2016). A hundred year record of industrial and urban development in French Alps combining Hg accumulation rates and isotope composition in sediment archives from Lake Luitel. *Chem. Geol.* 431, 10–19. doi:10.1016/j.chemgeo.2016.03.016

Gustin, M. S., Bank, M. S., Bishop, K., Bowman, K., Branfireun, B., Chételat, J., et al. (2020). Mercury biogeochemical cycling: A synthesis of recent scientific advances. *Sci. Total Environ.* 737, 139619. doi:10.1016/j.scitotenv.2020.139619

Hall, G. E. M., Pelchat, P., and Percival, J. B. (2005). The design and application of sequential extractions for mercury, part 1. Optimization of HNO_3 extraction for all non-sulphide forms of Hg. *Geochem. Explor. Environ. Anal.* 5, 107–113. doi:10.1144/1467-7873/03-061

Hall, G. E. M., and Pelchat, P. (2005). The design and application of sequential extractions for mercury, part 2. Resorption of mercury onto the sample during leaching. *Geochem. Explor. Environ. Anal.* 5, 115–121. doi:10.1144/1467-7873/03-062

Heckmann, G. (2002). *Sanierungsplan ehemaliges Betriebsgelände der Fa. Himmelsbach ("OKAL-Gelände") an der Freiburgerstraße in 79822 Titisee-Neustadt*. Landkreis Breisgau-Hochschwarzwald, Germany: Institut für Sanierung und Umweltschutz Dr. Eisele GmbH.

Hissler, C., and Probst, J. L. (2006). Chlor-alkali industrial contamination and riverine transport of mercury: Distribution and partitioning of mercury between water, suspended matter, and bottom sediment of the Thur River, France. *Appl. Geochem.* 21, 1837–1854. doi:10.1016/j.apgeochem.2006.08.002

Horvat, M., Covelli, S., Faganeli, J., Logar, M., Mandić, V., Rajar, R., et al. (1999). Mercury in contaminated coastal environments; a case study: The Gulf of Trieste. *Sci. Total Environ.* 237–238, 43–56. doi:10.1016/S0048-9697(99)00123-0

Hsu-Kim, H., Kucharzyk, K. H., Zhang, T., and Deshusses, M. A. (2013). Mechanisms regulating mercury bioavailability for methylating microorganisms in the aquatic environment: A critical review. *Environ. Sci. Technol.* 47, 2441–2456. doi:10.1021/es304370g

Issaro, N., Abi-Ghanem, C., and Bermond, A. (2009). Fractionation studies of mercury in soils and sediments: A review of the chemical reagents used for mercury extraction. *Anal. Chim. Acta X.* 631, 1–12. doi:10.1016/j.aca.2008.10.020

Janssen, S. E., Lepak, R. F., Tate, M. T., Ogorek, J. M., DeWild, J. F., Babiarz, C. L., et al. (2019). Rapid pre-concentration of mercury in solids and water for isotopic analysis. *Anal. Chim. Acta X.* 1054, 95–103. doi:10.1016/j.aca.2018.12.026

Janssen, S. E., Schaefer, J. K., Barkay, T., and Reinfelder, J. R. (2016). Fractionation of mercury stable isotopes during microbial methylmercury production by iron- and sulfate-reducing bacteria. *Environ. Sci. Technol.* 50, 8077–8083. doi:10.1021/acs.est.6b00854

Janssen, S. E., Tate, M. T., Krabbenhoft, D. P., DeWild, J. F., Ogorek, J. M., Babiarz, C. L., et al. (2021). The influence of legacy contamination on the transport and bioaccumulation of mercury within the Mobile River Basin. *J. Hazard. Mat.* 404, 124097. doi:10.1016/j.jhazmat.2020.124097

Jiskra, M., Saile, D., Wiederhold, J. G., Bourdon, B., Björn, E., and Kretzschmar, R. (2014). Kinetics of Hg(II) exchange between organic ligands, goethite, and natural organic matter studied with an enriched stable isotope approach. *Environ. Sci. Technol.* 48, 13207–13217. doi:10.1021/es503483m

Jiskra, M., Wiederhold, J. G., Bourdon, B., and Kretzschmar, R. (2012). Solution speciation controls mercury isotope fractionation of Hg(II) sorption to goethite. *Environ. Sci. Technol.* 46, 6654–6662. doi:10.1021/es3008112

Jiskra, M., Wiederhold, J. G., Skyllberg, U., Kronberg, R.-M. M., and Kretzschmar, R. (2017). Source tracing of natural organic matter bound mercury in boreal forest runoff with mercury stable isotopes. *Environ. Sci. Process. Impacts* 19, 1235–1248. doi:10.1039/c7em00245a

Jonsson, S., Skyllberg, U., Nilsson, M. B., Westlund, P. O., Shchukarev, A., Lundberg, E., et al. (2012). Mercury methylation rates for geochemically relevant HgII species in sediments. *Environ. Sci. Technol.* 46, 11653–11659. doi:10.1021/es3015327

Jung, S., Kwon, S. Y., Hong, Y., Yin, R., and Motta, L. C. (2021). Isotope investigation of mercury sources in a creek impacted by multiple anthropogenic activities. *Chemosphere* 282, 130947. doi:10.1016/j.chemosphere.2021.130947

Jung, S., Kwon, S. Y., Li, M. L., Yin, R., and Park, J. (2022). Elucidating sources of mercury in the west coast of Korea and the Chinese marginal seas using mercury stable isotopes. *Sci. Total Environ.* 814, 152598. doi:10.1016/j.scitotenv.2021.152598

Kallipoliti, L. (2010). Dry rot: The chemical origins of British preservation. *Future Anterior* 7, 1–19. doi:10.1353/fta.2010.0000

Kelly, C. A., and Rudd, J. W. M. (2018). Transport of mercury on the finest particles results in high sediment concentrations in the absence of significant ongoing sources. *Sci. Total Environ.* 637–638, 1471–1479. doi:10.1016/j.scitotenv.2018.04.234

Kim, C. S., Bloom, N. S., Rytuba, J. J., and Brown, G. E. (2003). Mercury speciation by X-ray absorption fine structure spectroscopy and sequential chemical extractions: A comparison of speciation methods. *Environ. Sci. Technol.* 37, 5102–5108. doi:10.1021/es0341485

Kocman, D., Horvat, M., Pirrone, N., and Cinnirella, S. (2013). Contribution of contaminated sites to the global mercury budget. *Environ. Res.* 125, 160–170. doi:10.1016/j.envres.2012.12.011

Kocman, D., Kanduč, T., Ogrinc, N., and Horvat, M. (2011). Distribution and partitioning of mercury in a river catchment impacted by former mercury mining activity. *Biogeochemistry* 104, 183–201. doi:10.1007/s10533-010-9495-5

Kritee, K., Blum, J. D., and Barkay, T. (2008). Mercury stable isotope fractionation during reduction of Hg(II) by different microbial pathways. *Environ. Sci. Technol.* 42, 9171–9177. doi:10.1021/es801591k

Kritee, K., Blum, J. D., Reinfelder, J. R., and Barkay, T. (2013). Microbial stable isotope fractionation of mercury: A synthesis of present understanding and future directions. *Chem. Geol.* 336, 13–25. doi:10.1016/j.chemgeo.2012.08.017

Lavoie, R. A., Bouffard, A., Maranger, R., and Amyot, M. (2018). Mercury transport and human exposure from global marine fisheries. *Sci. Rep.* 8, 6705–6709. doi:10.1038/s41598-018-24938-3

Lepak, R. F., Yin, R., Krabbenhoft, D. P., Ogorek, J. M., Dewild, J. F., Holsen, T. M., et al. (2015). Use of stable isotope signatures to determine mercury sources in the great lakes. *Environ. Sci. Technol. Lett.* 2, 335–341. doi:10.1021/acs.estlett.5b00277

LGRB Landesamt für Geologie Rohstoffe und Bergbau (2021). Hydrogeologische Großeinheiten. *LGRB-GeoPortal*. Available at: https://maps.lgrb-bw.de/.

Lin, Y., Larssen, T., Vogt, R. D., Feng, X., and Zhang, H. (2011). Transport and fate of mercury under different hydrologie regimes in polluted stream in mining area. *J. Environ. Sci.* 23, 757–764. doi:10.1016/S1001-0742(10)60473-1

Liu, G., Cai, Y., and O'Driscoll, N. (2011a). *Environmental Chemistry and toxicology of mercury*. Hoboken, NJ, USA: John Wiley & Sons. doi:10.1002/9781118146644

Liu, G., Li, Y., and Cai, Y. (2011b). Adsorption of mercury on solids in the aquatic environment. *Environ. Chem. Toxicol. Mercur.*, 367–387. doi:10.1002/9781118146644.ch11

Liu, J., Feng, X., Yin, R., Zhu, W., and Li, Z. (2011c). Mercury distributions and mercury isotope signatures in sediments of Dongjiang, the Pearl River Delta, China. *Chem. Geol.* 287, 81–89. doi:10.1016/j.chemgeo.2011.06.001

Liu, M., Zhang, Q., Maavara, T., Liu, S., Wang, X., and Raymond, P. A. (2021). Rivers as the largest source of mercury to coastal oceans worldwide. *Nat. Geosci.* 14, 672–677. doi:10.1038/s41561-021-00793-2

Ma, J., Hintelmann, H., Kirk, J. L., and Muir, D. C. G. (2013). Mercury concentrations and mercury isotope composition in lake sediment cores from the vicinity of a metal smelting facility in Flin Flon, Manitoba. *Chem. Geol.* 336, 96–102. doi:10.1016/j.chemgeo.2012.10.037

Marshall, B. G., Veiga, M. M., Kaplan, R. J., Adler Miserendino, R., Schudel, G., Bergquist, B. A., et al. (2018). Evidence of transboundary mercury and other pollutants in the Puyango-Tumbes River basin, Ecuador-Peru. *Environ. Sci. Process. Impacts* 20, 632–641. doi:10.1039/c7em00504k

McLagan, D. S., Biester, H., Navrátil, T., Kraemer, S. M., and Schwab, L. (2022a). Internal tree cycling and atmospheric archiving of mercury : Examination with concentration and stable isotope analyses. *Biogeosciences* 19, 4415–4429. doi:10.5194/bg-2022-124

McLagan, D. S., Schwab, L., Wiederhold, J. G., Chen, L., Pietrucha, J., Kraemer, S. M., et al. (2022b). Demystifying mercury geochemistry in contaminated soil–groundwater systems with complementary mercury stable isotope, concentration, and speciation analyses. *Environ. Sci. Process. Impacts* 24, 1406–1429. doi:10.1039/d1em00368b

Meng, M., Sun, R. Y., Liu, H. W., Yu, B., Yin, Y. G., Hu, L. G., et al. (2019). An integrated model for input and migration of mercury in Chinese coastal sediments. *Environ. Sci. Technol.* 53, 2460–2471. doi:10.1021/acs.est.8b06329

Motta, L. C., Kritee, K., Blum, J. D., Tsz-Ki Tsui, M., and Reinfelder, J. R. (2020). Mercury isotope fractionation during the photochemical reduction of Hg (II) coordinated with organic ligands. *J. Phys. Chem. A* 124, 2842–2853. doi:10.1021/acs.jpca.9b06308

Müller, G., and Gastner, M. (1971). The "Karbonat-Bombe", a simple device for the determination of carbonate content in sediment, soils, and other materials. *Neues Jahrb. für Mineral. - Monatsh.* 10, 466–469. doi:10.013/epic.27884

Nair, S. S., DeRolph, C., Peterson, M. J., McManamay, R. A., and Mathews, T. (2022). Integrated watershed process model for evaluating mercury sources, transport, and future remediation scenarios in an industrially contaminated site. *J. Hazard. Mat.* 423, 127049. doi:10.1016/j.jhazmat.2021.127049

Nehzati, S., Dolgova, N. V., Young, C. G., James, A. K., Cotelesage, J. J. H., Sokaras, D., et al. (2022). Mercury Lα1 high energy resolution fluorescence detected X-ray absorption spectroscopy: A versatile speciation probe for mercury. *Inorg. Chem.* 61, 5201–5214. doi:10.1021/acs.inorgchem.1c03196

Nowak, A. (1952). Die Kyanisierung von Leitungsmasten. *Holz als Roh- und Werkst* 10, 12–15. doi:10.1007/BF02605401

Obrist, D., Agnan, Y., Jiskra, M., Olson, C. L., Colegrove, D. P., Hueber, J., et al. (2017). Tundra uptake of atmospheric elemental mercury drives Arctic mercury pollution. *Nature* 547, 201–204. doi:10.1038/nature22997

Ortlepp, J. (1997). Fischereirechtlicher Hegeplan Wutach. Available at: https://docplayer.org/32635320-Fischereilicher-hegeplan-wutach.html.

Pelcová, P., Margetínová, J., Vaculovič, T., Komárek, J., and Kubáň, V. (2010). Adsorption of mercury species on river sediments - effects of selected abiotic parameters. *Open Chem.* 8, 116–125. doi:10.2478/s11532-009-0128-6

Petranich, E., Predonzani, S., Acquavita, A., Mashyanov, N., and Covelli, S. (2022). Rapid thermoscanning technique for direct analysis of mercury species in contaminated sediments: From pure compounds to real sample application. *Appl. Geochem.* 143, 105393. doi:10.1016/j.apgeochem.2022.105393

Poulin, B. A., Aiken, G. R., Nagy, K. L., Manceau, A., Krabbenhoft, D. P., and Ryan, J. N. (2016). Mercury transformation and release differs with depth and time in a contaminated riparian soil during simulated flooding. *Geochim. Cosmochim. Acta* 176, 118–138. doi:10.1016/j.gca.2015.12.024

Pribil, M. J., Rimondi, V., Costagliola, P., Lattanzi, P., and Rutherford, D. L. (2020). Assessing mercury distribution using isotopic fractionation of mercury processes and sources adjacent and downstream of a legacy mine district in Tuscany, Italy. *Appl. Geochem.* 117, 104600. doi:10.1016/j.apgeochem.2020.104600

Ravichandran, M. (2004). Interactions between mercury and dissolved organic matter - a review. *Chemosphere* 55, 319–331. doi:10.1016/j.chemosphere.2003.11.011

Reinfelder, J. R., and Janssen, S. E. (2019). Tracking legacy mercury in the Hackensack River estuary using mercury stable isotopes. *J. Hazard. Mat.* 375, 121–129. doi:10.1016/j.jhazmat.2019.04.074

Reis, A. T., Coelho, J. P., Rucandio, I., Davidson, C. M., Duarte, A. C., and Pereira, E. (2015). Thermo-desorption: A valid tool for mercury speciation in soils and sediments? *Geoderma* 237, 98–104. doi:10.1016/j.geoderma.2014.08.019

Reis, A. T., Davidson, C. M., Vale, C., and Pereira, E. (2016). Overview and challenges of mercury fractionation and speciation in soils. *TrAC Trends Anal. Chem.* 82, 109–117. doi:10.1016/j.trac.2016.05.008

Richard, J. H., Bischoff, C., Ahrens, C. G. M., and Biester, H. (2016a). Mercury (II) reduction and co-precipitation of metallic mercury on hydrous ferric oxide in contaminated groundwater. *Sci. Total Environ.* 539, 36–44. doi:10.1016/j.scitotenv.2015.08.116

Richard, J. H., Bischoff, C., and Biester, H. (2016b). Comparing modeled and measured mercury speciation in contaminated groundwater: Importance of dissolved organic matter composition. *Environ. Sci. Technol.* 50, 7508–7516. doi:10.1021/acs.est.6b00500

Riscassi, A., Miller, C., and Brooks, S. (2016). Seasonal and flow-driven dynamics of particulate and dissolved mercury and methylmercury in a stream impacted by an industrial mercury source. *Environ. Toxicol. Chem.* 35, 1386–1400. doi:10.1002/etc.3310

Rosera, T. J., Janssen, S. E., Tate, M. T., Lepak, R. F., Ogorek, J. M., Dewild, J. F., et al. (2022). Methylmercury stable isotopes: New insights on assessing aquatic food web bioaccumulation in legacy impacted regions. *ACS Environ. Sci. Technol. Water.* 2, 701–709. doi:10.1021/acsestwater.1c00285

Rumayor, M., Lopez-Anton, M. A., Díaz-Somoano, M., Maroto-Valer, M. M., Richard, J. H., Biester, H., et al. (2016). A comparison of devices using thermal desorption for mercury speciation in solids. *Talanta* 150, 272–277. doi:10.1016/j.talanta.2015.12.058

Schuler, D. (2012). Bericht 2012-69 Gefahrenverdachtserkundung Gewässeruntersuchung Gutach. Germany Unpublished report by Solum Büro für Boden + Geologie, Freiburg i. Br.

Selin, N. E. (2009). Global biogeochemical cycling of mercury: A review. *Annu. Rev. Environ. Resour.* 34, 43–63. doi:10.1146/annurev.environ.051308.084314

Skyllberg, U., Bloom, P. R., Qian, J., Lin, C. M., and Bleam, W. F. (2006). Complexation of mercury(II) in soil organic matter: EXAFS evidence for linear two-coordination with reduced sulfur groups. *Environ. Sci. Technol.* 40, 4174–4180. doi:10.1021/es0600577

Skyllberg, U. (2012). Chemical speciation of mercury in soil and sediment. *Environ. Chem. Toxicol. Mercur.*, 219–258. doi:10.1002/9781118146644.ch7

Smith, R. S., Wiederhold, J. G., Jew, A. D., Brown, G. E., Bourdon, B., and Kretzschmar, R. (2015a). Stable Hg isotope signatures in creek sediments impacted by a former Hg mine. *Environ. Sci. Technol.* 49, 767–776. doi:10.1021/es503442p

Smith, R. S., Wiederhold, J. G., and Kretzschmar, R. (2015b). Mercury isotope fractionation during precipitation of metacinnabar (β-HgS) and montroydite (HgO). *Environ. Sci. Technol.* 49, 4325–4334. doi:10.1021/acs.est.5b00409

Sonke, J. E. (2011). A global model of mass independent mercury stable isotope fractionation. *Geochim. Cosmochim. Acta* 75, 4577–4590. doi:10.1016/j.gca.2011.05.027

Stetson, S. J., Gray, J. E., Wanty, R. B., and Macalady, D. L. (2009). Isotopic variability of mercury in ore, mine-waste calcine, and leachates of mine-waste calcine from areas mined for mercury. *Environ. Sci. Technol.* 43, 7331–7336. doi:10.1021/es9006993

Streets, D. G., Horowitz, H. M., Lu, Z., Levin, L., Thackray, C. P., and Sunderland, E. M. (2019). Five hundred years of anthropogenic mercury: Spatial and temporal release profiles. *Environ. Res. Lett.* 14, 084004. doi:10.1088/1748-9326/ab281f

Tang, W. L., Liu, Y. R., Guan, W. Y., Zhong, H., Qu, X. M., and Zhang, T. (2020). Understanding mercury methylation in the changing environment: Recent advances in assessing microbial methylators and mercury bioavailability. *Sci. Total Environ.* 714, 136827. doi:10.1016/j.scitotenv.2020.136827

Troschel, E. (1916). *Handbuch der Holzkonservierung*. Berlin Heidelberg: Springer. doi:10.1007/978-3-662-42439-1

Tsui, M. T. K., Blum, J. D., Finlay, J. C., Balogh, S. J., Kwon, S. Y., and Nollet, Y. H. (2013). Photodegradation of methylmercury in stream ecosystems. *Limnol. Oceanogr.* 58, 13–22. doi:10.4319/lo.2013.58.1.0013

Tsui, M. T. K., Uzun, H., Ruecker, A., Majidzadeh, H., Ulus, Y., Zhang, H., et al. (2020). Concentration and isotopic composition of mercury in a blackwater river affected by extreme flooding events. *Limnol. Oceanogr.* 65, 2158–2169. doi:10.1002/lno.11445

Ullrich, S. M., Tanton, T. W., and Abdrashitova, S. A. (2001). Mercury in the aquatic environment: A review of factors affecting methylation. *Crit. Rev. Environ. Sci. Technol.* 31, 241–293. doi:10.1080/20016491089226

UN Environment (2019). Global mercury assessment 2018. UN environment programme, chemicals. *U. N. Environ. Program. Chem. heal. Branch Geneva* 58. doi:10.1021/acs.est.8b01246

Vermeesch, P. (2018). IsoplotR: A free and open toolbox for geochronology. *Geosci. Front.* 9, 1479–1493. doi:10.1016/j.gsf.2018.04.001

Wang, Y., Liu, J., Liem-Nguyen, V., Tian, S., Zhang, S., Wang, D., et al. (2022). Binding strength of mercury (II) to different dissolved organic matter: The roles of DOM properties and sources. *Sci. Total Environ.* 807, 150979. doi:10.1016/j.scitotenv.2021.150979

Washburn, S. J., Blum, J. D., Demers, J. D., Kurz, A. Y., and Landis, R. C. (2017). Isotopic characterization of mercury downstream of historic industrial contamination in the south river, Virginia. *Environ. Sci. Technol.* 51, 10965–10973. doi:10.1021/acs.est.7b02577

Washburn, S. J., Blum, J. D., Donovan, P. M., and Singer, M. B. (2019). Isotopic evidence for mercury photoreduction and retention on particles in surface waters of Central California, USA. *Sci. Total Environ.* 674, 451–461. doi:10.1016/j.scitotenv.2019.04.145

Washburn, S. J., Blum, J. D., Kurz, A. Y., and Pizzuto, J. E. (2018). Spatial and temporal variation in the isotopic composition of mercury in the South River, VA. *Chem. Geol.* 494, 96–108. doi:10.1016/j.chemgeo.2018.07.023

Wiederhold, J. G., Cramer, C. J., Daniel, K., Infante, I., Bourdon, B., and Kretzschmar, R. (2010). Equilibrium mercury isotope fractionation between dissolved Hg(II) species and thiol-bound Hg. *Environ. Sci. Technol.* 44, 4191–4197. doi:10.1021/es100205t

Wiederhold, J. G., Smith, R. S., Siebner, H., Jew, A. D., Brown, G. E., Bourdon, B., et al. (2013). Mercury isotope signatures as tracers for Hg cycling at the new idria Hg mine. *Environ. Sci. Technol.* 47, 6137–6145. doi:10.1021/es305245z

Woerndle, G. E., Tsz-Ki Tsui, M., Sebestyen, S. D., Blum, J. D., Nie, X., and Kolka, R. K. (2018). New insights on ecosystem mercury cycling revealed by stable isotopes of mercury in water flowing from a headwater peatland catchment. *Environ. Sci. Technol.* 52. doi:10.1021/acs.est.7b04449

Xu, J., Bland, G. D., Gu, Y., Ziaei, H., Xiao, X., Deonarine, A., et al. (2021). Impacts of sediment particle grain size and mercury speciation on mercury bioavailability potential. *Environ. Sci. Technol.* 55, 12393–12402. doi:10.1021/acs.est.1c03572

Yang, L., Yu, B., Liu, H., Ji, X., Xiao, C., Liang, Y., et al. (2022). Online determination of mercury isotopic compositions at ultratrace levels by automated purge and trap coupled with multicollector inductively coupled plasma-mass spectrometry. *J. Anal. At. Spectrom.* 37, 2480–2489. doi:10.1039/d2ja00148a

Yin, R., Feng, X., Hurley, J. P., Krabbenhoft, D. P., Lepak, R. F., Hu, R., et al. (2016). Mercury isotopes as proxies to identify sources and environmental impacts of mercury in sphalerites. *Sci. Rep.* 6, 18686. doi:10.1038/srep18686

Yin, R., Feng, X., Wang, J., Bao, Z., Yu, B., and Chen, J. (2013). Mercury isotope variations between bioavailable mercury fractions and total mercury in mercury contaminated soil in Wanshan Mercury Mine, SW China. *Chem. Geol.* 336, 80–86. doi:10.1016/j.chemgeo.2012.04.017

Yin, R., Guo, Z., Hu, L., Liu, W., Hurley, J. P., Lepak, R. F., et al. (2018). Mercury inputs to Chinese marginal seas: Impact of industrialization and development of China. *J. Geophys. Res. Oceans* 123, 5599–5611. doi:10.1029/2017JC013691

York, D., Evensen, N. M., Martińez, M. L., and De Basabe Delgado, J. (2004). Unified equations for the slope, intercept, and standard errors of the best straight line. *Am. J. Phys.* 72, 367–375. doi:10.1119/1.1632486

Yu, C., Liu, M., Guo, J., Lin, H., Yan, Y., Zhang, Q., et al. (2022). Transport of mercury in a regulated high-sediment river and its input to marginal seas. *Water Res.* 214, 118211. doi:10.1016/j.watres.2022.118211

Zhang, L., Wu, S., Zhao, L., Lu, X., Pierce, E. M., and Gu, B. (2019). Mercury sorption and desorption on organo-mineral particulates as a source for microbial methylation. *Environ. Sci. Technol.* 53, 2426–2433. doi:10.1021/acs.est.8b06020

Zhang, L., Yin, Y., Li, Y., and Cai, Y. (2022). Mercury isotope fractionation during methylmercury transport and transformation: A review focusing on analytical method, fractionation characteristics, and its application. *Sci. Total Environ.* 841, 156558. doi:10.1016/j.scitotenv.2022.156558

Zhang, R., Russell, J., Xiao, X., Zhang, F., Li, T., Liu, Z., et al. (2018). Historical records, distributions and sources of mercury and zinc in sediments of East China sea: Implication from stable isotopic compositions. *Chemosphere* 205, 698–708. doi:10.1016/j.chemosphere.2018.04.100

Zhang, Y., Chen, J., Zheng, W., Sun, R., Yuan, S., Cai, H., et al. (2020). Mercury isotope compositions in large anthropogenically impacted Pearl River, South China. *Ecotoxicol. Environ. Saf.* 191, 110229. doi:10.1016/j.ecoenv.2020.110229

Zheng, W., and Hintelmann, H. (2009). Mercury isotope fractionation during photoreduction in natural water is controlled by its Hg/DOC ratio. *Geochim. Cosmochim. Acta* 73, 6704–6715. doi:10.1016/j.gca.2009.08.016

Zheng, W., Demers, J. D., Lu, X., Bergquist, B. A., Anbar, A. D., Blum, J. D., et al. (2019). Mercury stable isotope fractionation during abiotic dark oxidation in the presence of thiols and natural organic matter. *Environ. Sci. Technol.* 53, 1853–1862. doi:10.1021/acs.est.8b05047

Zheng, W., and Hintelmann, H. (2010a). Isotope fractionation of mercury during its photochemical reduction by low-molecular-weight organic compounds. *J. Phys. Chem. A* 114, 4246–4253. doi:10.1021/jp9111348

Zheng, W., and Hintelmann, H. (2010b). Nuclear field shift effect in isotope fractionation of mercury during abiotic reduction in the absence of light. *J. Phys. Chem. A* 114, 4238–4245. doi:10.1021/jp910353y

Zhu, W., Li, Z., Li, P., Yu, B., Lin, C. J., Sommar, J., et al. (2018). Re-emission of legacy mercury from soil adjacent to closed point sources of Hg emission. *Environ. Pollut.* 242, 718–727. doi:10.1016/j.envpol.2018.07.002

frontiers | Frontiers in Environmental Chemistry

TYPE Original Research
PUBLISHED 09 February 2023
DOI 10.3389/fenvc.2023.1096199

OPEN ACCESS

EDITED BY
Ashu Dastoor,
Environment and Climate Change Canada (ECCC), Canada

REVIEWED BY
Dario Acha,
Universidad Mayor de San Andrés, Bolivia
Jackson Paul Webster,
California State University, Chico, United States

*CORRESPONDENCE
Chris S. Eckley,
eckley.chris@epa.gov

SPECIALTY SECTION
This article was submitted to Inorganic Pollutants, a section of the journal Frontiers in Environmental Chemistry

RECEIVED 11 November 2022
ACCEPTED 24 January 2023
PUBLISHED 09 February 2023

CITATION
Eckley CS, Eagles-Smith C, Luxton TP, Hoffman J and Janssen S (2023), Using mercury stable isotope fractionation to identify the contribution of historical mercury mining sources present in downstream water, sediment and fish. *Front. Environ. Chem.* 4:1096199. doi: 10.3389/fenvc.2023.1096199

Using mercury stable isotope fractionation to identify the contribution of historical mercury mining sources present in downstream water, sediment and fish

Chris S. Eckley[1]*, Collin Eagles-Smith[2], Todd P. Luxton[3], Joel Hoffman[4] and Sarah Janssen[5]

[1]U.S. EPA, Region 10, Seattle, WA, United States, [2]U.S. Geological Survey, Forest and Rangeland Ecosystem Science Center, Corvallis, OR, United States, [3]US EPA ORD, Center for Environmental Solutions and Emergency Response, Cincinnati, OH, United States, [4]U.S. EPA Office of Research and Development, Center for Computational Toxicology and Exposure, Great Lakes Toxicology and Ecology Division, Duluth, MN, United States, [5]U.S. Geological Survey, Mercury Research Lab, Upper Midwest Water Science Center, Madison, WI, United States

Ecosystems downstream of mercury (Hg) contaminated sites can be impacted by both localized releases as well as Hg deposited to the watershed from atmospheric transport. Identifying the source of Hg in water, sediment, and fish downstream of contaminated sites is important for determining the effectiveness of source-control remediation actions. This study uses measurements of Hg stable isotopes in soil, sediment, water, and fish to differentiate between Hg from an abandoned Hg mine from non-mine-related sources. The study site is located within the Willamette River watershed (Oregon, United States), which includes free-flowing river segments and a reservoir downstream of the mine. The concentrations of total-Hg (THg) in the reservoir fish were 4-fold higher than those further downstream (>90 km) from the mine site in free-flowing sections of the river. Mercury stable isotope fractionation analysis showed that the mine tailings (δ^{202}Hg: −0.36‰ ± 0.03‰) had a distinctive isotopic composition compared to background soils (δ^{202}Hg: −2.30‰ ± 0.25‰). Similar differences in isotopic composition were observed between stream water that flowed through the tailings (particulate bound δ^{202}Hg: −0.58‰; dissolved: −0.91‰) versus a background stream (particle-bound δ^{202}Hg: −2.36‰; dissolved: −2.09‰). Within the reservoir sediment, the Hg isotopic composition indicated that the proportion of the Hg related to mine-release increased with THg concentrations. However, in the fish samples the opposite trend was observed—the degree of mine-related Hg was lower in fish with the higher THg concentrations. While sediment concentrations clearly show the influence of the mine, the relationship in fish is more complicated due to differences in methylmercury (MeHg) formation and the foraging behavior of different fish species. The fish tissue δ^{13}C and Δ^{199}Hg values indicate that there is a higher influence of mine-sourced Hg in fish feeding in a more sediment-based food web and less so in planktonic and littoral-based food webs. Identifying the relative proportion of Hg from local contaminated site can help inform remediation decisions, especially when the relationship between total Hg concentrations and sources do not show similar covariation between abiotic and biotic media.

KEYWORDS

mercury, stable isotopes, contaminated sites, reservoirs, abandoned mines

1 Introduction

Mercury (Hg) is a pollutant of global concern due to its widespread atmospheric distribution and potential to impact remote areas (Obrist et al., 2018). Aquatic ecosystems exposed to Hg pollution are also often susceptible to the conversion of inorganic Hg to methylmercury (MeHg) by anaerobic microorganisms, which is modulated by Hg bioavailability, carbon sources, and terminal electron acceptor concentrations (e.g., sulfate, ferric iron) (Bravo and Cosio, 2020). After formation, MeHg is readily bioaccumulated in aquatic food webs, resulting in fish consumption advisories across the United States (US) and globally (Munthe et al., 2007). Mitigating Hg contamination and subsequent fish consumption advisories can be extremely difficult, particularly because Hg can enter the environment *via* numerous routes. In addition to inputs of atmospheric Hg, there are also local sources of Hg pollution that can contribute to Hg exposure and risk (Eckley et al., 2020). In the western US, there are hundreds of thousands of Hg contaminated sites that have contributed to elevated fish MeHg concentrations, often including defunct facilities such as abandoned mines and former industrial/manufacturing plants (Alpers et al., 2016; Eagles-Smith et al., 2016c).

Distinguishing the relative contributions of Hg from multiple sources that have accumulated in fish is complicated by differences in inorganic Hg bioavailability for methylation. The elevated Hg concentrations released from mining areas often have lower bioavailability than atmospheric sources (Suchanek et al., 2008; Eckley et al., 2017), though this is not the case for all types of contaminated sites (Janssen et al., 2021b). Uncertainties regarding the sources of MeHg that accumulates in fish obfuscates setting meaningful remediation goals at contaminated sites. Due to the unique biogeochemical conditions in a waterbody that govern how much MeHg is produced, it is very difficult to identify what "background" levels would be in the absence of releases from a local point source (Watras et al., 1995). As a result, a major challenge exists in determining the proportion of MeHg in fish that originated from local releases versus other sources such as atmospheric deposition. This is further complicated when the point of concern about elevated Hg in fish occurs many kilometers downstream (e.g., a reservoir or estuary) from the location of releases from a contaminated site (i.e., the abandoned mine or industry) (Park and Curtis, 1997; Foucher et al., 2009; Baptista-Salazar and Biester, 2019). As such, there remains large uncertainty regarding how far downstream from a contaminated site the fish Hg levels are impacted from a particular industrial source. Source attribution is further complicated by the multiple variables that influence the amount of Hg that accumulates in fish tissue, which includes the uptake and biomagnification of MeHg within the aquatic foodweb (Eagles-Smith et al., 2016a).

An approach used to help understand the cycling and sources of Hg in the environment involves the analysis of the fractionation of Hg stable isotopes (Blum et al., 2014; Yin et al., 2014). During kinetic and equilibrium reactions, Hg isotopes undergo mass dependent fractionation (MDF), which is commonly represented utilizing δ^{202}Hg (Blum and Bergquist, 2007). Mass independent fractionation (MIF) can also occur due to magnetic isotope and nuclear volume effects (Bergquist and Blum, 2007; Zheng and Hintelmann, 2010a; Zheng and Hintelmann, 2010b) and is most commonly observed in the odd-isotopes (^{199}Hg and ^{201}Hg). Separate to these processes and commonly detected first in atmospheric media, MIF of multiple isotopes occurs but due to complicating factors arising from odd-isotope MIF, are reported as even-isotope MIF (^{200}Hg and ^{204}Hg) (Fu et al., 2021) but the precise mechanisms are not well agreed upon. While MDF is often used to trace sources and processes, MIF is commonly used to identify photochemical reactions in aquatic environments (Bergquist and Blum, 2007; Zheng and Hintelmann, 2010a).

This study was designed to assess the potential contributions of point source Hg to fish tissue downstream from a historical mining site, the Black Butte mine. To effectively resolve mixed Hg sources and bioaccumulation differences driven by habitat, we used an integrated approach of examining foodweb dynamics alongside abiotic fate and transport processes. We were specifically interested in testing the hypothesis that fish in the river/reservoir system are impacted by releases of Hg sourced from Black Butte mine. This hypothesis was addressed by utilizing stable Hg isotope values in mine-site materials and downstream water, sediments, and fish tissue to assess the impacts of legacy contamination in the upper watershed on downstream fish concentrations. The holistic approach of examining multiple matrices for Hg stable isotopes will also provide valuable insight on how Hg is transformed through watershed transport away from contaminated point sources.

2 Materials and methods

2.1 Site description

The study area focuses on Black Butte mine and its downstream waterbodies, which are located within Oregon, United States

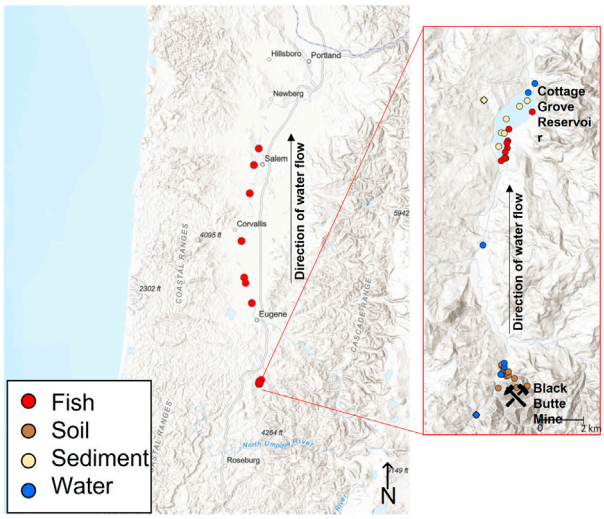

FIGURE 1
Map showing locations where samples were collected. Fish were collected over a larger geographic area than the abiotic parameters (soil, sediment, and water). Colors denote collection locations of different matrices. Circles represent locations downstream of the mine and diamonds represent background samples.

(Figure 1). Black Butte mine is a historical Hg mine and smelter that operated from the 1890s to the 1960s. The operation produced approximately 635,000 kg of Hg and over 200,000 m^3 of waste. There are three general types of mine-waste present at the site: Tailings that were generated from an older furnace (operated until 1909), tailings generated from a newer furnace, and mine waste material that was not processed (e.g., waste rock that was removed during the mining process but did not contain sufficient Hg to be sent to a furnace).

Furnace Creek drains directly through the mine tailings and flows into Little River and then the Coast Fork Willamette River 2 km further downstream. At approximately 15 km downstream of Black Butte mine is the Cottage Grove Reservoir. This study focuses on the reservoir because it contains some of the highest fish tissue Hg concentrations within this region and is a popular fishing destination (Ambers and Hygelund, 2001; Curtis et al., 2013). Previous studies have focused on Hg methylation dynamics within the reservoir (Eckley et al., 2015; Eckley et al., 2017); however, that work did not address the relative proportion of Hg that originated from the legacy mine site. Sampling of fish extended beyond Cottage Grove Reservoir to identify if there are potential impacts on fish isotopic Hg compositions over 90 km downstream of the mine site in the Willamette River.

The water level of Cottage Grove Reservoir varies significantly throughout the year because it is managed to control flooding. At full pool conditions (24 m at its deepest during May to September), vegetated wetland areas along the edges of the reservoir become inundated with water, covering approximately 8% (~36 ha) of the total surface area of the reservoir during the summer months (Eckley et al., 2017). To have storage capacity to prevent flooding, the reservoir water level is lowered before the part of the year that experiences higher rainfall (September through April). During the low pool conditions, over 60% of the reservoir area is exposed sediment and the dried wetlands are not directly hydrologically connected to the reservoir through surface water. During dryer years, the reservoir may not have enough inflow discharge to reach or maintain full pool conditions. If the reservoir does not fill up to reach a maximum depth over 19 m, then the wetland areas may remain dry and disconnected from the reservoir surface water.

2.2 Sample Collection

2.2.1 Fish collection

Fish were sampled from 11 locations within Cottage Grove Reservoir between June and August 2011, 2013, and 2014, and from seven downstream locations in the Willamette River in 2011. Fish were collected using a combination of beach seining and gill nets. Upon sampling, each fish was identified, measured to the nearest mm using a fish board, and frozen within 24 h in a uniquely labeled polyethylene zip close bag.

To estimate spatial and temporal variability in fish Hg concentrations, young-of-year (YOY) individuals (<100 mm) were sampled. The YOY fish collection focused on several species: Largemouth Bass (*Micropterus salmoides*), Northern Pikeminnow (*Ptychocheilus oregonensis*), Brown Bullhead (*Ameiurus nebulosus*), and Black Crappie (*Pomoxis nigromaculatus*). With the exceptions of Northern Pikeminnow, larger fish (>200 nm) of these species were also collected from the reservoir. Other adult fish species collected in the reservoir include: Yellow Perch (*Perca flavescens*), Bluegill (*Lepomis macrochirus*), and rainbow trout (*Oncorhynchus mykiss*).

2.2.2 Water collection

Water samples were collected between January 2017 and October 2019 at five locations that receive mine-related Hg inputs and one location located upstream. At the time of sampling, Furnace Creek ran directly through mine tailings and represented a purely mine-influenced waterbody (remediation actions have occurred in this watershed after sampling was conducted). Samples from Furnace Creek were used as a mine-signature endmember during mixing-model analysis (described in the Supplementary Material). Water was collected from one location on Little River 1.5 km downstream of the inputs from Furnace Creek and then further downstream (9 km) at on the Coast Fork Willamette River (at the London USGS gaging station). Water was collected within the Cottage Grove Reservoir and directly downstream of the reservoirs in the Coast Fork Willamette River. In addition, one location was sampled upstream (~3 km) of the mine-site on Garoutte Creek to obtain a background Hg concentrations and endmember isotopic signatures.

For the total-Hg (THg) analysis, between 0.5 and 20 L of water were collected at each location depending on the THg concentration following standard clean-hands dirty hands techniques using a peristaltic pump and Teflon sample line. The larger sample volumes were collected for Hg stable isotope measurements. An in-line filtration (0.45 μm disposable synthetic polymer filter capsule) was attached to the Teflon tubing for the collection of filtered samples (F-THg). All water samples were preserved immediately following collection (12 N trace metal grade hydrochloric acid (HCl); 0.5% acidification). Particulate-bound total-Hg (P-THg) was collected on the 0.45 μm filter and frozen following collection.

2.2.3 Sediment and soil collection

Soil samples were collected in October 2016. The soils were collected from 11 locations at the mine site and from two nearby background locations (<1 km from the historic mine operations). At each sample location, 60 individual samples were collected (0–15 cm depth—after removing the surface leaf litter layer) using a disposable plastic scoop from three 100-m transects (one sample collected approximately every 5 m). These samples were combined into a single composite which was sieved to <1.5 mm. Samples were stored in new double Ziploc bags.

Sediment samples were collected in May 2019. Sediment core samples were collected from seven locations within Cottage Grove Reservoir and from one background location upstream of the reservoir on Williams Creek. The sediments were collected using a gravity corer (polycarbonate cores, 9 cm diameter) deployed from a boat in Cottage Grove Reservoir, while the background location was shallow enough where the core was directly inserted into the sediment by hand. Each sediment core was sectioned using an incremental core extruding apparatus such that the top 4 cm were removed using a plastic spatula and transferred to a 4oz glass sample container. All soils and sediments were kept on ice in the field and frozen until analysis.

2.3 Sample Analysis

2.3.1 Mercury concentration analyses

At the USGS Forest and Rangeland Ecosystem Science Center in Corvallis, OR, each fish was rinsed with deionized water, blotted dry, measured for standard length (±1 mm), and weighed (±1 0.001 g). Fish were then dried to a constant weight (50°C for at least 48 h),

cooled to room temperature in a desiccator cabinet, and weighed again (± 10.001 g). Dried samples (either whole fish or fillets) were homogenized using stainless steel scissors and a porcelain mortar and pestle and stored in a desiccator cabinet until mercury determination. Total Hg concentrations were measured for each fish sample following EPA method 7473 on a Milestone tri-cell DMA-80 Direct Mercury Analyzer (Milestone Inc., Shelton, Connecticut, United States). Quality assurance measures included analysis of two certified reference materials [either fish muscle tissue (DORM-4; National Research Council of Canada, Ottawa, Canada) or lobster hepatopancreas (TORT-3; National Research Council of Canada, Ottawa, Canada)], two system and method blanks, and two duplicates per batch of 40 samples. Recoveries averaged 104.3% ± 1.44% (n = 32) and 100.2% ± 1.7% (n = 52) for certified reference materials and calibration checks, respectively. Absolute relative percent difference for duplicates averaged 4.6% ± 1.0% (n = 39).

2.3.2 Mercury stable isotopes

Mercury stable isotope measurements were performed by the USGS Mercury Research Laboratory (Madison, WI, United States) using the same methods as described in pervious publications (Lepak et al., 2019; Janssen et al., 2021a). A subset of all fish collected were analyzed for Hg stable isotopes, which are shown in Supplementary Table S1. Sediment and fish samples were acid digested (90°C for 8–10 h) prior to isotope analysis. The fish were acid digested using concentrated nitric acid (HNO_3) followed by a bromine monochloride (BrCl) addition (10% v/v) and the sediments were digested using an aqua regia solution (3HCl:HNO_3). Sample digests were diluted prior to isotope analysis (<10% acid and 0.5–1.2 ng mL−1 Hg). The certified reference materials (CRMs) used for sediment (IAEA SL-1 = 137 ± 3.1 standard deviation (1SD), 105% average recovery, n = 3 and NIST 1944 = 3,503 ± 62, 103% average recovery, n = 6), and fish (IAEA 407 = 213 ± 5, 1SD, 99% average recovery, n = 7) had acceptable concentration recoveries.

The Filtered-THg (F-THg) samples were processed using a modified resin pre-concentrated using an AG1-X4 (Chen et al., 2010; Štrok et al., 2014). Additional pre-treatment was needed to oxidize dissolved organic matter, which included an addition of 0.1% sodium persulfate followed by heating for 24 h at 55°C. After the initial sodium persulfate treatment, samples were oxidized with BrCl (1% v/v). The amount of THg within the sample was compared to the amount recovered post-processing to determine the percent recoveries for preconcentrated F-THg (107% ± 13%, 1SD, n = 6). Capsule filters containing suspended particulate matter were cut open using a heated nichrome wire and digested for particulate-THg (PTHg) in a 30% BrCl solution. The digests were heated for 14 days at 55°C before pre-concentration using a purge and trap method coupled to an oxidant trap (Janssen et al., 2019a). Percentage recoveries for P-THg were calculated by comparing the digestate to the final pre-concentrated oxidant trap (97% ± 7%, 1SD, n = 6).

A multicollector inductively coupled plasma mass spectrometer (MC-ICP-MS, Thermo Scientific Neptune Plus) was used for Hg stable isotope analysis. All solutions were diluted to 0.5–1 ng·mL^{-1} and <10% acid content. Samples were analyzed using standard-sample bracketing (Blum and Bergquist, 2007) with NIST 3133 and secondary standard NIST RM 8610 (UM Almaden) was analyzed every five samples, all solutions were matched within 10% Hg content and 1% acid content. Sample solutions were introduced into the instrument using stannous chloride reduction coupled to a custom-designed gas liquid separator, described elsewhere (Janssen et al., 2019a). For mass bias correction during analysis, a thallium standard (40 ng/ml, NIST 997) was simultaneously introduced into the gas liquid separator as an aerosol using an Apex-Q desolvating nebulizer. The MC-ICP-MS was tuned for optimal signal strength and stability for the analysis of Hg isotopes (1v^{202}Hg~ 1 ng·mL^{-1} of Hg). Instrument accuracy and precision were assessed by the NIST 8610 values (δ^{202}Hg = −0.52 ± 0.07, Δ^{199}Hg = −0.02 ± 0.05, Δ^{200}Hg = 0.01 ± 0.04, 2SD, n = 80), which agreed with the reference values. In addition, CRMs were analyzed within every sample batch (every five samples) to ensure digest efficiency. The secondary standard and the certified reference materials produced values in agreement with published literature (Blum and Bergquist, 2007; Estrade et al., 2010; Lepak et al., 2018) (see Supplementary Table S2).

2.3.3 Carbon and nitrogen stable isotopes

Analysis of carbon (C) and nitrogen (N) stable isotope ratios was conducted at the Great Lakes Toxicology and Ecology Division laboratory in Duluth (MN). Fish were dried (50°C for >24 h) and homogenized prior to analysis. Analysis was conducted using a Costech 4010 Elemental Analyzer, coupled to a Thermo Delta Plus XP isotope ratio mass spectrometer. Analytical error was based on the standard deviation of replicate lab standards and was ±0.2‰ for δ^{15}N and ±0.1‰ for δ^{13}C. To correct for the negative bias in δ^{13}C values associated with increasing lipid content, a mass-balance approach based on fish tissue C:N molar ratio was used to correct δ^{13}C values for lipid content (expressed as $\delta^{13}C_{lipid\text{-}free}$; fish C:N ratios ranged 3.6–5.2) (Hoffman et al., 2015).

2.3.4 X-ray absorption fine structure (XAFS) analysis

The speciation of Hg in the soils and tailings samples was determined by extended X-ray absorption fine structure (EXAFS) using methods described in detail elsewhere (Eckley et al., 2021). The spectra from the samples were compared to reference materials that included cinnabar, metacinnabar, elemental Hg, $HgCl_2$, $Hg(NO_3)_2$ (aq), Hg^{2+} -cysteine solution complex, Hg^{2+}-histidine solution complex, and a Hg^{2+}-citrate solution complex. The Hg L3-edge spectra were recorded at the Materials Research Collaborative Access Team (MRCAT) 10-ID line at the Advanced Photon Source (APS) operated by the U.S. Department of Energy (DOE) at the Argonne National Lab. The APS is a 7 GeV storage ring operating at 102 mA in top up mode. All samples and reference compounds analyzed (except elemental Hg) were initially ground to pass a 75 µm sieve. The materials were then mixed with polyvinylpyrrolidone and pressed into a 13 mm self-supporting pellet using a hand-held pellet press. The subsequent pellets were sealed between two pieces of Kapton® tape and stored at 4°C prior to analysis. The elemental Hg sample was prepared placing a droplet of Hg^0 between two polyethylene sheets and compressing the sheets together to disperse the droplet.

Incident X-rays were monochromatized using a cryogenically cooled Si (111) monochromator and a 250 mm long second crystal. A Si-coated flat harmonic rejection mirror was employed and a beam size of 400 µm × 400 µm was used. Incident beam energy was calibrated to the first derivative inflection point (12,284 eV) of elemental Hg. The monochromator was swept over the energy range 12,084 eV–13,084 eV at a rate of 1.5 eV per second. Data was collected in both fluorescence and transmission mode simultaneously.

Fluorescence data was collected using a Lytle Box purged with Ar gas. A minimum of 10 and maximum of 20 scans were collected for each sample. Merging of the spectra was first performed using LARCH, followed by re-binning, background removal, and normalization using the Demeter XAS software package (Ravel and Newville, 2005; Newville, 2013).

2.3.5 Statistical analyses for fish tissues

For the three primary fish species sampled (Largemouth Bass, Black Crappie, and Brown Bullhead) the fish were categorized as either YOY or adult based upon their lengths because the sampling design was heavily weighted towards the YOY size classes, and regression-based size-adjustments of Hg concentrations spanning the entire size spectra would introduce considerable bias. Prior to statistical analysis with the YOY fish, THg concentrations were size adjusted within each species using previously published methods (Eagles-Smith et al., 2016a; Eagles-Smith et al., 2016b). The larger size classes of fish were all very similar in size within species, so these samples did not necessitate size adjustment.

The THg concentrations (size adjusted for YOY individuals) were compared among species, size classes, and sites within Cottage Grove Reservoir using a general linear model (GLM) with the above factors as fixed effects. Because not all species were sampled across all years, the temporal variability was examined using a separate mixed-effects model that only included YOY Black Crappie and Largemouth Bass, which were sampled across three different years. This model included species, year, and a species × year interaction as fixed effects, and site ID as a random effect. The interaction term suggested that the two species may have had differing temporal responses ($F_{2,17.96} = 2.95$; $p = 0.07$); therefore, the separate models for each species were used. Finally, only YOY Largemouth Bass were sampled both within Cottage Grove Reservoir as well as downstream of the reservoir in the Willamette River. Size-adjusted concentrations between the reservoir fish and the downstream riverine fish were compared using analysis of variance. Calculations for the photochemical correction of δ^{202}Hg using Δ^{199}Hg (referred to as $\delta^{202}Hg_{COR}$) are outlined in the Supplementary Material.

3 Results and discussion

3.1 Mercury levels in river and reservoir fish

Total Hg concentrations in fish from Cottage Grove Reservoir ranged from 0.02 to 1.13 mg/kg wet weight (ww) across all species, size classes, and sampling locations. While THg is being measured, it is assumed that most of the Hg that has accumulated in the fish is MeHg (Driscoll et al., 2007). Total Hg concentrations of fish larger than 200 mm (those commonly targeted for human consumption) averaged 0.55 ± 0.07 mg/kg ww, and 65% of individuals exceeded US EPA MeHg criterion for the protection of human health (0.30 mg/kg ww). Within the reservoir, THg concentrations differed among species/size class groupings ($F_{8,37.8} = 31.5$, $p < 0.0001$) and sampling sites ($F_{10,106.6} = 71.0$; $p < 0.0001$). After accounting for site differences THg concentrations were highest in adult Black Crappie and adult Largemouth Bass, and lowest in both adult (>200 mm) and YOY (<52 mm) Brown Bullhead (Supplementary Figure S1). There was substantial spatial variability in fish THg concentrations across the reservoir. The highest concentrations were measured in three locations close to the reservoir inflow and were > 4-fold higher than the lowest sites which were closest to the dam.

Whereas YOY Black Crappie showed no differences in THg concentrations among years ($F_{2,13.41} = 1.45$; $p = 0.27$), Largemouth Bass YOY THg concentrations differed between 2013 and 2014 ($F_{1,2.04} = 22.61$; $p < 0.0001$). Specifically, concentrations were 1.5x higher in 2013 (0.017 ± 0.01 mg/kg ww) than in 2014 (0.11 ± 0.01 mg/kg ww). With only a few years of data its difficult to determine the cause of the variations in fish THg concentrations between years; however, it may be related to differences in MeHg production impacted by reservoir water-levels and wetland connectivity, which vary between wetter and drier years (Willacker et al., 2016; Eckley et al., 2017).

Young-of-year Largemouth Bass was the only species collected from both Cottage Grove Reservoir and downstream (>90 km) of the reservoir in the Willamette River. Total Hg concentration in the reservoir fish were 4-fold higher than those from the Willamette River ($F_{1,9.41} = 7.84$; $p = 0.02$; Figure 2A). The higher Hg concentrations in the reservoir fish compared to downstream could be a function of higher Hg inputs from in the mine and/or enhanced methylation processes occuring in a lentic compared to lotic system (Eckley et al., 2015; Hsu-Kim et al., 2018).

3.2 The impact of sources and foodweb dynamics on fish mercury levels

Mean $\delta^{13}C_{lipid\text{-}free}$ values ranged from −28.4‰ in YOY Brown Bullhead to −25.4‰ in YOY Black Crappie (Figure 3A). This suggests a food web difference among species, shifting from increasing planktonic sources (low δ^{13}C values) to increasing littoral sources (high δ^{13}C values) (Hoffman et al., 2007). Young-of-year Brown Bullhead had the lowest mean δ^{15}N value (4.27‰), whereas adult Largemouth Bass and Black Crappie had the highest mean δ^{15}N values (8.56‰ and 7.85‰, respectively), indicating these fishes occupied the lowest and highest trophic positions, respectively (Figure 3A). Total Hg concentrations in fish fillet tissues were highly correlated with δ^{15}N values ($F_{1,37} = 65.3$; $p < 0.0001$; $R^2 = 0.64$; Figure 3B), increasing 0.556 mg/kg ww from a δ^{15}N value of 4‰–8‰.

The higher YOY Largemouth Bass Hg concentrations in the reservoir compared to the free-flowing section of the river (Figure 2A) may be related to the higher Hg concentrations in water and sediment within the reservoir compared to downstream (Hope, 2006; Eckley et al., 2015); but may also be related to changes in Hg methylation and biomagnification related to shifting from a reservoir environment to a free-flowing river (Willacker et al., 2016; Hsu-Kim et al., 2018). However, because the comparison is being made on YOY fish of the same species, the impact of differences in foraging behavior would be very limited.

3.3 Characterizing the mercury isotopic composition in an upstream source area

Background soil samples collected from outside of the mining area had high mean Hg concentrations (1.6 μg/g) reflecting that the mine is situated within a naturally geologically enriched area (Figure 4A). The δ^{202}Hg values from the background soils were quite low (mean:

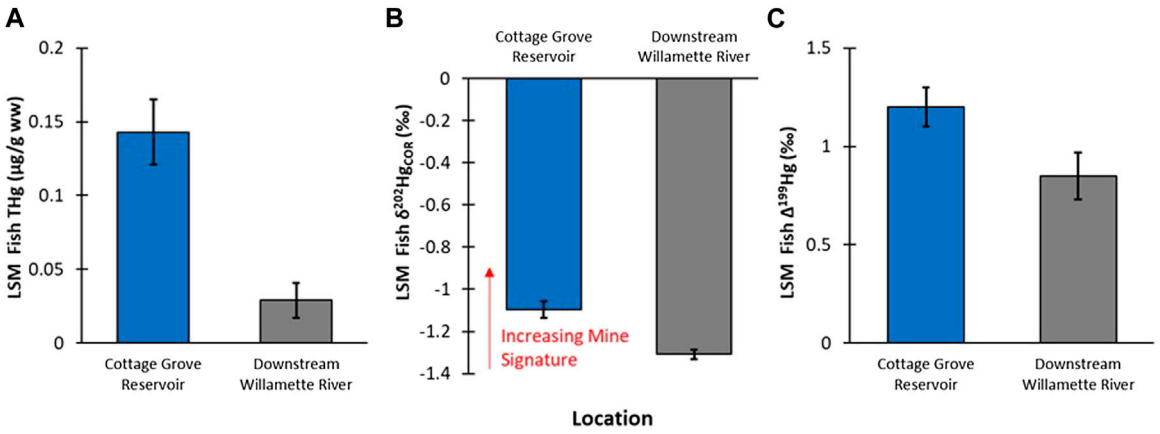

FIGURE 2
(A): Comparison of least square mean (LSM ± standard error—SE) of YOY Largemouth Bass fish tissue THg concentrations between Cottage Grove Resevoir (n = 14) and downstream sample locations in Willamette River (n = 38; fish length was a signficant covariate in the GLM analysis). **(B)**: Comparison of LSM ±SE of YOY fish tissue δ^{202}Hg compositions between Cottage Grove Resevoir and downstream sample locations in Willamette River (fish species was a significant covariate in the GLM analysis). **(C)**: Comparison of LSM ±SE of YOY fish tissue Δ^{199}Hg compositions between Cottage Grove Reservoir and downstream sample locations in Willamette River (fish species was a significant covariate in the GLM analysis).

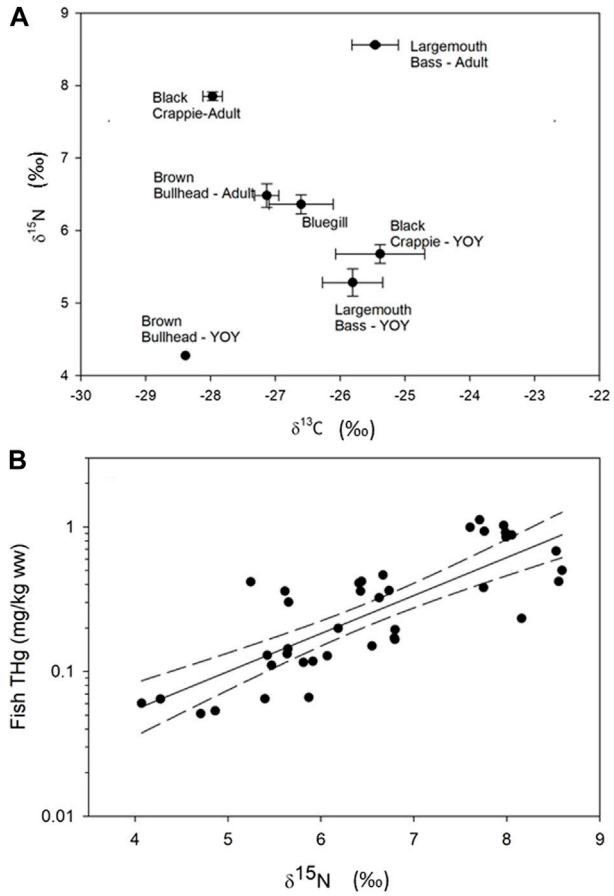

FIGURE 3
(A) shows the mean with standard error δ^{15}N versus δ^{13}C isotopic compositions in fish sampled in Cottage Grove Reservoir. **(B)** shows the relationship between tropic position (represented as δ^{15}N) versus THg concentrations (R^2 = 0.64, p < 0.0001; error bands represent 95% confidence intervals).

−2.55‰), indicating that they were not influenced by direct inputs from a mining/industrial source as seen in other contaminated sites (Eckley et al., 2020). However, it is noted that highly negative values for δ^{202}Hg have been observed in cinnabar ore as well as other Hg containing ore deposits (Smith et al., 2005; Smith et al., 2008). Given the geology of the area and the high Hg concentrations within the background soil, it is likely that the geogenic background of the region is highly depleted with regard to the δ^{202}Hg isotopic signature. The background sediment sample was collected from outside of the geologically enriched zone and has a much lower THg concentration (0.23 µg/g) and a lower δ^{202}Hg value (−1.81‰). The difference in isotopic compositions between these two types of background media may be related to differences in watershed processing of the geogenic source that impact the δ^{202}Hg isotopic signature (e.g., redox shifts during mineralization, elemental versus oxidized Hg inputs from air versus precipitation, etc.). It is difficult to ascertain potential processing or source differences using δ^{202}Hg because of the large overlap between values for ore material (Smith et al., 2005; Smith et al., 2008)and background reference values derived predominantly from atmospheric deposition (Eckley et al., 2020). However, examining Δ^{199}Hg values indicates there is more potential influence from terrestrial processing within the sediments due to lower values (soils: 0.06‰; sediment: −0.41‰) (Figure 4B). It is noted that no substantial differences were observed in Δ^{200}Hg values between the samples. Typically, negative Δ^{199}Hg values have been attributed to foliar uptake of gaseous elemental Hg (Demers et al., 2013; Enrico et al., 2016), which may indicate the sediments are reflective of mixed Hg sources (geogenic and atmospheric deposition), supported by the lower concentrations, or a subset of geogenic Hg pools are integrated and processed within the terrestrial environment, such as through soil re-emission.

Compared to the background samples, the mine tailings had a distinct δ^{202}Hg value (−0.35‰ ± 0.05‰), which is over a span of two ‰ different from the background soils and is more aligned with direct point sources measured at other contaminated sites (Eckley et al., 2020). The Hg isotopic composition of the tailings that originated

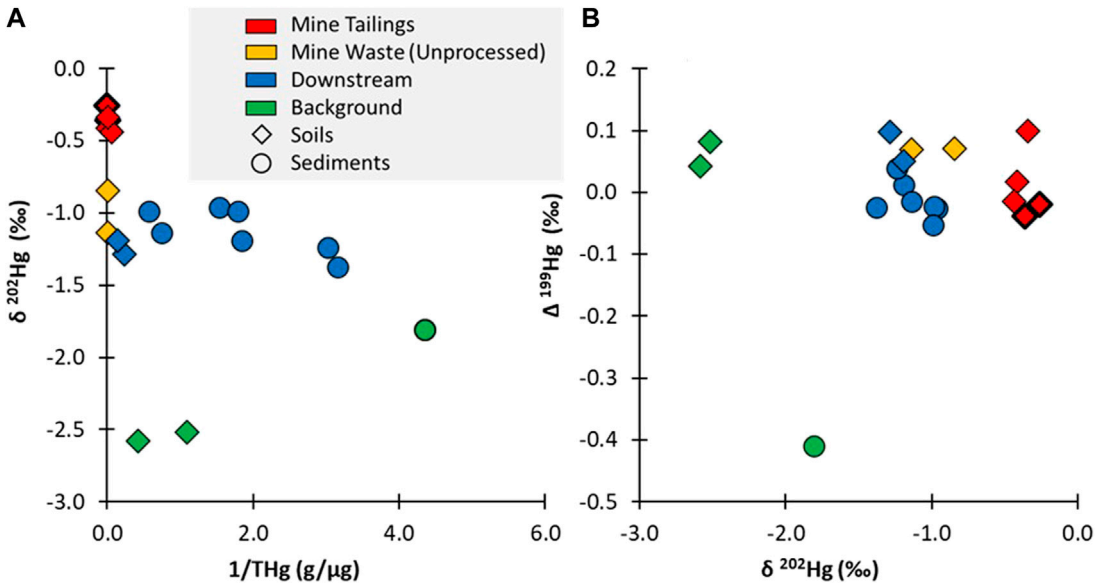

FIGURE 4
(A) showing the δ^{202}Hg values plotted against the inverse THg concentration (µg/g); and **(B)** showing the Δ^{199}Hg versus δ^{202}Hg values. Note: all soil samples are plotted as diamonds and all sediment samples are plotted as circles. The tailings samples from the old furnace are distinguished from the newer furnace with a heavier black outline.

from the newer versus the older furnaces had similar δ^{202}Hg values (old furnace tailings: −0.31‰; new furnace tailings: −0.40‰), indicating that there were no distinguishable differences between these two sources. There was a larger difference in the δ^{202}Hg value (> 0.5‰) when comparing the unprocessed mine waste (−0.99‰), indicating that the process of roasting the ore resulted in fractionation and contributed to the distinct isotopic composition of the tailings, as seen in other studies (Smith et al., 2014). The EXAFS data of the newer and older tailings and unprocessed mine waste confirms that there are distinctions in the Hg speciation in these materials (Supplementary Table S3). The tailings from the newer furnace is entirely composed of cinnabar; whereas the less efficient extraction process in the older furnace contained some metacinnabar. The unprocessed mine material is unique in that it contains Hg bound to organic material, which would have been easily removed during the ore-processing in a furnace.

The δ^{202}Hg value from water draining the mine site in Furnace Creek showed a similar isotopic signature as the tailings samples (particulate δ^{202}Hg: −0.58‰; filtered δ^{202}Hg: −0.89‰), which were much more enriched than the background stream samples (particulate −2.36‰; filtered: −2.09‰; Figures 4, 5A). The δ^{202}Hg value in these water samples shows a ~0.30‰ spread between the dissolved and particulate fractions, though the directionality differs between the two sites. Previous work has proposed that the difference between the filtered and particulate phases is a function of Hg sources, with dissolved phases represented atmospheric deposition while particulates are more similar to terrestrial runoff (Campeau et al., 2022). While this is possible, there was no evidence of differences in the Δ^{200}Hg ratios between the phases, which should be able to easily characterize precipitations pools of Hg (Kwon et al., 2020). Furthermore, the Δ^{199}Hg from the background water samples had a larger span in values between the filtered (−0.16‰) and particulate phases (0.58‰), which may indicate different levels of photochemical processing of the same source. It is unclear why there is higher photochemical processing (as indicated by Δ^{199}Hg) on the particulate matter rather than in the dissolved phase, but it indicates that environmental processing could have occurred during mobilization and sorption reactions resulting in the disconnect between the phases (Figure 5B). Further examination would be needed to assess if different Hg sources (e.g., precipitation and dry deposition) or *in situ* processing is contributing to the dissolved and particulate Hg isotope ratios observed.

3.4 Tracking the mercury isotopic composition in downstream water and sediment

Downstream sediment samples collected from the Cottage Grove Reservoir had higher δ^{202}Hg values compared to background samples (Figure 4A). While all the reservoir sediment samples were enriched in ^{202}Hg, there was some variability in this composition, which varied from −0.96‰ to −1.38‰, reflecting variations in sediment depositional patterns in the reservoir (see Supplementary Figure S2). For example, the two locations with the lowest δ^{202}Hg values were both located in wetlands along the edge of the reservoir, which are less impacted by the deposition of suspended particulates from the inflowing water. Enrichment in ^{202}Hg corresponded with increasing sediment THg concentration, indicating that particles mobilized from the mine site are a likely contributor to elevated THg in the reservoir (Supplementary Figure S3).

Mercury concentrations decrease with distance moving downstream from Black Butte Mine (Figure 5). While Furnace Creek, which drains through the mine site, contains elevated Hg concentrations (whole water THg: 391 ng/L), the creek had a very low

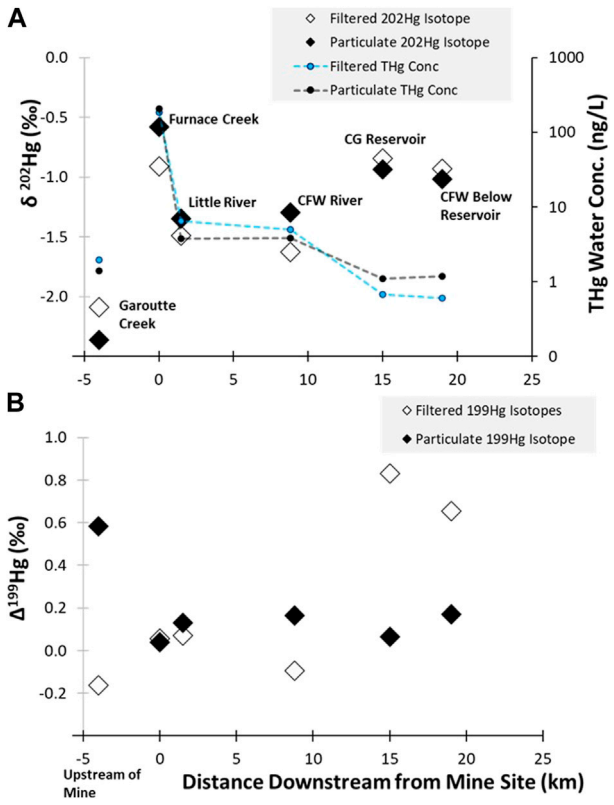

FIGURE 5
(A) shows the THg concentrations and δ^{202}Hg values in water samples for particulate and filtered phases and **(B)** shows this relationship for the Δ^{199}Hg values in water. The background samples were collected approximately 3 km upstream of the mine in Garoutte Creek (−3 km on the graph). The 0 km location marks the location of the Black Butte Mine and Furnace Creek. Furnace Creek flows into Little River, which was sampled 1 km downstream of the mine. Little River flows into the Coast Fork Willamette (CFW) river and was sampled 9 km downstream of the mine. The Cottage Grove (CG) reservoir is 15 km downstream of the mine and at 19 km downstream a sample was collected below the reservoir on the CFW River. Note that the secondary *y*-axis in **(A)** is plotted on a log-scale. Uncertainty of measurements was assessed by the 2SD of processing standard NIST 3133, which was 0.09‰ for both δ^{202}Hg and Δ^{199}Hg.

discharge (0.0028 m^3/s) and the Hg concentrations are quickly diluted (whole water THg: 10.3 ng/L) when it empties into Little River which has a much larger discharge (2.5 m^3/s). This dilution of the mine -related Hg inputs with low Hg content water from background sources results in a shift in the δ^{202}Hg values of both the filtered (−1.49‰) and particulate bound fractions (−1.35‰). However, mixing model calculations (see details in the Supplementary Material) indicate that even after being diluted by the larger downstream flows, 51% of F-THg and 63% of P-THg originated from mine-related sources. In addition, the Δ^{199}Hg value for the P-THg downstream of the mine site is consistent (0.13‰ ± 0.2‰) and similar to what was measured directly draining the tailings areas (0.04‰), confirming that the mine is an important source of Hg water further downstream of the mine.

The discharge of the river is further increased 9 km downstream of the mine site after Little River combines with Big River to form the Coast Fork Willamette River (9.3 m^3/s); however, the Hg concentrations (whole water THg: 8.9 ng/L) is only slightly lower than what was measured in Little River. The δ^{202}Hg values in dissolved and particulate samples are similar to the upstream site at Little River (3 km downstream from the site), indicating there is still a significant mining influence present. Dissolved and particulate phases do show divergence from one another in δ^{202}Hg and Δ^{199}Hg values, indicating that there may be integration of other runoff sources, potentially indicated by the negative Δ^{199}Hg in the dissolved phase, or *in situ* processing, such as photochemistry. The more stable Δ^{199}Hg values also indicates that the particles are more recalcitrant to environmental processing compared to Hg in the dissolved phase. Values in both matrices are still well above the established geogenic background soils in the region and approximately 40% of dissolved Hg and 70% of particulate Hg could be attributed to mine-related releases. (Figure 5A).

The water samples from the background/upstream location (Garoutte Creek) shows a larger Δ^{199}Hg value associated with the suspended particulate samples compared to the dissolved phase (Figure 5B). This may result from atmospheric Hg sources that efficiently sorb to the particles or that the particles represent a pool with a longer exposure time in comparison to the filtered water samples which is more transient. However, further investigation would be needed to provide a better understanding of the factors contributing to the upstream isotopic signature in water.

Once the water reaches the reservoir, there is an interesting divergence in the trends in Hg water concentrations and isotopic compositions. The whole water THg concentrations in and below the reservoir continue to decrease to levels that are similar to the background/upstream location (all < 4 ng/L). However, the Hg isotope ratios showed an increase in the δ^{202}Hg value in both the filtered (reservoir: −0.84‰; below reservoir: −0.93‰) and particulate phases (reservoir: −0.94‰; below reservoir: −1.02‰), which suggests that the Hg had had a greater contribution from the mine than the lotic locations closer to the mine. It is worth noting that the dissolved phase also had higher Δ^{199}Hg value (0.83‰ in the reservoir and 0.66‰ downstream of the reservoir), likely due to enhanced photochemical degradation of inorganic Hg in the reservoir, which likely explains the elevated δ^{202}Hg values. However, the particulates do not show any elevated Δ^{199}Hg values, indicating that there is no change in photochemical processing between the riverine particles and those collected in the reservoir. This observation indicates that the particulates are representative of a distinct source in the reservoir, different than what was observed in the lotic locations, whereas the dissolved Hg is related to riverine sources that are undergoing transformations in the reservoir. A potential source of mine-related Hg in and downstream of the reservoir is the reservoir sediment. The river system directly downstream of the mine is relatively high-energy and particles mobilized from the mine mostly stay in suspension. These particles are deposited/accumulated in the sediment of the reservoir (Curtis et al., 2013), which may also act as an ongoing secondary source to the reservoir water-column—especially when the reservoir is in low-pool conditions and the river cuts through previously deposited sediments.

3.5 Hg stable isotopes in fish

It is challenging to compare Hg isotopic composition in fish tissue to abiotic matrices such as water and sediments due to the net process of methylation as well as photodemethylation. To assess potential differences between the reservoir and the river, we opted to directly compare fish tissues from the same species and age classes (YOY).

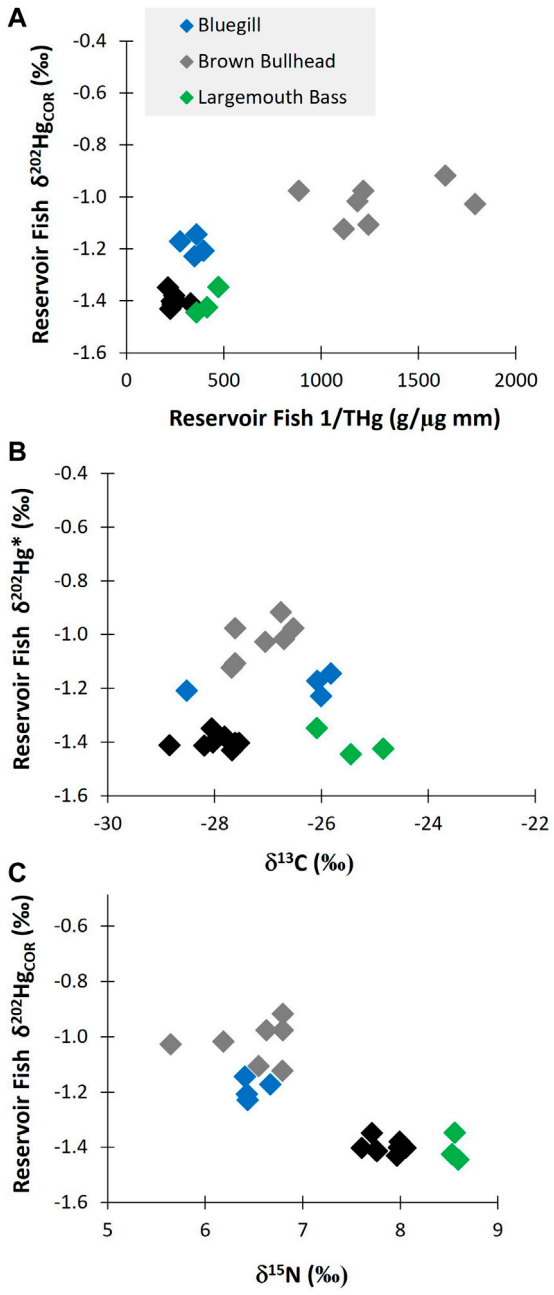

FIGURE 6
(A) shows the $\delta^{202}Hg_{COR}$ values for different adult fish species as a function of length normalized THg concentrations in Cottage Grove Reservoir. **(B)** shows the $\delta^{202}Hg_{COR}$ values for different fish species as a function of the $\delta^{15}N$ value. **(C)** shows the $\delta^{202}Hg_{COR}$ values for different fish species as a function of the $\delta^{13}C$ value.

While this allowed for an apt biological comparison, there were still obvious differences between the reservoir and riverine fish related to the extent of photochemistry (see plots of $\delta^{202}Hg$ versus $\Delta^{199}Hg$ values in Supplementary Figures S4, S5). All fish displayed positive $\Delta^{199}Hg$ values, which is typical of photodegradation of MeHg ($\Delta^{201}Hg/\Delta^{199}Hg$ slope of all fish = 1.31, $r^2 = 0.996$, $n = 75$) (Bergquist and Blum, 2007). The $\Delta^{199}Hg$ values in fish from Cottage Grove Reservoir were significantly higher (1.2‰) than those from downstream (0.85‰, $p = 0.018$; Figure 2C). Higher $\Delta^{199}Hg$ values in reservoir fish is reflective of photochemical processes, which can often be more pronounced in lentic relative to lotic systems due to higher water clarity and euphotic feeding (Lepak et al., 2018). Due to the fact that photochemical processes also produces MDF, $\delta^{202}Hg$ values are changed (Bergquist and Blum, 2007), so photochemical corrections (denoted as $\delta^{202}Hg_{COR}$) need to be applied to meaningfully compare fish Hg stable isotope ratios (Gehrke et al., 2011; Janssen et al., 2019b; Rosera et al., 2022). Whole body YOY fish from Cottage Grove Reservoir had a significantly higher $\delta^{202}Hg_{COR}$ value compared to fish collected further downstream (Figure 2B); which supports the interpretation that the mine-influence on Hg concentrations in YOY fish is larger in the reservoir and decreases downstream in the Willamette River. There are caveats to this approach; specifically, there could be different methylation environments (Rosera et al., 2022) within the lotic and lentic habitats or that photochemical corrections may vary due to differences in organic matter (Chandan et al., 2015). Nevertheless, this data provides the first evidence that there is a difference between the Hg sources bioaccumulated in the reservoir and lower Willamette River.

Within the reservoir, the degree of Black Butte mine-related Hg (as represented by $\delta^{202}Hg_{COR}$) varied with tissue THg concentration (Figure 6A). These results show that the fish with the highest THg concentrations were less influenced by mine sources than fish with lower THg concentrations. The relationship between fish THg concentrations and $\delta^{202}Hg_{COR}$ value is significantly ($p < 0.01$) influenced by differences in fish species, which was the primary driver of differences in isotopic composition (Supplementary Figures S5, S6). Among the fish species, Brown Bullhead had significantly lower $\Delta^{199}Hg$ values (0.77‰ ± 0.12‰) than Largemouth Bass, Bluegill, and Black Crappie (mean of all three species: 1.57‰ ± 0.15‰). The lower $\Delta^{199}Hg$ value in Brown Bullhead indicates that the source of Hg in their diet has more a benthic/sediment source than the other fish species, which appear to be more influenced by Hg uptake from the water-column (Supplementary Figure S7). This is consistent with the $\delta^{13}C$ data, such as the Brown Bullhead having $\delta^{13}C$ values that are intermediate between Black Crappie and Largemouth Bass (Figures 3A, 6B). Brown Bullhead $\delta^{13}C$ values (−25 to −28‰) are typically associated with riverine food web pathways based on terrestrial-derived, sediment sources, which is distinct from littoral-based food web (e.g., $\delta^{13}C > -22$) and a phytoplankton based food web (e.g., $\delta^{13}C > -30$) (Hoffman et al., 2007). As such, Bluegill is expected to be the most similar in food web pathways to Brown Bullhead, Black Crappie is interpreted to have a greater contribution from phytoplankton, and Largemouth Bass to have a greater contribution from littoral sources. Thus, differences in $\delta^{13}C$ values between fish species in the reservoir support the interpretation that food web pathways, $\Delta^{199}Hg$ values, and $\delta^{202}Hg_{COR}$ values are related, such that there is higher influence of mine-sourced Hg in fish feeding in a more sediment-based food web and less so in planktonic and littoral-based food webs.

The $\delta^{202}Hg_{COR}$ values had a negative relationship with $\delta^{15}N$ values (Figure 6C). This indicates that mine-related Hg burdens vary due to differences in trophic position, habitat usage and Hg cycling differences within habitats. The Hg isotopes shows that bullhead are disproportionally impacted by mine-related Hg, which is likely due to their comparatively greater preference for benthic habitats. The shift in diet/foraging behavior that is causing the decrease in mine-related influence on the higher trophic position fish is uncertain.

Notably, the two species with the lowest $\delta^{15}N$ values also had intermediate $\delta^{13}C$ values, indicating the potential for both trophic position and food web pathway to contribute to bioaccumulation of mine-sourced Hg.

Overall, the Hg isotopic composition data indicate that fish in Cottage Grove Resevoir are impacted from Hg releases associated with Black Butte mine (Figures 2, 6). However, the amount of mine-related Hg does not correlate with the total concentration of Hg in the fish and is more related to fish species and their different foraging behaviors (Figures 3, 6; Supplementary Figure S6). These results show that the lower trophic position species (i.e., Brown Bullhead) with a slightly larger dietary connection to the sediment could be more impacted by mine-related Hg sources; even though they have lower tissue THg concentrations than other fish species (i.e., Black Crappie). Whereas the sediment and surface water data for the reservoir indicate both media contain a large proportion of mine-related THg (see Figures 4, 5), the mine-related inorganic Hg may be much less available for methylation than Hg from other sources. This is consistent with findings from other contaminated sites, where the % MeHg decreases as the THg concentration increases (Eckley et al., 2020) and suggests the source of MeHg that the fish are exposed to differs from the primary source of THg in water and sediment.

We conclude that the examination of Hg transport from the Black Butte mining site has indicated that mine-derived Hg was transported downstream to lotic and lentic habitats (Curtis et al., 2013; Eckley et al., 2015). Mercury stable isotopes revealed that mining sources could be connected in different environmental compartments, but also showed there are a myriad of processes, specifically in waters and fish tissue, that can also be occurring. This work served as a first step to elucidating fate and transport of mine-related Hg to Cottage Grove Reservoir and the Willamette River.

Data availability statement

The raw data supporting the conclusion of this article will be made available by the authors, without undue reservation.

Author contributions

CE: Writing—original draft, visualization, conceptualization, sample collection, funding acquisition CE-S: Original draft, visualization, conceptualization, sample collection, sample analysis TL: Writing—review and editing, conceptualization, sample collection, sample analysis, funding acquisition JH: Writing—review and editing, conceptualization, sample analysis SJ: Writing—review and editing, conceptualization, visualization, sample analysis.

Funding

This work was supported by a US EPA Superfund Extramural Grant and the U.S. Geological Survey Toxic Substances Hydrology and Contaminants Biology Programs. Fish samples were collected under the authority of a state of Oregon Scientific Collection Permit (#1578) and Oregon State University Animal Care and Use Protocol #4147.

Acknowledgments

Thanks to CDM Smith (Kyle Vickstrom, Mary Lou Fox, Jason Silvertooth) for collecting all soil samples used in this study. For their support and input on the project we wish to thank David Krabbenhoft, Mike Tate, Jacob Ogorek, Branden Johnson, John Pierce, Kevin Donner, and James WIllacker (USGS), Dave Tomten and Rebecca Chu (R10 EPA Remediation Project Mangers); Jennifer Crawford (R10 EPA QA Chemist); Kira Lynch (R10 STL), John McKernan and Edwin Barth (ORD-NRMRLC-LMMD and ORD-ETSC) and Morgann Gordon (EPA ORD ORAU). Any use of trade, firm, or product names is for descriptive purposes only and does not imply the endorsement of the U.S. Government. Any opinions expressed in this paper are those of the author(s) and do not, necessarily, reflect the official positions and policies of the USEPA.

Conflict of interest

The authors declare that the research was conducted in the absence of any commercial or financial relationships that could be construed as a potential conflict of interest.

Publisher's note

Supplementary material

The Supplementary Material for this article can be found online at: https://www.frontiersin.org/articles/10.3389/fenvc.2023.1096199/full#supplementary-material

References

Alpers, C. N., Yee, J. L., Ackerman, J. T., Orlando, J. L., Slotton, D. G., and Marvin-DiPasquale, M. C. (2016). Prediction of fish and sediment mercury in streams using landscape variables and historical mining. *Sci. Total Environ.* 571, 364–379. doi:10.1016/j.scitotenv.2016.05.088

Ambers, R. K. R., and Hygelund, B. N. (2001). Contamination of two Oregon reservoirs by cinnabar mining and mercury amalgamation. *Environ. Geol.* 40, 699–707. doi:10.1007/s002540000173

Baptista-Salazar, C., and Biester, H. (2019). The role of hydrological conditions for riverine Hg species transport in the Idrija mining area. *Environ. Pollut.* 247, 716–724. doi:10.1016/j.envpol.2019.01.109

Bergquist, B. A., and Blum, J. D. (2007). Mass-dependent and -independent fractionation of hg isotopes by photoreduction in aquatic systems. *Science* 318, 417–420. doi:10.1126/science.1148050

Blum, J. D., and Bergquist, B. A. (2007). Reporting of variations in the natural isotopic composition of mercury. *Anal. Bioanal. Chem.* 388, 353–359. doi:10.1007/s00216-007-1236-9

Blum, J. D., Sherman, L. S., and Johnson, M. W. (2014). Mercury isotopes in earth and environmental sciences. *Annu. Rev. Earth Planet. Sci.* 42, 249–269. doi:10.1146/annurev-earth-050212-124107

Bravo, A. G., and Cosio, C. (2020). Biotic formation of methylmercury: A bio–physico–chemical conundrum. *Limnol. Oceanogr.* 65, 1010–1027. doi:10.1002/lno.11366

Campeau, A., Eklöf, K., Soerensen, A. L., Åkerblom, S., Yuan, S., Hintelmann, H., et al. (2022). Sources of riverine mercury across the Mackenzie River Basin; inferences from a combined HgC isotopes and optical properties approach. *Sci. Total Environ.* 806, 150808. doi:10.1016/j.scitotenv.2021.150808

Chandan, P., Ghosh, S., and Bergquist, B. A. (2015). Mercury isotope fractionation during aqueous photoreduction of monomethylmercury in the presence of dissolved organic matter. *Environ. Sci. Technol.* 49, 259–267. doi:10.1021/es5034553

Chen, J., Hintelmann, H., and Dimock, B. (2010). Chromatographic pre-concentration of Hg from dilute aqueous solutions for isotopic measurement by MC-ICP-MS. *J. Anal. Atomic Spectrom.* 25, 1402–1409. doi:10.1039/c0ja00014k

Curtis, L. R., Morgans, D. L., Thoms, B., and Villenueve, D. (2013). Extreme precipitation appears a key driver of mercury transport from the watershed to Cottage Grove Reservoir, Oregon. *Environ. Pollut.* 176, 178–184. doi:10.1016/j.envpol.2013.01.028

Demers, J. D., Blum, J. D., and Zak, D. R. (2013). Mercury isotopes in a forested ecosystem: Implications for air-surface exchange dynamics and the global mercury cycle. *Glob. Biogeochem. Cycles* 27, 222–238. doi:10.1002/gbc.20021

Driscoll, C. T., Han, Y-J., Chen, C. Y., Evers, D. C., Lambert, K. F., Holsen, T. M., et al. (2007). Mercury contamination in forest and freshwater ecosystems in the Northeastern United States. *Bioscience* 57, 17–28. doi:10.1641/b570106

Eagles-Smith, C. A., Ackerman, J. T., Willacker, J. J., Tate, M. T., Lutz, M. A., Fleck, J. A., et al. (2016a). Spatial and temporal patterns of mercury concentrations in freshwater fish across the Western United States and Canada. *Sci. Total Environ.* 568, 1171–1184. doi:10.1016/j.scitotenv.2016.03.229

Eagles-Smith, C. A., Herring, G., Johnson, B., and Graw, R. (2016b). Conifer density within lake catchments predicts fish mercury concentrations in remote subalpine lakes. *Environ. Pollut.* 212, 279–289. doi:10.1016/j.envpol.2016.01.049

Eagles-Smith, C. A., Wiener, J. G., Eckley, C. S., Willacker, J. J., Evers, D. C., Marvin-DiPasquale, M., et al. (2016c). Mercury in Western north America: A synthesis of environmental contamination, fluxes, bioaccumulation, and risk to fish and wildlife. *Sci. Total Environ.* 568, 1213–1226. doi:10.1016/j.scitotenv.2016.05.094

Eckley, C. S., Gilmour, C. C., Janssen, S., Luxton, T. P., Randall, P. M., Whalin, L., et al. (2020). The assessment and remediation of mercury contaminated sites: A review of current approaches. *Sci. Total Environ.* 707, 136031. doi:10.1016/j.scitotenv.2019.136031

Eckley, C. S., Luxton, T. P., Goetz, J., and McKernan, J. (2017). Water-level fluctuations influence sediment porewater chemistry and methylmercury production in a flood-control reservoir. *Environ. Pollut.* 222, 32–41. doi:10.1016/j.envpol.2017.01.010

Eckley, C. S., Luxton, T. P., McKernan, J. L., Goetz, J., and Goulet, J. (2015). Influence of reservoir water level fluctuations on sediment methylmercury concentrations downstream of the historical Black Butte mercury mine, OR. *Or. Appl. Geochem.* 61, 284–293. doi:10.1016/j.apgeochem.2015.06.011

Eckley, C. S., Luxton, T. P., Stanfield, B., Baldwin, A., Holloway, J., McKernan, J., et al. (2021). Effect of organic matter concentration and characteristics on mercury mobilization and methylmercury production at an abandoned mine site. *Environ. Pollut.* 271, 116369. doi:10.1016/j.envpol.2020.116369

Enrico, M., Roux, GlL., Marusczak, N., Heimburger, L. E., Claustres, A., Fu, X., et al. (2016). Atmospheric mercury transfer to peat bogs dominated by gaseous elemental mercury dry deposition. *Environ. Sci. Technol.* 50, 2405–2412. doi:10.1021/acs.est.5b06058

Estrade, N., Carignan, J., Sonke, J. E., and Donard, O. F. (2010). Measuring Hg isotopes in bio-geo-environmental reference materials. *Geostand. Geoanalytical Res.* 34, 79–93. doi:10.1111/j.1751-908x.2009.00040.x

Foucher, D., Ogrinc, N., and Hintelmann, H. (2009). Tracing mercury contamination from the idrija mining region (Slovenia) to the gulf of trieste using Hg isotope ratio measurements. *Environ. Sci. Technol.* 43, 33–39. doi:10.1021/es801772b

Fu, X., Jiskra, M., Yang, X., Marusczak, N., Enrico, M., Chmeleff, J., et al. (2021). Mass-independent fractionation of even and odd mercury isotopes during atmospheric mercury redox reactions. *Environ. Sci. Technol.* 55, 10164–10174. doi:10.1021/acs.est.1c02568

Gehrke, G. E., Blum, J. D., Slotton, D. G., and Greenfield, B. K. (2011). Mercury isotopes link mercury in san francisco bay forage fish to surface sediments. *Environ. Sci. Technol.* 45, 1264–1270. doi:10.1021/es103053y

Hoffman, J. C., Bronk, D. A., and Olney, J. E. (2007). Contribution of allochthonous carbon to American shad production in the Mattaponi River, Virginia, using stable isotopes. *Estuaries Coasts* 30, 1034–1048. doi:10.1007/bf02841394

Hoffman, J. C., Sierszen, M. E., and Cotter, A. M. (2015). Fish tissue lipid-C: N relationships for correcting δ13C values and estimating lipid content in aquatic food-web studies. *Rapid Commun. Mass Spectrom.* 29, 2069–2077. doi:10.1002/rcm.7367

Hope, B. K. (2006). An assessment of anthropogenic source impacts on mercury cycling in the Willamette Basin, Oregon, USA. *Sci. total Environ.* 356, 165–191. doi:10.1016/j.scitotenv.2005.03.023

Hsu-Kim, H., Eckley, C. S., Acha, D., Feng, X. B., Gilmour, C. C., Jonsson, S., et al. (2018). Challenges and opportunities for managing aquatic mercury pollution in altered landscapes. *Ambio* 47, 141–169. doi:10.1007/s13280-017-1006-7

Janssen, S. E., Hoffman, J. C., Lepak, R. F., Krabbenhoft, D. P., Walters, D., Eagles-Smith, C. A., et al. (2021a). Examining historical mercury sources in the Saint Louis River estuary: How legacy contamination influences biological mercury levels in Great Lakes coastal regions. *Sci. Total Environ.* 779, 146284. doi:10.1016/j.scitotenv.2021.146284

Janssen, S. E., Lepak, R. F., Tate, M. T., Ogorek, J. M., DeWild, J. F., Babiarz, C. L., et al. (2019a). Rapid pre-concentration of mercury in solids and water for isotopic analysis. *Anal. Chim. Acta* 1054, 95–103. doi:10.1016/j.aca.2018.12.026

Janssen, S. E., Riva-Murray, K., DeWild, J. F., Ogorek, J. M., Tate, M. T., Van Metre, P. C., et al. (2019b). Chemical and physical controls on mercury source signatures in stream fish from the northeastern United States. *Environ. Sci. Technol.* 53, 10110–10119. doi:10.1021/acs.est.9b03394

Janssen, S. E., Tate, M. T., Krabbenhoft, D. P., DeWild, J. F., Ogorek, J. M., Babiarz, C. L., et al. (2021b). The influence of legacy contamination on the transport and bioaccumulation of mercury within the Mobile River Basin. *J. Hazard. Mater.* 404, 124097. doi:10.1016/j.jhazmat.2020.124097

Kwon, S. Y., Blum, J. D., Yin, R., Tsui, M. T-K., Yang, Y. H., and Choi, J. W. (2020). Mercury stable isotopes for monitoring the effectiveness of the Minamata Convention on Mercury. *Earth-Science Rev.* 203, 103111. doi:10.1016/j.earscirev.2020.103111

Lepak, R. F., Hoffman, J. C., Janssen, S. E., Krabbenhoft, D. P., Ogorek, J. M., DeWild, J. F., et al. (2019). Mercury source changes and food web shifts alter contamination signatures of predatory fish from Lake Michigan. *Proc. Natl. Acad. Sci.* 116, 23600–23608. doi:10.1073/pnas.1907484116

Lepak, R. F., Janssen, S. E., Yin, R., Krabbenhoft, D. P., Ogorek, J. M., DeWild, J. F., et al. (2018). Factors affecting mercury stable isotopic distribution in piscivorous fish of the Laurentian Great Lakes. *Environ. Sci. Technol.* 52, 2768–2776. doi:10.1021/acs.est.7b06120

Munthe, J., Bodaly, R. A., Branfireun, B. A., Driscoll, C. T., Gilmour, C. C., Harris, R., et al. (2007). Recovery of mercury-contaminated fisheries. *Ambio* 36, 33–44. doi:10.1579/0044-7447(2007)36[33:romf]2.0.co;2

Newville, M. (2013). Larch: An analysis package for XAFS and related spectroscopies. *J. Phys. Conf. Ser.* 430, 012007. doi:10.1088/1742-6596/430/1/012007

Obrist, D., Kirk, J. L., Zhang, L., Sunderland, E. M., Jiskra, M., and Selin, N. E. (2018). A review of global environmental mercury processes in response to human and natural perturbations: Changes of emissions, climate, and land use. *Ambio* 47, 116–140. doi:10.1007/s13280-017-1004-9

Park, J. G., and Curtis, L. R. (1997). Mercury distribution in sediments and bioaccumulation by fish in two Oregon reservoirs: Point-source and nonpoint-source impacted systems. *Archives Environ. Contam. Toxicol.* 33, 423–429. doi:10.1007/s002449900272

Ravel, B., and Newville, M. (2005). *ATHENA*,*ARTEMIS*,*HEPHAESTUS*: Data analysis for X-ray absorption spectroscopy using*IFEFFIT*. *J. synchrotron Radiat.* 12, 537–541. doi:10.1107/s0909049505012719

Rosera, T. J., Janssen, S. E., Tate, M. T., Lepak, R. F., Ogorek, J. M., DeWild, J. F., et al. (2022). Methylmercury stable isotopes: New insights on assessing aquatic food web bioaccumulation in legacy impacted regions. *ACS ES&T Water* 2, 701–709. doi:10.1021/acsestwater.1c00285

Smith, C. N., Kesler, S. E., Blum, J. D., and Rytuba, J. J. (2008). Isotope geochemistry of mercury in source rocks, mineral deposits and spring deposits of the California Coast Ranges, USA. *Earth Planet. Sci. Lett.* 269, 399–407. doi:10.1016/j.epsl.2008.02.029

Smith, C. N., Kesler, S. E., Br, K., and Blum, J. D. (2005). Mercury isotope fractionation in fossil hydrothermal systems. *Geology* 33, 825–828. doi:10.1130/g21863.1

Smith, R. S., Wiederhold, J. G., Jew, A. D., Brown, G. E., Jr, Bourdon, B., and Kretzschmar, R. (2014). Small-scale studies of roasted ore waste reveal extreme ranges of stable mercury isotope signatures. *Geochimica Cosmochimica Acta* 137, 1–17. doi:10.1016/j.gca.2014.03.037

Štrok, M., Hintelmann, H., and Dimock, B. (2014). Development of pre-concentration procedure for the determination of Hg isotope ratios in seawater samples. *Anal. Chim. Acta* 851, 57–63. doi:10.1016/j.aca.2014.09.005

Suchanek, T. H., Eagles-Smith, C. A., and Harner, E. J. (2008). IS clear lake methylmercury DIStribution decoupled from bulk mercury loading? *Ecol. Appl.* 18, A107–A127. doi:10.1890/06-1649.1

Watras, C. J., Morrison, K. A., Host, J. S., and Bloom, N. S. (1995). Concentration of mercury species in relationship to other site-specific factors in the surface waters of northern Wisconsin lakes. *Limnol. Oceanogr.* 40, 556–565. doi:10.4319/lo.1995.40.3.0556

Willacker, J. J., Eagles-Smith, C. A., Lutz, M. A., Tate, M. T., Lepak, J. M., and Ackerman, J. T. (2016). Reservoirs and water management influence fish mercury concentrations in the Western United States and Canada. *Sci. Total Environ.* 568, 739–748. doi:10.1016/j.scitotenv.2016.03.050

Yin, R., Feng, X., Li, X., Yu, B., and Du, B. (2014). Trends and advances in mercury stable isotopes as a geochemical tracer. *Trends Environ. Anal. Chem.* 2, 1–10. doi:10.1016/j.teac.2014.03.001

Zheng, W., and Hintelmann, H. (2010a). Isotope fractionation of mercury during its photochemical reduction by low-molecular-weight organic compounds. *J. Phys. Chem. A* 114, 4246–4253. doi:10.1021/jp9111348

Zheng, W., and Hintelmann, H. (2010b). Nuclear field shift effect in isotope fractionation of mercury during abiotic reduction in the absence of light. *J. Phys. Chem. A* 114, 4238–4245. doi:10.1021/jp910353y

frontiers | Frontiers in Environmental Chemistry

TYPE Original Research
PUBLISHED 25 May 2023
DOI 10.3389/fenvc.2023.1109537

OPEN ACCESS

EDITED BY
Marc Amyot,
Montreal University, Canada

REVIEWED BY
Dario Acha,
Universidad Mayor de San Andrés, Bolivia
Igor Lehnherr,
University of Toronto Mississauga, Canada

*CORRESPONDENCE
Marissa C. Despins,
mdespins@ucsc.edu

RECEIVED 27 November 2022
ACCEPTED 17 May 2023
PUBLISHED 25 May 2023

CITATION
Despins MC, Mason RP, Aguilar-Islas AM, Lamborg CH, Hammerschmidt CR and Newell SE (2023), Linked mercury methylation and nitrification across oxic subpolar regions.
Front. Environ. Chem. 4:1109537.
doi: 10.3389/fenvc.2023.1109537

Linked mercury methylation and nitrification across oxic subpolar regions

Marissa C. Despins[1,2]*, Robert P. Mason[3], Ana M. Aguilar-Islas[4], Carl H. Lamborg[2], Chad R. Hammerschmidt[1] and Silvia E. Newell[1]

[1]Department of Earth and Environmental Sciences, Wright State University, Dayton, OH, United States, [2]Department of Ocean Sciences, University of California, Santa Cruz, Santa Cruz, CA, United States, [3]Department of Marine Science, University of Connecticut, Groton, CT, United States, [4]Oceanography Department, University of Alaska Fairbanks, Fairbanks, AK, United States

Methylmercury (MeHg) is a neurotoxin that bioaccumulates to potentially harmful concentrations in Arctic and Subarctic marine predators and those that consume them. Monitoring and modeling MeHg bioaccumulation and biogeochemical cycling in the ocean requires an understanding of the mechanisms behind net mercury (Hg) methylation. The key functional gene pair for Hg methylation, *hgcAB*, is widely distributed throughout ocean basins and spans multiple microbial phyla. While multiple microbially mediated anaerobic pathways for Hg methylation in the ocean are known, the majority of *hgcA* homologs have been found in oxic subsurface waters, in contrast to other ecosystems. In particular, microaerophilic *Nitrospina*, a genera of nitrite-oxidizing bacteria containing a *hgcA*-like sequence, have been proposed as a potentially important Hg methylator in the upper ocean. The objective of this work was therefore to examine the potential of nitrifiers as Hg methylators and quantify total Hg and MeHg across three Arctic and Subarctic seas (the Gulf of Alaska, the Bering Sea and the Chukchi Sea) in regions where *Nitrospina* are likely present. In Spring 2021, samples for Hg analysis were obtained with a trace metal clean rosette across these seas. Mercury methylation rates were quantified in concert with nitrification rates using onboard incubation experiments with additions of stable isotope-labeled Hg and NH_4^+. A significant correlation between Hg methylation and nitrification was observed across all sites (R^2 = 0.34, $p < 0.05$), with the strongest correlation in the Chukchi Sea (R^2 = 0.99, $p < 0.001$). *Nitrospina*-specific *hgcA*-like genes were detected at all sites. This study, linking Hg methylation and nitrification in oxic seawater, furthers understanding of MeHg cycling in these high latitude waters, and the ocean in general. Furthermore, these studies inform predictions of how climate and human interactions could influence MeHg concentrations across the Arctic in the future.

KEYWORDS

mercury, mercury methylation, nitrification, Arctic, Subarctic, *hgcA*, *Nitrospina*

1 Introduction

The harmful bioaccumulating neurotoxin, methylmercury (MeHg), has increased over the past 150 years in Arctic and subarctic mammals, resulting in high concentrations in the Canadian Arctic and Northern Gulf of Alaska (NGA) marine predators (Beckmen et al., 2002; Dietz et al., 2009; Lehnherr et al., 2011; Wang et al., 2018). Consumption of high trophic level marine organisms serves as the main MeHg exposure route to humans

(Sunderland and Mason, 2007). The health of indigenous communities that rely on marine predators, both fish and mammals, as a food source continues to be an area of concern as the MeHg blood concentrations of Arctic women remain high (AMAP, 2021). The largest source of inorganic mercury (Hg^{II}) to the global ocean is through atmospheric deposition (Mason et al., 2012). Rivers also serve as a large source of Hg^{II} to Arctic coastal zones compared to other ocean basins (Sørensen et al., 2016; Sonke et al., 2018; Dastoor et al., 2022; Zolkos et al., 2022). Mercury concentrations in ocean surface waters have been increasing since industrialization (Lamborg et al., 2014), with concurrent increases in marine MeHg concentrations (Médieu et al., 2022). Monitoring and modeling current and future MeHg production in the ocean requires an understanding of the mechanisms behind Hg methylation, but the pathways for MeHg formation are not clearly understood.

High MeHg concentrations have been observed just below the productive surface layer in the Arctic Ocean, Bering Sea, Northwest Atlantic and the North Pacific Ocean (Sunderland et al., 2009; Heimbürger et al., 2015; Schartup et al., 2015; Wang et al., 2018; Agather et al., 2019; Jonsson et al., 2022). These MeHg maxima residing within oxic layers are shallower than equatorial regions (Bowman et al., 2016; Kim et al., 2017) and result in a higher rate of MeHg bioaccumulation into the food chain (Heimbürger et al., 2015; Wang et al., 2018). Previous studies attribute higher MeHg concentrations in oxic layers to production in anoxic particle microenvironments or the resuspension and remineralization of MeHg bound to organic matter (Hammerschmidt and Fitzgerald, 2006; Ortiz et al., 2015; Motta et al., 2022). With low benthic-pelagic coupling in the central ocean, and given the rate of photo-degradation and demethylation of MeHg in the surface waters (DiMento and Mason, 2017; Munson et al., 2018), the question remains: by what mechanism is biotic Hg methylation occurring in the oxic surface waters at high latitudes? Lehnherr et al. (2011) developed a simple model based on their methylation and demethylation studies that estimated biotic MeHg formation accounts for a significant fraction of the MeHg present in polar marine waters but did not provide a mechanism for this process.

The presumed key functional gene pair for Hg methylation, *hgcAB*, is widely distributed throughout all ocean basins and spans multiple microbial phyla (Parks et al., 2013; Villar et al., 2020). All currently confirmed pathways for biotic marine MeHg production in marine water columns and sediment are anaerobic (Gilmour et al., 2013; Gionfriddo et al., 2020) and have been shown to coincide with oxygen minimum zones (Hammerschmidt and Bowman, 2012; Munson et al., 2018). However, across all ocean basins, 78% of discovered *hgcA* homologs have been found in oxic subsurface waters (Villar et al., 2020). In recent years, a new aerobic pathway for Hg methylation has been suggested in conjunction with nitrite-oxidation (Gionfriddo et al., 2016), the second, non-rate limiting reaction in nitrification (Delwiche, 1970). The putative Hg methylating microbes belong to two aerobic nitrite-oxidizing clades, *Nitrospina* and *Nitrospira* (Gionfriddo et al., 2016; Christiansen et al., 2019). While *Nitrospira hgcAB* genes have only been recovered in freshwater sediment and tidal marsh metagenomes (Gionfriddo et al., 2020), *Nitrospina hgcA*-like sequences have been found to be abundant across all ocean basins, including the Arctic (Bowman et al., 2020; Tada et al., 2020; Villar et al., 2020; Lin et al., 2021; Tada et al., 2021). As the most widely distributed microaerophilic putative Hg methylating microbe, it is hypothesized that *Nitrospina* could play a key role in global MeHg production in the ocean subsurface (Villar et al., 2020), although *in situ* measurements of Hg methylation rates by cultured *Nitrospina* have yet to be completed.

Recently, in the Equatorial Atlantic, a strong positive correlation was found between nitrification and Hg methylation at the chlorophyll *a* maximum and in surface waters (Starr et al., 2022). While *Nitrospina*-specific *16S* transcripts were recovered, *Nitrospina*-specific *hgcA*-like gene abundance was not assessed (Starr et al., 2022). Here, we further investigate the correlation between this putative microbially mediated aerobic Hg methylation pathway and nitrite oxidation across five nutrient-replete, polar regions (NGA, Unimak Pass, Bering Sea, Bering Strait and Chukchi Sea; Figure 1) where *Nitrospina hgcA*-like sequences have been previously reported (Bowman et al., 2020).

2 Methods

2.1 Sample collection

Seawater samples were collected between April and June 2021 in the NGA, Bering Sea, and Chukchi Sea aboard the *R/V Sikuliaq* during three oceanographic cruises: Northern Gulf of Alaska Long Term Ecological Research (NGA LTER), Bering and Aleutian Internal Tide Mixing, and Hg Cycling in the Arctic (Supplementary Table S1). All sampling stations were on the Alaskan continental shelf, except KOD10, which was on the slope in the NGA. The water column depth at the sampling locations in the Bering and Chukchi Seas were shallow (48 ± 6 m) compared to the NGA (610 ± 477 m) (Supplementary Table S2). Water samples were collected at a single depth, the chlorophyll *a* maximum (Figure 1; Supplementary Table S2), which was selected because previous studies have shown *in situ* Hg methylation at that depth (Munson et al., 2018; Starr et al., 2022). The ship's SeaBird 911+ CTD rosette was used to assess the chlorophyll *a* maximum during the down cast, which determined the sampling depth. During the downcast, other parameters were measured such as salinity, dissolved oxygen, photosynthetically active radiation (PAR), temperature, and pressure. Due to limited water allowances, Hg methylation, nitrification, and genetic samples were collected from the ship's regular CTD rosette (non-trace metal clean) in the NGA. Mercury methylation, nitrification, and genetic samples from the other 13 stations throughout the Bering and Chukchi Seas were collected using a trace metal clean SBE19plus V2 SeaCAT Profiler (SeaBird) CTD rosette equipped with Teflon-coated, external spring Niskin bottles (General Oceanics). Samples from the trace metal CTD rosette were transferred to acid washed sample bottles (Hammerschmidt et al., 2011) inside a positive-pressure, plastic enclosure (the bubble), constructed at the beginning of the NGA LTER cruise. Seawater samples for genetic analysis was collected in an acid washed 5-gallon collapsible polyethylene carboy. Using an Eppendorf peristaltic pump, 2 L of sample water was filtered through a 0.22 µM Sterivex filter pack (Millipore). The Sterivex was filled with RNAlater (ThermoFisher), stabilizing the nucleic acids, and stored at −80°C until extraction (Bowman et al., 2020). Seawater for Hg methylation rate experiments was collected in 4 2-L acid washed plastic bottles. Seawater samples for nitrification pool

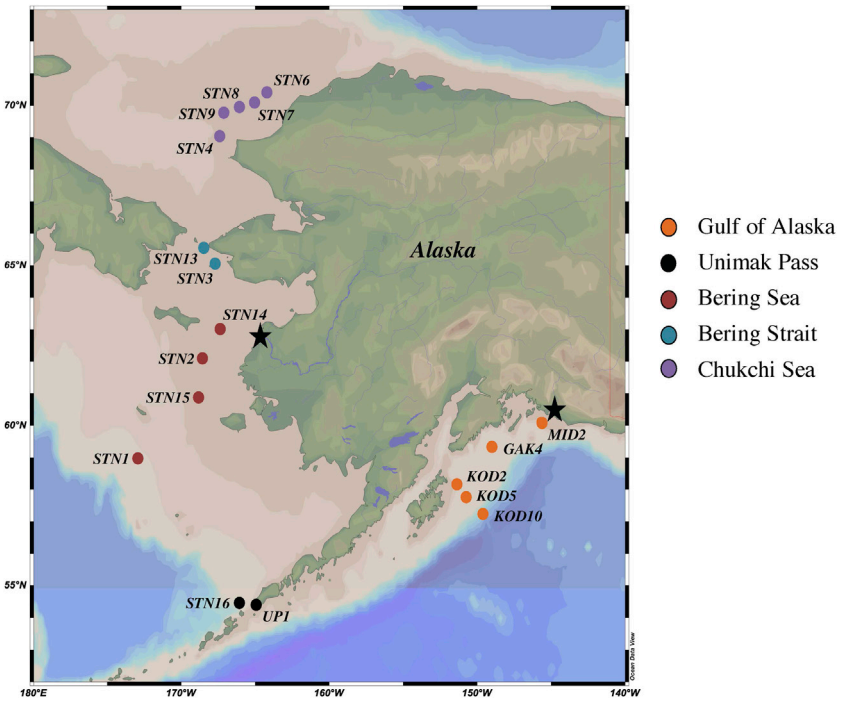

FIGURE 1
Map of NGA, Unimak Pass, Bering Sea, Bering Strait and Chukchi Sea 2021 sampling stations. Yukon and Copper River outflows denoted by black stars.

dilution experiments were collected into an acid washed 1-L and 3 125-mL polycarbonate incubation bottles. Incubation experiments occurred upon sample collection.

2.2 Mercury methylation experiments

Onboard dark incubation experiments were carried out with stable Hg isotope additions to quantify Hg methylation and demethylation rates. Four replicate 2-L unfiltered water samples were collected and promptly amended with 7.5 pM $^{200}Hg^{II}$ (Oak Ridge National Laboratory) and 7.7 pM $CH_3{}^{201}Hg$ by volume. MeHg synthesis was completed prior to the cruise with methyl-cobalamin and inorganic Hg isotopes (Oak Ridge National Laboratory). Initial sample volume was measured, and all samples were placed in a dark incubation chamber at *in situ* temperature (4°C) without further oxygenation. After 24 h, samples were removed, reduced to 1.5 L and immediately acidified to 1% H_2SO_4 by volume to stop biological transformations. Samples were stored unrefrigerated in a dark container until analysis.

Mercury methylation rate samples were analyzed at Wright State University (WSU) within 8 months of collection. Prior to analysis, these samples were neutralized to pH 4.9 ± 0.3 with 14 M potassium hydroxide, buffered with 14 mM acetate buffer by volume and amended with 0.1 mL of 2.5% ascorbic acid (Munson et al., 2014). Neutralized samples were derivatized with sodium tetraethylborate and purged with Hg-free N_2 gas. During the bubbling process, methylethylmercury was concentrated onto Tenax traps and analyzed on an optimized gas chromatography inductively coupled plasma mass spectrometer (GC-ICPMS; Perkin Elmer Elan 9000; Hintelmann and Evans, 1997). Ambient Hg standards and enriched isotope standards were analyzed on both the Tekran and ICP-MS to quantify both concentration and isotope abundance. Mercury methylation and demethylation rates were calculated from replicates at one time point using matrix methodology (Hintelmann and Evans, 1997; Ouerdane et al., 2009), as $CH_3{}^{200}Hg$ created and $CH_3{}^{201}Hg$ lost since amendment respectively: Hg methylation rate (pM day^{-1}) = k_m * $[Hg^{II}]$ and MMHg demethylation rate (pM day^{-1}) = k_d * [MMHg]. For Hg methylation rate potentials, first order specific rates (k_m) were also calculated as specific rate (day^{-1}) = Hg methylation rate * $[Hg^{II}]^{-1}$.

2.3 Nitrification experiments

The collected 1 L seawater samples were amended with 20 mM $^{15}NH_4Cl$ and inverted three times. The 20 µM spiked sample was transferred into three 125-mL polycarbonate incubation bottles. An initial sample was taken immediately from each incubation replicate via a 60 mL plastic syringe and filtered through a 0.22 µm filter into one 15-mL polypropylene tube and two 20-mL scintillation vials. An initial control was sampled from the 125 mL unamended seawater sample following the same methodology. Initial samples were frozen upon collection and stored until analysis. The four 125-mL

TABLE 1 Mean *Nitrospina*-specific *hgcA*-like gene abundance and rate potentials with standard error across five regions: NGA, Unimak Pass, Bering Sea, Bering Strait, and Chukchi Sea.

Region	k_m (10^{-3} d^{-1})	Hg methylation (10^{-2} pM d^{-1})	Nitrification (nM d^{-1})	Gene abundance (copies mL^{-1})
Gulf of Alaska	2.8 ± 0.6	1.8 ± 0.4	1.3 ± 0.6	2023 ± 957
Unimak Pass	8.3 ± 2.5	5.9 ± 1.9	N.D.	236
Bering Sea	4.3 ± 1.3	2.3 ± 0.5	1.7 ± 1.2	1895 ± 1,461
Bering Strait	5.3 ± 2.6	4.4 ± 1.2	0.5 ± 0.4	2,914 ± 278
Chukchi Sea	5.8 ± 1.7	4.2 ± 1.2	1.9 ± 0.8	1879 ± 784

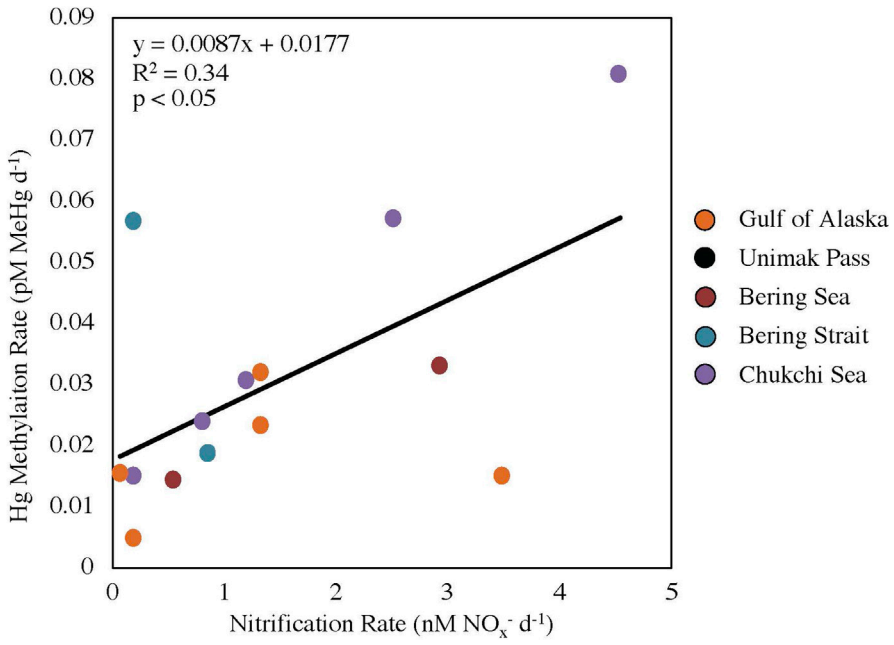

FIGURE 2
Linear regression between nitrification and mercury methylation rate potentials across five regions ($p < 0.05$, y = 0.0087x + 0.0177). Data points for Unimak Pass are not shown as nitrification rate experiments were not completed.

incubation bottles were incubated for 24 h in the onboard dark incubation chamber at *in situ* temperature. After the 24-h incubation, the four bottles were removed, final samples from the control and replicates were collected using the same methodology as the initial samples, and samples were frozen until analysis at WSU.

Cadmium (Cd) reductions (to reduce NO_3^- to NO_2^-) followed by sodium azide (NaN_3) reductions were completed on each sample to quantify the production of nitrous oxide (N_2O) from both nitrite and nitrate (NO_x^-; Heiss and Fulweiler, 2016; McIlvin and Altabet, 2005). To each sample, 100 mg and 6.6 g of dried magnesium and sodium chloride was added respectively and mixed. To complete the Cd reductions, 1 g of activated wet Cd powder was added to each sample and placed on a shaker table for 17 h. Samples were centrifuged for 15 min at 1,000 rpm to decant the reduced solution. 7.5 mL of supernatant was removed from the centrifuge tubes, transferred to a 12-mL Labco exetainer, and sealed with a single-wadded septa cap. Using a glass syringe with a needle, 0.25 mL of a solution containing 1:1 2 M sodium azide: 20% acetic acid purged with Argon gas was injected into the exetainer septa. Samples were shaken and incubated at 30°C for 1 h. Following incubation, the reaction was stopped by injecting 0.15 mL of 10 M NaOH through the exetainer septa with a clean needle and syringe (McIlvin and Altabet, 2005). Exetainers containing the reduced sample were stored upside down and shipped to the University of California—Davis Stable Isotope Facility for analysis of labeled $^{45,46}N_2O$ gas production using an isotope-ratio mass spectrometer (Hamilton and Ostrom, 2007). Incubation samples collected in falcon tubes were thawed and quantified for total NH_4^+ using colorimetric flow-injection analysis (Lachat Quikchem 8500) at WSU. Results from both analyses were used to calculate the $^{15}NH_4^+$ transformation and were corrected for NaN_3 reductions using Eq. 1, modified from Heiss and Fulweiler (2016), Beman et al. (2008), and Hampel et al. (2020). Nitrification rate experiments were only completed in the NGA, Bering Sea, Bering Strait, and Chukchi Sea.

$$NTR = \frac{\left(\left({}^{15}N/{}^{14}N * [NO_x^-]\right)_{tf} - \left({}^{15}N/{}^{14}N * [NO_x^-]\right)_{t0}\right)}{\alpha * t} \quad (1)$$
$$where\ \alpha = [{}^{15}NH_4^+]/([{}^{15}NH_4^+] + [{}^{14}NH_4^+])$$

2.4 Molecular analysis

DNA was extracted using the DNeasy PowerWater Sterivex Kit (Qiagen) and assessed for quality using 260/280 and 260/230 ratios, with a NanoDrop Microvolume Spectrophotometer (ThermoFisher), verified by Qubit. Extractions were stored at −18°C until assay. *Nitrospina*-specific *hgcA* primers (Supplementary Table S3), Nitro_SP14_1F and Nitro_SP14_1R, designed from sequences found in Antarctic Sea ice were used for amplification (Gionfriddo et al., 2016). The SP8 sequence, 504 bp, from Gionfriddo et al. (2016) was used as a positive control for the real-time polymerase chain reaction (qPCR) assay. A set of seven serial dilutions (10^{-4}–10^{-10} ng μL^{-1}) were prepared from the SP8 sequence and used to form a standard curve ($R^2 > 0.90$). With a reaction volume of 20 μL, the following chemical volumes were used for amplification: 10 μL Luna Universal qPCR Master Mix (New England BioLabs), 1 μL Nitro_SP14_1F and Nitro_SP14_1R, 1 μL of sample (5 ng DNA), diluted SP8, or Nuclease free water, and 7 μL of nuclease free water. Samples were amplified on a Mastercycler ep Realplex2 Real-Time PCR system (Eppendorf) with thermal cycling parameters (outlined in Gionfriddo et al., 2016) and a melting curve (Supplementary Table S3). Amplification efficiency was 95.6%, and sample amplicon concentration was calculated. Gene abundance was reported as *Nitrospina*-specific *hgcA* gene copies mL^{-1} and calculated using Eq. 2 and normalized to sample volume (mL).

$$Gene\ Abundance = \frac{5\,ng * (6.0221 * 10^{23}\ molecules/mol)}{504\,bp * 10^9\ ng/g * 650\ g/mol} \quad (2)$$

3 Results and discussion

3.1 Physiochemical oceanography

The NGA is heavily influenced by the Alaskan Coastal Current (ACC), which is driven by alongshore winds and characterized by freshwater inputs derived from coastal runoff and the Copper River outflow (Stabeno et al., 2004). From fall to spring the NGA is dominated by downwelling currents and Ekman transport from off-shelf surface waters (Stabeno et al., 2004). The downwelling dissipates as winds decrease throughout the spring, allowing for the resuspension of key nutrients (such as nitrate, phosphate, and silicate) promoting primary production (Stabeno et al., 2004). During the 2021 Spring NGA LTER cruise there was a large early season diatom bloom from late April to early May 2021, which was thought to be induced by the increased sunlight and reduced winds. Chlorophyll *a* concentrations at the sampling depth (chlorophyll *a* maximum) across the NGA ranged from 0.3–10.1 mg m^{-3} (Supplementary Table S2). The highest value (10.1 mg m^{-3}) was found at MID2, within the mixed waters under the Copper River plume. A small Copper River plume can be identified by a thin layer of nutrient deplete freshwater extending from the Copper River outflow. In the NGA, salinity increased with distance from the coastline, as the influence from runoff, freshwater inputs, and ACC wanes (Stabeno et al., 2016).

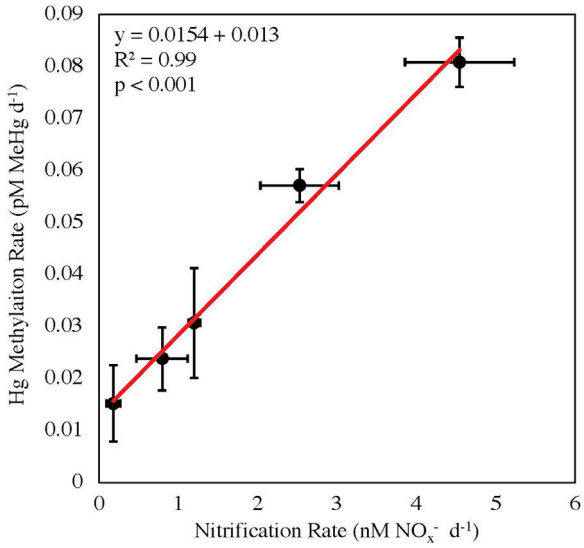

FIGURE 3
Linear regression between nitrification and mercury methylation rate potentials in the Chukchi Sea with standard errors ($p < 0.001$, y = 0.0154x + 0.013).

Water flows north across the Bering Sea shelf and Bering Strait, into the Chukchi Sea via the Bering Shelf Current and Chukchi Shelf current (Danielson et al., 2022). Higher concentrations of chlorophyll *a* and DO were seen in the surface waters in the southern Bering Sea near Unimak Pass (Supplementary Table S2). This can be attributed to the Aleutian North Slope current and deep mixing that resuspends key limited nutrients into the surface waters of this high nutrient low chlorophyll system (Aguilar-Islas et al., 2007; Danielson et al., 2022).

3.2 Mercury transformations

In situ Hg methylation occurred at all stations (0.003–0.008 d^{-1}). Specific (Hg-normalized) Hg methylation rate potentials (k_m) across all regions were comparable with previous measurements from the chlorophyll *a* maxima across the Arctic (0.004–0.010 d^{-1}; Lehnherr et al., 2011), Mediterranean Sea (0.004–0.038 d^{-1}; Monperrus et al., 2007) and the central Pacific Ocean (0.004–0.017 d^{-1}; Munson et al., 2018). Variability of k_m within each region is attributed to temporal and spatial heterogeneity between sampling stations impacting particle and nutrient distribution as a result of differing current dynamics (Stabeno et al., 2004; Strom et al., 2006). Differing assemblages of Hg methylating bacteria, Hg speciation, and demethylation rates also contribute to the variability of k_m within each sampled polar region. The highest k_m was measured at Unimak Pass (one-way ANOVA: $p < 0.05$; Table 1), which can be attributed to deep mixing, providing a substrate and microhabitat for Hg methylating anaerobic bacteria (Swift and Aagaard, 1976; Ortiz et al., 2015; Motta et al., 2022). The samples for incubation experiments in the NGA were collected in the early spring during

a diatom bloom. This increase in productivity could decrease the amount of Hg^{II} available for Hg methylation. This could potentially explain the lower k_m across the NGA, when compared to other regions. Changes in water chemistry across the regions could result in differing contributions of instantaneous Hg methylation to the measured Hg methylation rate potentials. This could explain the variability seen in Hg methylation rate potentials within and across regions.

Across all regions, correlations between k_m and oxygen, ambient Hg, ambient NH_4^+, salinity, and temperature were weak and not significant. The difference between predicted and measured MeHg concentrations is attributed to MeHg demethylation in the surface waters and mixing throughout the Bering Strait and Chukchi Sea (DiMento and Mason, 2017; Munson et al., 2018; Wang et al., 2018).

Methylmercury demethylation rate potentials are not reported as the demethylation rates were unrealistically high. Instantaneous demethylation could explain the low $CH_3{}^{201}Hg$ recovered in the samples (Munson et al., 2018). For future Hg rate experiments, adding additional time points, including a time zero, should be done as suggested by others (Munson et al., 2018).

3.3 Nitrification

Potential nitrification rates ranged 0.5–2.0 nM d^{-1} across all polar regions. These measurements are concurrent with *in situ* nitrification rates measured at deeper depths, 100–200 m, in oligotrophic regions such as the Sargasso Sea (2.0 ± 0.1 nM d^{-1}; Newell et al., 2013). The mean specific nitrification rate across all stations, 7.2×10^{-5} d^{-1} is lower than the global ocean estimate 0.195 d^{-1} (Yool et al., 2007), which is thought to be driven by high $^{15}NH^4Cl$ amendment. Nitrite and nitrate produced during nitrification pool dilution experiments are reported as potential nitrification rates to account for any bias from the high amendment, but the rates are low, suggesting that the nitrifiers become ammonium-saturated at low concentrations (Horak et al., 2013; Newell et al., 2013). In the Chukchi Sea (1.9 ± 0.8 nM d^{-1}), nitrification rate potentials were higher than previous measurements by Shiozaki et al. (2019) in the surface waters within the Chukchi and Beaufort Seas (<0.27 nM d^{-1}), which is not surprising as those rates are low for the open ocean (Yool et al., 2007). Nitrification rate experiments were not conducted at Unimak Pass, but it is hypothesized that Unimak Pass would have a higher apparent nitrification rate as deep mixing in this region would provide remineralized NH_4^+ and metals (Cu, Mo, and Fe) for enzymes involved in both steps of nitrification, ammonia monooxygenase and nitrite oxidoreductase (Musiani et al., 2020; Chicano et al., 2021). It is likely that at the chlorophyll *a* maximum, competition between microbes and plankton taking up various forms of N are driving the lower nitrification rates in this study. The nitrite maximum is typically seen at the base of the euphotic zone as many known ammonia oxidizing bacteria have been shown to be photo-inhibited, resulting in higher nitrification rates with reduced light (Horrigan and Springer, 1990; Lomas and Lipschultz, 2006; Merbt et al., 2012). Previous studies in the North Pacific and Arctic Ocean show nitrification maximum occurring below the chlorophyll *a* maximum, around the nitrite maximum, under <1% PAR (Grundle et al., 2013; Shiozaki et al., 2016; Shiozaki et al., 2019). The potential nitrification rates measured at the chlorophyll *a* maximum across all subpolar marine regions reported in this study are therefore not expected to reflect the highest nitrification rates in the water column.

3.4 Mercury methylation and nitrification

A positive linear relationship ($R^2 = 0.34$, $p < 0.05$; Figure 2) was seen between nitrification and Hg methylation rate potentials across all stations, suggesting a possible link between these two processes in surface waters surrounding Alaska (NGA, Bering Sea, Bering Strait and Chukchi Sea). The linear regression slope between nitrification and Hg methylation rate potentials across all regions ($m = 0.0087$ pM MeHg nM^{-1} NO_x^-; Figure 2) is the same order of magnitude as previous findings in the Amazon River Plume ($m = 0.0028$ pM MeHg nM^{-1} NO_x^-; Starr et al., 2022). This difference in slope can likely be attributed to differing ammonia oxidizing bacteria and archaea activities, substrate availability, and/or microbial assemblages including nitrifier community structure.

Station STN13 in the Bering Strait had a higher relative Hg methylation rate potential compared to nitrification rate potential (Figure 2). Chlorophyll *a* concentrations at STN13 were four times higher than those of STN3, the other station within the Bering Strait sampled 12 days prior to STN13 (Table 1; Supplementary Table S1). A higher chlorophyll *a* concentration suggests a general increase in microbial activity or decreased grazing pressure. Data from the USGS Yukon River Pilot Station show little change in Yukon River discharge throughout the 12-day period between sampling, suggesting riverine inputs were not the main driver in differing rate potentials or the high chlorophyll *a* concentrations. First year ice melt could influence the rate potentials between the two stations in the Bering Strait. A reduction in ice cover could change current dynamics driven by winds promoting water column mixing and resuspension of particles inhabited by Hg methylators. Although these are potential reasons for why STN13 had a higher Hg methylation rate potential compared to nitrification rate potentials, further investigation is needed to conclusively determine the decoupling of these rate potentials in the Bering Sea.

Station MID2, in the NGA near the Copper River outflow, had a higher relative nitrification rate potential compared to the Hg methylation rate potential. This higher relative nitrification rate potential can be attributed to nutrient resuspension, such as NH_4^+ and Cu, and differing communities of nitrifiers that can withstand freshwater plume dynamics (Bernhard et al., 2010). Lower substrate availability for Hg methylation associated the NGA diatom bloom could result from increased binding of Hg^{II} to particulate material, potentially accounting for the lower Hg methylation relative to nitrification rate potentials in the NGA. Overall, it is likely that the larger temporal and spatial differences among stations accounts for the higher variability in this study compared with the previous measurements in the Amazon River Plume ($R^2 = 0.78$; Starr et al., 2022).

The stations within the Chukchi Sea had less temporal and spatial variability than the other regions, as these stations were sampled within the shortest time period (6-day) and across the smallest distance (110 miles; Supplementary Table S1). The correlation between Hg methylation and nitrification rate potentials in the Chukchi Sea was highly significant ($R^2 = 0.99$, $p < 0.001$; Figure 3). Although the correlation between nitrification and Hg methylation rate potentials were strong, it cannot be concluded that nitrification rates alone are driving Hg methylation rates throughout these polar regions, as the functionality of *Nitrospina*-specific *hgcA*-like genes have not yet been confirmed. It is possible that the measured correlation between Hg methylation and nitrification may also be a result of other biogeochemical processes, such as general bacterial productivity, acting as a proxy (although nitrifiers are autotrophs,

while most known Hg methylators are heterotrophs; Yool et al., 2007; Monperrus et al., 2007).

3.5 *hgcA*-like genes

Nitrospina-specific *hgcA*-like genes were present across all stations. The Bering Strait had the highest average gene copy numbers (2,914 copies mL^{-1}) compared to the NGA (2023 copies mL^{-1}), Bering Sea (1895 copies mL^{-1}), and Chukchi Sea (1879 copies mL^{-1}). Unimak Pass had the lowest gene abundance (236 copies mL^{-1}), which was surprising as Unimak Pass had the highest k_m (Table 1). It is important to note that Hg methylation and nitrification rate potentials reported are a composite of the entire Hg methylator and nitrifier community, not just *Nitrospina*. Hg methylating microbes at Unimak Pass may be primarily anaerobic and particle-associated, as the station is characterized by deep water column mixing. We hypothesize that anaerobic and microaerophilic Hg methylating microbes inhabit settling or suspended particles, derived from sediment resuspension in the well mixed, shallow Bering Strait and Chukchi Sea, the well mixed waters of Unimak Pass, and the particle-rich Copper River plume. While this may include microaerophilic *Nitrospina* (Lücker et al., 2013), such particle microenvironments are likely dominated by anaerobic Hg methylating microbes such as *Desulfobacteraceae* and *Methanomassiliicoccus*, which have been found throughout the Bering Sea, Chukchi Sea, and Arctic Ocean water column (Bowman et al., 2020).

Across all sampled regions there was not a correlation between *Nitrospina*-specific *hgcA*-like genes and Hg methylation rate potentials. However, these *Nitrospina hgcA*-like amplicons only show gene presence, not enzyme function, so the lack of correlation may indicate that not all of these genes were active at the time of sampling. Despite a lack of correlation, the presence of *Nitrospina*-specific *hgcA*-like genes provides support for the potential for these organisms to be the primary methylators, given the relationship between Hg methylation and nitrification.

4 Conclusion

The link between Hg methylation and nitrification at the chlorophyll *a* maximum depth suggests a possible mechanism for Hg methylation in the oxic water column of these Alaskan Seas. The similarity between this link in subpolar waters and the Amazon River Plume further supports the hypothesis that nitrification and biotic Hg methylation are linked at the base of the oxic region of the euphotic (>1–9% PAR) ocean. As *Nitrospina hgcA*-like metagenomes have been recovered across all ocean basins (Villar et al., 2020), the presence of *Nitrospina* could be a major pathway for MeHg formation in the oxic ocean subsurface, provided these microbes are active (i.e., the conserved region of *hgcA* is functional). If these *Nitrospina*-specific *hgcA*-like genes are functional, then models utilizing current global specific nitrification rate estimates and *Nitrospina hgcA*-like amino acid sequence recoveries, could be used to predict global Hg methylation rate potentials in the ocean subsurface. However, until *Nitrospina*'s Hg methylating capabilities are confirmed in culture, more robust conclusions regarding Hg methylation by *Nitrospina* cannot be made. More research is needed to further examine the role of *Nitrospina* in the methylation of Hg in the global ocean.

Data availability statement

The original contributions presented in the study are included in the article/Supplementary Material, further inquiries can be directed to the corresponding author.

Author contributions

MD collected samples, carried out rate experiments, and completed analysis. RM and AA-I assisted in sample collection and contributed ambient Hg and nutrient data respectively. RM and CL helped with mercury rate experiments. SN aided in nitrification rate experiments. SN, CH, and MD conceived the project idea. All authors contributed to the article and approved the submitted version.

Funding

This research was partially supported by the U.S. National Science Foundation through OPP grant 1854454 to RM, and OCE grant 1656070 to AA-I.

Acknowledgments

We thank chief scientists, Russell Hopcroft and Tyler Hennon, the NGA LTER, and the Captain and crew of the *R/V Sikuliaq*. We also thank Yipeng He and Hannah Inman for help with sample collection and contributing ambient Hg data, Lauren Barrett for contributing nutrient data, Lindsay Starr and Justin Myers for help with analyses, Caitlin Gionfriddo for providing *Nitrospina*-specific *hgcA* amplicons, and the UC-Davis stable isotope laboratory.

Conflict of interest

The authors declare that the research was conducted in the absence of any commercial or financial relationships that could be construed as a potential conflict of interest.

Publisher's note

Supplementary material

The Supplementary Material for this article can be found online at: https://www.frontiersin.org/articles/10.3389/fenvc.2023.1109537/full#supplementary-material

References

Agather, A. M., Bowman, K. L., Lamborg, C. H., and Hammerschmidt, C. R. (2019). Distribution of mercury species in the western Arctic Ocean (U.S. GEOTRACES GN01). *Mar. Chem.* 216. doi:10.1016/j.marchem.2019.103686

Aguilar-Islas, A. M., Hurst, M. P., Buck, K. N., Sohst, B., Smith, G. J., Lohan, M. C., et al. (2007). Micro- and macronutrients in the southeastern Bering Sea: Insight into iron-replete and iron-depleted regimes. *Prog. Oceanogr.* 73, 99–126. doi:10.1016/j.pocean.2006.12.002

Amap (2021). *AMAP assessment 2021: Human health in the arctic*. Tromsø, Norway: Arctic Monitoring and Assessment Programme.

Beckmen, K. B., Duffy, L. K., Zhang, X., and Pitcher, K. W. (2002). Mercury concentrations is the Fur of Steller sea lions and northern Fur seals from Alaska. *Mar. Pollut. Bull.* 44, 1130–1135. doi:10.1016/S0025-326X(02)00167-4

Beman, J. M., Popp, B. N., and Francis, C. A. (2008). Molecular and biogeochemical evidence for ammonia oxidation by marine *Crenarchaeota* in the Gulf of California. *ISME J.* 2, 429–441. doi:10.1038/ismej.2007.118

Bernhard, A. E., Landry, Z. C., Blevins, A., de la Torre, J. R., Giblin, A. E., and Stahl, D. A. (2010). Abundance of ammonia-oxidizing *Archaea* and *Bacteria* along an estuarine salinity gradient in relation to potential nitrification rates. *Appl. Environ. Microbiol.* 76. doi:10.1128/AEM.02018-09

Bowman, K. L., Hammerschmidt, C. R., Lamborg, C. H., Swarr, G. J., and Agather, A. M. (2016). Distribution of mercury species across a zonal section of the eastern tropical South Pacific Ocean (U.S. GEOTRACES GP16). *Mar. Chem.* 186, 156–166. doi:10.1016/j.marchem.2016.09.005

Bowman, K. L., Lamborg, C. H., and Agather, A. M. (2020). A global perspective on mercury cycling in the ocean. *Sci. Total Environ.* 710. doi:10.1016/j.scitotenv.2019.136166

Chicano, T. M., Dietrich, L., de Almeida, N. M., Akram, M., Hartmann, E., Leidreiter, F., et al. (2021). Structural and functional characterization of the intracellular filament-forming nitrite oxidoreductase multiprotein complex. *Nat. Microbiol.* 6, 1129–1139. doi:10.1038/s41564-021-00934-8

Christensen, G. A., Gionfriddo, C. M., King, A. J., Moberly, J. G., Miller, C. L., Somenahally, A. C., et al. (2019). Determining the reliability of measuring mercury cycling gene abundance with correlations with mercury and methylmercury concentrations. *Environ. Sci. Technol.* 53, 8649–8663. doi:10.1021/acs.est.8b06389

Danielson, S. L., Grebmeier, J. M., Iken, K., Berchok, C., Britt, L., Dunton, K. H., et al. (2022). Monitoring Alaskan Arctic Shelf ecosystems through collaborative observation networks. *Oceanography* 35.

Dastoor, A., Angot, H., Bieser, J., Christensen, J. H., Douglas, T. A., Heimbürger-Boavida, L., et al. (2022). Arctic mercury cycling. *Nat. Rev. Earth Environ.* 3, 270–286. doi:10.1038/s43017-022-00269-w

Delwiche, C. C. (1970). The nitrogen cycle. *Sci. Am.* 233, 136–147.

Dietz, R., Outridge, P. M., and Hobson, K. A. (2009). Anthropogenic contributions to mercury levels in present-day Arctic animals – a review. *Sci. Total Environ.* 407, 6120–6131. doi:10.1016/j.scitotenv.2009.08.036

DiMento, B. P., and Mason, R. P. (2017). Factors controlling the photochemical degradation of methylmercury in coastal and oceanic waters. *Mar. Chem.* 196, 116–125. doi:10.1016/j.marchem.2017.08.006

Gilmour, C. C., Podar, M., Bullock, A. L., Graham, A. M., Brown, S. D., Somenahally, A. C., et al. (2013). Mercury methylation by novel microorganisms from new environments. *Environ. Sci. Technol.* 47, 11810–11820. doi:10.1021/es403075t

Gionfriddo, C. M., Stott, M. B., Power, J. F., Ogorek, J. M., Krabbenhoft, D. P., Wick, R., et al. (2020). Genome-resolved metagenomics and detailed geochemical speciation analyses yield new insights into microbial mercury cycling in geothermal springs. *Appl. Environ. Microbiol.* 86. doi:10.3389/fmicb.2020.541554

Gionfriddo, C. M., Tate, M. T., Wick, R. R., Schultz, M. B., Zemla, A., Thelen, M. P., et al. (2016). Microbial mercury methylation in Antarctic Sea ice. *Nat. Microbiol.* 1. doi:10.1038/nmicrobiol.2016.127

Grundle, D. S., Juniper, K., and Giesbrecht, K. E. (2013). Euphotic zone nitrification in the NE subarctic pacific: Implications for measurements of new production. *Mar. Chem.* 155, 113–123. doi:10.1016/j.marchem.2013.06.004

Hamilton, S. K., and Ostrom, N. E. (2007). Measurement of the stable isotope ratio of dissolved N_2 in ^{15}N tracer experiments. *Limnol. Oceanogr. Methods* 5, 233–240. doi:10.4319/lom.2007.5.233

Hammerschmidt, C. R., Bowman, K. L., Tabatchnick, M. D., and Lamborg, C. H. (2011). Storage bottles material and cleaning for determination of total mercury in seawater. *Limnol. Oceanogr.* 9, 426–431. doi:10.4319/lom.2011.9.426

Hammerschmidt, C. R., and Bowman, K. L. (2012). Vertical methylmercury distribution in the subtropical North Pacific ocean. *Mar. Chem.* 132-133, 77–82. doi:10.1016/j.marchem.2012.02.005

Hammerschmidt, C. R., and Fitzgerald, W. F. (2006). Methylmercury in freshwater fish linked to atmospheric mercury deposition. *Environ. Sci. Technol.* 40, 7764–7770. doi:10.1021/es061480i

Hampel, J. J., McCarthy, M. J., Aalto, S. L., and Newell, S. E. (2020). Hurricane disturbance stimulated nitrification and altered ammonia oxidizer community structure in Lake Okeechobee and St. Lucie Estuary (Florida). *Front. Microbiol.* 11. doi:10.3389/fmicb.2020.01541

Heimbürger, L., Sonke, J. E., Cossa, D., Point, D., Lagane, C., Laffont, L., et al. (2015). Shallow methylmercury production in the marginal sea ice zone of the central Arctic Ocean. *Sci. Rep.* 5. doi:10.1038/srep10318

Heiss, E. M., and Fulweiler, R. W. (2016). Coastal water column ammonium and nitrite oxidation are decoupled in summer. *Estuar. Coast. Shelf Sci.* 178, 110–119. doi:10.1016/j.ecss.2016.06.002

Hintelmann, H., and Evans, R. D. (1997). Application of stable isotopes in environmental tracer studies – measurement of monomethylmercury by isotope dilution ICP-MS and detection of species transformation. *Fresenius J. Anal. Chem.* 358, 378–385. doi:10.1007/s002160050433

Horak, R. E. A., Qin, W., Schauer, A. J., Armbrust, E. V., Ingalls, A. E., Moffett, J. W., et al. (2013). Ammonia oxidation kinetics and temperature sensitivity of a natural marine community dominated by Archaea. *ISME J.* 7, 2023–2033. doi:10.1038/ismej.2013.75

Horrigan, S. G., and Springer, A. L. (1990). Oceanic and estuarine ammonium oxidation: Effects of light. *Limnol. Oceanogr.* 35, 479–482. doi:10.4319/lo.1990.35.2.0479

Jonsson, S., Mastomonaco, M. G. N., Gardfeldt, K., and Mason, R. P. (2022). Distribution of total mercury and methylated mercury species in Central Arctic Ocean water and ice. *Mar. Chem.* 242. doi:10.1016/j.marchem.2022.104105

Kim, H., Sørensen, A. L., Hur, J., Heimbürger, L., Hahm, D., Siek Rhee, T., et al. (2017). Methylmercury mass budgets and distribution characteristics in the Western Pacific Ocean. *Environ. Sci. Technol.* 51, 1186–1194. doi:10.1021/acs.est.6b04238

Lamborg, C. H., Hammerschmidt, C. R., Bowman, K. L., Swarr, G. J., Munson, K. M., Ohnemus, D. C., et al. (2014). A global ocean inventory of anthropogenic mercury based on water column measurements. *Nature* 512, 65–68. doi:10.1038/nature13563

Lehnherr, I., Louis, V. L., Hintelmann, H., and Kirk, J. L. (2011). Methylation of inorganic mercury in polar marine waters. *Nat. Geosci.* 4, 298–302. doi:10.1038/ngeo1134

Lin, H., Ascher, D. B., Myung, Y., Lamborg, C. H., Hallam, S. J., Gionfriddo, C. M., et al. (2021). Mercury methylation by metabolically versatile cosmopolitan marine bacteria. *ISME J.* 15, 1810–1825. doi:10.1038/s41396-020-00889-4

Lomas, M. W., and Lipschultz, F. (2006). Forming the primary nitrite maximum: Nitrifiers or phytoplankton? *Limnol. Oceanogr.* 51, 2453–2467. doi:10.4319/lo.2006.51.5.2453

Lücker, S., Nowka, B., Rattei, T., Spieck, E., and Daims, H. (2013). The genome of *Nitrospina gracilis* illuminates the metabolism and evolution of the major marine nitrite oxidizer. *Front. Microbiol.* 4. doi:10.3389/fmicb.2013.00027

Mason, R. P., Choi, A. L., Fitzgerald, W. F., Hammerschmidt, C. R., Lamborg, C. H., Sørensen, A. L., et al. (2012). Mercury biogeochemical cycling in the ocean and policy implications. *Environ. Res.* 119, 101–117. doi:10.1016/j.envres.2012.03.013

McIlvin, M. R., and Altabet, M. A. (2005). Chemical conversion of nitrate and nitrite to nitrous oxide for nitrogen and oxygen isotopic analysis in freshwater and seawater. *Anal. Chem.* 77, 5589–5595. doi:10.1021/AC050528S

Médieu, A., Point, D., Itai, T., Angot, H., Buchanan, P. J., Allain, V., et al. (2022). Evidence that Pacific tuna mercury levels are driven by marine methylmercury production and anthropogenic inputs. *PNAS* 199. doi:10.1073/pnas.2113032119

Merbt, S. N., Stahl, D. A., Casamayor, E. O., Martí, E., Nicol, G. W., and Prosser, J. I. (2012). Differential photoinhibition of bacterial and archaeal ammonia oxidation. *FEMS Microbiol. Lett.* 327, 41–46. doi:10.1111/j.1574-6968.2011.02457.x

Monperrus, M., Tessier, E., Amouroux, D., Leynaert, A., Huonnic, P., and Donard, O. F. X. (2007). Mercury methylation, demethylation and reduction rates in coastal and marine surface waters of the Mediterranean Sea. *Mar. Chem.* 107, 49–63. doi:10.1016/j.marchem.2007.01.018

Motta, L. C., Blum, J. D., Popp, B. N., and Drazen, J. C. (2022). Mercury isotopic evidence for the importance of particles as a source of mercury to marine organisms. *PNAS* 119. doi:10.1073/pnas.2208183119

Munson, K. M., Babi, D., and Lamborg, C. H. (2014). Determination of monomethylmercury from seawater with ascorbic acid-assisted direct ethylation. *Limnol. Oceanogr.* 12, 1–9. doi:10.4319/lom.2014.12.1

Munson, K. M., Lamborg, C. H., Boiteau, R. M., and Saito, M. A. (2018). Dynamic mercury methylation and demethylation in oligotrophic marine water. *Biogeosciences* 15, 6451–6460. doi:10.5194/bg-15-6451-2018

Musiani, F., Broll, V., Evangelisti, E., and Ciurli, S. (2020). The model structure of the copper-dependent ammonia monooxygenase. *J. Biol. Inorg. Chem.* 25, 995–1007. doi:10.1007/s00775-020-01820-0

Newell, S. E., Fawcett, S. E., and Ward, B. B. (2013). Depth distribution of ammonia oxidation rates and ammonia-oxidizer community composition in the Sargasso Sea. *Limnol. Oceanogr.* 58, 1491–1500. doi:10.4319/lo.2013.58.4.1491

Ortiz, V. L., Mason, R. P., and Ward, J. E. (2015). An examination of the factors influencing mercury and methylmercury particulate distributions, methylation and demethylation rates in laboratory generated marine snow. *Mar. Chem.* 177, 753–762. doi:10.1016/j.marchem.2015.07.006

Ouerdane, L., Mester, Z., and Meija, J. (2009). General equation for multiple spiking isotope dilution mass spectrometry. *Anal. Chem.* 81. doi:10.1021/ac900205b

Parks, J. M., Johs, A., Podar, M., Bridou, R., Hurt, R. A., Smith, S. D., et al. (2013). The genetic basis for bacterial mercury methylation. *Science* 339, 1332–1335. doi:10.1126/science.1230667

Schartup, A. T., Ndu, U., Balcom, P. H., Mason, R. P., and Sunderland, E. M. (2015). Contrasting effects of marine and terrestrially derived dissolved organic matter on mercury speciation and bioavailability in seawater. *Environ. Sci. Technol.* 49, 5965–5972. doi:10.1021/es506274x

Shiozaki, T., Ijichi, M., Fujiwara, A., Makabe, A., Nishino, S., Yoshikawa, C., et al. (2019). Factors regulating nitrification in the Arctic Ocean: Potential impact of sea ice reduction and ocean acidification. *Glob. Biogeochem. Cy.* 33, 1085–1099. doi:10.1029/2018GB006068

Shiozaki, T., Ijichi, M., Isobe, K., Hashihama, F., Nakamura, K., Ehama, M., et al. (2016). Nitrification and its influence on biogeochemical cycles from the equatorial Pacific to the Arctic Ocean. *ISME J.* 10, 2184–2197. doi:10.1038/ismej.2016.18

Sonke, J. E., Teisserenc, R., Heimbürger-Boavida, L., Petrova, M. V., Marusczak, N., Le Dantec, T., et al. (2018). Eurasian river spring flood observations support net Arctic Ocean mercury export to the atmosphere and Atlantic Ocean. *PNAS* 115. doi:10.1073/pnas.1811957115

Sørensen, A. L., Jacob, D. J., Schartup, A. T., Fisher, J. A., Lehnherr, I., Louis, St.V. L., et al. (2016). A mass budget for mercury and methylmercury in the Arctic Ocean. *Glob. Biogeochem. Cy.* 30, 560–575. doi:10.1002/2015GB005280

Stabeno, P. J., Bell, S., Cheng, W., Danielson, S., Kachel, N., and Mordy, C. W. (2016). Long-term observations of Alaska coastal current in the northern Gulf of Alaska. *Deep Sea Res. II Top. Stud. Oceanogr.* 132, 24–40. doi:10.1016/j.dsr2.2015.12.016

Stabeno, P. J., Bond, N. A., Hermann, A. J., Kachel, N. B., Mordy, C. W., and Overland, J. E. (2004). Meteorology and oceanography of the northern Gulf of Alaska. *Cont. Shelf Res.* 24, 859–897. doi:10.1016/j.csr.2004.02.007

Starr, L. D., McCarthy, M. J., Hammerschmidt, C. R., Subramaniam, A., Despins, M. C., Montoya, J. P., et al. (2022). Mercury methylation linked to nitrification in the tropical North Atlantic Ocean. *Mar. Chem.* 247. doi:10.1016/j.marchem.2022.104174

Strom, S. L., Brady Olson, M., Macri, E. L., and Mordy, C. W. (2006). Cross-shelf gradients in phytoplankton community structure, nutrient utilization, and growth rate in the coastal Gulf of Alaska. *Mar. Ecol. Prog.* 328, 75–92.

Sunderland, E. M., Krabbenhoft, D. P., Moreau, J. W., Strode, S. A., and Landing, W. M. (2009). Mercury sources, distribution, and bioavailability in the North Pacific Ocean: Insights from data and models. *Glob. Biogeochem. Cy* 23. doi:10.1029/2008GB003425

Sunderland, E. M., and Mason, R. P. (2007). Human impacts on open ocean mercury concentrations. *Glob. Biogeochem. Cy.* 21. doi:10.1029/2006GB002876

Swift, J. H., and Aagaard, K. (1976). Upwelling near samalga pass. *Limnol. Oceanogr.* 21, 339–408. doi:10.4319/lo.1976.21.3.0399

Tada, Y., Marumoto, K., and Takeuchi, A. (2021). *Nitrospina*-like bacteria are dominant potential mercury methylators in both the Oyashio and Kuroshio regions of the Western North Pacific. *Environ. Microbiol.* 9. doi:10.1128/Spectrum.00833-21

Tada, Y., Marumoto, K., and Takeuchi, A. (2020). *Nitrospina*-like bacteria are potential mercury methylators in the mesopelagic zone in the East China Sea. *Front. Microbiol.* 11. doi:10.3389/fmicb.2020.01369

Villar, E., Cabrol, L., and Heimbürger-Boavida, L. (2020). Widespread microbial mercury methylation genes in the global ocean. *Environ. Microbiol. Rep.* 12, 277–287. doi:10.1111/1758-2229.12829

Wang, K., Munson, K. M., Beaupre-Laperriere, A., Mucci, A., Macdonald, R. W., and Wang, F. (2018). Subsurface seawater methylmercury maximum explains biotic mercury concentrations in the Canadian Arctic. *Sci. Rep.* 8. doi:10.1038/s41598-018-32760-0

Yool, A., Martin, A. P., Fernández, C., and Clark, D. R. (2007). The significance of nitrification for oceanic new production. *Nature* 447, 999–1002. doi:10.1038/nature05885

Zolkos, S., Zhulidov, A. V., Gurtovaya, T. Y., Gordeev, V. V., Berdnikov, S., Pavlova, N., et al. (2022). Multidecadal declines in particulate mercury and sediment export from Russian rivers in the pan-Arctic basin. *PNAS* 119. doi:10.1073/pnas.2119857119

frontiers | Frontiers in Environmental Chemistry

TYPE Original Research
PUBLISHED 13 June 2023
DOI 10.3389/fenvc.2023.1202957

OPEN ACCESS

EDITED BY
Robert Peter Mason,
University of Connecticut, United States

REVIEWED BY
Kenjiro Toyota,
Environment and Climate Change Canada, Canada
Christopher Holmes,
Florida State University, United States

*CORRESPONDENCE
Mae Sexauer Gustin,
mgustin@unr.edu

RECEIVED 09 April 2023
ACCEPTED 01 June 2023
PUBLISHED 13 June 2023

CITATION
Gustin MS, Dunham-Cheatham SM, Choma N, Shoemaker KT and Allen N (2023), Determining sources of reactive mercury compounds in Reno, Nevada, United States.
Front. Environ. Chem. 4:1202957.
doi: 10.3389/fenvc.2023.1202957

Determining sources of reactive mercury compounds in Reno, Nevada, United States

Mae Sexauer Gustin[1]*, Sarrah M. Dunham-Cheatham[2], Nicole Choma[1], Kevin T. Shoemaker[1†] and Natalie Allen[1]

[1]Department of Natural Resources and Environmental Science, University of Nevada, Reno, NV, United States, [2]College of Agriculture, Biotechnology and Natural Resources, University of Nevada, Reno, NV, United States

There is much uncertainty regarding the sources of reactive mercury (RM) compounds and atmospheric chemistry driving their formation. This work focused on assessing the chemistry and potential sources of reactive mercury measured in Reno, Nevada, United States, using 1 year of data collected using Reactive Mercury Active System. In addition, ancillary meteorology and criteria air pollutant data, Hybrid Single-Particle Lagrangian Integrated Trajectory (HYSPLIT) analyses, and a generalized linear model were applied to better understand reactive mercury observations. During the year of sampling, a fire event impacted the sampling site, and gaseous elemental Hg and particulate-bound mercury concentrations increased, as did Hg^{II}-S compounds. Data collected on a peak above Reno showed that reactive mercury concentrations were higher at higher elevation, and compounds found in Reno were the same as those measured on the peak. HYSPLIT results demonstrated RM compounds were generated inside and outside of the basin housing Reno. Compounds were sourced from San Francisco, Sacramento, and Reno in the fall and winter, and from long-range transport and the marine boundary layer during the spring and summer. The generalized linear model produced correlations that could be explained; however, when applying the model to similar data collected at two other locations, the Reno model did not predict the observations, suggesting that sampling location chemistry and concentration cannot be generalized.

KEYWORDS

GOM, HYSPLIT, PBM, RM chemistry, thermal desorption

Introduction

There are three different forms of mercury (Hg) in the atmosphere: gaseous elemental Hg (GEM), gaseous oxidized Hg (GOM), and particulate-bound mercury (PBM). The latter two, collectively known as reactive Hg (RM), have higher deposition velocities than GEM, are scrubbed from the air during precipitation, and are more readily methylated. Thus, GOM and PBM have a greater impact on ecosystems. The automated instrument (Tekran 1130/1135/2537) used for ~20 years to determine atmospheric Hg concentrations does not accurately measure GOM and PBM (Gustin et al., 2013; Gustin et al., 2019; Luippold et al., 2020a Luippold et al., 2020b; Osterwalder et al., 2021; Dunham-Cheatham et al., 2023). Because of the lack of accurate RM measurements by the Tekran system, alternative measurement systems have been developed. These include an active membrane-based system with which RM, GOM, and PBM concentrations and chemistry can be determined (Luippold et al., 2020a), and dual channel systems (DCS) that allow for

GRAPHICAL ABSTRACT

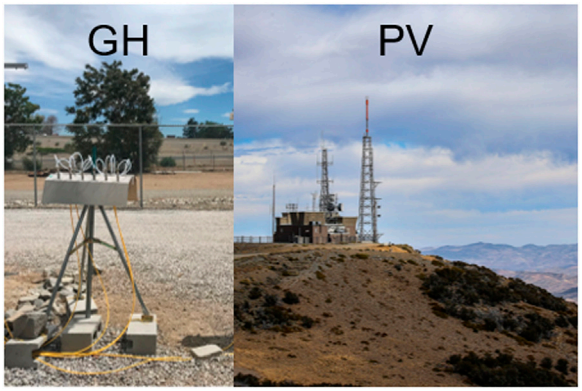

10–20 min resolution of operationally-defined GOM measurements (Ambrose et al., 2013; Gustin et al., 2023; Lyman et al., 2020).

Previous work with data reported here, using the University of Nevada, Reno (UNR)—Reactive Mercury Active System (RMAS), two DCS, and a Tekran 2537/1130 system co-located at the College of Agriculture, Biotechnology and Natural Resources Valley Road Greenhouse Complex (GH), assessed the comparability of the measurements and used a custom-designed calibrator to verify the accuracy of DCS measurements (Lyman et al., 2020; Dunham-Cheatham et al., 2023). RM and GOM concentrations measured by the RMAS were lower than those measured by the DCSs by 30% (UNR) and 50% (Utah State University). Because of these findings, we acknowledge that RMAS RM and GOM concentrations are underestimated.

Nylon membranes, used in the RMAS, are thermally desorbed to qualitatively identify potential RM and GOM compounds. Because it has been determined these membranes do not collect all compounds with equal efficiency (Huang et al., 2013; Gustin et al., 2023), observations using these surfaces have uncertainty. In addition, compounds are identified by comparing desorption profiles developed using purchased high purity compounds that may not reflect the chemistry in ambient air. Based on work by Jones and Lyman (2016), who used a GC-MS, it is known that $HgBr_2$ and $HgCl_2$ are emitted from permeation tubes housing these compounds; however, this has not been demonstrated for HgO, $HgN_2O6 \cdot H_2O$, or $HgSO_4$ that were added in Gustin et al. (2015), due to the fact that they cannot be loaded into the current GC-MS configuration. However, since high purity Hg compounds were used for the latter 3 compounds, it was assumed they represent oxide, nitrogen, and sulfur-based compounds, although the exact chemistry is not known. For example, is it unlikely HgO was permeated given its low vapor pressure, and it was suggested by Huang et al. (2013) that since what was emitted was a vapor it might be Hg_2O. Standard profiles developed using this permeation tube method are comparable to those developed using similar compounds added to coal fly ash (Rumayor et al., 2013; Rumayor et al., 2015). An additional uncertainty is whether reactions occur on the membranes. To test this accurately, a calibrator is needed. A custom-designed calibrator is now available and being used to test stability of compounds on the membranes. In order to do this quantitatively, the amount of the specific compound being added needs to be known and this requires permeation using a calibrator. Permeation of compounds is difficult and requires inert surfaces and controlled temperatures. Mao and Khalizov (2021) showed that GOM sorbed to a Cole-Parmer PES membrane surface exhibited exchange interactions with co-adsorbed GOM. Similar interactions could also influence our results. Mao and Khalizov's (2021) results were obtained using GOM concentrations that were 5-orders of magnitude higher than ambient background concentrations. More testing is necessary to determine whether similar reactions occur under ambient concentrations, and whether RMAS membrane surfaces influence RM retention. Despite the fact it is not known what the exact chemistry of the measured RMAS compounds are, this is currently the best method available for understanding Hg chemistry of oxidized Hg under ambient conditions.

Manuscripts with RMAS data from the GH have been published. One determined RM concentrations and chemistry, with data collected from March 2018 to March 2019, and focused on comparing data with those obtained at 3 other locations in Hawaii, Utah, and Maryland (Luippold et al., 2020a; Luippold et al., 2020b). Another reported on the ability of the RMAS system to measure PBM and GOM (Gustin et al., 2023). In addition, this location has been used for developing and testing methods for measurement of RM (*cf.* Dunham-Cheatham et al., 2020; Dunham-Cheatham et al., 2023).

In a recent paper, Lyman et al. (2022) did not observe a daily buildup of Hg^{II} concurrent with ozone build up during photochemical smog episodes in a remote location affected by oil and gas recovery, casting doubt on the current theory of gas-phase Hg oxidation kinetics and mechanisms. During an inversion, oxide-Hg^{II} compounds disappeared, leading to the conclusion that oxide-Hg^{II} compounds were sourced from the free troposphere. Halogenated, S, N, and organic Hg^{II} compounds were present during this time, indicating possible production. Data from the GH site, that is adjacent to a major interstate highway, allowed for testing whether this finding is applicable at a location impacted by road traffic.

Data for our analyses, collected from November 2019 to 2020, included: RM, GOM, and PBM chemistry and concentrations determined with two RMAS, and GEM measured using a Tekran 2537. Local air chemistry and meteorological measurements were compiled, and HYSPILT back trajectory analyses were done for 24 h and for the full duration of sampling. The latter allowed for estimating the time air spend at two heights [> or <2 km above ground level (agl)]

and in 6 source regions. During this time, a fire event impacted Reno, providing the opportunity to assess the impact on GEM and RM concentrations and chemistry. To further investigate sources of RM to Reno, two RMAS were deployed in Fall 2022 at the GH location and at Peavine Peak (PV; adjacent to and above Reno) to compare chemistry and concentrations.

Data collected were used within a generalized linear model (GLM) to test if this type of analysis could provide a means of characterizing conditions that lead to different RM concentrations and chemistry. The GLM developed for Reno was then applied to two other locations to determine if it could predict observations at other locations.

Our working hypothesis was that reactive -N, -S, and organic-based Hg^{II} compounds measured in Reno were locally/regionally sourced, oxide-based compounds were derived from the free troposphere, and halogenated compounds were sourced from the free troposphere and the marine boundary layer.

Materials and methods

Site descriptions

From 11/21/19 (month/day/year) to 11/24/20, two RMAS were deployed along with a Tekran 2537B to determine GOM, PBM, RM, and GEM at the University of Nevada, Reno Valley Road Greenhouse Complex [GH; 39.5375 N latitude, 119.8047 W longitude, elevation 1,368 m above sea level (masl)]. A fire event impacted Reno from 08/18/20 to 09/15/20 with two periods of heavy smoke. From 09/29/22 to 11/03/22, two RMAS were deployed simultaneously at the GH and on Peavine Peak (PV; 39.589389 N, 119.928797 W, 1940 masl).

A Tekran 2537B, used to measure GEM, was operated and maintained following protocols used by the National Atmospheric Deposition Program Atmospheric Mercury Network. The RMAS consists of a 25.4 mm-thick bent, anodized aluminum weather shield housing six dual- or triple-stage perfluoroalkoxy alkane (PFA) filter packs connected to vacuum pumps (KNF Neuberger Inc., 34 L per minute (Lpm) capacity; and Welch) stored inside or in a pump box. Ambient air flow was controlled by critical flow orifices (Teledyne API) at 1 Lpm, nominal. Flow rates through each filter pack were checked at the beginning and end of each deployment. All flow measurements were normalized to represent air flow at standard temperature and pressure conditions (0°C and 1 atm). For details, see Luippold et al. (2020b). Membranes used to collect GOM and PBM were cation exchange membranes (CEM; 0.8 µm pore size; Mustang-S, Pall Corporation®) and polytetrafluoroethylene (PTFE) membranes (0.2 µm pore size, 47 mm diameter; Sartorius Stedium Biotech®), respectively.

One RMAS was configured to measure RM concentrations and chemistry using triplicate two-in-line CEMs and triplicate two-in-line nylon membranes (0.2 µm pore size, Sartorius) in dual-stage filter packs, respectively. The second RMAS was identical to the first system, but used triple-stage filter packs that allowed for a PTFE membrane upstream of the two CEM or nylon membranes. The PTFE membrane was used to separate PBM (>0.2 µm) from GOM. Fourteen-day sampling periods were conducted from 12/17/19 through 07/15/20, and seven-day sampling periods occurred from 11/11/19 to 12/17/19 and 07/15/20 to 11/24/20. Deployment durations of 14 days during the winter were utilized due to low RM concentrations, and in the spring of 2020 were a result of institutional restrictions as a result of the COVID-19 pandemic.

Analyses

CEM, PTFE, and downstream nylon membranes were analyzed for total Hg following EPA Method 1631, Revision E (United States Environmental Protection Agency, 2002). Hg compounds were released by thermal desorption from upstream nylon membranes with subsequent thermal reduction through pyrolysis (388°C) to GEM and analyzed by cold vapor atomic fluorescence spectrometry using a Tekran 2537A (detection limit <0.1 $ng \cdot m^{-3}$). For details about both methods, see the Supplementary Material. It is important to note that compounds desorbed are described as specific classes of compounds (i.e., –O, –N, –S, halogenated, and organic). Since $HgBrNO_2$ and HgBrOH are thought to be abundantly produced in GEM oxidation (Shah et al., 2021), it is uncertain whether these would be identified as a N, halogen, or O-based Hg^{II} compound. More sophisticated methods are under development (e.g., GC-MS) to more definitively identify these compounds; however, until those methods have been developed and vetted for accuracy, the thermal desorption system presented here provides a basis for understanding RM compounds.

HYSPLIT back trajectories

Back trajectory simulations were performed for each sampling period for this study using the NOAA Air Resources Laboratory GDAS1° data archive and Hybrid Single-Particle Lagrangian Integrated Trajectory (HYSPLIT) model (http://ready.arl.noaa.gov/HYSPLIT.php, last access: 2023). Trajectories for the time of sampling were performed using a gridded frequency distribution method (Gustin et al., 2023). Trajectories were initiated every 4 h (00:00, 04:00, 08:00, 12:00, 16:00, 20:00 PST) from 9 points within a 0.5° × 0.5° horizontal grid centered on each site with four arrival heights (500, 1,000, 1,500, 2,000 magl), resulting in 216 trajectories per day. Generating a large number of trajectories provides for a reasonable representation of air mass transport (Stohl et al., 2002; Stohl et al., 2003; Weiss-Penzias et al., 2006).

Trajectory residence times were calculated for 6 source boxes (Eurasia, East Asia, north western and north eastern Pacific Ocean, Canada, and the United States; coordinate boundaries can be found in Supplementary Table S1). The boundary layer height was defined as 2,000 magl. Mixed layer depth was calculated in HYSPLIT. Two categories of trajectories were calculated for this study: 1) Twenty-four-h trajectories were generated to look at the path of regional air masses, and were calculated for the 24-hour period immediately before sample collection; and 2) trajectories were also calculated for the entire sampling duration (7 or 14 days) in order to determine the residence time of the sampled air that was above and below 2 km altitude and in the 6 source boxes. The 2 km boundary layer height was chosen because, due to high convective mixing, this is a typical boundary layer height for Reno.

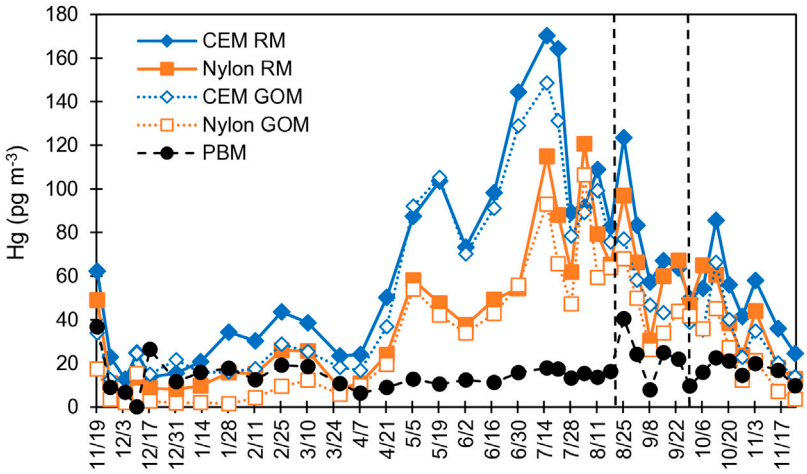

FIGURE 1
Time series of the CEM and nylon membrane-derived RM and GOM concentrations for the GH. PBM was derived from upstream PTFE membranes. Vertical lines delineate the start (left) and end (right) of the fire event. Dates indicate sample harvest dates.

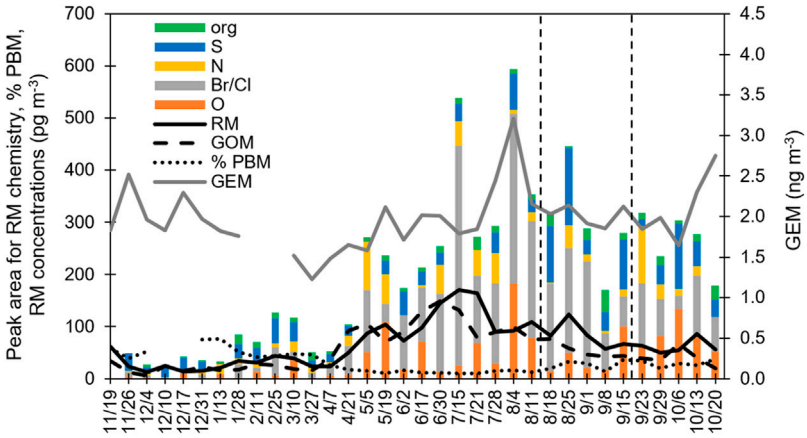

FIGURE 2
Time series of data developed at the GH: RM concentrations measured with the CEM; GEM measured by the Tekran 2537; %PBM, as determined using the Hg concentration on the PTFE membrane divided by the total Hg concentration for the PTFE membrane plus both CEM; and peak area for the different Hg^{II} compounds; and maximum mixing height (magl), calculated using HYSPLIT. Lines delineate the start (left) and end (right) of the fire event. Dates indicate sample harvest dates. Columns represent the RM chemistry based on peak area.

Ancillary data

Criteria air pollutant and meteorological data were downloaded from local monitoring stations. For complete details, see the Supplementary Material. During the PV-GH comparison, ancillary data for the GH site were obtained from the same locations as for the year-long measurements.

Statistical analyses and modeling

Statistical analyses, including correlations, regressions, and t-tests, were performed in Microsoft Excel using the data analysis tool.

A generalized linear model (GLM) was applied to better understand factors impacting RM chemistry. Response variables (RM, GOM, PBM, and specific chemistry of compounds) were modeled separately as a function of predictor variables (Supplementary Table S2). Predictor variables were first removed to maintain pairwise correlations (Pearson's ρ) $\leq$ 0.8 to reduce multicollinearity. For each response variable, a recursive feature elimination procedure was used ('rfe' function, with Random Forest method) and implemented in the 'caret' package (Kuhn, 2020) in R (R Core Team, 2020; version 4.0.2) to identify the set of predictor variables that optimized predictive performance under repeated cross-validation. Then, each response variable was modeled as a log-linear function of the top predictor variables identified above using a GLM with Gamma error distribution and an offset term (log of the number of sampling days) to account for

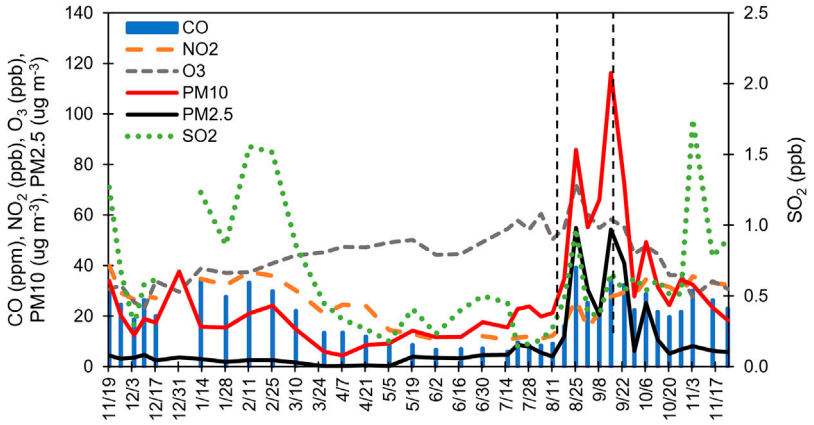

FIGURE 3
Criteria air pollutants measured by Washoe County and uploaded from EPA's Air Quality System database for the duration of the sampling campaign. Lines delineate the start (left) and end (right) of the fire event. Dates indicate sample harvest dates.

differences in sampling effort. Finally, reverse stepwise selection was used to remove any non-influential regression terms using Akaike's Information Criterion (Burnham and Anderson, 2002) as a model selection criterion. For each model, multiple goodness-of-fit tests were implemented in the 'DHARMa' package (Hartig, 2022) in R, including tests for uniformity of residuals, outliers, and overdispersion. The GLM was applied to similar data collected with RMAS at two additional field sites: 1) near Great Salt Lake at two locations, one adjacent to the lake at Antelope Island State Park marina (AISP; 41.060451 N, 112.238430 W, 1,283 masl) and another 11 km directly east of Antelope Island State Park location (41.084985, −112.111791, 1,288 masl); and 2) Georgia Tech campus in Atlanta, adjacent to a 14-lane highway (33.778463, −84.391425, 286 masl) (Gustin et al., 2023).

Results and discussion

General trends

In general, RM concentrations during this study were highest in the spring/summer (80–170 pg·m^{-3}), and lower in the fall/winter (20–80 pg·m^{-3}; Figures 1, 2). Comparing RMAS data from Gustin et al., 2023; October 2019 to January 2020), concentrations of up to 300 pg·m^{-3} were observed in October and declined to 25 pg·m^{-3} in January. Luippold et al. (2020a) and Luippold et al. (2020b) presented RMAS data from 2018 to 2019, with RM concentrations of 100–150 pg·m^{-3} from June to the end of October. Peterson et al. (2009) reported on Tekran Hg measurements made over 3 years (2005–2007) at Desert Research Institute (39.57 N, 119.80 W, 1,509 masl), 5 km north and 165 m above the GH site. Concentrations were highest in the summer, with the 3-year average for GOM being 26 ± 35 pg·m^{-3}, and ranging between 0 and 401 pg·m^{-3}. They also noted a diel pattern, with higher concentrations during the day, similar to ozone. Lyman and Gustin (2008) found, when comparing Tekran data collected at Desert Research Institute with that from a location 9 km east of Reno, that increased concentrations of GEM and PBM occurred when there was little atmospheric mixing, and suggested local sources were important for enhancing GEM and PBM concentrations in Reno. Concentrations of GOM and PBM measured with a Tekran system in Reno were on average 18 ± 22 and 7 ± 7 pg·m^{-3} (maximum of 177 pg·m^{-3}), respectively, and were higher during periods with higher temperature and lower dew point. Lyman and Gustin (2008) suggested higher GOM concentrations at the DRI location support the hypothesis that subsiding dry air from the free troposphere was a source of GOM to the surface.

Spring and summer

From 05/05/2020 to 07/21/20, RM concentrations were typically >100 pg·m^{-3} (Figure 1). During this time, halogenated compounds were dominant, making up 45%–78% of the compounds measured (Figure 2; Supplementary Material). Other compounds present were O, N, and S, with percentages varying week-to-week. Oxide-Hg^{II} compounds were, in general, higher during this time (Supplementary Figure S1; Supplementary Table S3). Organic compounds were typically ~5%.

High RM has been found to be associated with the tropopause (Lyman and Jaffe, 2012). NOAA operated their Tunable Optical Profiler for Aerosol and oZone lidar (TOPAZ) on June 17, 23, 24, and July 1, 2, 6, 8, 9, 10, and 16-17-2020. Elevated ozone layers consistent with stratospheric intrusions were observed on June 24 and July 8, but both remained above 7,000 masl and would not have impacted the surface anywhere near the sampling location (Andrew Langford, NOAA, personal communication). Thus, oxide compounds were not derived from the stratosphere.

During spring/summer, temperature and absolute humidity (or the mass of H_2O vapor per air volume) were higher, while RH (water vapor present relative to the amount of water needed for saturation) was lowest (Supplementary Figure S2) relative to the fall/winter. Wind speeds were also highest in the spring. Ozone concentrations were higher (50 ppbv) in the summer, compared to the fall/winter (30–40 ppbv; Figure 3). Fine et al. (2015) reported on sources of

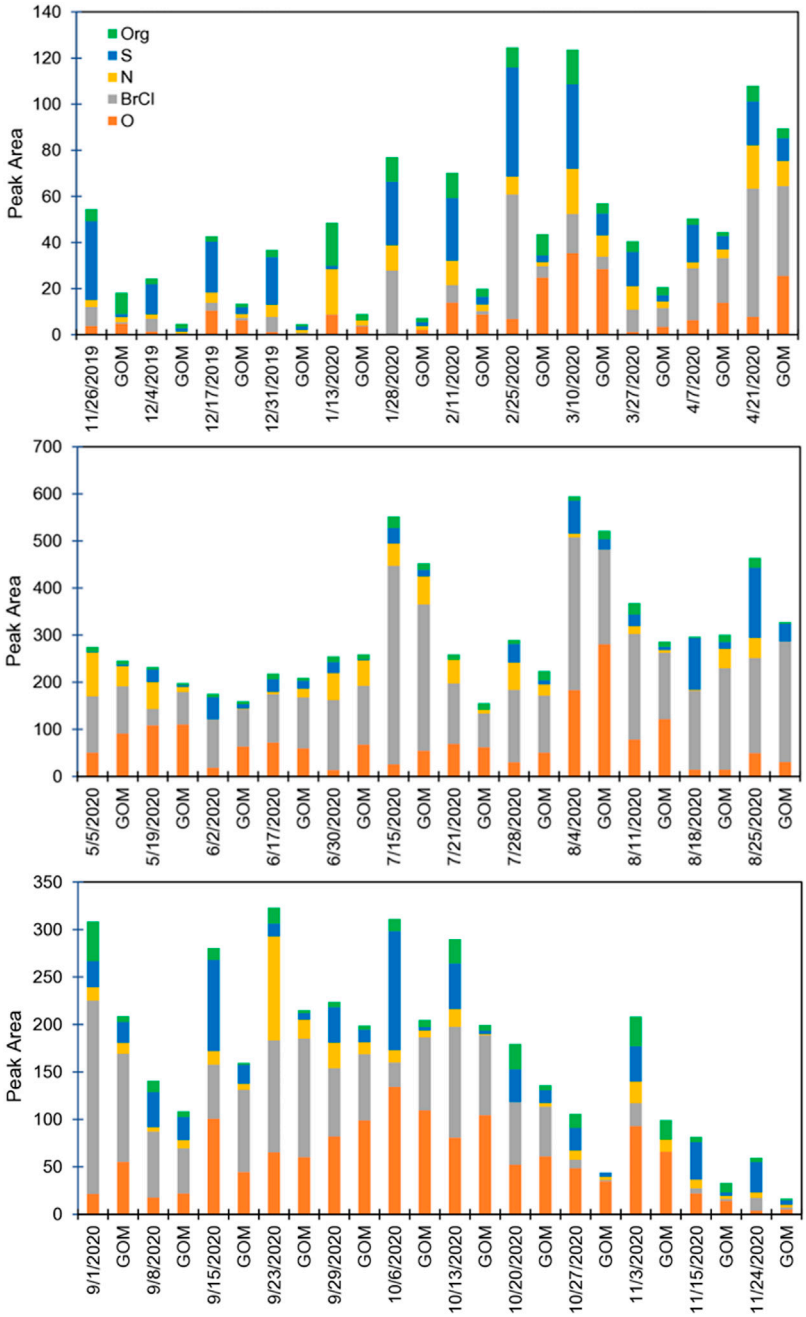

FIGURE 4
Peak areas of deconvoluted thermal desorption profiles for the specific compounds from nylon membranes at GH. Data associated with a date are RM measurements, with the corresponding GOM measurement to the right for the same sampling period. Dates indicate sample harvest dates.

ozone to Nevada and found peak ozone concentrations in late spring to early summer across the state due to long-range transport.

Most of the trajectory analyses during the spring and summer were done over the 14 days of sampling, with the exception being 07/21/20 (7 days). Trajectories for the duration of sampling were primarily (>50%) situated over the Pacific Ocean, with few exceptions (Supplementary Table S4). Mixing heights were higher during this time than in fall/winter (Supplementary Figure S3), which would allow for capture of air masses entering the area from >2,000 magl. The dry air and higher temperatures promoted vertical mixing. Ozone concentrations were also higher, indicating inputs from the free troposphere (*cf.* Fine et al., 2015).

Twenty-four h trajectories showed that when air masses originated from generally unpolluted areas, S-Hg^{II} compounds were present, suggesting, in this case, these compounds are not regionally sourced and were associated with long-range transport. When air was primarily over the United States and the Pacific Ocean (e.g., July and August), S-Hg^{II} compounds were less abundant. This

suggests that Eurasia/Asia was a likely source of these compounds. VanCuren and Gustin (2015), in a study investigating sources of ozone, using Interagency Monitoring of Protected Visual Environments network data, to Lassen and Great Basin National Parks, found that long-range transport contributed SO_4 aerosol that was associated with soil with reacted sea salt, mineral-bound SO_4, and mineral-bound NO_3. S-Hg^{II} compounds were primarily aerosol (Figure 4).

Since during this time long-range transport was the dominant air movement, and high convective mixing occurred, this indicates that halogenated compounds were derived from the marine boundary layer, and oxide and sulfur compounds were derived from long-range transport.

Fall and winter

During the fall and winter, RM concentrations were lower (<80 pg·m^{-3}) compared to spring/summer (Figure 1). CEM PBM was 40%–78% of RM, while from May to early September it was typically less than 20% (Figure 2). This indicates that during the fall/winter, local and regional pollution affected Reno air, while in the spring/summer, air from the free troposphere with little particulate matter was important. From mid-November through March, when sampling durations were predominantly 7 days, S-Hg^{II} compounds made up the highest percentage of RM compounds, ranging from 30% to 78% of total RM. In general, as PBM decreased so did S-Hg^{II}-based compounds, based on both peak area and proportion (Figure 2; Supplementary Material). S-Hg^{II} compounds also were highest for RM, indicating most of the S-based compounds were present as aerosol (Figure 4). It is important to note that when using the 7-day trajectories, we were not accounting for the air mass additions beyond the 7-day analyses, thus other areas could have contributed.

Oxide, N, halogenated, and organic-based Hg^{II} compounds were each typically 20% or less of the total RM, with a few time periods when values were higher. Oxide-based Hg^{II} compound concentrations were low in general, except for the fall 2020 when they were 25%–45% of the compounds present and long-range transport was important. For one sampling period, they were the dominant compound (5/19/20). O and halogenated compounds were often higher in concentration on the nylon membrane after the PTFE membrane, but not regularly, indicating the chemistries of PBM and GOM were different. This was not true for other compounds.

Local SO_2 concentrations were highest in the fall/winter, with concentrations up to 1.8 ppb, compared to spring/summer (<0.6 ppb; Figure 3). CO similarly had higher concentrations in the fall/winter (40 ppm) compared to the spring/summer (20 ppm). NO_2 concentrations were higher in the fall and winter (30 ppb), versus 10 ppb in spring/summer. During fall and winter, N-Hg^{II} compound peak areas were 10%–20%, higher than spring/summer when they were typically <10%.

During this time, maximum mixing heights were ~1,500–2,000 magl, lower than the spring/summer (2,000–4,000 magl; Supplementary Figure S3). Many of the 24 h trajectories during this time were from urban areas, including San Francisco-Sacramento (Supplementary Table S3), suggesting regional transport of Hg^{II} compounds. Since air masses from these highly populated areas were directly impacting Reno, it is possible these areas contributed to the observed oxide, N, and S-Hg^{II} compounds. Because PBM was high, and local SO_2 and NO_2 concentrations were also high, it is possible that N and S-Hg^{II} compounds were produced locally. In the winter, Reno is prone to inversions, and smoke and exhaust from wood burning is captured in the stagnant air mass. This also fits in with the observation by Lyman and Gustin (2008) that Tekran-based PBM measurements increased when there was little mixing in the valley where Reno is situated.

Specific membrane details

Percent PBM collected on the PTFE membrane in front of the nylon membrane was typically higher than that on the PTFE in front of the CEM (Supplementary Figure S4; Nylon PBM = 0.8 * CEM PBM, r^2 = 0.79, p < 0.001), due to the fact that the nylon membrane does not capture all compounds with equal efficiency, and typically exhibits lower concentrations than the CEM (Figure 1).

Nylon and CEM with and without upstream PTFE membranes demonstrated similar trends in concentrations (Figure 1). CEM and CEM + PTFE were correlated (CEM + PTFE = 1.0 * CEM, r^2 = 0.96 p < 0.001), as were nylon and nylon + PTFE (nylon + PTFE = 1.1 * nylon, r^2 = 0.95, p < 0.001). On average, nylon membranes were less efficient at capturing Hg^{II} than the CEM by 34%, as previously noted for this location (Gustin et al., 2023; Dunham-Cheatham et al., 2023). During the winter, the disparity between the concentrations measured on the CEM and nylon membranes was ~20 pg·m^{-3}, while in the spring this increased to 40 pg·m^{-3} (Figure 1), indicating that during spring there were compounds present the nylon membrane was not efficiently capturing. Breakthrough was consistent for both membrane types across the sampling period (for details see the Supplementary Material), indicating that the forms not being captured were likely reduced on the nylon membrane.

Specific case studies

Percent PBM for the PTFE membranes in front of the nylon and CEMs were most similar during the fire event (08/18/20 to 09/15/20; Supplementary Figure S4). $PM_{2.5}$ during the study was typically 5–10 and PM_{10} was 20–40 μg·m^{-3}, while concentrations during the fire were 30–55 and 120–160 μg·m^{-3}, respectively. Percent PBM increased to 30% during time periods when Reno was heavily impacted by wildfire smoke (Figures 1, 2). During this fire event, $PM_{2.5}$ and PM_{10} exceeded U. S. Environmental Protection Agency Air Quality Standard for $PM_{2.5}$ of 15 μg·m^{-3} during distinct time periods (August 16, 19–23, 25, 27–30, September 3, 7, 11–17, 2020; Washoe County, 2021). S-based Hg^{II} compounds increased during the fire event, corresponding with increases in GEM and PBM, indicating the potential for generation of these compounds associated with fire events (Figures 2; Supplementary Material). NO_2, CO, and SO_2 concentrations also increased during the fire event (Figure 3). RM and GOM concentrations did not increase.

When sampling in fire plumes, elevated GOM concentrations have not been measured (*cf.* Friedli et al., 2003). Observations indicated that RM chemistry could reflect inputs due to fire events, likely due to production of aerosol-based S-Hg^{II} compounds.

On 1/13/20, the 24 h trajectory showed air moving over the Pacific and Sacramento (Supplementary Figure S5). Halogenated, S, O, N, and organic-Hg^{II} compounds were 1, 3, 18, 40, and 38%, respectively, of the total RM chemistry (Supplementary Table S3), and PBM was 77% of the total RM concentrations. Trajectories showed air at < 2 km traveled over the Pacific Ocean and United States. During this time, the 14-day trajectories were fast-moving, starting north of Reno and traveling around the Northern Hemisphere over Eurasia. The high % PBM and lack of halogenated compounds suggests that S, O, N and organic-Hg^{II} compounds were derived regionally.

On 2/11/20, halogenated compounds were 11% of the RM compounds (Supplementary Table S3), while S-Hg^{II} compounds were high (40% of RM), and PBM was 41%. Twenty-four h trajectories showed that air was transported into the sampling location from rural areas in central Oregon and Washington (Supplementary Figure S5). Trajectories indicated that air <2 km was primarily over the United States and >2 km originated in Eurasia, then traveled over the Pacific Ocean into the United States. This suggests long-range transport as the origin of the S-based RM compounds.

On 5/19/20, O compounds were the dominant RM compound (48%), and Br/Cl (12%), N (25%), and S (10%) compounds were present at lower concentrations. PBM during this sampling period was low (10%). Twenty-four h trajectories indicated air moved in from the Central California Coast, over the Sierra Nevada Mountains, and into Reno (Supplementary Figure S5). Trajectories indicated that air at < 2 km passed primarily over the Pacific Ocean with some interaction with Asia/Eurasia at both below and above 2 km. Oxide and halogenated compounds were likely derived from the free troposphere and marine boundary layer, respectively, with N and S compounds coming from regional sources. S compounds could also be sourced from the marine boundary layer.

Lastly, for the week ending 10/6/20, O and S compounds were dominant, while N, halogenated, and organic compounds were <10%. The 24-h trajectory showed air moving in from San Francisco and Sacramento, while trajectories originated over the United States for <2 km (40% of the trajectory points) and predominately over the US for the >2 km (38%) with less time over the Eastern Pacific Ocean (Supplementary Figure S5). This suggests a local/regional source for these compounds.

Peavine-greenhouse comparison

In the 2022 PV-GH comparisons, samples were collected weekly and on the same day at both locations. RM concentrations at PV and GH ranged from 33 to 182 and 32–80 $pg{\cdot}m^{-3}$, respectively (Supplementary Figure S6 top panel). Concentrations decreased as temperatures cooled and a storm front moved in. RM concentrations at PV were always higher than at GH, except for the last sampling period due to the fast-moving storm that came in during the previous sampling period with average wind speeds of 2.3 $m{\cdot}s^{-1}$ that was followed by 0.2 mm of precipitation; concentrations at the GH and PV were the same during this time due to turbulent mixing, and RM concentrations decreased due to removal by precipitation.

PBM concentrations were always higher at the GH (9–45 $pg{\cdot}m^{-3}$) than at PV (4–6 $pg{\cdot}m^{-3}$), with the exception being the time period impacted by the storm event when it was 6 and 5 $pg{\cdot}m^{-3}$, respectively. The higher concentrations at the greenhouse were due to local aerosol production.

Comparing the chemistry for the two locations demonstrated that O-Hg^{II} compounds were dominant during the sampling campaign, with Br/Cl, N, S, and organic compounds being of lesser amounts (Supplementary Figure S7). High O compounds were likely due to long-range transport that occurred during this time. Concentrations of O-Hg^{II} compounds were greater at PV than at GH, as were Br/Cl compounds at times, while N, S, and organic compounds were similar in concentration between the two locations (Supplementary Figure S7). For the last sampling event, chemistry and total peak area for both locations were the same due to mixing with the storm event. Since O compounds were typically highest for PV relative to the GH, it is thought that this was derived from outside of the basin. Br/Cl, N, S, and organic compounds were comparable in concentration or at times higher at the GH relative to PV. These compounds could have been derived from the valley and transported to PV by upslope winds. This is supported by maximum mixing heights of 2,000–3,000 m that were well above the top of Peavine Peak that is 570 m above Reno (Supplementary Figure S3).

GLM model results

The model was developed using the 2019–2020 GH dataset presented here. A goal was to see if a model developed from one location could be applied to accurately predict observations at other locations. The model was applied to two datasets, one developed at Guadalupe Mountains National Park and one for a site adjacent to a highway in Atlanta, Georgia (Gustin et al., 2023).

Response variables included RM, GOM, PBM, and the chemistry of the compounds. These were compared with meteorology, percent of trajectory points in source boxes, and criteria pollutants (Supplementary Table S2). The major influencing factor that was correlated with most variables was temperature, and was removed from model consideration. Another strongly correlated variable was NO_2, so the model was performed with and without this variable. Supplementary Table S7 provides details of the analyses, along with the webpage where the model is available.

RM and GOM concentrations were positively correlated with absolute humidity and ozone, all of which increase in the summer, and negatively correlated with CO that decreases in the summer. RM and GOM were also negatively correlated with NO_2 concentrations, that was a major driver of the model and decreased in the summer.

In terms of chemistry, O and N-Hg^{II} compounds were correlated with ozone. Br/Cl compounds were correlated with ozone and absolute humidity, due to the Br/Cl compounds dominating in the summer when ozone was higher and RH lower. S and organic-Hg^{II} compounds were positively correlated with $PM_{2.5}$,

and S compounds were linked with transport from Eurasia. Besides these correlations, the GLM did not result in any conclusions that would help predict concentrations nor sources of RM based on ancillary data measurements and HYSPLIT trajectories. Lastly, the GH GLM did not accurately predict observations at the other locations, indicating that a singular simplistic GLM approach cannot be developed from a dataset from one location and applied universally.

Conclusion

There are several caveats to consider regarding use of data collected using the RMAS system. Since we are not certain regarding the exact chemistry of the RM compounds and the membrane measurements have not been calibrated, the interpretation of the chemistry observed with the RMAS system must be used with caution. In addition, RM concentrations collected with the CEM are underestimated based on the intercomparison conducted with a calibrated DCS (Dunham-Cheatham et al., 2023). The nylon membrane does not collect all compounds with equal efficiency. It is also possible that GOM could be captured on particulates collected on the PTFE membrane.

Based on data analysis, N compounds were locally/regionally sourced, while S compounds were derived from long-range transport, fires, regional production, local production, and possibly from the marine boundary layer. This suggests that chemistry associated with highway smog production could lead to formation of RM compounds. O compounds were derived from long-range transport, and halogenated compounds were from the marine boundary layer. This work showed that RM may also be derived and/or produced from both local and regional air masses. This is an important point that modelers should consider. This lack of prediction of RM concentrations and chemistry by the GEOS-Chem model is demonstrated in a forthcoming paper (Gustin et al., 2023).

Most of the mechanisms and products for production of RM are uncertain. Theoretical calculations suggest that in the atmosphere, GEM can be converted to Hg^{II} compounds by a mechanism that requires multiple oxidation steps involving Br and OH* (Shah et al., 2021). Recently, Castro et al. (2022) suggested that $OH^{\cdot}$ and ozone together account for significant conversion of Hg(0) to Hg^{II}. The compounds defined in this work are not explained in theoretical calculations. Thus, being able to definitively identify the compounds would greatly improve our understanding of RM and GOM chemistry.

The GLM modeling exercise showed that each site requires its own data collection in order to create a model, thus more monitoring sites with the RMAS could help fill data gaps as new methods are developed that can better measure RM concentrations and chemistry. Lastly, despite the limitations of the RMAS data, it is a useful step in the path to more accurate and comprehensive measurements of Hg^{II} chemistry and concentrations.

Data availability statement

The original contributions presented in the study are included in the article/Supplementary Material. Further inquiries can be directed to the corresponding author.

Author contributions

MG compiled data for the paper and wrote the paper. SD-C collected the field data, analyzed the samples, and compiled data into spreadsheets and edited the paper. NC compiled all the HYSPLIT analyses and contributed to the paper. KS prepared the GLM model and ran the model. KS wrote modeling sections of the paper. NA did the Peavine-Greenhouse comparison and contributed to the paper. All authors contributed to the article and approved the submitted version.

Funding

Funding for this work was provided by the National Science Foundation, Grant Nos. 1700711 and 1700722.

Acknowledgments

The authors would like to thank Ben Ingle for his assistance with taking measurements and collecting samples throughout the sampling campaign; Lei Zhang and Weikang Zhang for their help validating the updated peak deconvolution method; and Andrew Langford of NOAA for investigating whether stratospheric intrusions were influencing observations. The authors thank the three reviewers for their constructive comments.

Conflict of interest

The authors declare that the research was conducted in the absence of any commercial or financial relationships that could be construed as a potential conflict of interest.

Publisher's note

Supplementary material

The Supplementary Material for this article can be found online at: https://www.frontiersin.org/articles/10.3389/fenvc.2023.1202957/full#supplementary-material

References

Ambrose, J. L., Lyman, S. N., Huang, J., Gustin, M. S., and Jaffe, D. A. (2013). Fast time resolution oxidized mercury measurements during the Reno atmospheric mercury intercomparison experiment (RAMIX). *Environ. Sci. Technol.* 47, 7285–7294. doi:10.1021/es303916v

Burnham, K. P., and Anderson, D. R. (2002). *Model selection and inference: A practical information-theoretic approach*. New York: Springer-Verlag.

Castro, P. J., Kello, V., Cernusak, I., and Dibble, T. S. (2022). Together, not separately, OH and O_3 oxidize $Hg^{(0)}$ to $Hg^{(II)}$ in the atmosphere. *J. Phys. Chem. A* 126, 8266–8279. doi:10.1021/acs.jpca.2c04364

County (2021). 2011-20 Washoe county, Nevada air quality trends report. Available at: https://www.washoecounty.gov/health/programs-and-services/air-quality/air-quality-reports-and-data.php.

Dunham-Cheatham, S. M., Lyman, S., and Gustin, M. S. (2023). Comparison and calibration of methods for ambient reactive mercury quantification. *Sci. Total Environ.* 856, 159219. doi:10.1016/j.scitotenv.2022.159219

Dunham-Cheatham, S. M., Lyman, S., and Gustin, M. S. (2020). Evaluation of sorption surface materials for reactive mercury compounds Atmospheric Environment. *Atmos. Environ.* 241, 117836. doi:10.1016/j.atmosenv.2020.117836

Fine, R., Miller, M. B., Burley, J., Jaffe, D. A., Pierce, R. B., Lin, M. Y., et al. (2015). Variability and sources of surface ozone at rural sites in Nevada, USA: Results from two years of the Nevada rural ozone initiative. *Sci. Total Environ.* 530, 471–482. doi:10.1016/j.scitotenv.2014.12.027

Friedli, H. R., Radke, L. F., Lu, J. Y., Banic, C. M., Leaitch, W. R., and MacPherson, J. I. (2003). Mercury emissions from burning of biomass from temperate north American forests: Laboratory and airborne measurements. *Atmos. Environ.* 37, 253–267. doi:10.1016/s1352-2310(02)00819-1

Gustin, M. S., Allen, N., Dunham Cheatham, S. M., Choma, N., Lyman, S. N., Johnson, W., et al. (2023). *Observations of the chemistry and concentrations of reactive Hg at locations with different ambient air chemistry*. submitted to STOTEN.

Gustin, M. S., Dunham-Cheatham, S. M., and Zhang, L. (2019). Comparison of 4 methods for measurement of reactive, gaseous oxidized, and particulate bound mercury. *Environ. Sci. Technol.* 53, 14489–14495. doi:10.1021/acs.est.9b04648

Gustin, M. S., Dunham-Cheatham, S. M., Zhang, L., Lyman, S., Choma, N., and Castro, M. (2020). Use of membranes and detailed HYSPLIT analyses to understand atmospheric particulate, gaseous oxidized, and reactive mercury chemistry. *Environ. Sci. Technol.* 55, 893–901. doi:10.1021/acs.est.0c07876

Gustin, M. S., Huang, J., Miller, M. B., Peterson, C., Jaffe, D. A., Ambrose, J., et al. (2013). Do we understand what the mercury speciation instruments are actually measuring? Results of RAMIX. *Environ. Sci. Technol.* 47, 7295–7306. doi:10.1021/es3039104

Gustin, M. S., Amos, H. M., Huang, J., Miller, M. B., and Heidecorn, K. (2015). Measuring and modeling mercury in the atmosphere: a critical review. *Atmos. Phys. Chem.* 15, 5697–5713. doi:10.5194/acp-15-5697-2015

Hartig, F. (2022). DHARMa: Residual diagnostics for hierarchical (Multi-Level/mixed) regression models. Available at: https://CRAN.R-project.org/package=DHARMa.

Huang, J., Miller, M. B., Weiss-Penzias, P., and Gustin, M. S. (2013). Comparison of gaseous oxidized Hg measured by KCl-coated denuders, and nylon and cation exchange membranes. *Environ. Sci. Technol.* 47, 7307–7316. doi:10.1021/es4012349

Jones, C. P., Lyman, S. N., Jaffe, D. A., Allen, T., and O'Neil, T. L. (2016). Detection and quantification of gas-phase oxidized mercury compounds by GC/MS. *Atmos. Meas. Tech.* 9–2205. doi:10.5194/amt-9-2195-2016

Kuhn, M. (2020). *caret: Classification and regression training*. Available at: https://CRAN.R-project.org/package=caret.

Luippold, A., Gustin, M. S., Dunham-Cheatham, S. M., Castro, M., Luke, W., Lyman, S., et al. (2020a). Use of multiple lines of evidence to understand reactive mercury concentrations and chemistry in Hawai'I, Nevada, Maryland, and Utah, USA. *Environ. Sci. Technol.* 54, 7922–7931. doi:10.1021/acs.est.0c02283

Luippold, A., Gustin, M. S., Dunham-Cheatham, S. M., and Zhang, L. (2020b). Improvement of quantification and identification of atmospheric reactive mercury. *Atmos. Environ.* 224, 117307. doi:10.1016/j.atmosenv.2020.117307

Lyman, S. N., Elgiar, T., Gustin, M. S., Dunham-Cheatham, S. M., David, L. M., and Zhang, L. (2022). Evidence against rapid mercury oxidation in photochemical smog. *Environ. Sci. Technol.* 56, 11225–11235. doi:10.1021/acs.est.2c02224

Lyman, S. N., Gratz, L., Dunham-Cheatham, S. M., Gustin, M. S., and Luippold, A. (2020). Improvements to the accuracy of atmospheric oxidized mercury measurements. *Environ. Sci. Technol.* 54, 13379–13388. doi:10.1021/acs.est.0c02747

Lyman, S. N., and Gustin, M. S. (2008). Speciation of atmospheric mercury at two sites in northern Nevada, USA. *Atmos. Environ.* 42, 927–939. doi:10.1016/j.atmosenv.2007.10.012

Lyman, S. N., and Jaffe, D. A. (2012). Formation and fate of oxidized mercury in the upper troposphere and lower stratosphere. *Nat. Geosci.* 5, 114–117. doi:10.1038/ngeo1353

Mao, N., and Khalizov, A. (2021). Exchange reactions alter molecular speciation of gaseous oxidized mercury. *ACS Earth Sp. Chem.* 5, 1842–1853. doi:10.1021/acsearthspacechem.1c00178

Osterwalder, S., Dunham-Cheatham, S. M., Araujo, B. F., Magand, O., Thomas, J. L., Baladima, F., et al. (2021). Fate of springtime atmospheric reactive mercury: Concentrations and deposition at zeppelin, svalbard. *ACS Earth Space Chem* 5, 3234–3246. doi:10.1021/acsearthspacechem.1c00299

Peterson, C., Gustin, M. S., and Lyman, S. (2009). Atmospheric mercury concentrations and speciation measured from 2004 to 2007 in Reno, Nevada, USA. *Atmos. Environ.* 43, 4646–4654. doi:10.1016/j.atmosenv.2009.04.053

Rumayor, M., Diaz-Somoano, M., Lopez-Anton, M. A., and Martinez-Tarazona, M. R. (2015). Application of thermal desorption for the identification of mercury species in solids derived from coal utilization. *Chemosphere* 119, 459–465. doi:10.1016/j.chemosphere.2014.07.010

Rumayor, M., Diaz-Somoano, M., Lopez-Anton, M. A., and Martinez-Tarazona, M. R. (2013). Mercury compounds characterization by thermal desorption. *Talanta* 114, 318–322. doi:10.1016/j.talanta.2013.05.059

Shah, V., Jacob, D. J., Thackray, C. P., Wang, X., Sunderland, E. M., Dibble, T. S., et al. (2021). Improved mechanistic model of the atmospheric redox chemistry of mercury. *Environ. Sci. Technol.* 55, 14445–14456. doi:10.1021/acs.est.1c03160

Stohl, A., Eckhardt, S., Forster, C., James, P., Spichtinger, N., and Seibert, P. (2002). A replacement for simple back trajectory calculations in the interpretation of atmospheric trace substance measurements. *Atmos. Environ.* 36, 4635–4648. doi:10.1016/s1352-2310(02)00416-8

Stohl, A., Forster, C., Eckhardt, S., Spichtinger, N., Huntrieser, H., Heland, J., et al. (2003). A backward modeling study of intercontinental pollution transport using aircraft measurements. *J. Geophys. Res.* 108, 4370. doi:10.1029/2002jd002862

United States Environmental Protection Agency (Epa) (2002). *EPA method 1631, revision E: Mercury in water by oxidation, purge and trap, and cold vapor atomic fluorescence spectrometry*.

VanCuren, R., and Gustin, M. S. (2015). Identification of sources contributing to PM2.5 and ozone at elevated sites in the Western US by receptor analysis: Lassen volcanic national Park, California, and Great Basin National Park, Nevada. *Sci. Total Environ.* 530, 505–518. doi:10.1016/j.scitotenv.2015.03.091

Weiss-Penzias, P., Jaffe, D. A., Swartzendruber, P., Dennison, J. B., Chand, D., Hafner, W., et al. (2006). Observations of Asian air pollution in the free troposphere at Mount Bachelor Observatory during the spring of 2004. *J. Geophys. Res.* 111, D10304. doi:10.1029/2005jd006522

frontiers | Frontiers in Environmental Chemistry

TYPE Original Research
PUBLISHED 30 August 2023
DOI 10.3389/fenvc.2023.1242813

OPEN ACCESS

EDITED BY
Robert Peter Mason,
University of Connecticut, United States

REVIEWED BY
Brett Poulin,
University of California, Davis,
United States
Svetoslava Todorova,
Syracuse University, United States

*CORRESPONDENCE
Andrew M. Graham,
grahaman@grinnell.edu

†PRESENT ADDRESS
Katherine Smith, Department of Crop and Soil Sciences, College of Agricultural, Human, and Natural Resource Sciences, Washington State University, Pullman, WA, United States

RECEIVED 19 June 2023
ACCEPTED 17 August 2023
PUBLISHED 30 August 2023

CITATION
Graham AM, Van Helten S, Wadle A, Mamrak E, Morsch J, Lopez S and Smith K (2023), Mercury transport and methylmercury production in the lower Cedar River (Iowa) floodplain. *Front. Environ. Chem.* 4:1242813. doi: 10.3389/fenvc.2023.1242813

Mercury transport and methylmercury production in the lower Cedar River (Iowa) floodplain

Andrew M. Graham*, Seth Van Helten, Austin Wadle, Emily Mamrak, Jacob Morsch, Samuel Lopez and Katherine Smith†

Grinnell College Department of Chemistry, Grinnell, IA, United States

Scant attention has been paid to cycling of total mercury (THg) and methylmercury (MeHg) in agriculturally intensive watersheds. Monitoring of Hg and MeHg in river basins provides valuable information on the efficacy of environmental policy and the impacts of land use and climate change on Hg fluxes and biogeochemistry. We report on Hg and MeHg yields in the Cedar River (Iowa), a major tributary of the Upper Mississippi River, and on Hg biogeochemistry in a floodplain of the lower Cedar River, with emphasis on Hg cycling in groundwater and wetland ponds. For the period 2016 to 2018, total Hg yields for the 21,000 km^2 Cedar River watershed ranged from 2.6 to 6.9 $\mu g\ m^{-2}\ yr^{-1}$, or 25% to 70% of estimated wet deposition, and MeHg yields ranged from 0.09 to 0.18 $\mu g\ m^{-2}\ yr^{-1}$. High watershed transfer efficiencies for THg are driven by soil erosion and suspended sediment delivery. Policies and land management practices targeting soil conservation are thus likely to have significant impacts on downstream transport of Hg. Within alluvial groundwaters, Hg and MeHg concentrations were highly spatiotemporally variable, ranging from 0.5 to 2.0 ng/L for THg and 0.03–1.50 ng/L for MeHg. Microtopography exerted strong control on groundwater geochemistry and Hg biogeochemical cycling, with groundwater sampled from lower lying swales exhibiting less dissolved oxygen (DO), higher conductivity, higher dissolved organic carbon (DOC), and higher THg and MeHg. The alluvial aquifer exhibits high hydrologic connectivity with the river and groundwater THg and MeHg concentrations responded rapidly to hydrologic events, with MeHg concentrations increasing with a rising water table. Concentrations of THg and MeHg in wetland ponds were elevated compared to groundwater and most strongly correlated with DOC and UV-absorbance. Methylation potentials in pond sediments were among the highest reported for freshwater sediments, up to 0.15 d^{-1}, which we hypothesize to be linked to high primary productivity associated with nutrient enrichment. Floodplain groundwaters and wetlands constitute important ecosystem control points for downstream MeHg delivery, the magnitude of which is sensitive to changing hydroclimate, especially flood frequency.

KEYWORDS

mercury, methylmercury, floodplain, groundwater, climate change

1 Introduction

Mercury (Hg) contamination of aquatic and terrestrial ecosystems has deleterious consequences for wildlife and human health (Driscoll et al., 2013). Emissions inventories indicate that human activities (especially gold and silver production and coal combustion) have increased Hg in the present-day atmosphere by at least a factor of 3 relative to 1850 (Streets et al., 2017). Owing to its long residence time in the atmosphere, mercury can be deposited far from emission sources, resulting in contamination of remote terrestrial, freshwater, and marine ecosystems (Driscoll et al., 2013). Methylation of Hg by diverse bacteria and archaea carrying the *hgcAB* genes to produce bioaccumulative methylmercury (MeHg), predominantly in anoxic environments like sediments, wetlands, and saturated soils (Gilmour et al., 2013), is the main driver of risk associated with Hg contamination. The Minamata Convention on Mercury entered into force in 2017, and represents a global effort to significantly reduce anthropogenic Hg emissions. The effectiveness of the Minamata Convention will depend both on realizing intended emissions reductions and the impacts of changing climate and land use on the release and transport of large legacy Hg stores (Bishop et al., 2020). Climate and land use change also have potential to impact biogeochemical processing of Hg (e.g., Hg methylation and demethylation) and Hg bioaccumulation and trophic transfer (Krabbenhoft and Sunderland, 2013). In this paper, we explore unresolved aspects of terrestrial Hg cycling within a large river and its flood plain in the Upper Midwest United States–the Cedar River in Iowa.

Long-term monitoring of Hg and MeHg fluxes in large rivers has great utility for quantifying the export of Hg and MeHg from terrestrial watersheds and system response to environmental policy and climate change. In a review of terrestrial Hg cycling, Bishop et al. (2020) reported a global summary of MeHg and THg yields from rivers and streams. These workers reported median yields for diverse ecosystems (Arctic, forested, agricultural, and urban) to range from 1.45 to 4.77 $\mu g\ m^{-2}\ y^{-1}$ for unfiltered THg and 0.017–0.080 $\mu g\ m^{-2}\ y^{-1}$ for unfiltered MeHg. There are relatively few reports of THg and MeHg yields in agroecosystems, where yields for agricultural watersheds were reported to range from 0.53 to 4.90 $\mu g\ m^{-2}\ y^{-1}$ (median = 2.69 $\mu g\ m^{-2}\ y^{-1}$) for unfiltered THg and 0.026–0.120 $\mu g\ m^{-2}\ y^{-1}$ (median = 0.063 $\mu g\ m^{-2}\ y^{-1}$) for unfiltered MeHg (Bishop et al., 2020). In the Upper Mississippi River Basin (UMRB), work has focused mostly on Minnesota and Wisconsin rivers (Hurley et al., 1995; Babiarz et al., 1998; Balogh et al., 1998; Brigham et al., 2009), and is non-existent to our knowledge for rivers within the state of Iowa. Annual wet deposition of Hg in the UMRB is elevated. At the National Atmospheric Deposition Program (NADP) Mercury Deposition Network (MDN) station closest to the study site (station WI-031 in southern Wisconsin), Hg deposition has averaged 11.0 ± 2.7 $\mu g/m^2$ between 2001–2018, with no discernible trend in either Hg wet deposition or precipitation Hg concentration (NADP, 2019). While Hg deposition has declined in portions of the eastern United States and Canada, increasing emissions outside of North America and long-range Hg transport have resulted in stable or increasing wet Hg deposition in the upper Midwestern United States (Weiss-Penzias et al., 2016). Earlier studies in the UMRB reported lower watershed transfer efficiencies for THg (the ratio of watershed export to wet deposition) in agricultural watersheds (Hurley et al., 1995) and increasing MeHg export with increasing wetland land cover (Hurley et al., 1995; Brigham et al., 2009). THg and MeHg export from agriculturally-dominated watersheds in the UMRB have since received little attention. Total suspended solids (TSS) yields in Minnesota and Wisconsin rivers are 4–20 times lower than that of Iowa and Illinois rivers (Heimann et al., 2011). We argue that determination of THg and MeHg export in high TSS rivers of the UMRB is worthy of further attention, as such watersheds may play a larger role in downstream THg and MeHg transport than previously recognized.

The impacts of climate change on terrestrial export of THg and MeHg are uncertain. Significant increases in river discharge (Jones et al., 2018b) and flood frequency (Mallakpour and Villarini, 2015) have occurred in the UMRB over the late 20th and early twenty-first centuries. Downscaled general circulation climate models project further increases in spring and winter flood events in this region (Neri et al., 2019). Within the Cedar River basin, the focus of this study, mean annual discharge from 1980–2019 was 61% higher than the period 1940–1979. Extreme discharge events within the basin have also increased, with about half of the top 1% discharge days and nearly 60% of the top 0.1% discharge days occurring within just the last 20 years. Increased flood events almost certainly lead to greater downstream THg and MeHg delivery. Quantifying the impact of increased flood frequency on THg and MeHg transport is a priority for assessing how climate change may impact the global biogeochemical cycle of Hg (Krabbenhoft and Sunderland, 2013). Furthermore, flood events may also represent "hot moments" of *in situ* MeHg production within river floodplains (Balogh et al., 2006; Gygax et al., 2019). Clarifying the timing of peak MeHg production relative to peak discharge is important for determining the scale of flooding impact on downstream MeHg delivery. There are few (Balogh et al., 2006) investigations of Hg biogeodynamics with respect to flooding within large river floodplains of the UMRB. Notably, there are no studies in river systems with exceptionally high nitrate loads, as is typical (Jones et al., 2018a) of Iowa rivers–whether high nitrate delivery to floodplains suppresses Hg methylation associated with iron and sulfate reduction remains an open question.

Lastly, the role of groundwater in THg and MeHg transport in the riparian zone warrants further attention. We are aware of only a handful of observational studies (Creswell et al., 2008; Bradley et al., 2010; 2011; 2012; Vidon et al., 2013) of MeHg and THg riparian groundwaters. In hydrologically connected floodplains, groundwater inputs may be an important source of riverine MeHg (Bradley et al., 2010). Groundwater geochemistry (e.g., alkalinity, redox active solutes like dissolved oxygen (DO), nitrate, Fe, and Mn, and dissolved organic carbon (DOC)) in floodplains can vary substantially over small spatial scales due to differences in sediment lithology (Schilling and Jacobson, 2012). Microtopographic variation in MeHg production is well documented for northern peatlands (Branfireun, 2004), and, given microtopographic control of other biogeochemical processes, we hypothesize that THg and MeHg concentrations in groundwater of temperate river floodplains likely show strong fine scale spatial variability. Characterizing the magnitude of this

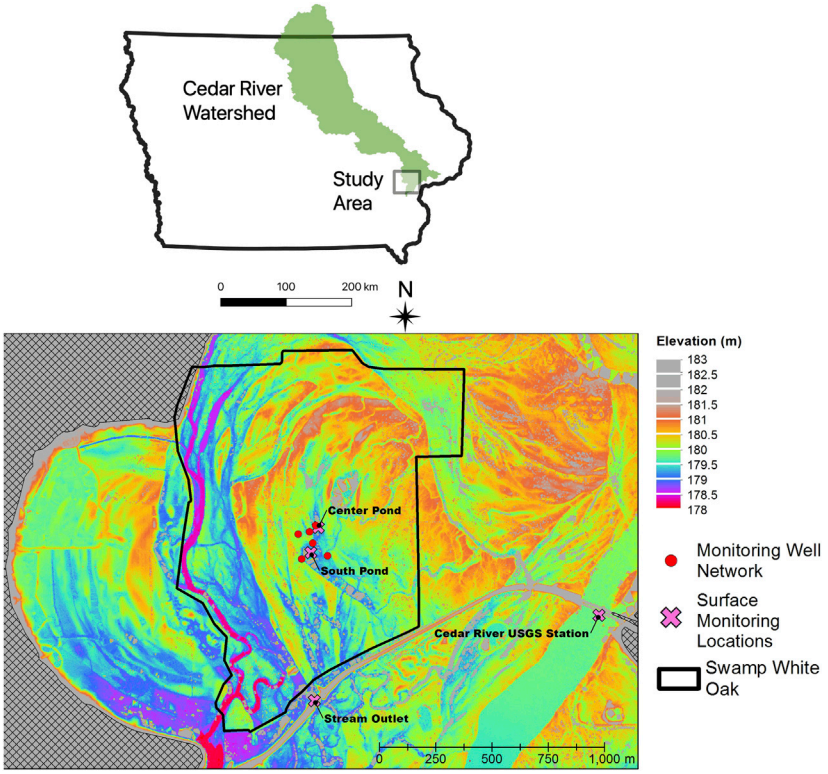

FIGURE 1
Map of Cedar River watershed showing approximate location of study area and detailed LiDAR digital elevation model of study area, showing locations of groundwater monitoring wells (red circles) and surface water monitoring stations (pink crosses).

variability is important for designing sampling programs to quantify groundwater transport of THg and MeHg through terrestrial ecosystems.

In summary, our work has three major objectives, spanning multiple temporal and spatial scales.

1) To characterize THg and MeHg fluxes in a large river of the UMRB, in a region (the state of Iowa) for which little information on THg and MeHg fluxes exists.
2) To evaluate THg and MeHg transport, and MeHg production, within the river floodplain across seasons and in response to flood events.
3) To determine to what extent, if any, microtopography controls THg and MeHg dynamics

2 Methods

2.1 Description of study area

Sampling of shallow alluvial groundwaters and shallow wetland ponds occurred periodically from June 2016 to September 2018 at the Swamp White Oak (SWO) Nature Preserve, a Nature Conservancy-owned restored savanna oak forest dominated by *Quercus bicolor* (Dettman and Mabry, 2008), occupying the floodplain of the lower Cedar River in east-central Iowa near Conesville, Iowa (lat. 41°24′36″, long. 91°17′06″, see map in Figure 1). Samples were also collected nearby from the main channel of the Cedar River at the site of a United States Geological Survey (USGS) gaging station (USGS station number 05465000), for which continuous discharge measurements have been available since 1940. The Cedar River is a major tributary of the Upper Mississippi River, with a watershed area of approximately 20,200 km^2 at the sampling station. Corn and soybean cultivation comprise the major land cover (72.5% of land area) with smaller areas of grasslands (14.9%, including pasture), forest (7%) and impervious surface (2.7%). The climate of the region is temperate, with hot, humid summers and cold, dry winters. Mean annual precipitation in nearby Muscatine, Iowa is 810 mm/year, with May, June, and July typically the wettest months of the year (NCEI Climatology Database). Long-term mean annual discharge of the Cedar River at Conesville, Iowa is 164 $m^3\ s^{-1}$ (5,800 $ft^3\ s^{-1}$).

A monitoring well network encompassing microtopographic highs (sandy ridges) and lows (silty swales) was installed in 2005 as part of studies of riparian hydrology, nutrient processing, and carbon dynamics within the SWO preserve (Schilling and Jacobson, 2009; 2012; 2015). Monitoring wells were installed to a depth of approximately 2 m with a 1.5 m long polyvinyl chloride (PVC) well-screen and 1.5 m long PVC riser (Schilling and Jacobson, 2009). The water table in these floodplain monitoring wells responds rapidly to Cedar River stage indicating a high level of hydrologic connectivity between the floodplain and the river (Schilling and Jacobson, 2009). Significant differences in

groundwater quality, with respect to nitrate, DO, and DOC, exist between ridges and swales, with wells in microtopographic depressions exhibiting lower DO and nitrate and higher DOC (Schilling and Jacobson, 2012). Schilling and Jacobson (2009)A subset of three topographically "high" wells (>180.5 m land surface elevation; Center, West, and South) and three "low" wells (<180.5 m land surface elevation; North, East, and Swale) were selected for our study of Hg biogeochemistry.

2.2 Sampling and sample processing

All samples were collected utilizing a clean hands/dirty hands approach (Fitzgerald, 1999) to minimize sample contamination. Monitoring wells were sampled using a peristaltic pump with acid-washed Teflon tubing and a short piece of silicone tubing on the pump head. Prior to sampling, depth to water table was measured to the nearest cm using an electronic water level tape (Solinst Model 101). Wells were flushed for 2–3 min and allowed to recharge for a minimum of 1 h prior to sampling. Samples from the two ponds were collected by wading and filling a sample bottle at maximal reach from the area of sediment suspension caused by wading. Samples from the Cedar River and the SWO outlet stream were collected by lowering a virgin polyethylene terephthalate glycol (PETG) bottle or acid-washed Teflon bottle to a depth of about 30 cm below the water surface. All samples were stored in PETG bottles with zero headspace on ice until return to laboratory to minimize sample oxidation. DO, pH, specific conductance, and water temperature were measured immediately on a separate subsample using a multimeter (YSI Pro DSS or PASCO Xplorer GLX) with optical DO sensor. Samples for dissolved Fe(II) and sulfide were immediately filtered in the field through a 0.2 µm nylon membrane filter and preserved in ferrozine colorimetric reagent (1 mM ferrozine, 10 mM HEPES buffer) for Fe(II) analysis (Stookey, 1970) and sulfide antioxidant buffer (SAOB) for sulfide analysis (Clesceri et al., 2000).

Samples were returned to the laboratory, refrigerated, and processed within 24 h of collection. Samples were filtered through 0.45 µm glass fiber filters (baked for 4 h at 550°C in a muffle furnace and stored at room temperature in a double-bagged sealed plastic container) using an acid-washed PFA filtration assembly (Savillex; Eden Prairie, MN) into virgin PETG bottles. A known volume (generally about 150 mL) of filtrate was collected for both THg and MeHg and analyses and preserved with 1% trace metal grade HCl. Filters corresponding to particulate THg and MeHg were retrieved and stored frozen until analysis. All MeHg analyses were completed within 60 days, within the acceptable holding time (180 days) per EPA Method 1630 (US EPA, 1998). For THg, the majority of samples were analyzed with 90 days, the EPA recommended holding time (US EPA, 2002). 25% of samples (corresponding to THg samples from 7/7/17, 8/17/17, 7/19/18, and 9/4/18) were held acid-preserved and refrigerated up to 10–18 months prior to analysis. Prior work indicates that preserved THg samples are stable for at least 10 months (Parker and Bloom, 2005). Filtered THg samples for the Cedar River on 6/3/16 and 7/17/17 and particulate MeHg on 6/3/16 and 9/8/16 were lost during processing. A separate subsample of the filtrate was preserved with 2% HNO_3 for other major and trace element analysis, carried out within 6 months of sample collection. Samples for anions and DOC were collected in 50 mL polypropylene tubes and stored frozen until analysis, typically within 30 days of sample collection.

2.3 Sediment collection and enriched isotope methylation rate experiments

In June and July of 2018, sediment cores were retrieved from the Center and South ponds at SWO via hand-coring with 5 cm diameter, 45 cm long polycarbonate tubes, predrilled at 1 cm intervals with openings sealed with silicone. Sediment cores were 12–16 cm in length and filled with overlying water leaving no headspace, capped with plastic seals wrapped in vinyl tape, and transported to the laboratory at ambient temperature. Upon return to the laboratory, cores were stored overnight at 4°C, then transferred the next day to incubators at field temperature (22.5°C–23.7°C) for *in situ* methylation potential determination or sectioned at 2 cm intervals for ambient total Hg (THg) and MeHg analyses. Sub-sectioned sediment core samples were homogenized and stored frozen until analysis.

Core injections for methylation potential (k_m) determination followed the method of Mitchell and Gilmour (2008). Sediment cores were injected at 1 cm intervals through the silicone septa with 100 µL of 4 µg/mL enriched $^{201}HgCl_2$ (pre-equilibrated for 1 hour with 0.2 µm-filtered overlying water from the respective ponds). Injections were performed while moving the syringe needle in a back-and-forth motion while withdrawing the needle to try to evenly inject the ^{201}Hg spike across the core's entire cross-sectional area at each depth. After injection, the cores were incubated at site temperature in the dark for 3 h. Cores were then sectioned at 2 cm intervals and samples frozen for analysis.

2.4 Methods for Hg analyses

Samples for MeHg (either filtered water, filters with particulate matter, or sediments) were analyzed by steam distillation, ethylation with sodium tetraethylborate, and isotope dilution gas chromatography inductively coupled plasma mass spectrometry (Hintelmann and Evans, 1997) using enriched $Me^{199}Hg$ as the internal standard (Oak Ridge National Laboratories, 91.95% ^{199}Hg). All MeHg analyses were carried out with a manual purge and trap GC system as described in Kanzler et al. (2018) interfaced to an Agilent 7500ce ICP-MS. Quality assurance/quality control (QA/QC) measures included analysis of field blanks (filter blanks), distillation blanks, a certified reference material (NIST 1566b oyster tissue), and duplicate sample analyses. QA/QC data for MeHg analyses is summarized in Supplementary Table S1.

Sample digestion and analysis protocols for THg analyses differed depending on the subsample type. Filtered water samples for total Hg analysis were digested overnight in 1% BrCl. Filters (for particulate THg) and sediments were digested in 7:4 v/v HNO_3:H_2SO_4 at 190°C for 2 h, diluted with deionized water (resistivity of 18.2 MΩ-cm), then preserved with 1% BrCl. For filtered water samples and filters, THg was determined by isotope dilution purge and trap dual gold trap Hg amalgamation coupled to ICP-MS. Briefly, a 50–100 mL sample was

added to a bubbler with 100 µL of 20% w/v hydroxylamine hydrochloride (to reduce excess BrCl), 300 µL of 60 g/L $SnCl_2$ reductant, and a known amount of enriched $^{201}HgCl_2$ (Oak Ridge National Laboratories, 98.11% ^{201}Hg) and purged for 15 min onto a sample trap containing glass beads coated with gold (Brooks Rand Instruments, Seattle WA). Gold sample traps were heated via a nichrome wire to release amalgamated Hg in a stream of argon gas onto a second gold trap (the analytical trap), which was heated to release Hg directly into the Agilent 7500ce ICP-MS. A small subset of filtered THg samples were analyzed by an automated total mercury analysis system (Brooks Rand Instruments MERX-T using $SnCl_2$ reduction and dual gold trap amalgamation) interfaced to a Perkin Elmer Nexion 2000 ICP-MS. Sediment samples which had higher THg concentrations were analyzed by ICP-MS with flow injection reduction of Hg(II) to Hg(0) using 60 g/L $SnCl_2$ in 1% HCl (Graham et al., 2012). QA/QC measures for THg analyses were identical to those for MeHg (except that NIST 2709a San Joaquin soil was used as certified reference material) and are summarized in Supplementary Table S1.

2.5 Other geochemical analyses

Dissolved Fe(II) was measured colorimetrically at 562 nm following complexation with ferrozine reagent (Stookey, 1970). Dissolved sulfide concentrations were measured using a sulfide ion selective electrode calibrated against a Pb-titrated sulfide standard (Clesceri et al., 2000). Major anion concentrations (chloride, nitrate, and sulfate) were determined using isocratic ion chromatography (Latchat 8000 series) with a carbonate eluent (2.6 mM Na_2CO_3 and 2.0 M $NaHCO_3$, pH = 10.44) with conductivity detection and ion suppression. Major and trace element concentrations other than Hg were determined by ICP-MS using either an Agilent 7500 ce or Perkin Elmer Nexion 2000. DOC concentrations were determined using a Shimadzu TOC-$V_{CSH/CSN}$ analyzer. UV-Vis absorbance spectra were measured in quartz cuvettes on a Cary 60 UV-Vis spectrophotometer following addition of 0.2% w/v hydroxylamine hydrochloride to the sample to minimize interference due to formation of light scattering Fe(III) (oxy)hydroxides (Doane and Horwáth, 2010) upon sample storage after filtering. QA/QC measures for DOC, anions, and trace elements are provided in Supplementary Table S2.

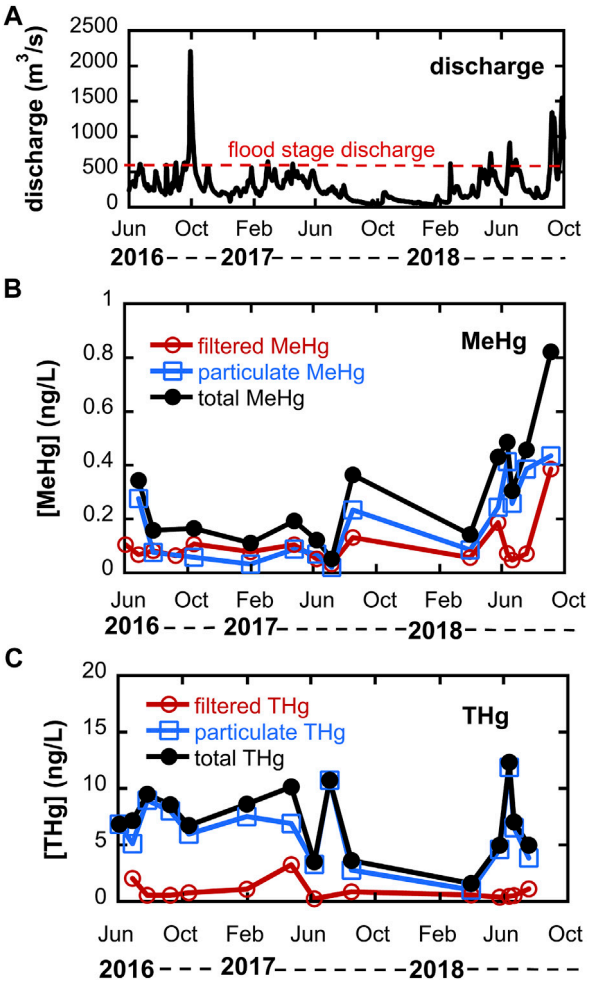

FIGURE 2
(A) hydrograph for Cedar River near Conesville, Iowa (USGS station number 05465000) during study period. Flood stage is 3.96 m, corresponding to a discharge of ~594 m^3/s. **(B)** Methylmercury (MeHg) distribution between 0.45 µm filtered and particulate phases; and **(C)** Total Hg (THg) distribution between 0.45 µm filtered and particulate phases. Note that summed totals for total MeHg or total THg do not include filtered THg data on 6/3/16 and 7/7/17 or particulate MeHg data for 6/3/16 and 9/8/16 due to sample loss.

2.6 THg and MeHg flux and yield estimation for Cedar River

Three methods were utilized for computing fluxes of THg and MeHg in the Cedar River. First, fluxes were estimated using the program LOADEST (Runkel et al., 2004) as implemented in *R* (R Core Team, 2019). LOADEST has the advantage of automated selection from multiple regression models using the Akaike Information Criterion, with computation of model coefficients using an adjusted maximum likelihood estimation (AMLE). A downside is the risk of overfitting given the relatively small number of observations (n = 16 across 3 years).

In a second approach, we calculated daily fluxes based on daily discharge and median THg or MeHg concentration. A third approach relied on using high resolution turbidity (5 min time interval) and discharge (at 15 min intervals) to estimate instantaneous fluxes at 15 min intervals. Turbidity data were available for a portion of 2018 (late February through mid-November), measured at the Conesville station at 5 min intervals (data retrieved from the Iowa Water Quality Information System; IWQIS: https://iwqis.iowawis.org/app/). The turbidity-based approach is discussed further in the results and discussion below. Fluxes were converted to yields by dividing the flux by the watershed area.

3 Results and discussion

3.1 Hg and MeHg dynamics and yields in the Cedar River

A hydrograph for the Cedar River during the study period is shown in Figure 2, and shows that discharge exceeded that required

TABLE 1 Summary of annual Hg yields for the Cedar River watershed. Error estimates are standard errors derived from the LOADEST model.

Calendar year	LOADEST predicted THg yield (μg m^{-2} yr^{-1})	THg yield based on median THg conc (μg m^{-2} yr^{-1})	LOADEST predicted MeHg yield (μg m^{-2} yr^{-1})	MeHg yield based on median MeHg conc (μg m^{-2} yr^{-1})
2016	5.2 ± 1.0	3.75	0.15 ± 0.05	0.13
2017	2.6 ± 0.3	2.5	0.09 ± 0.02	0.09
2018	6.9 ± 1.6	4.2	0.18 ± 0.07	0.15

for overbank flow on several occasions during 2016–2018. The Fall 2016 event corresponds to the second largest discharge on record. Total unfiltered Hg concentrations in the Cedar River are also shown in Figure 2 and ranged from 1.6 to 14.6 ng/L (mean = 8.6 ± 3.4 ng/L, where uncertainty represents one standard deviation); median = 7.1 ng/L, n = 16), the bulk (nearly 80% on average) of which was particulate THg (mean = 6.7 ± 3.4 ng/L; median = 6.7 ng/L). No obvious seasonal trend is apparent, though few samples were collected during low flow winter months due to ice cover. Measured unfiltered THg concentrations are within the range reported by others during the 1990s and early 2000s for UMRB rivers at varying discharge scales (Hurley et al., 1995; Balogh et al., 1998; 2005). Particulate THg concentrations were strongly correlated to measured total suspended solids (TSS; r^2 = 0.71, p = 0.0005), as shown in Supporting Information Supplementary Figure S2. Unfiltered THg concentrations were well correlated with discharge (r^2 = 0.46, p = 0.004), likely due to a positive relationship between discharge and TSS.

Unfiltered MeHg concentrations in the Cedar River ranged from 0.05 to 0.82 ng/L (mean = 0.30 ± 0.21 ng/L; median = 0.25 ng/L, n = 14), with the particulate fraction accounting for about 64% of total MeHg. Total unfiltered MeHg was not strongly correlated with unfiltered THg (Supplementary Figure S2). The lower fraction of particulate MeHg compared to THg reflects stronger solid-solution partitioning for inorganic Hg relative to MeHg–calculated log K_d's based on TSS (distribution coefficients with units of L kg^{-1}) for THg averaged 4.89 vs 4.21 for MeHg. Measured log K_d's are similar to that reported for Wisconsin rivers by Babiarz et al. (1998). The mean unfiltered MeHg concentration for the Cedar River is similar to the 0.20 ng/L reported for the Minnesota River (Balogh et al., 2005) but higher than that reported for agriculture-intensive watersheds in Wisconsin (mean MeHg = <0.03–0.085 ng/L) (Hurley et al., 1995). Approximately 4.8% of unfiltered THg was MeHg, also higher than that reported for predominantly agricultural watersheds in Wisconsin rivers (Hurley et al., 1995). The highest filtered MeHg concentrations were observed in October 2016 May 2018 and September 2018 following overbank flow events, consistent with the idea that the floodplain is a significant MeHg source area.

Annual THg and MeHg yields were estimated using the daily discharge data and measured concentrations (Table 1). Automated model selection for both THg and MeHg in LOADEST resulted in a model of the form:

$$\ln(flux) = \alpha_0 + \alpha_1 lnQ \quad (1)$$

where lnQ is the ln(observed daily discharge)—center of ln(daily discharge). In the case of THg, this model described 81.2% of the variability in THg flux (p < 0.0001), whereas the model for MeHg only explained 40.6% of the variability in MeHg flux (p = 0.0039). Yields calculated using LOADEST-derived fluxes ranged from 2.6 to 6.9 μg m^{-2} y^{-1} for THg and 0.09–0.18 μg m^{-2} y^{-1} for unfiltered MeHg. Using the median concentrations of unfiltered THg and MeHg, yields were estimated to be between 2.5 and 4.2 μg m^{-2} y^{-1} for THg and 0.09–0.15 μg m^{-2} y^{-1} for MeHg. The median concentration and LOADEST approaches agree closely for MeHg, but the median concentration approach results in lower yields for THg in wet years.

An alternative approach for estimating THg yields is to use turbidity as a proxy measure of particulate THg concentration. Turbidity is strongly linearly correlated with TSS (Supplementary Figure S3, r^2 = 0.96, p < 0.001) and TSS is strongly correlated with particulate THg (Supplementary Figure S2). A potential advantage of this approach is that turbidity and discharge measures are only weakly correlated (r^2 = 0.01), an observation that is likely driven by significant discharge-TSS hysteresis, so the high-resolution turbidity measurements provide a more accurate real-time estimate of sediment flux not captured by the regression models. For example, during 2018, high turbidity occurred on the rising limb of the hydrograph, but fell much more quickly than discharge (Supplementary Figure S4). For 2018, where high resolution turbidity data were available, the particulate THg yield was estimated at 3.1 μg m^{-2} y^{-1} for the period 3/1 through 11/14/18. Assuming that the particulate THg flux is 80% of the total Hg flux (supported by concentration measurements in Figure 2C), the total Hg yield for this period would be 3.9 μg m^{-2} y^{-1}, within 10% of the yield predicted based on median THg concentration (3.6 μg m^{-2} y^{-1} for the same interval). The LOADEST estimate for this same period is significantly higher, about 6.1 μg m^{-2} y^{-1}. High resolution turbidity monitoring may be a useful proxy measure for THg in some watersheds (Riscassi and Scanlon, 2013; Vermilyea et al., 2017), as also demonstrated for phosphorus (Schilling et al., 2017), providing more accurate estimates of Hg fluxes especially under circumstances where suspended sediment delivery shows complex relationships with discharge (see Supplementary Figure S4).

Total unfiltered Hg and MeHg yields for the Cedar River are toward the higher end of what has been reported for agriculturally-dominated watersheds elsewhere in the Upper Midwest United States and even for many watersheds with much larger proportions of forests and wetlands (Bishop et al., 2020). Unfiltered MeHg and THg yields are above the 75th percentile (3.12 μg m^{-2} y^{-1} for THg, n = 80 and 0.091 μg m^{-2} y^{-1} for MeHg, n = 67) for all watersheds reviewed by Bishop et al. (2020). Hurley et al. (1995) reported mean watershed yields of 0.05 (fall) to 3.2 (spring) μg m^{-2} y^{-1} for unfiltered THg in agricultural watersheds in Wisconsin in the early 1990s. Balogh et al. (2005) reported THg yields of 0.3–6.4 μg m^{-2} y^{-1} for the Minnesota River and its tributaries in the early 2000s. Reported unfiltered MeHg yields range from 0.002 to 0.05 μg m^{-2} y^{-1} in Wisconsin rivers (Hurley et al., 1995) to 0.03–0.09 μg m^{-2} y^{-1} in

Minnesota Rivers (Balogh et al., 2005). Wet deposition for the Cedar River watershed is estimated at 10–14 μg m^{-2} y^{-1} for the period 2016 to 2018 (NADP, 2019). Dry deposition and litter fall inputs of Hg within this watershed are not known [but are often similar in magnitude to wet deposition (Bishop et al., 2020)]. We are not aware of any local point sources of Hg within the watershed. Relative to wet deposition, observed THg yields thus represent watershed transfer efficiencies of about 25% to nearly 70%.

High THg yields likely reflect high TSS loads in rivers of this region. For 2018, we estimated TSS yield to be about 60 tons/km^2, similar to long-term observations of sediment yields for Iowa rivers contributing to the Upper Mississippi River Basin (Heimann et al., 2011; Jones and Schilling, 2011). High TSS loads can drive high THg and MeHg yields even when mean Hg concentrations of soil particles are fairly low (median THg concentration of suspended sediments was 48 ng/g and median MeHg concentration was 1.5 ng/g). Changing climate (increased frequency of intense rainfall events (Mallakpour and Villarini, 2015)) and land management practices (e.g., bringing conservation reserve program (CRP) lands back into production) have potential to increase sediment yields, and hence Hg yields, in this region.

3.2 Floodplain groundwater hydrology and geochemistry

Riparian groundwaters and wetlands may be important sources of MeHg to the Cedar River. In order to understand biogeochemical processes controlling MeHg production, we monitored geochemistry in groundwater and surface waters within the adjacent river floodplain. Groundwater geochemistry was monitored in six shallow monitoring wells, representing three microtopographically "high" wells and three "low" wells over the period June 2016 through July 2018. The south well has the highest land elevation, but geochemistry was more similar to low wells. Hereafter, we exclude the south well from our analysis when discussing differences between low and high wells. Aquifer sediments at high wells tend to be coarser grained and have greater depth to water table (DWT) than low wells. Mean DWT was about 0.6 m greater in high wells (1.10 m) compared to low wells (0.47 m; $p < 0.001$ for one-way ANOVA). The rapid response of the water table elevation to Cedar River discharge is indicative of high hydrologic connectivity between the floodplain and the river. Supplementary Figure S5 shows the strong linear relationship (r^2 = 0.78) between 5-day prior discharge of Cedar River and DWT at the swale well. Our results are in close agreement with insights provided by continuous monitoring of the water table in the center well from 2005–2007, which suggested a lag of 1–6 days between river discharge and water table elevation (Schilling and Jacobson, 2009).

Low and high wells also showed contrasting geochemistry. High wells had significantly lower specific conductance, higher DO, and lower DOC compared to low wells averaged across all sampling events (Supplementary Figure S6). Specific conductance was about 60% higher ($p < 0.001$ for one-way ANOVA) in low wells (mean = 352 ± 62 μS/cm) vs high wells (mean = 218 ± 51 μS/cm). DOC was about double ($p < 0.001$ for one-way ANOVA) in low wells (mean = 4.07 ± 1.74 mg/L) compared to high wells (mean = 2.09 ± 1.25 mg/L). Groundwater pH was similar across all wells (mean = 6.60 ± 0.34). Analysis of major cations and anions suggested similar distribution of ions (see Piper diagram in Supplementary Figure S7), though absolute concentrations were significantly higher in low wells compared to high wells, consistent with conductivity data. Alkalinity, estimated for these relatively hard groundwaters as the difference between strong base cation equivalents and strong acid anion equivalents, was nearly double for low wells (mean alkalinity = 2.74 meq/L) vs high wells (mean alkalinity = 1.35 meq/L). We posit that higher alkalinity and dissolved solids for low wells reflect greater rates of carbon mineralization at these sites, resulting in higher P_{CO2} in groundwater, thus driving increased dissolution of carbonate minerals. Increased dissolved inorganic carbon and carbonate mineral dissolution in shallow aquifers in response to increased

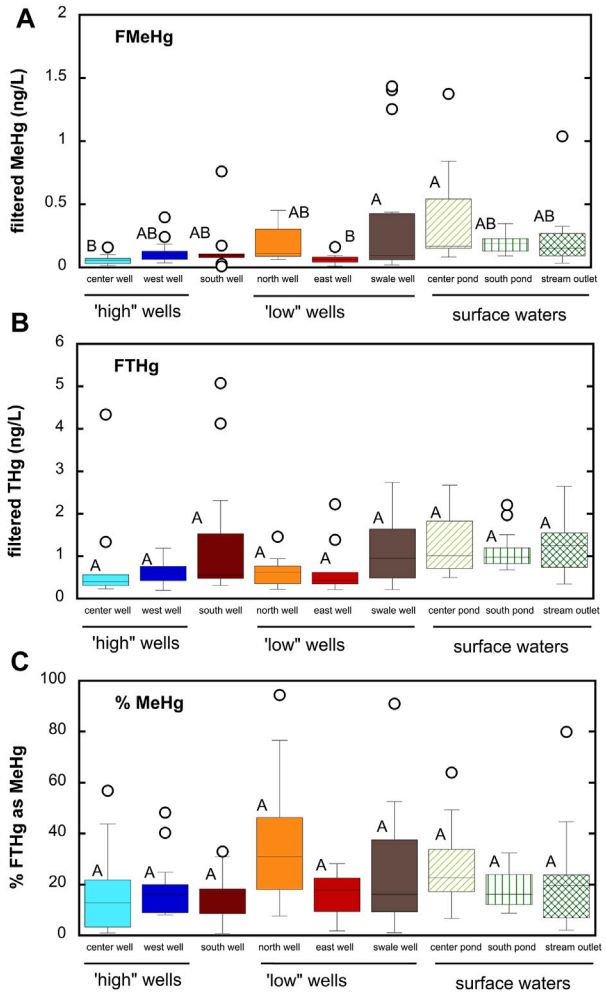

FIGURE 3
Box and whisker plots summarizing differences in MeHg and THg between microtopographically "high" and "low" wells and surface waters. South well is not classified as either "high" or "low". **(A)** filtered MeHg; **(B)** filtered THg; **(C)** percent filtered THg as MeHg. Boxes represent 25th and 75th percentiles, line the median, and whiskers the 10th and 90th percentiles; points represent outliers. Stations that do not share a common letter are significantly different (α = 0.05) from one another based on one-way ANOVA and Tukey *post hoc* comparison.

soil respiration in summer months are well-documented in other similar systems (Tsypin and Macpherson, 2012). Alluvial sediments at the high and low sites contain similar organic carbon in surficial sediments, but low sites have 2–5 times more carbon at depths greater than or equal to 0.5 m (Schilling and Jacobson, unpublished data), supporting the idea that increased carbon availability leads to greater subsurface microbial activity in the low wells. This hypothesis is further supported by observations of DO in these shallow groundwaters, as an indicator of aerobic microbial activity. DO was about 60% higher (p = 0.001 for one-way ANOVA) across all high wells (mean = 3.5 ± 1.9 mg/L) compared to all low wells (mean = 2.2 ± 1.4 mg/L). No significant differences were observed between low and high wells for other indicators of terminal electron accepting processes, including nitrate, dissolved Fe(II), dissolved Mn, and sulfate (Supplementary Figure S6).

3.3 Hg dynamics in groundwater

Filtered THg concentrations in shallow groundwater (mean = 0.87 ± 0.92 ng/L; median = 0.57 ng/L across all sampling sites and dates) were similar to that observed in the Cedar River (mean = 0.94 ± 0.83 ng/L). Filtered MeHg concentrations (mean = 0.16 ± 0.26 ng/L; median = 0.087 ng/L) were slightly higher than that observed for Cedar River (mean = 0.10 ± 0.08 ng/L). MeHg represented about 22% of filtered THg for all groundwater samples. These averages, however, may mask significant difference in Hg and MeHg concentrations in time and space within the alluvial aquifer. Figure 3 shows differences in THg and MeHg concentrations averaged across all sampling dates. Filtered THg concentrations generally ranged from 0.5 to 2 ng/L, with only a few exceptions, and were not significantly different between wells, though both the south well and swale well did have larger median concentrations. Greater spatial variability existed for MeHg concentrations, with MeHg concentrations ranging from below detection (0.029 ng/L) to nearly 1.5 ng/L (a 50-fold difference). MeHg represented as little as 1% of filtered THg to as much as 94%, with a mean of 22% across all sites and sampling dates. MeHg concentrations were greatest in the low-lying north and swale wells.

There are few studies of Hg and MeHg in alluvial groundwater with which to compare our findings. Vidon et al. (2013) measured THg and MeHg in alluvial groundwaters at three sites in central Indiana and observed lower filtered THg concentrations medians ranging from 0.28 to 1.05 ng/L) and filtered MeHg concentrations (medians ranging from 0.01 to 0.05 ng/L (Vidon et al., 2013). The highest MeHg concentrations in groundwater at these sites were observed during the summer months of July and August. Creswell et al. (2008) reported THg concentrations in hyporheic wetland sediments from northern Wisconsin of 2–10 ng/L and MeHg concentrations of <0.05 to as much as 3 ng/L, more similar to the range of MeHg and THg concentrations we observe in these alluvial groundwaters in Iowa. Bradley et al. (2010) reported filtered MeHg concentrations ranging from 0.1 to greater than 1.5 ng/L in riparian pools fed by groundwater in a coastal plain floodplain of a blackwater stream in South Carolina. Filtered THg concentrations were reported to range from 1 to 10 ng/L in groundwater in a follow-up study (Bradley et al., 2012). Of these studies, the work of Vidon et al. (2013) is most similar in terms of geomorphic setting–a river floodplain developed on glacial outwash/alluvium with significant agriculture in upland portions of the watershed. Vidon et al. (2013) concluded that riparian zones in regions with low groundwater DOC may not contribute appreciable MeHg. Here, we show higher MeHg in groundwaters, especially in response to rapid groundwater table rise (see section 3.6 below), and suggest that such hydrologically connected floodplains do constitute important sources of MeHg during critical moments. For the Cedar River system, the moments of highest MeHg in groundwaters immediately precede the highest observed filtered MeHg concentrations in the Cedar River (Figure 2).

Comparing wells sampled on the same date (see Supplementary Figure S8), MeHg concentrations were on average about 2.5–7.9 times higher in the microtopographically low north and swale wells compared to the microtopographically high center and west wells. The low east well and unclassified south well were on average 1.8–3.7 times higher compared to the center well, but similar to the west well. Just as microtopography can influence carbon and nutrient cycling (Schilling and Jacobson, 2012), Hg dynamics are influenced by microtopography over very small spatial scales in this alluvial aquifer. We hypothesize that these microtopographic differences in groundwater MeHg reflect underlying geomorphic control on biogeochemical processing of carbon and other redox active solutes, as illustrated in the geochemical data in Supplementary Figure S6. Our finding highlights the need for consideration of microtopography in sampling design when investigating Hg biogeochemistry in groundwaters where small-scale spatial heterogeneity is likely to be important (e.g., river floodplains).

To better understand the controls on Hg speciation in these groundwaters, we examined relationships between MeHg and other geochemical variables (Table 2). Significant positive correlations were observed between filtered MeHg (FMeHg) and THg, DOC, absorbance at 254 nm (A_{254}, a parameter that depends on both DOM concentration and DOM character, especially aromatic carbon content (Weishaar et al., 2003)), dissolved Fe(II), and temperature. The fraction of filtered THg as MeHg (%MeHg) positively correlated with DOC, A_{254}, dissolved Fe(II) and Mn. The strong link between MeHg and DOC (r = 0.603) or A_{254} (r = 0.640) has been noted in numerous studies of surface waters and wetlands (Hall et al., 2008) and may relate to the role of DOM as a principal control of microbial community structure and function, including Hg methylation (Graham et al., 2018), the role of DOM in altering the bioavailability of inorganic Hg(II) for methylation (Graham et al., 2012), and/or increased aqueous partitioning of MeHg due to MeHg complexation by thiols in DOM (Skyllberg, 2008).

Interestingly, we did not observe any significant correlation of MeHg or %MeHg with sulfate concentrations. The mean sulfate concentration across all groundwater sites was 20.7 ± 20.9 mg/L, about 35% lower than mean sulfate in the Cedar River. Sulfate reduction was evidenced by minima in sulfate during the summer months, as reflected in the inverse correlation of groundwater sulfate with temperature shown in Table 2. Dissolved sulfide was rarely detected above 2 μM (mean = 0.5 ± 1.9 μM; Supplementary Figure S6) and showed no significant correlation with sulfate. Precipitation of Fe-S minerals (e.g., mackinawite, FeS(s) (Rickard, 2006)) via reaction of sulfide with dissolved Fe(II) produced from dissimilatory

TABLE 2 Correlation matrix for groundwater samples. Correlation coefficients in bolded-italics indicate significance at α = 0.05 level.

	FMeHg	% MeHg	FTHg	DO	DOC	Sulfate	Fe(II)	Mn	Nitrate	pH	Conductivity	T	Abs_{254}
FMeHg													
%MeHg	*0.634*												
FTHg	***0.336***	−0.142											
DO	−0.109	−0.029	−0.18										
DOC	***0.603***	***0.439***	***0.366***	−0.205									
sulfate	−0.082	−0.003	−0.178	***0.481***	−0.093								
Fe(II)	***0.240***	***0.326***	0.028	***−0.375***	***0.484***	−0.216							
Mn	0.208	***0.259***	0.06	***−0.273***	0.098	***−0.251***	***0.558***						
nitrate	−0.136	−0.216	−0.089	***0.346***	−0.184	−0.051	−0.175	***−0.244***					
pH	−0.038	−0.029	−0.056	−0.055	−0.024	−0.057	−0.104	−0.021	−0.037				
conductivity	0.119	0.087	0.219	***−0.367***	***0.579***	−0.046	***0.333***	0.073	−0.209	0.061			
T	***0.237***	0.228	***0.261***	***−0.578***	***0.378***	***−0.512***	0.229	0.236	***−0.307***	0.048	0.155		
Abs_{254}	***0.640***	***0.500***	0.212	***−0.263***	***0.628***	0.021	***0.479***	***0.272***	−0.139	0.143	***0.284***	0.176	
water table elevation	0.195	0.014	***0.302***	−0.221	***0.359***	−0.001	***0.258***	0.009	0.133	−0.156	***0.282***	0.037	0.445

Fe reduction may explain the low sulfide concentrations in these groundwaters. The highest sulfate concentrations, occasionally exceeding 100 mg/L, occurred during early spring, when groundwaters were more oxygen rich, suggesting internal cycling of sulfur stores in aquifer sediments (e.g., oxidation of reduced Fe-S minerals accumulating from prior sulfate and iron reduction). Compared to many sulfate-limited freshwater wetlands where Hg methylation has been extensively studied, sulfate supply may not limit Hg methylation in these systems and/or Hg methylation may be driven by microorganisms other than SRB (e.g., Fe-reducers, methanogens, or fermentative bacteria (Gilmour et al., 2013)). Recent studies investigating the diversity of *hgcA* in a variety of freshwater environments have shown that while *Deltaproteobacteria* (which includes SRB and FeRB) are often well-represented amongst Hg-methylators, other organisms, with diverse metabolisms, including those belonging to *Firmicutes, Spirochaetota, Chloroflexota, Nitrospirota,* and *Methanomicrobia,* can comprise an important fraction of the Hg-methylator community (Schaefer et al., 2014; Christensen et al., 2019; Jones et al., 2020; Xu et al., 2021).

Significant positive correlations between %MeHg and dissolved Fe(II) and Mn concentrations suggest that dissimilatory metal reduction may be important to Hg methylation in this system. Strong correlations between MeHg concentrations and dissolved Mn have been noted in agricultural wetlands (i.e., rice fields; (Alpers et al., 2014); and in a eutrophic reservoir (Beutel et al., 2020). We note that *Geobacter*, which include a number of species capable of Hg methylation (Gionfriddo et al., 2019), can reduce both Fe(III) and Mn(III,IV) (hydr)oxides (Richter et al., 2012). Mn(III,IV) hydroxides may also be reduced by dissolved Fe(II) (Schaefer et al., 2017), complicating interpretation of relationships between dissolved Mn and MeHg.

3.4 Hg dynamics in shallow wetland ponds

Wetland ponds represent another possible source of MeHg to the Cedar River. Total Hg and MeHg concentrations in the shallow wetland ponds tended to be greater than in groundwaters (Figure 3). Across all three wetland ponds, mean filtered MeHg was 0.26 ± 0.27 ng/L (median = 0.17 ng/L, n = 45) and mean filtered THg was 1.24 ± 0.65 ng/L (median = 1.02 ng/L, n = 45). Due to a combination of sediment suspension and primary production within these shallow wetland ponds and streams, these waters contain appreciable suspended particulate matter (Figure 4; mean SPM = 54.5 ± 71.4 mg/L; median SPM = 21.6 mg/L). Whole, unfiltered THg and MeHg concentrations are thus appreciably higher than filtered concentrations, averaging 4.89 ± 4.25 ng/L for THg (median = 2.96 ng/L) and 0.50 ± 0.48 ng/L for MeHg (median = 0.32 ng/L) respectively. Filtered MeHg comprised 55% ± 21% (median = 53%) of the total MeHg; for total Hg, this fraction was slightly lower, at 38% ± 24% (median = 37%). Distribution coefficients (log K_D's) for partitioning between the dissolved phase and suspended sediments averaged 4.5 ± 0.6 and 4.9 ± 0.5 for MeHg and THg respectively, similar to that observed for the Cedar River. In general, no significant differences in MeHg and THg concentrations or partitioning behavior were observed across the three wetland ponds, excepting higher THg in the south pond that had the highest suspended particulate matter.

Similar to groundwater samples, we examined a correlation matrix of Hg species concentrations and associated geochemical and physical parameters for these wetland ponds (Table 3). Total MeHg was significantly correlated with dissolved Mn and the absorbance at 254 nm (Abs_{254}), a parameter that reflects both DOM concentration and aromaticity (Weishaar et al., 2003). Total Hg was most strongly correlated with SPM and DOC.

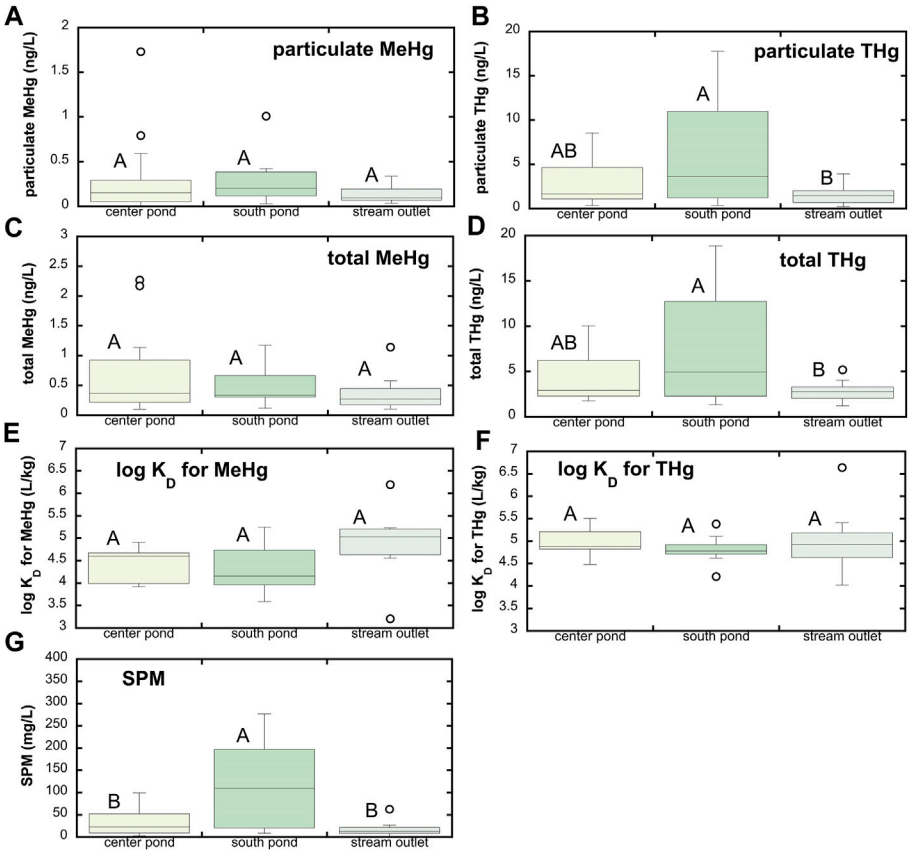

FIGURE 4
Hg speciation associated with suspended particulate matter (SPM) at SWO surface water sites. **(A)** Particulate MeHg; **(B)** particulate THg; **(C)** total MeHg (sum of filtered and particulate MeHg); **(D)** total THg (sum of filtered and particulate THg); **(E)** distribution coefficient (K_D) for partitioning between dissolved phase and SPM for MeHg; **(F)** K_D for THg; and **(G)** SPM. Boxes represent 25th and 75th percentiles, line the median, and whiskers the 10th and 90th percentiles; points represent outliers. Stations that do not share a common letter are significantly different ($\alpha = 0.05$) from one another based on one-way ANOVA and Tukey *post hoc* comparison. Note that SPM was sampled beginning 4/25/17 and through last sample collection on 9/4/18, so panels e, f, and g correspond to that time frame only. Panels a–d include data from the full study period beginning in June 2016.

Several earlier studies have highlighted the link between DOM and MeHg in wetland systems. Hall et al. (2008) found that MeHg in wetlands in coastal Louisiana was highly correlated with the hydrophobic acid fraction of DOM, but weakly correlated with bulk DOC. Mitchell and Gilmour (2008) observed strong correlation of Hg methylation rates in wetland sediments with $SUVA_{280}$ and slope ratio (S_R) (Helms et al., 2008), spectroscopic measures mostly strongly related to DOM molecular weight and aromaticity. Our results suggest tight coupling of DOM and MeHg in inland wetlands within agriculturally-dominated regions of the UMRB. Recent advances in measuring individual low molecular weight (LMW) thiols (Liem-Nguyen et al., 2021) and sulfur-containing compounds in DOM by high-resolution mass spectrometry (HR-MS) (Mangal et al., 2022) indicate the importance of thiols to Hg methylation in freshwater wetlands, presumably by controlling Hg bioavailability to Hg-methylating organisms (Graham et al., 2012; 2017). Increased anthropogenic sulfur inputs in regions with intensive corn and soy cultivation appear likely as soils may become sulfur-depleted following acid deposition recovery (Hinckley et al., 2020). Such sulfur inputs could induce changes in microbial community structure (Jones et al., 2020) and/or Hg bioavailability for methylation due to complex linkages between sulfide, DOM, and Hg (Graham et al., 2017; Poulin et al., 2017) that alter MeHg production in terrestrial ecosystems.

3.5 Hg methylation potentials in wetland pond sediments

Observations of Hg speciation in wetland waters were supplemented by measurements of Hg speciation and Hg methylation potentials in shallow sediment cores. Total Hg concentrations in wetland sediments were generally between 70 and 100 ng/g dry weight and generally decreased slightly with depth (Figure 5). MeHg concentrations were greatest in near surface sediments, reaching 1 ng/g dry weight, up to 1.6% of THg. Methylation potentials were determined in short term incubations with injection of enriched ^{201}Hg pre-equilibrated with filtered surface water from each site and were greatest (k_{meth} exceeding 0.15 d^{-1}) in surface sediments.

Surficial sediments in the SWO ponds have methylation potentials toward the upper end of the range reported previously for other freshwater wetlands (Hoggarth et al., 2015), indicative of robust Hg methylation potential within wetlands of the Cedar River

TABLE 3 Correlation matrix for SWO surface water samples. Correlation coefficients in bolded-italics indicate significance at $\alpha = 0.05$ level.

	F MeHg	% FTHg as MeHg	F THg	SPM	P MeHg	P THg	Total MeHg	Total THg	DO	DOC	SO_4^{2-}	Fe(II)	Mn	NO_3^-	pH	Conductivity	T
% MeHg	*0.772*																
FTHg	***0.463***	−0.103															
SPM	−0.059	−0.099	0.055														
PMeHg	***0.355***	0.270	0.110	***0.367***													
PTHg	−0.073	−0.058	−0.102	***0.841***	0.299												
total MeHg	***0.794***	***0.607***	***0.333***	0.148	***0.850***	0.138											
total THg	−0.002	−0.074	0.050	***0.849***	***0.318***	***0.988***	0.191										
DO	***−0.420***	−0.204	***−0.317***	0.208	−0.110	0.195	−0.303	0.149									
DOC	−0.088	−0.065	−0.135	0.265	0.174	***0.438***	0.066	***0.420***	0.174								
sulfate	0.060	−0.070	0.155	−0.052	−0.122	−0.083	−0.032	−0.059	0.255	−0.273							
Fe(II)	0.202	0.064	0.151	−0.123	0.257	−0.094	0.280	−0.071	***−0.421***	0.198	−0.147						
Mn	***0.368***	0.270	0.176	−0.100	0.223	−0.113	***0.349***	−0.087	***−0.442***	0.220	−0.047	***0.538***					
nitrate	0.142	0.114	0.288	0.018	−0.122	−0.218	0.009	−0.175	0.015	***−0.322***	0.071	−0.133	−0.211				
pH	0.051	0.282	−0.218	−0.113	0.080	−0.054	0.113	−0.085	***0.385***	0.142	−0.185	−0.045	−0.078	−0.081			
conductivity	−0.062	−0.139	0.202	−0.238	−0.052	−0.192	−0.062	−0.165	0.146	−0.205	0.136	−0.111	−0.048	0.225	0.002		
T	0.160	***0.391***	−0.100	−0.056	0.192	0.103	0.211	0.089	0.095	***0.388***	***−0.460***	0.036	−0.007	0.044	***0.479***	0.272	
Abs_{254}	***0.503***	***0.369***	0.207	0.066	***0.568***	0.100	***0.652***	0.131	***−0.447***	***0.708***	−0.193	***0.398***	***0.515***	***−0.341***	0.194	−0.255	***0.389***

10.3389/fenvc.2023.1242813

10.3389/fenvc.2023.1242813

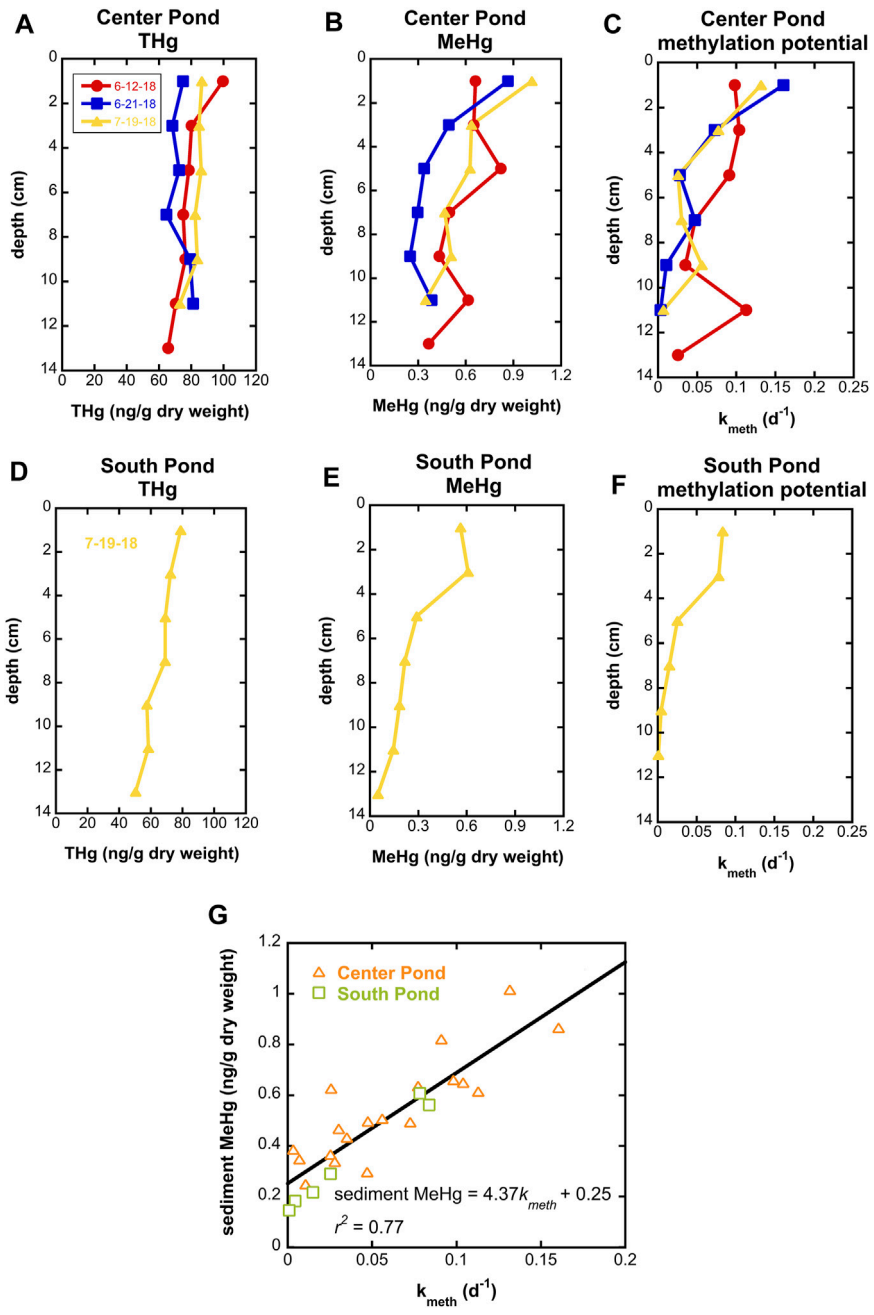

FIGURE 5
Total Hg, MeHg, and Hg methylation potential in center pond sediment cores on three dates in summer 2018 (**(A-C)** respectively) and a south pond sediment core on 7/19/18 **(D-F)**. **(G)** shows correlation between Hg methylation potential (k_{meth}) and MeHg concentrations for all samples.

floodplain. Interestingly, the %MeHg observed in sediments (not exceeding 1.6%) is relatively low given the large values of k_{meth} observed. We hypothesize that MeHg degradation in SWO sediments may be comparatively fast and relatively invariant with depth, leading to the strong correlation between k_{meth} and MeHg in sediment (Figure 5G). Future studies at SWO will investigate biological and dark abiotic MeHg degradation processes, which, apart from MeHg degradation by *merB* containing organisms, remain poorly understood (Barkay and Gu, 2022).

3.6 Response to hydrologic events

Geochemistry in groundwaters and wetlands can change rapidly in riparian zones with high hydrologic connectivity. During the summer of 2018, we sampled at SWO just before and after overbank flow events of the Cedar River (Figure 6). We observed that filtered Hg and MeHg concentrations in groundwater increased markedly immediately following flood conditions. In the low-lying swale well (Figure 6B), groundwater MeHg concentrations increased 17 to 35-

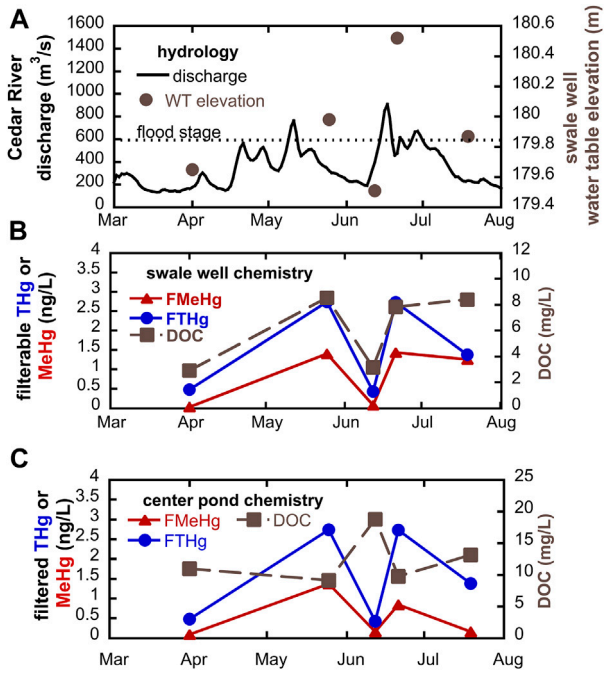

FIGURE 6
Response to flood events during summer 2018, showing **(A)** water table rise and fall in swale well; **(B)** groundwater chemistry in swale well; and **(C)** surface water chemistry in center pond.

fold (from as little as 0.04 ng/L to 1.4 ng/L) following flood events. THg concentrations also showed significant increases, about 5-fold (from 0.5 to 2.7 ng/L) following flooding. During this period, we observed tight coupling with DOC concentrations. We hypothesize that water table rise into the OM-rich surface soils results in leaching of both DOM and THg and supports high MeHg production. A similar trend for MeHg and THg following flooding was observed within the center pond wetland, but DOC was actually highest during the June sampling with the lowest MeHg (Figure 6C). Apparent mismatch between peak DOC and peak MeHg and THg at this site may relate to shifting sources of DOM within the pond that have differential impact on Hg bioavailbity for methylation. DOM may be transported into the pond via both overland flow and groundwater, as well as being produced autochthonously via leakage from phytoplankton. Periods of groundwater table rise or overland flow are likely to increase the delivery of allocthonous DOM. During dry periods, groundwater recharge of the pond will be reduced, and DOM will be mostly derived from algal biomass produced within the pond. Laboratory experiments indicate that high molecular weight, more aromatic allocthonous DOM is especially effective at enhancing Hg methylation by Hg-methylating bacteria (Graham et al., 2013).

Importantly, we see no evidence that delivery of nitrate rich water suppresses Hg methylation during flooding. Nitrate concentrations in the Cedar River averaged 6.5 ± 1.7 mg N/L during the 2018 sampling dates but were markedly lower in wetlands (0.43 ± 1.0 mg N/L) and alluvial groundwaters (0.21 ± 0.51 mg N/L) over the same period. Nitrate inputs have potential to suppress other less-energetically favorable terminal electron acceptor processes. If the suppressed processes are the dominant metabolisms associated with Hg methylation, then nitrate addition may inhibit microbial Hg methylation. Nitrate addition to a sulfate-rich stratified freshwater lake resulted in lowered MeHg concentrations in hypolimnetic waters, likely related to both shifts in terminal electron acceptor processes and the formation/stability of iron-oxide layers at the sediment-water interface that adsorb and store MeHg (Todorova et al., 2009; Matthews et al., 2013). In this system, we see no buildup of nitrate in either alluvial groundwaters or wetland surface waters at or near flood conditions. The supply of labile organic carbon in this system is likely sufficient to allow for rapid denitrification and less-energetically favorable microbial metabolisms associated with Hg methylation (e.g., iron and sulfate reduction and methanogenesis).

Clearly, flood events result in significant increases in Hg and MeHg available for transport within the Cedar River floodplain. We posit that river floodplains are important "control points" (Bernhardt et al., 2017) for downstream delivery of Hg and MeHg. Hydrologic connectivity between floodplain and river likely plays an important role in the efficiency of both stimulation of Hg methylation and subsequent Hg and MeHg transport. Flood frequency has increased in the central United States over the last 50-plus years (Mallakpour and Villarini, 2015). Streamflow estimates derived from coupled downscaled precipitation projects and a hillslope link model for the Cedar River basin project a 50% increase in the Cedar River discharge during a flood with a 100-year recurrence interval by the end of the 21st century (Quintero et al., 2018). While increased streamflow will almost certainly lead to increased fluxes of Hg and MeHg (see section 3.1), our results suggest this effect may be amplified, especially for MeHg, by increased MeHg production within riparian zones during floods. Climate change thus has potential to partially offset reductions in export of Hg and MeHg from terrestrial ecosystems achieved by emissions reductions via implementation of the Minamata Convention. Long-term monitoring of Hg and MeHg in fluvial systems could serve an important role in measuring the effectiveness of the Minamata Convention and climate-change driven changes in Hg biogeochemistry and transport.

4 Conclusion

There are few, if any, reports of MeHg or THg in rivers of Iowa or wetlands of the UMRB. MeHg concentrations measured at SWO (<0.03 to as much as 1.5 ng/L) fall within the range reported for lakes and wetlands in the upper plains region of the United States and Canada (Sando et al., 2007; Hall et al., 2009; Cowdery and Brigham, 2013; Hoggarth et al., 2015). MeHg concentrations in SWO groundwaters and wetlands were strongly correlated with DOC and reduced metal (Fe and Mn) species, suggesting a role for dissimilatory metal reduction in Hg methylation at these sites. Groundwater transport of dissolved MeHg and THg in river systems with high hydrologic connectivity between river and floodplain may play an underappreciated role in Hg and MeHg export from terrestrial ecosystems. Hg speciation and other geochemical variables show significant spatiotemporal variability on small scales (meters and days), linked to landscape position (geomorphic control) and water table elevation (hydrologic control).

While fine-scale variability of DO and nutrient biogeochemistry within this landscape has been noted previously (Schilling and Jacobson, 2012) we extend that understanding to include trace element biochemistry. The reality of such fine-scale spatiotemporal variability highlights the importance of adequate sampling density in environmental monitoring and assessment for Hg in patchy landscapes, like ridge and swale floodplains.

We contend that riparian groundwaters and wetlands act as critical ecosystem control points (Bernhardt et al., 2017) for Hg trophic transfer in terrestrial ecosystems and downstream export of MeHg. MeHg concentrations increase rapidly in response to flood events, leading to increased transport and potential wildlife exposure. The SWO preserve is a high-value ecosystem that provides critical habitat for waterfowl and endangered reptiles and amphibians (SWO is part of a designated Amphibian and Reptile Conservation Area within the state of Iowa). Further studies on the impacts on wildlife in these ecosystems are warranted.

Total Hg and MeHg fluxes for the Cedar River watershed ranged from 2.6 to 6.9 $\mu g\ m^{-2}\ yr^{-1}$ for THg and 0.09–0.18 $\mu g\ m^{-2}\ yr^{-1}$ for MeHg. The THg flux can represent near 50% of total wet deposition in this region. The high watershed transfer efficiency of THg is almost certainly linked to high rates of soil loss and sediment transport. Our findings suggest that agricultural watersheds may be overlooked contributors of export of THg and MeHg from terrestrial ecosystems. Given the importance of suspended sediment to THg transport (and MeHg to a lesser extent), land use and management (e.g., soil conservation practices vs new land in production) and climate change (e.g., increased frequency and shifts in seasonality of extreme precipitation events) have the potential to alter riverine Hg and MeHg fluxes in this region. Long-term monitoring of Hg and MeHg fluxes in intermediate and large-scale watersheds like the Cedar River is a valuable tool for evaluating changes in the global biogeochemical cycle of Hg, such as land to sea fluxes, that are likely to change in response to implementation of the Minamata Convention and climate change.

Data availability statement

The raw data supporting the conclusion of this article will be made available by the authors, without undue reservation.

Author contributions

AG designed and supervised the study. All authors contributed to field work, analytical work, and data analysis. AG wrote the first draft of the paper. All authors contributed to the article and approved the submitted version.

Acknowledgments

The authors gratefully acknowledge support from the Grinnell College Mentored Advanced Project program and National Science Foundation grant EAR 1919696. We appreciate additional field work and laboratory assistance from Vivian Cheslack, Ania Szlembarska, and Feven Getachew and helpful conversations with Peter Jacobson and Keith Schilling that improved the quality of this study.

Conflict of interest

The authors declare that the research was conducted in the absence of any commercial or financial relationships that could be construed as a potential conflict of interest.

Publisher's note

Supplementary material

The Supplementary Material for this article can be found online at: https://www.frontiersin.org/articles/10.3389/fenvc.2023.1242813/full#supplementary-material

References

Alpers, C. N., Fleck, J. A., Marvin-DiPasquale, M., Stricker, C. A., Stephenson, M., and Taylor, H. E. (2014). Mercury cycling in agricultural and managed wetlands, yolo bypass, California: spatial and seasonal variations in water quality. *Sci. Total Environ.* 484, 276–287. doi:10.1016/j.scitotenv.2013.10.096

Babiarz, C. L., Benoit, J. M., Shafer, M. M., Andren, A. W., Hurley, J. P., and Webb, D. A. (1998). Seasonal influences on partitioning and transport of total and methylmercury in rivers from contrasting watersheds. *Biogeochemistry* 41, 237–257. doi:10.1023/a:1005940630948

Balogh, S. J., Meyer, M. L., and Johnson, D. K. (1998). Transport of mercury in three contrasting river basins. *Environ. Sci. Technol.* 32, 456–462. doi:10.1021/es970506q

Balogh, S. J., Nollet, Y. H., and Offerman, H. J. (2005). A comparison of total mercury and methylmercury export from various Minnesota watersheds. *Sci. Total Environ.* 340, 261–270. doi:10.1016/j.scitotenv.2004.08.013

Balogh, S. J., Swain, E. B., and Nollet, Y. H. (2006). Elevated methylmercury concentrations and loadings during flooding in Minnesota rivers. *Sci. Total Environ.* 368, 138–148. doi:10.1016/j.scitotenv.2005.09.045

Barkay, T., and Gu, B. (2022). Demethylation-the other side of the mercury methylation coin: A critical review. *Acs Environ. Au* 2, 77–97. doi:10.1021/acsenvironau.1c00022

Bernhardt, E. S., Blaszczak, J. R., Ficken, C. D., Fork, M. L., Kaiser, K. E., and Seybold, E. C. (2017). Control points in ecosystems: moving beyond the hot spot hot moment concept. *Ecosystems* 20, 665–682. doi:10.1007/s10021-016-0103-y

Beutel, M., Fuhrmann, B., Herbon, G., Chow, A., Brower, S., and Pasek, J. (2020). Cycling of methylmercury and other redox-sensitive compounds in the profundal zone of a hypereutrophic water supply reservoir. *Hydrobiologia* 847, 4425–4446. doi:10.1007/s10750-020-04192-3

Bishop, K., Shanley, J. B., Riscassi, A., Wit, H. A., Eklöf, K., Meng, B., et al. (2020). Recent advances in understanding and measurement of mercury in the environment: terrestrial Hg cycling. *Sci. Total Environ.* 721, 137647. doi:10.1016/j.scitotenv.2020.137647

Bradley, P. M., Burns, D. A., Murray, K. R., Brigham, M. E., Button, D. T., Chasar, L. C., et al. (2011). Spatial and seasonal variability of dissolved methylmercury in two

stream basins in the eastern United States. *Environ. Sci. Technol.* 45, 2048–2055. doi:10.1021/es103923j

Bradley, P. M., Journey, C. A., Chapelle, F. H., Lowery, M. A., and Conrads, P. A. (2010). Flood hydrology and methylmercury availability in coastal plain rivers. *Environ. Sci. Technol.* 44, 9285–9290. doi:10.1021/es102917j

Bradley, P. M., Journey, C. A., Lowery, M. A., Brigham, M. E., Burns, D. A., Button, D. T., et al. (2012). Shallow groundwater mercury supply in a coastal plain stream. *Environ. Sci. Technol.* 46, 7503–7511. doi:10.1021/es301540g

Branfireun, B. A. (2004). Does microtopography influence subsurface pore-water chemistry? Implications for the study of methylmercury in peatlands. *Wetlands* 24, 207–211. doi:10.1672/0277-5212(2004)024[0207:dmispc]2.0.co;2

Brigham, M. E., Wentz, D. A., Aiken, G. R., and Krabbenhoft, D. P. (2009). Mercury cycling in stream ecosystems. 1. Water column chemistry and transport. *Environ. Sci. Technol.* 43, 2720–2725. doi:10.1021/es802694n

Christensen, G. A., Gionfriddo, C. M., King, A. J., Moberly, J. G., Miller, C. L., Somenahally, A. C., et al. (2019). Determining the reliability of measuring mercury cycling gene abundance with correlations with mercury and methylmercury concentrations. *Environ. Sci. Technol.* 53, 8649–8663. doi:10.1021/acs.est.8b06389

Clesceri L., Greenberg A. E., and Eaton, A. D. (Editors) (2000). *Standard methods for the examination of water and wastewater* (American Public Health Association).

Cowdery, T. K., and Brigham, M. E. (2013). *Mercury in wetlands at the glacial Ridge National wildlife refuge, northwestern Minnesota, 2007-9*. United States Geological Survey Scientific Investigations. Report 2013-5068.

Creswell, J. E., Kerr, S. C., Meyer, M. H., Babiarz, C. L., Shafer, M. M., Armstrong, D. E., et al. (2008). Factors controlling temporal and spatial distribution of total mercury and methylmercury in hyporheic sediments of the allequash creek wetland, northern Wisconsin. *J. Geophys Res. Biogeosciences* 113. doi:10.1029/2008jg000742

Dettman, C. L., and Mabry, C. M. (2008). Lessons Learned about Research and Management: A Case Study from a Midwest Lowland Savanna, U.S.A. *Restor. Ecol.* 16, 532–541. doi:10.1111/j.1526-100x.2008.00478.x

Doane, T. A., and Horwáth, W. R. (2010). Eliminating Interference From Iron(III) for Ultraviolet Absorbance Measurements of Dissolved Organic Matter. *Chemosphere* 78, 1409–1415. doi:10.1016/j.chemosphere.2009.12.062

Driscoll, C. T., Mason, R. P., Chan, H. M., Jacob, D. J., and Pirrone, N. (2013). Mercury as a Global Pollutant: sources, Pathways, and Effects. *Environ. Sci. Technol.* 47, 4967–4983. doi:10.1021/es305071v

Fitzgerald, W. F. (1999). "Clean hands, dirty hands: clair Patterson and the aquatic biogeochemistry of mercury," in *Clean hands: Clair patterson's crusade against environmental lead contamination*. Editor C. I. Davidson, 119–137.

Gilmour, C. C., Podar, M., Bullock, A. L., Graham, A. M., Brown, S. D., Somenahally, A. C., et al. (2013). Mercury Methylation by Novel Microorganisms from New Environments. *Environ. Sci. Technol.* 47, 11810–11820. doi:10.1021/es403075t

Gionfriddo, C., Podar, M., Gilmour, C., Pierce, E., and Elias, D. (2019). *ORNL compiled mercury methylator Database*. Available at: https://www.osti.gov/dataexplorer/biblio/dataset/1569274.

Graham, A. M., Aiken, G. R., and Gilmour, C. C. (2013). Effect of Dissolved Organic Matter Source and Character on Microbial Hg Methylation in Hg–S–DOM Solutions. *Environ. Sci. Technol.* 47, 5746–5754. doi:10.1021/es400414a

Graham, A. M., Aiken, G. R., and Gilmour, C. C. (2012). Dissolved Organic Matter Enhances Microbial Mercury Methylation Under Sulfidic Conditions. *Environ. Sci. Technol.* 46, 2715–2723. doi:10.1021/es203658f

Graham, A. M., Cameron-Burr, K., Hajic, H., Lee, C., Msekela, D., and Gilmour, C. C. (2017). Sulfurization of Dissolved Organic Matter Increases Hg–Sulfide–Dissolved Organic Matter Bioavailability to a Hg-Methylating Bacterium. *Environ. Sci. Technol.* 51, 9080–9088. doi:10.1021/acs.est.7b02781

Graham, E. B., Gabor, R. S., Schooler, S., McKnight, D. M., Nemergut, D. R., and Knelman, J. E. (2018). Oligotrophic Wetland Sediments Susceptible to Shifts in Microbiomes and Mercury Cycling with Dissolved Organic Matter Addition. *Peerj* 6, e4575. doi:10.7717/peerj.4575

Gygax, S., Gfeller, L., Wilcke, W., and Mestrot, A. (2019). Emerging Investigator Series: mercury Mobility and Methylmercury Formation in a Contaminated Agricultural Flood Plain: influence of Flooding and Manure Addition. *Environ. Sci. Process Impacts* 21, 2008–2019. doi:10.1039/c9em00257j

Hall, B. D., Aiken, G. R., Krabbenhoft, D. P., Marvin-DiPasquale, M., and Swarzenski, C. M. (2008). Wetlands as Principal Zones of Methylmercury Production in Southern Louisiana and the Gulf of Mexico Region. *Environ. Pollut.* 154, 124–134. doi:10.1016/j.envpol.2007.12.017

Hall, B. D., Baron, L. A., and Somers, C. M. (2009). Mercury Concentrations in Surface Water and Harvested Waterfowl from the Prairie Pothole Region of Saskatchewan. *Environ. Sci. Technol.* 43, 8759–8766. doi:10.1021/es9024589

Heimann, D. C., Sprague, L. A., and Blevins, D. W. (2011). *Trends in suspended-sediment loads and concentrations in the Mississippi River Basin, 1950-2009*. U.S. Geological Survey Scientific Investigations. Report 2011-5200.

Helms, J. R., Stubbins, A., Ritchie, J. D., Minor, E. C., Kieber, D. J., and Mopper, K. (2008). Absorption Spectral Slopes and slope Ratios as Indicators of Molecular Weight, Source, and Photobleaching of Chromophoric Dissolved Organic Matter. *Limnol. Oceanogr.* 53, 955–969. doi:10.4319/lo.2008.53.3.0955

Hinckley, E.-L. S., Crawford, J. T., Fakhraei, H., and Driscoll, C. T. (2020). A Shift in Sulfur-Cycle Manipulation From Atmospheric Emissions to Agricultural Additions. *Nat. Geosci.* 13, 597–604. doi:10.1038/s41561-020-0620-3

Hintelmann, H., and Evans, R. D. (1997). Application of Stable Isotopes in Environmental Tracer Studies – Measurement of Monomethylmercury (CH3Hg+) by Isotope Dilution ICP-MS and Detection of Species Transformation. *Fresenius' J. Anal. Chem.* 358, 378–385. doi:10.1007/s002160050433

Hoggarth, C. G. J., Hall, B. D., and Mitchell, C. P. J. (2015). Mercury Methylation in High and Low-Sulphate Impacted Wetland Ponds Within the Prairie Pothole Region of North America. *Environ. Pollut.* 205, 269–277. doi:10.1016/j.envpol.2015.05.046

Hurley, J. P., Benoit, J. M., Babiarz, C. L., Shafer, M. M., Andren, A. W., Sullivan, J. R., et al. (1995). Influences of Watershed Characteristics on Mercury Levels in Wisconsin Rivers. *Environ. Sci. Technol.* 29, 1867–1875. doi:10.1021/es00007a026

Jones, C. S., Nielsen, J. K., Schilling, K. E., and Weber, L. J. (2018a). Iowa Stream Nitrate and the Gulf of Mexico. *PLOS One* 13, e0195930. doi:10.1371/journal.pone.0195930

Jones, C. S., and Schilling, K. E. (2011). From Agricultural Intensification to Conservation: sediment Transport in the Raccoon River, Iowa, 1916–2009. *J. Environ. Qual.* 40, 1911–1923. doi:10.2134/jeq2010.0507

Jones, C. S., Schilling, K. E., Simpson, I. M., and Wolter, C. F. (2018b). Iowa Stream Nitrate, Discharge and Precipitation: 30-Year Perspective. *Environ. Manage* 62, 709–720. doi:10.1007/s00267-018-1074-x

Jones, D. S., Johnson, N. W., Mitchell, C. P. J., Walker, G. M., Bailey, J. V., Pastor, J., et al. (2020). Diverse Communities of hgcAB + Microorganisms Methylate Mercury in Freshwater Sediments Subjected to Experimental Sulfate Loading. *Environ. Sci. Technol.* 54, 14265–14274. doi:10.1021/acs.est.0c02513

Kanzler, C. R., Lian, P., Trainer, E. L., Yang, X., Govind, N., Parks, J. M., et al. (2018). Emerging Investigator Series: methylmercury Speciation and Dimethylmercury Production in Sulfidic Solutions. *Environ. Sci. Process Impacts* 20, 584–594. doi:10.1039/c7em00533d

Krabbenhoft, D. P., and Sunderland, E. M. (2013). Global Change and Mercury. *Science* 341, 1457–1458. doi:10.1126/science.1242838

Liem-Nguyen, V., Skyllberg, U., and Björn, E. (2021). Methylmercury formation in boreal wetlands in relation to chemical speciation of mercury(II) and concentration of low molecular mass thiols. *Sci. Total Environ.* 755, 142666. doi:10.1016/j.scitotenv.2020.142666

Mallakpour, I., and Villarini, G. (2015). The Changing Nature of Flooding Across the Central United States. *Nat. Clim. Change* 5, 250–254. doi:10.1038/nclimate2516

Mangal, V., Lam, W. Y., Huang, H., Emilson, E. J. S., Mackereth, R. W., and Mitchell, C. P. J. (2022). Molecular Correlations of Dissolved Organic Matter with Inorganic Mercury and Methylmercury in Canadian Boreal Streams. *Biogeochemistry* 160, 127–144. doi:10.1007/s10533-022-00944-6

Matthews, D. A., Babcock, D. B., Nolan, J. G., Prestigiacomo, A. R., Effler, S. W., Driscoll, C. T., et al. (2013). Whole-Lake Nitrate Addition for Control of Methylmercury in Mercury-Contaminated Onondaga Lake, NY. *Environ. Res.* 125, 52–60. doi:10.1016/j.envres.2013.03.011

Mitchell, C. P. J., and Gilmour, C. C. (2008). Methylmercury Production in a Chesapeake Bay Salt Marsh. *J. Geophys Res. Biogeosciences* 113. doi:10.1029/2008jg000765

National Atmospheric Deposition Program (2019). *National atmospheric deposition program 2018 annual summary*. Madison, WI: Wisconsin State Laboratory of Hygiene, University of Wisconsin-Madison.

Neri, A., Villarini, G., and Napolitano, F. (2019). Statistically-Based Projected Changes in the Frequency of Flood Events Across the U.S. Midwest. *J. Hydrol.* 584, 124314. doi:10.1016/j.jhydrol.2019.124314

Parker, J. L., and Bloom, N. S. (2005). Preservation and Storage Techniques for Low-level Aqueous Mercury Speciation. *Sci. Total Environ.* 337, 253–263. doi:10.1016/j.scitotenv.2004.07.006

Poulin, B. A., Ryan, J. N., Nagy, K. L., Stubbins, A., Dittmar, T., Orem, W. H., et al. (2017). Spatial Dependence of Reduced Sulfur in Everglades Dissolved Organic Matter Controlled by Sulfate Enrichment. *Environ. Sci. Technol.* 51, 3630–3639. doi:10.1021/acs.est.6b04142

Quintero, F., Mantilla, R., Anderson, C., Claman, D., and Krajewski, W. (2018). Assessment of Changes in Flood Frequency Due to the Effects of Climate Change: implications for Engineering Design. *Hydrology* 5, 19. doi:10.3390/hydrology5010019

R Core Team (2019). *R: A language and environment for statistical computing*. Vienna, Austria: R Foundation for Statistical Computing. Available at: https://www.R-project.org/.

Richter, K., Schicklberger, M., and Gescher, J. (2012). Dissimilatory Reduction of Extracellular Electron Acceptors in Anaerobic Respiration. *Appl. Environ. Microb.* 78, 913–921. doi:10.1128/aem.06803-11

Rickard, D. (2006). The Solubility of FeS. *Geochim. Cosmochim. Ac* 70, 5779–5789. doi:10.1016/j.gca.2006.02.029

Riscassi, A. L., and Scanlon, T. M. (2013). Particulate and Dissolved Mercury Export in Streamwater Within Three Mid-Appalachian Forested Watersheds in the US. *J. Hydrol.* 501, 92–100. doi:10.1016/j.jhydrol.2013.07.041

Runkel, R. L., Crawford, C. G., and Cohn, T. A. (2004). *Load Estimator (LOADEST): A FORTRAN Program for Estimating Constituent Loads in Streams and Rivers. U.S. Geological Survey*. doi:10.3133/tm4A5

Sando, S. K., Krabbenhoft, D. P., Johnson, K. M., Lundgren, R. F., and Emerson, D. G. (2007). *Mercury and methylmercury in water and bottom sediments of wetlands at lostwood national wildlife refuge, north Dakota, 2003-04*. United States Geological Survey Scientific Investigations. Report 2007-5219.

Schaefer, J. K., Kronberg, R. M., Morel, F. M. M., and Skyllberg, U. (2014). Detection of a key Hg methylation gene,*hgcA*, in wetland soils: detection of the Hg methylation gene, hgcA, in soils. *Env. Microbiol. Rep.* 6, 441–447. doi:10.1111/1758-2229.12136

Schaefer, M. V., Handler, R. M., and Scherer, M. M. (2017). Fe(II) Reduction of Pyrolusite (β-MnO2) and Secondary Mineral Evolution. *Geochem T* 18, 7. doi:10.1186/s12932-017-0045-0

Schilling, K. E., and Jacobson, P. J. (2015). Temporal Variations in Dissolved Oxygen Concentrations Observed in a Shallow Floodplain Aquifer. *River Res. Appl.* 31, 576–589. doi:10.1002/rra.2759

Schilling, K. E., and Jacobson, P. (2012). Spatial Relations of Topography, Lithology, and Water Quality in a Large River Floodplain. *River Res. Appl.* 28, 1417–1427. doi:10.1002/rra.1531

Schilling, K. E., and Jacobson, P. (2009). Water Uptake and Nutrient Concentrations Under a Floodplain Oak Savanna During a Non-Flood Period, lower Cedar River, Iowa. *Hydrol. Process* 23, 3006–3016. doi:10.1002/hyp.7403

Schilling, K. E., Kim, S.-W., and Jones, C. S. (2017). Use of Water Quality Surrogates to Estimate Total Phosphorus Concentrations in Iowa Rivers. *J. Hydrol. Reg. Stud.* 12, 111–121. doi:10.1016/j.ejrh.2017.04.006

Skyllberg, U. (2008). Competition Among Thiols and Inorganic Sulfides and Polysulfides for Hg and MeHg in Wetland Soils and Sediments Under Suboxic Conditions: illumination of Controversies and Implications for MeHg Net Production. *J. Geophys Res. Biogeosciences* 113. doi:10.1029/2008jg000745

Stookey, L. L. (1970). Ferrozine -- A New Spectrophotometric Reagent for Iron. *Anal. Chem.* 42, 779–781. doi:10.1021/ac60289a016

Streets, D. G., Horowitz, H. M., Jacob, D. J., Lu, Z., Levin, L., Schure, A. F. H. T., et al. (2017). Total Mercury Released to the Environment by Human Activities. *Environ. Sci. Technol.* 51, 5969–5977. doi:10.1021/acs.est.7b00451

Todorova, S. G., Driscoll, C. T., Matthews, D. A., Effler, S. W., Hines, M. E., and Henry, E. A. (2009). Evidence for Regulation of Monomethyl Mercury by Nitrate in a Seasonally Stratified, Eutrophic Lake. *Environ. Sci. Technol.* 43, 6572–6578. doi:10.1021/es900887b

Tsypin, M., and Macpherson, G. L. (2012). The effect of Precipitation Events on Inorganic Carbon in Soil and Shallow Groundwater, Konza Prairie LTER Site, NE Kansas, USA. *Appl. Geochem.* 27, 2356–2369. doi:10.1016/j.apgeochem.2012.07.008

United States Environmental Protection Agency (1998). *Method 1630: Methyl mercury in water by distillation aqueous ethylation purge and trap and cold vapor atomic fluorescence spectrometry*. Washington, D.C. United States Environmental Protection Agency.

United States Environmental Protection Agency (2002). *Cold vapor atomic fluorescence spectrometry*. Washington, D.C. United States Environmental Protection Agency.Method 1631, Revision E: mercury in Water by Oxidation, Purge and Trap

Vermilyea, A. W., Nagorski, S. A., Lamborg, C. H., Hood, E. W., Scott, D., and Swarr, G. J. (2017). Continuous Proxy Measurements Reveal Large Mercury Fluxes from Glacial and Forested Watersheds in Alaska. *Sci. Total Environ.* 599, 145–155. doi:10.1016/j.scitotenv.2017.03.297

Vidon, P. G., Mitchell, C. P. J., Jacinthe, P.-A., Baker, M. E., Liu, X., and Fisher, K. R. (2013). Mercury Dynamics in Groundwater Across Three Distinct Riparian Zone Types of the US Midwest. *Environ. Sci. Process Impacts* 15, 2131–2141. doi:10.1039/c3em00254c

Weishaar, J. L., Aiken, G. R., Bergamaschi, B. A., Fram, M. S., Fujii, R., and Mopper, K. (2003). Evaluation of Specific Ultraviolet Absorbance as an Indicator of the Chemical Composition and Reactivity of Dissolved Organic Carbon. *Environ. Sci. Technol.* 37, 4702–4708. doi:10.1021/es030360x

Weiss-Penzias, P. S., Gay, D. A., Brigham, M. E., Parsons, M. T., Gustin, M. S., and Schure, A. ter (2016). Trends in Mercury Wet deposition and Mercury Air Concentrations across the U.S. and Canada. *Sci. Total Environ.* 568, 546–556. doi:10.1016/j.scitotenv.2016.01.061

Xu, J., Liem-Nguyen, V., Buck, M., Bertilsson, S., Björn, E., and Bravo, A. G. (2021). Mercury Methylating Microbial Community Structure in Boreal Wetlands Explained by Local Physicochemical Conditions. *Front. Environ. Sci.* 8, 518662. doi:10.3389/fenvs.2020.518662

frontiers | Frontiers in Environmental Chemistry

TYPE Original Research
PUBLISHED 14 September 2023
DOI 10.3389/fenvc.2023.1242915

OPEN ACCESS

EDITED BY
Claude Fortin,
Université du Québec, Canada

REVIEWED BY
Marc Amyot,
Montreal University, Canada
Andrew Mitchell Graham,
Grinnell College, United States

*CORRESPONDENCE
Anne Helene Fostier,
annehfostier@gmail.com

†These authors have contributed equally to this work and share senior authorship

RECEIVED 19 June 2023
ACCEPTED 29 August 2023
PUBLISHED 14 September 2023

CITATION
Fostier AH, Amouroux D, Tessier E, Viana JLM and Richter L (2023), Methylmercury content in soil and litter from the Amazonian rainforest and its potential fate during forest fires. *Front. Environ. Chem.* 4:1242915. doi: 10.3389/fenvc.2023.1242915

Methylmercury content in soil and litter from the Amazonian rainforest and its potential fate during forest fires

Anne Helene Fostier[1*†], David Amouroux[2†], Emmanuel Tessier[2], José Lucas Martins Viana[1] and Larissa Richter[1]

[1]Institute of Chemistry, University of Campinas (UNICAMP), Campinas, São Paulo, Brazil, [2]Université de Pau et des Pays de l'Adour, E2S UPPA, CNRS, Institut des Sciences Analytiques et de Physico-chimie pour l'Environnement et les Matériaux (IPREM), Pau, France

Methylmercury in soils and vegetation from the Amazonian rainforest is still poorly studied. Hence, the aim of this work was to determine the total mercury [THg] and methylmercury [MeHg] concentrations in litter and surface soil, MeHg deposition via litterfall, and the MeHg fate during a forest fire in the Amazonian rainforest. Sampling of litter, soil (0–1, 1–2, and 2–5 cm), and ash was carried out before (BB) and after (AB) a prescribed forest fire. The results showed a low [THg] (34 ± 8 ng g^{-1}) and [MeHg] (0.16 ± 0.03 ng g^{-1}) value in litter, with a correspondingly low estimate of the MeHg litterfall flux (0.13 ± 0.03 µgm^{-2} yr^{-1}) which has been probably underestimated due to potential losses during the field experiment. In ashes, [THg] and [MeHg] values were 23 ± 8 ng g^{-1} and 0.11 ± 0.04 ng g^{-1}, respectively. Although a significant part of Hg contained in the biomass was lost during the fire, the [MeHg]/[THg] ratio was not affected by it and was the same in litterfall and ash (~0.5%). In soil, the average [THg] BB value was 149 ± 12 ng g^{-1} in the three layers and [MeHg] was between 0.8 and 1.0 ng g^{-1}. The forest fire only affected the superficial soil, with a significant decrease of [THg] and [MeHg] in the 0-1 cm layer. Similarly, the decrease of the [MeHg]/[THg] ratio in the surface soil layer suggested that MeHg was more readily emitted or degraded than the other Hg species present.

KEYWORDS

mercury, methylmercury, litterfall, soil, ash, forest fire, tropical forest

1 Introduction

Forests have been recognized as key ecosystems in the global biogeochemical Hg cycle (Wang et al., 2016; Outridge et al., 2018; Bishop et al., 2020; Zhou et al., 2021). The forest canopy is highly efficient in trapping atmospheric Hg through the stomatal uptake of gaseous elemental mercury (Hg^0) and by the adsorption of particulate-bounded mercury (PBM) and reactive gaseous mercury onto leaf surfaces (Jiskra et al., 2018; Zhou et al., 2021). Methylmercury (MeHg), one of the most toxic and bioaccumulating Hg species, is also expected in tree leaves, mainly originating from MeHg atmospheric depositions (Graydon et al., 2008; Tsui et al., 2012; Ma et al., 2015; Gerson et al., 2022). As the root absorption of Hg is very low, in noncontaminated sites, a significant contribution in this manner is not expected (Graydon et al., 2009; Tabatchnick et al., 2012). Mercury fixed in the foliage is then transferred to the forest floor via litterfall and throughfall (rain that washes plant surfaces

off). Some studies showed the total mercury (THg) and MeHg fluxes in throughfall and litterfall are many times higher than those in direct wet deposition in open areas (Branfireun et al., 1998; Louis et al., 2001; Mowat et al., 2011; Gerson et al., 2022). Mercury is then sequestered in soil generally associated with organic matter (Bishop et al., 2020). However, in ferralitic soils (Oxisols), which are largely present in the Amazonian region, Hg mainly adsorbs onto Fe-oxy-hydroxides, while the MeHg concentration seems to be more dependent on the organic matter quality and quantity (Roulet and Lucotte, 1995; Roulet et al., 2001).

Global mercury deposition through litterfall has been estimated to be between 1,000 and 1,200 Mg yr^{-1} (Wang et al., 2016; Obrist et al., 2018) with 30% of the total deposition in temperate/boreal forests and 70% in tropical/subtropical forests. This accounts for approximately one-third of the total Hg deposition on land (Mason et al., 2012), also equivalent to 50%–60% of global anthropogenic emissions (Pirrone et al., 2010). A higher efficiency of tropical/subtropical forests in transferring atmospheric Hg via litterfall is mainly attributed to the higher litterfall biomass production (Wang et al., 2016; Schneider et al., 2023). Biological factors such as the presence of evergreen broadleaf species with long leaf lifespans and strong foliage assimilation also result in higher Hg concentrations in the foliage and litterfall (Fostier et al., 2015; Wang et al., 2016; Teixeira et al., 2017; Pleijel et al., 2021; Gerson et al., 2022). As for other Hg species, [MeHg] in tree leaves and litter also largely depend on the forest type (Witt et al., 2009). As tropical forests are commonly rich in perennial broadleaved species with high litter production, relatively high atmospheric MeHg inputs are expected in these environments (Zhou and Obrist, 2021). However, to our knowledge, [MeHg] has not yet been measured in tree leaves from tropical forests, and only one dataset of [MeHg] in litter samples from the Amazonian rainforest is available (Roulet et al., 2001).

Forests can also provide favorable environments for Hg methylation processes (Eklöf et al., 2018), enhancing the potential risk to the terrestrial biota (Rieder et al., 2011; Ackerman et al., 2016). Lowland forests are frequently pointed out as hotspots for Hg methylation due to soil saturation and anoxic conditions that favor the methylation process (Bishop et al., 2020). In the Amazonian region, some studies showed that seasonal flooding of the forest results in high [MeHg] in litter and organic horizons of forest soils (Guimaraes et al., 2000; Roulet et al., 2001; Guedron et al., 2011). Mercury methylation can also take place in organic surface soils in uplands (Bishop et al., 2020); however, this process was poorly studied, especially in forested tropical uplands (Shanley et al., 2020).

Deforestation and some forest management practices can enhance the mobilization of Hg stocked in soils through leaching and runoff processes, therefore increasing Hg transport toward the streams (Fostier et al., 2000; Roulet et al., 2001; Patry et al., 2013; Bishop et al., 2020), where the methylation process results in the production of MeHg (Bishop et al., 2020). By studying the long-term impact of forest fires on Hg concentrations at Acadia National Park (United States), Patel et al. (2019) suggested that fire enhanced MeHg production in superficial soil. However, the sources and fate of MeHg in forests are still poorly known, especially in tropical areas (Schneider et al., 2023). As far as we know, the effects of fire on MeHg volatilization and degradation have never been studied, albeit biomass burning was suggested as a possible source of atmospheric MeHg (Zhang et al., 2019).

The Amazonian rainforest represents over half of the planet's remaining rainforest. The vegetation in the region is mainly semi-deciduous or evergreen tropical forests, but the species composition varies widely due to the differences in the soil type and altitude across the basin (Sombroek, 2000). From the different vegetation types, it was estimated that approximately 66% of soils are covered by the so-called old-growth terra firme forests (Saatchi et al., 2007; Chave et al., 2010), which are part of the upland (never flooded) forests. For this biome, the total Hg deposition via litterfall was estimated to be 268 ± 77 Mg y^{-1} (Fostier et al., 2015), whereas the total Hg input from the atmosphere was estimated to be 332 Mg y^{-1} (Feinberg et al., 2023). Conversely, in the Brazilian Amazon, which accounts for the main part of this tropical forest, approximately 8 × 10^3 km^2 were deforested yearly over the 2008–2022 period, which was mainly performed by clearing and biomass burning (INPE, 2023). Although a growing body of evidence has shown the importance of tropical forests in the global Hg cycle, Hg in soils and vegetation from the Amazonian rainforest has still been poorly studied and very few data are available for MeHg in these regions. Therefore, the aim of this work was two-fold: 1) to determine THg and MeHg concentrations in litter and soil in an upland forest located in the Brazilian Amazon basin and 2) to calculate the fluxes of MeHg via litterfall, as well as the impact of prescribed forest burning on the MeHg fate at the interface soil/ash/atmosphere in the same region.

2 Materials and methods

2.1 Experimental area and sampling

This study was performed in the western Brazilian Amazon region within a 150 m × 150 m native forest area (8°38'S 63°11'W) located approximately 20 km from Candeias do Jamari city (Rondônia state, Brazil) (Figure 1). The vegetation type present in the experimental area is old-growth terra firme forests (Chave et al., 2010) and the soil is classified as Oxisols (Almeida et al., 2005). The prescribed fire experiment was conducted according to the slash-and-burn practice commonly applied for deforestation in this region (Fire experiment authorization 204/2014 Secretaria de Estado do Desenvolvimento Ambiental). Details on the complete experiment can be found in the work of Carvalho et al. (2016). In brief, the first step was to perform a forest inventory of the trees with the diameter at breast height (DBH) being >10 cm in the central 1 ha (Supplementary Figure S1). The forest was then cleared at the beginning of the dry season (July), and burning was performed at the end of August when the vegetation was sufficiently dry. Although the total area (2.5 ha) was burned, the combustion completeness (CC) of the fine material (branches with diameter <10 cm, litter, and leaves) was estimated in 12 different 4 m^2 subareas distributed in the 1 ha central area, as shown in Supplementary Figure S1. In each area, the biomass was weighted before (BB) and after the burning (AB) (both in August) and CC was calculated as the percentage of the burned biomass, as detailed in Supplementary Table S1. Details on fuel loading and ash mass in

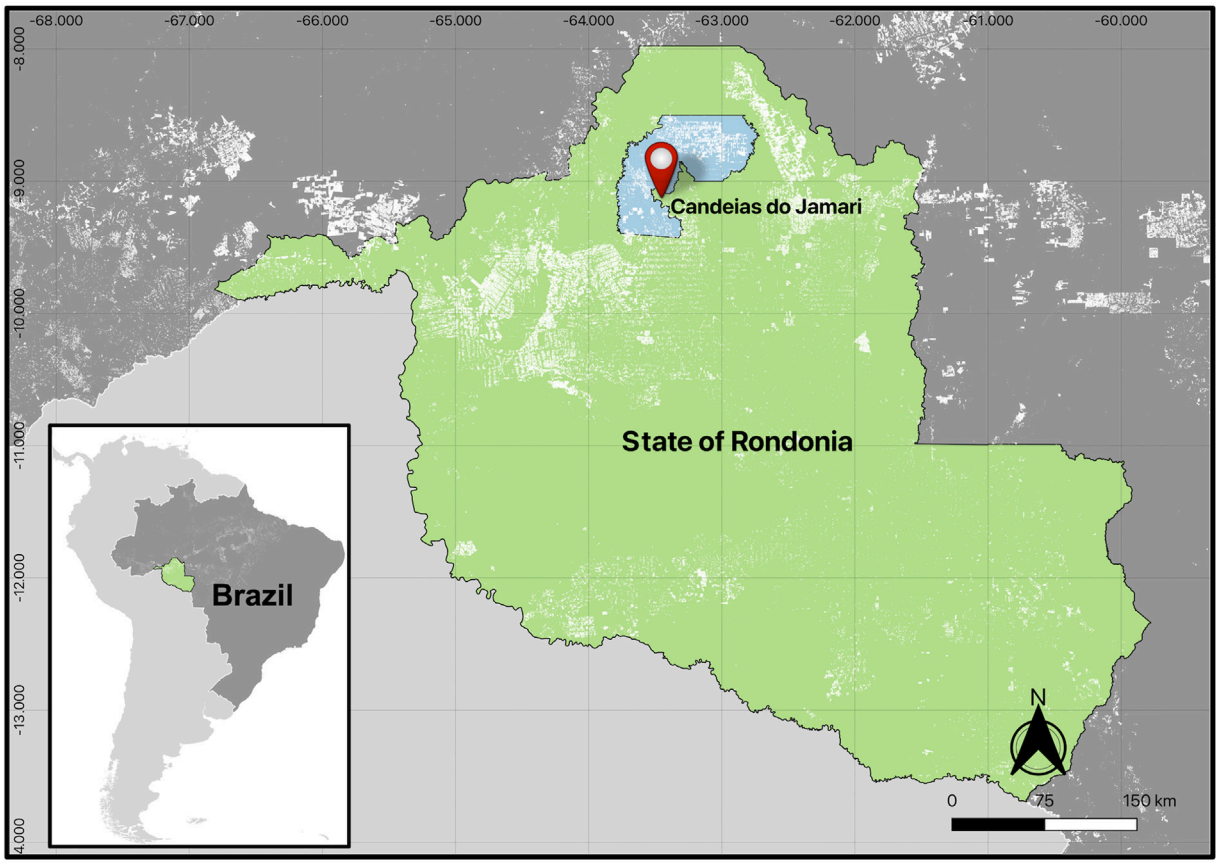

FIGURE 1
Location of the study area (Candeias do Jamari, RO).

each subarea are presented in Supplementary Table S1. The consumption of logs (DBH >10 cm) and larger branches (D >10 cm) in the 1 ha central area was also estimated as detailed in the work of Carvalho et al. (2016). Litter, soil (0–1, 1–2, and 2–5 cm), and ash sampling was carried out in nine of these subareas (Supplementary Figure S1). In each area, each sample was composed of three subsamples that were mixed and homogenized. Soil was collected using an acid-washed plastic shovel and litter was collected with hands using gloves. The samples were stored in doubled plastic bags for transport to the laboratory, dried at room temperature in a laminar flow hood, milled in a mortar (with the aid of liquid N_2 for litter), and stocked in decontaminated HDPE flasks.

2.2 Analyses and quality control

2.2.1 Total mercury

The determination of the total mercury concentration [THg] was carried out through thermodesorption atomic absorption spectrometry (DMA-80 Tri-Cell, Milestone), according to the work of Melendez-Perez and Fostier (2013). Accuracy, expressed as the average percentage of recovery (±1 standard deviation, s) of the THg certified concentration, was assessed by analyzing standard reference materials (SRMs). It was 113% ± 8% for NIST-2689 (coal fly ash), 113% ± 5% for NIST-1632d (trace elements in coal), 99% ± 5% for IAEA-433 (trace elements in marine sediments), and 93% ± 2% for IAEA-336 (trace and minor elements in lichens). Precision was calculated as the relative standard deviation (1 s) of three analytical replicates and was always <10%. The limit of detection (LOD) and of quantification (LOQ), calculated based on the angular coefficient of analytical curves, were 1.7 ± 0.1 and 5.6 ± 0.5 ng g^{-1}, respectively, for litter analyses, 1.3 ± 0.1 ng g^{-1} and 4.5 ± 0.4 ng g^{-1} for ash, and 0.75 ± 0.06 and 2.5 ± 0.2 ng g^{-1} for soil.

2.2.2 Methylmercury

A precise and accurate method based on species-specific isotope dilution and gas chromatography coupled to inductively coupled plasma mass spectrometry (GC-ICPMS), which allows the simultaneous determination of the methylmercury concentration [MeHg] and inorganic Hg [iHg], was used for MeHg quantification in the different matrices studied in this work (Rodriguez Martin Doimeadios et al., 2003; Monperrus et al., 2008; Clemens et al., 2011). This analytical methodology has already been assessed for soil and vegetal samples (Feng et al., 2016) and more details on the protocol are briefly given in Supplementary Text S1 and in more detail in the previous works (Monperrus et al., 2008; Clemens et al., 2011). For MeHg, the analytical method recovery was assessed by

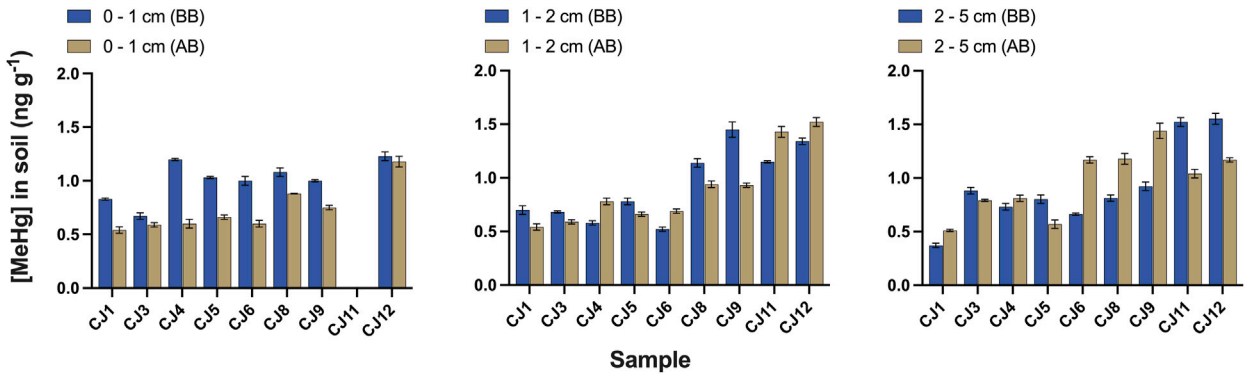

FIGURE 2
Methylmercury concentration (ng g^{-1}) in soil samples from the experimental subareas before and after burning in the three sampled layers (0–1, 1–2, and 2–5 cm). The CJ11 0–1 cm layer was not analyzed.

analyzing the SRM IAEA-405 (trace elements and MeHg in marine sediments) and calculating the ratio (%) between the obtained and certified [MeHg]. Total Hg species (THg_{sp}) recovery was also calculated for IAEA-405, IAEA-336, and litter, ash, and soil samples as the ratio between [MeHg] + [iHg] and [THg]. The precision was calculated as the relative standard deviation of three analytical replicates. The limit of detection and quantification were calculated based on the parameters of the analytical curves. For MeHg, LOD and LOQ were 0.006 and 0.020 ng g^{-1}, respectively. Recovery for IAEA-405 was 100.4%, and the precision was <5%; detailed data are given in Supplementary Table S2.

For iHg, LOD was 0.07 ng g^{-1} and LOQ was 0.23 ng g^{-1}. For THg_{sp}, it was 95.4% and 89.1% for IAEA-405 and IAEA-336, respectively, and the precision was <5%. For litter and ash samples, THg_{sp} recovery ([MeHg] + [iHg]) × 100/[THg]) was 73% ± 8% and 50% ± 12%, respectively (Supplementary Tables S3, S4). For soil, it ranged from 46% ± 7% to 52% ± 7% (Supplementary Table S5).

2.2.3 Determination of the organic matter content

The organic matter content was determined in litter, ash, and soil samples via gravimetric analysis. The previously dried samples were burned for 2 h at 360°C in a muffle furnace; then, the percentage lost on ignition was used to estimate the organic matter content (North Central Regional Research, 2012).

2.3 Statistical data treatment

Data processing was conducted using PAST (Paleontological Statistics, version 4.11) (Hammer et al., 2001), GraphPad Prism version 10.0.0 (Boston, MA, United States), and XLSTAT® software. The normality of the datasets was assessed using the Shapiro–Wilk test. To evaluate the statistical differences between normally distributed datasets, Student's *t*-test was employed. Furthermore, one-way ANOVA was used to assess the differences among more than three sets of normally distributed data. All statistical analyses were carried out with a significance level of 95% (α = 0.05). Pearson's correlation coefficient (r) was also analyzed to assess the degree of dependence between pairs of variables (i.e., combustion completeness (%), total biomass (kg m^{-2}), OM lost from vegetation (%), THg lost from vegetation (%), MeHg lost from vegetation (%), OM lost from 0–1 cm soil (%), THg lost from 0–1 cm soil, and MeHg lost from 0–1 cm soil).

3 Results

3.1 Total [THg] and methylmercury concentrations

All the results presented a normal distribution, except the dataset of [MeHg] in the 0–1 cm soil layer AB, in which the CJ12 [MeHg] (1.18 ng g^{-1}) appeared as an outlier (Grubbs' test for outliers; p <0.05) (Figure 2). However, the rest of the data were normally distributed after removing this value. Paired Student's *t*-test was then applied to compare the different datasets (i.e., litter and ash, soil BB or AB at different depths, and soil BB and AB at the same depth).

[THg] in litter ranged from 25.0 to 50.0 ng g^{-1} (Table 1) and was significantly higher than that in ash (paired Student's *t*-test, p <0.05). In soil, the overall average [THg] was 149 ± 12 ng g^{-1} (Table 2), and there was no difference among layers. After burning, a significant decrease was only observed in the 0–1 cm layer (p <0.05).

The average [MeHg] was 0.16 ± 0.03 ng g^{-1} in litter, ranging from 0.11 to 0.21 ng g^{-1} (Table 1). Following the same trend observed for [THg], it was significantly higher than the [MeHg] in ash (p <0.05), where the average was 0.11 ± 0.04 ng g^{-1}, ranging from 0.04 to 0.18 ng g^{-1}. Before burning, in the superficial soil layer (0–1 cm), the average [MeHg] was 1.0 ± 0.2 ng g^{-1} (Table 2), ranging from 0.67 to 1.23 ng g^{-1} (Figure 2), which was not significantly different from [MeHg] in the other two layers BB. After burning, a significant decrease was only observed in the 0–1 cm layer (paired Student's *t*-test; p <0.05), in which the average [MeHg] value was 0.7 ± 0.1 ng g^{-1}, ranging from 0.54 to 0.88 ng g^{-1}, albeit it should be noted that in this layer, MeHg was not determined in the CJ11

TABLE 1 Concentrations of total mercury [THg] and methylmercury [MeHg] (ng g^{-1}) in litter and ash, with their respective [MeHg]/[THg] ratios expressed in %.

Experimental area	Litter			Ash		
	THg	MeHg	MeHg/THg	THg	MeHg	MeHg/THg
	(ng g^{-1})	(ng g^{-1})	(%)	(ng g^{-1})	(ng g^{-1})	(%)
CJ1	40.0	0.19	0.48	23.9	0.11	0.46
CJ3	50.0	0.15	0.30	11.8	0.09	0.76
CJ4	25.0	0.15	0.61	30.7	0.08	0.26
CJ5	36.8	0.16	0.43	28.8	0.14	0.49
CJ6	31.0	0.21	0.68	27.5	0.13	0.47
CJ8	25.2	0.19	0.76	21.8	0.18	0.82
CJ9	32.9	0.13	0.39	11.7	0.10	0.85
CJ11	28.0	0.11	0.39	16.5	0.04	0.24
CJ12	34.7	0.16	0.46	30.3	0.10	0.33
Average ± 1 s	33 ± 8	0.16 ± 0.03	0.5 ± 0.2	23 ± 8	0.11 ± 0.04	0.5 ± 0.2

TABLE 2 Average concentrations of THg, MeHg (ng g^{-1}), and MeHg/THg (%) in the 0–1, 1–2, and 2–5 cm soil layers before and after burning.

Soil layer		[THg]	[MeHg]	[MeHg]/[THg]
		(ng g^{-1})	(ng g^{-1})	(%)
0–1 cm[a]	BB	148 ± 13	1.0 ± 0.2	0.7 ± 0.1
	AB	134 ± 21	0.7 ± 0.2	0.5 ± 0.1
1–2 cm	BB	148 ± 12	0.9 ± 0.4	0.6 ± 0.2
	AB	146 ± 16	0.8 ± 0.3	0.5 ± 0.2
2–5 cm	BB	149 ± 12	0.8 ± 0.3	0.5 ± 0.2
	AB	150 ± 13	0.9 ± 0.3	0.6 ± 0.2

[a]In this layer, [MeHg] was not determined in CJ11, and as [MeHg] in CJ12 AB was an outlier (Grubbs' test for outliers; $p < 0.05$), it was not included in the average [MeHg] calculation.

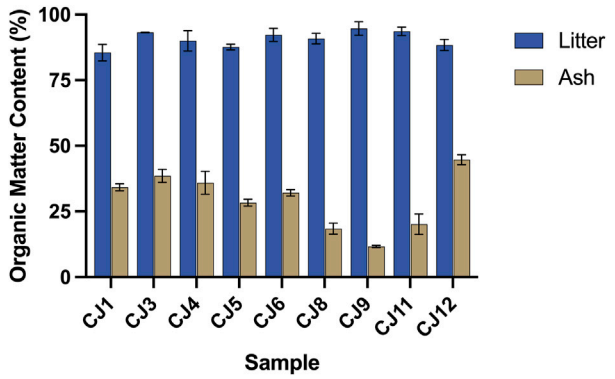

FIGURE 3
Organic matter content (%, w w^{-1}) in litter and ash samples in the 4 m^2 subplots.

sample. Furthermore, as CJ12 [MeHg] AB (1.18 ng g^{-1}) appeared as an outlier, it was not included in the average calculation.

The average [MeHg]/[THg] ratio in litter (0.5 ± 0.2 ng g^{-1}) (Table 1) was the same as in ash (0.5 ± 0.2 ng g^{-1}). In the 0–1 cm soil layer, the average ratio was 0.7 ± 0.1 ng g^{-1} before (0.50–0.74 ng g^{-1}) and 0.5 ± 0.1 ng g^{-1}, ranging from 0.36 to 0.65 ng g^{-1} after burning. In the other soil layers, the average ratio varied between 0.5 ± 0.2 ng g^{-1} and 0.6 ± 0.2 ng g^{-1} BB and AB.

3.2 Organic matter content in litter, ash, and soil samples

The average OM content in litter was 91% ± 3% (w w^{-1}), which significantly decreased to 29% ± 11% in ash (paired Student's *t*-test, $p < 0.05$) (Figure 3). In soil, before burning, it was 21% ± 5%, 10% ± 2%, and 7% ± 2% in the 0–1, 1–2, and 2–5 cm layers, respectively.

After burning, it was 14% ± 4%, 8% ± 1%, and 7% ± 2% in the 0–1, 1–2, and 2–5 cm layers, respectively.

4 Discussion

4.1 Speciation method recovery

The extraction method used for Hg speciation presented high THg_{sp} recovery for both CRM IAEA-405 (sediment) and IAEA-336 (lichens). However, THg_{sp} recovery was lower in litter, soil, and ash samples (Supplementary Table S5). For Hg as for other heavy metals, the liquid/solid extraction efficiency depends on the reagent type and its ability to solubilize the different forms (i.e., more or less labile), in which the metal is present in the sample (Song et al., 2015; Ku et al., 2018; Zhou et al., 2018). Conversely, a complete release of Hg is expected with the thermodesorption method being used (Zhou et al., 2018).

A sequential extraction applied to fresh and dried leaves aiming at Zn, Cd, and Cu determination showed that for most extractants, the extraction efficiency was higher in fresh leaves than that in dried leaves, which could be related to the storage of the metals in vacuoles (Song et al., 2015). The authors also pointed out that the finer particle size of the dried samples may have increased the extraction efficiency. As our litter samples were ground manually, this latter point could explain the relatively low extraction efficiency (73% ± 8%) when compared to IAEA-336 (93 ± 2%). However, plant metal fractions have still been poorly studied (Zhou et al., 2018), and it is probable that many factors, such as plant species and the age of tissues, can have an impact on the metal lability. For soil and ash samples, recovery was approximately 50%, showing that only Hg species soluble in oxidizing and moderately acid media (HNO_3 6 mol L^{-1}) were extracted. This method is expected to solubilize Hg bound to the organic matter and Hg adsorbed by amorphous iron oxides and by clay in soil (Reis et al., 2016), but not the Hg present in the recalcitrant pools, which includes HgSe and HgS (Ku et al., 2018). Conversely, this method is not expected to digest charcoal or recalcitrant black carbon originating from biomass burning (Ku et al., 2018), and these authors reported that a recalcitrant Hg pool significantly increased in wildfire ash when compared with the unburned vegetation (litter and wood). In our study, a recalcitrant pool was calculated as 100 – [TH_{sp}] recovery (%) (Supplementary Table S5), which increased from 27% in litter to 50% in ash. So, our results suggest that a large part of Hg was likely present in the recalcitrant pool in the soil samples and included in charcoal and ash.

4.2 Total and methylmercury concentrations in litter

The average total Hg concentration in litter (33 ± 8 ng g^{-1}) was lower than that reviewed by Fostier et al. (2015) for the Amazonian upland forests, which ranged from 40 ± 5 to 119 ± 29 ng g^{-1} (average = 75 ± 30 ng g^{-1} and median = 61 ng g^{-1}). As the tree species composition has a strong influence on Hg uptake by the foliage and because tree species are not homogeneously distributed in the forest, variations in the Hg concentration can result from the variations in litter composition. The relative high coefficient of variation (CV %) generally observed for any set of data on litter [THg] can largely be attributed to this factor. In our study, CV was 24%, which was lower than the data reported by Fostier et al. (2015) in the Amazonian forest. Conversely, previous results on [THg] in litter were obtained near the experimental site but under forested areas (Fostier et al., 2015), which showed that [THg] was higher in the forest area (61 ± 11 ng g^{-1}) than that in our experimental conditions (33 ± 8 ng g^{-1}). This difference could, therefore, be due to the exposure to solar radiation and rain washout for some months after the forest was cut, resulting in Hg loss. Richter et al. (2023) reached the same conclusion when comparing the isotopic composition of litter sampled in the same experimental site at CJ and in a forest site. Furthermore, Carpi et al. (2014) showed significant increases in Hg emissions when soils (covered or not by litter) were exposed to solar radiation after cutting the tree and suggested that solar UV radiation was the main driver responsible for these emissions.

As for [THg], the average [MeHg] in litter (0.16 ± 0.03 ng g^{-1}) was also in the low range of those reviewed in other remote regions (Zhou et al., 2018), e.g., from 0.18 ng g^{-1} in the coniferous forest of Canada (Louis et al., 2001) to 0.84 ng g^{-1} in a subtropical altitude forest in China (Ma et al., 2015). In addition, Graydon et al. (2008) reported [MeHg] ranging from 0.22 ± 0.02 to 0.49 ± 0.14 ng g^{-1} in litter from jack pine and deciduous forests, respectively, in a remote boreal Canadian region. However, the average [MeHg]/[THg] ratio (%) in litter (0.5% ± 0.1%) was in the same range as for other remote regions, i.e., between 0.25% and 1.0% (Graydon et al., 2008; Zhou et al., 2018). This shows that Hg losses due to direct atmospheric exposure (solar radiation and rain washout) probably happen at the same rate for THg and MeHg. In Amazonian flooded forests (i.e., hydromorphic soils), a much higher [MeHg]/[THg] ratio in litter (2%–5%) has been reported by Roulet et al. (2001), suggesting that this environment is very favorable for Hg methylation and/or MeHg accumulation.

4.3 Total and methylmercury litterfall deposition

The total mercury annual deposition via litterfall (D_{THg}) can be estimated as D_{THg} = [THg_{lit}] × M_{lit}, where [THg_{lit}] is the average [THg] in litter and M_{lit} is the annual mass of litter deposited on the forest floor, which was estimated to be 8 ± 2 Mg ha^{-1} yr^{-1} by Fostier et al. (2015) for the Brazilian Amazonian rainforest. Then, the estimated D_{THg} value was 28 ± 14 μg m^{-2} yr^{-1}. This value can be considered low compared to 49 ± 14 μg m^{-2} yr^{-1} estimated by Fostier et al. (2015) and to 84 ± 48 μg m^{-2} yr^{-1} by Wang et al. (2016) for different locations in the Amazonian rainforest. The MeHg litterfall deposition (D_{MeHg}), calculated the same way, but using the average [MeHg] in litter, resulted in a net deposition of 0.13 ± 0.04 μg m^{-2} yr^{-1}. This value is within the range of the previous estimations from 0.08 to 0.34 μg m^{-2} yr^{-1} reported by Zhou et al. (2018) for MeHg litterfall deposition in other remote regions. Nevertheless, as already pointed out, the litter exposed, for several months, to sun radiation and rain washout may have resulted in some loss of Hg and, consequently, to an underestimation of the initial net THg and MeHg depositions. Conversely, an estimate of Hg deposition based on a limited dataset obtained in the specific

TABLE 3 Total (Hg_{Tot}) and methylmercury (MeHg) concentrations (average ± 1 SD) and the percentage of MHg/Hg_{Tot} in soil reported in the literature and from the present study for Amazonian flooding forests and upland forests.

	Forest type	Location		N	Hg_{Tot} (ng g^{-1})	MeHg (ng g^{-1})	MeHg/ Hg_{Tot} (%)
This study[a]	UF	Candeias do Jamari (RO)	Oxisols (0–5 cm)	9	149 ± 1	0.93 ± 0.01	0.63 ± 0.01
Roulet and Lucotte (1995)	UF	French Guiana	Oxisols (0–15 cm)	6	250 ± 27	2.1 ± 0.8	0.8 ± 0.3
	FF	French Guiana	Oxisols (0–15 cm)	12	192 ± 18	2 ± 2	1 ± 1
	FF	French Guiana	Hydromorphic soils (0–15 cm)	6	123 ± 30	10 ± 10	7 ± 6
Roulet et al. (2001)	FF	Tapajós basin	Unclassified alluvial soils	1	190	2.24	1.11
				1	112	0.55	0.45
				1	209	0.59	0.26
Guedron et al. (2011) [b]	UF	French Guiana	Oxisols	6	350 ± 40	-	-
		French Guiana	Interstitial water from Oxisols	6	1.70 ± 1.23 (ng L^{-1})	0.005 ± 0.002 (ng L^{-1})	0.29 ± 0.24
Araujo et al. (2018)	UF	Amazon basin	Unclassified soils	4	19–68	0.51–1.01	1.48–3.57
Guyoneaud et al. (2023) (submitted)	UF	French Guiana	Oxisols	3	419 ± 164	3 ± 1	0.9 ± 0.5
	UF	French Guiana	Acrisols	4	269 ± 123	2 ± 2	0.8 ± 0.3
Gerson et al. (2022) [c]	UF	Peruvian Amazon	Not informed			1.1; 1.4	0.79; 1.4

[a]Average concentrations for 0–5 cm, when considering only soil data before burning.
[b]Guedron et al. (2011) did not assess the MeHg concentration in soils, but rather in the interstitial water from the studied soils. For this reason, the concentrations are expressed in ng L-1.
[c]These data are the only ones detailed by the authors for superficial soils (0–5 cm) of forest sites in two mining zones and are the highest values measured in these sites.

condition (after the vegetation was felled and dried) may be not representative of the Amazonian upland forest; however, it is paramount to highlight that this is the first dataset obtained on [MeHg] in litterfall in this ecosystem.

4.4 Total and methylmercury concentrations in soil before burning

The total Hg concentrations in soil before burning (149 ± 12 ng g^{-1}) are within the values expected in Amazonian soils, which are highly variable, i.e., 61 ± 25 to 304 ± 62 ng g^{-1} for superficial (0–10 cm) pristine forest soils (Schneider et al., 2023). MeHg (~1 ng g^{-1}) and [MeHg]/[THg] (0.6%) concentrations obtained in the present study are in accordance with those reported for Oxisols from other locations of the Amazonian forest (Table 3), which are dominant in Candeias do Jamari (Roulet and Lucotte, 1995; Almeida et al., 2005). In contrast, higher [MeHg]/[THg] ratios were reported in hydromorphic soils, but the processes governing mercury methylation and/or accumulation in those soils are still unknown (Roulet et al., 2001; Guedron et al., 2011). The data presented in this work also agree with MeHg concentrations in soils from uncontaminated temperate and boreal forests, in which MeHg concentrations are generally below 1 ng g^{-1}, although some values up to 10 ng g^{-1} have been reported under specific conditions, such as around fumarolic areas (Kodamatani et al., 2018), in a boreal coniferous clear-cut forest (Kronberg et al., 2016), and wetland forests (Bishop et al., 2020).

As expected, [THg] and [MeHg] concentrations were significantly higher in soil than those in litter (paired Student's *t*-test; p <0.05) because the litter mass decreases during its decomposition and is then incorporated into the superficial soil (Zhou et al., 2021). However, the dynamics of Hg in soil strongly depend on the soil composition. The decomposition of the litter results in the formation of organic horizons (Oh), and Hg originating from this litter may bind to the organic matter, accumulating in superficial soil. Nevertheless, in Oxisols, Hg can mainly be adsorbed onto Fe-oxy-hydroxides (Roulet and Lucotte, 1995).

Methylmercury in litterfall can originate from MeHg atmospheric depositions on tree leaves (Graydon et al., 2008; Tsui et al., 2012; Ma et al., 2015), but this process has never been evaluated in the Amazonian forest. In addition to the atmospheric input, MeHg in soil can also increase due to the methylation process, mainly driven by anaerobic bacteria (Kronberg et al., 2016; Gerson et al., 2017; Eklöf et al., 2018). High [MeHg] and [THg] were observed in dried superficial soils in an Amazonian forest area, where a high atmospheric Hg input was attributed to the proximity to artisanal small gold mining (Gerson et al., 2022). However, as [MeHg]% (0.79%) was in the same order as in remote areas around the globe, the authors concluded that the methylation rate did not increase in the study area and that high [MeHg] and [THg] can mainly be attributed to a high Hg input, litter decomposition, and high storage capacity of Hg in soil. However, the examination of the sources of MeHg in forest soils via either atmospheric depositions or *in situ*

methylation pathways and the importance of each source still remain to be clearly assessed to better understand the Hg cycle in terrestrial environments (Tsui et al., 2012; Tao et al., 2018; Zhou et al., 2018). This aspect is a critical gap in the knowledge of tropical soils and forests, for which the available studies and data are very scarce (Gerson et al., 2022).

4.5 Combustion completeness and fire severity

In forest fires, the combustion process depends on several factors, such as initial mass, nature, and moisture of fuel; air temperature and humidity; wind speed; and the topography of the site (Certini, 2005). The impact of fire on the physical, chemical, and biological properties of the soil (the fire severity) depends on the heat release from the combusting biomass (the fire intensity) and on the duration of combustion (Neary et al., 2005). A low-to-moderate severity is expected in the prescribed fire experiments (Certini, 2005). In our experimental site, the fine material (D <10 cm) accounted for 13.3% of the total fresh biomass estimated to 701.5 t ha^{-1}, which was in the upper range of the average forest biomass in western Amazonia (612.4 ± 142.5 t ha^{-1}) (Carvalho et al., 2016). In the nine 4-m^2 areas considered in the present study, the CC of the fine material ranged from 66.6% to 100%, showing the heterogeneity of the combustion process. Consumption completeness showed no correlation (p >0.05) with any of the other variables (Supplementary Table S6). In two other prescribed fire experiments conducted in the same way in western Amazonia, Carvalho et al. (2016) reported the CC of small size materials of 85.5% and 89.2%. Conversely, when also considering logs (DBH >10 cm) and larger branches (D >10 cm), the overall CC was only 16.0% (Carvalho et al. (2016). The typical superficial soil temperature in forest fires rises 200–300°C (Rundel, 1983), although the temperature up to 500–700°C can be reached in case of heavy fuels (Certini, 2005). One of the first effects of forest fires on soil properties is the removal of OM, whose substantial consumption begins at 250–300°C and completes at approximately 460°C (Giovannini et al., 1988). The organic matter release can, therefore, be used as an indicator of fire severity. In our experiment, the OM content significantly decreased only in the 0–1 cm layer (paired Student's t-test; p <0.05). However, the average decrease of the OM content in this layer was only 33% ± 25%, indicating a moderate fire in the sampled subareas. It also suggests that, at these places, relatively low temperatures were reached, as complete combustion of soil only occurs at temperatures >450–500°C (Gonzalez-Perez et al., 2004; Mataix-Solera et al., 2011).

4.6 Total and methylmercury release due to forest burning

In soil, a significant decrease of [THg] and [MeHg] was only observed in the 0-1 cm layer, indicating that the fire intensity was only able to promote Hg release from the very superficial soil, which is in accordance with the observed OM decrease in the same layer. However, no correlation was observed between the OM lost and [THg] and [MeHg] lost in this soil layer (Supplementary Table S6). The impacts of the prescribed forest fires on the very superficial soil in the Amazonian rainforest were also reported by Melendez-Perez et al. (2014) and Michelazzo et al. (2010). A significant decrease (paired Student's t-test; p <0.05) of the [MeHg]/[THg] ratio was observed in the 0–1 cm layer after burning (Table 2), suggesting that with the increase in temperature, MeHg was more easily degraded and/or emitted than other Hg species (i.e., iHg compounds) present in such soils. The impact of fire on soil OM (and others soil components) is a complex issue, as it depends on many parameters, such as soil properties and composition, the temperature reached during the fire, and the burning duration. It was reported that the distillation of volatiles and the loss of organic carbon in soils start at temperatures between 100 and 200°C and that the charring process starts above 190–200°C (Gonzalez-Perez et al., 2004). So, the effects of forest fire on MeHg release and degradation can also vary with fire severity. Mercury speciation by thermodesorption shows that different species are released at different temperature ranges (Reis et al., 2016). Applying this technique to Amazonian soil spiked with Hg^{2+}, Do Valle et al. (2005) showed that Hg bound to the mineral phases was released at a lower temperature than Hg bound to humic acids. Therefore, our results suggest that MeHg was mainly bound to weak organic matter ligands and/or mineral phases. It is important to notice that after burning, the 0-1 cm layer visually corresponded to the partially burned O-horizon, while newly formed ashes were mainly produced from the burned overlaying biomass. Both [THg] and [MeHg] were significantly lower in ash than in litter (30% and 31% decrease for [THg] and [MeHg], respectively), clearly showing that the fire conditions in our experimental site were able to remobilize a significant part of Hg sequestered in the vegetation, with likely a larger fraction of it emitted into the atmosphere (Outridge et al., 2018). Furthermore, as [MeHg]/[THg] ratios were not different in litter and ash, one can conclude that MeHg was released with a similar efficiency as the main fraction of the inorganic Hg species. Biomass burning was pointed out as a potential source of MeHg in atmospheric fine particles (Zhang et al., 2019). However, the release of MeHg from soil and litter does not imply that it was directly emitted into the atmosphere. First, MeHg can be readsorbed into ash particles that have a high adsorption capacity for organic and inorganic Hg compounds (Ku et al., 2018). Furthermore, MeHg under heating conditions can be transformed into gaseous and volatile Hg forms (i.e., mainly Hg^0). However, to our knowledge, the effects of the high temperature generated by biomass burning on MeHg present in the vegetation have not yet been studied in detail. Recently, a study performed on the same litter, ash, and soil samples (Richter et al., 2023) using the Hg stable isotopic composition suggested that Hg emission and reallocation during forest fire is quite complex and demonstrated that the Hg present in newly produced ash was mainly originating from Hg emitted from the superficial soil layer (0-1 cm).

5 Conclusion

Total and MeHg concentrations in litter from the study area were relatively low compared to other Amazonian rainforest areas. Consequently, the estimated MeHg litterfall flux was also low,

possibly due to the extended exposure time of litter to solar radiation and rain washout after forest cutting. Conversely, the [MeHg]-to-[THg] ratio in soil and litter was of the same order as that in many remote forests from upland temperate and boreal forests. For the first time, it was shown that the release of MeHg occurs with a similar efficiency as the primary fraction of inorganic Hg species from litter. Although the forest fire promoted a significant decrease in [THg] and [MeHg] in the very superficial soil layer (0-1 cm), in such organic topsoil MeHg was more readily emitted or degraded compared to the other Hg species. The complexity of understanding the MeHg dynamics and fate in fire-impacted soils was highlighted, especially considering the strong modifications that fire can induce in soil OM, as MeHg in soils is primarily linked to OM. This study sheds new light on the behavior of MeHg in the fire-affected areas of the Amazonian rainforest and emphasizes the need for further research to fully comprehend the intricate interplay between fire, soil, and Hg dynamics.

Data availability statement

The original contributions presented in the study are included in the article/Supplementary Material; further inquiries can be directed to the corresponding author.

Author contributions

AF: conceptualization, project administration, writing—original draft, writing—review and editing, and supervision. DA: conceptualization, project administration, writing—original draft, writing—review and editing, and supervision. LR: methodology, investigation, and formal analysis. ET: methodology and investigation. JV: statistical analysis, writing—review and editing. All authors contributed to the article and approved the submitted version.

Funding

This work was funded by the São Paulo Research Foundation (FAPESP) (projects 2008/04490-4, 2010/19040-4) and also partially supported by The University of Campinas (UNICAMP/FAEPEX 2932/23), the CNRS, French ANR, and New Aquitaine Region council. LR received a fellowship from the Brazilian Coordination for the Improvement of Higher Education Personnel, CAPES (financing code 001). JV received a fellowship from FAPESP (2019/18124-4). The burning in Candeias do Jamari was conducted under permission 204/2014 from the Secretaria de Estado do Desenvolvimento Ambiental de Rondônia (SEDAM) and under permission from CNPq.

Acknowledgments

The authors also thank their coworkers from the Brazilian Institute of Environment and Renewable Natural Resources (IBAMA) and the Brazilian National Institute of Spatial Research (INPE). Jim Hesson edited the manuscript (https://www.academicenglishsolutions.com/editing-service).

Conflict of interest

The authors declare that the research was conducted in the absence of any commercial or financial relationships that could be construed as a potential conflict of interest.

Publisher's note

Supplementary material

The Supplementary Material for this article can be found online at: https://www.frontiersin.org/articles/10.3389/fenvc.2023.1242915/full#supplementary-material

References

Ackerman, J. T., Eagles-Smith, C. A., Herzog, M. P., Hartman, C. A., Peterson, S. H., Evers, D. C., et al. (2016). Avian mercury exposure and toxicological risk across western north America: A synthesis. *Sci. Total Environ.* 568, 749–769. doi:10.1016/j.scitotenv.2016.03.071

Almeida, M. D., Lacerda, L. D., Bastos, W. R., and Herrmann, J. C. (2005). Mercury loss from soils following conversion from forest to pasture in Rondônia, Western Amazon, Brazil. *Environ. Pollut.* 137 (2), 179–186. doi:10.1016/j.envpol.2005.02.026

Araujo, B. F., Hintelmann, H., Dimock, B., de Lima Sobrinho, R., Bernardes, M. C., de Almeida, M. G., et al. (2018). Mercury speciation and Hg stable isotope ratios in sediments from Amazon floodplain lakes—Brazil. *Limnol. Oceanogr.* 63 (3), 1134–1145. doi:10.1002/lno.10758

Bishop, K., Shanley, J. B., Riscassi, A., de Wit, H. A., Eklöf, K., Meng, B., et al. (2020). Recent advances in understanding and measurement of mercury in the environment: terrestrial Hg cycling. *Sci. Total Environ.* 721, 137647. doi:10.1016/j.scitotenv.2020.137647

Branfireun, B. A., Hilbert, D., and Roulet, N. T. (1998). Sinks and sources of methylmercury in a boreal catchment. *Biogeochemistry* 41, 277–291. doi:10.1023/a:1005964603828

Carpi, A., Fostier, A. H., Orta, O. R., dos Santos, J. C., and Gittings, M. (2014). Gaseous mercury emissions from soil following forest loss and land use changes: field experiments in the and Brazil. *Atmos. Environ.* 96, 423–429. doi:10.1016/j.atmosenv.2014.08.004

Carvalho, J. A., Amaral, S. S., Costa, M. A. M., Soares Neto, T. G., Veras, C. A. G., Costa, F. S., et al. (2016). CO2 and CO emission rates from three forest fire-controlled experiments in Western Amazonia. *Atmos. Environ.* 135, 73–83. doi:10.1016/j.atmosenv.2016.03.043

Certini, G. (2005). Effects of fire on properties of forest soils: a review. *Oecologia* 143, 1–10. doi:10.1007/s00442-004-1788-8

Chave, J., Navarrete, D., Almeida, S., Alvarez, E. ´, Aragão, L. E. O. C., Bonal, D., et al. (2010). Regional and seasonal patterns of litterfall in tropical South America. *Biogeosciences* 7, 43–55. doi:10.5194/bg-7-43-2010

Clémens, S., Monperrus, M., Donard, O. F. X., Amouroux, D., and Guérin, T. (2011). Mercury speciation analysis in seafood by species-specific isotope dilution: method validation and occurrence data. *Anal. Bioanal. Chem.* 401 (9), 2699–2711. doi:10.1007/s00216-011-5040-1

Do Valle, C. M., Santana, G. P., Augusti, R., Egreja Filho, F. B., and Windmöller, C. C. (2005). Speciation and quantification of mercury in oxisol, ultisol, and spodosol from Amazon (manaus, Brazil). *Chemosphere* 58 (6), 779–792. doi:10.1016/j.chemosphere.2004.09.005

Eklöf, K., Bishop, K., Bertilsson, S., Björn, E., Buck, M., Skyllberg, U., et al. (2018). Formation of mercury methylation hotspots as a consequence of forestry operations. *Sci. Total Environ.* 613, 1069–1078. doi:10.1016/j.scitotenv.2017.09.151

Feinberg, A., Jiskra, M., Borrelli, P., and Biswakarma, J. (2023). *Land use change as an anthropogenic driver of mercury pollution*. arXiv. doi:10.31223/X5TQ03

Feng, C., Pedrero, Z., Li, P., Du, B., Feng, X., Monperrus, M., et al. (2016). Investigation of Hg uptake and transport between paddy soil and rice seeds combining Hg isotopic composition and speciation. *Elementa* 2016. doi:10.12952/journal.elementa.000087

Fostier, A.-H., Forti, M. C., Guimaraes, J. R. D., Melfi, A. J., Boulet, R., Santo, C. M. E., et al. (2000). Mercury fluxes in a natural forested amazonian catchment serra do navio, amapa state, Brazil. *Sci. Total Environ.* 260, 201–211. doi:10.1016/s0048-9697(00)00564-7

Fostier, A. H., Melendez-Perez, J. J., and Richter, L. (2015). Litter mercury deposition in the Amazonian rainforest. *Environ. Pollut.* 206, 605–610. doi:10.1016/j.envpol.2015.08.010

Gerson, J. R., Driscoll, C. T., Demers, J. D., Sauer, A. K., Blackwell, B. D., Montesdeoca, M. R., et al. (2017). Deposition of mercury in forests across a montane elevation gradient: elevational and seasonal patterns in methylmercury inputs and production. *J. Geophys. Res. Biogeosciences* 122 (8), 1922–1939. doi:10.1002/2016JG003721

Gerson, J. R., Szponar, N., Zambrano, A. A., Bergquist, B., Broadbent, E., Driscoll, C. T., et al. (2022). Amazon forests capture high levels of atmospheric mercury pollution from artisanal gold mining. *Nat. Commun.* 13 (1), 559. doi:10.1038/s41467-022-27997-3

Giovannini, G., Lucchesi, S., and Giachetti, M. (1988). Effects of heating on some physical and chemical parameters related to soil aggregation and erodibility. *Soil Sci.* 146, 255–261. doi:10.1097/00010694-198810000-00006

Gonzalez-Perez, J. A., Gonzalez-Vila, F. J., Almendros, G., and Knicker, H. (2004). The effect of fire on soil organic matter—A review. *Environ. Int.* 30, 855–870. doi:10.1016/j.envint.2004.02.003

Graydon, J. A., Louis, V. L., Hintelmann, H., Lindberg, S. E., Sandilands, K. A., Rudd, J. W. M., et al. (2008). Long-term wet and dry deposition of total and methyl mercury in the remote boreal ecoregion of Canada. *Environ. Sci. Technol.* 42 (22), 8345–8351. doi:10.1021/es801056j

Graydon, J. A., Louis, V. L., Hintelmann, H., Lindberg, S. E., Sandilands, K. A., Rudd, J. W. M., et al. (2009). Investigation of uptake and retention of atmospheric Hg(II) by boreal forest plants using stable Hg isotopes. *Environ. Sci. Technol.* 43 (13), 4960–4966. doi:10.1021/es900357s

Guedron, S., Grimaldi, M., Grimaldi, C., Cossa, D., Tisserand, D., and Charlet, L. (2011). Amazonian former gold mined soils as a source of methylmercury: evidence from a small scale watershed in French guiana. *Water Res.* 45 (8), 2659–2669. doi:10.1016/j.watres.2011.02.022

Guimaraes, J. R. D., Roulet, M., Lucotte, M., and Mergler, D. (2000). Mercury methylation along a lakeforest transect in the tapajos river floodplain, Brazilian Amazon: seasonal and vertical variations. *Sci. Total Environ.* 261, 91–98. doi:10.1016/s0048-9697(00)00627-6

Guyoneaud, R., Tessier, E., Colin, Y., Gassie, C., Guédron, S., Monperrus, M., et al. (2023). Microbial communities and environmental factors controlling methylmercury fate in an Amazonian watershed (Crique Combat, French Guyana) in wet and dry season. *Soil syst.* (in preparation 2023).

Hammer, O., Harper, D. A., and Ryan, P. D. (2001). Past: paleontological statistics software pack-age for education and data analysis. *Palaeontol. Electron.* 4, 9. doi:10.1016/j.bcp.2008.05.025

INPE (Instituto Nacional de Pesquisas Espaciais) (2023). *TerraBrasilis. PRODES (desmatamento)*. Available at http://terrabrasilis.dpi.inpe.br/app/dashboard/deforestation/biomes/legal_amazon/rates (Accessed May 15, 2023).

Jiskra, M., Sonke, J. E., Obrist, D., Bieser, J., Ebinghaus, R., Myhre, C. L., et al. (2018). A vegetation control on seasonal variations in global atmospheric mercury concentrations. *Nat. Geosci.* 11 (4), 244–250. doi:10.1038/s41561-018-0078-8

Kodamatani, H., Katsuma, S., Shigetomi, A., Hokazono, T., Imura, R., Kanzaki, R., et al. (2018). Behavior of mercury from the fumarolic activity of Mt. Myoko, Japan: production of methylmercury and ethylmercury in forest soil. *Environ. Earth Sci.* 77 (13), 478. doi:10.1007/s12665-018-7616-y

Kronberg, R. M., Jiskra, M., Wiederhold, J. G., Björn, E., and Skyllberg, U. (2016). Methyl mercury formation in hillslope soils of boreal forests: the role of forest harvest and anaerobic microbes. *Environ. Sci. Technol.* 50 (17), 9177–9186. doi:10.1021/acs.est.6b00762

Ku, P., Tsui, M. T. K., Nie, X., Chen, H., Hoang, T. C., Blum, J. D., et al. (2018). Origin, reactivity, and bioavailability of mercury in wildfire ash. *Environ. Sci. Technol.* 52 (24), 14149–14157. doi:10.1021/acs.est.8b03729

Louis, V. L. S. T., Rudd, J. W. M., Kelly, C. A., Hall, B. D., Rolfhus, K. R., Scott, K. J., et al. (2001). Importance of the forest canopy to fluxes of methyl mercury and total mercury to boreal ecosystems. *Environ. Sci. Technol.* 35 (15), 3089–3098. doi:10.1021/es001924p

Ma, M., Wang, D., Du, H., Sun, T., Zhao, Z., and Wei, S. (2015). Atmospheric mercury deposition and its contribution of the regional atmospheric transport to mercury pollution at a national forest nature reserve, southwest China. *Environ. Sci. Pollut. Res.* 22 (24), 20007–20018. doi:10.1007/s11356-015-5152-9

Mason, R. P., Choi, A. L., Fitzgerald, W. F., Hammerschmidt, C. R., Lamborg, C. H., Soerensen, A. L., et al. (2012). Mercury biogeochemical cycling in the ocean and policy implications. *Environ. Res.* 119, 101–117. doi:10.1016/j.envres.2012.03.013

Mataix-Solera, J., Cerd_a, A., Arcenegui, V., Jord_an, A., and Zavala, L. M. (2011). Fire effects on soil aggregation: a review. *Earth-Science Rev.* 109, 44–60. doi:10.1016/j.earscirev.2011.08.002

Melendez-Perez, J. J., and Fostier, A. H. (2013). Assessment of direct Mercury Analyzer® to quantify mercury in soils and leaf samples. *J. Braz. Chem. Soc.* 24 (11), 1880–1886. doi:10.5935/0103-5053.20130235

Melendez-Perez, J. J., Fostier, A. H., Carvalho, J. A., Windmöller, C. C., Santos, J. C., and Carpi, A. (2014). Soil and biomass mercury emissions during a prescribed fire in the Amazonian rain forest. *Atmos. Environ.* 96, 415–422. doi:10.1016/j.atmosenv.2014.06.032

Michelazzo, P. A. M., Fostier, A. H., Magarelli, G., Santos, J. C., and De Carvalho, J. A. (2010). Mercury emissions from forest burning in southern Amazon. *Geophys. Res. Lett.* 37 (9). doi:10.1029/2009GL042220

Monperrus, M., Rodriguez Gonzalez, P., Amouroux, D., Garcia Alonso, J. I., and Donard, O. F. X. (2008). Evaluating the potential and limitations of double-spiking species-specific isotope dilution analysis for the accurate quantification of mercury species in different environmental matrices. *Anal. Bioanal. Chem.* 390 (2), 655–666. doi:10.1007/s00216-007-1598-z

Mowat, L. D., Louis, V. L., Graydon, J. A., and Lehnherr, I. (2011). Influence of forest canopies on the deposition of methylmercury to boreal ecosystem watersheds. *Environ. Sci. Technol.* 45 (12), 5178–5185. doi:10.1021/es104377y

Neary, D. G., Ryan, K. C., and Debano, L. F. Editors (2005). Wildland fire in ecosystems: effects of fire on soils and water. *Gen. Tech. Rep.* RMRS-GTR-42-vol.4. Ogden, UT: U.S. Department of Agriculture, Forest Service, Rocky Mountain Research Station, 250.

North Central Regional Research (2012). *Recommended chemical soil test procedures for the north central region*. United States of America: North Central Regional Research.

Obrist, D., Kirk, J. L., Zhang, L., Sunderland, E. M., Jiskra, M., and Selin, N. E. (2018). A review of global environmental mercury processes in response to human and natural perturbations: changes of emissions, climate, and land use. *Ambio* 47 (2), 116–140. doi:10.1007/s13280-017-1004-9

Outridge, P. M., Mason, R. P., Wang, F., Guerrero, S., and Heimbürger-Boavida, L. E. (2018). Updated global and oceanic mercury budgets for the united nations global mercury assessment 2018. *Environ. Sci. Technol.* 52 (20), 11466–11477. doi:10.1021/acs.est.8b01246

Patel, K. F., Jakubowski, M. D., Fernandez, I. J., Nelson, S. J., and Gawley, W. (2019). Soil nitrogen and mercury dynamics seven decades after a fire disturbance: a case study at Acadia national Park. *Water, Air, Soil Pollut.* 230 (2), 29. doi:10.1007/s11270-019-4085-1

Patry, C., Davidson, R., Lucotte, M., and Béliveau, A. (2013). Impact of forested fallows on fertility and mercury content in soils of the Tapajós River region, Brazilian Amazon. *Sci. Total Environ.* 458 (460), 228–237. doi:10.1016/j.scitotenv.2013.04.037

Pirrone, N., Cinnirella, S., Feng, X., Finkelman, R. B., Friedli, H. R., Leaner, J., et al. (2010). Global mercury emissions to the atmosphere from anthropogenic and natural sources. *Atmos. Chem. Phys.* 10 (13), 5951–5964. doi:10.5194/acp-10-5951-2010

Pleijel, H., Klingberg, J., Nerentorp, M., Broberg, M. C., Nyirambangutse, B., Munthe, J., et al. (2021). Mercury accumulation in leaves of different plant types-the significance of tissue age and specific leaf area. *Biogeosciences* 18 (23), 6313–6328. doi:10.5194/bg-18-6313-2021

Reis, A. T., Davidson, C. M., Vale, C., and Pereira, E. (2016). Overview and challenges of mercury fractionation and speciation in soils. *TrAC - Trends Anal. Chem.* 82, 109–117. doi:10.1016/j.trac.2016.05.008

Richter, L., Amouroux, D., Tessier, E., and Fostier, A. H. (2023). Impact of forest fire on the mercury stable isotope composition in litter and soil in the Amazon. *Chemosphere* 339, 139779. doi:10.1016/j.chemosphere.2023.139779

Rieder, S. R., Brunner, I., Horvat, M., Jacobs, A., and Frey, B. (2011). Accumulation of mercury and methylmercury by mushrooms and earthworms from forest soils. *Environ. Pollut.* 159 (10), 2861–2869. doi:10.1016/j.envpol.2011.04.040

Rodríguez Martin-Doimeadios, R. C., Monperrus, M., Krupp, E., Amouroux, D., and Donard, O. F. X. (2003). Using speciated isotope dilution with GC-inductively coupled plasma MS to determine and unravel the artificial formation of monomethylmercury in certified reference sediments. *Anal. Chem.* 75 (13), 3202–3211. doi:10.1021/ac026411a

Roulet, M., Guimarães, J.-R. D., and Lucotte, M. (2001). Methylmercury production and accumulation in sediments and soils of an amazonian floodplain-effect of seasonal inundation. *Water, Air Soil Pollut.* 128, 41–60. doi:10.1023/a:1010379103335

Roulet, M., and Lucotte, M. (1995). Geochemistry of mercury in pristine and flooded ferralitic soils of a tropical rain forest in French Guiana, South America. *Air Soil Pollut.* 80, 1079–1088. doi:10.1007/bf01189768

Rundel, P. W. (1983). "Impact of fire on nutrient cycles in mediterranean-type ecosystems with reference to chaparral," in *Mediterranean-type ecosystems: The role of nutrients*. Editors F. J. Kruger, D. T. Mitchell, and J. U. M. Jarvis (New York, USA: Springer-Verlag), 192–2207.

Saatchi, S., Houghton, R. A., Dos Santos Alvalá, R. C., Soares, J. V., and Yu, Y. (2007). Distribution of aboveground live biomass in the Amazon basin. *Glob. Change Biol.* 13 (4), 816–837. doi:10.1111/j.1365-2486.2007.01323.x

Schneider, L., Fisher, J. A., Diéguez, M. C., Fostier, A.-H., Guimaraes, J. R. D., Leaner, J. J., et al. (2023). A synthesis of mercury research in the southern hemisphere, part 1: natural processes. *Ambio* 52, 897–917. doi:10.1007/s13280-023-01832-5

Shanley, J. B., Marvin-DiPasquale, M., Lane, O., Arendt, W., Hall, S., and McDowell, W. H. (2020). Resolving a paradox—High mercury deposition, but low bioaccumulation in northeastern Puerto Rico. *Ecotoxicology* 29 (8), 1207–1220. doi:10.1007/s10646-019-02108-z

Sombroek, W. (2000). Amazon landforms and soils in relation to biological diversity. *Acta Amaz.* 30 (1), 81–100. doi:10.1590/1809-43922000301100

Song, Z. W., Zhong, Z. P., ZhongXu, D. W., Hua, L., and Luo, Y. (2015). Comparison between sequential and single extraction procedures for metal speciation in fresh and dried Sedum Plumbizincicola. *J. Central South Univ.* 22 (2), 487–494. doi:10.1007/s11771-015-2547-1

Tabatchnick, M. D., Nogaro, G., and Hammerschmidt, C. R. (2012). Potential sources of methylmercury in tree foliage. *Environ. Pollut.* 160 (1), 82–87. doi:10.1016/j.envpol.2011.09.013

Tao, Z., Bian, R., and Chai, X. (2018). Methylmercury levels in cover soils from two landfills in Xi'an and Shanghai, China: implications for mercury methylation potentials. *Waste Manag.* 78, 331–336. doi:10.1016/j.wasman.2018.06.008

Teixeira, D. C., Lacerda, L. D., and Silva-Filho, E. V. (2017). Mercury sequestration by rainforests: the influence of microclimate and different successional stages. *Chemosphere* 168, 1186–1193. doi:10.1016/j.chemosphere.2016.10.081

Tsui, M. T. K., Blum, J. D., Kwon, S. Y., Finlay, J. C., Balogh, S. J., and Nollet, Y. H. (2012). Sources and transfers of methylmercury in adjacent river and forest food webs. *Environ. Sci. Technol.* 46 (20), 10957–10964. doi:10.1021/es3019836

Wang, X., Bao, Z., Lin, C. J., Yuan, W., and Feng, X. (2016). Assessment of global mercury deposition through litterfall. *Environ. Sci. Technol.* 50 (16), 8548–8557. doi:10.1021/acs.est.5b06351

Witt, E. L., Kolka, R. K., Nater, E. A., and Wickman, T. R. (2009). Influence of the forest canopy on total and methyl mercury deposition in the boreal forest. *Water, Air, Soil Pollut.* 199 (1–4), 3–11. doi:10.1007/s11270-008-9854-1

Zhang, H., Wang, Z., and Zhang, X. (2019a). Methylmercury concentrations and potential sources in atmospheric fine particles in Beijing, China. *Sci. Total Environ.* 681, 183–190. doi:10.1016/j.scitotenv.2019.05.128

Zhou, J., Obrist, D., Dastoor, A., Jiskra, M., and Ryjkov, A. (2021). Vegetation uptake of mercury and impacts on global cycling. *Nat. Rev. Earth Environ.* 2 (4), 269–284. doi:10.1038/s43017-021-00146-y

Zhou, J., and Obrist, D. (2021). Global mercury assimilation by vegetation. *Environ. Sci. Technol.* 55 (20), 14245–14257. doi:10.1021/acs.est.1c03530

Zhou, J., Wang, Z., and Zhang, X. (2018). Deposition and fate of mercury in litterfall, litter, and soil in coniferous and broad-leaved forests. *J. Geophys. Res. Biogeosciences* 123 (8), 2590–2603. doi:10.1029/2018JG004415

frontiers | Frontiers in Environmental Chemistry

TYPE Correction
PUBLISHED 28 September 2023
DOI 10.3389/fenvc.2023.1296650

OPEN ACCESS

APPROVED BY
Frontiers Editorial Office,
Frontiers Media SA, Switzerland

*CORRESPONDENCE
Anne Helene Fostier,
annehfostier@gmail.com

†These authors have contributed equally to this work and share senior authorship

RECEIVED 18 September 2023
ACCEPTED 19 September 2023
PUBLISHED 28 September 2023

CITATION
Fostier AH, Amouroux D, Tessier E, Viana JLM and Richter L (2023), Corrigendum: Methylmercury content in soil and litter from the Amazonian rainforest and its potential fate during forest fires.
Front. Environ. Chem. 4:1296650.
doi: 10.3389/fenvc.2023.1296650

Corrigendum: Methylmercury content in soil and litter from the Amazonian rainforest and its potential fate during forest fires

Anne Helene Fostier[1*†], David Amouroux[2†], Emmanuel Tessier[2], José Lucas Martins Viana[1] and Larissa Richter[1]

[1]Institute of Chemistry, University of Campinas (UNICAMP), Campinas, São Paulo, Brazil, [2]Université de Pau et des Pays de l'Adour, E2S UPPA, CNRS, Institut des Sciences Analytiques et de Physico-chimie pour l'Environnement et les Matériaux (IPREM), Pau, France

KEYWORDS

mercury, methylmercury, litterfall, soil, ash, forest fire, tropical forest

A Corrigendum on
Methylmercury content in soil and litter from the Amazonian rainforest and its potential fate during forest fires

by Fostier AH, Amouroux D, Tessier E, Viana JLM and Richter L (2023). Front. Environ. Chem. 4: 1242915. doi: 10.3389/fenvc.2023.1242915

In the published article, there was an error in the **Funding** statement. The University of Campinas (UNICAMP/FAEPEX 2932/23) was left out of the original statement inadvertently.

"This work was funded by the São Paulo Research Foundation (FAPESP) (projects 2008/04490-4, 2010/19040-4) and also partially supported by the CNRS, French ANR, and New Aquitaine Region council." The correct Funding statement appears below.

"This work was funded by the São Paulo Research Foundation (FAPESP) (projects 2008/04490-4, 2010/19040-4) and also partially supported by the University of Campinas (UNICAMP/FAEPEX 2932/23), the CNRS, French ANR, and New Aquitaine Region council."

The authors apologize for this error and state that this does not change the scientific conclusions of the article in any way. The original article has been updated.

Publisher's note

All claims expressed in this article are solely those of the authors and do not necessarily represent those of their affiliated organizations, or those of the publisher, the editors and the reviewers. Any product that may be evaluated in this article, or claim that may be made by its manufacturer, is not guaranteed or endorsed by the publisher.

frontiers | Frontiers in Environmental Chemistry

TYPE Original Research
PUBLISHED 23 October 2023
DOI 10.3389/fenvc.2023.1241176

OPEN ACCESS

EDITED BY
Robert Peter Mason,
University of Connecticut, United States

REVIEWED BY
John Dodson,
Chinese Academy of Sciences (CAS), China
Carl Lamborg,
University of California, Santa Cruz, United States

*CORRESPONDENCE
Jalene Nalbant,
jalene.nalbant@anu.edu.au

RECEIVED 20 June 2023
ACCEPTED 02 October 2023
PUBLISHED 23 October 2023

CITATION
Nalbant J, Schneider L, Hamilton R, Connor S, Biester H, Stuart-Williams H, Bergal-Kuvikas O, Jacobsen G and Stevenson J (2023), Fire, volcanism and climate change: the main factors controlling mercury (Hg) accumulation rates in Tropical Lake Lantoa, Sulawesi, Indonesia (~16,500–540 cal yr BP). *Front. Environ. Chem.* 4:1241176. doi: 10.3389/fenvc.2023.1241176

Fire, volcanism and climate change: the main factors controlling mercury (Hg) accumulation rates in Tropical Lake Lantoa, Sulawesi, Indonesia (~16,500–540 cal yr BP)

Jalene Nalbant[1]*, Larissa Schneider[1,2], Rebecca Hamilton[1,2], Simon Connor[1,2], Harald Biester[3], Hilary Stuart-Williams[4], Olga Bergal-Kuvikas[5], Geraldine Jacobsen[6] and Janelle Stevenson[1,2]

[1]School of Culture, History and Language, Australian National University, Canberra, ACT, Australia, [2]ARC Centre of Excellence for Australian Biodiversity and Heritage, Australian National University, Canberra, ACT, Australia, [3]Institut für Geoökologie, AG Umweltgeochemie, Technische Universität Braunschweig, Braunschweig, Germany, [4]Research School of Biology, Australian National University, Canberra, ACT, Australia, [5]Institute of Volcanology and Seismology FEB RAS, Petropavlovsk-Kamchatsky, Russia, [6]Centre for Accelerator Science, Australian Nuclear Science & Technology Organisation, Sydney, NSW, Australia

The effects of climate change on long-term mercury (Hg) cycling are still not well understood, as climate changes are usually gradual and can only be assessed using high-resolution archives. Our study site (a small, lowland tectonic lake in Sulawesi, Indonesia) provides a unique opportunity to further understanding of Hg cycling in the Southeast Asian (SEA) tropics during the transition from the Pleistocene to the Holocene, a period of significant climate variability. We present a high-resolution record of Late Glacial and Holocene Hg deposition within the sediments of tropical Lake Lantoa, Sulawesi. Using a multi-proxy framework (including pollen, charcoal, carbon:nitrogen ratio and high-resolution geochemistry records) we investigate the response of Hg accumulation rates (HgAR) in sediments to shifts in climate between ~16,488 and 538 cal BP. This period encompasses the Bølling-Allerød (BA) warming, Younger Dryas (YD) cooling and Holocene warming events, providing new insights into the effects of global climatic transitions on HgAR in SEA sediments. The Pleistocene Termination had the highest HgAR and substantial variability (μ = 11.32, 5.38–33.91 μg m^{-2} yr^{-1}), when drier conditions and high charcoal accumulation rates suggest that fire activity was the main source of Hg to the lake. The Holocene Transition was marked by a decrease in HgAR (μ = 8, 3.50–18.84 μg m^{-2} yr^{-1}) as humid conditions precluded forest burning, followed by high HgAR (μ = 11.35, 3.30–158.32 μg m^{-2} yr^{-1}) in the Early Holocene. Mercury accumulation rate in the Late Holocene (μ = 3.80, 1,67–43.65 μg m^{-2} yr^{-1}) was the lowest in the Lake Lantoa record, marked by the lowest fire events and a stable catchment. An increase in carbon:nitrogen ratios during the Late Holocene, coupled with a decrease in HgAR, suggests that the establishment of lowland forest resulted in suppressed Hg erosion/leaching. Our results demonstrate that forest fires, vegetation change and volcanism are

important drivers of Hg inputs to Lake Lantoa, a relationship which is strongly mediated by climate and lake-catchment dynamics.

KEYWORDS

volcanic mercury emissions, long-term mercury deposition, Southeast Asian mercury cycle, primary productivity and mercury accumulation, forest fire mercury emissions, effects of climate change on mercury

1 Introduction

Over the last two decades, our understanding of the biogeochemical cycling of mercury (Hg) has advanced significantly in temperate areas of the Northern Hemisphere (Lindberg et al., 2007; Obrist et al., 2018). Few studies, however, have targeted sites in the tropics (Schneider et al., 2023). This knowledge gap has meant that Hg regulatory frameworks within tropical regions have had to rely on inferences about the Hg cycle from temperate areas (Fisher and Nelson, 2020). This is problematic as there are unique processes affecting the biogeochemical cycle of Hg in the tropics, such as higher Hg uptake rates via litterfall and greater ecological heterogeneity (Lacerda et al., 1999; Wang et al., 2016; Schütze et al., 2021).

Lake systems are central to the terrestrial cycle of Hg (Parkman and Meili, 1992). They receive Hg from the atmosphere and catchment, working as natural archives that capture long-term temporal trends in Hg accumulation rates (HgAR) (Swain et al., 1992; Engstrom et al., 2007; Hermanns and Biester, 2013; Schütze et al., 2021). The HgAR is directly affected by climatic and environmental changes which play an important role in the transport of Hg from soils to lake sediments. While atmospheric deposition of Hg in lakes is a relatively straightforward process, Hg derived from the lake-catchment is dependent on complex environmental processes that need to be fully understood when reconstructing the relationship between past Hg cycling and its climatic drivers (Roulet et al., 1998; Schütze et al., 2021).

The major climatic and environmental processes that influence Hg deposition in lakes include: i) catchment erosion, ii) wet and dry deposition, iii) lake primary productivity, and iv) forest fires (Parkman and Meili, 1992; Lintern et al., 2020; Pérez-Rodríguez and Biester, 2022). Understanding these processes and how they affect HgAR over time is critical to understanding the impacts of anthropogenically-induced environmental and climatic changes on the natural Hg cycle. This is particularly relevant in the tropics, where catchment erosion is known to be intensified by high temperatures and precipitation rates, further magnifying the effects of climate and environmental changes on HgAR (Lal, 1990; Labrière et al., 2015). Furthermore, these processes are not necessarily independent, and HgAR is the net result of these dynamic processes, their proximity to the lake, and their Hg contents.

Mercury stored in soils is deposited into lakes via direct litterfall input and/or via production of dissolved organic matter (DOM), with the quantity of stored Hg dependent on the amount of Hg bound to each unit of organic matter (OM). Wet and dry Hg deposition also play an important role in regulating HgAR. Isotopic analyses indicate that 50%–80% of Hg in vegetation and soil derives from atmospheric Hg(0) uptake by plants, with the remainder from wet and aerosol deposition (Demers et al., 2013; Jiskra et al., 2015; Enrico et al., 2016; Obrist et al., 2017). This has direct implications for HgAR in tropical lakes as tropical regions have the highest global litterfall fluxes (Wang et al., 2016), resulting in higher soil Hg concentrations facilitated by the rapid breakdown of litterfall. Mercury stored in soils is deposited into lakes via direct litterfall input and/or via production of dissolved organic matter (DOM), with the quantity of stored Hg dependent on the amount of Hg bound to each unit of OM (Schütze et al., 2021).

Mercury accumulation rates in lake sediments are also mediated by primary productivity. Mercury scavenging from the water column by algae and detrital suspended particulate OM, followed by settlement and sedimentation, is recognised as an important process for Hg transfer into the hypolimnia of temperate lakes (Outridge et al., 2007; Schütze et al., 2021). Globally there is no consensus on the relationship between Hg and primary productivity in lakes, but it has been hypothesized that higher productivity results in higher HgAR (Melack and Forsberg, 2001; Schütze et al., 2021). These studies show that water column Hg scavenging by algae is the major reason for the intense Hg export to the sediments of productive lakes, making them significantly larger sedimentary sinks than oligotrophic lakes.

Forest fires are a major source of Hg deposited into lake sediments. Fires re-emit Hg sequestered in catchment vegetation and soils via volatilisation and thermal desorption (Outridge et al., 2019). Deforestation associated with forest fires promotes catchment erosion and Hg leaching into lakes (Lindberg and Stratton, 1998; Amirbahman et al., 2004), further contributing to HgAR in lake sediments. Studies have reported the coeval increase in HgAR and charcoal accumulation rates (CHAR) with peaks in charcoal counts, demonstrating the positive correlation between forest fires and HgAR (Ribeiro Guevara et al., 2010; Daga et al., 2016; Thomas et al., 2022).

Natural events (e.g., volcanic degassing, flood events, increase in catchment runoff) can also increase both direct and indirect deposition of Hg into lakes (Guédron et al., 2019). For example, a volcanic eruption emits Hg into the atmosphere, contributing to direct atmospheric Hg deposition, while volcanic ash accompanied by a release of sulphuric acid (SO_2) can trigger secondary deposition of Hg from soils via catchment erosion and Hg leaching into lakes (Guédron et al., 2019).

Southeast Asia (SEA) is critical to the global Hg cycle because it supports tropical rainforest vegetation (which facilitates Hg uptake by plants and subsequent transfer to soils and lakes) and has high regional volcanic activity (which directly contributes to atmospheric Hg emissions and subsequent deposition in terrestrial and aquatic environments). Despite the important role of tropical zones in the global Hg cycle, there are very few studies that track the long-term dynamics of Hg in relation to volcanic eruptions, landscape change and industrial activity in these areas (Pérez-Rodríguez et al., 2015; Lacerdada et al., 2017; Fadina et al., 2019; Schneider et al., 2020).

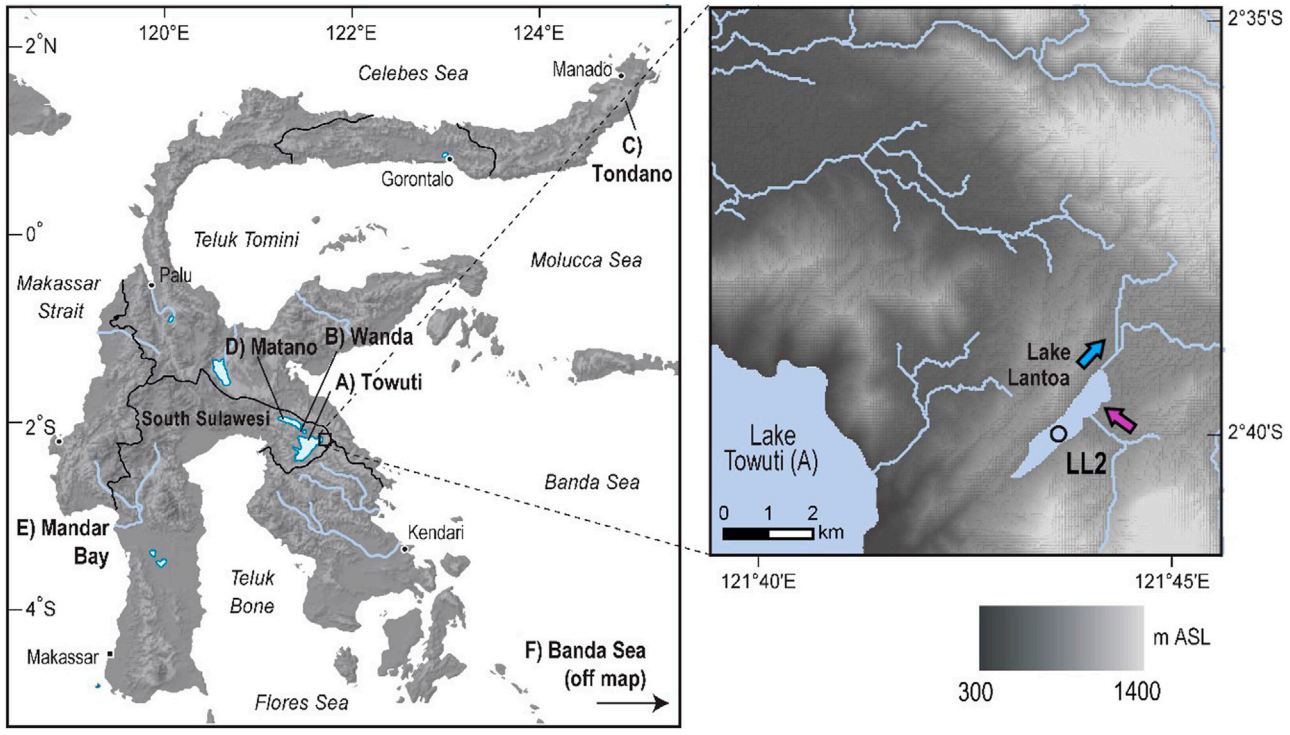

FIGURE 1
The location of the study area in South Sulawesi, Indonesia. On the right panel is a detailed figure of Lake Lantoa's catchment and its proximity to the Malili Lakes system (Lake Towuti). The coring site (LL2) is indicated by a black circle. The blue arrow on the right panel indicates the outflow of water from Lake Lantoa, and the pink arrow indicates the lake's inflow.

Long-term studies from tropical zones are crucial as they do not have the same temporal or spatial limitations as current observational studies, which typically focus on temperate regions and recent decades (Schneider et al., 2023).

We assess the impact of climate change on HgAR in tropical SEA through a long-term, multi-proxy analysis of a sediment core from a tropical lowland lake: Lake Lantoa, in Sulawesi, Indonesia. This sediment record spans ~16,500–540 cal BP, recording periods of rapid climate fluctuations from the end of the Last Glacial Maximum (Pleistocene Termination; ~18ka) into the Holocene which began ~11.7ka (Russell et al., 2016; Hamilton et al., 2019b). This provides a unique opportunity to examine the influence of highly variable climate and environmental drivers, such as vegetation and fire, on Hg cycling in the lowland tropics of SEA. In doing so we hope to expand current understanding of the relationship between lake-catchment dynamics and HgAR in tropical lake sediments, and offer insight into the effects of modern land use on Hg transport to aquatic environments.

2 Materials and methods

2.1 Study location and regional setting

Lake Lantoa (Danau Lontoa) (2.6647°S, 121.7292°E) is a low-latitude, north-east to south-east oriented lake that forms part of the much larger tectonic Malili Lakes system in South Sulawesi, Indonesia (Figure 1) (Hamilton et al., 2019b). The lake is shallow (~4 m maximum depth), small (~1.5 km^2), and sits at ~600 m above sea level (ASL). Lake Lantoa is an ideal site to study historical Hg deposition as it has a small catchment area (~5 km^2) and is fairly remote, yet it is surrounded by sub-montane vegetation on neighbouring peaks which reach up to 800 m ASL. The lake is ~29 km from the Banda Sea coast (Figure 1). Lake Lantoa receives stream inflow at the south-east and water outflows from the northern most extent of the lake (Figure 1) (Russell et al., 2016). Core LL2 was taken from the south-west of the lake, away from the inflow and outflow of water (Figure 1) (Hamilton et al., 2019b).

The Malili Lakes catchment formed approximately 1.5 Ma from a series of trans-tensional basins in response to the Matano strike-slip fault (Russell et al., 2016; Russell et al., 2020). The catchment is located within the East Sulawesi Ophiolite formation and contains ultramafic gabbros, basalts, and peridotites (Costa et al., 2015). Consequently, the catchment soils are nutrient-poor and heavy metal-rich (Van der Ent et al., 2013). Although there is archaeological evidence of human occupation in this area since 40,000 cal BP, land use prior to the development of mining in the 1970s mostly consisted of small-scale agriculture (Hope, 2001; Van Den Bergh et al., 2016). Therefore, we do not expect anthropogenic activities, such as broad-scale forest clearing, to influence our proxies. This inference is supported by pollen data published from Lake Lantoa in Hamilton et al. (2019b), which shows no obvious clearance of catchment vegetation over the past 16,500 years.

Sulawesi has a heterogenous temperature and precipitation gradient across the island, resulting in high humidity at low-

elevations and milder climate in mountainous terrain with higher altitudes (Whitten et al., 1988). As there are only 2 months where the average rainfall is <100 mm/month (September and October), Sulawesi is considered to be mildly seasonal (Walsh and Lawler, 1981).

Regional climate patterns within Sulawesi are dictated by changes in the Indo-Pacific Warm Pool (IPWP), shifts in the International Convergence Zone (ITCZ), and the El Niño Southern Oscillation (ENSO) cycle (De Deckker, 2016). Sulawesi is surrounded by the IPWP, which has a permanent sea surface temperature (SST) of >28°C (De Deckker, 2016). The IPWP directly influences the Australian-Indonesian Summer Monsoon (AISM) strength, as monsoons are generated in response to the temperature difference between the land and sea, with precipitation falling over the area with the higher surface temperature. The AISM drives a north-easterly flowing air current from the Northern Hemisphere into the Southern. Changes in AISM strength can mediate the transportation of Hg from the Northern Hemisphere into the Southern Hemisphere. This is particularly pertinent to interpreting the HgAR record in Sulawesi as it can potentially record Hg emissions from local and regional volcanism. Volcanic Hg is primarily emitted as gaseous elemental mercury (GEM) allowing it to travel long distances (Ansmann et al., 1997; Slemr and Scheel, 1998; Polvani et al., 2019).

2.2 Core location and extraction

A 600 cm long sediment core (LL2) was collected from the southern end of the lake. The core was extracted using a Geocorer in six drives, each 1 m long, as detailed in Hamilton et al. (2019b). The first metre was unconsolidated and subsampled on site at 11 cm intervals. The five basal drives were capped, sealed, and transported to the Australian National University (ANU) for storage and analysis. Cores were split lengthways, and half of the core was stored in a cool room at 4°C at the School of Culture, History and Language at the ANU, while the other half was scanned for XRF elemental analysis using an Avaatech core-scanner at the Research School of Earth Sciences at the ANU. Sediment recovery within each of the first five 1 m drives ranged from 85% to 95%. Five "no core" gaps are highlighted in the figures presented in this study for the sections with less than 100% recovery (Figure 3; Figure 4; Figure 7).

2.3 Core chronology

The original chronology for the core, based on AMS ^{14}C analysis of 10 samples (bulk sediment samples), published in Hamilton et al. (2019b) has since been refined through the radiocarbon analysis of an additional 10 bulk sediment samples from the upper portion of the core (OZY codes in Table 1). These

TABLE 1 Laboratory ID, sample type, depth and conventional ^{14}C (1σ) ages of LL2 samples used for the chronological model used in this study.

Laboratory code	Depth (cm)	Material	Reference	^{14}C date BP (±1 σ)
OZY956	3	Bulk sediment	This study	655 ± 20
OZY957	9	Bulk sediment	This study	725 ± 30
45723	16	Bulk sediment	Hamilton et al. (2019)	1138 ± 21
OZY958	26.5	Bulk sediment	This study	1375 ± 30
OZY959	33.5	Bulk sediment	This study	1770 ± 30
OZY960	39.5	Bulk sediment	This study	2425 ± 30
OZY961	44.5	Bulk sediment	This study	2635 ± 25
45724	48	Bulk sediment	Hamilton et al. (2019)	2960 ± 22
OZY962	53.5	Bulk sediment	This study	3260 ± 30
OZY963	58.5	Bulk sediment	This study	3385 ± 30
OZY964	65.5	Bulk sediment	This study	3555 ± 30
OZY965	69.5	Bulk sediment	This study	3735 ± 30
DAMS008500	70	Bulk sediment	Hamilton et al. (2019)	3858 ± 29
45725	132	Bulk sediment	Hamilton et al. (2019)	4778 ± 24
45726	232	Bulk sediment	Hamilton et al. (2019)	7627 ± 28
45727	332	Bulk sediment	Hamilton et al. (2019)	10346 ± 32
45729	432	Bulk sediment	Hamilton et al. (2019)	12098 ± 37
45730	532	Bulk sediment	Hamilton et al. (2019)	12734 ± 40
45731	580	Bulk sediment	Hamilton et al. (2019)	13471 ± 42
DAMS008501	600	Bulk sediment	Hamilton et al. (2019)	13779 ± 54

samples underwent acid-base-acid (ABA) treatment prior to conversion of the organic carbon to graphite for AMS analysis on the NEC 1 MV Vega accelerator at the Australian Nuclear Science and Technology Organisation Centre for Accelerator Science (Wilcken et al., 2015) (Table 1). A Bayesian age-depth model was produced for core sediments between 0 and 600 cm at 0.5 cm intervals using the ages returned from the twenty bulk sediment samples (Table 1). This model was produced in the package Bacon 2.5 (Blaauw and Christen, 2011) in R (Core Team, 2013), using the Southern Hemisphere calibration curve (Hogg et al., 2020) (SHCal20) and a mean accumulation rate of 20 years/cm.

The top 5 cm of the core was analysed using ^{210}Pb dating. Unsupported ^{210}Pb activities were too low for dating calculations (see Supplementary Table S3). This supports the age-model based on ^{14}C dating. For this reason, this study excludes any interpretation of the industrial era (defined here as 200 BP).

2.4 Charcoal and pollen analyses

Charcoal and palynological analysis of core sediments are reported in Hamilton et al. (2019b), the results of which are used against the updated chronological model for this study. Briefly, 31 pollen and spore samples were extracted from the core sediments for palynological analysis at approximately 20 cm intervals using standard methods (Fægri and Iverson, 1989; Caffrey and Horn, 2013). Plant microfossils were enumerated under a Zeiss AxioImager M.1 light microscope fitted with an AxioCam MRc5 camera under x400 magnification and identified using published literature from the region (Huang, 1972; Wang et al., 1995; Hamilton, et al., 2019a; Hamilton et al., 2019b; Hamilton and Stevenson, 2020). A minimum count target of 200 pollen and spores (with a minimum of 100 arboreal taxa) was set for the analysis. The pollen and spore data were classified into functional groups and habitat types through comparison with a digitised herbarium list of 28,000 specimens collected from Sulawesi and compiled by the Naturalis Biodiversity Center in Leiden, Netherlands.

Macro-charcoal (>125 µm), a proxy for local fire activity, was wet sieved contiguously from 2.5 cm^3 sediment samples (Hamilton et al., 2019b). Samples between 1 and 10 cm depth were taken from 2 cm intervals while those between 10 and 600 cm were taken from 1 cm intervals (Hamilton et al., 2019b). Macro-charcoal fragments were isolated from the subsamples following methods outlined in Stevenson and Haberle (2005). Charcoal fragments were then enumerated under a Zeiss Stemi Stereo microscope at ×20 magnification (Stevenson and Haberle, 2005).

2.5 Organic matter

The organic matter (OM) content of each sediment sub-sample was determined using weight loss-on-ignition (Wang et al., 2011) at the Palaeoworks Laboratory at the ANU. Samples were freeze dried for 48 h using the Alpha 1-2 LDplus (Martin Christ, Germany) freeze drier. Approximately 0.5 g of sediment was weighed and heated for 7 h in a muffle furnace (LABEC, model CEMLL) at 550°C. After samples cooled to room temperature, they were re-weighed to determine OM %.

2.6 Carbon and nitrogen percentage

Samples of dried sediment were weighed to the closest microgram in folded tin foil cups. These were then combusted in a Carlo-Erba EA-1110 Elemental Analyser (Carlo Erba, Milan, Italy). Gases were separated using a packed gas chromatograph (HayesSep D 80/100, Grace Davison, Australia) at room temperature and passed to a stable isotope ratio mass spectrometer (Isoprime, Micromass U.K., Manchester, U.K.). Percentages of nitrogen and carbon were calculated using the heights and areas of the mass spectrometer peaks. Carbon and nitrogen ratios (C:N) were derived by dividing %C by %N. This ratio was used to characterise the source of OM to lake sediments (i.e., allochthonous vs. autochthonous) (Riddle et al., 2022). Carbon and nitrogen percentages and C:N values are presented in Supplementary Table S1.

2.7 Mercury analysis

Mercury analysis was conducted using a Milestone Direct Mercury Analyser (DMA-80 Tri-Cell; Milestone, Bergamo, Italy) at the Palaeoworks Laboratory at the ANU. Samples were analysed using the USEPA method 7,473 (USEPA, 1998). Approximately 50 mg of each sample were weighed into nickel boats. Two blanks, two Standard Reference Materials (SRMs) and 10 replicas were run every 40 samples. Certified soil reference material NIST 2706 and SECCC WQB-1 (soil and sediment matrix) were analysed, and the results agreed well with published values (Supplementary Table S2).

Mercury accumulation rate (HgAR) in this study was defined as the deposition of Hg (concentration in ng g^{-1}) per centimetre of sediment accumulation (sedimentation rate in cm yr^{-1}). Accumulation rates (µg m^{-2} yr^{-1}) were calculated using the following equation:

$$HgAR = 10 \times SR \times DBD \times Hg$$

where SR = sedimentation rate (cm yr^{-1}); DBD = dry bulk density (g cm^{-3}); Hg = Hg concentration (ng g^{-1}).

2.8 Visual inspection for glass shards

A visual inspection for volcanic tephra was conducted in the full LL2 core. As no tephra was identified visually, sediments from the two depths with the highest Hg concentrations and HgAR (depths 220 and 241 cm) were checked for cryptotephras. These sediments were digested with hydrogen peroxide and HCl, and analysed under a scanning electron microscope (SEM) JEOL JCM-6000 at 400 X magnification and an accelerating voltage 15 kV for the identification of fine glass shards.

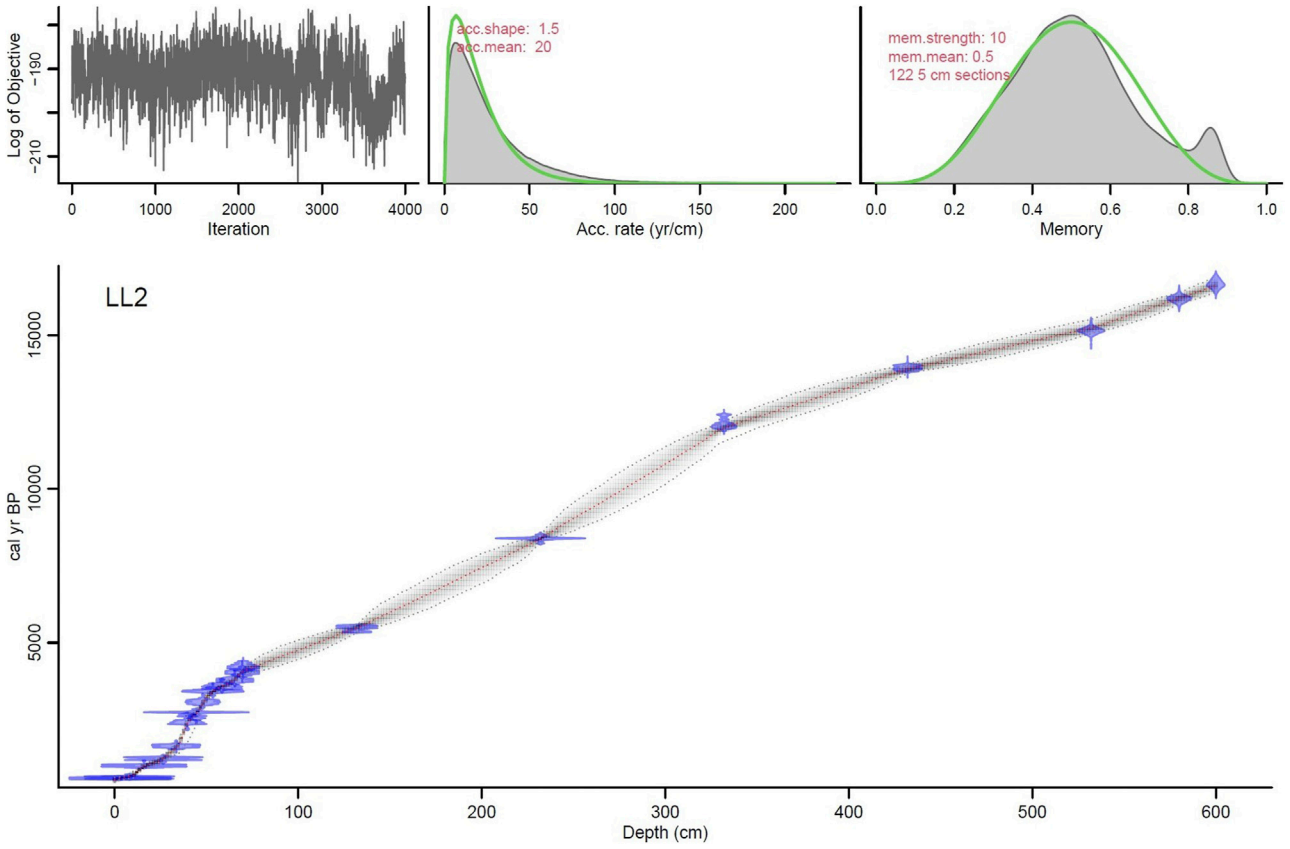

FIGURE 2
Age-depth model for Lake Lantoa sediments using R package *rbacon* 2.2 (Blaauw and Christen, 2011). The ^{14}C ages were calibrated against the Southern Hemisphere calibration (SHCal20) data set (Hogg et al., 2020). The main panel shows the age-depth model with 95% credible interval and mean as grey and red dashed line. Blue symbols indicatet the calibrated radiocarbon dates. Top panels, from left to right, show: Markov Chain Monte Carlo iterations, the accumulation rate panel with prior (green) and posterior (grey) distributions of the accumulation rate, and the memory panel (dependence of accumulation rate between neighbouring depths) showing the prior (green) and posterior (grey) distributions of the memory parameter.

2.9 X-ray fluorescence data processing and analyses

Surfaces of five core sections (100 cm–594 cm) were scanned using an Avaatech core-scanner for X-ray fluorescence (XRF) elemental analysis at the Australian National University Research School of Earth Sciences (20 s count time 10 kV voltage). The methods used to correlate and standardise these data are outlined in Hamilton et al. (2019b). In summary, this first entailed normalising each elemental variable using total count per second (cps) as the denominator, which statistical correlation determined to be a valid means of correcting for the dilution effects of water and organic material in the core sediments. Select elements that were consistently above detection limit (i.e., those that consistently returned positive count values) were then standardised using a z-score. Exceptions to this were the elements S and P which, though returning largely negative values, were included in the original study due to the interactions with redox-sensitive elements (Hamilton et al., 2019b). A running mean (centralised) was applied to the variables following normalisation (5pt for Ca, Mn, Fe, Ni, Cr; 20 pt for Al, Si, P, S, and Ti), depending on detectability and the noisiness of the dataset (Hamilton et al., 2019b). In this study any values <0 were recorded as 'below detection limits' and not included in the statistical analyses.

Lake Lantoa has a catchment characterised by ultramafic soils, composed mainly of mafic minerals (e.g., manganese [Mn], iron [Fe] and siderophilic elements such as nickel [Ni]) (Van der Ent et al., 2013). In this study, these elements (Mn, Fe, Ni) are used as a proxy for erosion ofof the Lake Lantoa catchment (Hamilton et al., 2019b).

2.10 Numerical analyses and plots

All data analyses were performed using R Statistical Software (Core Team, 2013). Stratigraphic plots were built using the R package *analogue*. Principal Component Analysis (PCA) was performed on log-transformed data using R packages *vegan*, *ggplot2* and *ggfortify*. One PCA was run with pollen, OM, C:N and charcoal data (proxies with low temporal resolution) and a second on OM, C:N charcoal and geochemical data (proxies with high resolution).

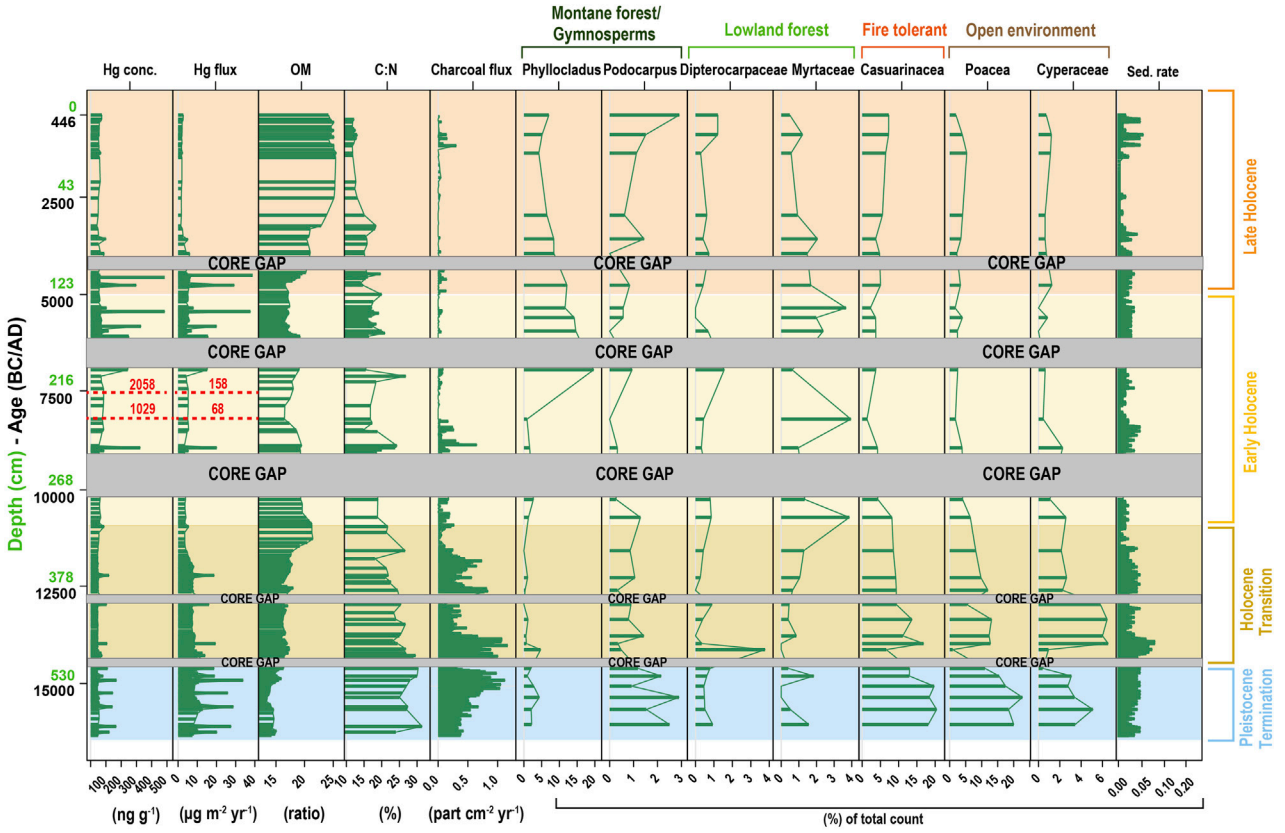

FIGURE 3
Mercury (Hg) concentrations (ng g^{-1}), mercury accumulation rate (µg m^{-2} yr^{-1}), organic matter (OM, %), carbon and nitrogen ration (C:N), charcoal flux (particle cm^{-2} yr^{-1}) and pollen data (%) for Lake Lantoa (LL2) sediment core for the last 16,477 years. The two highest peaks in Hg and HgAR (at 8,015 and 8,722 cal BP) were removed for clearer plotting of these proxies. They are represented as red dashed lines with their values and are plotted off scale.

3 Results and discussion

3.1 Core chronology, sedimentation and XRF geochemistry

The ^{14}C age-depth model for LL2 demonstrates increasing age with depth, with the smoothly varying slope indicating no, or temporally invariant, post-depositional mixing of sediments (Figure 2). The median chronological model produced for the core estimates that the age range of the sediments span 16,488–538 cal BP. The core therefore includes the Pleistocene Termination (considered to be the period between 16,488 and 14,000 cal BP in this paper), a period of significant climate variability (Russell et al., 2016).

The base of the core (594 cm) generated a mean radiocarbon age of 16,488 (16,259–16,736) cal BP and the top sample (0 cm) generated a mean radiocarbon age of 538 (446–607) cal BP. The very top part of the mud-water interface core was lost during extrusion.

The updated chronology produced for the core sediments estimates that the five core gaps capture the time periods between 14,843–14,516 cal BP, 13,293–12,967 cal BP, 10,835–9,547 cal BP, 7,475–6,552 cal BP, and 4,837–4,219 cal BP.

The age-depth model suggests a mean sedimentation rate of approximately 3 mm/yr and steadily decreases up-core. Sediments between 594 and 345 cm depth (modelled at 16,488 to 12,247 cal BP) show the fastest sedimentation rate of 4 mm/yr, slowing to 3 mm/yr between 345 and 259 cm depth (modelled at 12,247–9,378 cal BP) before slowing again to 2 mm/yr between 259 and 0 cm depth (modelled at 9,378–538 cal BP).

The XRF geochemistry results are discussed in (Hamilton et al., 2019b) and the reader is referred to the original publication for more detail. To summarise, the Lake Lantoa XRF record demonstrates that sulphur (S), manganese (Mn) and nickel (Ni) are better indicators of detrital input than some traditional elements in the Lake Lantoa catchment (Hamilton et al., 2019b). Typically, studies using XRF core scanning data report that increases in aluminium (Al), silicon (Si), calcium (Ca), titanium (Ti), magnesium (Mg), manganese (Mn) and iron (Fe) are good proxies for an increase in detrital input to lake sediments (Davies et al., 2015). As outlined in Hamilton et al. (2019b), this discrepancy is driven by the ultramafic local geology and soil type in the Lake Lantoa catchment.

3.2 Environmental and ecological changes

The results for the new proxies analysed as part of this study (Hg concentration, HgAR, organic matter, CHAR and C:N ratios) are presented in Supplementary Table S4. The cross-comparative pollen

TABLE 2 Mean of quantitative proxies (min–max) per period for core LL2.

Quantitative proxies	Pleistocene Termination (16,477–14,000 cal BP)	Holocene Transition (14,000–11,700 cal BP)	Early Holocene (11,700–5,000 cal BP)	Late Holocene (5,000–538 cal BP)
Mercury concentration (ng g^{-1})	61 (28.92–169.78)	50 (29.40–120.43)	164 (49.36–2558.59)	72 (41.13–604.70)
Mercury accumulation rate (μg m^{-2} yr^{-1})	11 (5.38–33.92)	8 (3.50–18.84)	11 (3.30–158.32)	4 (1.67–43.65)
Charcoal flux (particle cm^{-2} yr^{-1})	0.59 (0.12–1.31)	0.34 (0.01–1.00)	0.05 (0.00–0.63)	0.02 (0.00–0.24)
C:N ratio	27 (23.20–31.40)	23 (18.10–26.70)	18 (14.10–26.80)	14 (11.70–19.70)
Organic matter (%)	16 (13.36–17.39)	17 (15.66–21.45)	18 (16.48–21.28)	23 (18.36–25.53)

and XRF count data are included in the publication where these data were originally produced and interpreted (Hamilton et al., 2019b).

The Pleistocene Termination was a period characterised by relatively high local fire activity, indicated by elevated charcoal counts with a more seasonal, drier, cooler climate than the Holocene (Figure 3). In the lowlands these conditions supported a seasonal, more fire-tolerant lowland forest (e.g., Casuarinaceae) and open savanna taxa (e.g., Poaceae and Cyperceae), limiting the range of moisture-demanding, fire-exclusionary lowland and montane forest taxa (e.g., *Phyllocladus* and Dipterocarpaceae, as described in Hamilton et al., 2019b) (Figure 3). The pollen data indicate that the *Podocarpus* forest likely grew in cool, high elevation zones (Hamilton et al., 2019b).

The high C:N ratios (μ = 27, 1σ = 2.46) for the Pleistocene Termination indicate that there was significant contribution of catchment-derived organic matter (OM) to the lake (Figure 3). Typically autochthonous (within lake production) OM, like algae and phytoplankton, have more nitrogen (N) than terrestrial OM, returning a C:N ratio between 4 and 10 (Devesa-Rey and Barral, 2012). Conversely, allochthonous (catchment-derived) OM tend to be nitrogen-poor (dependent on lignin and cellulose structure) and are characterised by C:N ratios of >20 (Devesa-Rey and Barral, 2012). The C:N ratio decreases from the Pleistocene Termination to the Holocene Transition (μ = 27, 1σ = 2.46, to μ = 23, 1σ = 2.58, respectively), indicating a slight decrease in catchment-derived OM in the sediments (Figure 3 and Table 2).

Vegetation change from the Pleistocene Termination to the Holocene Transition (between 14,000 and 11,000 cal BP) suggests a gradual increase in humidity at the site (Hamilton et al., 2019b). Montane forest taxa (e.g., *Podocarpus*) and lowland ultramafic forest angiosperms (e.g., Dipterocarpaceae and Myrtaceae) gradually increase in this period, concurrent with a decline in grasses and sedges (e.g., Poaceae and Cyperaceae) and reduction in fire activity (e.g., Casuarinaceae and CHAR, as described in Hamilton et al., 2019b) (Figure 3). This climate shift is concurrent with the Bølling-Allerød, which was likely a gradual warming event in Southeast Asia (SEA) (Russell et al., 2014; Wicaksono et al., 2015; Hamilton et al., 2019b) and as a more abrupt warming event in the mid-high latitudes of the Northern Hemisphere (Benson et al., 1997).

The Early Holocene (~11,700 to 5,000 cal BP) climate of the region appears to have been relatively warm and wet (Figure 3). The pollen record indicates a shift from a more seasonal forest during the Pleistocene Termination to an everwet, fire-precluding lowland forest which persists to the top of the record (Figure 3) (Hamilton et al., 2019b). The Late Holocene (interpreted here as the period after ~5,000 BP) is characterised by a more stable climate and local catchment, with an increase in primary productivity, as indicated by the lowest C:N ratios (μ = 14, 1σ = 2.17) in the core (Figure 3 and Table 2). A slight increase in secondary/seasonal taxa (e.g., Casuarinaceae) in the pollen records after 5,000 cal BP suggests either a slight increase in aridity or heightened human activity in the catchment (Hamilton et al., 2019b).

3.3 Mercury concentration and accumulation rates

Mercury concentrations and HgAR varied along the core from 29 to 2,558 ng g^{-1} (1σ = 201.09) and 1.67–158 μg m^{-2} yr^{-1} (1σ = 13.30), respectively. For a better visualisation of the data and clearer recognition of patterns and trends for the full core, the two largest HgAR peaks (158 and 68 μg m^{-2} yr^{-1} at ~ 8,015 and ~8,722 cal BP, respectively) were plotted out of scale in Figure 3, Figure 4 and Figure 7. No XRF data is available for the top section of the core (0–100 cm) as its unconsolidated nature required this section to be sliced in the field. The contribution of catchment input in Hg concentration and accumulation rates in Lake Lantoa can be tracked through C:N ratios, which varied between 11.70 and 31.40 (1σ = 5.24) (Figure 4 and Table 2).

3.3.1 Pleistocene Termination (~16,488 to 14,000 cal BP; 594–439 cm)

The abundance of open environment pollen taxa (Poaceae and Cyperceae), limited moisture-demanding tropical taxa (Myrtaceae and *Phyllocladus*) and high charcoal counts (Figure 3) indicate that this period was characterised by a drier, more seasonal environment with relatively more forest fires (Hamilton et al., 2019b). Our results agree with global (Power et al., 2008) and regional charcoal records (Figure 3) which suggest that fire increased in the tropics during the Pleistocene Termination. This is supported by the XRF data (Figure 4) which indicate that the Lake Lantoa catchment received relatively less precipitation during the Pleistocene Termination (Hamilton et al., 2019b). These data in conjunction with the coeval increase in CHAR and HgAR demonstrate that forest fires were the main drivers of high HgAR in Lake Lantoa during the Pleistocene Termination.

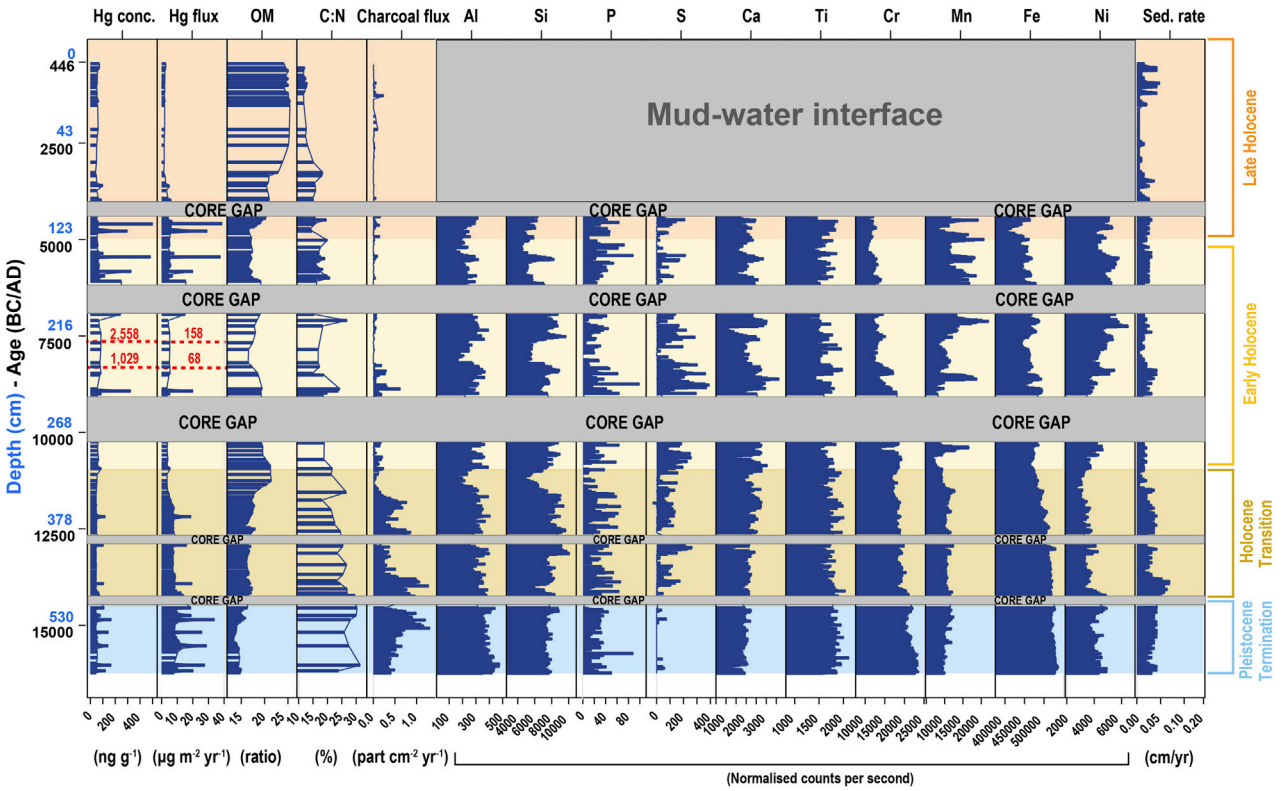

FIGURE 4
Mercury (Hg) concentrations (ng g^{-1}), mercury accumulation rate (µg m^{-2} yr^{-1}), organic matter (OM, %), charcoal flux (particle cm^{-2} yr^{-1}) and XRF data (counts per second) for Lake Lantoa (LL2) sediment core for the last 16,488 years. The two highest peaks in Hg and HgAR (at 8,015 and 8,722 cal BP) were removed to allow better visualisation of Hg concentration and accumulation rate along the core. They are represented as red dashed lines with their values and are plotted off scale.

In the Lake Lantoa record, more open, seasonal forests with grass in the understorey co-occur with higher variability in HgAR (Figure 3). This vegetation type, which burns and potentially exposes soils, may facilitate soil erosion (decreased catchment stability). Catchment stability directly impacts the type of OM (i.e., allochthonous vs. autochthonous) that is deposited into the lake, with an increase in allochthonous OM indicating an increase in catchment input to lake sediments. During the Pleistocene Termination, the C:N ratio values (μ = 27, 1σ = 2.46) indicate that Lake Lantoa received the most catchment-derived OM for the entire record (Figure 3 and Table 2). Furthermore, the sedimentation rate is the highest during the Pleistocene Termination (Figure 2), suggesting that this was a period characterised by an unstable catchment. Together these data indicate that the vegetation type in the Lake Lantoa catchment mediates the role of catchment soils as long-term Hg sinks.

The increased catchment input to Lake Lantoa sediments, as inferred from C:N ratios, OM and sedimentation rates, suggests that the Hg record is a mixture of atmospheric Hg directly deposited into the lake and secondary deposition of Hg from the catchment soils. Low manganese (Mn) and nickel (Ni) counts (Figure 4) indicate that overall there was little catchment erosion (i.e., few high precipitation/flood events) during the Pleistocene Termination (Hamilton et al., 2019b), likely due to the dry climate limiting precipitation in the Lake Lantoa catchment. The pollen, CHAR, XRF and C:N ratio data indicate that during the Pleistocene Termination the majority of the Hg in the Lake Lantoa sediments was derived from the catchment and deposited via dry or aeolian deposition. The relationship between CHAR and HgAR in the Pleistocene Termination appears to mediate aeolian deposition of Hg, with high intensity fire events associated with an increase in HgAR and C:N ratios (Figure 3). The contribution of volcanic emissions to this period is unlikely given the low sulphur (S) counts for this period (Figure 4). Therefore, dry or aeolian deposition and forest fires are the primary drivers of HgAR in Lake Lantoa sediments during the Pleistocene Termination.

3.3.2 Transition to the Holocene (~14,000 to 11,700 cal BP; 439–310 cm)

For the period between 14,000 and 11,700 cal BP, the pollen data suggest an increase in humidity, with a vegetation shift to a closed, ultramafic, lowland rainforest (Hamilton et al., 2019b) (Figure 3). While the pollen data potentially indicate an abrupt shift at ~14,000 cal BP, this is not picked up by geochemical interpretations of lake level fluctuations (Hamilton et al., 2019b) or other records from the Southern Hemisphere tropics (Colinvaux et al., 1996; Anhuf et al., 2006; Chabangborn et al., 2014; Russell et al., 2014; Partin et al., 2015; Renssen et al., 2018; Turu et al., 2021).

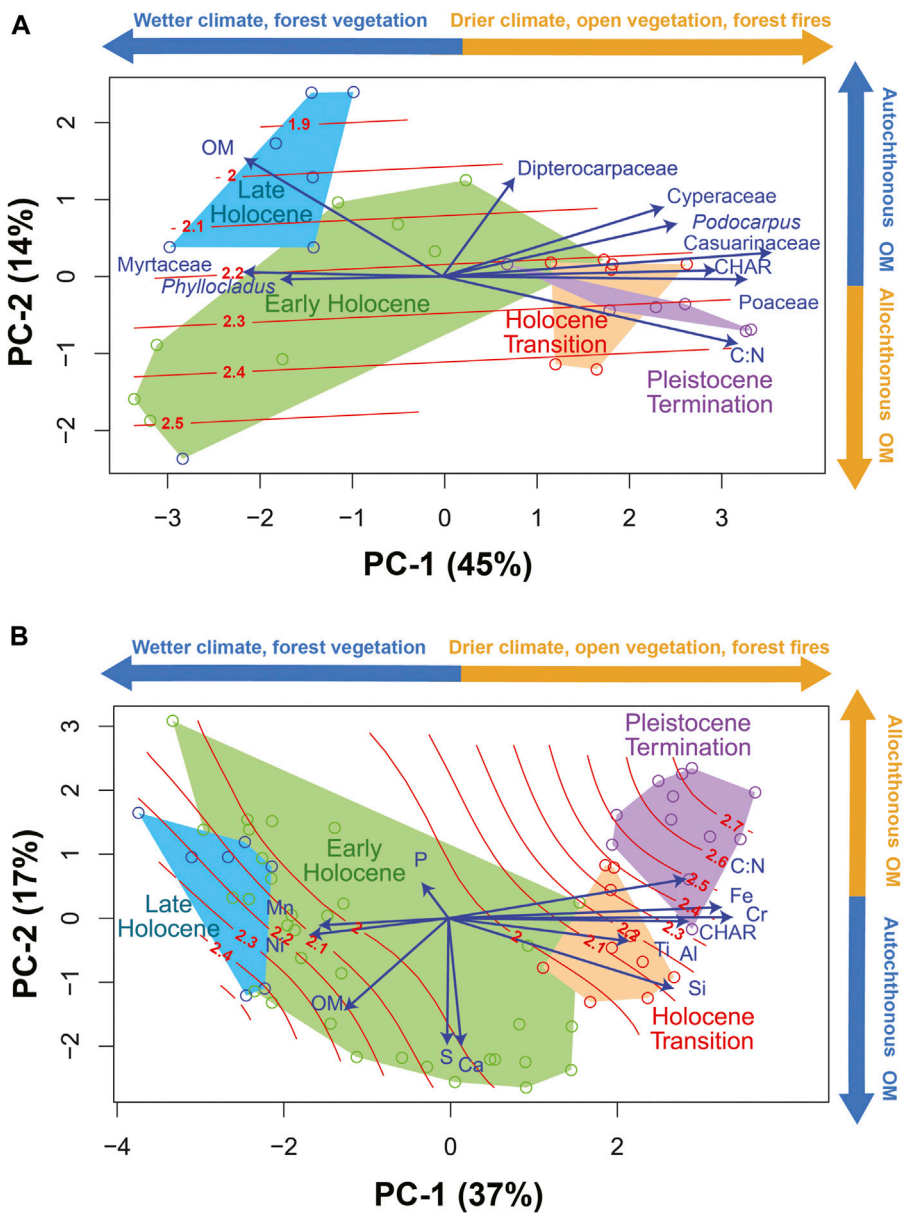

FIGURE 5
Principal Components Analysis of **(A)** charcoal flux, organic matter, C:N ratios and pollen and **(B)** charcoal flux, organic matter, C:N ratios and geochemistry from sediment samples of Lake Lantoa. A fitted surface (red) of mercury flux (μg m^{-2} yr^{-1}) is plotted passively within the ordination space using a thin-plate spline, indicating mercury's relationship to ordination scores.

The relatively high C:N ratios (μ = 23, 1σ = 2.28) indicate that there was still a significant amount of catchment-derived OM in the sediments. There is an increase in sulphur (S) counts from the Pleistocene Termination to the Holocene Transition, however manganese (Mn) and nickel (Ni) counts appear to remain similar between these two periods, suggesting that catchment input to the lake sediments was also similar (Hamilton et al., 2019b) (Figure 4). Therefore, the XRF counts indicate that the slight decrease in C:N ratios in the Holocene Transition was driven by an increase in primary productivity within the lake, rather than an increase in catchment input (Hamilton et al., 2019b).

The range in Hg concentrations and HgAR for the Holocene Transition decreased compared to the Pleistocene Termination (7.54 μg m^{-2} yr^{-1}, 1σ = 6.02 vs. 11.32 μg m^{-2} yr^{-1}, 1σ = 2.53, respectively, Table 2), a trend coeval with a decrease in CHAR compared to the Pleistocene Termination (0.34 m^{-2} yr^{-1}, 1σ = 0.25 vs. 0.59 m^{-2} yr^{-1}, 1σ = 0.21, respectively, Table 2). This trend in the Hg and CHAR records was likely driven by the progressive onset of increasingly humid conditions around the site during this period (Figure 4), reinforcing interpretations made from the pollen record (Hamilton et al., 2019b).

3.3.3 The Early Holocene (~11,700 to 5,000 cal BP; 321–110 cm)

The average HgAR in Lake Lantoa in the Early Holocene increased compared to the Holocene Transition (11.35 μg m^{-2} yr^{-1} vs. 7.54 μg m^{-2} yr^{-1}, respectively) and is marked by greater variability. The Early

Holocene has the highest average HgAR for the whole core, however this average is largely driven by isolated HgAR peaks within this period, with the highest peaks occurring at 8,015 cal BP (2,558 μg m^{-2} yr^{-1}) and 8,722 cal BP (1,029 μg m^{-2} yr^{-1}). When outliers are removed, the average HgAR is 6.30 μg m^{-2} yr^{-1}, similar to the Holocene Transition (7.54 μg m^{-2} yr^{-1}).

Our multiproxy data suggest two probable explanations for this increase in HgAR: 1) as this period is characterised by increasingly humid conditions in the Lake Lantoa catchment, flood pulses could have contributed to increasing Hg through in-wash of organic material from the catchment into the lake, including litterfall; and 2) as the Early Holocene is a period of intense volcanic activity in Southeast Asia (Ninkovich, 1979; Ku et al., 2009), volcanic emissions could also be a major contributor of Hg into the lake (either directly or via litterfall uptake and in-wash to the lake) (Figure 4).

The increases in S, Mn and Ni counts (Figure 4) are interpreted as an increase in catchment input to the sediments (Hamilton et al., 2019b). The decrease in C:N ratios (μ = 18, 1σ = 2.71) indicates that there was relatively more autochthonous OM in the sediments than in the Holocene Transition (μ = 23, 1σ = 2.58) or Pleistocene Termination (μ = 27, 1σ = 2.46 Table 2). These proxies (XRF counts, OM% and C:N ratio) demonstrate that there was an increase in catchment input to the lake sediments and lake primary productivity (Figure 4). This is reinforced by the pollen record, which illustrates that montane forest was expanding at this time (Figure 3) and represents the continuation of increasing humidity around the site (Hamilton et al., 2019b). We propose that the trends in the XRF counts and C:N ratios were driven by an increase in primary productivity within the lake, itself driven by increasing temperatures.

The environmental reconstruction for the Lake Lantoa catchment during the Early Holocene demonstrates a nuanced relationship between the proxies used in this study (Figure 5). The PCA results (Figure 5B) indicate that the catchment was less stable during the Early Holocene compared to the Holocene Transition. Indicators of catchment runoff and erosion in the Lake Lantoa sediments (S, Mn and Ni) are positively correlated with warmer and wetter conditions (Figure 5B), demonstrating that these conditions facilitate catchment input to the lake (Hamilton et al., 2019b). This relationship appears to be mediated by montane forest cover (Figure 3, Figure 5A).

3.3.4 The Late Holocene (~5,000–538 cal BP; 110–0 cm)

A marked difference in Hg concentrations and accumulation rates between the Early and Late Holocene can be seen in Lake Lantoa (Table 2, Figure 4). Average HgAR decreased during the Late Holocene compared to the Early Holocene (4 μg m^{-2} yr^{-1}, 1σ = 6.63 vs. 11 μg m^{-2} yr^{-1}, 1σ = 23.01, respectively), demonstrating the lowest average HgAR recorded in the entire core. This decrease is likely linked to an environmental shift at Lake Lantoa from wet climate conditions with an unstable catchment in the Early Holocene to wet conditions with a more stable catchment in the Late Holocene (Figure 3). This marked climate shift, dated at around 5,000 cal BP in Lake Lantoa, has been recorded globally in paleoclimate records from other parts of the world (Hermanns and Biester, 2013).

Organic matter (OM) increases distinctly in this period from the Early Holocene (μ = 23, 1σ = 2.32 vs. μ = 18, 1σ = 1.36, respectively), accompanied by a significant decrease in C:N ratios (μ = 14, 1σ = 2.17 vs. μ = 18, 1σ = 2.71, respectively), suggesting that the increase in OM during the Late Holocene was driven by a significant increase in primary productivity within the lake, rather than an increase in catchment input (Figure 4 and Table 2). The pollen record demonstrates a simultaneous increase in tropical forest cover during the Late Holocene (Figure 3), which appears to have promoted a more stable catchment (Hamilton et al., 2019b)).

The Late Holocene is characterised by established montane and lowland forests, suggesting that this period had the warmest and most humid conditions in the past 16,488 years. The significantly low C:N ratios for this period (Table 2), however, demonstrate that this period also received the lowest contribution of catchment input for the core. Therefore, while warmer and wetter conditions promote catchment runoff and erosion, vegetation establishment appears to mediate this relationship.

The significant increase in OM is concomitant with decreases in C:N ratios and HgAR during the Late Holocene. This decrease in HgAR and C:N (meaning more OM of autochthonous origin) suggest that the lake received less Hg input from the catchment, likely a result of a more established lowland forest. A decrease in HgAR means that the amount of Hg in the lake decreased (e.g., smaller Hg flux from the catchment), independent of Hg concentrations in the sediment. A more established forest (demonstrated by pollen data, Figure 5) means more stable soil, hindering Hg transfer from soil to the water phase. Alternatively, this decrease in HgAR could be a result of in-lake processes promoting Hg^{2+} reduction to Hg^0 and consequent Hg evasion, resulting in a decrease in the net Hg load to the lake. The link between primary productivity and HgAR in tropical lake sediments is poorly studied. More studies are needed to better understand the important relationship between lake-catchment dynamics, lake primary productivity and Hg deposition in freshwater lakes.

3.4 Main drivers of HgAR in Lake Lantoa sediments

The variability of HgAR in Lake Lantoa sediments appears to be heavily mediated by catchment dynamics such as vegetation cover and type, fire activities, and changes in precipitation. Previous studies have demonstrated the important role of vegetation and litterfall contributing to Hg concentrations in soils, a relationship mediated by vegetation type (Fostier et al., 2015; Zhang et al., 2016; Zheng et al., 2016; Zhang et al., 2019). Plant species, leaf age and leaf placement are biological factors that significantly influence Hg uptake by foliage (Laacouri et al., 2013; Zhu et al., 2016) and can be reflected in HgAR in lake sediments with densely vegetated catchments. While we recognise that changes in vegetation can influence HgAR in the lake, a this signal is indistinguishable from other signals and will not be discussed in this manuscript.

For a better spatial and temporal assessment of Hg patterns in our multi-proxy dataset, we plotted two principal component analyses (Figures 5A,B): the first is based on pollen data, and the second on geochemical data. Both graphs show the relationship between the ordination result and HgAR as an environmental variable. For the pollen PCA (Figure 5A), the samples from the Pleistocene Termination are positively loaded on axis 1 with open vegetation pollen taxa and charcoal, reinforcing that the dry climate and fire activity of the Pleistocene Termination were key drivers of HgAR. Mercury

TABLE 3 Comparison of the timing of peaks in mercury accumulation in Lake Lantoa sediments with the timing of volcanic eruptions reported for Southeast Asia (as reported in De Maisonneuve and Bergal-Kuvikas, 2020).

Mercury peak date (cal BP)	Potential source eruption (cal BP)	Volcano of origin	Reference
9,450 (10,056–9,434)	9,410 ± 150	Mount Pinatubo	Newhall et al. (1996)
8,722 (8,453–9,143)	Unknown	Banda Api and Banda Awu?	Global volcanism program, Smitsonian Institution, 2022
8,015 (7,611–8,304)	Unknown	Banda Api or Banda Awu?	Global volcanism program, Smitsonian Institution, 2022
6,254 (5,830–6,712)	6,875 ± 859	Taal Caldera	Martinez and Williams (1999)
5,708 (5,457–6,024)	5,500 ± 500	Mount Pinatubo	Newhall et al. (1996)
5,203 (4,887–5,453)	5,260 ± 780	Tengger caldera	Global volcanism program, Smitsonian Institution, 2022
5,107 (4,785–5,384)	5,479 ± 140	V5d eruption from unknown volcano	Salisbery et al. (2012)
4,769 (4,441–5,096)	4,860 ± 60	V5 eruption from unknown volcano	Salisbery et al. (2012)

sediment accumulation rates, passively plotted, have high concentrations during the Pleistocene Termination and Late Holocene, indicating the importance of fire and catchment runoff as drivers of HgAR in Lake Lantoa.

For the geochemistry PCA, Mn, Ni, S are negatively loaded on axis 1 (Figure 5B). These loadings are positioned in the Early Holocene area, at the time of several isolated HgAR peaks (likely of volcanic origin) and catchment runoff. Charcoal accumulation rates are loaded positively on axis 1, indicating a disconnect between fires and HgAR for the entire Holocene. This reinforces the interpretation that fires were unlikely to be primary contributors to Holocene HgAR in Lake Lantoa.

3.5 Possible volcanic contributions to mercury deposition in Lake Lantoa

The isolated peaks in Hg concentrations and accumulation rates in Lake Lantoa during the Early Holocene do not appear to be driven by lake-catchment processes. These peaks are associated with low fire activities, indicating that forest fires were not a major contributor to these peaks (Figure 3). This is supported by the pollen record which demonstrates that the Lake Lantoa catchment experienced warm and wet climate conditions during the Early Holocene (Figure 3) (Hamilton et al., 2019b). Furthermore, there are no significant abrupt perturbations in any of the other proxy records for Lake Lantoa (Figure 3; Figure 4) which suggest that these peaks in the Hg record are being driven by external catchment processes. We propose that a process that would result in an unsustained drastic increase in Hg deposition in the Lake Lantoa sediments, with minor impact on proxies of lake-catchment dynamics, is volcanism. That is not to say that is the only possible external process that could result in a significant abrupt increase in HgAR, however, given the high volcanic activity of the SEA region it appears to be the most reasonable explanation. Further exploration of this theory is outside the scope of this paper, however we do present a series of hypotheses that can be used to assess the validity of this theory.

A valid explanation for four statistically significant peaks in the Hg record (43 μg m^{-2} yr^{-1} at 5,203 cal BP, 37 μg m^{-2} yr^{-1} at 5,708 cal BP, 158 μg m^{-2} yr^{-1} at 8,015 cal BP, and 68 μg m^{-2} yr^{-1} at 1,029 cal BP) should be able to address why these peaks are two standard deviations above the average HgAR for the entire core (μ = 9, 1σ = 13.30). Figures 3 and 4 demonstrate that there are no perturbations in the multiproxy record proportional to the Hg peaks, further supporting the theory that these peaks are driven by processes that other proxies are not sensitive enough to capture.

Volcanic degassing and eruptions primarily emit mercury in its elemental form, Hg(0) (Ansmann et al., 1997; Slemr and Scheel, 1998; Polvani et al., 2019). In this form, Hg can be transported long distances from the original emission source (Ci et al., 2011). The following discussion explores the feasibility of regional volcanism contributing to the Lake Lantoa Hg record.

To facilitate future investigations aimed at identifying sources of volcanic Hg in the region, Table 3 presents known volcanic eruptions in SEA (as reported by De Maisonneuve and Bergal Kuvikas, 2020) coincident with eight distinct peaks in the Hg record. More data is needed to confirm the drivers of these isolated extrusions in the Hg record (Table 3), which may be outside of the SEA region.

Several volcanoes in Southeast Asia could have contributed to higher HgAR in Lake Lantoa sediments during the Early Holocene (Figure 6). As atmospheric pressure gradients are weak in the tropics (Phadke et al., 2003), the wind is variable and can transport Hg emitted by volcanoes in several directions (Figure 6). Known eruptions for the early Holocene period for Southeast Asia are presented in Figure 7 together with geochemical proxies for the LL2 core. The trend in elements seen from the XRF counts indicate strong variability during the Early Holocene, supported by high S counts. The above hypothesis could be supplemented by a secondary study investigating instrumental differences in tracking volcanic emissions, and focusing on elements of volcanic origin such as sulphur.

The validity of our hypothesis that isolated peaks in the Lake Lantoa Hg record during the Early Holocene were driven by volcanism could be investigated by comparing the geochemical fingerprint of the eruption and the geochemical fingerprint of the sediments associated with the Hg peaks in question. Studies could

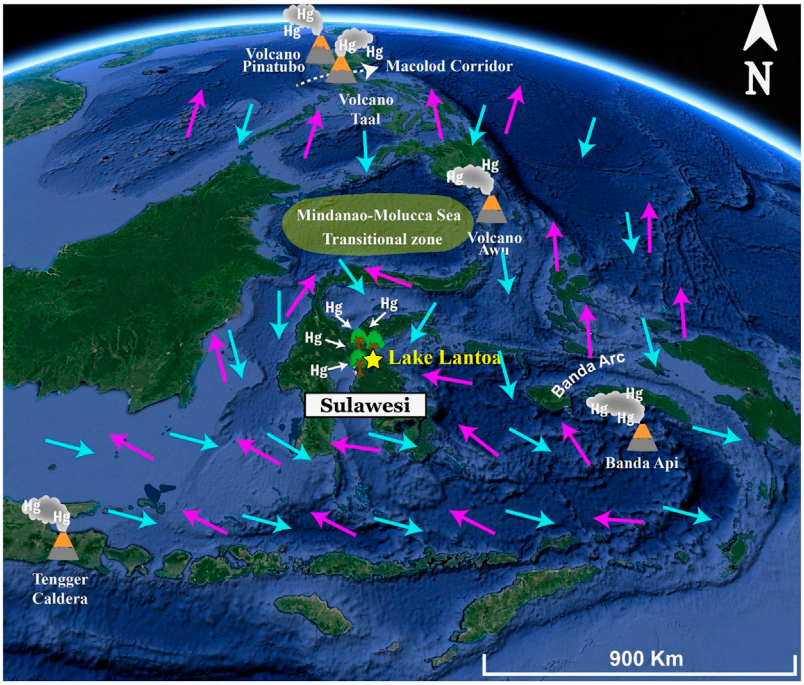

FIGURE 6
Location of Southeast Asia volcanoes with potential mercury (Hg) emission and transport to Lake Lantoa (yellow star) in the early Holocene. Trees represent dry Hg deposition throught litterfall. Cyan arrows indicate the direction of monsoon winds toward east-southeast during wet season (mean wind direction January 1946–1989). Pink arrows indicate the direction of monsoon winds toward north-northwest during dry season (mean wind direction August 1946–1989). Wind data adapted from Klicpera and Westphal. (2017) and originally derived from COADS Monthly Climatology dataset (Woodruff et al., 1998).

also use different methods of characterising soil geochemistry (e.g., Inductively Coupled Plasma Mass Spectrometry vs. Laser Ablation Inductively Coupled Plasma Mass Spectrometry vs. XRF) to assess if one method is more sensitive to regional (vs. local) events.

Such studies would benefit from a modelling study to demonstrate the transportation and subsequent fallout and deposition of volcanic emissions, mediated by changes in trade winds. They would also clarify the plausibility of regional volcanism impacting the Hg record in Lake Lantoa without affecting the XRF or pollen records. These studies might also indicate which elements/molecules/compounds are best suited to tracking the range of volcanic emissions from a given eruption.

It is important to note that no reported eruptions in SEA for this period were found in the literature for the two highest peaks in HgAR for the entire LL2 core (at ~ 8,015 cal BP and ~8,722 cal BP). These peaks in HgAR (158 μg m^{-2} yr^{-1} and 68 μg m^{-2} yr^{-1} respectively) are ~13 and 6 times higher than the average HgAR (11.35 μg m^{-2} yr^{-1}) for the Early Holocene (Table 2). The suggestions mentioned above may be able to clarify which, if any, volcanoes could have contributed to these Hg peaks. Two Hg peaks are coeval with eruptions of Mount Pinatubo in the Philippines (Table 3, Figure 7): the eruptions of 9,410 ± 150 and 5,500 ± 500 cal BP (Newhall et al., 1996). We use the dominant direction of ash cloud distribution to infer the direction of volcanic gas transportation, including Hg(0), for the 9,410 ± 150 cal BP eruption. The ash cloud associated with this eruption is distributed southwest of the Philippines (De Maisonneuve and Bergal-Kuvikas, 2020), implying that Hg emissions from volcanoes in the Philippines could have been transported to Indonesia.

The Hg peak at ~ 4,769 cal BP potentially corresponds to the 4,860 ± 60 cal BP V5 eruption, which is recorded in a marine core close to Sumatra (Salisbury et al., 2012). The authors report one significant ash layer (V5) dating to 4,860 ± 60 BP and another ash layer (V5d) dating to 5,479 ± 140 BP was identified in another core (Salisbery et al., 2012).

The potential contribution of volcanic events listed in Figure 7 to the Lake Lantoa Hg record could be investigated via fingerprinting the chemical signature of these eruptions. Modelling studies examining the transportation and subsequent fallout and deposition of volcanic emissions, mediated by changes in trade winds, would also clarify the plausibility of regional volcanism impacting the Hg record in Lake Lantoa without affecting the XRF or pollen records.

Fingerprinting a potential eruption for these Hg peaks is difficult considering the limited number of studies on pre-historic eruptions or tephra layers documented in Indonesia (De Maisonneuve and Bergal-Kuvikas, 2020). The Hg peaks could be either a result of secondary catchment processes and reworked material being transported to the lake, or a case of unknown volcanic sources. The Banda Api and Banda Awu calderas, both in the Sunda-Banda arc, are believed to have erupted during this period. These two calderas are near Lake Lantoa (Figure 6) and of a significant size: Banda Api caldera is 7 km wide and Banda Awu 4.5 km wide (Smithsonian Institution, 2020). Unfortunately, there is no information on the dates of their caldera-forming eruptions or spatial distributions of pyroclastic deposits. Despite the abundance of

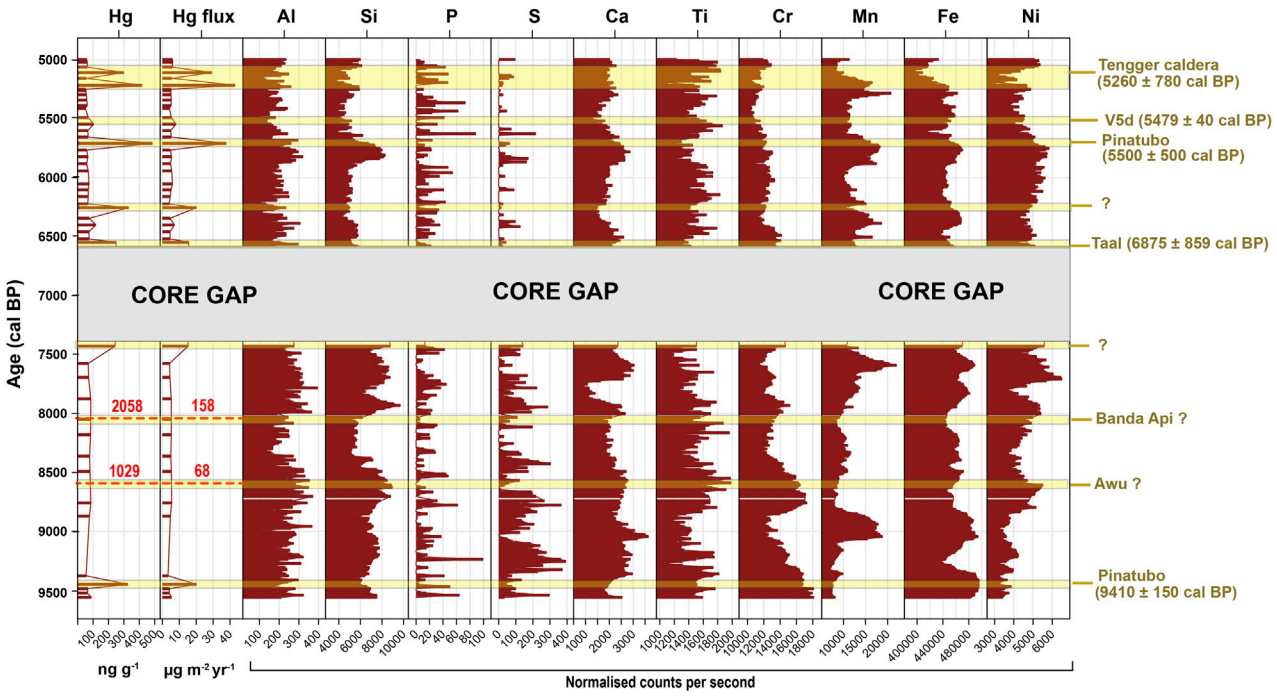

FIGURE 7
Geochemical profile for the early-mid Holocene at Lake Lantoa, showing mercury profile and known volcanic eruptions that could potentially have contributed to mercury inputs. Mercury peaks are highlighted in yellow, and known volcanic eruptions are indicated on the right of the figure. The two highest peaks in Hg and HgAR (at 8,015 and 8,722 cal BP) were removed for clearer plotting of these proxies. They are represented as red dashed lines with their values and are plotted off scale.

volcanoes recorded Southeast Asia (147 alone in Indonesia, according to Hariyono and Liliasari, 2018), Banda Api and Banda Awu are the most promising candidates due to their location and wind direction, and further studies should investigate these two volcanoes as significant potential Hg sources for Sulawesi.

Two other Hg peaks (at ~7,429 and 6,254 cal BP) also do not correspond to any known volcanic eruptions. This highlights the gap in our understanding of the role secondary catchment processes have on HgAR in tropical lakes. For instance, soil acidification from volcanic aerosols can cause significant leaching of nutrients after volcanic eruptions (Yagasaki et al., 2006; Guédron et al., 2019). This is particularly a problem in the Lake Lantoa catchment, where ultramafic soils are reported to be already nutrient poor (Van der Ent et al., 2013). Extreme nutrient limitation and increase in sulphur input can trigger a breakdown in forest vegetation, with trees losing foliage and widespread soil erosion (Guédron et al., 2019). This may have been the case in Lake Lantoa at the time of major Hg input pulses to the lake. The sulphur counts for LL2 appear to support this hypothesis, with the highest counts at recorded during the Early Holocene relative to the rest of the core (Figure 4).

The acidification of Indonesian soils as a result of volcanic activities has been reported for the island of Sumatra (Setyaningsih et al., 2018). In this case, volcanic activities reduced vegetation diversity with volcanophile taxa (e.g., Casuarinaceae and Myrtaceae) thriving and other rainforest taxa only outcompeting the volcanophile taxa several centuries after volcanic deposition ceased (Setyaningsih et al., 2018). This pattern results from the volcanic aerosols depleting the soils of nitrogen, with Casuarinaceae and Myrtaceae better adapted to these soils than rainforest taxa (Setyaningsih et al., 2018). It should also be noted that rainforest taxa may take longer to recover after volcanic deposition and deforestation, relative to volcanophile taxa, due to the change in the amount of sunlight reaching the ground, as many require semi-shaded areas to germinate or establish.

The impact of soil acidification from volcanic activities may be compounded if the area is dominated by taxa that do not thrive in nitrogen-depleted soils, like *Podocarpus* (Li et al., 2021). These conditions promote litterfall and organic decomposition of these taxa, facilitated by the warm temperatures and humid climate of the tropics, which has direct implications for Hg sequestered in catchment soils that can be transported into the lake through catchment runoff (Guédron et al., 2019). The effects of ash cover on vegetation, germination and establishment must also be considered, however, a comprehensive analysis of the relationship between volcanic activity and lake-catchment dynamics is outside the scope of this paper.

4 Conclusions and future directions

This study presents the first long-term record of HgAR in a tropical lake in Southeast Asia (SEA). It is also one of the few studies globally to combine Hg records with a comprehensive set of ecological and geochemical data (i.e., pollen, charcoal, multi-element geochemistry, and C:N ratio). The results describe a dynamic relationship between HgAR, lake-catchment conditions,

forest fires and regional volcanism. These relationships are mediated by climate conditions which can promote or inhibit the accumulation of Hg in lake sediments.

Our results indicate that the highest HgAR in Lake Lantoa are associated with high seasonality (i.e., the catchment experiences both fire and high precipitation events annually), wet climates (i.e., flood pulse events) and an unstable catchment area. Established forest taxa have the greatest capacity to uptake and sequester atmospheric Hg, reducing the amount of Hg deposited on surface soils that can be re-deposited into the lake via precipitation or flood events. Therefore, non-seasonal climates with established forests are likely to act as long-term Hg sinks, reducing Hg accumulation in lake sediments. These results suggest that areas with non-seasonal wet climates in established forests serve as long-term Hg sinks. Therefore, shifts in climate to drier and more variable conditions in these areas have the potential to trigger a dramatic increase in Hg accumulation into aquatic systems and the atmosphere.

Additionally, the Lake Lantoa record reinforces studies demonstrating that algae production can bio-dilute Hg accumulation in lake sediments (e.g., Outridge et al., 2019). The C:N ratios dramatically decrease while OM% dramatically increases during the Late Holocene, indicating a significant rise in autochthonous OM in lake sediments, which is attributed to an increase in primary productivity (Figure 3). This shift in primary productivity proxies is associated with the lowest HgAR for the entire core (Table 2). This suggests that a more stable catchment hindering Hg inputs to the lake, or inlake processes resulting in Hg evasion.

Volcanism appears to be an important source of Hg to Lake Lantoa, via both direct (atmospheric) and secondary (terrestrial) HgAR. More datasets from the SEA region would elucidate the response of HgAR to the interplay between volcanism and ecological processes. More studies fingerprinting eruption signals in SEA sediments are needed to further examine this relationship.

Data availability statement

The original contributions presented in the study are included in the article/Supplementary Material, further inquiries can be directed to the corresponding author.

Author contributions

JN–analysis, acquisition and interpretation of the mercury record and comparison with new and published geochemical and palynological records. LS–drafting and critical revision of the manuscript and interpretation of the mercury record, and comparison of southern hemisphere mercury records. RH–acquisition, analysis and interpretation of the palynological (pollen and charcoal) and XRF-scanning records, approval for publication of the content. SC–drafting and critical revision of the manuscript, assisted with selection of pollen data relevant to understanding the mercury record. HB - drafting and critical revision of the manuscript and interpretation of the mercury record. HS-W–acquisition, analysis and interpretation of the Carbon:Nitrogen ratio data. OB-K–interpretation of the mercury and XRF record, particularly with reference to possible volcanic sources of mercury peaks in the Holocene. GJ–acquisition, analysis and interpretation of the age-depth model. JS–acquisition of the LL2 sediment core, analysis and interpretation of the palynological record, approval for publication of the content. All authors contributed to the article and approved the submitted version.

Funding

This project has been funded by the Australian Research Council Discovery Early Career Researcher Award (DE180100573) granted to LS. The original recovery of the Lake Lantoa material was carried out under RISTEK permit number 267 and Australian Research Council Funding (DP110101357) to JS. AMS radiocarbon dates at ANSTO were funded by ANSTO Research grant AP12188 to RH.

Acknowledgments

We acknowledge the financial support from the Australian Government for the Centre for Accelerator Science at ANSTO through the National Collaborative Research Infrastructure Strategy (NCRIS). Thanks are given to the office of Bupati Luwu Timur as well as Camat Nuha and Camat Towuti and to the Mahalona community for their consent, hospitality and logistical support.

Conflict of interest

Author HB was employed by AG Umweltgeochemie.

The remaining authors declare that the research was conducted in the absence of any commercial or financial relationships that could be construed as a potential conflict of interest.

Publisher's note

Supplementary material

The Supplementary Material for this article can be found online at: https://www.frontiersin.org/articles/10.3389/fenvc.2023.1241176/full#supplementary-material

References

Amirbahman, A., Ruck, P. L., Fernandez, I. J., Haines, T. A., and Kahl, J. S. (2004). The effect of fire on mercury cycling in the soils of forested watersheds: acadia National Park, Maine, U.S.A. *Water, Air, Soil Pollut.* 152 (1-4), 315–331. doi:10.1023/b:wate.0000015369.02804.15

Anhuf, D., Ledru, M. P., Behling, H., Da Cruz, F., Cordeiro, R., Van der Hammen, T., et al. (2006). Paleo-environmental change in Amazonian and African rainforest during the LGM. *Palaeogeogr. Palaeoclimatol. Palaeoecol.* 239, 510–527. doi:10.1016/j.palaeo.2006.01.017

Ansmann, A., Mattis, I., Wandinger, U., Wagner, F., Reichardt, J., and Deshler, T. (1997). Evolution of the Pinatubo aerosol: raman lidar observations of particle optical depth, effective radius, mass, and surface area over central Europe at 53.4°N. *J. Atmos. Sci.* 54 (22), 2630–2641. doi:10.1175/1520-0469(1997)054<2630:EOTPAR>2.0.CO;2

Benson, L., Burdett, J., Lund, S., Kashgarian, M., and Mensing, S. (1997). Nearly synchronous climate change in the Northern Hemisphere during the last glacial termination. *Nature* 388, 263–265. doi:10.1038/40838

Blaauw, M., and Christen, J. A. (2011). Flexible paleoclimate age-depth models using an autoregressive gamma process. *Bayesian Anal.* 6, 457–474. doi:10.1214/11-ba618

Caffrey, M. A., and Horn, S. P. (2013). The use of lithium heteropolytungstate in the heavy liquid separation of samples which are sparse in pollen. *Palynology* 37 (1), 143–150. doi:10.1080/01916122.2012.736417

Chabangborn, A., Brandefelt, J., and Wohlfarth, B. (2014). Asian monsoon climate during the Last Glacial Maximum: palaeo-data-model comparisons. *Boreas* 43 (1), 220–242. doi:10.1111/bor.12032

Ci, Z., Zhang, X., Wang, Z., and Niu, Z. (2011). Atmospheric gaseous elemental mercury (GEM) over a coastal/rural site downwind of East China: temporal variation and long-range transport. *Atmos. Environ.* 45 (15), 2480–2487. doi:10.1016/j.atmosenv.2011.02.043

Colinvaux, P. A., De Oliveira, P. E., Moreno, J. E., Miller, M. C., and Bush, M. B. (1996). A long pollen record from lowland Amazonia: forest and cooling in glacial times. *Science* 274 (5284), 85–88. doi:10.1126/science.274.5284.85

Core Team (2013). *R: a language and environment for statistical computing*. Vienna: R: A language and environment for statistical computing.

Costa, K. M., Russell, J., Vogel, H., and Bijaksana, S. (2015). Hydrological connectivity and mixing of Lake Towuti, Indonesia in response to paleoclimatic changes over the last 60,000 years. *Palaeogeogr. Palaeoclimatol. Palaeoecol.* 417, 467–475. doi:10.1016/j.palaeo.2014.10.009

Daga, R., Ribeiro Guevara, S., Pavlin, M., Rizzo, A., Lojen, S., Vreča, P., et al. (2016). Historical records of mercury in southern latitudes over 1600 years: lake Futalaufquen, Northern Patagonia. *Sci. Total Environ.* 553, 541–550. doi:10.1016/j.scitotenv.2016.02.114

Davies, S. J., Lamb, H. F., and Roberts, S. J. (2015). "Micro-XRF Core Scanning in Palaeolimnology: recent Developments," in *Micro-XRF studies of sediment cores: applications of a non-destructive tool for the environmntal sciences* (Netherlands: Springer), 189–226. doi:10.1007/978-94-017-9849-5_7

De Deckker, P. (2016). The Indo-Pacific Warm Pool: critical to world oceanography and world climate. *Geosci. Lett.* 3, 20. doi:10.1186/s40562-016-0054-3

De Maisonneuve, C. B., and Bergal-Kuvikas, O. (2020). Timing, magnitude and geochemistry of major Southeast Asian volcanic eruptions: identifying tephrochronologic markers. *J. Quat. Sci.* 35 (1–2), 272–287. doi:10.1002/jqs.3181

Demers, J. D., Blum, J. D., and Zak, D. R. (2013). Mercury isotopes in a forested ecosystem: implications for air-surface exchange dynamics and the global mercury cycle. *Glob. Biogeochem. Cycles* 27 (1), 222–238. doi:10.1002/gbc.20021

Devesa-Rey, R., and Barral, M. T. (2012). Allochthonous versus autochthonous naturally occurring organic matter in the Anllóns river bed sediments (Spain). *Environ. Earth Sci.* 66 (3), 773–782. doi:10.1007/s12665-011-1286-3

Engstrom, D. R., Balogh, S. J., and Swain, E. B. (2007). History of mercury inputs to Minnesota lakes: influences of watershed disturbance and localized atmospheric deposition. *Limnol. Oceanogr.* 52 (6), 2467–2483. doi:10.4319/lo.2007.52.6.2467

Enrico, M., Roux, G. L., Marusczak, N., Heimbürger, L. E., Claustres, A., Fu, X., et al. (2016). Atmospheric Mercury Transfer to Peat Bogs Dominated by Gaseous Elemental Mercury Dry Deposition. *Environ. Sci. Technol.* 50 (5), 2405–2412. doi:10.1021/acs.est.5b06058

Fadina, O. A., Venancio, I. M., Belem, A., Silveira, C. S., Bertagnolli, D. d. C., Silva-Filho, E. V., et al. (2019). Paleoclimatic controls on mercury deposition in northeast Brazil since the Last Interglacial. *Quat. Sci. Rev.* 221, 105869. doi:10.1016/j.quascirev.2019.105869

Fægri, K., and Iverson, J. (1989). *Textbook of pollen analysis*. 4th edn. Chester, UK: John Wiley & Sons, Ltd.

Fisher, J. A., and Nelson, P. F. (2020). Atmospheric mercury in Australia: recent findings and future research needs. *Elementa* 8, 1–20. doi:10.1525/elementa.2020.070

Fostier, A. H., Melendez-Perez, J. J., and Richter, L. (2015). Litter mercury deposition in the Amazonian rainforest. *Environ. Pollut.* 206, 605–610. doi:10.1016/j.envpol.2015.08.010

Guédron, S., Tolu, J., Brisset, E., Sabatier, P., Perrot, V., Bouchet, S., et al. (2019). Late Holocene volcanic and anthropogenic mercury deposition in the western Central Andes (Lake Chungará, Chile). *Sci. Total Environ.* 662, 903–914. doi:10.1016/j.scitotenv.2019.01.294

Hamilton, R., Hall, T., Stevenson, J., and Penny, D. (2019a). Distinguishing the pollen of Dipterocarpaceae from the seasonally dry and moist tropics of south-east Asia using light microscopy. *Rev. Palaeobot. Palynology* 263, 117–133. doi:10.1016/j.revpalbo.2019.01.012

Hamilton, R., Stevenson, J., Stevenson, J., and Bijaksana, S. (2019b). A 16,000-year record of climate, vegetation and fire from Wallacean lowland tropical forests. *Quat. Sci. Rev.* 224, 105929. doi:10.1016/j.quascirev.2019.105929

Hamilton, R., and Stevenson, J. (2020). The challenge of the enigmatic tricolporate tropical pollen type: A case study from Sulawesi, Indonesia. *Rev. Palaeobot. Palynology* 273, 104146–104221. doi:10.1016/j.revpalbo.2019.104146

Hariyono, E., and Liliasari, S. (2018). "The Characteristics of Volcanic Eruption in Indonesia," in *Volcanoes - geological and geophysical setting, theoretical aspects and numerical modeling, applications to industry and their impact on the human health* (London: IntechOpen). doi:10.5772/intechopen.71449

Hermanns, Y. M., and Biester, H. (2013). A 17,300-year record of mercury accumulation in a pristine lake in southern Chile. *J. Paleolimnol.* 49 (4), 547–561. doi:10.1007/s10933-012-9668-4

Hogg, A., Heaton, T. J., Hua, Q., Palmer, J. G., Turney, C. S., Southon, J., et al. (2020). SHCal20 Southern Hemisphere Calibration, 0–55,000 Years cal BP. *Radiocarbon* 62 (4), 759–778. doi:10.1017/RDC.2020.59

Hope, G. (2001). Environmental change in the late Pleistocene and later Holocene at wanda site, soroako, South Sulawesi, Indonesia. *Palaeogeogr. Palaeoclimatol. Palaeoecol.* 171 (3–4), 129–145. doi:10.1016/S0031-0182(01)00243-7

Huang, T.-C. (1972). *Pollen flora of taiwan*. Taiwan: National Taiwan University Botany Department Press.

Jiskra, M., Wiederhold, J. G., Skyllberg, U., Kronberg, R. M., Hajdas, I., and Kretzschmar, R. (2015). Mercury Deposition and Re-emission Pathways in Boreal Forest Soils Investigated with Hg Isotope Signatures. *Environ. Sci. Technol.* 49 (12), 7188–7196. doi:10.1021/acs.est.5b00742

Ku, Y. P., Chen, C. H., Song, S. R., Iizuka, Y., and Shen, J. J. S. (2009). A 2 Ma record of explosive volcanism in southwestern Luzon: implications for the timing of subducted slab steepening. *Geochem. Geophys. Geosystems* 10 (6), 2486. doi:10.1029/2009GC002486

Laacouri, A., Nater, E. A., and Kolka, R. K. (2013). Distribution and Uptake Dynamics of Mercury in Leaves of Common Deciduous Tree Species in Minnesota, U.S.A. *Environ. Sci. Technol.* 47 (18), 10462–10470. doi:10.1021/es401357z

Labrière, N., Locatelli, B., Laumonier, Y., Freycon, V., and Bernoux, M. (2015). Soil erosion in the humid tropics: A systematic quantitative review. *Agric. Ecosyst. Environ.* 203, 127–139. doi:10.1016/j.agee.2015.01.027

Lacerda, L. D., Ribeiro, M. G., and Sifeddine, A. (1999). Atmospheric mercury deposition over Brazil during the past 30,000 years. *Cienc. Cult.* 30, 000.

Lacerda, L. D., Turcq, B., Sifeddine, A., and Cordeiro, R. C. (2017). Mercury accumulation rates in Caço Lake, NE Brazil during the past 20.000 years. *J. S. Am. Earth Sci.* 77, 42–50. doi:10.1016/j.jsames.2017.04.008

Lal, R. (1990). *Soil erosion in the tropics: principles and management*. New York: McGraw-Hill.

Li, R., Han, J., Zhu, L., Zhao, L., Huang, X., Zhang, M., et al. (2021). Does nitrogen fertilization impact nonstructural carbohydrate storage in evergreen Podocarpus macrophyllus saplings? *J. For. Res.* 32 (4), 1653–1661. doi:10.1007/s11676-020-01181-z

Lindberg, S., Bullock, R., Ebinghaus, R., Engstrom, D., Feng, X., Fitzgerald, W., et al. (2007). A Synthesis of Progress and Uncertainties in Attributing the Sources of Mercury in Deposition. *Ambio* 36 (1), 19–33. doi:10.1579/0044-7447(2007)36[19:asopau]2.0.co;2

Lindberg, S. E., and Stratton, W. J. (1998). Atmospheric mercury speciation: concentrations and behavior of reactive gaseous mercury in ambient air. *Environ. Sci. Technol.* 32 (1), 49–57. doi:10.1021/es970546u

Lintern, A., Schneider, L., Beck, K., Mariani, M., Fletcher, M. S., Gell, P., et al. (2020). Background concentrations of mercury in Australian freshwater sediments: the effect of catchment characteristics on mercury deposition. *Elementa* 8 (1), 19. doi:10.1525/elementa.019

Martinez, M. M. L., and Williams, S. N. (1999). "Basaltic andesite to andesite scoria pyroclastic flow deposits from Taal caldera, Philippines." *Journal of Geological Society Philippines* 54 (1 & 2), 1–18.

Melack, J. M., and Forsberg, B. R. (2001). "Biogeochemistry of the Amazon Floodplain," in *The biogeochemistry of the amazon basin*. Editors M. E. McClain, R. Victoria, and J. E. Richey (New York: Oxford University Press), 235–274. doi:10.1093/oso/9780195114317.003.0017

Newhall, C., Dagg, A. S., and Delfin, F. G. (1996). "Eruptive History of Mount Pinatubo," in *Fire and mud. Eruptions and lahars of Mount Pinatubo, Philippines.*

Editor R. Punongbayan (Seattle: University of Washington Press and Philippine Institute of Volcanology and Seismology), 165–195.

Ninkovich, D. (1979). Distribution, age and chemical composition of tephra layers in deep-sea sediments off Western Indonesia. *J. Volcanol. Geotherm. Res.* 5, 67–86. doi:10.1016/0377-0273(79)90033-7

Obrist, D., Agnan, Y., Jiskra, M., Olson, C. L., Colegrove, D. P., Hueber, J., et al. (2017). Tundra uptake of atmospheric elemental mercury drives Arctic mercury pollution. *Nature* 547 (7662), 201–204. doi:10.1038/nature22997

Obrist, D., Kirk, J. L., Zhang, L., Sunderland, E. M., Jiskra, M., and Selin, N. E. (2018). A review of global environmental mercury processes in response to human and natural perturbations: changes of emissions, climate, and land use. *Ambio* 47 (2), 116–140. doi:10.1007/s13280-017-1004-9

Outridge, P. M., Sanei, H., Stern, H., and Goodarzi, F. (2007). Evidence for control of mercury accumulation rates in Canadian High Arctic lake sediments by variations of aquatic primary productivity. *Environ. Sci. Technol.* 41 (15), 5259–5265. doi:10.1021/es070408x

Outridge, P. M., Stern, G. A., Hamilton, P. B., and Sanei, H. (2019). Algal scavenging of mercury in preindustrial Arctic lakes. *Limnol. Oceanogr.* 64 (4), 1558–1571. doi:10.1002/lno.11135

Parkman, H., and Meili, M. (1992). Mercury in Macroinvertebrates from Swedish Forest Lakes: influence of Lake Type, Habitat, Life Cycle, and Food Quality. *Can. J. Fish. Aquat. Sci.* 50, 521–534. doi:10.1139/f93-061

Partin, J. W., Quinn, T., Shen, C. C., Okumura, Y., Cardenas, M., Siringan, F., et al. (2015). Gradual onset and recovery of the Younger Dryas abrupt climate event in the tropics. *Nat. Commun.* 6, 8061. doi:10.1038/ncomms9061

Pérez-Rodríguez, M., and Biester, H. (2022). Sensitivity of river catchments to discharge-controlled dissolved carbon export: a study of eight catchments in southern Patagonia. *Biogeochemistry* 160 (2), 177–197. doi:10.1007/s10533-022-00947-3

Pérez-Rodríguez, M., Horák-Terra, I., Rodríguez-Lado, L., Aboal, J. R., and Martínez Cortizas, A. (2015). Long-Term (~57 ka) controls on mercury accumulation in the souther hemisphere reconstructed using a peat record from pinheiro mire (minas gerais, Brazil). *Environ. Sci. Technol.* 49 (3), 1356–1364. doi:10.1021/es504826d

Phadke, A. C., Martino, C. D., Cheung, K. F., and Houston, S. H. (2003). Modeling of tropical cyclone winds and waves for emergency management. *Ocean. Eng.* 30, 553–578. doi:10.1016/s0029-8018(02)00033-1

Polvani, L. M., Banerjee, A., and Schmidt, A. (2019). Northern Hemisphere continental winter warming following the 1991 Mt. Pinatubo eruption: reconciling models and observations. *Atmos. Chem. Phys.* 19 (9), 6351–6366. doi:10.5194/acp-19-6351-2019

Power, M. J., Marlon, J., Ortiz, N., Bartlein, P. J., Harrison, S. P., Mayle, F. E., et al. (2008). Changes in fire regimes since the last glacial maximum: an assessment based on a global synthesis and analysis of charcoal data. *Clim. Dyn.* 30 (7–8), 887–907. doi:10.1007/s00382-007-0334-x

Renssen, H., Goosse, H., Roche, D. M., and Seppä, H. (2018). The global hydroclimate response during the Younger Dryas event. *Quat. Sci. Rev.* 193, 84–97. doi:10.1016/j.quascirev.2018.05.033

Ribeiro Guevara, S., Meili, M., Rizzo, A., Daga, R., and Arribére, M. (2010). Sediment records of highly variable mercury inputs to mountain lakes in Patagonia during the past millennium. *Atmos. Chem. Phys.* 10 (7), 3443–3453. doi:10.5194/acp-10-3443-2010

Riddle, B., Fox, J., Mahoney, D. T., Ford, W., Wang, Y. T., Pollock, E., et al. (2022). Considerations on the use of carbon and nitrogen isotopic ratios for sediment fingerprinting. *Sci. Total Environ.* 817 (152640), 152640–152719. doi:10.1016/j.scitotenv.2021.152640

Roulet, M., Lucotte, M., Saint-Aubin, A., Tran, S., Rhéault, I., Farella, N., et al. (1998). The geochemistry of mercury in central Amazonian soils developed on the Alter-do-Chão formation of the lower Tapajós River Valley, Pará state, Brazil. *Sci. Total Environ.* 223, 1–24. doi:10.1016/s0048-9697(98)00265-4

Russell, J. M., Bijaksana, S., Vogel, H., Melles, M., Kallmeyer, J., Ariztegui, D., et al. (2016). The Towuti Drilling Project: paleoenvironments, biological evolution, and geomicrobiology of a tropical Pacific lake. *Sci. Drill.* 21, 29–40. doi:10.5194/sd-21-29-2016

Russell, J. M., Vogel, H., Bijaksana, S., Melles, M., Deino, A., Hafidz, A., et al. (2020). The late quaternary tectonic, biogeochemical, and environmental evolution of ferruginous Lake Towuti, Indonesia. *Palaeogeogr. Palaeoclimatol. Palaeoecol.* 556, 109905. doi:10.1016/j.palaeo.2020.109905

Russell, J. M., Vogel, H., Konecky, B. L., King, J. W., Huang, Y., Melles, M., et al. (2014). Glacial forcing of central Indonesian hydroclimate since 60,000 y B.P. *PNAS* 111 (14), 5100–5105. doi:10.1073/pnas.1402373111

Salisbury, M. J., Patton, J. R., Kent, A. J., Goldfinger, C., Djadjadihardja, Y., and Hanifa, U. (2012). Deep-sea ash layers reveal evidence for large, late Pleistocene and Holocene explosive activity from Sumatra, Indonesia. *J. Volcanol. Geotherm. Res.* 231 (232), 61–71. doi:10.1016/j.jvolgeores.2012.03.007

Schneider, L., Cooke, C. A., Stansell, N. D., and Haberle, S. G. (2020). Effects of climate variability on mercury deposition during the Older Dryas and Younger Dryas in the Venezuelan Andes. *J. Paleolimnol.* 63 (3), 211–224. doi:10.1007/s10933-020-00111-7

Schneider, L., Fisher, J. A., Diéguez, M. C., Fostier, A. H., Guimaraes, J. R. D., Leaner, J. J., et al. (2023). A synthesis of mercury research in the Southern Hemisphere, part 1: natural processes. *Ambio* 52, 897–917. doi:10.1007/s13280-023-01832-5

Schütze, M., Gatz, P., Gilfedder, B., and Biester, H. (2021). Why productive lakes are larger mercury sedimentary sinks than oligotrophic brown water lakes. *Limnol. Oceanogr.* 66 (4), 1316–1332. doi:10.1002/lno.11684

Setyaningsih, C. A., Biagioni, S., Saad, A., Achnopha, Y., Sabiham, S., and Behling, H. (2018). The effect of volcanism on submontane rainforest vegetation composition: paleoecological evidence from Danau Njalau, Sumatra (Indonesia). *Holocene* 28 (2), 293–307. doi:10.1177/0959683617721329

Slemr, F., and Scheel, H. E. (1998). Trends in atmospheric mercury concentrations at the summit of the Wank mountain, Southern Germany. *Atmos. Environ.* 32 (5), 845–853. doi:10.1016/S1352-2310(97)00131-3

Smithsonian Institution (2020). *Global volcanism program*. Washington: National Museum of Natural History. doi:10.5860/choice.45-6183

Stevenson, J., and Haberle, S. G. (2005). Palaeoworks Technical Papers 5: macro Charcoal Analysis: a Modified Technique Used by the Department of Archaeology and Natural History. Technical Papers.

Swain, E. B., Engstrom, D. R., Brigham, M. E., Henning, T. A., and Brezonik, P. L. (1992). Increasing rates of atmospheric mercury deposition in midcontinental North America. *Science* 257 (5071), 784–787. doi:10.1126/science.257.5071.784

Thomas, Z. A., Mooney, S., Cadd, H., Baker, A., Turney, C., Schneider, L., et al. (2022). Late Holocene climate anomaly concurrent with fire activity and ecosystem shifts in the eastern Australian Highlands. *Sci. Total Environ.* 802, 149542. doi:10.1016/j.scitotenv.2021.149542

Turu, V., Carrasco, R. M., López-Sáez, J. A., Pontevedra-Pombal, X., Pedraza, J., Luelmo-Lautenschlaeger, R., et al. (2021). Palaeoenvironmental changes in the Iberian central system during the Late-glacial and Holocene as inferred from geochemical data: A case study of the Navamuño depression in western Spain. *Catena* 207, 105689. doi:10.1016/j.catena.2021.105689

Van Den Bergh, G. D., Li, B., Brumm, A., Grün, R., Yurnaldi, D., Moore, M. W., et al. (2016). Earliest hominin occupation of Sulawesi, Indonesia. *Nature* 529 (7585), 208–211. doi:10.1038/nature16448

Van der Ent, A., Baker, A., van Balgooy, M., and Tjoa, A. (2013). Ultramafic nickel laterites in Indonesia (Sulawesi, Halmahera): mining, nickel hyperaccumulators and opportunities for phytomining. *J. Geochem. Explor.* 128, 72–79. doi:10.1016/j.gexplo.2013.01.009

Walsh, R. P. D., and Lawler, D. M. (1981). Rainfall seasonality: description, spatial patterns and change through time. *Weather* 36 (7), 201–208. doi:10.1002/j.1477-8696.1981.tb05400.x

Wang, F., Qian, N., and Zhan, Y. (1995). *Pollen flora of China*. Beijin, China: Science China Press.

Wang, Q., Li, Y., and Wang, Y. (2011). Optimizing the weight loss-on-ignition methodology to quantify organic and carbonate carbon of sediments from diverse sources. *Environ. Monit. Assess.* 174, 241–257. doi:10.1007/s10661-010-1454-z

Wang, X., Bao, Z., Lin, C. J., Yuan, W., and Feng, X. (2016). Assessment of Global Mercury Deposition through Litterfall. *Environ. Sci. Technol.* 50 (16), 8548–8557. doi:10.1021/acs.est.5b06351

Whitten, A. J., Mustafa, M., and Henderson, G. S. (1988). *The ecology of Sulawesi*. Indonesia: Gadjah Mada University Press.

Wicaksono, S. A., Russell, J. M., and Bijaksana, S. (2015). Compound-specific carbon isotope records of vegetation and hydrologic change in central Sulawesi, Indonesia, since 53,000 yr BP. *Palaeogeogr. Palaeoclimatol. Palaeoecol.* 430, 47–56. doi:10.1016/j.palaeo.2015.04.016

Wilcken, K. M., Hotchkis, M., Levchenko, V., Fink, D., Hauser, T., and Kitchen, R. (2015). From carbon to actinides: A new universal 1MV accelerator mass spectrometer at ANSTO. *Nucl. Instrum. Methods Phys. Res. Sect. B Beam Interact. Mater. Atoms* 361, 133–138. doi:10.1016/j.nimb.2015.04.054

Yagasaki, Y., Mulder, J., and Okazaki, M. (2006). The role of soil organic matter and short-range ordered aluminosilicates in controlling the activity of aluminum in soil solutions of volcanic ash soils. *Geoderma* 137 (1–2), 40–57. doi:10.1016/j.geoderma.2006.07.001

Zhang, H., Holmes, C., and Wu, S. (2016). Impacts of changes in climate, land use and land cover on atmospheric mercury. *Atmos. Environ.* 141, 230–244. doi:10.1016/j.atmosenv.2016.06.056

Zhang, H., Nizzetto, L., Feng, X., Borgå, K., Sommar, J., Fu, X., et al. (2019). Assessing Air-surface exchange and fate of mercury in a subtropical forest using a novel passive exchange-meter device. *Environ. Sci. Technol.* 53 (9), 4869–4879. doi:10.1021/acs.est.8b06343

Zheng, W., Obrist, D., Weis, D., and Bergquist, B. A. (2016). Mercury isotope compositions across North American forests: mercury Isotopes Across U.S. Forests. *Glob. Biogeochem. cycles* 30 (10), 1475–1492. doi:10.1002/2015GB005323

Zhu, W., Lin, C. J., Wang, X., Sommar, J., Fu, X., and Feng, X. (2016). Global observations and modeling of atmosphere–surface exchange of elemental mercury: a critical review. *Atmos. Chem. Phys.* 16 (7), 4451–4480. doi:10.5194/acp-16-4451-2016

Frontiers in
Environmental Chemistry

Explores chemical technologies and tools to prevent and treat pollutants

Investigates the analysis, prevention, treatment and control of anthropogenic and natural pollutants across all environmental matrices - air, water, soil, and sediment - using cutting-edge chemical technologies and tools.

Discover the latest Research Topics

See more →

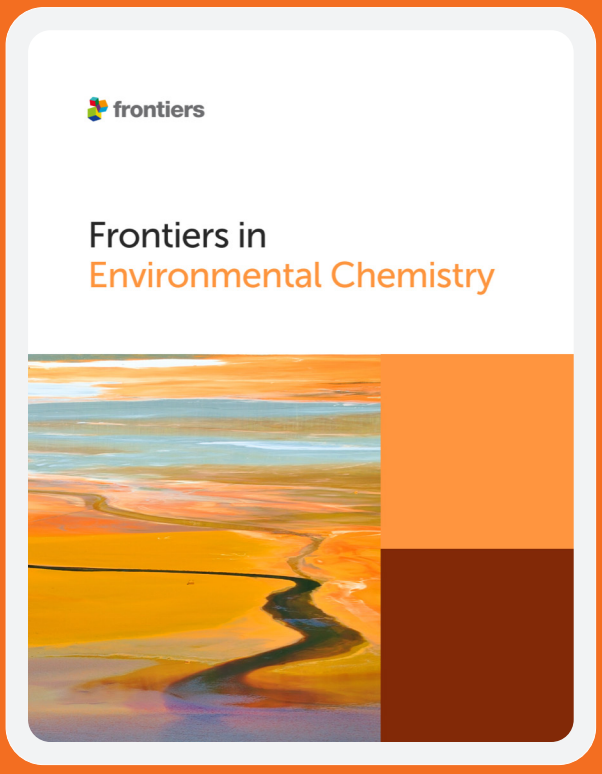

Frontiers

Avenue du Tribunal-Fédéral 34
1005 Lausanne, Switzerland
frontiersin.org

Contact us

+41 (0)21 510 17 00
frontiersin.org/about/contact